MARTIN MARIETTA ENERGY SYSTEMS LIBRARIES

3 4456 0289171 6

ORNL/TM-10838

ornl

OAK RIDGE
NATIONAL
LABORATORY

MARTIN MARIETTA

OAK RIDGE NATIONAL LABORATORY
CENTRAL RESEARCH LIBRARY
CIRCULATION SECTION
4500N ROOM 175
LIBRARY LOAN COPY
DO NOT TRANSFER TO ANOTHER PERSON
If you wish someone else to see this report, send in name with report and the library will arrange a loan.

Ceramic Technology for Advanced Heat Engines Project Semiannual Progress Report for October 1987 Through March 1988

Prepared for
U.S. Department of Energy
Assistant Secretary for
Conservation and Renewable Energy
Office of Transportation Systems
Advanced Materials Development Program

CERAMIC TECHNOLOGY FOR
ADVANCED HEAT ENGINES

CERAMIC TECHNOLOGY PROJECT
DOE/ORNL

OPERATED BY
MARTIN MARIETTA ENERGY SYSTEMS, INC.
FOR THE UNITED STATES
DEPARTMENT OF ENERGY

Printed in the United States of America. Available from
National Technical Information Service
U.S. Department of Commerce
5285 Port Royal Road, Springfield, Virginia 22161
NTIS price codes: Printed Copy: A20; Microfiche: A01

This report was prepared as an account of work sponsored by an agency of the United States Government. Neither the United States Government nor any agency thereof, nor any of their employees, makes any warranty, express or implied, or assumes any legal liability or responsibility for the accuracy, completeness, or usefulness of any information, apparatus, product, or process disclosed, or represents that its use would not infringe privately owned rights. Reference herein to any specific commercial product, process, or service by trade name, trademark, manufacturer, or otherwise, does not necessarily constitute or imply its endorsement, recommendation, or favoring by the United States Government or any agency thereof. The views and opinions of authors expressed herein do not necessarily state or reflect those of the United States Government or any agency thereof.

ORNL/TM-10838

Metals and Ceramics Division

CERAMIC TECHNOLOGY FOR ADVANCED HEAT ENGINES PROJECT SEMIANNUAL PROGRESS REPORT FOR OCTOBER 1987 THROUGH MARCH 1988

D. R. Johnson
Project Manager

Date Published: December 1988

NOTICE: This document contains information of a preliminary nature. It is subject to revision or correction and therefore does not represent a final report.

Prepared for
U.S. Department of Energy
Assistant Secretary for Conservation and Renewable Energy
Office of Transportation Systems
Advanced Materials Development Program
EE 04 00 00 0

Prepared by the
OAK RIDGE NATIONAL LABORATORY
Oak Ridge, Tennessee 37831
operated by
MARTIN MARIETTA ENERGY SYSTEMS, INC.
for the
U.S. DEPARTMENT OF ENERGY
under Contract DE-AC05-84OR21400

MARTIN MARIETTA ENERGY SYSTEMS LIBRARIES

3 4456 0289171 6

REPORTS PREVIOUSLY ISSUED

ORNL/TM-9325	Period March 1983–September 1983
ORNL/TM-9466	Period October 1983–March 1984
ORNL/TM-9497	Period April 1984–September 1984
ORNL/TM-9673	Period October 1984–March 1985
ORNL/TM-9947	Period April 1985–September 1985
ORNL/TM-10079	Period October 1985–March 1986
ORNL/TM-10308	Period April 1986–September 1986
ORNL/TM-10469	Period October 1986–March 1987
ORNL/TM-10705	Period April 1987–September 1987

CONTENTS

SUMMARY 1

0.0 PROJECT MANAGEMENT AND COORDINATION 3

1.0 MATERIALS AND PROCESSING 5

INTRODUCTION 5

1.1 MONOLITHICS 7

1.1.1 Silicon Carbide 7

Synthesis of High-Purity Sinterable Silicon Carbide Powders (SOHIO) 7

Turbomilling of SiC Whiskers and SiC Whisker/Alumina Composites (University of Southern Illinois) 10

1.1.2 Silicon Nitride 12

Sintering of Silicon Nitride (AMTL) 12

Synthesis of High Purity Sinterable Si_3N_4 Powders (Ford) 14

Microwave Processing of Silicon Nitride (ORNL) . . . 22

1.1.4 Processing of Monolithics 25

Improved Processing (ORNL) 25

1.2 CERAMIC COMPOSITES 27

1.2.2 Silicon Nitride Matrix 27

Silicon Nitride-Metal Carbide Composites (GTE) . . . 27

Development of Toughened Si_3N_4 Composites by Glass Encapsulated Hot Isostatic Pressure (Norton) 39

1.2.3 Oxide Matrix 60

Dispersion-Toughened Oxide Composites (ORNL) 60

Processing of Improved Transformation-Toughened Ceramics (Norton) 67

Processing and Characterization of Transformation-Toughened Ceramics with Strength Retention to Elevated Temperatures (Ceramatec) 75

1.2.4 Silicate Matrix 86

Low Expansion Ceramics for Diesel Engine Applications (VPI) 86

1.3 THERMAL AND WEAR COATINGS 117

1.3.1 ZrO_2 Base Coatings 117

Development of Adherent Ceramic Coatings to Reduce Contact Stress Damage of Ceramics (GTE Laboratories) 117

Advanced Coating Technology (ORNL) 127

Wear-Resistant Coatings (Caterpillar) 131

Development of Wear-Resistant Ceramic Coatings for Diesel Engine Components (Cummins) 135

1.4 JOINING 157

1.4.1 Ceramic-Metal Joints 157

Joining of Ceramics for Heat Engine Applications (ORNL) 157

Analytical and Experimental Evaluation of Joining Silicon Nitride to Metal and Silicon Carbide to Metal for Advanced Heat Engine Applications (GTE) 180

Analytical and Experimental Evaluation of Joining Ceramic Oxides to Ceramic Oxides and Ceramic Oxides to Metal for Advanced Heat Engine Applications (BCL) 214

Analytical and Experimental Evaluation of Joining Silicon Carbide to Silicon Carbide and Silicon Nitride to Silicon Nitride for Advanced Heat Engine Applications (Norton) 224

2.0 MATERIALS DESIGN METHODOLOGY 241

INTRODUCTION 241

2.1 MODELING 243

2.1.1 Modeling 243

Microstructural Modeling of Cracks (UT) 243

2.2 CONTACT INTERFACES 249

2.2.2 Dynamic Interfaces 249

Studies of Dynamic Contact of Ceramics and Alloys for Advanced Heat Engines (Battelle) 249

2.3 NEW CONCEPTS 253

Advanced Statistical Concepts of Fracture in Brittle Materials (GE) 253

3.0 DATA BASE AND LIFE PREDICTION 261

INTRODUCTION 261

3.1 STRUCTURAL QUALIFICATION 263

Failure Analysis (NBS) 263

Physical Properties of Structural Ceramics (ORNL) . . 269

Effect of Translucence of Engineering Ceramics on Heat Transfer in Diesel Engines (ITI) 281

3.2 TIME-DEPENDENT BEHAVIOR 289

Characterization of Advanced Transformation Toughened Zirconias (AMTL) 289

Fracture Behavior of Toughened Ceramics (ORNL) . . . 290

Cyclic Fatigue of Toughened Ceramics (ORNL) 294

Rotor Data Base Generation (ORNL) 302

3.3 ENVIRONMENTAL EFFECTS 307

Environmental Effects in Toughened Ceramics (University of Dayton) 307

3.4 FRACTURE MECHANICS 345

Improved Methods for Measuring the Fracture Resistance of Structural Ceramics (University of Washington) 345

Testing and Evaluation of Advanced Ceramics at High Temperature in Uniaxial Tension (North Carolina A&T State University) 347

Standard Tensile Test Development (NBS) 361

3.5 NONDESTRUCTIVE EVALUATION DEVELOPMENT 373

Nondestructive Characterization (ORNL) 373

Computed Tomography (ANL) 381

Nuclear Magnetic Resonance Imaging (ANL) 389

Powder Characterization (ORNL) 398

4.0 TECHNOLOGY TRANSFER 401

Technology Transfer (ORNL) 401

IEA Annex II Management (ORNL) 402

Standard Reference Materials (NBS) 410

Ceramic Characterization (NBS) 415

CERAMIC TECHNOLOGY FOR ADVANCED HEAT ENGINES PROJECT SEMIANNUAL PROGRESS REPORT FOR OCTOBER 1987 THROUGH MARCH 1988

SUMMARY

The Ceramic Technology For Advanced Heat Engines Project was developed by the Department of Energy's Office of Transportation Systems (OTS) in Conservation and Renewable Energy. This project, part of the OTS's Advanced Materials Development Program, was developed to meet the ceramic technology requirements of the OTS's automotive technology programs.

Significant accomplishments in fabricating ceramic components for the Department of Energy (DOE), National Aeronautics and Space Administration (NASA), and Department of Defense (DOD) advanced heat engine programs have provided evidence that the operation of ceramic parts in high-temperature engine environments is feasible. However, these programs have also demonstrated that additional research is needed in materials and processing development, design methodology, and data base and life prediction before industry will have a sufficient technology base from which to produce reliable cost-effective ceramic engine components commercially.

An assessment of needs was completed, and a five-year project plan was developed with extensive input from private industry. The objective of the project is to develop the industrial technology base required for reliable ceramics for application in advanced automotive heat engines. The project approach includes determining the mechanisms controlling reliability, improving processes for fabricating existing ceramics, developing new materials with increased reliability, and testing these materials in simulated engine environments to confirm reliability. Although this is a generic materials project, the focus is on the structural ceramics for advanced gas turbine and diesel engines, ceramic bearings and attachments, and ceramic coatings for thermal barrier and wear applications in these engines. This advanced materials technology is being developed in parallel and close coordination with the ongoing DOE and industry proof-of-concept engine development programs. To facilitate the rapid transfer of this technology to U.S. industry, the major portion of the work is being done in the ceramic industry, with technological support from government laboratories, other industrial laboratories, and universities.

This project is managed by ORNL for the Office of Transportation Systems, Heat Engine Propulsion Division, and is closely coordinated with complementary ceramics tasks funded by other DOE offices, NASA, DOD, and industry. A joint DOE and NASA technical plan has been established, with DOE focus on automotive applications and NASA focus on aerospace applications. A common work breakdown structure (WBS) was developed to facilitate coordination. The work described in this report is organized according to the following WBS project elements:

0.0 Management and Coordination

1.0 Materials and Processing

- 1.1 Monolithics
- 1.2 Ceramic Composites
- 1.3 Thermal and Wear Coatings
- 1.4 Joining

2.0 Materials Design Methodology

- 2.1 Modeling
- 2.2 Contact Interfaces
- 2.3 New Concepts

3.0 Data Base and Life Prediction

- 3.1 Structural Qualification
- 3.2 Time-Dependent Behavior
- 3.3 Environmental Effects
- 3.4 Fracture Mechanics
- 3.5 NDE Development

4.0 Technology Transfer

This report includes contributions from all currently active project participants. The contributions are arranged according to the work breakdown structure outline.

0.0 PROJECT MANAGEMENT AND COORDINATION

D. R. Johnson
Oak Ridge National Laboratory

Objective/scope

This task includes the technical management of the project in accordance with the project plans and management plan approved by the Department of Energy (DOE) Oak Ridge Operations Office (ORO) and the Office of Transportation Systems. This task includes preparation of annual field task proposals, initiation and management of subcontracts and interagency agreements, and management of ORNL technical tasks. Monthly management reports and bimonthly reports are provided to DOE; highlights and semiannual technical reports are provided to DOE and program participants. In addition, the program is coordinated with interfacing programs sponsored by other DOE offices and federal agencies, including the National Aeronautics and Space Administration (NASA) and the Department of Defense (DOD). This coordination is accomplished by participation in bimonthly DOE and NASA joint management meetings, annual interagency heat engine ceramics coordination meetings, DOE contractor coordination meetings, and DOE Energy Materials Coordinating Committee (EMaCC) meetings, as well as special coordination meetings.

1.0 MATERIALS AND PROCESSING

INTRODUCTION

This portion of the project is identified as project element 1.0 within the work breakdown structure (WBS). It contains four subelements: (1) Monolithics, (2) Ceramic Composites, (3) Thermal and Wear Coatings, and (4) Joining. Ceramic research conducted within the Monolithics subelement currently includes work activities on green state ceramic fabrication, characterization, and densification and on structural, mechanical, and physical properties of these ceramics. Research conducted within the Ceramic Composites subelement currently includes silicon carbide and oxide-based composites, which, in addition to the work activities cited for Monolithics, include fiber synthesis and characterization. Research conducted in the Thermal and Wear Coatings subelement is currently limited to oxide-base coatings and involves coating synthesis, characterization, and determination of the mechanical and physical properties of the coatings. Research conducted in the Joining subelement currently includes studies of processes to produce strong stable joints between zirconia ceramics and iron-base alloys.

A major objective of the research in the Materials and Processing project element is to systematically advance the understanding of the relationships between ceramic raw materials such as powders and reactant gases, the processing variables involved in producing the ceramic materials, and the resultant microstructures and physical and mechanical properties of the ceramic materials. Success in meeting this objective will provide U.S. companies with new or improved ways for producing economical highly reliable ceramic components for advanced heat engines.

1.1 MONOLITHICS

1.1.1 Silicon Carbide

Synthesis of High-Purity Sinterable Silicon Carbide (SiC) Powders
H. A. Lawler and B. L. Mehosky [Standard Oil Engineered Materials Company (Carborundum)]

Objective/Scope

The objective of this program is to develop a volume scaleable process to produce high purity, high surface area sinterable silicon carbide powder.

The program is organized in two phases. Phase I, completed in July, 1986, included the following elements:

- Verify the technical feasibility of the gas phase synthesis route.
- Identify the best silicon feedstock on the basis of performance and cost.
- Optimize the production process at the bench scale.
- Fully characterize the powders produced and compare with commercially available alternatives.
- Develop a theoretical model to assist in understanding the synthesis process, optimization of operating conditions and scale-up.

Phase II, authorized in August, 1986, will scale the process to five to ten times the bench scale quantities in order to perform confirmatory experiments, produce process flowsheets and to perform economic analysis.

Technical Progress

Task 8. Process Scale-up

During this reporting period, the Phase II reactor system could not be consistently started up and operated under controlled conditions. The initial problem centered on the fact that the plasma torch would not remain in operation when the high frequency starter signal was discontinued.

Originally, this was attributed to a possible conflict between the power supply control circuit and the supervisory control circuit or an inductive/impedance interaction between the plasma torch and the power supply.

In order to identify the source of the problem, a testing matrix was developed using the old Phase I torch and power supply and the new Phase II torch, power supply, reactor, etc. Initially, the Phase I unit was re-assembled and successfully operated.

Upon instrumenting the Phase II unit, it was discovered that the control signal was not providing a linear output to the saturable core reactors and that at less than 30% of input signal range, there was no current signal output at all.

Since all of the previous start-ups were at 20-30% of input signal range, it became obvious that there was no way that the main power supply had even turned on. Confirmation of this was attempted by installing a 0-10A D.C. power supply and ammeter in the control circuit.

With the Phase I torch mounted in the Phase II system, an attempt to start the torch resulted in a starter and cooling water failures. The Phase I power supply was then connected to the new system through a set of cables with no better results.

Inspection of the torch uncovered appreciable damage to the internals -- probably caused on the initial start-up attempts.

Further attempts with modified starting procedures resulted in a torch start, however, control current fluctuations were noted after 5 minutes. The system could not be re-started, and again, torch erosion was evident.

A 500V 400A variable resistance load was rented locally and each of the secondary transformers were individually tested. All exhibited stable operation.

Additions and revisions to the power supply system approved by Walker Power were made in an attempt to identify and stabilize the power supply control system. These included a resistor wired in series with the saturable reactors and manual control system along with multipoint recorders and a High Speed Data Acquisition System.

The Phase II torch was again mounted and tested at which time it ran for twenty minutes while wave forms were collected. Torch damage occurred and from subsequent two-second runs it was concluded that torch erosion occurred at start-up during unstable operation. Very high current transients of up to 4500 amp at 60 volts over a period of 700 milliseconds were identified.

Although revisions to the controller were made as recommended by the vendor, the current surge was not eliminated. A decision was made to operate through this problem and commence making powder.

Nitrogen operation was therefore attempted, however, the torch would not light off at 480V, 720V or 960V. Further efforts to operate with the Walker Power supply were then abandoned and the Phase I Miller power supply was reinstalled into the system. The available 65KW is considered adequate and represents a 3-1/2 to 4x scale-up over the Phase I operation.

The system was repeatedly started on argon and then switched to nitrogen as a qualifying gas prior to switching to hydrogen. The last torch build successfully completed fifteen start-ups. Additional start-ups were made to better define the argon-to-nitrogen transition operating window since during this transition the arc is very unstable.

At the same time, the methyl trichlorosilane system was hydrostatically tested. Although the lines were flushed with air followed by trichloroethane, a number of plugs were identified when the system was charged with methyl trichlorosilane. These plugged lines are presently being cleaned.

Status of Milestones

The milestone schedule below reflects a contract extension from December 31, 1987 to June 30, 1988 as approved in Supplemental Agreement No. 7.

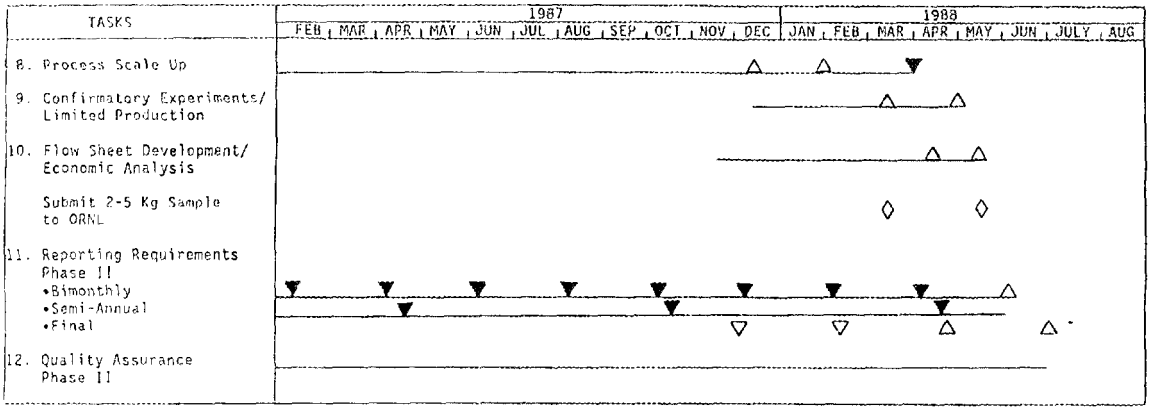

MILESTONE CHART

Publications

None during this reporting period.

Turbomilling of SiC Whiskers and SiC Whisker/Alumina Composites

D. E. Wittmer (Associate Professor, SIU-C, Carbondale, IL)

Objective/scope

The purpose of this work is to investigate the turbomilling process as a means of improved processing for SiC whisker-ceramic matrix composites, and to design and fabricate prototype turbomilling units.

Technical progress

During the previous reporting period the initial subcontract involving a feasibility study to determine the effectiveness of using the turbomilling concept for processing SiC whisker/alumina matrix composites was completed. It was demonstrated in these feasibility trials that the strength and fracture toughness could be increased due to improved dispersion, deagglomeration and homogenization. The milestone for this subcontract (the feasibility report) was completed ahead of schedule.

On the basis of this success, an additional award was requested to continue turbomilling investigations. The supplemental agreement requested in September (FY 87) was finalized in January (FY 88).

The supplemental agreement contains three tasks:

Task 1. Design, fabrication and testing of prototype turbomills.

Task 2. Dispersion and homogenization of SiC whisker/alumina matrix composites.

Task 3. Dispersion and homogenization of SiC whisker/silicon nitride matrix composites.

In Task 1 developmental turbomills have been designed and are presently being fabricated to allow the use of various sized rotor, shaft and body assemblies which shall make it possible to make smaller batches and determine the effects of upscaling on the processing parameters. Additional design considerations will allow for real-time data acquisition of the turbomill operating parameters.

During Task 2 the small volume (approximately 1 liter) turbomill produced in Task 1 will be utilized to determine the solids loading limit for SiC whiskers in water alone. This will be followed by the processing of several batches of SiC whisker/alumina matrix mixes to determine the relationship between solids loading, whisker volume, and turbomilling parameters on dispersion and homogenization. The results of these trials will be monitored through visual inspection with optical and scanning electron microscopes and by fracture results on hot-pressed specimens.

For Task 3 the matrix material will be silicon nitride and similar experiments to those of Task 2 will be conducted. Initially a 20 vol. % whisker loading will be investigated, followed by incremental

increases in whisker loading. The silicon nitride will be high purity UBE powder with alumina and yttria sintering aids. Again, microscopic and fracture results will be used as a means of measuring the effectiveness of turbomilling for dispersion and homogenization.

To date the design/machine drawings have been 80% completed for 4 in., 6 in., and 8 in. diameter turbomills and the work orders for the fabrication of the prototype turbomilling units have been submitted. The metal machine work for the turbomill base units is proceeding on schedule with the recent receipt of a new welding machine in the university machine shop. Most of the construction materials, motors and controllers, transducers and data acquisition electronics have been received. The balance of the materials and electronics are expected to be delivered within the next two months.

Status of milestones

Design, fabrication and testing of prototype turbomills.	July 1988
Dispersion and homogenization of SiC whisker/ alumina matrix composites.	November 1988
Dispersion and homogenization of SiC whisker/ silicon nitride matrix composites.	November 1988

Publications

D.E. Wittmer, "Improved Dispersion Technique for Ceramic Whisker-Ceramic Matrix Composites", Proceedings of the 12 Annual Conference on Composites and Advanced Ceramics, Cocoa Beach, FL, Jan. 20-22, 1988 (in press).

1.1.2 Silicon Nitride

Sintering of Silicon Nitride
G. E. Gazza (Army Materials Technology Laboratory)

Objective/scope

The program is concentrating on sintering compositions in the Si_3N_4-$Y_2O_3SiO_2$ system using a two-step sintering method where the N_2 gas pressure is raised to 7-8 MPa during the second step of the process. During the sintering, dissociation reactions are suppressed by the use of high N_2 pressure and cover powder of suitable composition over the specimen. Variables in the program include the sintering process parameters, source of starting powders, milling media and time, and specimen composition. Resultant properties determined are room temperature modulus of rupture, high temperature stress-rupture, oxidation resistance, and fracture toughness. Successful densification of selected compositions with suitable properties will lead to densification of injection molded or slip cast components for engine testing.

Technical progress

Sintering

The composition selected for further scale-up and extensive evaluation was the 85.8m/o Si_3N_4-4.73m/o Y_2O_3-9.47m/o SiO_2 composition designated as composition 39. It was also observed that the addition of 1.0m/o Mo_2C promotes densification of this composition. Wet milling of powder components is accomplished in RBSN milling jars using hot isostatically pressed Si_3N_4 balls. Milling time varies from 100 to 300 hours. Powders are dried, screened and pressed into cold compacts as previously reported. Starting Si_3N_4 powder used is Toyo-Soda TS-7. A recently developed TS-10 powder has been substituted in some of the sintering studies. Sintering is accomplished using a two-step procedure where temperatures of 1925-1960C are used with N_2 gas pressures of 2.0/8.0 MPa for times of 60/30 minutes, respectively. Sintered density of these specimens are determined to be 3.30+0.01 g/cc.

Stress-rupture testing

Stress-rupture testing was completed during this period. Long term stress-rupture tests were conducted at temperatures of 1200-1250C under 300 MPa stress for times up to 750 hours. STSR testing was also performed at temperatures starting at 700C. Of the composition 39 specimens tested under the various stress-rupture conditions, 15 of 16 survived with 4 surviving the 750 hour test. The surfaces of the specimens showed a thin, coherent oxide layer with residual machining marks still clearly visible. A residual permanent strain of 0.1.0.2% was measured for specimens surviving 750 hours at 1250C under 300 MPa stress.

Room temperature MOR tests were conducted with stress-rupture survivors to determine retained strength. A dozen values were obtained for specimens that had been stress-rupture tested at 1200C and 1250C for between 300-500 hours under 300 MPa stress. Values usually ranged from 800-900 MPa (830 MPa mean) with one value of 1030 MPa recorded.

The increase in MOR values over those determined for specimens not subjected to stress-rupture testing (700-780 MPa) may be associated with residual stress in the specimens.

Room-temperature modulus of rupture (MOR)

Room temperature MOR values were determined for machined specimens in the as-sintered condition, and for stress-rupture survivors to determine retained strength. From data obtained thusfar, MOR values for specimens of compositions No. 39 containing 1m/o Mo_2C and sintered at 1850-1900C fell in the 475-575 MPa range while those of the same composition sintered at 1925-1960C fell in the 700-780 MPa range. Compositions containing 1m/o Mo_2C additions had the highest strengths with values falling off to the 550-625 MPa range as Mo_2C levels were reduced to the 0.35-0.75m/o range.

Status of milestones

(a) The composition designated as No. 39 has been selected for scale-up for extensive generation of property data. The existance of 1-2um particles resulting from incorporation of Mo_2C in the starting material have been tentatively identified as $MoSi_3$ and $MoSi_2$.

(b) Stress-rupture tests have been completed. Composition 39 bars have survived 750 hours under 300 MPa stress at 1250C.

(c) Numerous fractographs of MOR specimens are being examined to determine relative size and morphology of Si_3N_4 grains and minor phases. Fracture origins are being determined. Polished and etched surfaces are being examined for grain size measurements and for compositional analysis of minor phases.

Future plans

Continue fractographic analysis of as-sintered and stress-rupture specimens. Continue microstructural analysis of polished and etched surfaces.

Further explore the effect of post heat treatments on composition, phase development, and resultant properties.

Generate extensive amounts of mechanical property data for analysis of process reproducibility.

Preliminary fabrication and densification of some complex shapes.

Synthesis of High Purity Sinterable Si_3N_4 Powders -- G. M. Crosbie, J. M. Nicholson, R. L. Predmesky, and E. D. Stiles (Research Staff, Ford Motor Company, Dearborn, Michigan)

Objective/scope

The goal of this task is to achieve major improvements in the quantitative understanding of how to produce sinterable Si_3N_4 powders having highly controlled particle size, shape, surface area, impurity content and phase content. Through the availability of improved powders, new ceramic materials are expected to be developed to provide reliable and cost-effective structural ceramics for application in advanced heat engines.

Of interest to the present powder needs is a silicon nitride powder of high cation and anion purity without carbon residue.

The process study is directed towards a modification of the low temperature reaction of $SiCl_4$ with liquid NH_3 which is characterized 1) by absence of organics (a source of carbon contamination), 2) by pressurization (for improved by-product extraction efficiency), and 3) by use of a non-reactive gas diluent for $SiCl_4$ (for reaction exotherm control).

In the "further development" phase begun October 1987, our goal is to test for unique properties of the ceramics sintered from the low carbon powders, before committing to a pilot plant of the 110 L scale designed. In view of powder quantities needed to allow tests of the ceramics, the major task is to design and implement a scaled-up version of the silicon nitride synthesis processing equipment to produce greater amounts of powders with high cation and anion purity and low carbon residue.

Technical progress

Introduction

Silicon nitride based ceramics are often considered to represent the toughest of the high-temperature (above $1000^{o}C$) monolithic ceramics intended for advanced heat engine use. Also, due to a desirable combination of lower temperature properties (wear resistance, low density, high hardness, and toughness), the nitride ceramics are already finding commercial applications in certain passenger vehicles.

Ceramic reliability and cost depend on powder qualities and subsequent processing. Because powders can limit the capability to achieve unique sintered properties and to fabricate complex shapes, the availability of appropriate powders is critical to advanced ceramics research. In the case of silicon nitride ceramics, the powder purity is especially important, since a low solubility in silicon nitride for many impurities leads to high concentrations of those impurities in grain boundary phases. Also, carbon residues (which are found in some otherwise high purity powders) are considered to be detrimental to second phase oxynitride development, thermal stability, and mechanical properties.

Previous work

The primary points of reference for the previous process work are the 1986 and 1987 Automotive Technology Development Contractors' Coordination Meeting proceedings papers[1,2] and the previous semiannual report.[3]

In the previous lab demonstration work, we prepared a novel process

flowsheet for preparation of Si_3N_4 with a block flow diagram and a mathematical model of mass and heat balances for the "vapor chloride--liquid ammonia" process. We observed that the cooling from latent heat of vaporization of NH_3 more than offsets the heat of reaction at 0^oC and 75 psig.

Powder characteristics met or were approaching target values. Key results were achieved in the areas of phase and microstructure, and carbon purity. Si_3N_4 powder was produced with phase content, particle size and shape which are close to those characteristics considered desirable for pressureless sinterability. An overpressure sintering to 83% T.D. was obtained.

Specifically, the powder derived by thermal decomposition of an intermediate imide product (from reaction of $SiCl_4$ with liquid NH_3 at 0^oC and 75 psig) was principally alpha silicon nitride (as determined by x-ray diffraction, which has little sensitivity to amorphous phases) with crystallite size of 0.2 to 0.3 µm and primarily equi-axed particle shape.

The process was identified to have features which are important for scale-up. Key features of near-neutral heat balance and liquid-like materials handling were demonstrated.

Also, improvements were achieved in yield, laboratory production rate, cation purity, and alpha/beta ratios.

In the extension period work, we prepared a pilot plant design for the "vapor-chloride - liquid ammonia" process, carried out additional process development including the "liquid chloride - liquid ammonia" direct reaction, campaigned runs to test process stability, carried out sintering tests, and reported on a new analytical method for discriminating amorphous and crystalline phases in silicon nitride powders.

Summary of current period work

In this period, we have installed the pre-pilot plant at 4 L scale, found continued high oxygen contents in powders from the modified 500 mL scale equipment, analyzed the imide intermediate for Si-Cl bonding and found none, extended the baseline sintering and ceramic characterization, begun transient flow modeling of saturator performance at the pre-pilot scale, and extended the economic analysis.

Pre-pilot plant commissioning

In the "further development" phase begun in this period, we have increased reactor volume, taken steps to improve quality of sealing of vessels and piping, and incorporated direct mechanical agitation while under pressure. By this means, we have equipment to produce 100 g lots of powder (by liquid-liquid and vapor-liquid routes) for sintering tests and characterization of the sintered materials.

Through joint work with an engineering firm, the 4 L scale skid-mounted imide reactor system was installed onto a dynamometer test cell bed plate and pressure tested to 225 psig (1.65 MPa absolute) with nitrogen in March 1988.

The pressure test demonstrates basic performance of the system and can be considered to be a demonstration of commissioning of the apparatus. Auxiliary items are being installed and tested to allow its safe use in powder preparation. Therefore, the milestone of commissioning in March is met, but with qualification that powder has not been made with it yet.

In the design of this system, the reactor working volume is increased to one gallon (4 L) and a pressure-sealed mechanical agitator is provided. The piping system is of welded construction with flanged fittings that are mostly of a type to allow simplified helium leak testing. All vessels are jacketed and pressure-rated to 300 psig (2.2 MPa absolute) to permit tests with ammonia remaining liquid to room temperature (to demonstrate reduced refrigeration requirement). The equipment was received with certification plates and corresponding rupture disks for these pressure ratings.

The pre-pilot plant is located in larger quarters in a nearby building at the Research and Engineering Center in Dearborn. The new location is a dynamometer test cell which provides suitable facilities for the pre-pilot scale plant. These facilities include: 1) a high volumetric air flow rate (with up to three air changes per minute), 2) a high ceiling to accommodate the condenser (4 meter height) and other desired lay-out features, 3) adequate floor space to allow access to all sides of the equipment, and 4) an adjacent control room with a large window for monitoring.

In the October-November 1987 period, a major portion of the test cell was cleared. This clearing operation involved dismantling and removing various test rigs, their associated hardware, and certain support equipment. The room air heaters are now operational and new air filters have been installed.

In January 1988, final drawings were accepted from the engineering firm doing the construction. The firm had received the agitated reactor and all the necessary jacketed pressure vessels and had mounted the waste and product tanks on the skid. The agitated reactor vessel stand was reworked to fit on the same mounting.

In the December 1987 - January 1988 period at Ford, the following site preparation work was completed: As part of the clearing of the test cell, overhead tubing and wiring were removed to allow for an open path between the test cell and the control room. In the control room, unnecessary and unused equipment was removed and stored. An analytical balance has been purchased for cell use. Discussions were held to determine what facilities are needed to best meet the required safety-related alterations.

Installation and pressure testing of the skid-mounted system took place in March 1988.

Subsystems tested okay by end of March 1988 (with feature tested): Agitated reactor, bottom valve, product tank, wastage tank, the condenser cooling system, the vessel jacket heating/cooling system. Subsystems in process of installation were the $SiCl_4$ introduction system, temperature readouts, a vacuum pump, and data acquisition connections.

Powder results for upgraded lab apparatus

In lab work which continued at the 500 mL reactor scale, we reported in the August-September 1987 period that the imide synthesis and thermal decomposition systems had been re-built to eliminate 95% of the polymer tubing previously present. Also, a non-alumina decomposition vessel had been installed. These changes are intended to decrease water vapor permeability and oxygen contamination of the powder product. These and subsequent changes were not effective in reducing the Cl and O contamination of the powders produced. The imide intermediate from certain of these runs was further analyzed (next section).

This equipment was to complete two powdermaking runs by the "liquid $SiCl_4$ - liquid NH_3" route. The resulting powder characteristics are shown in Table I.

In the first of the two runs, a quantity of powder was obtained which had two distinct fractions of light and dark appearance. The light fraction was identified by x-ray diffraction (XRD) as NH_4Cl. The dark fraction (#5259-85-2) had a 64/36 ratio of alpha/beta silicon nitride, with a diffracted halo of a non-crystallized species. Because of the small quantity of powder, an attempt to identify the amorphous species by magic angle spinning n.m.r. (MAS-NMR) was unsuccessful.

In the second of the two, 6.9 g of product powder was obtained, with obvious deterioration of portions of the Mo decomposition vessel liner. By XRD, the sample had alpha- and no beta-silicon nitride, some NH_4Cl and Mo compounds (not further identified), and a much flatter amorphous halo. Additional analyses are pending.

Table I. Powder synthesis characterization results (partial)

Powder product -- Characteristic	#5259-85-2	#5259-86-3
X-ray diffraction:		
% alpha/(alpha+beta)	64%	89%
Amorphous background	present	trace
Mo_5Si_3 (JCPDS 34-371)	not detected	minor
NH_4Cl	trace	present
MAS-NMR: status	insuff. qty.	N.A.
Product mass	4.8 g	6.9 g
Si_3N_4-rich mass (analyzed)	<0.5 g	6.9 g

In subsequent lab work continuing at the 500 mL reactor scale, the equipment was used in January 1988 in two powdermaking runs by the "liquid $SiCl_4$ - liquid NH_3" route:

In Run #5289-89, a stainless sampling tee and valve were installed between the reactor and the intermediate product tank in order to collect an imide sample without any exposure to air. Also, a moly endcap liner was omitted from the hot zone of the decomposition vessel in order to reduce Mo contamination.

In this run, after the first of two planned sequences of $SiCl_4$ additions, the injector plugged. Upon transfer out of the reactor, no imide was retained in the sampling tee for characterization of the intermediate product. Approximately, 5.7 g of product was obtained. The (A/(B+A)) ratio was 79%. However, the oxygen content was 18 wt.%.

In Run #5289-90, a 150 psig gas injection was made after each sequence of $SiCl_4$ injections. Also, heat tape was wrapped around the decomposition vessel after transfer to help speed up the boil off of NH_3, and allow sampling from the decomposition tube before heating.

In this case, a total of 3 sequences of $SiCl_4$ additions were made (not the planned two). The 150 psig N_2 gas injections apparently kept the injector clear. However, the run was aborted when the decomposition tube fractured at the last stage of NH_3 boiloff. Apparently, the heat which was applied caused an excess of solids to be carried off and to plug the exit valve. Emphasis was then placed on installation of the new build.

Characterization of the imide intermediate

It has been suggested that characterization of the intermediate product would be useful for a better understanding of the causes of retained chlorine after rinsing. Residual chlorine is known to affect adversely yields and microstructure. In the pre-pilot stage of build in progress, a pressurized and agitated reactor vessel is included which should expedite NH_4Cl extraction. If, however, the chlorine is bound up in the cross-linked imide network, removal may still be slow. We report here first-cut attempts to locate Cl in the cross-linked imide intermediate, using product from the non-agitated 500 mL scale equipment.

In these initial analyses of the intermediate compound, exposure to air was minimized but not eliminated. The imide sample was transferred from a residue in the 500 mL reactor (under a N_2 positive pressure) to a PTFE-stoppered quartz cuvette with less than 10 seconds exposure to ambient.

Analyses of the imide from run 5259-86 were made by Raman, IR, and MAS-NMR at Ford Research in co-operation with W. H. Weber and B. D. Poindexter (Physics); R. O. Carter III and M. Peck (Chemical Analysis); and K. R. Carduner (Chemical Analysis Section), respectively.

No evidence of Si-Cl bonding was observed in this sample by any of these three techniques.

Thus, characterization of the imide intermediate product points to little, if any, Si-Cl bonding, which, in turn, suggests that agitation in the 4 L build will be effective in removing NH_4Cl.

Baseline sintering and ceramic characterization

We have been carrying out a partial factorial designs of experiments to identify key time-temperature (t-T) factors in the pressureless sintering of commercially available silicon nitride powders with our equipment. Samples of 96-97% of theoretical density were prepared by dry-mixing with oxide aids, die-pressing, and subsequent isostatic pressing. All samples reported here are of a nominal composition of 10 wt.% Y_2O_3 and 2.25 wt.% Al_2O_3 and of sintering times of less than or equal to 2 h at 1800°C.

To demonstrate the reproducibility of the sintering process, a subset of the density and phase development data is shown in Table II. All samples in this subset have been sintered with a single (t-T) schedule.

For the three powder mixes and five billets tests, the densities are all within a narrow range. This density range corresponds to a variation of less than 0.25% of the theoretical density (taken to be 3.3 g/cm^3). This consistency of results also extends to the relative proportions of beta- and alpha- silicon nitride. However, the grain boundary (g.b.) phase development is consistent only within a mixed powder batch. Within the batch designated 5162-73-2, the results are consistent in spite of different packing powder lots. But, differences appear between different mixed powder batches in spite of use of the same packing powder lot.

Table II. Density and phase development (reproducibility subset)

Powder Batch	Sintering Run	Billet #	Density g/cm^3	B/(A+B) %	K/(H+K)[1] %
5162-73-	AVR-	5325-73-			g.b. phases
2	171	2-1	3.182	74	100
2	178	2-6	3.173	72	100
2	185	2-8	3.178	73	100
3	187	3-2	3.178	73	22
4	190	4-1	3.173	79	75
4	191	4-2	3.163	74	68

To help understand the differences between powder batches, chemical analyses of Table III were performed. The higher oxygen and lower carbon in batch 5162-73-3 are consistent with the higher oxygen content direction which is expected for a lower %K/(H+K) grain boundary phase proportion in billets from this powder mix.

Table III. Chemical composition of dry milled powder mixtures by Leco method (Note: each datum is the average of two duplicate analyses)

Powder Batch	Carbon wt.%	Oxygen wt.%	Nitrogen wt.%
5162-73-2	0.1615	4.815	34.65
5162-73-3	0.148	4.875	34.9
5162-73-4	not analyzed	not analyzed	not analyzed

To establish routines for mechanical property testing, we have carried out fast fracture modulus of rupture (MOR) tests from room temperature to 1300°C with samples from the baseline sintering. Stress rupture tests in the MOR configuration (at a nominal 60 ksi (414 MPa) stress level) indicate no glassy grain-boundary-phase behavior at 1000°C after more than 350 h exposure. However, at 1200°C, sample bending was observed after 40 h. Patch-type oxidation was seen in 1200°C and 1300°C samples. This oxidation is attributed, at least in part, to the carbon content of the commercial powder used.

In subsequent work, we established the capability to make 6 - 9 bars for mechanical testing in the larger "Ford B" design configuration with slightly less than 100 g quantities of input powder using a new die. (The "Ford B" design has a cross-section 4 mm X 3 mm and inner and outer spans

---

[1] Estimated as follows: $\%K/(H+K) = 100\% \times I\,K_{av} / (I\,H_{av} + I\,K_{av})$, where $I\,H_{av}$ is the average of diffracted intensities at 32.6° and 47.2° (CuK_α radiation) and $I\,K_{av}$ is the average of intensities at 25.35° and 44.7° of two-theta. The values reported here are subject to change as a result of calibration work in progress. Note: "H" designates the compound $Y_{10}(SiO_4)_6N_2$ and "K" designates $YSiO_2N$.

of 20 and 40 mm with minimum bar length of 60 mm.)

To demonstrate the reproducibility of the sintering process with the new die, a subset of the density and phase development data is shown in Table II as run 191. It appears that the new die has little, if any, effect on the density and grain boundary phase development.

In February and March, additional equipment was received for preparation of powder mixtures for dry pressing before sintering. A laboratory spray drier and a freeze drier are included.

A sintering run was made to check utility of a new lot of Y_2O_3. Based upon density, the new lot passed this screening test.

Saturator transient flow modeling

A series of discussions was initiated with L.-F. Chen of the Control Systems Department (Ford Research) to begin to model flow transients for the saturator built for use with the pre-pilot plant build. In previous laboratory demonstration tests of the "vapor $SiCl_4$ - liquid NH_3" process, flow transients have caused clogging when the vapor supersaturates at the reactor entry during operation. It had been suggested by D. K. Hrovat (Control Systems Dept.) that a computer simulation could aid in designing a system to minimize the supersaturation transients.

Mr. Chen proposed the use of a state function approach to model the gas flows in the reactor system for the vapor-liquid process. We have provided him with various system size parameters and steady-state mass balance calculations for use as input to the digital simulation.

Initial modeling results show that supersaturations can readily occur with less than 2 psi (13.8 kPa) step changes in system pressure. The model is currently being used to examine means to adjust system parameters to minimize these transient supersaturations.

Economic analysis

As part of the preparation for licensing discussions, we are adapting and refining previous cost estimates into formats of likely interest to particular companies. Where possible, we are formulating quantitative models for capital and utility costs. We plan, then, to tie these models with process options in the range that is testable for process feasibility with the pre-pilot plant. For example, operation under higher pressure allows less refrigeration but requires thicker pressure vessel walls.

Status of milestones

This two-year follow-on contract was initiated October 1, 1987 for the "Further Development of Synthesis of High-Purity Sinterable Silicon Nitride (Si_3N_4) Powders for Application in Ceramic TEchnology for Advanced Heat Engines Project." Key milestones are the commissioning of scale-up equipment and the modeling of saturator transient performance.

The milestones are on schedule. We met, with qualification, the March 1988 milestone of commissioning the 4 L scale equipment.

Publications

G. M. Crosbie, J. M. Nicholson, R. L. Predmesky, and E. D. Stiles, "Silicon Nitride Powder Synthesis Program," presented at the 25th Automotive Technology Development Contractors' Coordination Meeting, Dearborn, Michigan, Oct. 26-29, 1987. Manuscript submitted for inclusion in the Post-Conference Proceedings to be published in 1988 by the Society of Automotive Engineers, Warrendale, Pennsylvania.

K. R. Carduner, R. O. Carter III, M. E. Milberg, G. M. Crosbie, "Determination of Silicon Nitride Crystallinity and Silicon Phase Composition of Silicon Nitride Powder by ^{29}Si MASNMR," *Analytical Chemistry*, 59 [23] 2794-97 (1987).

G. M. Crosbie, "Synthesis of High Purity Sinterable Si_3N_4 Powders," pp. 17-23 in *Ceramic Technology for Advanced Heat Engines Project Semiannual Report for October 1986 Through March 1987*, ORNL/TM-10469, Oak Ridge National Laboratory, Oak Ridge, Tenn., August 1987.

K. R. Carduner, R. O. Carter III, G. M. Crosbie, M. E. Milberg, T. J. Whalen, L. C. Westwood, E. N. Boulos, and M. F. Best, "Analytical Applications of Solution and Solid State ^{29}Si NMR," presented at the Pittsburgh Conference to be held in New Orleans, February 22-26, 1988.

G. M. Crosbie and R. L. Predmesky, "Method of Making High Purity Silicon Nitride Precursor," U.S. Patent No. 4,732,746, March 22, 1988.

G. M. Crosbie, J. M. Nicholson, R. L. Predmesky, E. D. Stiles, "Pre-Pilot Scale Synthesis of Low-Carbon Si_3N_4," to be presented at the 90th Annual Meeting of the American Ceramic Society, May 1-5, 1988, at Cincinnati, Ohio.

References

1. G. M. Crosbie, "Silicon Nitride Powder Synthesis," pp.255-265 in: *Proc. of the 24th Automotive Technology Development Contractors' Coordination Meeting*, Soc. of Automotive Engineers, Warrendale, Pa., 1987. (P-197).

2. G. M. Crosbie, J. M. Nicholson, R. L. Predmesky, and E. D. Stiles, "Silicon Nitride Powder Synthesis Program," presented at the 25th Automotive Technology Development Contractors' Coordination Meeting, Dearborn, Michigan, Oct. 26-29, 1987. Manuscript submitted for inclusion in the Post-Conference Proceedings to be published in 1988 by the Society of Automotive Engineers, Warrendale, Pennsylvania.

3. G. M. Crosbie, "Synthesis of High Purity Sinterable Si_3N_4 Powders," pp. 17-23 in *Ceramic Technology for Advanced Heat Engines Project Semiannual Report for October 1986 Through March 1987*, ORNL/TM-10469, Oak Ridge National Laboratory, Oak Ridge, Tenn., August 1987.

Microwave Processing of Silicon Nitride

H. D. Kimrey, M. A. Janney, and M. K. Ferber (Oak Ridge National Laboratory)

Objective/scope

The objective of this research element is to identify those aspects of microwave processing of silicon nitride that might (1) accelerate densification, (2) permit sintering to high density with much lower levels of sintering aids, (3) lower the sintering temperature, or (4) produce unique microstructures.

Technical progress

This is a new start for FY 1988.

Background - The application of microwave processing to ceramic materials represents an exciting new method for sintering, joining, melting, and heat treating. In microwave heating, energy is absorbed throughout the volume of a material; therefore, the material heats uniformly without gradients in temperature. In contrast, in radiant or convection heating, energy is absorbed only at the surface of the material and must be transferred into the bulk of the part by conduction; therefore, gradients in temperature within the part must exist until the part achieves thermal equilibrium. For the processing of ceramic materials, the more uniform temperature distribution afforded by microwave processing should lead to more uniform shrinkage upon sintering and to more uniform microstructures.

Most of the ceramic microwave processing efforts to date have focused on the use of tuned-cavity microwave applicators operating at 2.45 GHz (i.e., the microwave oven frequency). Tuned cavities are inherently small in size (<10 cm^3) and produce severe gradients in the microwave field intensity within the cavity, which lead to extreme variations in temperature within the parts being heated.

Based on experience gathered in the microwave heating tasks associated with the DOE Fusion Energy Program, we have developed methods and hardware (namely an untuned cavity operating at 28 GHz) for uniformly heating ceramic parts of large volume (>300 cm^3) to temperatures in excess of 1600°C, in vacuum, or in reducing, neutral, or oxidizing atmospheres.

A detailed sintering study of high purity alumina doped with 0.1 wt % MgO was conducted in 1987 using support from the ORNL Director's Discretionary Fund. It was shown in that study that the sintering temperature required to achieve high density could be reduced by up to 400°C by microwave sintering at 28 GHz as compared to conventional sintering. Small samples (2-3 g) were used for the conventional sintering studies to reduce the variations in density due to thermal gradients in the parts; larger samples (100-120 g) were used in the microwave sintering studies. All of the sintering experiments used the same powder (Sumitomo AKP 50), formed in the same manner (isostatic pressing at 30,000 psi), with the same additive (0.1 wt % MgO), heated to the sintering temperature at the same rate (50°C per min), in the same type of atmosphere (diffusion pump vacuum). The differences in sintering behavior are illustrated as

follows: a 1-h hold at 1200°C in the conventional furnace produced a part that was 71.4% dense; in contrast, a 1-h hold at 1200°C in the microwave furnace yielded a part that was 98.2% dense. Furthermore, in the microwave sintering case, significant sintering occurred even at temperatures as low as 950°C (69.3% dense after 1 min, and 92.0% dense after 1 h); in conventional sintering, virtually no densification occurred at this temperature even after prolonged heating.

Approach - Silicon nitride poses several challenges to microwave processing. First, silicon nitride is inherently a very low-loss material; in its pure state silicon nitride is very difficult to heat even in a microwave cavity. Hence, we must develop methods for coupling to the silicon nitride if we are to successfully sinter it. Second, silicon nitride possesses a significant vapor pressure at its normal sintering temperatures; thus, methods to suppress vaporization of silicon nitride without interfering with the transmission of microwaves through the cavity will need to be developed. Third, there are currently no insulating materials available that possess both the thermal resistance properties and the low-loss dielectric properties required to act as an insulating barrier for silicon nitride; these materials will have to be developed within the context of this project.

This research element will examine the sintering and heat treatment of silicon nitride in the ORNL 200-kW, 28-GHz microwave furnace. The types of experiments that will be performed include the following: (1) annealing of dense silicon nitride (and/or sialon) parts to examine the effects of microwave heating on grain growth and grain boundary recrystallization; these experiments can be performed early in our investigation while the microwave furnace dilatometer (see #2) is being developed for the sintering experiments, and will provide valuable data on the methods needed to process silicon nitride in a microwave environment; (2) development of a microwave furnace dilatometer to provide the capability to monitor the densification of silicon nitride at all stages in the sintering process; (3) sintering of conventional silicon nitride compositions (e.g., $6Y_2O_3$ and $2Al_2O_3$) to establish a baseline of densification rates and microstructural states for microwave-sintered materials; and (4) sintering of silicon nitride with reduced levels of sintering aids (e.g., <2% Y_2O_3) to produce a dense sintered body with superior mechanical properties at elevated temperatures.

Progress - Our efforts to date have focused on two areas: (1) design and construction of a microwave-compatible dilatometer for sintering studies and (2) development of an insulation technique for silicon nitride that is compatible with silicon nitride.

The dilatometer poses several design problems that are unique to a microwave furnace. First, the materials of construction must be compatible with the microwave field. We have chosen boron nitride as the most likely candidate that will satisfy the needs of high-temperature stability as well as low microwave absorption. Second, no leakage of microwaves can be allowed along the feedthroughs for the dilatometer. Several designs for blocking the transmission of microwaves are being considered. It is likely that the final design selection will depend on actual low power leakage tests of the various designs. Third, the components of the dilatometer must be compatible with high vacuum, as well as furnace atmosphere, operation.

Development of a proper insulation system is an important part of developing microwave processing technology for a new material. The insulating system must provide appropriate thermal insulation and must have the appropriate microwave absorption characteristics. For example, if the microwave absorption of the insulation is significantly higher than that of the part being processed, then only the insulation will be heated by the microwaves and the part will simply be heated by conduction and radiation from the hot insulation. In addition, the insulation must be relatively easy to handle. In particular for silicon nitride, we must have an insulation that will not foul the dilatometer that is being designed for the sintering studies. To date, we have demonstrated that two types of insulation will work for silicon nitride having either 6 wt % yttria or 6 wt % yttria and 2 wt % alumina added as sintering aids.

The insulation is based on Ube or Toyo Soda high purity silicon nitride powders. We have used the powder in two forms: (1) granules made by isopressing and screening and (2) dry pressed blocks that were subsequently fired at 1700°C to bond the particles together. The dielectric properties of the Ube powder and the granules or blocks made from that powder are superb. Essentially no microwave energy is absorbed by the silicon nitride powder. As an example, we have placed a block of high purity silicon nitride on top of a block of high purity boron nitride and then heated that assembly in our 28 GHz microwave furnace. Boron nitride has one of the lowest microwave absorptions of any commercially available material. On applying power to the furnace, the boron nitride heated to about 1200°C. The silicon nitride block that was sitting on top of the boron nitride was heated only by conduction from below, and its temperature never exceeded 200°C. Both types of insulation have been used successfully for heating silicon nitride parts to temperatures in excess of 1600°C.

1.1.4 Processing of Monolithics

Improved Processing

R. L. Beatty and R. A. Strehlow (Oak Ridge National Laboratory)

Objective/scope

The objective of this project is to determine and develop the reliability of selected advanced ceramic processing methods. This project is intended to be conducted on a scale that will permit the potential for manufacturing use of candidate processes to be evaluated.

Technical progress

For this new program several processes were considered and one technique was selected that utilizes the gelation of a slip casting as part of the method. Laboratory space was arranged and much of the needed equipment was procured.

The experimental plan is directed toward the manufacture of a set of specimens for each group of process variables, such as milling and formulation, other pretreatment of starting powders, casting conditions, mold types, drying, binder removal procedure, and sintering schedules. A sufficient number of tensile test bars and gage block castings are to be produced in each run so that characterization of the products from each processing may be feasibly conducted to yield statistics that permit conclusions to be drawn about the reliability of the process.

Because the gel-casting method is generic and not restricted to the high-temperature materials of greatest interest, it was possible to begin experimental work before all of the necessary high-temperature furnaces, equipment, and special materials were obtained. A tensile bar specimen was designed and fabricated to permit exploration of various mold-making techniques. A suitable mold-making procedure was selected after examination of several possibilities. The materials considered for this function included unfilled styrene and polyester resins, silicone resin polymer, and plaster impregnated with paraffin. The unfilled polymers exhibited too high a shrinkage and the silicone was found to produce an inadequate cast surface. Paraffin-impregnated plaster, however, appeared to be suitable.

An alternate design for a tensile bar was also developed that would utilize adhesive joining of a machined specimen to metallic end pieces. If this alternate design proves to be effective, it is expected to provide a simpler routine for specimen preparation. This would permit the development of near-net-shape casting development separately from the study of the process variables. This alternate design is to be tested using purchased specimens as well as those fabricated using the gel-casting technique.

Several experimental castings were made of an alumina-silica mixture. They were air dried, and sintering was attempted in a furnace with a usable temperature limit of 1400°C. Maximum density achieved was about

92%. Although the expected conversion to mullite occurred, this density was not adequate. Because a graphite element furnace has now been made available, we are now proceeding toward initial attempts to apply the process to silicon-nitride along with a comparable fine-grained alumina for development studies.

Status of milestones

Decision on mold preparation procedures, June 30, 1988, is on schedule. Work has proceeded on other milestone tasks.

Publications

None.

1.2 CERAMIC COMPOSITES

1.2.2 Silicon Nitride Matrix

Silicon Nitride–Metal Carbide Composites
S. T. Buljan (GTE Laboratories, Inc.)

Objective/Scope

The objective of this effort is to study the effect of sintering aids on the microstructure and properties of Si_3N_4-SiC(w) composites and utilize the results obtained to design and synthesize an advanced composite of improved properties. It is also an objective of this effort to refine forming and consolidation processes and develop technology for prototype part fabrication.

Research conducted in the period from June 1985 to date has generated substantial information regarding toughening/strengthening mechanisms of ceramic matrix composites and resulted in the development of an improved silicon nitride composite material. A process route for fabrication of complex parts from this material for automotive engine applications has been demonstrated. These studies have also identified critical issues and defined direction for further materials optimization and process refinement.

In the course of previous investigations, it has been shown that in composites such as Si_3N_4-SiC(w) the ceramic matrix microstructure plays a crucial role in determining the properties. The effectiveness of dispersoid additions for improved toughness depends on the matrix microstructure and the fracture mode. In the absence of intergranular fracture, the matrix acts as a homogeneous continuum, and the degree of toughening depends solely on crack interaction with the dispersoid. Ceramics, however, rarely fail exclusively by transgranular fracture.

In a material with intergranular fracture, the energy expended to propagate a crack is a function of the grain size, shape, and the strength of the intergranular bond. Intergranular bond strength also plays an important role in determining the degree of intergranular fracture.

Si_3N_4-SiC material is a ternary composite consisting of β-Si_3N_4, SiC, and an intergranular glass phase. In a composite which fracture transgranularly, the fracture toughness is (to a first approximation) a sum of the component properties. If fracture proceeds through the intergranular phase, the toughness will be not only grain size-dependent but also strongly affected by the properties of grain boundaries or grain boundary phase. Strong bonding at grain boundaries reduces the amount of intergranular fracture while, on the other hand, weak boundaries reduce the surface energy. This requires that the properties of grain boundary phase be carefully tailored for maximum fracture toughness.

The success of composite optimization depends on precursor materials as well as processing. In the process of execution of the current program, it has become increasingly apparent that reliance of the development on a single source of whiskers (ARCO) is at best impractical. The supplier's decision to restrict sales and internalize the use of whiskers has imposed a need to identify and qualify alternate sources. It is for this reason that it is also proposed that future research incorporate evaluation of alternate sources of raw materials, both SiC whiskers and silicon nitride.

The current program has demonstrated that Si_3N_4-based composites containing up to 30 volume percent of SiC whiskers could be injection-molded and densified by HIP to over 99% of theoretical density. This work has also pointed at several areas where further process development is needed to bring injection-molded composites from the feasibility demonstration stage to a technology ready for prototype fabrication. In view of the preceding discussion, it is also apparent that additional process adaptations will be

required to accommodate and fabricate new developmental materials. This effort will address optimization of the binder system, compounding and molding techniques, as well as the densification procedures.

Technical Progress

Initial quantities of UBE-Si_3N_4, a potential replacement for SN-502 Si_3N_4 used previously as the matrix material for composite research, have been characterized. Three grades, E-03, E-05, and E-10, of high purity powder were selected for the first studies. Table 1 compares the analyses for these powders and the SN-502. All powders appear to have the same purity except for the oxygen levels, which are considerably lower for the UBE E-03 and E-05 powders. As determined by x-ray diffraction, the UBE powders do not contain detectable levels of β-Si_3N_4. All three UBE powder grades have an equiaxed morphology.

Alternate SiC whiskers to replace ARCO SC-9 have also been evaluated. Table 2 shows the analyses for two potential whisker-replacement materials and compares the data to that for the SC-9. The average diameter of American Matrix SiC whiskers is considerably larger than the others.

Table 1: Analysis of silicon nitride powders

Manufacturer	**GTE[a]**	**UBE[b]**	**UBE[b]**	**UBE[b]**
Grade	**SN-502**	**E-03**	**E-05**	**E-10**
Lot No.	**SN-185**	**B-20208**	**F-610074**	**A-610342**
Impurities				
Metallic (PPM)				
Fe	< 50	60	60	60
Al	< 100	< 5	< 5	< 5
Ca	ND	< 10	< 10	< 10
Ni	ND	< 10	< 10	< 10
Cr	ND	< 5	< 5	< 5
Mg	ND	< 5	< 5	< 5
Non Metallic (wt. %)				
Oxygen	1.5	0.65	0.80	1.37
Carbon	ND	ND	ND	ND
Phase Content (wt. %)				
α-Si_3N_4	94.1	100	100	100
β-Si_3N_4	5.8	ND	ND	ND
Si	0.1	ND	ND	ND
Surface Area				
BET (m^2/g)	4.0	3.6	4.6	10.5

[a]GTE Chemical and Metallurgical Division, Towanda, PA
[b]UBE Industries, Ltd., Ube City, Japan

Table 2: Analysis of SiC whiskers

Manufacturer Grade	ARCO[a] SC-9	Tokai[b] Toka	AMI[c] -
Impurities			
Non Metallic (wt. %)			
Oxygen	1.2	0.3	1.0
Metallic (ppm)			
B	-	-	1000
Ca	300	-	400
Mg	100	-	100
Fe	300	-	-
Mn	30	-	-
Ti	-	300	-
Size (μm)			
Avg. Lg. (Std. Dev.)	17.3 (±9.7)	7.4 (±5.8)	14.1 (±14.5)
Avg. Dia. (Std. Dev.)	0.5 (±0.2)	0.4 (±0.1)	1.0 (±0.7)

[a]Advanced Composite Materials Corporation (formerly ARCO), Greer, SC
[b]Tokai, Tokai Carbon American, Inc., New York, NY
[c]American Matrix Incorporated, Knoxville, TN

Representative blends of monolithic AY6 have been prepared from E-10, E-03 and an 80%:20% mixture of E-03 and E-10 Si_3N_4 powders using the GTEL standard milling procedures and hot pressing schedule.

Table 3 shows the surface area values of the raw powders and the values after milling the AY6 composition. The higher values of the milled powders reflect the surface area of the Y_2O_3 and Al_2O_3 additions, as well as comminution of the Si_3N_4. The particle size distribution for the as-received and milled AY6 compositions containing the E-10 and E-03 powders were measured and the results are compared in Figure 1. The general trend observed is a reduction in particle size for both milled AY6 compositions when compared to the as-received powders. However, the milled AY6 composition prepared from the E-10 shows the presence of ≈4% of particles larger than the sizes observed in the as-received material. These results suggest that agglomeration is occurring during processing of the finer E-10 material.

Hot pressing of these AY6 powders was performed at 1725°C/34.5 MPa with a hold time of 100 minutes. Measured densities of all materials were greater than 99% of theoretical. Figure 2 shows densification curves for the three materials examined. The finer E-10 material densifies very rapidly, with the 80/20 mixture showing an intermediate rate, while the coarsest E-03 material exhibits the slowest rate. Duplicate runs showed good agreement. The hot-pressed billets prepared from coarser precursor materials retained a much higher fraction of α-Si_3N_4 (Table 3).

Fracture toughness measurements by the Controlled Surface Flaw technique (CSF) showed the E-10 and 80/20 mixture to have values which were higher than the E-03 (Table 3). Average strength was found to be higher for the coarser materials. The flaw size range was calculated for all materials using the maximum and minimum values of frac-

ture toughness and MOR. The somewhat larger processing flaw size and slightly reduced MOR of the E-10-based AY6 may be a consequence of the observed agglomeration in the powders.

Table 3: Evaluation of Si_3N_4 AY6 made with different Ube grades, hot pressed 1725°C/34.5 MPa/100 min.

Ube Grade	BET Si_3N_4 (m^2/g)	BET Milled AY6 (m^2/g)	Density (g/cm^3)	Mechanical Properties K_{IC} (CSF) ($MPa \cdot m^{1/2}$)	Mechanical Properties MOR* (MPa)	Flaw Size Calc. Range (μm)	Phase Identification (XRD)
E-10	10.5	14.0	3.25	4.7±0.3	845±51	18-29	Minor α-Si_3N_4 Major β-Si_3N_4
E-03/ E-10 80/20	(5.0) Calc.	8.0	3.25	4.7±0.2	932±92	14-25	Major α-Si_3N_4 Major β-Si_3N_4
E-03	3.6	6.4	3.25	4.1±0.3	995±30	10-15	Major α-Si_3N_4 Major β-Si_3N_4

*Average of 5 measurements

Baseline data (Table 4) pertaining to the study of the effect of Si_3N_4 glass phase composition on microstructural development and mechanical properties has been established. Three compositions were prepared using Ube E10 Si_3N_4 powder employing yttria, ceria and magnesia sintering aids. The AC8 and AM4 materials contain ceria and magnesia substituted on a volume basis for yttria, respectively.

Table 4: Room temperature property characterization of Si_3N_4 ceramics containing different sintering aids, hot pressed 1725°C/34.5 MPa/90 min.

Material Designation	Composition	Hot Press Density (g/cm^3)	Young's Modulus (GPa)	Mechanical Properties K_{IC} (CSF) ($MPa \cdot m^{1/2}$)	Mechanical Properties MOR* (MPa)
AY6	Y_2O_3 - 6.0 w/o Al_2O_3 - 1.5 w/o;Bal Si_3N_4	3.25	293	5.0±0.1	983±138
AC8	CeO_2 - 8.3 w/o Al_2O_3 - 1.5 w/o;Bal Si_3N_4	3.30	284	5.1±0.1	879±118
AM4	MgO - 4.4 w/o Al_2O_3 - 1.5 w/o;Bal Si_3N_4	3.12	251	3.6±0.1	706±68

*Average of six bars

All compositions were hot pressed by a schedule which employs a 90-minute hold at 1725°C at a pressure of 34.4 MPa (5 ksi). Figure 3 shows relative density as a function of time at maximum temperature for the three materials investigated. The MgO (AM-4) containing body was observed to densify very rapidly during the initial stages of densification, reaching greater than 96% of calculated theoretical density by the time the hold temperature was achieved. The Y_2O_3 (AY6) and CeO_2 (AC8) bodies appear to densify at the same rate during the early stages of densification, which is slower than that of the MgO-containing AM4. The slower densification rates observed for these materials (AY6 and AC8) are related to the formation of a more viscous intergranular glass phase. For all three materials, analysis (XRD) shows that α-Si_3N_4 was completely converted to beta.-Si_3N_4 during hot pressing. No other phases were detected.

The substitution of MgO for Y_2O_3 on a volume-equivalent basis was observed to lower Young's modulus, fracture toughness and MOR, while the CeO_2-containing material exhibited equivalent or higher room temperature mechanical properties.

Elevated temperature fracture toughness testing by controlled surface flaw techniques (Table 5) shows that the species of sintering aid has a dramatic effect on K_{IC} at and above 1000°C. The MgO-containing bodies show increased K_{IC} at 1000°C and 1200°C, believed to be related to crack blunting by a glass phase. The AY6 data exhibits an increase in K_{IC} at somewhat higher temperature (1200°C) due to a higher softening temperature of the Y_2O_3-containing glass. The CeO_2-containing Si_3N_4 exhibits a reduced K_{IC} at elevated temperature. This effect seems to be related to the even more refractory ceria-containing glass.

Table 5: Room and elevated fracture toughness of Si_3N_4 ceramics containing equivalent volumes of different sintering aids

	Fracture Toughness ($MPa \cdot m^{1/2}$)		
Material	**25°C**	**1000°C**	**1200°C**
AY6	5.0 ± 0.1	5.0 ± 0.1	7.1 ± 0.1
AC8	5.1 ± 0.1	4.6 ± 0.1	4.3 ± 0.3
AM4	3.6 ± 0.1	6.8 ± 0.1	8.0 ± 0.4

Fabrication experiments utilizing AY6 (SN502 Si_3N_4) whisker composite material which was injection molded and densified by hot isostatic pressing (HIP) have demonstrated the feasibility of shaping complex Si_3N_4-SiC whisker components (Figure 4). The major fabrication issue identified during these studies was distortion observed after densification by HIP. Turbine blades fabricated in this manner show areas of distortion in the form of curvature along the airfoil trailing edge, in the platform and dovetail. Test bars also showed distortion in the form of curvature along the bar length with the concave surface always on the gate side of the bar (Figure 5).

Shrinkage measurements of AY6 + 30 SiC whisker samples have shown that shrinkage along the test bar length was smaller relative to test bar width and thickness. This shrinkage anisotropy suggested a preferred alignment of the whiskers.

An injection molding trial was then made using SiC whiskers which had been milled to a near-equiaxed state prior to blending with AY6. This material, after HIPing by the same schedule, reached the same density but had uniform linear shrinkage in all directions (Table 6), which indicates that the whisker alignment played a major role in non-uniform densification shrinkage.

Table 6: Normalized densification shrinkage of composites Containing Whisker or Particulate SiC Additions

Shrinkage Direction	AY6 SiC Whiskers	AY6 + Milled SiC Whiskers
Bar Length	0.843	1.005
Bar Width	1.074	1.000
Bar Thickness	1.204	0.995

To determine the exact mechanism leading to test bar bending, a detailed quantitative microstructural evaluation of whisker orientation as a function of position in the test bar was performed. Sections of the HIPed composites, 30 v/o whiskers, were cut from test bars. Multiple regions of the samples (Figure 6) were evaluated. Each whisker image was digitized and a computer program was used to determine aspect ratio and orientation angle for approximately 200 whiskers per field of view.

Figure 7 illustrates the whisker alignment determined along the bar length. The orientation observed is parabolic, but the side gate location causes the parabolic flow and the whisker orientation to be off center with respect to the test axis. The side opposite the gate has whisker orientation parallel to the bar length, while the gate side, containing the parabola vertex, has a greater number of whiskers orientated perpendicular to the bar length. Whiskers, when aligned in a matrix, restrict densification shrinkage parallel to their alignment. It is the nonsymmetrical nature of the orientation which is responsible for the observed distortion.

Methods to alleviate the whisker-orientation effect are being investigated. The previous experiments used a die having a single side gate configuration with the gate above the center axis of the bar thickness. A die is currently being modified which will incorporate the four gate configurations illustrated in Figure 8.

The single side-gate configuration (Figure 8a) is similar to that used in initial studies but will be fabricated with the gate shifted to a position on the center axis of the bar thickness. The flow pattern during mold fill should approximate classic "plug flow."

The opposing side gates (Figure 8b) will provide a similar fill pattern, but a more rapid fill and symmetrical orientation effect. The end-gate configuration (Figure 8c) will initiate a thin stream into the bar cavity which will compress into multiple folds during filling. This should create a more random whisker orientation than the plug flow case, but may lead to air entrapment and increased flaws.

A final test configuration will utilize a thin gate along the entire bar length (Figure 8d). As this stream folds into the cavity, it is expected that the minimal level of whisker orientation will be created.

Test bars will be injection molded using the four gate configurations and evaluated for whisker orientation and distortion.

Status of Milestones

Program execution is on schedule.

Communications/Visits/Travel

S.T. Buljan and J.G. Baldoni attended the 25th Automotive Technology Development Contractors' Coordination Meeting, October 26-29, 1987.

S.T. Buljan, J.G. Baldoni, M.L. Huckabee, J.T. Neil, and G. Zilberstein presented a paper entitled "SiC Whisker-Reinforced Si_3N_4" at the aforementioned meeting.

Problems Encountered

None.

Publications

None.

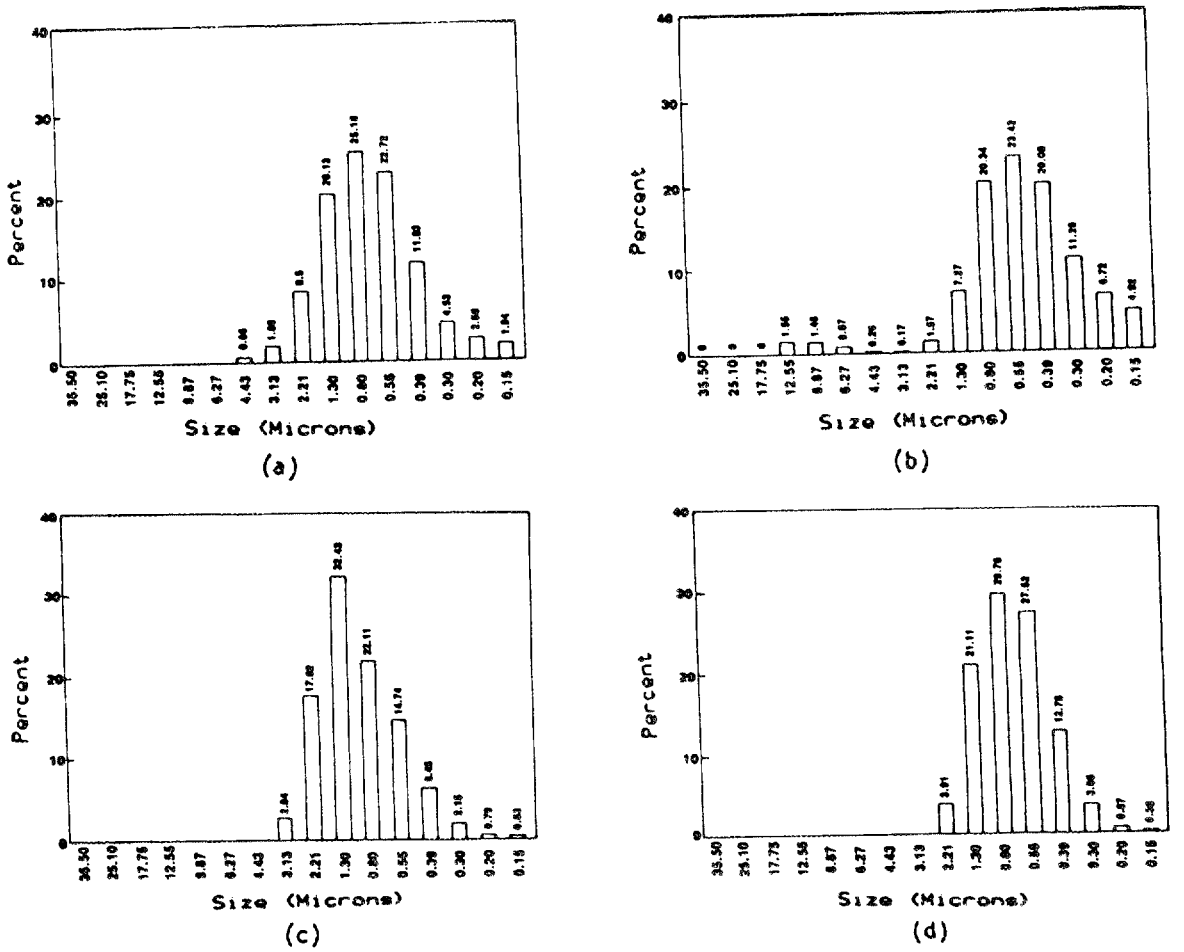

Figure 1: Microtrac particle size analysis of Ube Si_3N_4 grades E-10 (a) unmilled raw powder, (b) milled in AY6 composition and E-03, (c) unmilled raw powder, (d) milled in AY6 composition

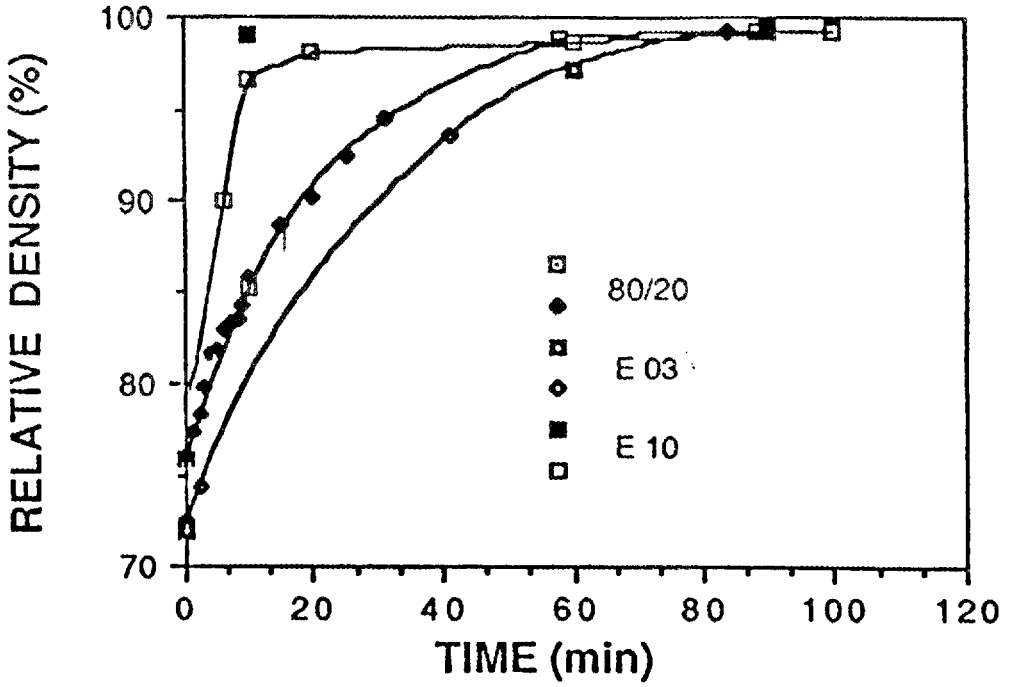

Figure 2: Densification rates for AY6 compositions containing UBE E-03, E-10, and a mixture of 80%/20%:E-03/E-10 Si_3N_4

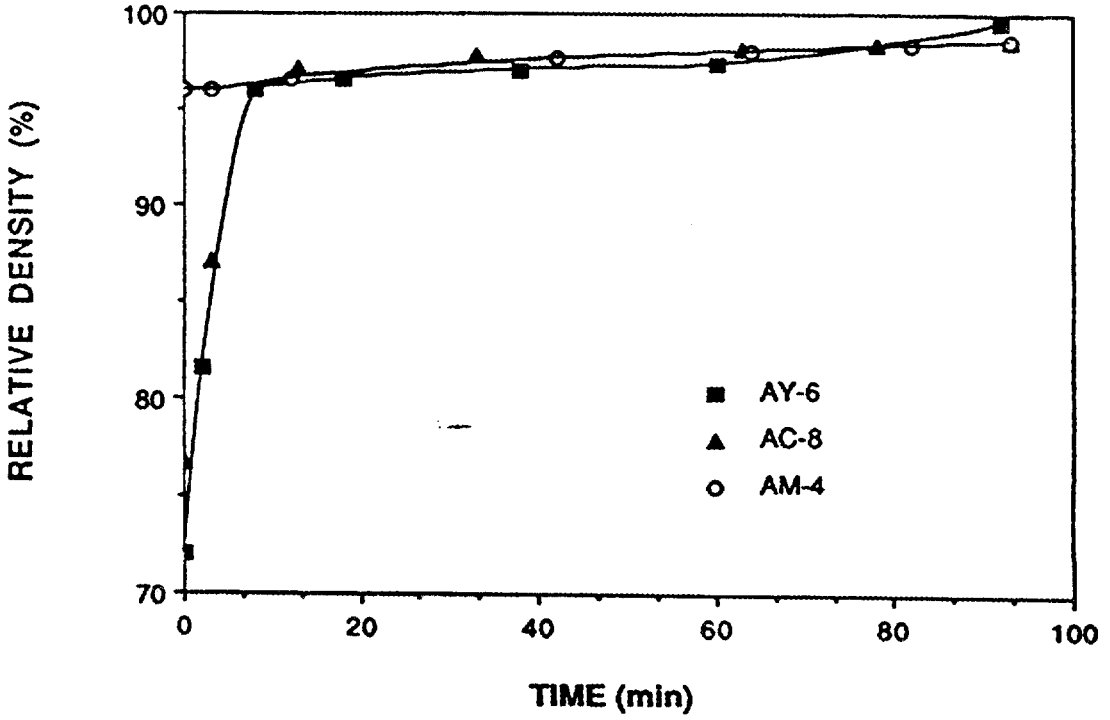

Figure 3: Relative density as a function of time at constant hot-pressing temperature (1725°C) for Si_3N_4-containing equivalent volumes of Y_2O_3 (AY6), CeO_2 (ACB), and MgO (AM4)

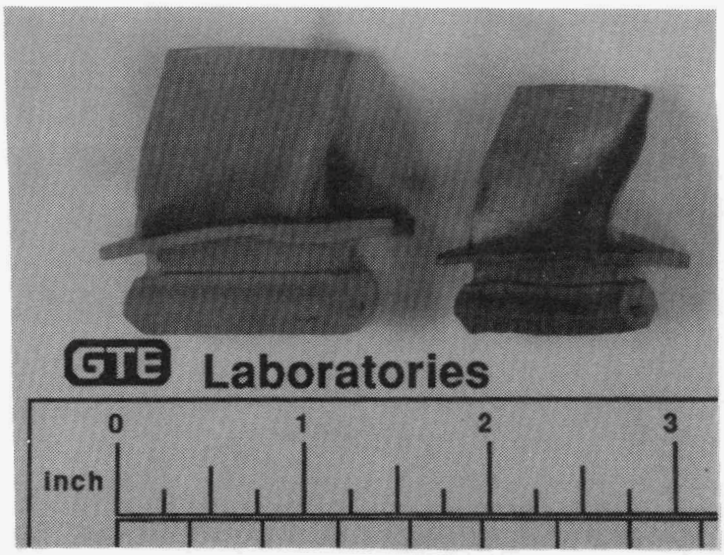

Figure 4: **Turbine blade containing Si_3N_4-30 v/o SiC whiskers (a) as injection-molded and (b) after HIPing**

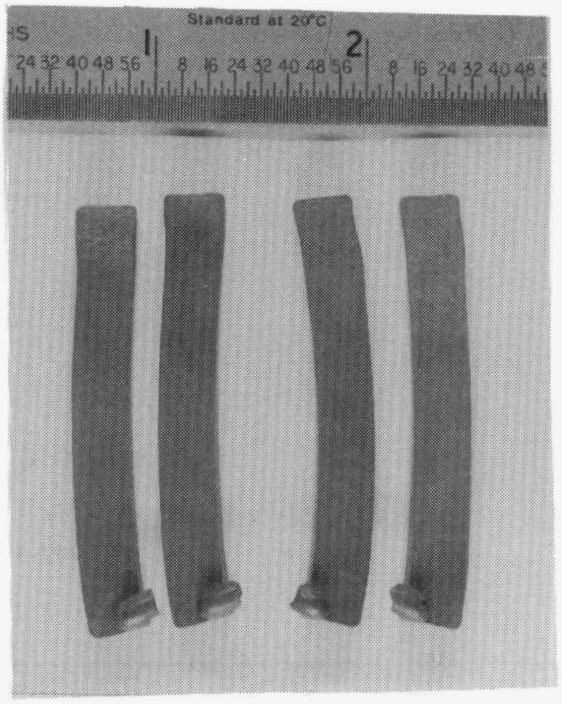

Figure 5: **Injection-molded bars containing Si_3N_4-30 v/o SiC whiskers illustrating bar curvature after hot isostatic pressing**

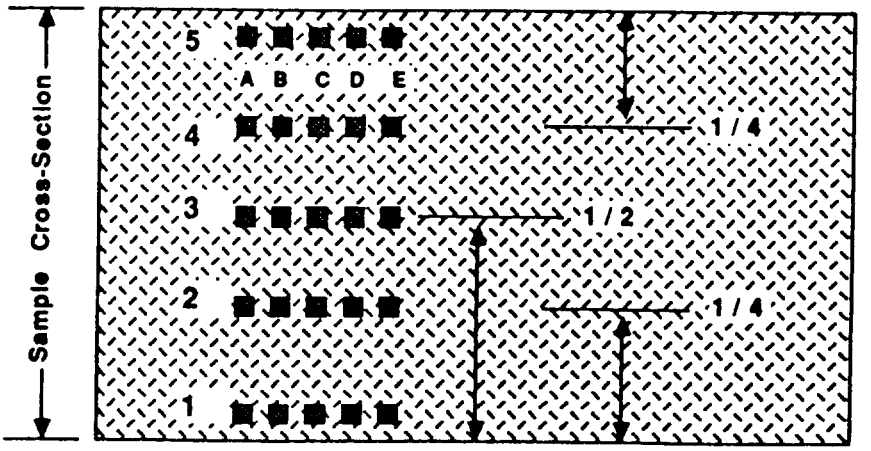

Figure 6: Regions photographed on bar cross section

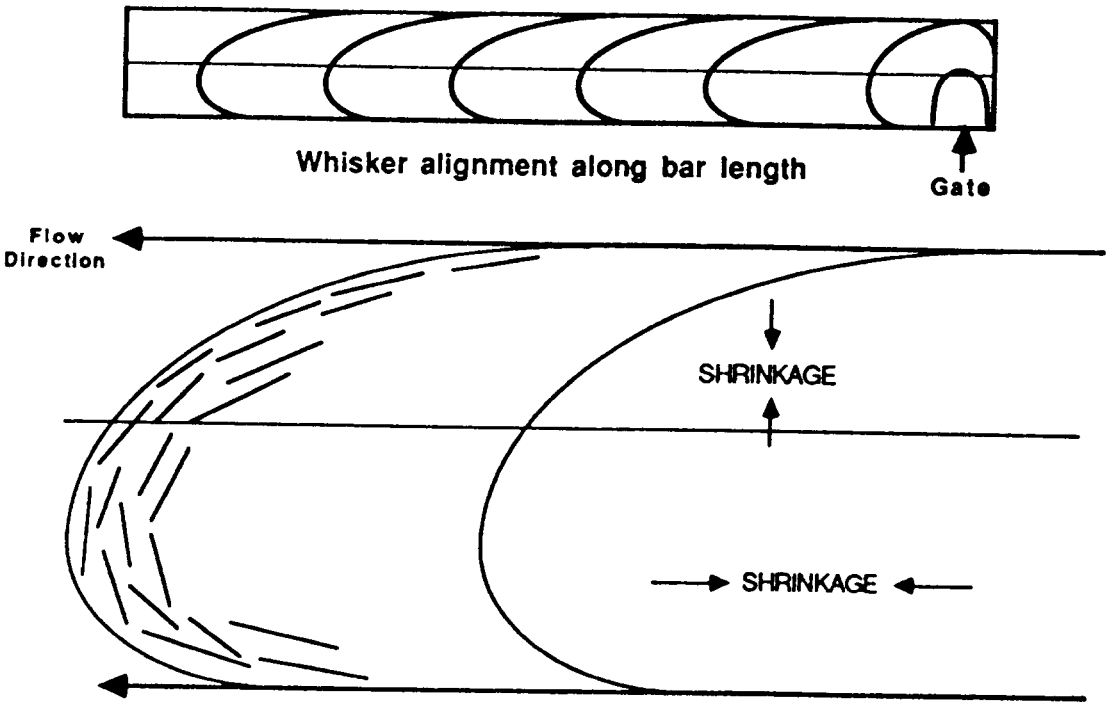

Figure 7: Whisker orientation model for test bar

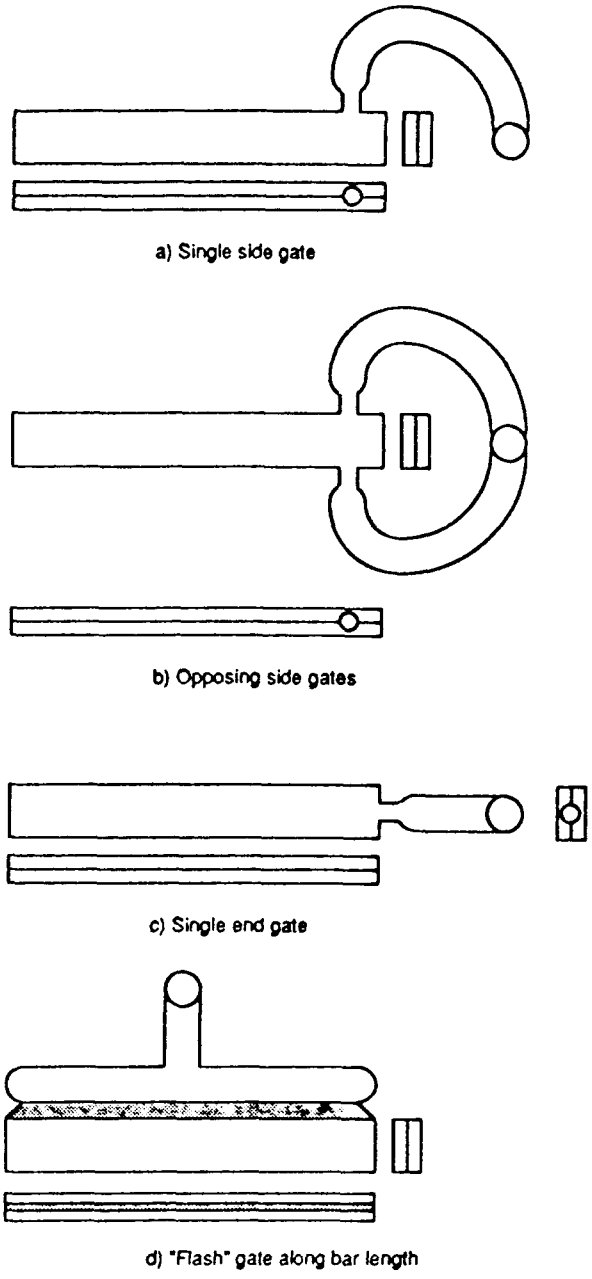

Figure 8: Test-bar gating configurations for whisker composite-molding study

Development of Toughened Si_3N_4 Composites by
Glass Encapsulated Hot Isostatic Pressure

N. D. Corbin, C. A. Willkens, V. K. Pujari, G. A. Rossi, J. S. Hansen, and K. N. Siebein (Norton Company)

Objective/scope

This two year program is to develop fully dense Si_3N_4 matrix SiC whisker composites which show enhanced properties over monolithic Si_3N_4 materials. Materials will be processed using an RBSN approach followed by high pressure glass encapsulation HIPing. The primary goal is to develop a composite with a fracture toughness >10 MPa $(m)^{.5}$ and capable of operating up to 1400°C.

Studies will be conducted to tailor the whisker/matrix interface and determine the optimum whisker morphology for fracture toughness improvements. The effect of forming on whisker orientation, fracture toughness, and shape distortion will also be addressed.

Technical progress

This report covers the later portion of our Phase I effort and the initiation of our Phase II effort.

1.0 EVALUATION PROCEDURES

Procedures for analytical evaluations and mechanical property determinations have previously been described in detail[1]. Depending on material availability, flexural strength is determined using either the U. S. Army recommended procedure for a cross-section of $3x4mm^2$ or a NORTON CO. standard procedure for bars with a 3x3.1mm cross-section. Fracture toughness is determined by either an indentation method[3] or a controlled flaw method[4] depending on material availability.

During this reporting period a technique was developed for determining the surface composition of individual SiC whiskers by Scanning Auger Microanalysis (SAM)[5]. SiC whiskers are dispersed on a copper grid which eliminates sample charging problems during

evaluation. The portion of the whiskers suspended away from the copper are analyzed as shown in Figure 1. This allows sputtering of the whiskers to proceed without contamination from the substrate. This technique has been successfully applied to evaluate the surface composition of different whisker sources and coated whisker materials.

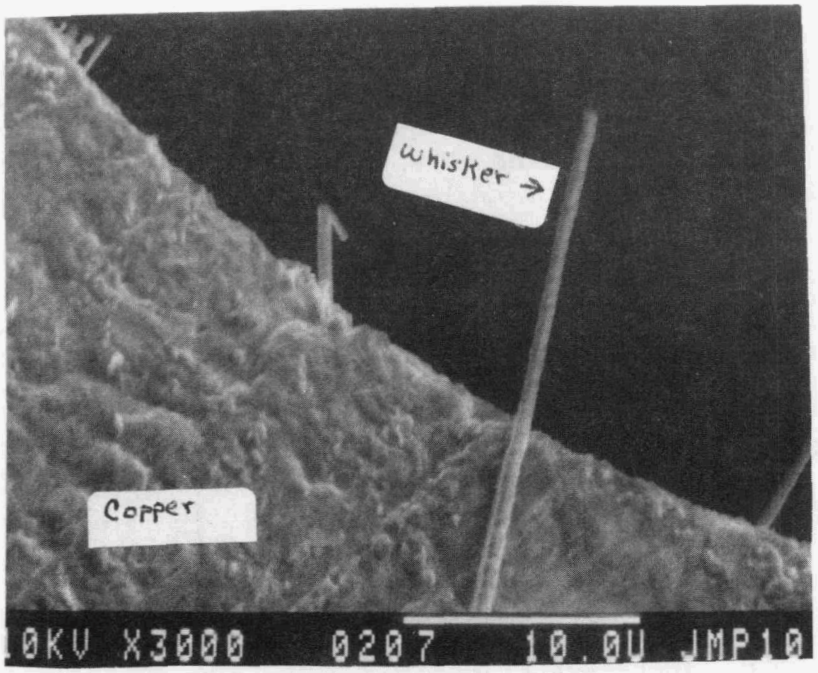

Figure 1: Whisker configuration for Auger analysis.

2.0 REINFORCEMENTS

Whisker Sources - Additional whisker sources have been evaluated in a standard 4 w/o Y_2O_3 matrix at a 20 v/o loading. Whiskers were evaluated from Tokai Carbon (Grade 3), Shin Etsu Chemical Co. and Advanced Composite Materials (ACM). Composite properties are listed in Table 1. An unreinforced monolith and 20% v/o Tateho T44 composite were also made for baseline comparison. Both the Tokai Grade 3 and ACM composite had slightly higher toughness values than the Tateho T44 baseline and were ~20% tougher than the monolith.

Table 2 lists the impurity contents for various whisker sources as analyzed by emission spectroscopy. Impurity levels of Fe, Al and Ca are relatively high as compared to the matrix powder. High levels of aluminum and calcium will degrade high temperature strength and stress-rupture performance of the composite.

TABLE 1

COMPOSITE PROPERTIES

Whisker*	(MPa(m)$^{.5}$) Controlled Flaw Toughness	Specimen Code
Monolith	4.6 ± 0.3	2139-38
Tateho T44 (h)	5.1 ± 0.1	2138-38
Tokai - Grade 3[a]	5.4 ± 0.2	2134-38
Shin Etsu[b]	4.9 ± 0.2	2137-38
ACM[c]	5.4 ± 0.2	2132-38
Kobe[d]	4.9 ± 0.2	2100-30
Nikkei[e]	4.4 ± 0.4	2104-30
American Matrix[f]	5.0 ± 0.2	2101-30
Coarse Huber[g]	5.0 ± 0.3	2131C-38,37
Fine Huber	4.9 ± 0.3	2131F-38,37

[a] Tokai Carbon Co., Tokyo, Japan
[b] Shin-Etsu Chemical Co., Japan
[c] Advanced Composite Materials (formerly Arco) Greer, SC
[d] Kobe Steel, Kobe, Japan
[e] Nikkei Techno Research Co., Shinozuoko, Japan
[f] American Matrix Inc., TN, Rec 7/87
[g] J. M. Huber Corp., Borger, TX
[h] Tateho Chemical Ind. Co. JAPAN
*Composites made with 20 v/o SiC whiskers, CIP/HIP

TABLE 2

Whisker Source Analysis

Manufacturer	Grade	Rec.	(%) Oxygen	(%) Nitrogen	(%) Free Carbon	Fe	Ca	(ppm) Al	Mg	B	Ni
Tateho	T144	11/86	0.4	0.9	0.4	340	810	3100	84	ND	30
Tokai	Gr.3	12/87	0.27	0.87	0.3	143	593	300	39	10	10
Shinetsu		11/87	4.21	0.1	0.43	129	492	10	68	10	12
ACM (Arco)		1/88	1.21	1.01	0.19	187	1200	2000	449	ND	9
American Matrix	Gen.4	2/88	1.48	0.07	0.09	170	730	470	390	>1000	180
Huber	XPWZ	5/87	0.1	0.9	6.16	1000	11	10	45	11	670
Kobe		5/87	1.21	0.71	0.15	720	320	43	9	ND	2229
Tokai		7/86	0.31	0.68	0.25	72	24	32	32	10	9

Various whisker sources were evaluated as to surface chemistry. Table 3 compares the surface compositions as determined by ESCA. The carbon contents of the Tateho products are significantly higher (~50 vs ~31%) than the other sources, while their oxygen content is significantly lower (~20 vs. ~40). Silicon contents for all materials are similar. The surface chemistry of the Advanced Composite Materials and American Matrix SiC whiskers are very similar. Surface composition is expected to influence dispersion behavior and possibly composite fracture toughness. Data obtained from AUGER analysis shows a variation in whisker surface composition from whisker to whisker within the same lot. Examples of this variation are given in Table 4. Data from individual Advanced Composite Materials whiskers consistently showed 100% carbon on their surfaces. It should be noted that ESCA and AUGER data are not identical. The reason for this is unclear but may be related to electron beam heating in AUGER which causes desorption of hydrated species and the small spacial resolution of AUGER (.05 um diameter) as compared to ESCA (~3mm).

TABLE 3

ESCA DATA ON SiC WHISKERS

	Advanced Composite Materials[1]	American Matrix[2]	Tateho 0.8 um[3]	Tateho T44[4]
Oxygen (A/O)	41.5	45.5	19.6	24.0
Carbon (A/O)	32.7	31.4	49.7	49.1
Silicon (A/O)	24.9	22.0	28.2	26.8
Other (A/O)	0.6	0.9	2.3	--

[1]Advanced Composite Materials, Rec. 1/88
[2]American Matrix, Generation 4, Rec. 2/88
[3]Tateho 0.8 um, SCW #1-S105, Lot 1020, Rec. 11/87
[4]Tateho T44, SCW #1=S105, Lot S178, Rec. 11/86

TABLE 4

AUGER ANALYSIS OF INDIVIDUAL WHISKERS

	American Matrix[1]			Tateho[2]		
Whisker	A	B	C	A	B	C
Oxygen (A/O)	54.9	13.8	34.4	-	12.5	-
Carbon (A/O)	33.9	57.4	35.2	54.5	70.9	100
Silicon (A/O)	11.1	28.8	30.4	45.5	16.6	-

[1]American Matrix, Generation 4, Rec. 2/88
[2]Tateho 0.8 um, SCW #1-S-105, Lot 1020, Rec. 11/87

American Matrix SiC whiskers (rec. 7/87) were evaluated by TEM to determine their structure. Evaluations on Tateho, Advanced Composite Materials, and Huber whiskers were reported earlier.[1] The whiskers were incorporated into a dense Si_3N_4 matrix for their evaluation. They contain many planar faults and twins perpendicular to the growth axis. A longitudinal view of an American Matrix whisker in the SRBSN matrix is presented in Fig. 2. The core of the whisker appears solid, although it contained many small cavities, see Fig. 3. The cavities are usually attributed to gas bubble evolution during whisker growth.[6] These whiskers appear very similar in structure to materials prepared from rice hull processes[6,1] and are dissimilar from the previously reported structure of the Huber product.[1] The American Matrix whiskers are relatively large. SEM photomicrographs show them to be between 1-3 micron in diameter which agrees with the product literature.[7]

2.0 Aspect Ratio - Fine particle classification techniques were applied to size a given whisker source into various size classes. Huber SiC whiskers were separated into a coarse fraction ($d_{50} \simeq$ 1.5 um) and a fine fraction ($d_{50} \simeq$ 0.4 um).[1] These two extremes were incorporated into composites at a 20 v/o loading (Fig. 4). The composites were formed by cold isopressing, yielding a random whisker distribution. Controled flaw fracture toughness values are listed in Table 1 and show no significant difference.

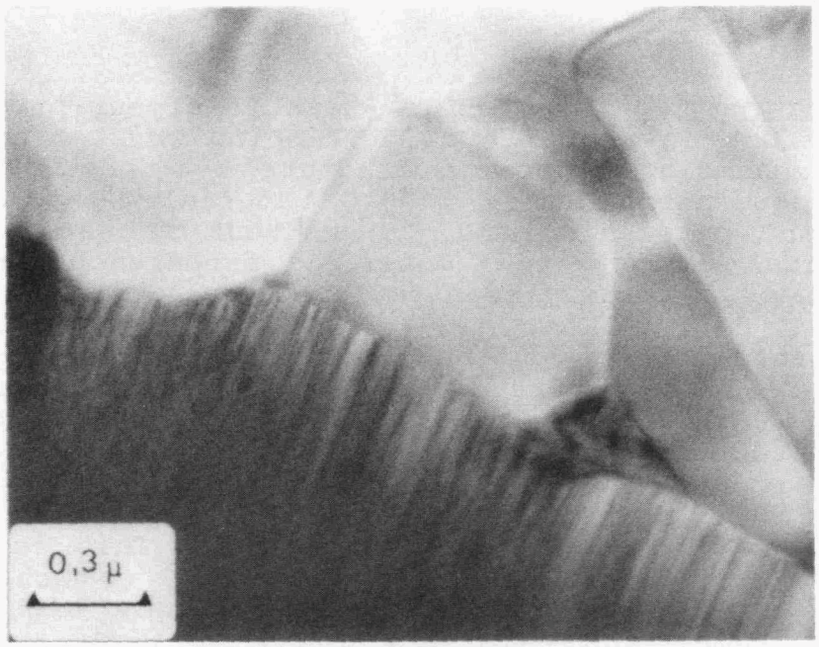

Figure 2: Bright field TEM micrograph of an American Matrix whisker in SRBSN showing planar faulting.

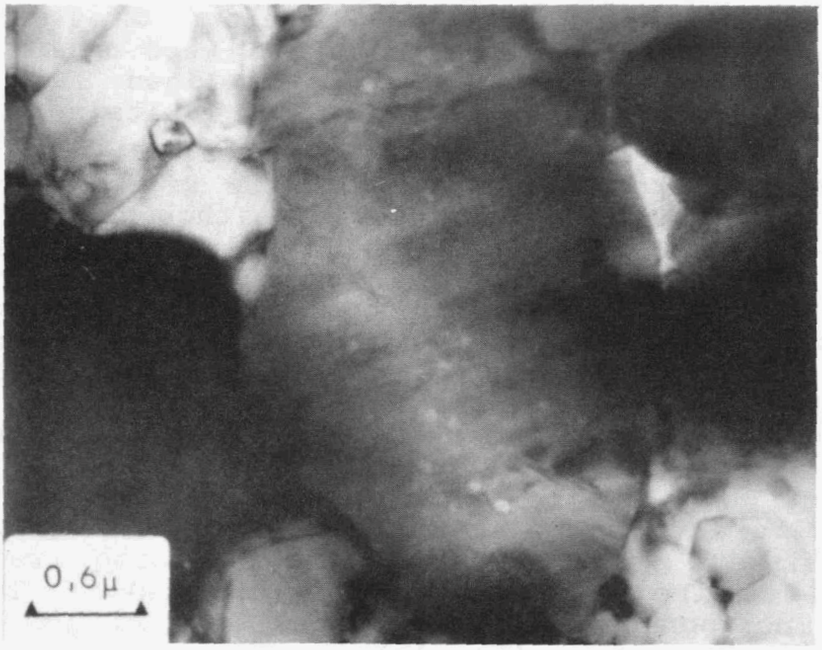

Figure 3: Bright field TEM micrograph of an American Matrix whisker in SRBSN containing cavities.

Whisker Coating Technology - In Phase II of our program we have an expanded effort in the area of developing whisker coating technologies for enhancing composite fracture toughness while meeting the program requirement for a 1400°C material. We are investigating solution, pyrolysis, and CVD methods for coating application. Analytical evaluation of materials prepared under Phase I of this project have previously been reviewed[1].

CVD coating work is continuing at SYNTERIALS[8]. Two batches of CVD coated SiC whiskers were received during this current contract period. For the batch labeled #2-88 the coating was applied to Tateho SiC whiskers[9]. Fig. 5 is an SEM photograph showing that a coating was deposited on these whiskers. The bulk oxygen content was significantly lower than observed in similar material prepared in Phase I (3.2 vs 8.1%). This is significant since the oxygen most likely exists as B_2O_3 which can form a low melting glass at the grain boundaries reducing high temperature properties. Auger analysis was combined with sputtering to determine composition as a function of depth. The results in Figure 6 show that both carbon and BN were deposited on the whiskers. The data does not represent the desired multilayer configuration of SiC over BN. It appears as though carbon and BN were co-deposited on the whiskers. The BN stoichiometry is improved over earlier samples (B:N, 1.4:1 vs 2:1).

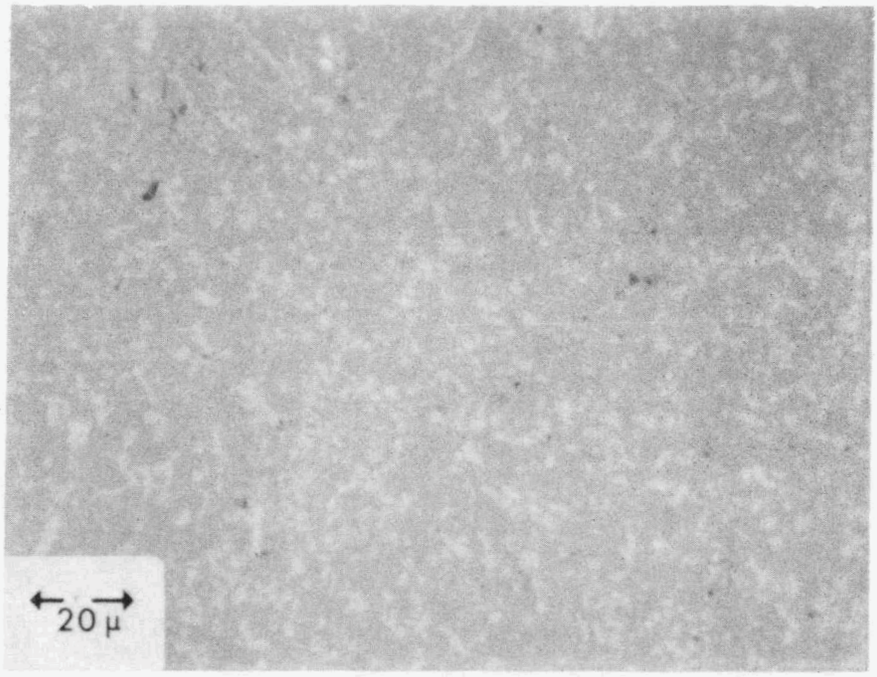

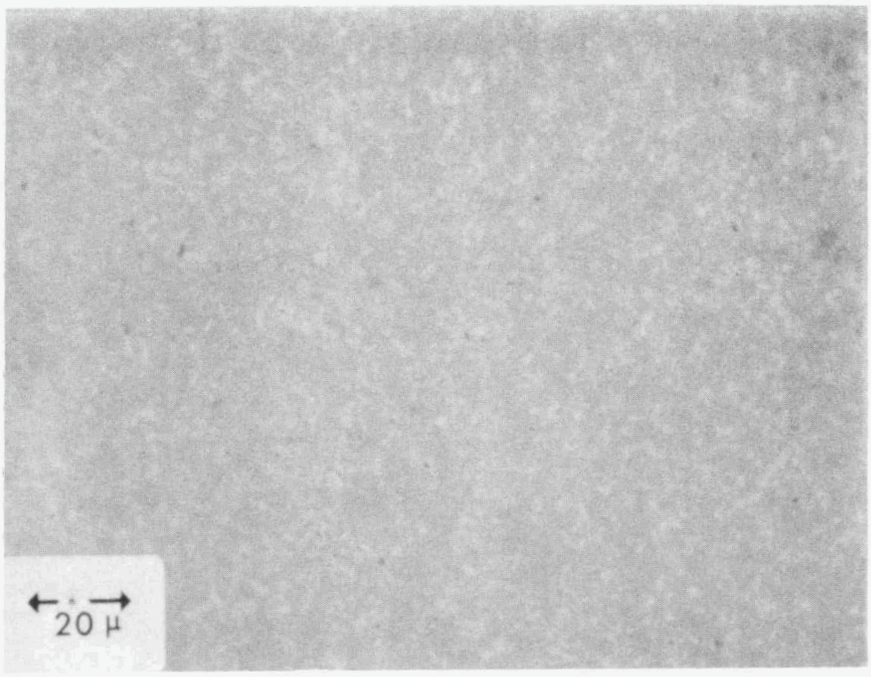

Figure 4: Composite microstructures with sized Huber SiC whiskers.
TOP: Coarse fraction BOTTOM: Fine fraction

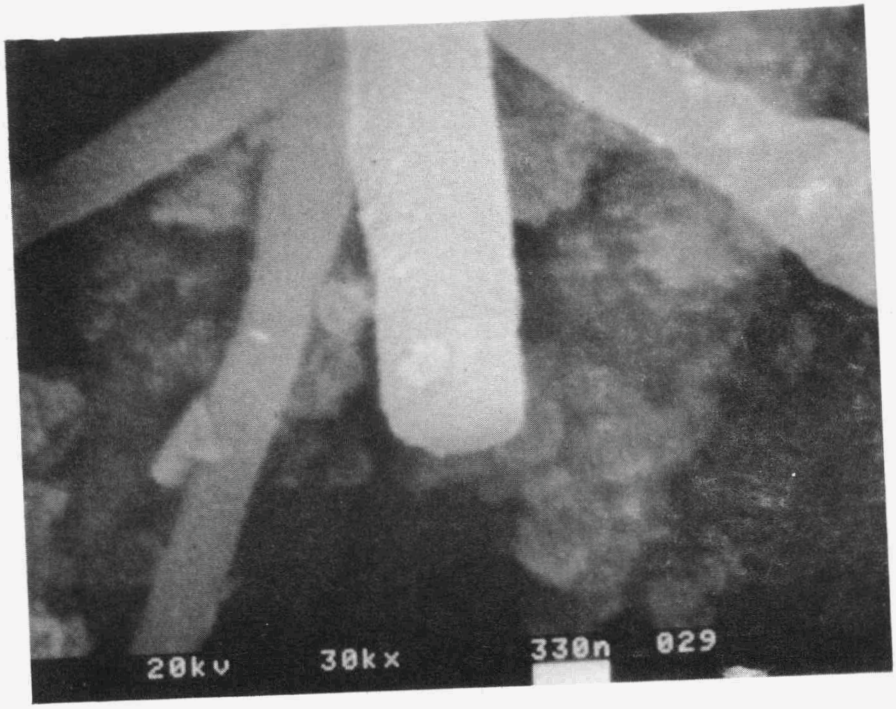

Figure 5: SEM of CVD coated Tateho SiC whisker received 2/88.

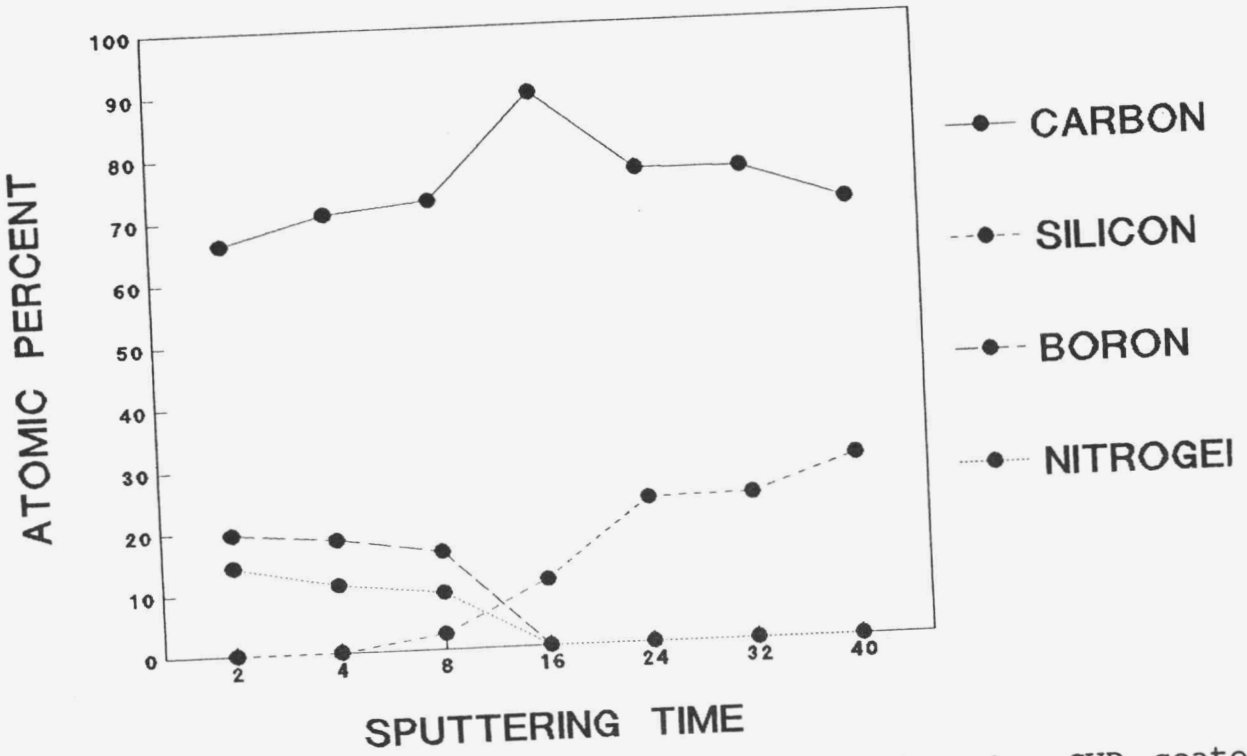

Figure 6: Surface composition vs. sputtering time for CVD coated Tateho SiC whisker received 2/88.

A second lot of CVD coated whiskers (LOT #3/88) utilized American Matrix SiC whiskers.[10] Auger analysis combined with sputtering was conducted on four different whiskers within the lot to determine surface composition. In general, surface composition varied from whisker to whisker. For example, Auger data in Fig. 7 shows boron and nitrogen at the surface of a whisker which gradually changes to silicon and carbon with sputtering time. Another whisker (Fig. 8) shows only a small quantity of boron and nitrogen at the surface with the balance being carbon. The different results demonstrate the difficulty in coating all whiskers within a batch. As with the other batch of coated whisker just described, it appears that carbon rather than SiC was deposited on the whiskers as an over coating. SEM analysis of this batch confirms the Auger data that some whiskers are coated where others are not (see Fig. 9).

The current status of this coating effort is that the deposition of BN is improving as evidenced by its better stoichiometry and lower oxygen content over earlier work. There is still difficulty in the deposition of a SiC overcoat and coating all whiskers within a batch. It has been demonstrated that coatings can be applied to different whisker materials having different diameters (Tateho ~0.4um, Amer. Mat. ~2.0um). Composites will be prepared using these coated whiskers to determine if enhancements in fracture toughness are observed.

In addition to the CVD effort being conducted at SYNTERIALS Norton is developing in-house whisker coating technologies. An effort in CVD coatings is being developed at Norton Diamond Technology Research Center in Salt Lake City, Utah. This group has extensive experience in the application of CVD coatings in a fluidized bed reactor. The initial effort will be in modifying the current process for the deposition of BN on SiC grit to be followed by coating SiC whisker. It is anticipated that alternatives to fluidization will be required for coating the whisker materials.[11] To date the CVD system has been modified to accommodate this project. The gases, and mass-flow controllers used in BN deposition were added to the system. The RF generator was serviced and the CVD cabinet was modified for the temperatures needed for BN deposition. The first BN coating runs have been completed on SiC grit. This material is currently under evaluation.

The application of coatings to whiskers by solution methods is also being conducted at Norton utilizing our experience in this area. Initial work is focussed on modifying grain boundary composition and thickness by coating whiskers with oxides. SEM revealed that most whiskers have been coated using this process, however, whisker bundles were also engulfed in what appeared to be large precipitates. Figure 10 shows a coated whisker from this process. Efforts to increase coating thickness and morphology are under way.

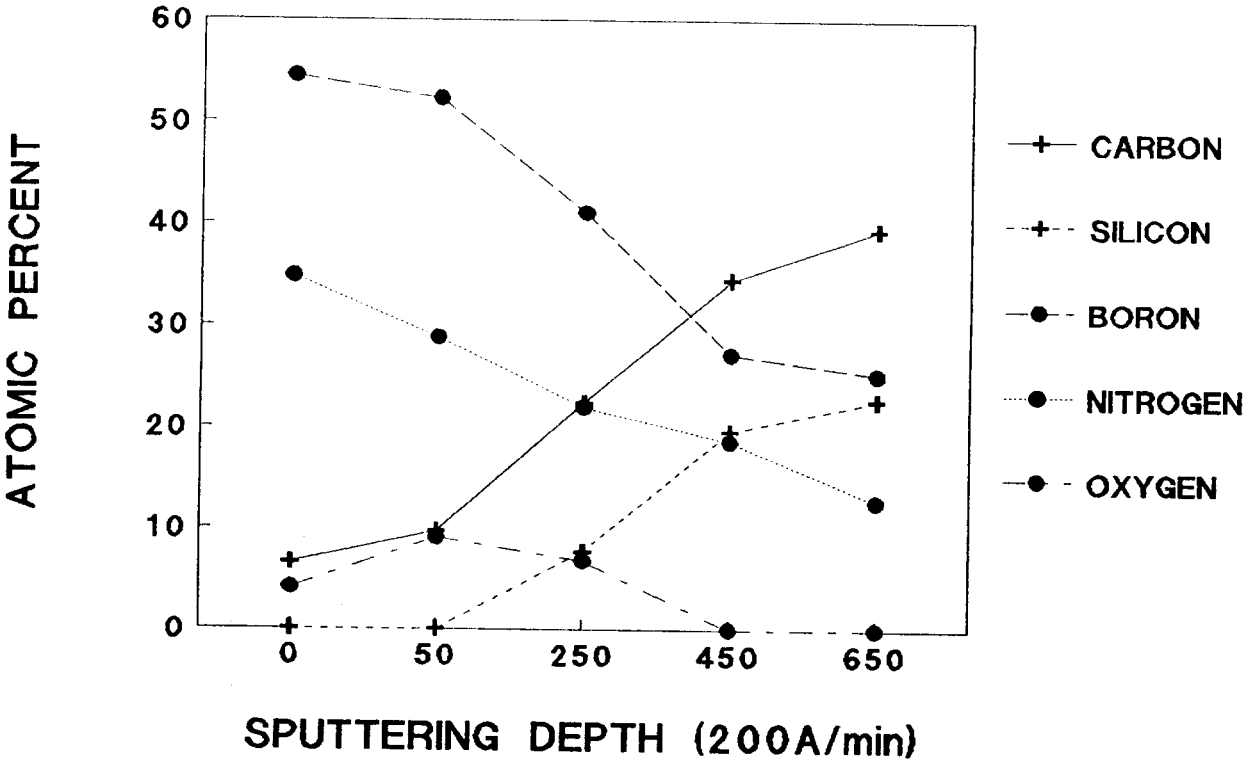

Figure 7: Surface composition vs. sputtering depth for CVD coated American Matrix whisker with BN rich surface.

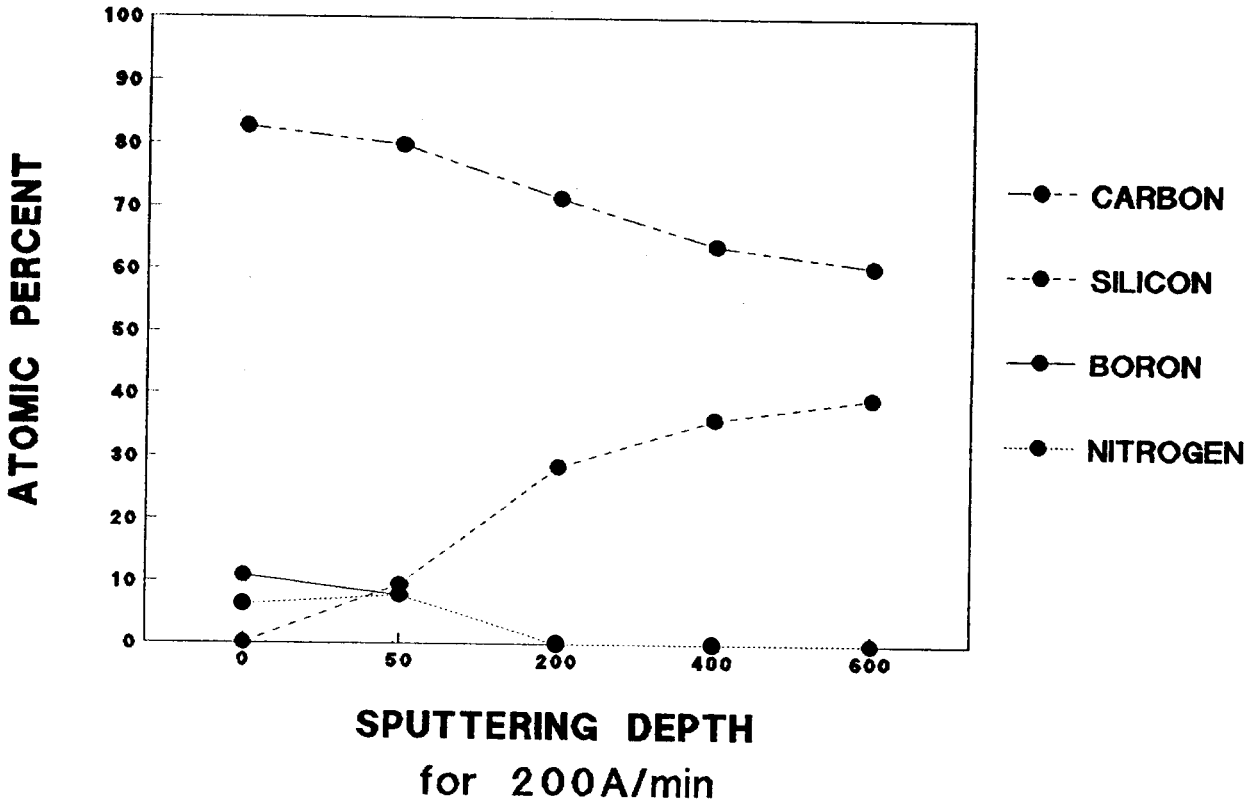

Figure 8: Surface composition vs. sputtering depth for CVD coated American Matrix whisker with carbon rich surface.

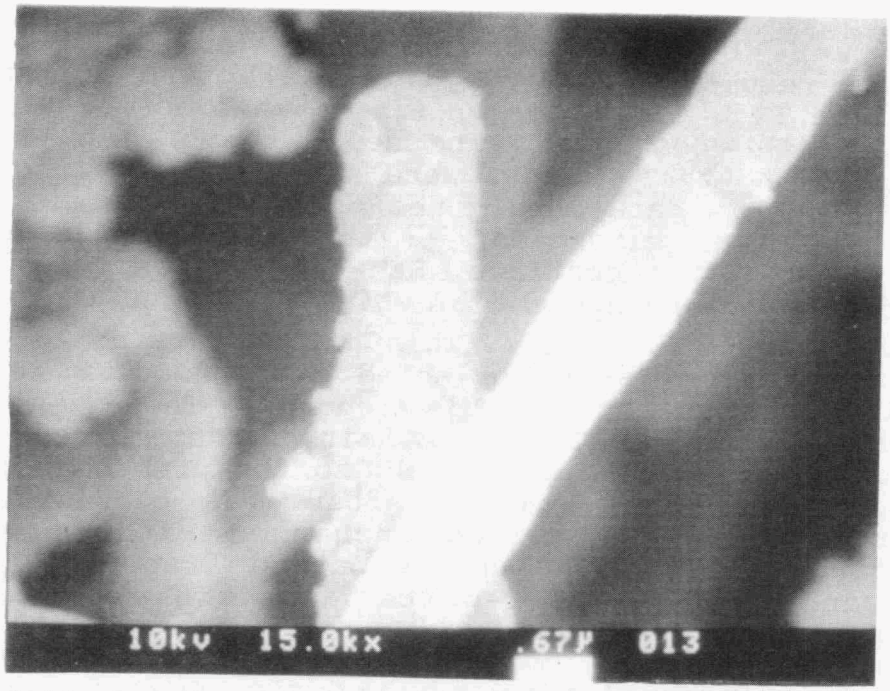

Figure 9: SEM of CVD coated American Matrix whisker received 3/88.

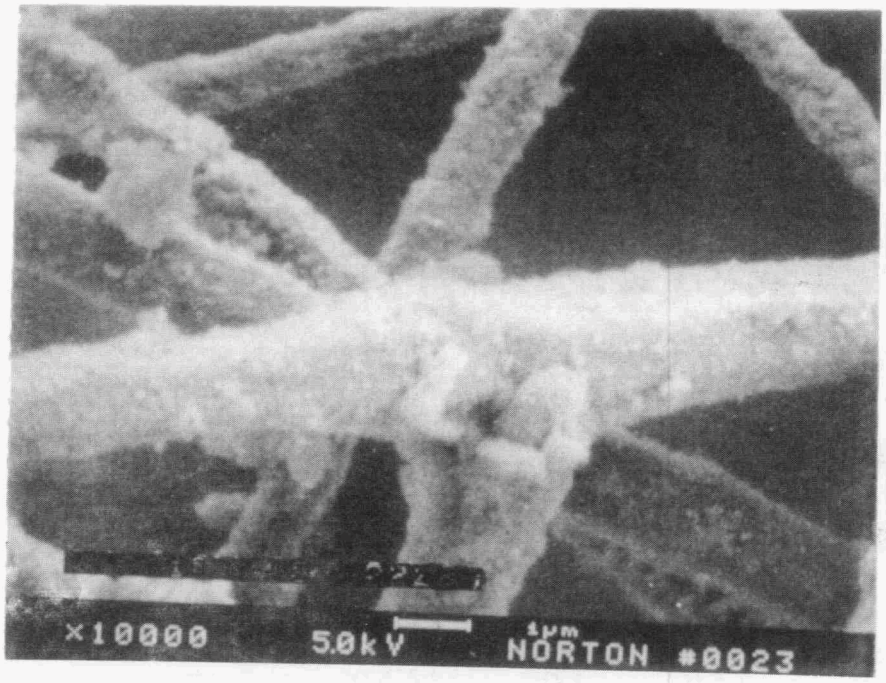

Figure 10: SEM of solution coated American Matrix whisker.

Composites with Coated Whiskers - The coated whiskers evaluated previously[1] were blended into Si_3N_4 powder and HIPed to full density. The resulting controlled flaw fracture toughness values are reported in Fig. 11. No significant influence can be detected as a result of the coatings. It should be noted that the actual coatings applied to the whiskers were not stoichiometric BN nor SiC and as a result this data should not be interpreted as representative of an optimized situation. Although these results did not show much effect of the coatings, SEM observations of the fracture surfaces did show an enhancement of whisker pullout in these composites as shown in Fig. 12. This discrepancy could be a result of the quantity of whiskers oriented perpendicular to the crack plane as discussed later in this report. These materials were oxidized for 100 hrs. at 1000°C in air to determine if a catastrophic oxidation problem results due to the presence of carbon as reported by Knoch and Gazza[12]. After this oxidation treatment sample microstructures remained unchanged with no evidence of sample bloating. The weight change data is reported in Table 5. The discrepancy for these results with the reported data of Knoch[12] is not understood at this time.

Composites reinforced with treated SiC whiskers show promise for increasing the fracture toughness of these materials. As shown in Fig. 13 the fracture toughnesses are ~6 MPa(m)$^{.5}$ where typical results for similar materials are generally less than 5 MPa(m)$^{.5}$

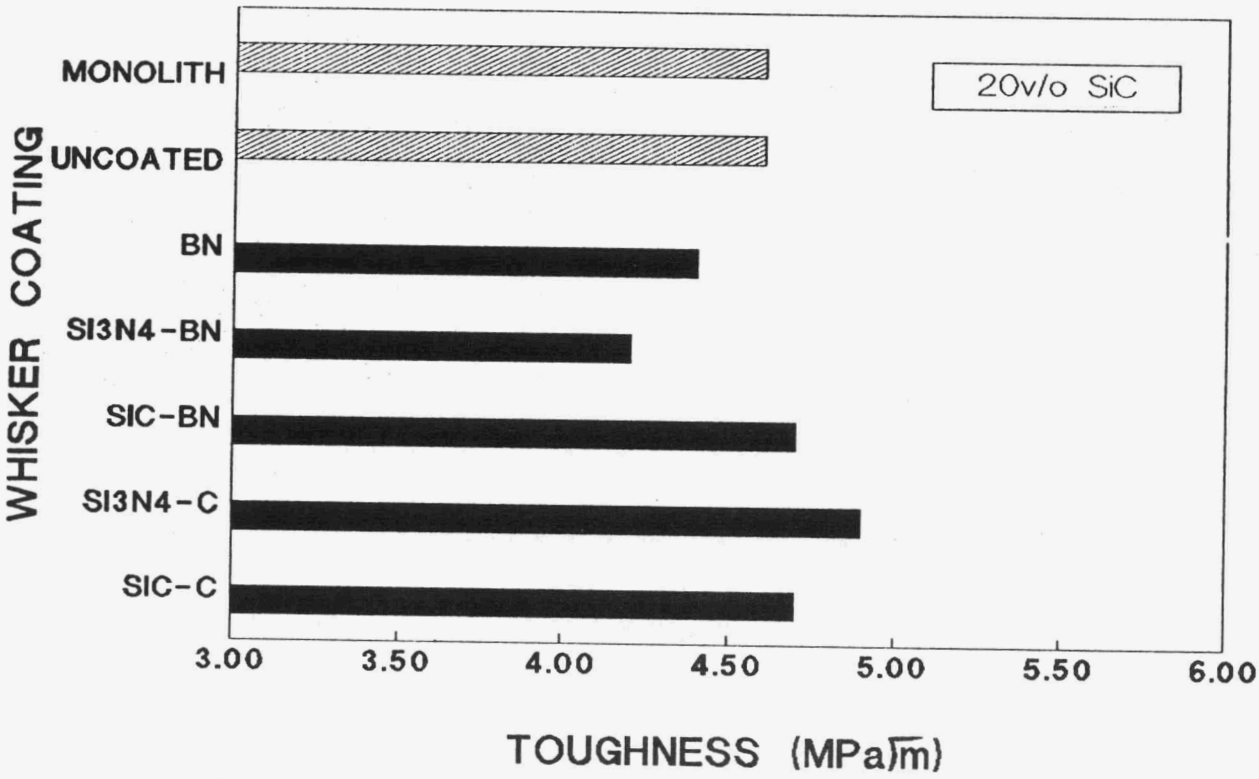

Figure 11: Control flaw fracture toughness of coated whisker reinforced Si_3N_4 composites.

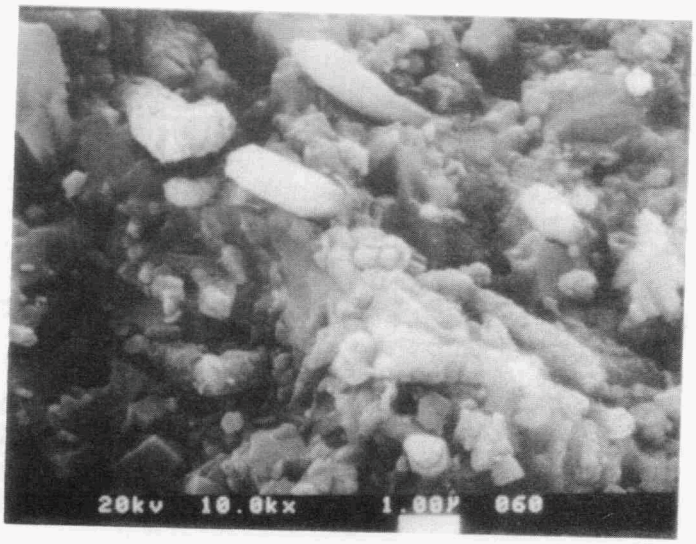

Figure 12: Fracture surface of an Si_3N_4 matrix composite reinforced with CVD coated (SiC over C) SiC whiskers.

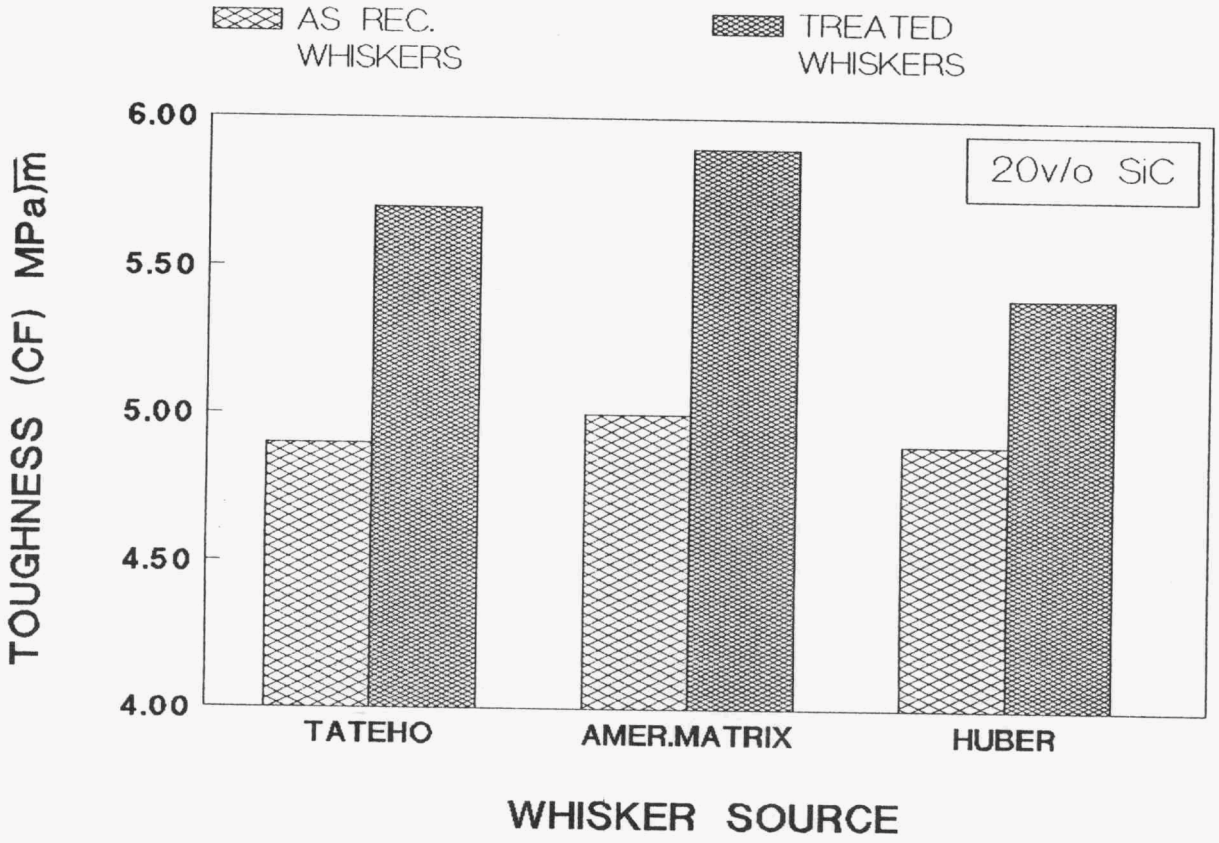

Figure 13: Control flaw fracture toughness of treated whisker reinforced Si_3N_4.

3.0 GREEN BODY

Forming - Table 6 lists the porosity of both green and nitrided samples, and densification shrinkage as a function of forming process (IM, CIP). Typical values for Si_3N_4 powder monoliths and composites are also listed for comparison and clarification. Currently neither the matrix powder or whisker size distribution have been optimized to maximize packing. A high packing density will minimize densification shrinkage. Decreasing the current shrinkage values for both the monolith and for the composite is a goal. Use of an SRBSN matrix can result in lower shrinkage during densification as compared to a Si_3N_4 powder matrix. For CIP, higher whisker loadings lower the packing density significantly. The whisker loading does not decrease the packing density of injection molded mixtures (IM) as severely as cold isostatically pressed (CIP). The reasons probably relate in some manner to improved dispersion and/or whisker orientation in the former case.

Injection Molding - The IM process was employed to achieve better whisker/matrix dispersion uniformity, higher green density and preferential whisker alignment to optimize microstructure and toughness. Monolith (Si + 4% Y_2O_3) and composite (Si + 4% Y_2O_3 + 30 v/o SiC whiskers) test bars were injection molded into net shape dimensions of 3mm x 4mm x 50 mm. Prior to injection molding, wettability/dispersability of silicon powder and SiC whiskers with the presence of various dispersants (in the binder system) was evaluated using Brookfield viscometry. A paraffin based binder system was employed in the molding process. Suspensions were prepared using up to 60 w/o silicon powder or SiC whiskers and resulting viscosities were measured at three different shear rates. From these tests compatible surfactants were identified which helped reduce the viscosity by a factor of three at 60 w/o solids loading in the suspension. It is anticipated that an optimized powder/whisker mixture packing density will result in lower binder requirements for molding.

The injection molded bars were debinderized in a vacuum furnace with a controlled heating cycle. Visual examination did not reveal any cracking problem. Subsequent to dewaxing, test bars were nitrided and densified by HIP to full theoretical density. Microstructural evaluation of the IM composite showed a very homogeneous dispersion of the whiskers (Fig. 14), as well as a moderate degree of whisker orientation. Controlled flaw K_{IC} values were measured for both the IM monolith (4.5 ± 0.5 MPa $(m)^{.5}$) and composite (6.3 ± 0.3 MPa $(m)^{.5}$) bars. The composite K_{IC} value was 40% higher than the monolith. Orientation of the whisker axis perpendicular to the crack plane may account for this relatively large K_{IC} increase.

4.0 DENSIFICATION STUDIES

Studies to determine the effect of sintering aid composition and quantity on fracture toughness are underway. At this time materials are in process and awaiting microstructural and property evaluations.

TABLE 5

Weight Changes After 100 hr. Oxidation in Air at 1000°C

MATRIX[a]	WHISKER	WHISKER COATING	% WT[b]	SPECIMEN CODE
SRBSN	Mono	-	0	25 #35
SRBSN	Tateho	No coating	0	9C #35
Si_3N_4	Tateho	BN/SN	0	2090B #23
Si_3N_4	Tateho	C/SiC	-3.0%	2090C #23
Si_3N_4	Tateho	C/Si_3N_4	-1.7%	2090D #23

a = 4 w/o Y_2O_3 in matrix, HIPed materials.

b = specimen 3mm x 4mm x ~25mm

TABLE 6

GREEN POROSITY VS. FORMING TECHNIQUE

FORMING PROCESS	MATERIAL	(% POROSITY) GREEN	(% POROSITY NITRIDED	(% SHRINKAGE)
CIP	SRBSN	42	32	
CIP	30% SiC-w/SRBSN	49	40	
CIP	Si_3N_4	47	NA	
CIP	30% SiC-w/Si_3N_4	48	NA	
IM	SRBSN	41	29	9.3
IM	30% SiC-w/SRBSN	47	37	16.0

*All materials made using 4 w/o Y_2O_3 as sintering aid and Tateho T44 Grade SiC whiskers. Densified using HIP.

CIP - Cold Isostatic Press (30 ksi)
IM - Injection Mold

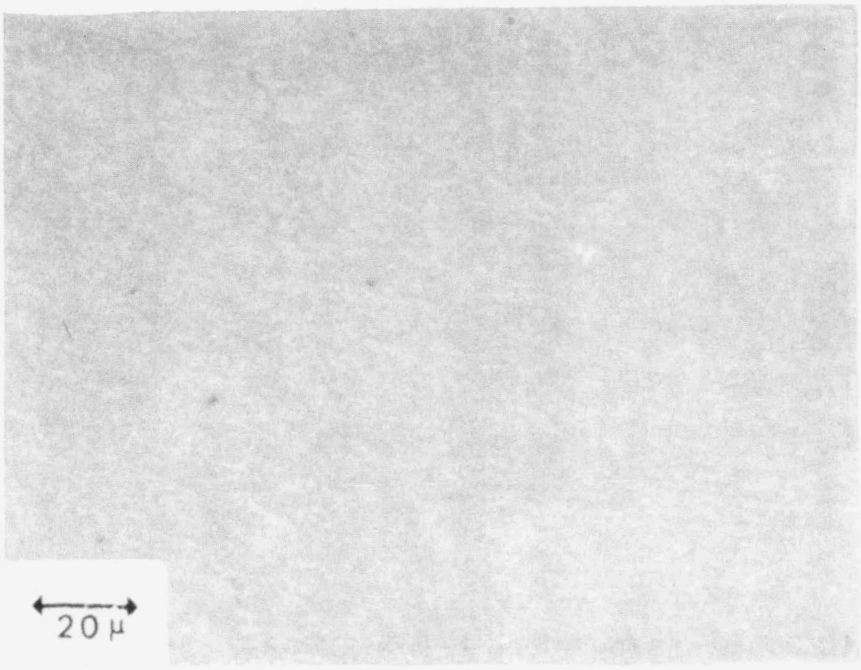

Figure 14: Microstructure of injection molded SRBSN/SiC whisker composite after densification by HIP.

5.0 PROPERTY PROGRESS

Composites which show promise from the screening studies will be prepared into large batches to allow for extensive property evaluations. Of particular emphasis are Weibull modulus, fracture toughness to 1400°C, oxidation resistance, and stress rupture behavior at 1400°C. Three materials were prepared under Phase I and the data is reported elsewhere[1].

The recent materials (Vintage August 87) consist of a monolith and composite prepared by the HIPed SRBSN route. Table 7 lists the data available on these materials. Fracture toughness of the composite is 24% greater than the monolith. The composite also has a higher room temperature flexural strength. Fractography revealed that the strength limiting flaws in the composite were either machining flaws or SiC particulates on the order of 10 to 20 microns. The flaw origins of the monoliths were either machining flaws or ~10 micron porous regions with a high iron content. Stress rupture life was determined at 1370°C. The monolith could survive a 250 MPa load for >200 hrs with the composite able to withstand a 225 MPa load for >260 hrs. Testing was suspended after

TABLE 7

LARGE BATCH MATERIAL - Vintage Aug. 87

	Monolith (3x015)	Composite (7x014)
RT[a]	662 ± 14 MPa (3)*	772 ± 55 MPa (3)
1370°C[a]	517 ± 62 MPa (3)	420 ± 21 MPa (3)
K_{IC} (CF)[b]	4.2 ± .3 MPa(m)$^{.5}$ (3)	5.2 ± .1 MPa(m)$^{.5}$ (3)
K_{IC} (IN)[c]	3.9 ± .1 MPa(m)$^{.5}$	4.2 ± .1 MPa(m)$^{.5}$
Hardness[d]	16.0 ± .2 GPa	18.4 ± .3 GPa
Density	3.24 g/cc	3.23 g/cc
Oxygen	2.5 w/o	1.7 w/o
Nitrogen	37.9 w/o	27.8 w/o
XRD (major)	β-Si_3N_4	β-Si_3N_4, β-SiC
XRD (trace)	$Y_2Si_2O_7$	α-Si_3N_4

Stress rupture life
at 1370°C

Load		
225 MPa	N/A	>260 hrs.
250 MPa	>200 hrs.	5.2 hrs.
275 MPa	~150 hrs.	N/A
300 MPa	3.5 hrs.	N/A

- 4% Y_2O_3 in matrix, 30 v/o Tateho T44 SiC(w)
*number of data points in parenthesis.

a) Mil-STD-1942 (MR), 3x4mm bar, 40/20 span

b) Chantikul et al, J. Amer.Cer.Soc. 64, #9, p539 (1981) with 10 kg indent and MIL-STD-1942 (MR) bar

c) Antis et al J. Amer.Cer.Soc.64, #9, p533 (1981), with 10 kg indent, average of five indents, crack length measured at 400x magnification.

d) Vickers indent at 10 kg

these respective times. Identical stress rupture testing conditions resulted in the composite undergoing more deformation than the monolith. Considering the high temperature property results of the composite, it is felt that the most important parameter for improving high temperature srength, stress rupture life, and creep resistance, is lowering the impurity content of the whiskers. The whiskers used in this composite have a rather high concentration of aluminum, calcium, and iron (see Table 2). These impurities are known to lower the the high temperature performance of Si3N4 based materials. Future efforts to lower the impurity concentrations in SiC whiskers are being planned.

6.0 TOUGHENING ISSUES

As shown in Table 8 there are many microstructural issues which need to be addressed when considering toughening Si_3N_4 with SiC whiskers. Recent studies[13,14,15] have observed the effect of whisker uniaxial, planar and random orientations on fracture toughness in the Si_3N_4/SiC whisker system. As shown in Fig. 15, taken from reference 15 fracture toughness is maximized when the whisker axes are 90 degrees to the crack plane for a composite with uniaxially aligned whiskers. If one uses a window for optimum orientation (e.g. ±15 degrees), knows the quantity of whiskers in the composite (volume % loading) and knows the orientation of whiskers in the composite (random, planar, uniaxial), then the quantity of whiskers 90 degrees (± window) to the crack plane can be calculated from simple geometry. This is done in Table 9 for the case of random alignment with different whisker loadings and different windows for optimum orientation. As shown, the quantity of whiskers available for crack wake bridging is much lower than the whisker loading in the composite. Considering this, major increases in the fracture toughness of composites with random whisker orientation appear unlikely unless toughening mechanisms, in addition tothe whisker bridging of cracks are present or the optimum angle window is expanded. It is anticipated that mechanisms observed in coarse grained alumina[16] would be beneficial for Si_3N_4 based composite systems.

7.0 SUMMARY

The effort on applying coatings by CVD is showing improvement in terms of BN stochiometry and lower oxygen content. There is still difficulty in depositing a SiC overlayer and in coating all whiskers within a batch. Initial attempts using solution methods to apply oxide coatings show promise. Treatments of whiskers to modify their surface composition prior to incorporation into the matrix have demonstrated significant improvements in fracture toughness (~6.0 $MPa(m)^{.5}$) over untreated whiskers (~5.0 $MPa(m)^{.5}$.

Whisker orientation has a large effect on fracture toughness. Whisker alignment as a result of injection molding has consistently resulted in composites with a fracture toughness of 6.3 $MPa(m)^{.5}$. For this result, unmodified interfaces are used. It is anticipated that higher fracture toughness values will be obtained when the interfacial bond strength is lowered.

Finally, the composite processing route we are using (HIP'ed SRBSN) can consistently prepare fully dense composites with uniform whisker distributions. The current properties of composites with randomly oriented whiskers and unmodified interfaces have a fracture toughness of 5.2 $MPa(m)^{.5}$ and room temperature flexural strengths of 772 MPa. Improvements in the high temperature properties of the composites will require higher purity SiC whiskers.

TABLE 8

Microstructural Features
In Si_3N_4/SiC Composites

SiC Whisker	Si_3N_4 Matrix	Intergranular Phases
Diameter*	Vol. Frac.*	Y_2O_3*
Vol. Frac.*	Size	Vol. Frac.
Length	Shape	SiO_2
Total#		Thickness
Spacing		Crystalline
Aspect Ratio		Amorphous
Orientation		Distribution

*Processing Independent Variable

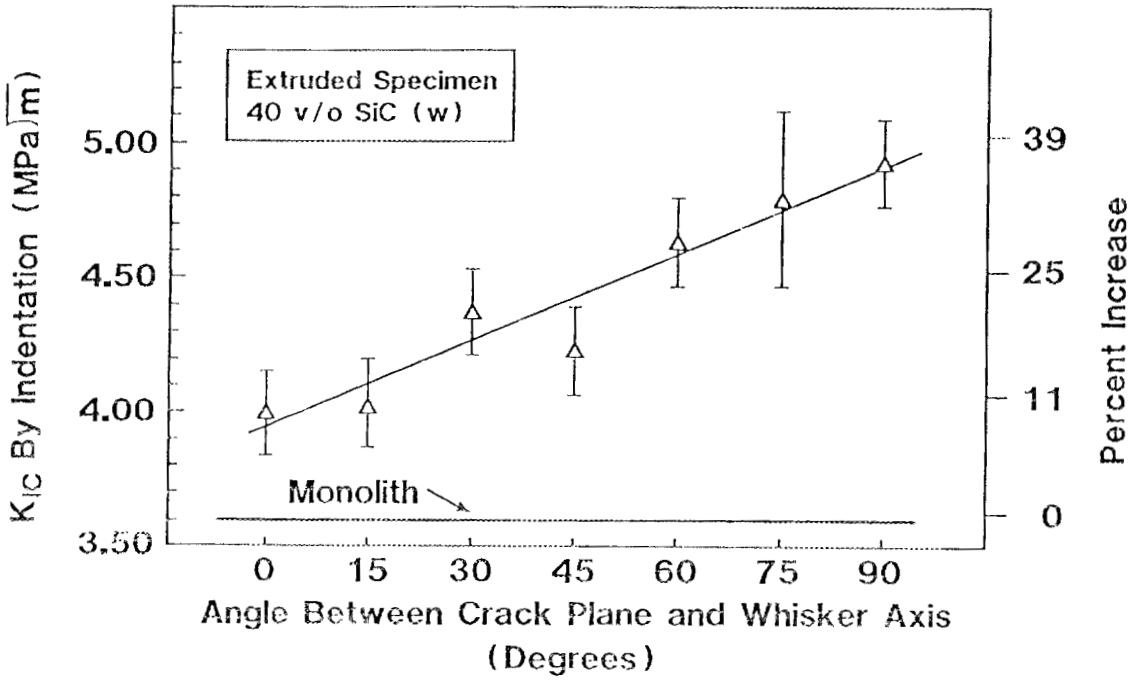

Figure 15: Effect of the angle between whisker axis and crack plane on fracture toughness in SiC whisker reinforced Si_3N_4.

TABLE 9

WHISKERS AVAILABLE FOR BRIDGING IN
COMPOSITES WITH RANDOMLY ORIENTED WHISKERS

Optimum Toughness Window	Whisker Loading in Composite		
	100 v/o SiC	40 v/o SiC	20 v/o SiC
90 ± 15°	3.4% v/o	1.4 v/o	0.7 v/o
90 ± 30°	13.4 v/o	5.4 v/o	2.7 v/o
90 ± 45°	29.3 v/o	11.7 v/o	5.9 v/o

Status of milestones

All milestones are on schedule.

Publications

1. C. A. Willkens and N. D. Corbin, "Development of Toughened Si_3N_4 Composites by Glass Encapsulated Hot Isostatic Pressure," to be published in The Proceedings of the Twenty-Fifth Automotive Technology Development Contractors' Coordination Meeting, Detroit, MI, October, 1987.

2. N. D. Corbin and C. A. Willkens, "Development of Toughened Si_3N_4 Composites by Glass Encapsulated Hot Isostatic Pressure," Final Report for Contract #86X-95906C-Phase I, In Process.

References

1. N. D. Corbin and C. A. Willkens, "Development of Toughened Si_3N_4 Composites by Glass Encapsulated Hot Isostatic Pressure", Final Report for Contract #86X-95906C-Phase I, In Process.

2. MIL-STD-1942 (MR), Flexural Strengths of High Performance Ceramics at Ambient Temperature, November 21, (1983).

3. Antis, G., Chantikul, P., Lawn, B., Marshall, D., "A Critical Evaluation of Indentation Techniques for Measuring Fracture Toughness: I, Direct Crack Measurements," Journal of the American Ceramic Society, Vol. 64, #9, p.533-538, Sept. 1981.

4. Chantikul, P. Anstis, G., Lawn, B., and Marshall, D., "A Critical Evaluation of Indentation Techniques for Measuring Fracture Toughness: II, Strength Method," Journal of the American Ceramic Society, Vol. 64, #9, P.539-543, Sept. 1981.

5. Developed by J. Geller of Geller Microanalytical Laboratory, Peabody, MA.

6. Nutt, S.R., "Defects in Silicon Carbide Whiskers," J. Amer. Ceram. Soc., Vol. 67, No. 6, June (1984).

7. Product Literature, American Matrix Inc., Knoxville, TN.

8. Synterials, Herndon, VA

9. Tateho Chemical Industries Co., Ltd., JAPAN, SCW #1, Rec. 12/85.

10. American Matrix Inc., Knoxville, TN, SiC Whisker Generation 4, Rec. 2/88.

11. Zachrich, D., "Personal Communication," Norton Company, Diamond Technology Center, Salt Lake City, UT.

12. H. Knoch and G. Gazza, "Carbon Impurity Effect on the Thermal Degradation of A Si_3N_4-Y_2O_3 Ceramic", AMMRC TR #79-27, May, 1979, Army Materials and Mechanics Research Center, Watertown, MA.

13. V. K. Pujari, C. A. Willkens, and N. D. Corbin, "Injection Molding of Si_3N_4-SiC Whisker Composite", presented at the 89th Annual Meeting of the American Ceramic Society, April 26-30, 1987, Pittsburg, PA.

14. C. A. Willkens, N. D. Corbin, and V. K. Pujari, "Properties of Injection Molded Si_3N_4-SiC Whisker Composites", presented at the 40th Pacific Coast Regional Meeting of the American Ceramic Society, November 1-4, 1987, San Diego, CA.

15. N. D. Corbin, et al, "The Influence of Microstructure Orientation on the Fracture Toughness of Si_3N_4 Based Materials", to be published in The Proceedings of the 12th AnnualConference on Composites and Advanced Ceramic Materials, January 18-20, 1988, Cocoa Beach, FL.

16. Swanson, P.L., Fairbanks, C.J., Lawn, B.R., Mai, Y.W., Hockey, B.J., "Crack-Interface Grain Bridging as a Fracture Resistance Mechanism in Ceramics: I, Experimental Study on Alumina, J. Amer. Ceram. Soc., Vol. 70, No. 4, p279-89 (1987).

1.2.3 Oxide Matrix

Dispersion-Toughened Oxide Composites

T. N. Tiegs, L. A. Harris, and J. W. Geer (Oak Ridge National Laboratory)

Objective/scope

This work involves development and characterization of SiC whisker reinforced oxide composites for improved mechanical performance. To date, most of the work has dealt with alumina as the matrix because it was deemed a promising material for initial study. However, a new effort in SiC whisker reinforced-sialon is being initiated. Emphasis in the new system will be on pressureless sintering and control of the whisker-matrix interface properties.

Technical progress

SiC whiskers – Previous results showed that SiC whisker surface chemistries could be modified by heat treatments to improve the fracture toughness of alumina-matrix composites. The effect is also being examined in sialon-matrix composites as previously described. Three batches of whiskers from different sources were treated and examined for bulk chemistry mistry changes (Table 1). The surface chemistry changes by ESCA will be also be determined. As shown in Table 1, the overall impurity levels are generally reduced by the treatment.

Table 1. Chemical analysis of selected SiC whiskers (ppm)[a]

Chemical	American Matrix[b]		ARCO Chemical[c]		Tateho Chemical[d]	
	As received	After treatment	As received	After treatment	As received	After treatment
Al	20	100	50	200	100	200
B	>1000	200	3	3	3	3
Ca	400	200	400	400	400	400
Co	<1	<1	1	1	<1	<1
Cr	50	3	100	50	20	20
Fe	200	5	200	200	200	200
K	100	10	100	20	20	20
Mg	100	10	100	30	30	10
Mn	3	1	300	100	30	30
Na	100	10	100	30	5	30
Ni	20	3	20	20	5	10
Zn	5	<3	50	1	<3	1
Zr	10	<1	3	<1	<1	30

[a]Analysis by spark source mass spectrometry, accuracy ±50%.

[b]American Matrix, Inc., Knoxville, TN, Grade #1, received 9/87.

[c]ARCO Chemical Co., Greer, SC, Grade SC-9, received 2/84.

[d]Tateho Chemical Co., Ako, Japan, Grade SCW-1S, received 1/86 (cleaned by sedimentation).

In addition to the effect on bulk chemistry, the heat treatments also affect the surface chemistry of the whiskers. The changes in fracture toughness with different heat treatments for alumina matrix composites using Tateho SiC whiskers was described previously.[1] The surfaces of the as-received and heat-treated American Matrix SiC whiskers were examined with X-ray photoelectron spectroscopy (XPS). The results showed that the heat treatment reduced the surface silica content to near zero (Fig. 1). At the same time the surface carbon peaks showed a shift to a more SiC-like surface with a reduction of the bonding attributable to C-C and C-H bonds (Fig. 2). These whiskers were used in the composites described below.

Sialon-SiC whisker composites - It has been determined that the fracture toughness improvements of alumina-SiC whisker composites were a direct result of increased crack-whisker interactions. For the toughening mechanisms to operate, debonding along the whisker-matrix interface is necessary. The same requirements are believed to be necessary in sialon/silicon nitride-SiC whisker composites for improved toughness. Previous results showed that SiC whisker surface chemistries could be modified by heat treatments to change the bonding behavior and the fracture toughness of alumina matrix composites.

The effect of changing the whisker surface chemistry of a silicon nitride (6% Y_2O_3/2% Al_2O_3) with 20 vol % SiC whiskers is shown in Table 2. As illustrated, modifying the surface did little to improve the fracture toughness in those composites. Examination of the fracture surfaces with an SEM revealed no apparent difference in the level of crack interaction (Fig. 3). Evidently in these composites where considerable amounts of liquid phases are present during densification, the bonding at the whisker-matrix interface is controlled by that liquid phase and the surface chemistry of the whisker is secondary. Additional composites have been fabricated and are currently being tested to further clarify these conclusions. Fractography of the test bars showed that the composites contained numerous defects apparently introduced with the whiskers which resulted in the somewhat low flexural strengths obtained. Procedures are being initiated to remove these prior to composite fabrication.

Additional Si_3N_4-matrix composites were fabricated with whisker contents of 10, 20, and 30 vol %. The results on the mechanical properties show improved toughness for the 20 and 30 vol % loadings as compared to the 10 vol % loaded composite (Table 3).

Table 2. Comparison of mechanical properties of Si_3N_4-20 vol % SiC whisker composites[a] using as received and heat-treated whiskers

	As-received whiskers	Heat-treated whiskers
Fracture toughness, K_{IC} (MPa$\sqrt{m}$)	5.5 ± 0.3	5.6 ± 0.6
Flexural strength, MPa	770 ± 39	764 ± 83

[a]Si_3N_4-6% Y_2O_3/2% Al_2O_3-20 vol % SiC; whiskers from American Matrix, received 9/87.

ORNL-DWG 88-2260

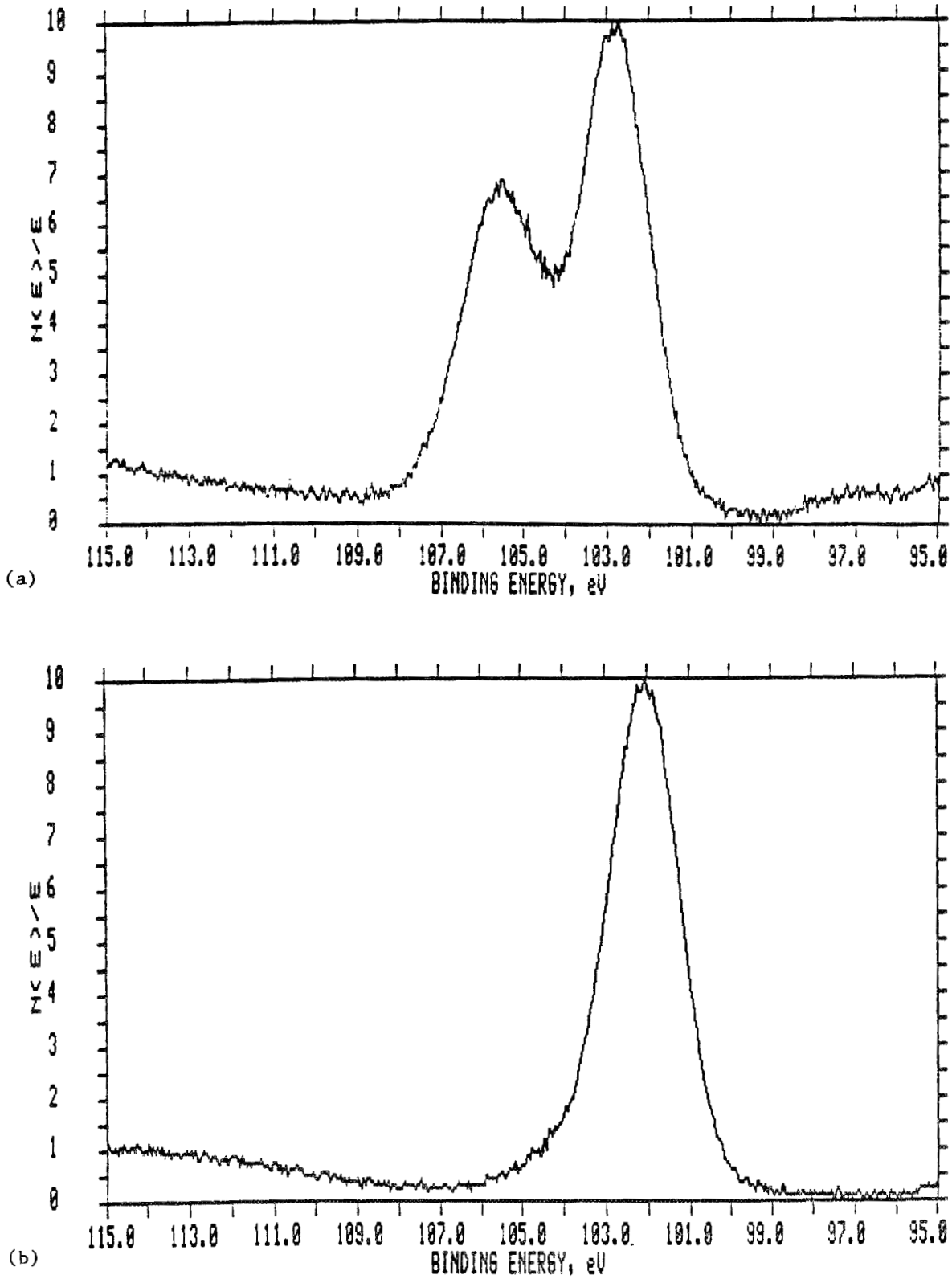

Fig. 1. X-ray photoelectron spectroscopy of silicon bonding energy peak on American Matrix SiC whiskers showing reduced surface silica content after heat treatment. (a) As-received surface. (b) Heat-treated surface.

ORNL-DWG 88-2261

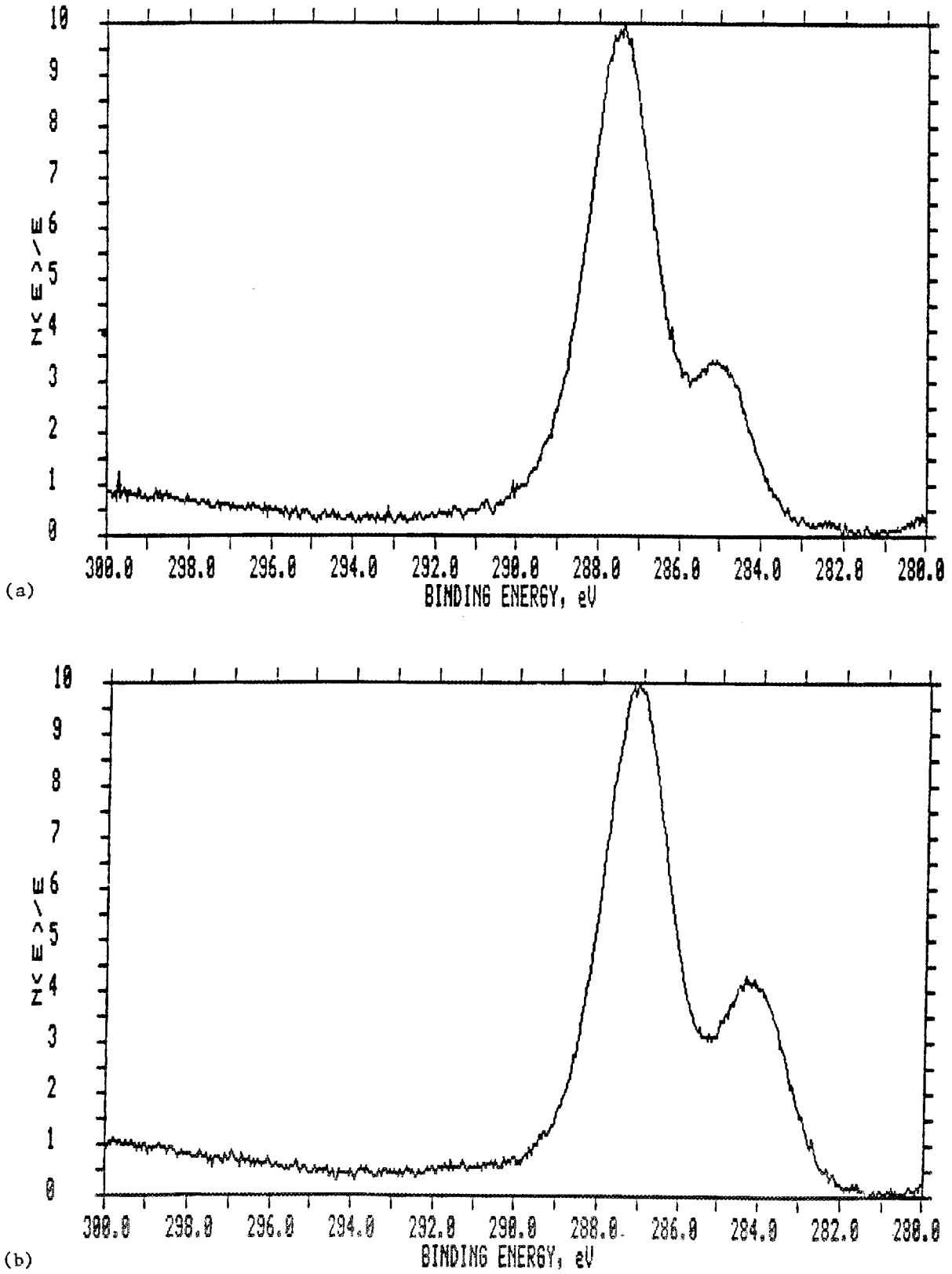

Fig. 2. X-ray photoelectron spectroscopy of carbon bonding energy peak on American Matrix SiC whiskers showing very little change in the nature of the surface carbon with heat treatment. (a) As-received surface. (b) Heat-treated surface.

M27683

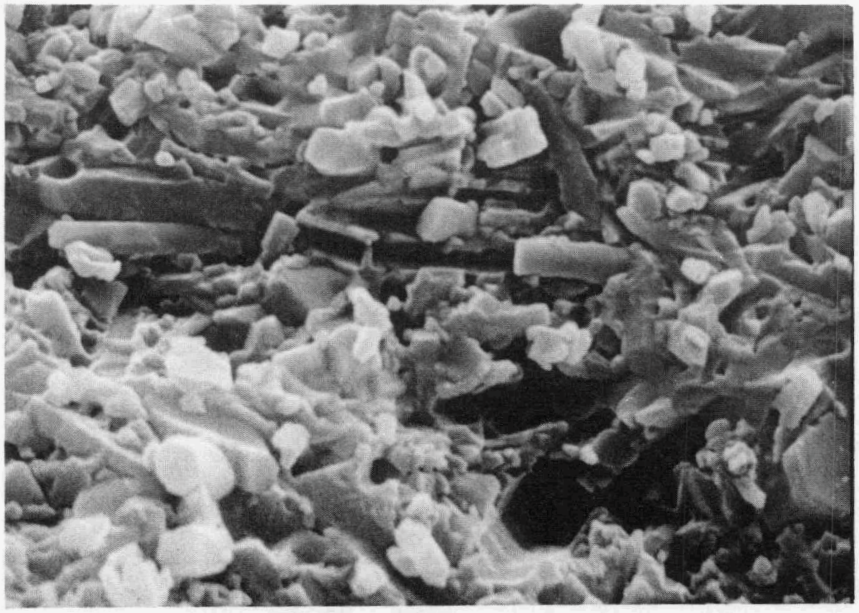

(a)

1.0 μm

M27678

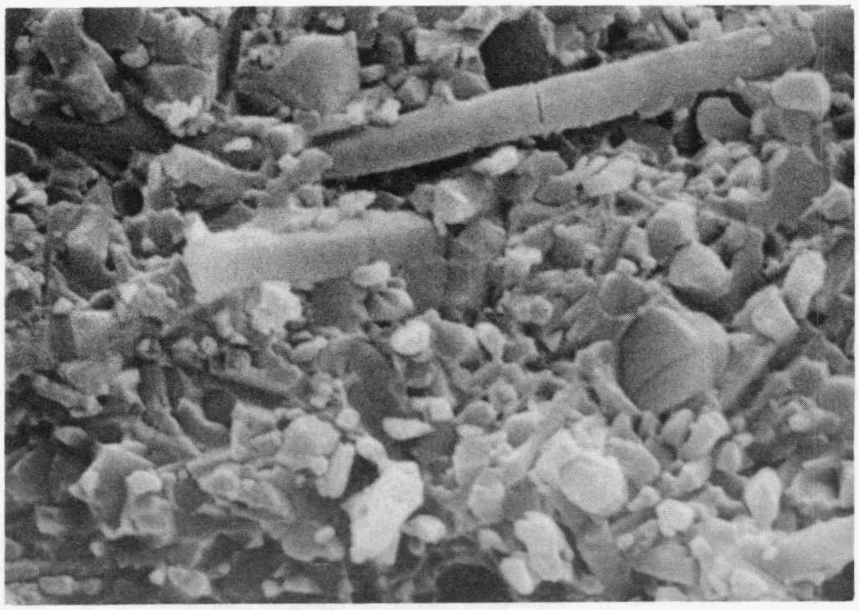

(b)

Fig. 3. Fracture surfaces of Si_3N_4-20 vol % American Matrix SiC whisker composites. (a) Using as-received whiskers. (b) Using heat-treated whiskers.

Table 3. Comparison of mechanical properties of Si_3N_4-matrix composites reinforced with SiC whiskers[a]

	Flexure toughness, K_{Ic} (MPa$\sqrt{m}$)[b]	Flexural strength (MPa)[c]
Si_3N_4-10 vol % SiC_w	4.8 ± 0.4	722 ± 44
Si_3N_4-20 vol % SiC_w	5.6 ± 0.6	764 ± 83
Si_3N_4-30 vol % SiC_w	5.7 ± 0.3	726 ± 58

[a]Si_3N_4 matrix had 6% Y_2O_3/2% Al_2O_3 added as sintering aids. Whiskers were heat-treated American Matrix, received 9/87.

[b]Fracture toughness determined by controlled flaw indent flexure test.

[c]Four-point flexure test.

Pressureless sintering - Pressureless sintering of the silicon nitride-SiC whisker composites is being examined as an alternative densification method to hot pressing or encapsulated HIPing. The initial results are given in Table 4. As shown, the densification is dependent on the whisker volume fraction and the liquid phase sintering aid content. These results are essentially identical to those generated for the alumina matrix composites. No apparent difference was observed between the two whisker types. The low densities noted at the higher sintering temperatures are attributable to excessive weight losses from matrix volatilization that inhibited densification.

Status of milestones

Due to problems with hot-pressing during the December 1987-January 1988 period, completion of Milestone 123106 has been delayed two months. All other milestones on schedule.

Publications

T. N. Tiegs, P. F. Becher, and P. Angelini, "Microstructures and Propertie of SiC Whisker-Reinforced Mullite," to be published in proceedings of Firs International Workshop on Mullite, Tokyo, Japan, November 9-10, 1987.

Reference

1. T. N. Tiegs, L. A. Harris, and J. W. Geer, "Dispersion Toughened Oxide Composites," *Ceramic Technology for Advanced Heat Engines Project Semiannual Progress Report for October 1986 Through March 1987*, pp. 86-93, ORNL/TM-10469 (August 1987).

Table 4. Summary of results of pressureless sintering of SiC whisker-reinforced Si_3N_4-matrix composites

Whisker content (vol %)	Sintering aid content (wt %)	Sintering temperature (°C)	Sintered density (% T.D.)	Weight loss (%)
10[a]	$6Y_2O_3$, $2Al_2O_3$	1700	70.7	3.5
10[a]	$6Y_2O_3$, $2Al_2O_3$	1750	71.1	3.6
10[a]	$6Y_2O_3$, $2Al_2O_3$	1800	70.5	13.4
10[a]	$6Y_2O_3$, $2Al_2O_3$	1850	69.9	20.7
10[a]	$12Y_2O_3$, $4Al_2O_3$	1700	86.0	2.5
10[a]	$12Y_2O_3$, $4Al_2O_3$	1750	93.6	2.8
10[a]	$12Y_2O_3$, $4Al_2O_3$	1800	87.3	8.3
10[a]	$12Y_2O_3$, $4Al_2O_3$	1850	85.5	11.8
20[a]	$12Y_2O_3$, $4Al_2O_3$	1700	71.7	1.8
20[a]	$12Y_2O_3$, $4Al_2O_3$	1750	70.6	6.0
20[a]	$12Y_2O_3$, $4Al_2O_3$	1800	69.5	15.3
20[a]	$12Y_2O_3$, $4Al_2O_3$	1850	71.7	30.0
20[b]	$12Y_2O_3$, $4Al_2O_3$	1700	68.9	2.4
20[b]	$12Y_2O_3$, $4Al_2O_3$	1750	72.9	6.1
20[b]	$12Y_2O_3$, $4Al_2O_3$	1800	72.3	16.2
20[b]	$12Y_2O_3$, $4Al_2O_3$	1850	63.7	30.1

[a]American Matrix whiskers, acid-leached, received 9/87, no aspect ratio modification.

[b]Tateho Chemical Whiskers, received 1/86, no aspect ratio modification.

Processing of Improved Transformation-Toughened Ceramics

E. Lilley and G. A. Rossi (Norton Company)

Objective/scope

The objective of Phase IIA is to optimize the properties of two classes of transformation toughened ceramics, which were already studied in Phase I of this contract. These ceramics are Y-TZP (Y_2O_3 stabilized Tetragonal Zirconia Polycrystals) and Ce-ZTA (CeO_2-ZrO_2 toughened Al_2O_3).

For the Y-TZP materials one of the main efforts will be to study the low temperature degradation and understand how it is affected by microstructure and composition. In the case of the Ce-ZTA ceramics, the main goal is to optimize the high tempera-ture mechanical properties by minimizing the flaw size and con-trolling the microstructure.

The scope includes powder synthesis and characterization, shape forming, pressureless sintering, characterization of the ceramics and reporting of results.

Technical progress

Since Phase IIA was officially started on March 1st 1988, this report gives the results obtained in little more than a month of work.

1. Y-TZP CERAMICS

Yttria doped zirconia crude has been prepared by arc melting and rapid solidification for compositions of 4.5 and 5.3 wt.% Y_2O_3. This crude was Sweco milled to produce powder with an average diameter of 0.7 microns, measured by a Sedigraph. The resulting powders were dry pressed and CIPped at 30 ksi and fired at 1500°C. In subsequent studies, gas pressure sintering will also be used.

The fired billets have been machined into MOR bars for low temperature degradation studies. Some tests have just begun in which the bars are held in an oven at 250°C through which nitrogen is slowly passed. The nitrogen is previously bubbled through water at room temperature. Holding times of up to 2000 hours are planned after which the bars will be tested for MOR and the results compared with a control group of bars that are integrated. At least 10 bars for each holding time are required to get meaningful statistics.

The tetragonal to monoclinic low temperature degradation reaction will also be tracked using a Raman microprobe to measure the depth of the monoclinic layer as a function of holding times.

Variations will be made in grain size, yttria concentration, purity and density to study their influence on LTD and the results compared with those on Japanese materials.

2. Ce-ZTA CERAMICS

Two CeO_2-ZrO_2 crudes (about 50 lbs. each) were made in our facility in Chippawa, Ontario by co-fusion and rapid solidification (R/S). The compositions of these two crudes are 16 w/o CeO_2-ZrO_2 (Z16CE) and 24 w/o CeO_2-ZrO_2 (Z24CE). The crudes were wet milled in a vibratory (Sweco) mill and we are now in the process of characterizing the powder obtained (particle size distribution, phase content by XRD, BET surface area) and classifying it to get the desired fineness.

Figs. 1 and 2 show the particle size distribution curves for the two powders after Sweco milling in water for 48 and 96 hrs., respectively, using Mg-PSZ media. It appears that the high CeO_2 crude is harder to mill. Figs. 3 and 4 show the XRD patterns of the Z16CE and Z24CE crudes, respectively. The two patterns are virtually identical and show only the presence of t-ZrO_2 (possibly t'-ZrO_2 due to rapid solidification). Slight changes in the d spacings (see Figs. 3A and 3B) could be caused by the different CeO_2 content.

The next step will be to mix these two powders with submicron alpha alumina in different proportions, in order to study the effect of composition of the Ce-ZTA ceramics on their room temperature and high temperature mechanical properties.

Status of milestones

All milestones are on schedule. The list of milestones for Phase IIA is reported below.

Phase IIA Milestones

I. Y-TZP (YZ-110 Study

1) Complete preliminary evaluation of low temperature degradation (LTD). Obtain rapidly solidified (R/S) crude from Chippawa of different Y_2O_3 compositions for microstructural studies..... June '88

2) Choose best YZ-110 composition and forming method based on previous measurements of LTD and mechanical properties to be used in optimizational studies in the remaining period. At Penn State prepare and carry out initial mechanical testing of TiO_2/ZrO_2 ceramic bodies made from R/S Chippawa crude..... Oct. '88

3) Complete, (i) processing/microstructural studies for optimization of mechanical properties; (ii) measurements of MOR, K_{IC} between RT and 700°C; (iii) low temperature degradation testing. ..... Feb. '89

4) Finish all documentation and supply test bars to ORNL..... May '89

Ceria-Zirconia Toughened Alumina Ceramics

1) Choose best composition on the basis of mechanical properties obtained at room temperature and at high temperature. Use HIPping to quickly evaluate compositions. Demonstrate and perfect Moffatt's technique..... June '88

2) Evaluate rapidly solidified powders made in Chippawa and PMI and choose between chemically derived and rapidly solidified powders, based on mechanical properties obtained at RT and high temperature..... Oct. '88

3) Complete study on processing/microstructure/-property optimization..... Feb. '89

4) Finish all documentation and supply test bars to ORNL..... May '89

Publications

None

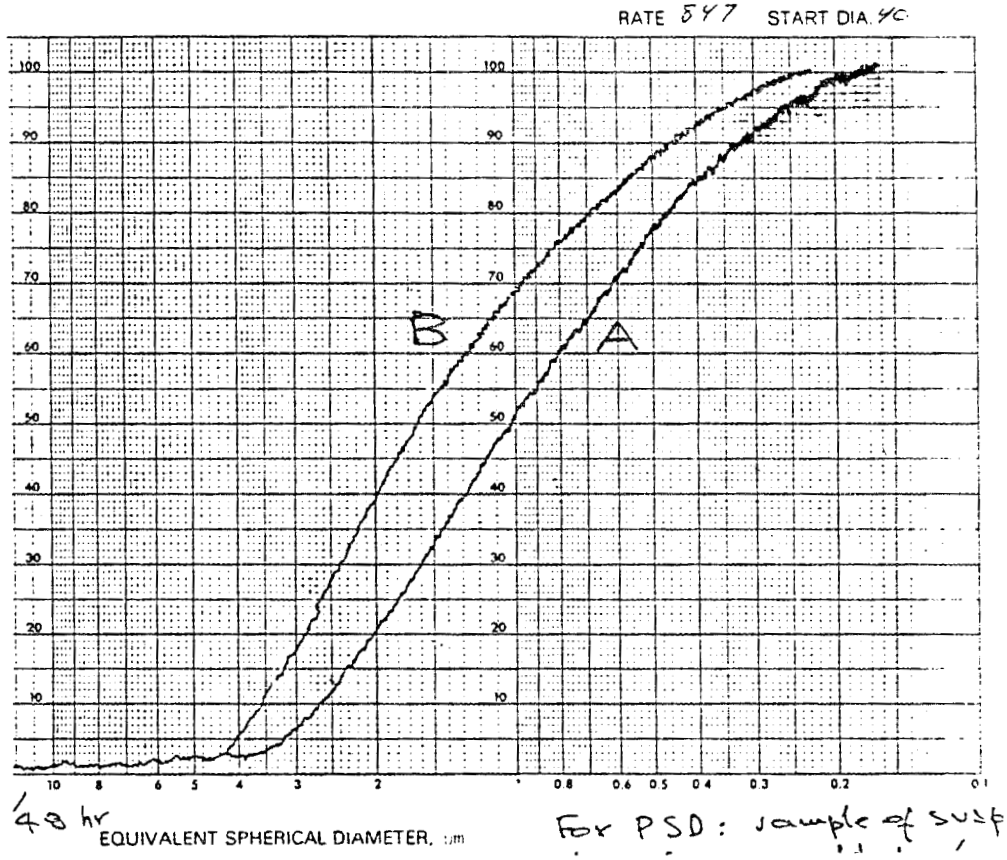

Fig.1 Particle size distribution (Sedigraph) of Z16CE (A) and Z24CE (B) after Sweco milling for 48 hrs.

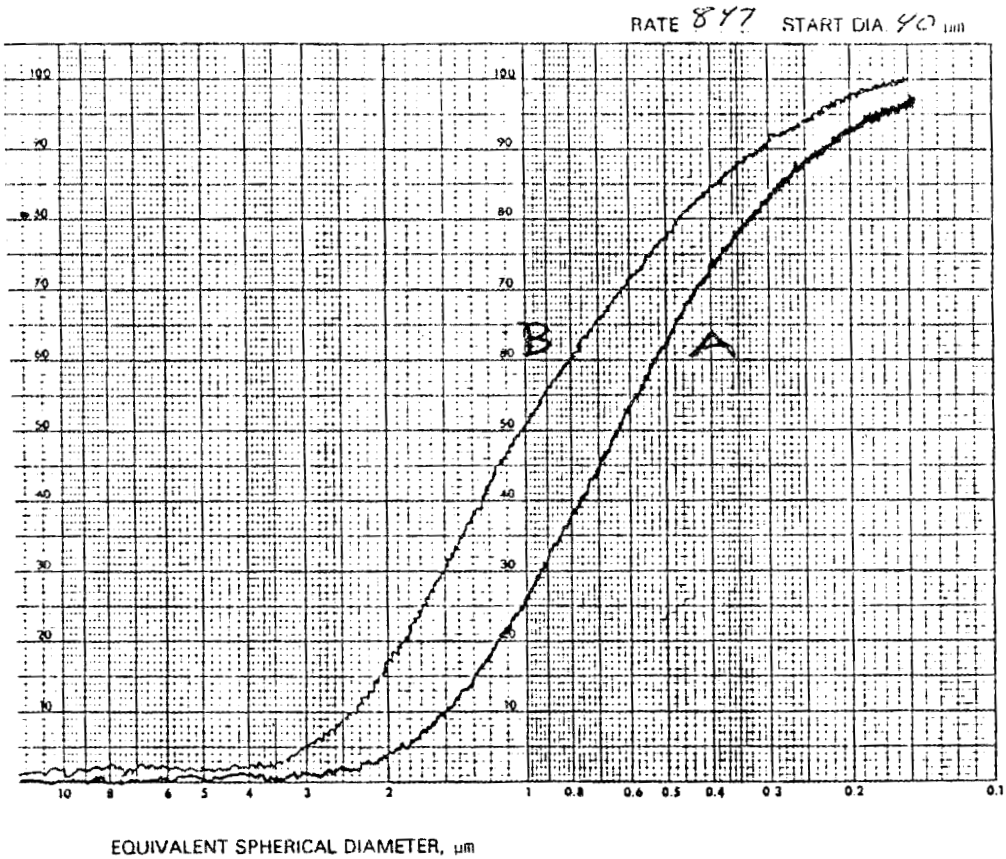

Fig. 2 Particle size distribution (Sedigraph) of Z16CE (A) and Z24CE (B) after Sweco milling for 96 hrs.

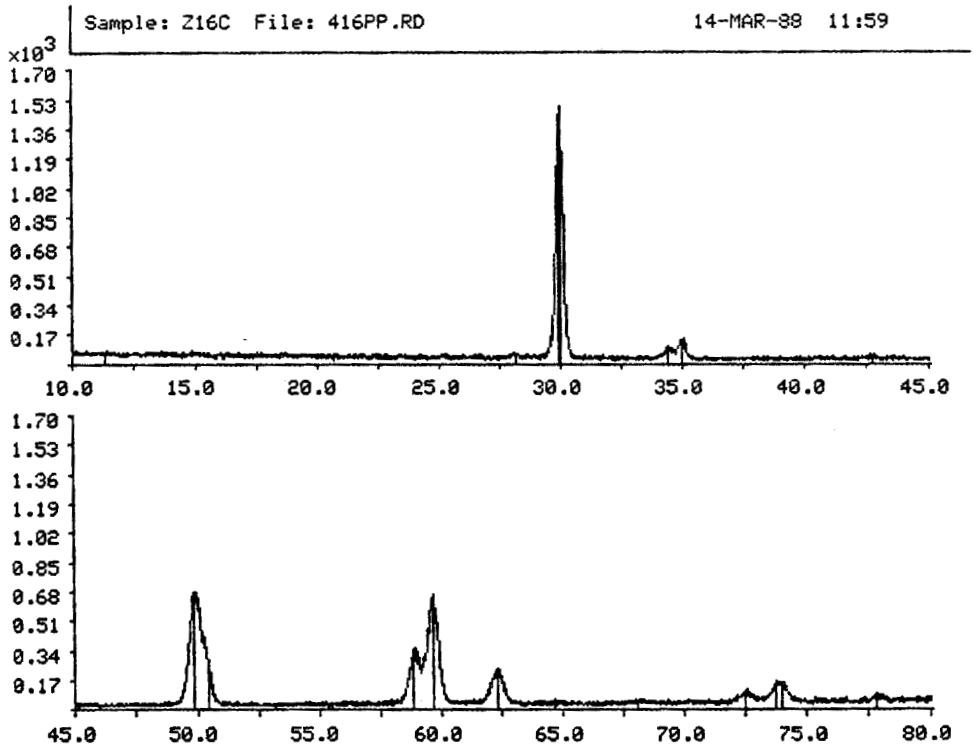

Fig. 3 XRD pattern of rapidly solidified Z16CE crude (16 w/o CeO_2-ZrO_2)

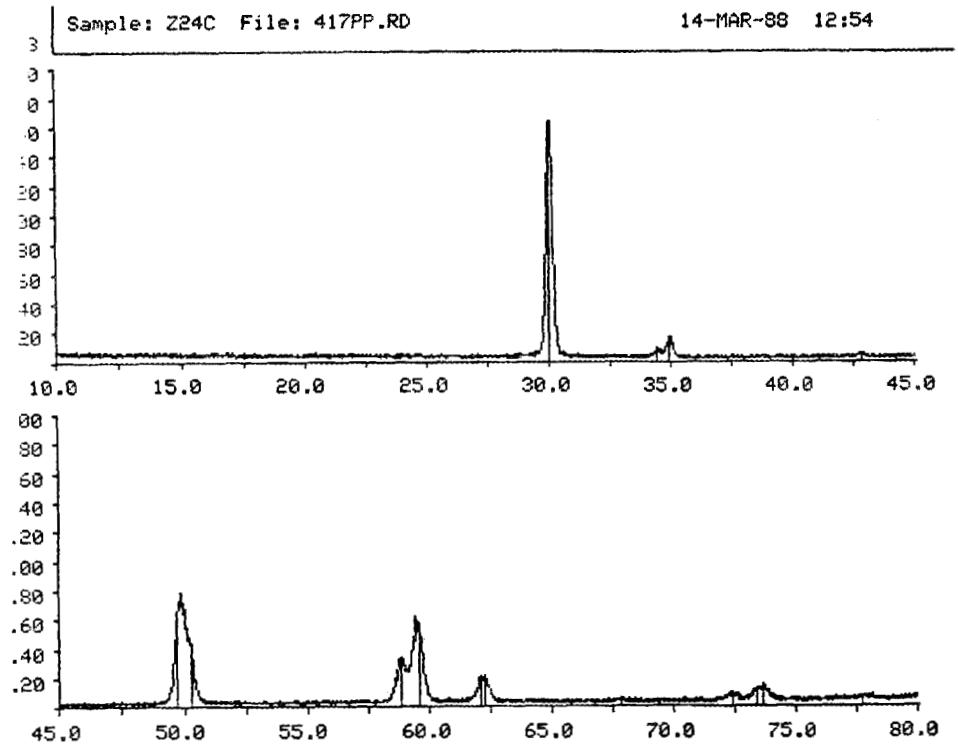

Fig. 4 XRD pattern of rapidly solidified Z24CE crude

(24 w/o CeO_2-ZrO_2)

Peak no	Peak angle	Tip width	Peak int.	Backgr. int.	D space	I/Imax (%)	Type A1	Type A2	Type Ot	Qual
1	11.3075	0.12	16	55	7.8188	1.13	X	X		0.85
2	28.1400	0.32	21	34	3.1685	1.50	X	X		1.48
3	29.8825	0.06	1170	36	2.9876	82.79	X			1.29
4	29.9700	0.12	1414	36	2.9864	100.00		X		4.17
5	34.4175	0.24	66	27	2.6036	4.64	X	X		2.14
6	34.9900	0.28	108	27	2.5623	7.65	X	X		4.90
7	42.7375	0.24	15	26	2.1140	1.08	X	X		0.79
8	49.8575	0.44	640	29	1.8275	45.28	X	X		22.39
9	50.4275	0.28	272	31	1.8082	19.26	X	X		3.02
10	58.8425	0.36	276	37	1.5681	19.49	X	X		7.08
11	59.6675	0.48	595	40	1.5484	42.11	X	X		29.51
12	62.3725	0.36	174	44	1.4875	12.32	X	X		5.89
13	64.6875	0.96	10	36	1.4398	0.72	X	X		1.26
14	68.1050	0.64	15	34	1.3756	1.08	X	X		0.81
15	72.5050	0.12	66	41	1.3026	4.64	X	X		0.79
16	73.7475	0.20	88	61	1.2837	6.25	X			0.93
17	73.9725	0.28	88	61	1.2835	6.25		X		1.20
18	77.7750	0.32	36	45	1.2270	2.55	X	X		1.00

18 Crystalline peaks in file
All peaks listed

Fig. 3A D spacings of Z16CE rapidly solidified crude

Peak no	Peak angle	Tip width	Peak int.	Backgr. int.	D space	I/Imax (%)	Type A1	Type A2	Type Ot	Qual
1	30.0250	0.20	1616	32	2.9737	100.00	X	X		44.67
2	34.4325	0.24	49	28	2.6025	3.03	X	X		1.91
3	34.9325	0.28	119	27	2.5664	7.35	X	X		6.61
4	42.7750	0.32	18	25	2.1122	1.09	X	X		1.10
5	49.7225	0.14	605	29	1.8322	37.45	X	X		2.00
6	50.2650	0.16	392	29	1.8137	24.26	X	X		1.10
7	58.8400	0.24	296	30	1.5681	18.31	X	X		3.72
8	59.6225	0.08	493	30	1.5494	30.50	X			1.10
9	62.0725	0.12	156	40	1.4940	9.67	X			1.15
10	62.2525	0.24	156	40	1.4938	9.67		X		1.70
11	67.8475	0.96	10	36	1.3802	0.63	X	X		1.45
12	72.4125	0.40	44	40	1.3040	2.70	X	X		1.86
13	73.3525	0.28	83	38	1.2896	5.12	X			1.35
14	73.6700	0.12	85	52	1.2880	5.24		X		0.81
15	77.7325	0.24	24	52	1.2275	1.49	X	X		1.02

15 Crystalline peaks in file
All peaks listed

Fig. 4A D spacings of Z24CE rapidly solidified crude

Processing and Characterization of Transformation-Toughened Ceramics with Strength Retention to Elevated Temperatures

R. A. Cutler, J. J. Hansen, and D. W. Prouse (Ceramatec, Inc.) A. V. Virkar and D. K. Shetty (University of Utah)

Objective/Scope

Previous work[1] has shown that it is possible to increase the strength of Al_2O_3-ZrO_2 ceramics by incorporating transformation-induced residual stresses in sintered specimens consisting of three layers. The outer layers contained Al_2O_3 and unstabilized ZrO_2, while the central layer contained Al_2O_3 and partially stabilized ZrO_2. When cooled from the sintering temperature, some of the zirconia in the outer layers transformed to the monoclinic form while zirconia in the central layer was retained in the tetragonal polymorph. The transformation of zirconia in the outer layers led to the establishment of surface compressive stresses and balancing tensile stresses in the bulk. In theory, the residual stress will not decrease with temperature until the monoclinic to tetragonal transformation temperature is reached since monoclinic and tetragonal ZrO_2 polymorphs have nearly the same coefficients of thermal expansion. The demonstration of the retention of residual stresses with temperature is a primary purpose of this project.

Previous work was accomplished using dry pressing techniques. The development of slip casting technology for layered composites will allow for better dispersion of zirconia in alumina and thereby facilitate higher volume fraction monoclinic ZrO_2 in outer layers without strength degrading microcracking. A comparison between slip casting and dry pressing techniques will be made to identify higher strength materials for more detailed characterization during the second year of the project.

Technical Highlights

Slip Casting

A substantial effort was directed at slip casting Al_2O_3-15 vol. % ZrO_2 three layer composites since previous results had shown that strengths greater than 1 GPa were attainable[2]. Previous slip casting, however, was hindered by plates cracking during drying. In order to solve these problems, dispersion of the three materials used in the composites (alumina, unstabilized zirconia, and partially stabilized zirconia) was investigated individually as a function of dispersant used. Each of the four dispersants (pH adjusted to 2.0-2.5 using HNO_3, an ammonium polyelectrolyte (Darvan 821A from R. T. Vanderbilt), Darvan C (higher molecular weight

polyelectrolyte from same company) in combination with citric acid, and sodium hexametaphosphate) dispersed alumina well at solids contents of at least 70 wt. %. These dispersants also dispersed partially stabilized (3 mol. % Y_2O_3) zirconia but none of the dispersants were successful in dispersing unstabilized ZrO_2 at solids contents greater than 65 wt. %. Initial efforts were therefore directed at obtaining high density outer layer[3,4] specimens without cracking.

The effect of dispersant type on the sintered density of ball milled powders was investigated by slip casting bars of the outer layer composition (Al_2O_3-15 vol. % ZrO_2) at a solids content of 60 wt. % with each of the four dispersants. Density and open porosity are given as a function of dispersant used in Table 1. Three of the four dispersants resulted in composites with similar density, while little sintering occurred when sodium hexametaphosphate was used (see Table 1 and Figure 1). The green densities were similar for all four dispersants, with the sodium hexametaphosphate slip having the highest green density. Scanning electron microscopy of composites dispersed with sodium hexametaphosphate showed that ZrO_2 was well dispersed throughout the alumina matrix, indicating that Na and P contaminants inhibited sintering.

Further slip casting experiments using Darvan C/citric acid and vibratory milled powders showed that by proper selection of the binder and by rounding the edges of slip cast plates, the outer layer material could be sintered to densities greater than 98% of theoretical without cracking. It was also demonstrated that high

Table 1
Effect of Dispersants on Density of Al_2O_3-15 vol. % ZrO_2[a]

Dispersant	After Bisquing[b]		After Sintering		
	Density(g/cc)	%TD[c]	Density(g/cc)	%TD	o.p.(%)[b]
$(NaPO_3)_6$[d]	2.54	59.1	3.32	77.2	19.1
Darvan C/ citric acid	2.44	56.7	4.15	96.5	1.9
Darvan 821A	2.46	57.2	4.12	95.8	2.5
HNO_3	2.40	55.8	4.12	95.8	2.2

a. DK1 (Daiichi Kagaku Kogyo Co., Ltd., Osaka, Japan).
b. After bisquing at 850°C.
c. Percent theoretical density.
d. Sodium hexametaphosphate is more accurately described by $(NaPO_3)_n$ where n indicates a mixture of metaphosphates.

(a)

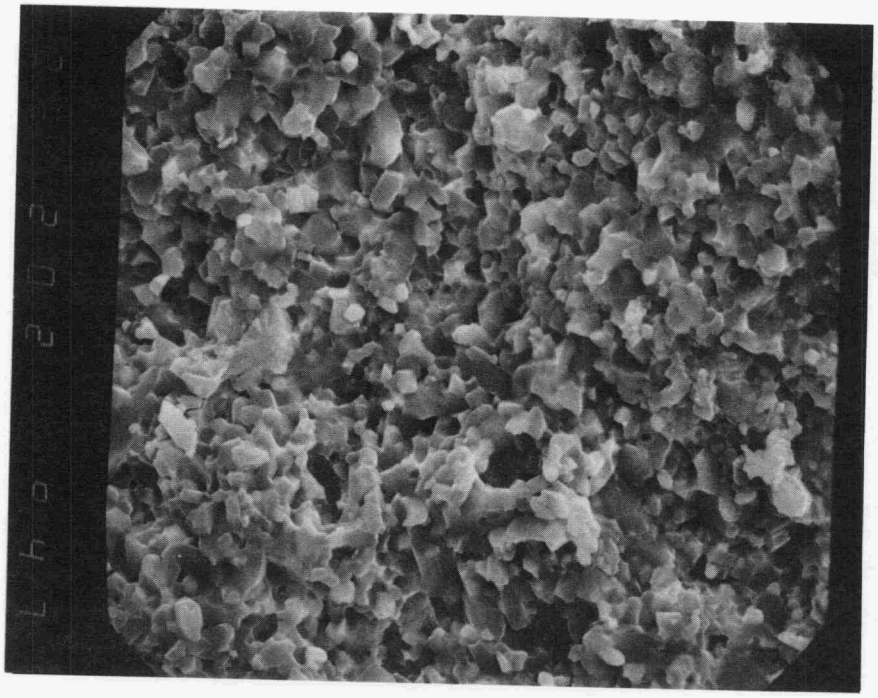

(b)

Figure 1. Fracture surfaces of Al_2O_3-15 vol. % ZrO_2 composite slip cast using (a) sodium hexametaphosphate, and (b) Darvan C/citric acid, as dispersants showing poor sintering when $(NaPO_3)_6$ is used as a dispersant (2000X).

density outer layer plates could be made using a two step slip casting technique, as is required for three layer composites.

Using the same technique, monolithic inner layer (Al_2O_3-15 vol. % ZrO_2 (3.0 mol. % Y_2O_3)) bars and three layer composites were slip cast and sintered to densities greater than 98.8% of theoretical. No cracks were observed in any of the slip cast plates and HIPing increased the density to greater than 99.5 % of theoretical. The plates were sectioned into test bars and tested in four-point bending at room temperature. Table 2 gives density and strength data for the three compositions. These strengths for unground bars indicate that residual compressive stresses on the order of 420 MPa are present in the outer layers of three layer slip cast bars, as compared to stresses of 375 MPa for bars prepared using dry pressing techniques[3,4]. Fractography revealed that voids, believed to result from foaming of the binder, limited strength in all three compositions. Further efforts are underway to eliminate voids and optimize water removal from green slip cast bars. Testing of monolithic and three layer slip cast bars which have been ground will then be conducted as a function of temperature.

Elevated Temperature Testing

Improvement in high temperature strength of die pressed Al_2O_3-15 vol. % ZrO_2 was achieved by using a ZrO_2 powder (Teledyne Albany K 906) with an average particle size of 1.4 microns (prior to vibratory milling with alumina). High temperature x-ray diffraction data showed that the m->t transformation of ZrO_2 was shifted to higher temperatures for monolithic outer layer composition bars made using this coarser zirconia[3]. The three layer

Table 2
Density and Strength of Slip Cast Al_2O_3-15 vol. % ZrO_2

Composition	Density (g/cc)	Strength (MPa) #[a]	Mean	Std. Dev.
Outer Layer[b]	4.25	7	491	29
Inner Layer[c]	4.28	7	481	46
Three Layer[d]	4.28	7	853	104

a. Number of specimens tested.
b. Al_2O^3-15 vol. % ZrO_2
c. Al_2O_3-15 vol. % ZrO_2(3 mol. % Y_2O_3)
d. 1/12-5/6-1/12 (outer-inner-outer).

specimens had an outer layer thickness of approximately 375 microns (4.5 mm total thickness) so as to be comparable to three layer specimens previously tested at elevated temperatures[3,4]. The density after HIPing was 4.29 g/cc with microstructure as shown in Figure 2. The bars were surface ground and then annealed at 1200°C for 30 minutes prior to testing in four-point bending[3,4]. The strength of three layer composites was 815 MPa (52 MPa std. dev.) before annealing and 787 MPa (100 MPa std. dev.) after the annealing treatment. The strength of the three layer composites (see Table 3) was improved by over 100 MPa at 950°C as compared to previously reported data[4], due to the change in zirconia size.

The data in Table 3 show the strength hysteresis expected[4] due to the temperature differential for the m-->t transformation upon heating and the t-->m transformation upon cooling. Figure 3 shows expansion and contraction curves as a function of temperature for the two monolithic materials. Thermal contraction of the monolithic inner and outer materials are nearly identical between 1200 and 600°C (see Table 4) since both materials contain tetragonal zirconia over that range. Approximately 75% of the tetragonal zirconia transforms to monoclinic in the outer layers between 550 and 350°C upon cooling. Thermal expansion data for the two materials are similar upon heating until the monoclinic zirconia

Table 3
Strength Retention of Three Layer Al_2O_3-15 vol. % ZrO_2 Composites at Elevated Temperatures

Specimen	Test Temp. (°C)	No. Spec. Tested	Strength (MPa)	Normalized Strength[a]	Compressive Stress(MPa)
Monolithic outer layer	25	5	531±19	1.00	
	750	3	355±25	0.67	
	950	3	415±28	0.79	
Three layer composite specimens	25	5	787±100	1.00	256
	750	3	636±55	0.82	283
	850	3	617±62	0.78	232[b]
	950	3	495±23	0.63	80
	1200->750[c]	3	442±19	0.57	--[d]

a. Strength divided by strength at 25°C.
b. Assuming strength of outer layer bars as average of strength measured at 750 and 950°C.
c. Specimens heated to 1200°C and then cooled to 750°C before testing.
d. Testing has not been performed on monolithic outer layer bars, but transformation-induced stresses should not be present under these conditions.

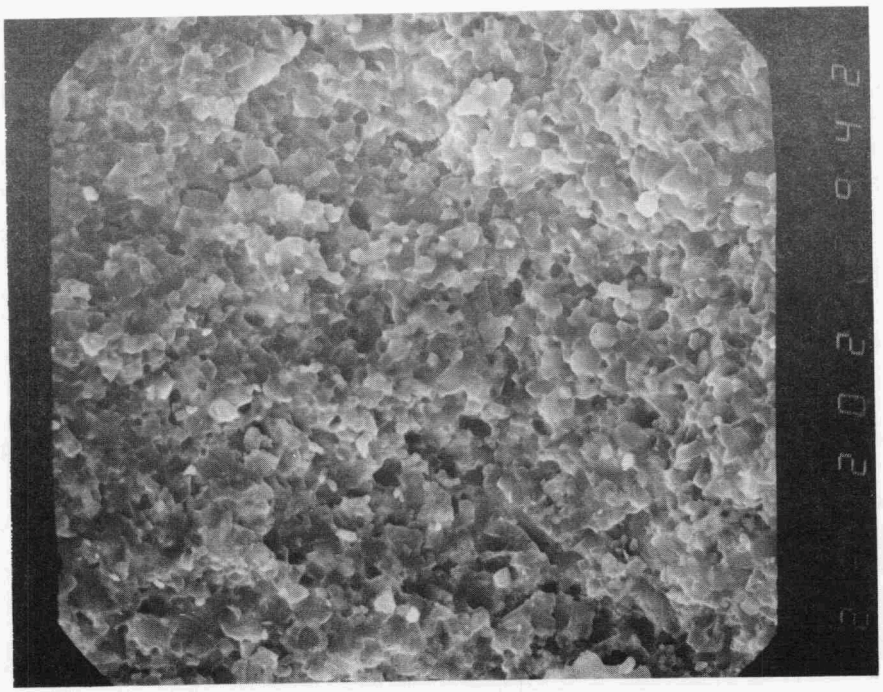

(a)

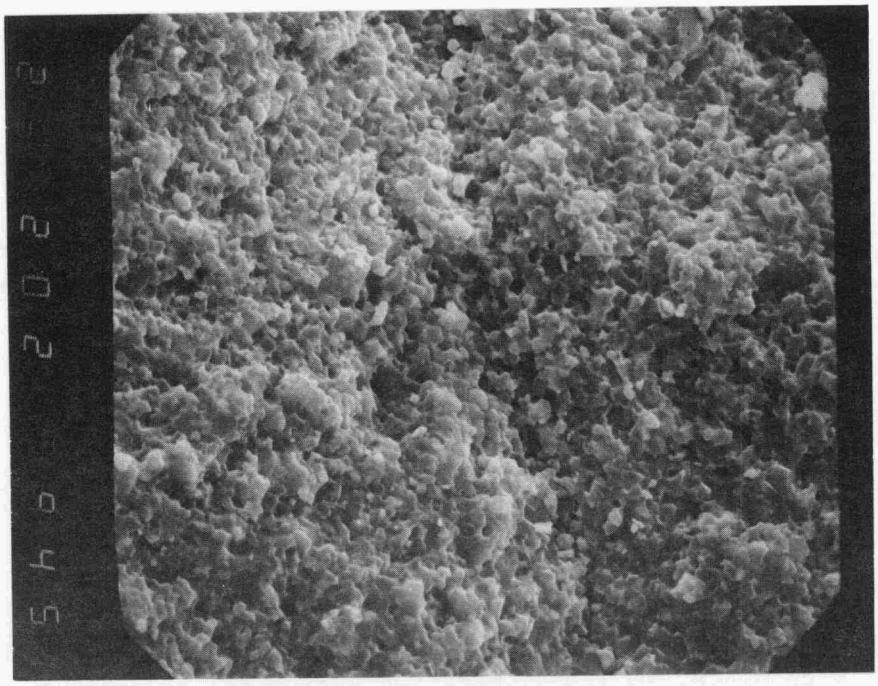

(b)

Figure 2. Fracture surfaces of three layer Al_2O_3-15 vol. % ZrO_2 composites made via dry pressing (2000x). (a) Outer layer containing Teledyne K906 ZrO_2[3] and (b) inner layer containing Daiichi HSY-3.0 ZrO_2.

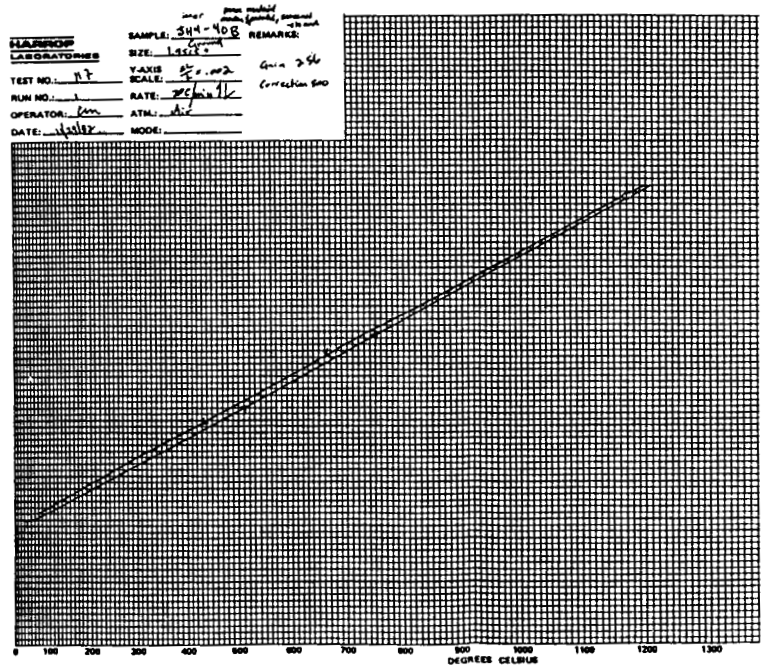

(a)

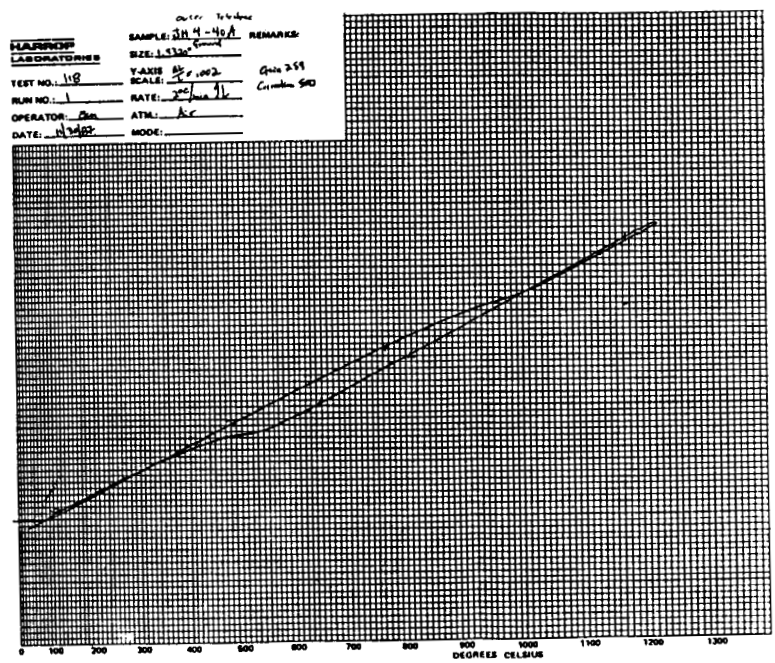

(b)

Figure 3. Thermal expansion and contraction curves for monolithic (a) inner layer Al_2O_3-15 vol. % ZrO_2(3 mol. % Y_2O_3) and (b) outer layer Al_2O_3-15 vol. % ZrO_2.

Table 4
Thermal Expansion/Contraction for Monolithic
Al_2O_3-15 vol. % ZrO_2

Thermal Expansion(100°C-Temp) Temperature (°C)	Outer[a] ($x10^6$/°C)	Inner[b]	Thermal Contraction(1200°C-Temp) Temperature (°C)	Outer[a] ($x10^6$/°C)	Inner[b]
100	---	---	1200	---	---
200	7.0	7.0	1100	10.4	10.4
300	7.5	7.5	1000	10.4	10.5
400	7.7	7.9	900	10.3	10.3
500	7.9	8.1	800	10.1	10.2
600	8.0	8.4	700	10.0	9.9
700	8.2	8.6	600	9.8	9.9
800	8.2	8.7	500	9.3	9.8
900	8.1	8.9	400	8.7	9.7
1000	7.9	9.0	300	8.5	9.6
1100	8.0	9.2	200	8.2	9.4
1200	8.2	9.3	100	8.2	9.3

a. Outer layer composition (Al_2O^3-15 vol. % ZrO_2)
b. Inner layer composition (Al_2O_3-15 vol. % ZrO_2(3 mol. % Y_2O_3))

transforms back to the tetragonal polymorph, which occurs between 750 and 1000°C. The assumption of similar thermal expansion for the two materials is good, as is the assumption of similar elastic moduli (Young's modulus of 348 GPa measured for the outer material and 346 GPa measured for the inner layer material) as determined by strain gaging monolithic bars.

Assuming a square wave stress distribution, it is possible to calculate the expected residual stress, σ_c, by

$$\sigma_c = -d_2 E \Delta\varepsilon_o / d(1-\upsilon) \qquad (1)$$

where d_2 is the thickness of the inner layer, d, is the total thickness of the bar, E is Young's modulus, υ is Poisson's ratio (taken as 0.25), and $\Delta\varepsilon_o$ is the free expansion of the outer layers per unit length. Taking the deviation from linear thermal contraction (see Figure 3(b)) as $\Delta\varepsilon_o$, a value of $1.0x10^{-3}$ is obtained at room temperature, in good agreement with data obtained by x-ray diffraction, strain gaging, and strength testing[3]. Similarly, the deviation from linearity in the thermal expansion curve was used to measure $\Delta\varepsilon_o$ upon heating. Using these data, the predicted stresses are compared with measured stresses in Figure 4. The predicted stresses due to the temperature hysteresis between the m-->t transformation upon heating and the t-->m transformation upon cooling show the same hysteresis effect as the strength data. Distinctly higher strengths were measured for three layer composites tested by heating to 750°C as compared the strength of bars first heated to 1200°C and then cooled to 750°C for strength testing. These data

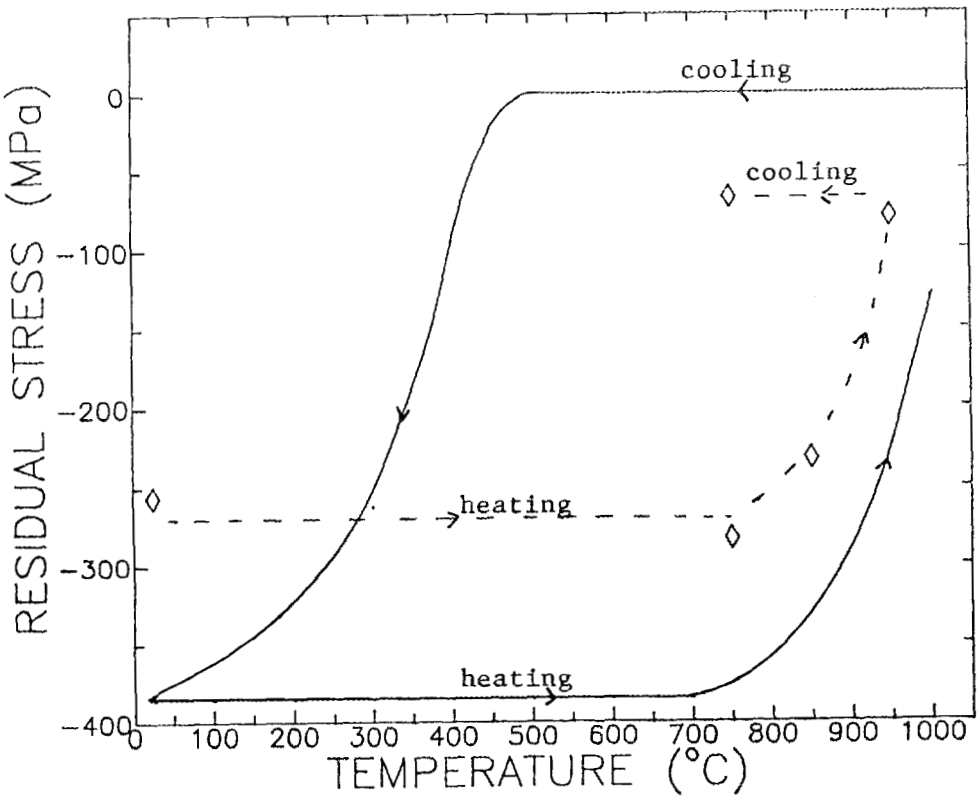

Figure 4. Compressive residual stresses calculated (solid line (based on thermal expansion (contraction) data using Equation (1))) and strength measurements (dotted line (see Table 2)). Note that strength data follow same trend as predicted behavior.

suggest that HfO_2 should be substituted for ZrO_2 for applications where thermal cycling occurs or where the use temperature is above 750°C, such as for adiabatic diesel engines. Future efforts will be directed at substituting hafnia for zirconia.

Strength testing of ground bars showed an unexpected feature with respect to the monolithic inner layer composition (see Table 5). Previous testing[3,4] of both monolithic and three layer compositions was performed in the as-sintered condition to avoid transformation of the outer layer upon grinding. Strength data (see Table 5) show that the strength of monolithic inner layer bars nearly double upon grinding. The strength degraded slightly with temperature (see Table 5) but testing at 750°C (after cooling from 1200°C) showed that transformation-induced stresses are not the primary strengthening mechanism since strength was identical to that measured upon heating to 750°C. This is consistent with x-ray diffraction data which showed no transformation to monoclinic zirconia upon grinding.

Table 5
Strengthening of Al_2O_3-15 vol. % ZrO_2(3 mol. % Y_2O_3) Due to Grinding

Specimen Preparation	Test Temp. (°C)	No. Spec. Tested	Strength (MPa)
Unground	25	6	452±11
Ground (220 Grit)	25	6	835±85
Ground,1200°C Anneal	25	5	731±168
Ground,1600°C Anneal	25	6	666±68
Ground,1200°C Anneal	750	3	621±47
Ground,1200°C Anneal	850	3	606±5
Ground,1200°C Anneal	950	3	528±21
Ground,1200°C Anneal	1200->750	3	627±95

Specimens polished to a 1 micrometer finish without grinding showed only a moderate strength improvement (strength of 551±49 MPa) despite a significant improvement in surface finish, demonstrating that grinding does more than improve surface finish. It is possible that grinding introduces compressive stresses due to plastic deformation, although it is not understood why monolithic and three layer composites do not show the same effect (monolithic and three layer composites increased approximately 100 MPa in strength upon grinding). The strength of bars machine ground on one side and hand ground on the other side was 841±109 MPa when the machine ground side was placed in tension and 579±68 MPa when the hand ground side was placed in tension, showing that the stresses are near the surface. While others[5-8] have observed significant residual stresses after grinding transformation toughened ceramics, these stresses were always been accompanied by an increase the monoclinic ZrO_2 content. Further work is underway to explain these compressive surface stresses and to learn how to optimize their depth.

Status of Milestones

High temperature testing of slip cast composites is behind schedule.

Publication

A. V. Virkar, J. F. Jue, J. J. Hansen and R. A. Cutler, "Measurement of Residual Stresses in Oxide-ZrO_2 Three-Layer Composites," J. Am. Ceram. Soc., 71[3] C-148-C-151 (1988).

References

1. A. V. Virkar, J. L. Huang, and R. A. Cutler, "Strengthening of Oxide Ceramics by Transformation Induced Stresses," J. Am. Ceram. Soc., 70 [3] 164-170 (1987).

2. R. A. Cutler, J. J. Hansen, A. V. Virkar, and D. K. Shetty, "Processing and Characterization of Transformation Toughened Ceramics with Strength Retention to Elevated Temperatures," in Ceramic Technology for Advanced Heat Engines Project Bimonthly Technical Progress Report ORNL/CF-87/327 (Aug.-Sept. 1987), Oak Ridge National Laboratory, Oak Ridge, Tenn. pp. 107-110 (1987).

3. R. A. Cutler, J. J. Hansen, A. V. Virkar, D. K. Shetty, and R. C. Winterton, "Strength Improvement in Transformation Toughened Ceramics using Compressive Residual Surface Stresses," Advanced Structural Ceramics Vol. 78, ed. by P.F. Becher, M. V. Swain, and S. Somiya (Materials Research Society, Pittsburgh, PA, 155-163, 1987).

4. R. A. Cutler, J. D. Bright, A. V. Virkar, and D. K. Shetty, "Strength Improvement in Transformation-Toughened Alumina by Selective Phase Transformation," J. Am. Ceram. Soc., 70 [10] 714-18 (1987).

5. T. K. Gupta, "Strengthening by Surface Damage in Metastable Tetragonal Zirconia," J. Am. Ceram. Soc., 63 [1-2] 117 (1980).

6. N. Claussen and M. Ruhle, "Design of Transformation-Toughened Ceramics," Advances in Ceramics Vol. 3, ed. by A. H. Heuer and L. W. Hobbs, The Am. Ceram. Soc., Columbus, Ohio, pp 137-163 (1981).

7. D. J. Green, F. F. Lange, and M. R. James, "Residual Surface Stresses in Al_2O_3-ZrO_2 Composites," Advances in Ceramics Vol. 12, ed. by N. Claussen, M. Ruhle, and A. H. Heuer, The Am. Ceram. Soc., Columbus, Ohio, pp. 240-250 (1983).

8. D. J. Green, F. F. Lange, and M. R. James, "Factors Influencing Residual Surface Stresses due to a Stress-Induced Phase Transformation," J. Am. Ceram. Soc., 66 [9] 625-629 (1983).

1.2.4 Silicate Matrix

Low Expansion Ceramics for Diesel Engine Applications

J. J. Brown, R. E. Swanson (Virginia Polytechnic Institute and State University), and F. A. Hummel (Consultant)

Objective/scope

The major objective of this research is to investigate selected oxide systems for the development of a low expansion, high thermal shock resistant ceramic. Specifically, it is the goal of this study to develop an isotropic, ultra-low expansion ceramic which can be used above 1200°C and which is relatively inexpensive.

Technical progress

This research program includes the synthesis, property characterization, and fabrication of candidate low thermal expansion ceramics from four systems based upon aluminum phosphate, silica, mullite, and zircon. In the first two systems, the goal is to stabilize low thermal expansion, high temperature, high crystal symmetry phases via solid solution formation. In mullite, deviation from stoichiometry and solid solution formation are utilized to reduce the thermal expansion. In zircon, the crystal anisotropy and thermal expansion are reduced via solid solution formation. Based upon earlier data of the investigators, compositional ranges are evaluated by fabricating experimental specimens and determining phase content plus microstructure, thermal expansion, solidus temperature, and density. Those compositions which exhibit acceptable sintering, phase composition, and expansion characteristics are studied in more detail, including flexure strength, creep, thermal conductivity, and crystal structure. Finally, those ceramic compositions exhibiting the best combination of properties are evaluated as to their fabrication behavior in the form of specimens having masses up to about 0.5 kg.

Aluminum Phosphate System

$AlPO_4$ is a well-known high melting compound with crystal structures and polymorphism similar to that of SiO_2. Solid solutions of BPO_4 and β-eucryptite ($Li_2O \cdot Al_2O_3 \cdot 2SiO_2$) with $AlPO_4$ are being studied in an effort to stabilize the high temperature polymorphs such as β-cristobalite. The β-cristobalite solid solution phase, known to exist at high temperatures,[1] may provide a low thermal expansion, high melting ceramic.

It was previously reported that β-eucryptite-$AlPO_4$ solid solutions formed the β-cristobalite structure.[2] It was also shown that SiO_2- β-eucryptite solid solutions possessed a thermal expansion coefficient of nearly zero.[3] During the present reporting period, the effect of adding BPO_4 and SiO_2 to these solid solutions was examined.

Experimental

Both solid-state and sol-gel methods were used in preparing samples. Using the sol-gel technique, samples were formed directly from the raw materials without the pre-formation of $AlPO_4$, BPO_4, and β-eucryptite. The starting materials included 1-tetraethyl orthosilicate $(C_2H_5O)_4Si$, aluminum isopropoxide $[(CH_3)_2CHO]_3Al$, trimethyl phosphate $(CH_3O)_3P(O)$, trimethyl borate $(CH_3O)_3B$, and Li_2CO_3. The sol-gel reactions proceeded at room temperature for 24 to 48h; the reaction products were then fired at 1000-1200°C for more than 24h.

Using the solid-state reaction technique, samples without BPO_4 were formed directly from the raw materials. The starting materials included $Al(OH)_3 \cdot H_2O$, $(NH_4)_2HPO_4$ or $NH_4H_2PO_4$, silica gel or silicic acid, and Li_2CO_3. When BPO_4 was introduced, the samples were made from the pre-formed $AlPO_4$, BPO_4, and $LiAlSiO_4$ (β-eucryptite). The starting materials for each sample were mixed with acetone using a mortar and pestle, and subsequently fired.

Following firings, x-ray diffraction (XRD) phase identification was made on ground samples prepared by either solid-state reaction or the sol-gel methods. The samples having multiphase compositions were refired, ground, and analyzed again by XRD to ensure equilibrium.

The samples having a final single phase composition (and in some cases, a trace second phase) were prepared for thermal expansion measurement by pressing the sample powders into bars. The bars were pressed in a stainless steel die, using 3 wt% of a cellulose ether powder (Methocel) as a binder, and sintered at 1180 to 1220°C for 8 to 24h. The sintered bars were cut to appropriate lengths, and thermal expansion measurements were made using a dual push rod differential dilatometer from 30 to 1000°C. Each bar was measured twice, and the average coefficient of thermal expansion (CTE) is reported herein. Thermal expansion measurements were not performed on specimens in which more than one phase was detected after three heat treatments.

Results and Discussion

<u>$AlPO_4$-BPO_4-β-eucryptite ternary compositions</u>. Table 1 summarizes the phase identification results and thermal expansion data for compositions studied in the $AlPO_4$-BPO_4-β-$LiAlSiO_4$ ternary system. When the content of β-$LiAlSiO_4$ was not greater than 30 mol% and the content of $AlPO_4$ was not less than that of BPO_4, a single phase ($AlPO_4$) solid solution (in some cases with trace amounts of β-$LiAlSiO_4$ solid solution) was formed. When the content of β-$LiAlSiO_4$ was equal to or greater than 40 mol% (YS-43), a single phase solid solution was not formed even after 108h of heat treatment. All work was done in an open system, and weight losses were observed.

Thermal expansion data for the sample bars having an $AlPO_4$ solid solution phase composition are shown in Table 1. The occurrence of a phase transformation in all samples between 190 to 220°C probably suggests that these solid solutions have the low-cristobalite structure.

Horn and Hummel[1] investigated the system $AlPO_4$-BPO_4 in a closed system and reported that a complete series of solid solutions between $AlPO_4$ and BPO_4 exists above 1200°C. These solid solutions have the high-cristobalite structure and can be quenched metastably to room temperature. The discrepancies between the results of our work and those of Horn and Hummel may be due to: (1) our work was done in an

open system, and (2) $LiAlSiO_4$ was included in our compositions.

Table 1. Summary of thermal expansion data for samples in the $AlPO_4$-BPO_4-β-eucryptite ternary system.

Sample No.	Initial Composition	Sample Processing (Temp, °C/Time, h)	Weight Loss (%)	Phase Composition	Thermal expansion $\alpha(x10^{-7}/^{o}C)$
YS-32	$Li_{0.1}Al_{0.7}B_{0.3}P_{0.9}Si_{0.1}O_4$[a]	1200/24	C[b]	S.S.[c]	P.T[d] at 210°C
YS-34	$Li_{0.1}Al_{0.6}B_{0.4}P_{0.9}Si_{0.1}O_4$	1200/72 + 1200/76	C	S.S.	P.T at 192°C
YS-35	$Li_{0.15}Al_{0.6}B_{0.4}P_{0.85}Si_{0.15}O_4$	1200/76	1.17	S.S.	P.T at 193°C
YS-36	$Li_{0.2}Al_{0.6}B_{0.4}P_{0.8}Si_{0.2}O_4$	1200/76	11.9	S.S.	P.T at 220°C
YS-37	$Li_{0.2}Al_{0.8}B_{0.2}P_{0.8}Si_{0.2}O_4$	1200/72	C	S.S.	P.T at 215°C
YS-38	$Li_{0.3}Al_{0.9}B_{0.1}P_{0.7}Si_{0.3}O_4$	1200/74	C	S.S.	P.T at 224°C
YS-40	$Li_{0.3}Al_{0.8}B_{0.2}P_{0.7}Si_{0.3}O_4$	1200/74	0.3	S.S. + tr $LiAlSiO_4$	P.T at 220°C
YS-43	$Li_{0.4}Al_{0.9}B_{0.1}P_{0.6}Si_{0.4}O_4$	1200/72 + 1180/36	C	Multiphase	--

[a]Sample YS-32 prepared by sol-gel with starting materials = $[(CH_3)_2CHO]_3Al$, $(C_2H_5O)_4Si$, $(CH_3O)_3P(O)$, Li_2CO_3, $(CH_3O)_3B$; other samples prepared by solid-state reaction with starting materials = preformed $AlPO_4$, BPO_4, and β-$LiAlSiO_4$

[b]C = Crucible damaged

[c]S.S. = Solid solution

[d]P.T. = Phase transformation

<u>Al_2O_3-P_2O_5-SiO_2-Li_2O system</u>. A summary of the experimental work completed to date on the phase composition and the thermal expansion of the samples formed from this system is presented in Table 2.

Phase identification results in identical compositions containing 60 mol% $AlPO_4$ prepared by solid-state reaction (YS-12) and the sol-gel method (YS-26) showed more than one phase present after extended heat treatments. Multiphase composition was also detected by XRD analysis for a sample containing 70 mol% $AlPO_4$ prepared by solid-state reaction (YS-25). Samples of identical compositions containing 55 mol% $AlPO_4$ prepared by solid-state reaction (YS-13) and sol-gel processing (YS-29) were composed of more than one phase after

long heat treatments. However, according to XRD analysis, the relative content of the second phase in the samples containing 55 mol% $AlPO_4$ was much less than that in samples containing 60 mol% $AlPO_4$.

Table 2. Summary of thermal expansion data for samples in the Al_2O_3-P_2O_5-SiO_2-Li_2O system.

Sample No.	Initial Composition	Sample Processing (Temp, °C/Time, h)	Phase Composition	Thermal Expansion $\alpha(\times 10^{-7}/°C)$
YS-12	$Li_{0.4}AlP_{0.6}Si_{0.4}O_4$ [a]	1200/50, 1200/52, 1380 20/48, 1250/72	Multiphase	NA
YS-26	$Li_{0.4}AlP_{0.6}Si_{0.4}O_4$ [b]	1250/72	Multiphase	NA
YS-25	$Li_{0.3}AlP_{0.7}Si_{0.3}O_4$ [a]	1200/72, 1250/72, 1250/48	Multiphase	NA
YS-13	$LI_{0.45}AlP_{0.55}Si_{0.45}O_4$ [a]	1200/48, 1380 20/48, 1250/72	Multiphase	NA
YS-29	$Li_{0.45}AlP_{0.55}Si_{0.45}O_4$ [b]	1200/48	Multiphase	NA
YS-11*	$Li_{0.5}AlP_{0.5}Si_{0.465}O_{3.93}$ [a]	1200/48	S.S.[d] + tr $AlPO_4$, Al_2O_3	-0.96
YS-14	$Li_{0.5}AlP_{0.5}Si_{0.58}O_{4.16}$ [a]	1200/72, 1200/96	S.S.	-17
YS-19	$Li_{0.5}AlP_{0.5}Si_{0.695}O_{4.39}$ [a]	1280/96, 1200/56	S.S. + tr $AlPO_4$, Al_2O_3	-21
YS-15**	$Li_{0.48}AlP_{0.52}Si_{0.445}O_{3.93}$ [a]	1280/96, 1200/56	S.S. + tr $AlPO_4$, Al_2O_3	-3.21
YS-50	$Li_{0.48}AlP_{0.52}Si_{0.48}O_4$ [c]	1200/50	S.S.	-5.3
YS-20	$Li_{0.48}Al_{0.52}Si_{0.67}O_{4.38}$ [a]	1200/72, 1200/96, 1200/48	Multiphase	NA
YS-31	$Li_{0.51}AlP_{0.49}Si_{0.765}O_{4.51}$ [b]	1200/24	Multiphase	NA
YS-48	$Li_{0.46}AlP_{0.54}Si_{0.69}O_{4.46}$ [c]	1200/50, 1200/48, 1200/52	Multiphase	NA
YS-56	$Li_{0.47}AlP_{0.53}Si_{0.47}O_4$ [c]	1200/58	S.S. + tr $AlPO_4$	-5.16

[a]Starting materials = $Al(OH)_3$ nH_2O, $(NH_4)_2HPO_4$, silica gel, Li_2CO_3

[b]Sol-gel processing: starting materials = $[(CH_3)_2CHO]_3Al$, $(C_2H_5O)_4Si$, $(CH_3O)_3P(O)$, Li_2CO_3

[c]Starting materials = $Al(OH)_3$ nH_2O, $NH_4H_2PO_4$, silicic acid, Li_2CO_3

[d]S.S. = Solid solution

*YS-11 composition reported incorrectly in Dec. 87-Jan. 88 bimonthly report.

**YS-15 composition reported incorrectly in Dec. 87-Jan. 88 bimonthly report.

Although Perrotta[2] has patented a series of solid solutions extending from 5 to 65 mol% $AlPO_4$ with β-$LiAlSiO_4$, the results of our work indicate that it is likely that a single phase solid solution cannot form in the system within the $AlPO_4$ content range of 60-70 mol%, and that the solid solubility limit is in the vicinity of $AlPO_4$ content of 55 mol%.

Moay, Verduch, and Hortal[3] report that by increasing the solid solution SiO_2 content in β-eucryptite, one can approach a value of zero for the coefficient of thermal expansion. However, the opposite effect was observed in experimental results of the present work. As shown in Table 2, with an increase in SiO_2 content, samples YS-11, YS-14, and YS-19, the average CTE value decreased from $-0.96 \times 10^{-7}/^{o}C$ to $-17 \times 10^{-7}{}^{o}C$ to $-21 \times 10^{-7}/^{o}C$, respectively. The situation was similar in the case of samples YS-15 and YS-50 where only a slight increase in SiO_2 content resulted in a change in CTE from $3.21 \times 10^{-7}/^{o}C$ to $-5.3 \times 10^{-7}/^{o}C$. Sample YS-20, containing considerably more SiO_2 than samples YS-15 and YS-50, showed multiphase phase composition after a long heat treatment.

The effect of SiO_2 content on the phase composition and thermal expansion will be further investigated.

<u>Ionic Substitution for Li^+</u>. Due to the instability of the Li^+ ion at high temperatures, it would appear appropriate to substitute it with a non-alkali ion. According to the XRD analysis, the solid solution formed in our experimental work is β-$LiAlSiO_4$, which has a high-quartz structure. In this structure, Li^+ is stuffed into interstices.[4] Considering the factors of ionic radius ratio, coordination number, and valency, the Be^{++} ion should be a suitable choice to substitute for the Li^+ ion. However, considering its toxicity, Be^{++} will unlikely be introduced to replace Li^+ in this system. Thus, the most promising choice is probably the Mg^{++} ion.

Table 3 presents a summary of the compositions tested for Li^+ substitution. One sample (YS-52) was prepared by solid-state reaction in which 20.4 mol% of Li^+ was replaced by Mg^{++} ($2Li^+ \rightleftharpoons Mg^{++}$). This

composition formed β-$LiAlSiO_4$ solid solution with a trace amount of $AlPO_4$; the average thermal expansion coefficient of the sample was $-2.31 \times 10^{-7}/^{o}C$.

Table 3. Summary of thermal expansion data for samples with ionic substitutions for Li^+.

Sample No.	Initial Composition	Sample Processing (Temp, °C/Time, h)	Phase Composition	Thermal Expansion $\alpha(\times 10^{-7}/^{o}C)$
YS-21	$Li_{0.364}Mg_{0.078}AlP_{0.48}Si_{0.52}O_4$ [a]	1200/96, 1200/120	Multiphase	NA
YS-22	$Li_{0.416}Mg_{0.052}AlP_{0.48}Si_{0.78}O_4$ [a]	1200/96, 1200/120	Multiphase	NA
YS-52	$Li_{0.39}Mg_{0.05}AlP_{0.51}Si_{0.49}O_4$ [b]	1200/54, 1200/60	S.S.[d] + tr $AlPO_4$	-2.81
YS-53	$Li_{0.33}Mg_{0.08}AlP_{0.51}Si_{0.49}O_4$ [b]	1200/54, 1200/60, 1200/40	Multiphase	NA
YS-55	$Li_{0.33}Mg_{0.075}AlP_{0.52}Si_{0.48}O_4$ [b]	1200/58, 1200/60, 1200/40	Multiphase	NA
YS-27	$Li_{0.45}Na_{0.05}AlP_{0.5}Si_{0.5}O_4$ [c]	1200/40, 1200/40, 1200/40	Multiphase	NA
YS-28	$Li_{0.4}Na_{0.1}AlP_{0.5}Si_{0.5}O_4$ [c]	1200/40, 1200/40, 1200/40	Multiphase	NA
YS-49	$Li_{0.42}Mg_{0.04}AlP_{0.5}Si_{0.5}O_4$ [b]	1200/50	S.S + tr $AlPO_4$	-6.1

[a] $Al(OH)_3$ nH_2O, $(NH_4)_2HPO_4$, silica gel, Li_2CO_3, MgO

[b] $Al(OH)_3$ nH_2O, $NH_4H_2PO_4$, silicic acid, Li_2CO_3 $MgSO_4$

[c] $Al(OH)_3$ nH_2O, $(NH_4)_2HPO_4$, silica gel, Li_2CO_3, Na_2CO_3

[d] S.S. = Solid solution

Additional samples prepared using multiple, extended heat treatments of compositions containing Mg^{++} substitutions of 32.65 mol% (YS-53) and 31 mol% (YS-55) formed multiphases. Thus it appears likely that the replaceable amount of Li^+ by Mg^{++} is less than 30 mol%. Work is continuing on the substitution of Mg^{++} for Li^+ in this system.

Attempts to substitute Na^+ for Li^+ (samples YS-27 and YS-28 in Table 3) have resulted in multiphase compositions. It was likely that, due to the differences of radius ratio and coordination state of the two ions, Na^+ cannot replace Li^+ in this system.

Summary

Samples formed from the $AlPO_4$-BPO_4-β-eucryptite ternary compositions in open systems do not show good phase composition or improved thermal expansion. Increasing the content of β-eucryptite in the compositions has resulted in the lowering of both softening points and melting points.[5]

Several samples formed in the Al_2O_3-P_2O_5-SiO_2-Li_2O and Al_2O_3-P_2O_5-SiO_2-Li_2O-MgO systems show promising phase compositions and low thermal expansion results. More work shall be done in these two systems.

Silica System

The high-low crystallographic inversion of cristobalite remains the greatest barrier to its high-temperature application. Although the high-temperature phase (β-cristobalite) is highly desirable because of its isotropic low thermal expansion behavior, large volume changes always occur upon the high-low phase transition, which is characterized by changes in the configuration of secondary coordination. The inversion temperature seems to follow a statistical distribution, implying local inhomogeneities or domain structure. Like most compounds exhibiting high-low inversions, high cristobalite cannot be brought to room temperature without mechanical constraints.

Two factors are known to affect the inversion temperature: heat treatment and formation of solid solution. Therefore, present studies involve the formation of cristobalite solid solution at different temperatures with different combinations of compounds isostructural with cristobalite. Three systems were studied, SiO_2-$AlPO_4$-TiO_2, SiO_2-BPO_4-TiO_2, and SiO_2-$AlPO_4$-BPO_4. It is hoped that the inversion temperature can be lowered significantly, and that the amount of

expansion associated with the high-low inversion can be reduced by forming solid solution at the maximum solubility limit.

Experimental

Raw materials used included silicic acid, TiO_2, H_3BO_3, $(NH_4)_2HPO_4$, and $Al(OH)_3 \cdot nH_2O$. $AlPO_4$ was made by reacting $Al(OH)_3 \cdot nH_2O$ and $(NH_4)_2HPO_4$, and BPO_4 was prepared using H_3BO_3 and $(NH_4)_2HPO_4$. XRD examinations of the synthetic compounds show pure phase formation and good crystallinity. Compositions studied for the three systems were prepared from silicic acid, $AlPO_4$, BPO_4, and TiO_2. After being mixed in acetone, samples were calcined at 1000°C for 2 hours for the SiO_2-$AlPO_4$-TiO_2 system, and at 800°C for 10 hours for those containing BPO_4. The calcined samples were sealed in platinum tubes and heat treated at different temperatures for 72 hours, followed by quenching in cold water.

Standard XRD and petrographic analyses were performed for phase identification. The inversion temperatures of cristobalite were measured by differential scanning calorimetry (DSC) at a heating rate of 20°C/min. For thermal expansion measurements, reacted powders were pressed into bars and sintered at the temperatures shown in Tables 4-6 for 10 hours. Measurements were carried out in an automatic dual push rod dilatometer (Netzsch 402 ED). Indium and sapphire standards were used to calibrate both the DSC and the dilatometer.

Results and Discussion

<u>SiO_2-$AlPO_4$-TiO_2 System.</u> Phase analyses and inversion temperatures of cristobalite solid solutions heat treated at different temperatures are shown in Table 4. The crystallographic features of SiO_2 cristobalite and $AlPO_4$ cristobalite are so similar that, even at a low scan rate (0.25°/min), the two phases cannot be clearly distinguished in the x-ray patterns. Phase identifications are therefore largely based on petrographic and DSC analyses since these two phases can be easily distinguished using polarized light and by inversion temperatures.

Table 4. Phase analyses and inversion temperatures of cristobalite solid solution for the SiO_2-$AlPO_4$-TiO_2 system.

Sample No.	Composition (wt%) SiO_2	$AlPO_4$	TiO_2	Temp(°C)	Phase	Inversion Temp(°C)
TS-72	93	5	2	1413	α-crist.(s.s.) + $AlPO_4$(s.s.)	196
TS-73				1475	α-crist.(s.s.) + $AlPO_4$(s.s.)(tr)	193
TS-74				1492	α-crist.(s.s.)	193
TS-75				1513	α-crist.(s.s.) + glass	194
TS-76	90	7	3	1413	α-crist.(s.s.) + $AlPO_4$(s.s.)	183.6
TS-58				1475	α-crist.(s.s.) + $AlPO_4$(s.s.)	180
TS-77				1492	α-crist.(s.s.) + glass (tr)	185
TS-54				1513	α-crist.(s.s.) + glass	179
TS-78	90	5	5	1413	α-crist.(s.s.) + TiO_2	192
TS-59				1475	α-crist.(s.s.) + TiO_2	167
TS-79				1492	α-crist.(s.s.)	165
TS-55				1513	α-crist.(s.s.) + glass	174
TS-80	90	3	7	1413	α-crist.(s.s.) + TiO_2	190
TS-60				1475	α-crist.(s.s.) + TiO_2	170
TS-81				1492	α-crist.(s.s.) + TiO_2	162
TS-56				1513	α-crist.(s.s.) + glass	164
TS-82	87	10	3	1413	α-crist.(s.s.) + $AlPO_4$(s.s.) + TiO_2	196
TS-83				1475	α-crist.(s.s.) + $AlPO_4$(s.s.)	179
TS-84				1492	α-crist.(s.s.) + $AlPO_4$(s.s.)(tr)	174
TS-85				1513	α-crist.(s.s.) + glass + $AlPO_4$(s.s.)(tr)	181
TS-86	80	15	5	1413	α-crist.(s.s.) + $AlPO_4$(s.s.) + TiO_2	191
TS-87				1475	α-crist.(s.s.) + $AlPO_4$(s.s.) + TiO_2	181
TS-88				1492	α-crist.(s.s.) + $AlPO_4$(s.s.) + TiO_2(tr)	163
TS-89				1513	α-crist.(s.s.) + $AlPO_4$(s.s.) + glass	175
TS-90	80	10	10	1413	α-crist.(s.s.) + $AlPO_4$(s.s.) + TiO_2	191
TS-61				1475	α-crist.(s.s.) + $AlPO_4$(s.s.) + TiO_2	171
TS-57				1513	α-crist.(s.s.) + $AlPO_4$(s.s.) + glass	168
TS-91	78	17	5	1413	α-crist.(s.s.) + $AlPO_4$(s.s.) + TiO_2	190
TS-92				1475	α-crist.(s.s.) + $AlPO_4$(s.s.) + TiO_2	180
TS-93				1492	α-crist.(s.s.) + $AlPO_4$(s.s.) + TiO_2(tr)	162
TS-94				1513	α-crist.(s.s.) + $AlPO_4$(s.s.) + glass	175
TS-95	78	15	7	1413	α-crist.(s.s.) + $AlPO_4$(s.s.) + TiO_2	192
TS-96				1475	α-crist.(s.s.) + $AlPO_4$(s.s.) + TiO_2	187
TS-97				1513	α-crist.(s.s.) + $AlPO_4$(s.s.) + glass	173
TS-98	70	15	15	1413	α-crist.(s.s.) + $AlPO_4$(s.s.) + TiO_2	191
TS-99				1475	α-crist.(s.s.) + $AlPO_4$(s.s.) + TiO_2	173
TS-100				1492	glass	
TS-101	60	20	20	1413	α-crist.(s.s.) + $AlPO_4$(s.s.) + TiO_2	191
TS-102				1475	α-crist.(s.s.) + $AlPO_4$(s.s.) + TiO_2	174
TS-103				1513	glass + TiO_2(tr) + $AlPO_4$(tr)	--

For all samples, the inversion temperatures of cristobalite solid solutions show a continuous decrease with increasing concentration of $AlPO_4$ and TiO_2. The lowest inversion temperature occurs at 162°C for the SiO_2-$AlPO_4$-TiO_2 system. Beyond solubility limits, the presence of second phases does not seem to change the inversion temperature. Although the solubility of $AlPO_4$ is higher than that of TiO_2 in cristobalite, the lowering of the inversion temperature is mainly attributed to the effects of TiO_2.

As shown in Table 4, samples with TiO_2 concentrations lower than 5% exhibit high inversion temperatures (above 174°C), even though the $AlPO_4$ concentration is high. When the TiO_2 content is sufficiently high (around 5%), the inversion temperature can be lowered to 162°C with only 3% $AlPO_4$. This is also made clear by the SiO_2-TiO_2 and SiO_2-$AlPO_4$ binary systems. [In the present investigation, it was found that in the SiO_2-TiO_2 system, the inversion temperature was lowered from 260°C to about 190°C with less than 5% TiO_2, whereas in the SiO_2-$AlPO_4$ system, 15% $AlPO_4$ was required to lower the inversion temperature to only 244°C (reported in last semiannual report[5]). These results indicate that TiO_2 is more efficient than $AlPO_4$ in lowering the inversion temperature.]

For temperatures and compositions studied, the SiO_2-$AlPO_4$-TiO_2 system appears to be a true ternary system with the eutectic plane at 1492°C, at which the lowest inversion temperature was obtained. The solubility limit is approximately 4-5% TiO_2 and 7-8% $AlPO_4$.

<u>SiO_2-BPO_4-TiO_2 System</u>. Phase analyses and inversion temperatures of cristobalite solid solution are presented in Table 5. It was expected that TiO_2 would lower the inversion temperature as in the SiO_2-$AlPO_4$-TiO_2 system; however, the inversion temperatures remained high for the SiO_2-BPO_4-TiO_2 system due to the formation of TiP_2O_7. The formation of TiP_2O_7 consumes both TiO_2 and BPO_4. As a result, only a limited amount of TiO_2 or BPO_4 can enter the cristobalite lattice.

It is likely that the low stability of BPO_4 at high temperatures results in the formation of TiP_2O_7, which is not found in the SiO_2-$AlPO_4$-TiO_2 system. The inversion temperature cannot be

significantly lowered without the simultaneous presence of sufficient amounts of both TiO_2 and BPO_4 in the cristobalite lattice. The presence of TiP_2O_7 indicates either non-equilibrium conditions or that the SiO_2-BPO_4-TiO_2 system is not a true ternary system. Long heat treatments at low temperatures as well as recrystallization from glass will be continued for this system to test equilibrium conditions.

Table 5. Phase analyses and inversion temperatures of cristobalite solid solution for the SiO_2-BPO_4-TiO_2 system.

Sample No.	Composition (wt%) SiO_2	BPO_4	TiO_2	Temp(°C)	Phase	Inversion Temp(°C)
TS-62	90	7	3	1000	α-crist.(s.s.) + TiP_2O_7 + B_2O_3(tr)	197
TS-63				1050	α-crist.(s.s.) + TiP_2O_7 + glass(tr)	201
TS-104				1195	α-crist.(s.s.) + TiP_2O_7(tr) + glass(tr)	180
TS-64	90	5	5	1000	α-crist.(s.s.) + TiP_2O_7	193
TS-65				1050	α-crist.(s.s.) + TiP_2O_7	200
TS-105				1195	α-crist.(s.s.) + TiP_2O_7	184
TS-66	90	3	7	1000	α-crist.(s.s.) + TiP_2O_7	194
TS-67				1050	α-crist.(s.s.) + TiP_2O_7	200
TS-106				1195	α-crist.(s.s.) + TiP_2O_7	222
TS-68	80	10	10	1000	α-crist.(s.s.) + TiP_2O_7 + glass (tr)	192
TS-69				1050	α-crist.(s.s.) + TiP_2O_7 + glass	201
TS-107				1195	α-crist.(s.s.) + TiP_2O_7(tr) + glass	180
TS-70	70	15	15	1000	α-crist.(s.s.) + TiP_2O_7(tr) + glass	193
TS-71				1050	α-crist.(s.s.) + TiP_2O_7(tr) + glass	200
TS-108				1195	glass + α-crist.(tr)	--

<u>SiO_2-$AlPO_4$-BPO_4 System</u>. Phase analyses and inversion temperatures of cristobalite solid solution are shown in Table 6. The average inversion temperature for this system is around 200°C except for those of composition $90SiO_2 \cdot 7AlPO_4 \cdot 3BPO_4$, which are even higher. The low stability of BPO_4 causes glass formation at low temperatures, and $AlPO_4$ has little effect on lowering the inversion temperature.

Table 6. Phase analyses and inversion temperatures of cristobalite solid solution for the SiO_2-$AlPO_4$-BPO_4 system.

Sample No.	Composition (wt%) SiO_2	$AlPO_4$	BPO_4	Temp(°C)	Phase	Inversion Temp(°C)
TS-109	90	3	7	1050	α-crist.(s.s.) + glass(tr)	203
TS-110				1160	α-crist.(s.s.) + glass	195
TS-111				1300	α-crist.(s.s.) + glass	193
TS-112				1431	glass	--
TS-113	90	5	5	1050	α-crist.(s.s.)	197
TS-114				1160	α-crist.(s.s.) + BPO_4(s.s.)(tr)	205
TS-115				1300	α-crist.(s.s.) + glass	197
TS-116				1430	α-crist.(s.s.) + glass	192
TS-117	90	7	3	1050	α-crist.(s.s.)	219
TS-118				1160	α-crist.(s.s.)	226
TS-119				1300	α-crist.(s.s.) + glass(tr)	238
TS-120				1431	α-crist.(s.s.) + glass	239
TS-121	80	10	10	1050	α-crist.(s.s.) + glass	197
TS-122				1160	α-crist.(s.s.) + glass	196
TS-123				1300	α-crist.(s.s.) + glass	207
TS-124				1431	glass	--

Summary

It can be concluded from the experimental results of the present work that the high-low inversion temperature of cristobalite solid solution is mainly determined by solute concentrations. Heat treatment does not appear to play an important role since no correlation between the inversion and formation temperature of cristobalite is apparent from the present study. The lowest inversion temperature achieved is 162°C from the SiO_2-$AlPO_4$-BPO_4 system. The high inversion temperatures result from either compound (TiP_2O_7) or solid solution [$(Al,B)PO_4$] formation. The thermal expansion behavior associated with the high-low inversion of cristobalite solid solution appears to be independent of the inversion temperature. Samples with different inversion temperatures show thermal expansion behavior similar to that of pure cristobalite. It is apparent that the extent of solid solution is determined by a number of variables in addition to isotructural effects. A study of the overall chemistry must be considered.

Thus far, work has been concentrated only on the cation substitution of Si^{+4}. In addition to anion substitution, such as N^{-3}

for O^{-2}, the effects of substitutions of silica by its stuffed derivative compounds on inversion behaviors will be studied.

Mullite System

The thermal expansion behavior of various mullite solid solutions was investigated. The work on mullite modified with $AlPO_4$, BPO_4, $CrPO_4$, $BAsO_4$, $AlAsO_4$, and $GaAsO_4$ has been completed. TiO_2-modified mullite has been studied in order to optimize the results in the system $Al_xTi_ySi_7O_{13}$ as shown in the previous semiannual report.[5] A processing technique using the hydrolysis of alkoxide to develop the mullite solid solution was employed in synthesizing various compositions of oxide-modified mullite.

Experimental

The starting materials were $Si(OC_2H_5)_4$, $Al[(CH_5)_2CHO]_3$, $Al[C_2H_5CH(CH_3)O]_3$, $Ti[OCH(CH_3)_2]_4$, $(CH_3O)PO$, and $(CH_3O)_3B$. The procedures for synthesizing the modified mullite are presented in the flow chart shown in Figure 1.

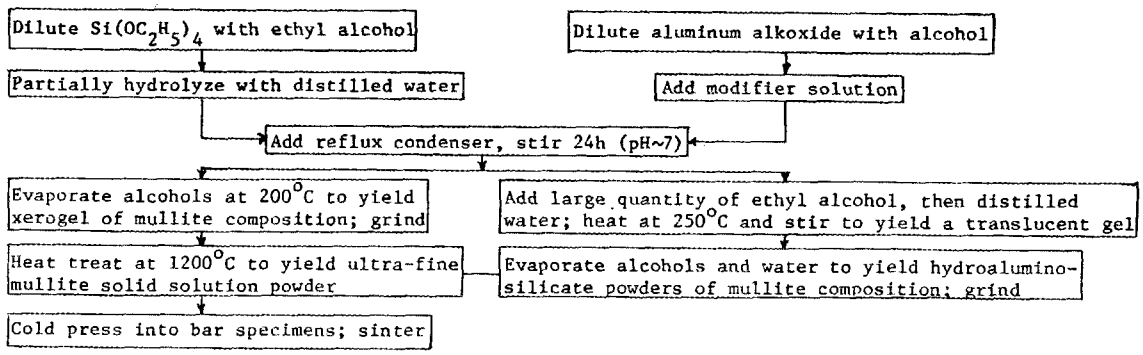

Figure 1. Sol-gel processing of chemically modified mullite.

XRD phase analysis and petrographic microscopy were performed after each sintering. The latter was mainly used to detect the possible presence of glassy phase. If a glassy phase was formed, a recrystallization procedure was performed to achieve phase equilibrium.

The linear aggregate CTE of bar specimens having single-phase mullite solid solutions was measured on an automatic differential dilatometer. Duplicate measurements were taken on all specimens.

Results and Discussion

Since the initial results in the Al_2O_3-TiO_2-SiO_2 system showed a decrease in thermal expansion with an increase in TiO_2 content in single-phase mullite and mullite with Al_2TiO_5, the study on single-phase mullite was intensified. A series of new compositions was examined based on the following stoichiometries:

$$Al_6Si_{2-x}Ti_xO_{13}$$
$$Al_{6-4y}Ti_{3y}\square_ySi_2O_{13}$$

The above expressions include the assumption that, crystal-chemically, there are two available sites in the mullite crystal structure in which Ti^{4+} may substitute. They are the octahedral and the tetrahedral sites of Al and Al/Si, respectively. The 3:2 mullite stoichiometry was selected because 3:2 mullite is readily synthesized at a reasonably low temperature (below that of 2:1 mullite) and, more importantly, 3:2 mullite has a lower CTE value than other x:2 mullites ($3<x\leq4$), as reported previously.[6]

Tests to determine the effect of sintering temperature on phase composition and thermal expansion of Ti-modified mullite were conducted. Specimens having the composition $Al_{5.6}Ti_{0.3}\square_{0.1}Si_2O_{13}$ were sintered at temperatures ranging from 1350 to >1650°C, as shown in Table 7. It was observed that sintering at 1550°C for 72 hours resulted in the least amount of Al_2TiO_5 formation and the highest degree of mullitization. The presence of Al_2TiO_5 as a second phase is undesirable because its high expansion anisotropy generates local stress causing grain-boundary microcracking, thus weakening the structure, although its aggregate CTE is very low.

Table 7. Summary of thermal expansion data for the Ti-modified mullite system synthesized by sol-gel processing.

Sample No.	Composition	Al_2O_3/SiO_2 molar ratio	Sintering (temp,°C/time,h)	Phase(s) Present	CTE $\alpha(x10^{-6}/°C)$ R.T.-1000°C
J-0901	$Al_{5.6}Ti_{0.3}\square_{0.1}Si_2O_{13}$	1.40	1350/72	M + R(mi)	N.A.
J-0902	$Al_{5.6}Ti_{0.3}\square_{0.1}Si_2O_{13}$	1.40	1450/72	M + AT(tr)	N.A.
J-0903	$Al_{5.6}Ti_{0.3}\square_{0.1}Si_2O_{13}$	1.40	1500/72	M + AT(tr)	N.A.
J-0904	$Al_{5.6}Ti_{0.3}\square_{0.1}Si_2O_{13}$	1.40	1550/72	M + AT(tr)	4.8
J-0905	$Al_{5.6}Ti_{0.3}\square_{0.1}Si_2O_{13}$	1.40	1600/72	M + AT(tr) + R(tr)	N.A.
J-0906	$Al_{5.6}Ti_{0.3}\square_{0.1}Si_2O_{13}$	1.40	1650/20	M + R(tr)	N.A.
J-0907	$Al_{5.6}Ti_{0.3}\square_{0.1}Si_2O_{13}$	1.40	melted	M + R(tr)	N.A.
J-082	$Al_6Ti_{0.1}Si_{1.9}O_{13}$	1.58	1500/72	M	5.0
J-083	$Al_6Ti_{0.2}Si_{1.8}O_{13}$	1.67	1500/72	M	5.1
J-084	$Al_6Ti_{0.3}Si_{1.7}O_{13}$	1.76	1500/72	M + AT(tr)	N.A.
J-091	$Al_{5.73}Ti_{0.19}\square_{0.07}Si_2O_{13}$	1.44	1550/72	M	4.6

M = Mullite solid solution
AT = Al_2TiO_5 (Aluminum Titanate)
R = rutile
N.A. = not available
tr = trace
mi = minor amount

The results also indicate that Al_2TiO_5 coexists with Ti-modified mullite from 1450°C to 1600°C. At a temperature greater than 1600°C, Al_2TiO_5 decomposes, then a Ti-modified mullite (rich in Al) coexists with rutile. To confirm these results, the specimens were reground and sintered at the same temperature for the same length of time. The final phases present remained unchanged, indicating complete phase equilibrium.

Specimens J-082, J-083, and J-084 were prepared according to the formula $Al_6Si_{1-x}Ti_xO_{13}$, which assumed that Ti ions substitute for Si ions in tetrahedral sites. The resulting compositions would be SiO_2 deficient corresponding to higher Al_2O_3/SiO_2 values. As shown in Table

7, the thermal expansion behavior of the samples was comparable to that of the 3:2 mullite.

Specimen J-091 ($Al_{5.73}Ti_{0.19}\square_{0.07}Si_2O_{13}$) based on the formula $Al_{6-4x}Ti_{3x}\square_xSi_2O_{13}$ showed the lowest CTE value, 4.6 x $10^{-6}/^oC$, 13% lower than that of the $Al_6Si_2O_{13}$ specimen. As indicated in Table 7, Ti^{4+} appears to be less soluble (2 wt%) in the specimen having a higher Al_2O_3/SiO_2 molar ratio, and more soluble (4 wt%) in the specimen having a lower Al_2O_3/SiO_2 ratio. Thus it was concluded that a deficiency in Al_2O_3 is favored over a deficiency in SiO_2 in lowering the CTE of mullite.

In order to further lower the CTE of the Ti-modified mullite, B_2O_3 was used as a ternary addition. The specimens having compositions of $Al_{5.2}B_{0.8}Si_2O_{13}$ and $Al_{4.8}B_{1.2}Si_2O_{13}$ had CTE values of $5.0x10^{-6}/^oC$ and $5.1x10^{-6}/^oC$, respectively. These results indicate that B^{3+} substitution for Al^{3+} or Si^{4+} in tetrahedral sites, when Al^{3+} is deficient, does not increase the CTE of mullite. Therefore, a series of Ti-B-modified mullite was prepared. As shown in Table 8, B_2O_3 additions do not appear to affect the CTE of Ti-modified mullite.

Table 8. Summary of thermal expansion data for the B-Ti-modified mullite system.

Sample No.	Composition	Al_2O_3/SiO_2 molar ratio	Sintering (temp,°C/time,h)	Phase(s) Present	CTE $\alpha(x10^{-6}/°C)$ R.T.-1000°C
J-054*	$Al_{5.2}B_{0.8}Si_2O_{13}$	1.3	1500/24	M + g(tr)	5.0
J-055*	$Al_{4.8}B_{1.2}Si_2O_{13}$	1.2	1500/24	M + g(tr)	5.1
J-072	$Al_{5.2}B_{0.8}Si_2O_{13}$	1.3	1550/72	M	5.2
J-086	$Al_{5.1}B_{0.9}Si_{1.7}Ti_{0.3}O_{13}$	1.5	1550/80	M + AT(tr)	N.A.
J-089	$Al_{4.94}B_{0.80}Ti_{0.2}\square_{0.07}Si_2O_{13}$	1.24	1550/80	M	4.9
J-092	$Al_{5.14}B_{0.6}Ti_{0.2}\square_{0.07}Si_2O_{13}$	1.29	1550/72	M	5.1**

* synthesized by solid-state reaction
** average value from 10 identical bar specimens

The compositions $3Al_2O_3 \cdot (2-2x)SiO_2 \cdot xXYO_4$ were synthesized by solid-state reaction where x = 0.1 and XYO_4 = either $AlPO_4$, BPO_4, $GaPO_4$, $CrPO_4$, $BAsO_4$, $AlAsO_4$, or $GaAsO_4$. Synthesized compounds XYO_4 of high purity were mixed with $Al(OH)_3 \cdot nH_2O$ and $SiO_2 \cdot nH_2O$. For the compounds $AlPO_4$, BPO_4, $GaPO_4$, and $CrPO_4$, starting materials such as $Al(OH)_3 \cdot nH_2O$, $(NH_4)_2HPO_4$, H_3BO_3, Ga_2O_3, and Cr_2O_3 were mixed directly with $Al(OH)_3 \cdot nH_2O$ and $SiO_2 \cdot nH_2O$. A step-heating schedule was used to prevent the loss of P_2O_5 on ignition. $AlPO_4$- and BPO_4-modified mullites were also prepared by sol-gel processing to compare the results with those of samples prepared by solid-state synthesis.

All specimens were fired for three 3-day periods at 1500°C. Between each firing, the powders were reground and examined by XRD and transmission optical microscopy. Although mullite was the major phase in the final phase assemblage, minor amounts of Al_2O_3 were always present. For specimens modified by XPO_4 compounds, $(X,Al)PO_4$ solid solution was always found in trace amounts, indicating that XPO_4 forms solid solution with Al_2O_3.

Summary

1. TiO_2 additions lower the CTE of mullite by 13%.
2. In TiO_2-modified mullite, a deficiency in Al in stoichiometry is favored over a deficiency in Si in lowering the CTE of mullite.
3. Addition of B_2O_3 (more than 10 mol%) did not lower the CTE of Ti-modified mullite (ss).
4. XYO_4 compounds substituting for SiO_2 show no solubility.

Zircon-Based System

As previously reported,[5] an investigation of the linear aggregate thermal expansion of the $NaZr_2(PO_4)_3$-type (hereafter NZP) system is underway. Substitutions of elements with the electron valence from +1 to +5 for Na^+ in the NZP structure were previously investigated and reported. Currently, the solid solubility formed by substituting alkali and/or alkaline earth ions for Na^+ ion in the NZP structure is

being studied. CTE measurements were performed on compositions showing single phase.

Experimental

During sample preparation, the raw materials were heat treated at 100°C for 24h, and at 1300°C for 4h. The samples were then reground and sintered at 1300°C for 8h. To aid sintering, 1 to 2 wt% ZnO was added to the reground powder.

XRD patterns were obtained to determine the phases present after sample preparation. A fused silica dilatometer was used to measure CTE from room temperature to 1000°C using a heating rate of 5 to 6°C/min. Thermal expansion values were corrected by adding the thermal expansion of fused silica ($5.0 \times 10^{-7}/°C$). Thermal expansion values less than $10 \times 10^{-7}/°C$ in absolute value were verified by repeated testing.

Results and Discussion

After sample synthesis, phases present were identified by XRD. The linear CTE values for compounds were measured. Table 9 presents the experimental data. For the convenience of analysis, systems are classified into 4 groups.

Group A consists of systems substituted with several mole combinations of alkali ions for the Na^+ ion in the first part of the NZP structure. From the XRD pattern analysis, compounds modified by [Rb^+(1.49Å) - Cs^+(1.65Å)] and [Na^+(0.98Å) - K^+(1.33Å)][7] (ionic radii are based on a coordination number of 6 because of the octahedral structure of NaO_6 in the NZP structure[8]) showed single phase, and the sample substituted by ($1/2Rb^+$-$1/2K^+$) showed solid solution.

The tendency for solid-solution formation between alkali-alkali ions in the NZP-type structure was not due to the complex structure of NZP. The difference in the radii of the ions showing solubility was 9.7% for (Rb^+-Cs^+) and 26.3% for (Na^+-K^+). In systems substituted by (Rb^+-K^+), the composition ($1/2Rb^+$-$1/2K^+$) showed solubility in spite of the ionic size difference of 10.7%; the compositions ($3/4Rb^+$-$1/4K^+$) and ($1/4Rb^+$-$3/4K^+$) did not show solid solubility.

Table 9. Phase analysis and thermal expansion results for the NZP-modified compounds.

Group	Sample Designation	Composition (Moles)	Phase	Thermal Expansion $\alpha(x10^{-7}/°C)$	Temp Range (°C)
A	JK-RN1	$Rb_{0.25}Na_{0.75}Zr_2(PO_4)_3$	$RbZr_2(PO_4)_3 + NaZr_2(PO_4)_3$	N.A.	N.A.
	JK-RN2	$Rb_{0.5}Na_{0.5}Zr_2(PO_4)_3$	$RbZr_2(PO_4)_3 + NaZr_2(PO_4)_3$	N.A.	N.A.
	JK-RN3	$Rb_{0.75}Na_{0.25}Zr_2(PO_4)_3$	$RbZr_2(PO_4)_3 + NaZr_2(PO_4)_3$	N.A.	N.A.
	JK-RK1	$Rb_{0.25}K_{0.75}Zr_2(PO_4)_3$	$RbZr_2(PO_4)_3 + KZr_2(PO_4)_3$	N.A.	N.A.
	JK-RK2	$Rb_{0.5}K_{0.5}Zr_2(PO_4)_3$	$(Rb_{0.5}K_{0.5})Zr_2(PO_4)_3$	- 15	R.T.-1000°C
	JK-RK3	$Rb_{0.75}K_{0.25}Zr_2(PO_4)_3$	$RbZr_2(PO_4)_3 + KZr_2(PO_4)_3$	N.A.	N.A.
	JK-RC1	$Rb_{0.25}Cs_{0.75}Zr_2(PO_4)_3$	$(Rb_{0.25}Cs_{0.75})Zr_2(PO_4)_3$	2	R.T.-1000°C
	JK-RC2	$Rb_{0.5}Cs_{0.5}Zr_2(PO_4)_3$	$(Rb_{0.5}Cs_{0.5})Zr_2(PO_4)_3$	-0.3	R.T.-1000°C
	JK-RC3	$Rb_{0.75}Cs_{0.25}Zr_2(PO_4)_3$	$(Rb_{0.75}Cs_{0.25})Zr_2(PO_4)_3$	- 2	R.T.-1000°C
	JK-CN1	$Cs_{0.25}Na_{0.75}Zr_2(PO_4)_3$	$CsZr_2(PO_4)_3 + NaZr_2(PO_4)_3$	N.A.	N.A.
	JK-CN2	$Cs_{0.5}Na_{0.5}Zr_2(PO_4)_3$	$CsZr_2(PO_4)_3 + NaZr_2(PO_4)_3$	N.A.	N.A.
	JK-CN3	$Cs_{0.75}Na_{0.25}Zr_2(PO_4)_3$	$CsZr_2(PO_4)_3 + NaZr_2(PO_4)_3$	N.A.	N.A.
	JK-CK1	$Cs_{0.25}Na_{0.75}Zr_2(PO_4)_3$	$CsZr_2(PO_4)_3 + KZr_2(PO_4)_3$	N.A.	N.A.
	JK-CK2	$Cs_{0.5}K_{0.5}Zr_2(PO_4)_3$	$CsZr_2(PO_4)_3 + KZr_2(PO_4)_3$	N.A.	N.A.
	JK-CK3	$Cs_{0.75}K_{0.25}Zr_2(PO_4)_3$	$CsZr_2(PO_4)_3 + KZr_2(PO_4)_3$	N.A.	N.A.
	JK-NK1	$Na_{0.25}K_{0.75}Zr_2(PO_4)_3$	$(Na_{0.25}K_{0.75})Zr_2(PO_4)_3$	N.A.	N.A.
	JK-NK2	$Na_{0.5}K_{0.5}Zr_2(PO_4)_3$	$(Na_{0.5}K_{0.5})Zr_2(PO_4)_3$	N.A.	N.A.
	JK-NK3	$Na_{0.75}K_{0.25}Zr_2(PO_4)_3$	$(Na_{0.75}K_{0.25})Zr_2(PO_4)_3$	N.A.	N.A.
B	JK-RMM	$Rb_{0.5}Mg_{0.25}Zr_2(PO_4)_3$	$RbZr_2(PO_4)_3 + MgZr_4(PO_4)_6$	N.A.	N.A.
	JK-RCM	$Rb_{0.5}Ca_{0.25}Zr_2(PO_4)_3$	$RbZr_2(PO_4)_3 + CaZr_4(PO_4)_6$	N.A.	N.A.
	JK-RSM	$Rb_{0.5}Sr_{0.25}Zr_2(PO_4)_3$	$RbZr_2(PO_4)_3 + SrZr_4(PO_4)_6$	N.A.	N.A.
	JK-RBM	$Rb_{0.5}Ba_{0.25}Zr_2(PO_4)_3$	$RbZr_2(PO_4)_3 + BaZr_4(PO_4)_6$	N.A.	N.A.
	JK-CMM	$Cs_{0.5}Mg_{0.25}Zr_2(PO_4)_3$	$CsZr_2(PO_4)_3 + MgZr_4(PO_4)_6$	N.A.	N.A.
	JK-CCM	$Cs_{0.5}Ca_{0.25}Zr_2(PO_4)_3$	$CsZr_2(PO_4)_3 + CaZr_4(PO_4)_6$	N.A.	N.A.
	JK-CSM	$Cs_{0.5}Sr_{0.25}Zr_2(PO_4)_3$	$CsZr_2(PO_4)_3 + SrZr_4(PO_4)_6$	N.A.	N.A.
	JK-CBM	$Cs_{0.5}Ba_{0.25}Zr_2(PO_4)_3$	$CsZr_2(PO_4)_3 + BaZr_4(PO_4)_6$	N.A.	N.A.
	JK-CNM	$Ca_{0.25}Na_{0.5}Zr_2(PO_4)_3$	$(Ca_{0.25}Na_{0.5})Zr_2(PO_4)_3$	1	R.T.-900°C
	JK-CKM	$Ca_{0.25}K_{0.5}Zr_2(PO_4)_3$	$CaZr_4(PO_4)_6 + KZr_2(PO_4)_3$	N.A.	N.A.
	JK-MNM	$Mg_{0.25}Na_{0.5}Zr_2(PO_4)_3$	$MgZr_4(PO_4)_6 + NaZr_2(PO_4)_3$	N.A.	N.A.
	JK-MKM	$Mg_{0.25}K_{0.5}Zr_2(PO_4)_3$	$MgZr_4(PO_4)_6 + KZr_2(PO_4)_3$	N.A.	N.A.
	JK-BNM	$Ba_{0.25}Na_{0.5}Zr_2(PO_4)_3$	$(Ba_{0.25}Na_{0.5})Zr_2(PO_4)_3$	-17	R.T.-900°C
	JK-BKM	$Ba_{0.25}K_{0.5}Zr_2(PO_4)_3$	$(Ba_{0.25}K_{0.5})Zr_2(PO_4)_3$	N.A.	N.A.
	JK-SNM	$Sr_{0.25}Na_{0.5}Zr_2(PO_4)_3$	$(Sr_{0.25}Na_{0.5})Zr_2(PO_4)_3$	N.A.	N.A.
	JK-SKM	$Sr_{0.25}K_{0.5}Zr_2(PO_4)_3$	$SrZr_4(PO_4)_6 + KZr_2(PO_4)_3$	N.A.	N.A.

Table 9 (continued)

Group	Sample Designation	Composition (Moles)	Phase	Thermal Expansion $\alpha(x10^{-7}/°C)$	Temp Range (°C)
C	JK-MCC	$Mg_{0.25}Ca_{0.25}Zr_2(PO_4)_3$	$(Mg_{0.25}Ca_{0.25})Zr_2(PO_4)_3$	- 7	R.T.-1000°C
	JK-MSC	$Mg_{0.25}Sr_{0.25}Zr_2(PO_4)_3$	$(Mg_{0.25}Sr_{0.25})Zr_2(PO_4)_3$	18	R.T.-1000°C
	JK-MBC	$Mg_{0.25}Ba_{0.25}Zr_2(PO_4)_3$	$(Mg_{0.25}Ba_{0.25})Zr_2(PO_4)_3$	20	R.T.-1000°C
	JK-CSC	$Ca_{0.25}Sr_{0.25}Zr_2(PO_4)_3$	$(Ca_{0.25}Sr_{0.25})Zr_2(PO_4)_3$	13	R.T.-1000°C
	JK-CBC	$Ca_{0.25}Ba_{0.25}Zr_2(PO_4)_3$	$(Ca_{0.25}Ba_{0.25})Zr_2(PO_4)_3$	37	R.T.- 900°C
	JK-BSC	$Ba_{0.25}Sr_{0.25}Zr_2(PO_4)_3$	$(Ba_{0.25}Sr_{0.25})Zr_2(PO_4)_3$	32	R.T.- 950°C
D	JK-CNM4	$(\frac{1}{8}Ca\bullet\frac{3}{4}Na)Zr_2(PO_4)_3$	$(\frac{1}{8}Ca\bullet\frac{3}{4}Ca)Zr_2(PO_4)_3$	-51	R.T.-1000°C
	JK-CNMC	$(\frac{3}{8}Ca\bullet\frac{1}{4}Na)Zr_2(PO_4)_3$	$(\frac{3}{8}Ca\bullet\frac{1}{4}Na)Zr_2(PO_4)_3$	-31	R.T.-1000°C
	JK-CMC4	$(\frac{1}{8}Ca\bullet\frac{3}{8}Mg)Zr_2(PO_4)_3$	$CaZr_4(PO_4)_6 + MgZr_4(PO_4)_6$	N.A.	N.A.
	JK-CMCC	$(\frac{3}{8}Ca\bullet\frac{1}{8}Mg)Zr_2(PO_4)_3$	$(\frac{3}{8}Ca\bullet\frac{1}{8}Mg)Zr_2(PO_4)_3$	-10	R.T.-1000°C
	JK-CMN22	$(\frac{1}{16}Ca\bullet\frac{1}{16}Mg\bullet\frac{3}{4}Na)Zr_2(PO_4)_3$	$(\frac{1}{16}Ca\bullet\frac{1}{16}Mg\bullet\frac{3}{4}Na)Zr_2(PO_4)_3$	-25	R.T.-1000°C
	JK-CMN44	$(\frac{1}{8}Ca\bullet\frac{1}{8}Mg\bullet\frac{1}{2}Na)Zr_2(PO_4)_3$	$CaZr_4(PO_4)_6 + NaZr_2(PO_4)_3$	N.A.	N.A.
	JK-CMN66	$(\frac{3}{16}Ca\bullet\frac{3}{16}Mg\bullet\frac{1}{4}Na)Zr_2(PO_4)_3$	$CaZr_4(PO_4)_6 + NaZr_2(PO_4)_3$	N.A.	N.A.

Two explanations are presented for this solid solubility behavior. The first possible cause is due to weight difference of the two ions selected. Another possibility is an order-disorder transition characteristic. Most of the systems showing solid solution had one or two extra diffraction peaks which are not from impurity or unreactivity of the raw materials. The tendency to form a more ordered state by the substitution of two ions, for example (Rb^+-K^+), instead of one (Na^+) ion in the NZP structure was different for different compositions.

Thermal expansion results are shown in Table 9 for the compositions showing single phase. Compounds modified by (Na^+-K^+) were not considered because the $NaZr_2(PO_4)_3$ and $KZr_2(PO_4)_3$ compounds showed large negative expansion in our previous investigations whereas Rb^+-Cs^+ substitutions showed very low linear thermal expansion.[5] The linear thermal expansion values for $RbZr_2(PO_4)_3$ and $CsZr_2(PO_4)_3$ were 2 x $10^{-7}/°C$ and 5 x $10^{-7}/°C$, respectively.

The thermal expansion of $KZr_2(PO_4)_3$ was reported previously as -23 x $10^{-7}/°C$,[5] but the CTE of $(Rb_{0.5}K_{0.5})Zr_2(PO_4)_3$ was measured as -15 x

$10^{-7}/^{o}C$. This result is related to the basic theory of thermal expansion for mixed composites[4] and also to the reduction of thermal expansion by solid solution formation. Detailed thermal expansion behavior is shown in Figure 2.

Systems substituted by combining one-half mole of alkali with one-quarter mole of alkaline earth ions are classified in Group B. Only compounds combining large alkaline earth ions with small alkali ions showed complete solubility; these were Ca^{2+}(1.04Å)-Na^{+}(0.98Å), Ba^{2+}(1.38Å)-Na^{+}(0.98Å), Ba^{2+}(1.38Å)-K^{+}(1.33Å), and Sr^{2+}(1.20Å)-Na^{+}(0.98Å). The substitution of alkaline earth ions into the NZP skeletal framework creates vacancies. In order to form a stable single phase, the combinations of large alkaline earth ions with small alkali ions are more desirable than the opposite combination. Linear thermal expansions were measured and are shown in Figure 3. Due to the combination of two different ions with different electron valence values of +1 and +2, they showed phase instability above about 900°C.

Group C consists of the systems substituted by mixed alkaline earth ions. Irrespective of ionic size differences of the two elements, they showed solubility. The tendency of approaching complete solid solution by modification of alkaline earth-alkaline earth ions is related to vacancy formation by substitution of ions with electron valence of +2. That tendency appears related to the ease of replacing half of the positions of Na^{+} ions.

Figures 4 and 5 show the linear thermal expansion behavior of systems substituted by mixed alkaline earth ions. Compounds containing Ba^{2+}, which is a dense and large ion, showed phase instability or more drastic increase of thermal expansion in the high temperature range. Compositions containing Sr^{2+} [$Mg_{0.25}Sr_{0.25}Zr_2(PO_4)_3$ and $Ca_{0.25}Sr_{0.25}Zr_2(PO_4)_3$] show similar thermal expansion behavior, but $Ca_{0.25}Sr_{0.25}Zr_2(PO_4)_3$ shows a much smaller CTE value up to about 500°C. (It is reported that a U.S. patent has been filed for the system of $Ca_{0.25}Sr_{0.25}Zr_2(PO_4)_3$ for relatively low temperature application up to 550°C.[9]) The system $Mg_{0.25}Ca_{0.25}Zr_2(PO_4)_3$ showed linear expansion behavior of $-7 \times 10^{-7}/^{o}C$ up to 1000°C.

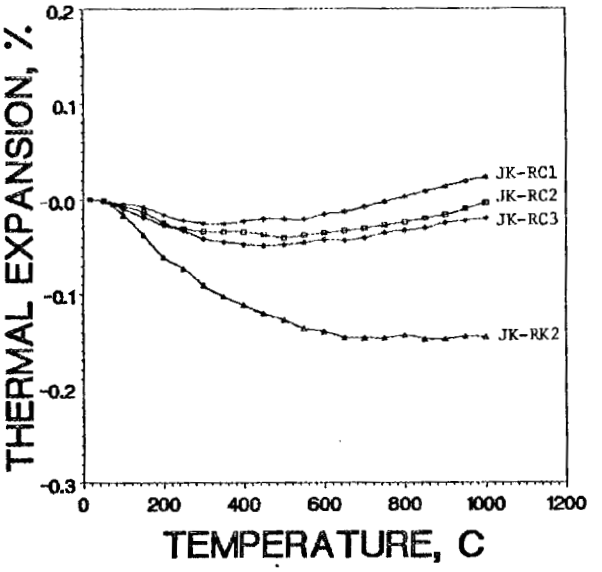

Figure 2. Linear thermal expansion behavior of NZP-type compounds modified by mixed alkali ions.

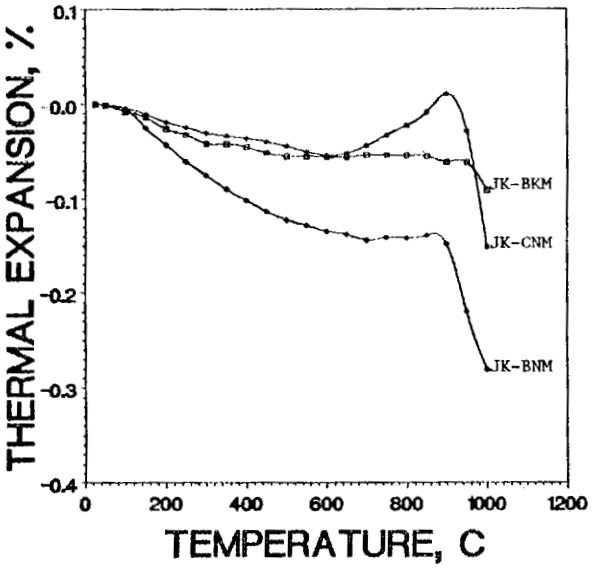

Figure 3. Linear thermal expansion behavior of NZP-type compounds modified by mixed alkali and alkaline earth ions.

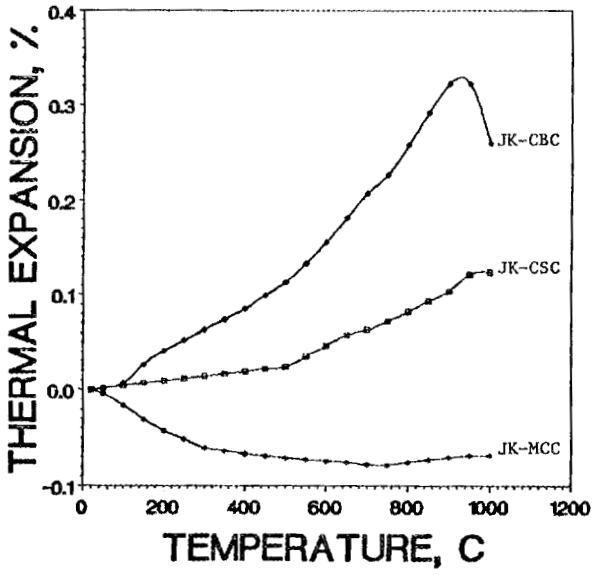

Figure 4. Linear thermal expansion behavior of NZP-type compounds modified by mixed alkaline earth ions.

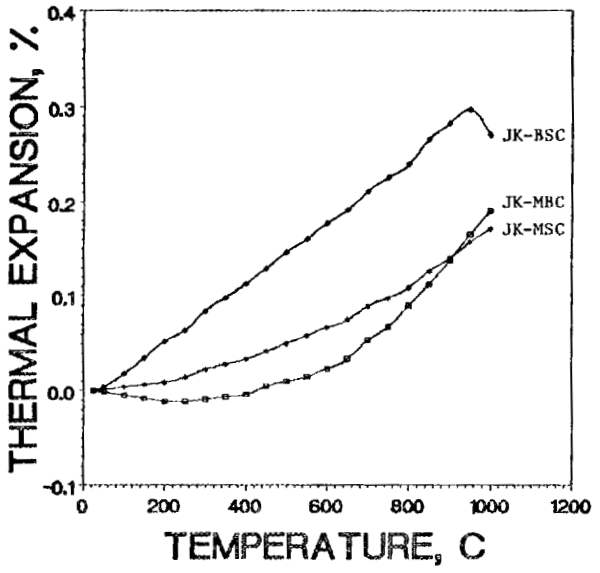

Figure 5. Linear thermal expansion behavior of NZP-type compounds modified by mixed alkaline earth ions.

From the significant result of $Mg_{0.25}Ca_{0.25}Zr_2(PO_4)_3$ and the economic considerations of its raw materials, several more systems based on (Ca-Na), (Ca-Mg) and (Ca-Mg-Na) substitutions were considered and are tabulated in Group D of Table 9. The quarternary compounds modified by Ca-Na or Ca-Mg for the first part of the NZP structure showed solid-solution behavior except for the $[(1/8Ca.3/8Mg)Zr_2(PO_4)_3]$.

For the compositions containing Ca-Mg-Na, only one preparation $[(1/16Ca,1/16Mg,3/4Na)Zr_2(PO_4)_3]$ showed single phase. From the results of Group B, the combination of large alkaline earth ions and small alkali ions seems to form a solid solution. In addition, the combination of Mg^{2+} (0.74Å) with Na^{+}(0.98Å) does not form a solid solution. Thermal expansion behaviors for the systems modified by (Ca-Mg-Na), (Ca-Mg), and (Ca-Na) are shown in Figure 6. All of the compounds showed negative expansion.

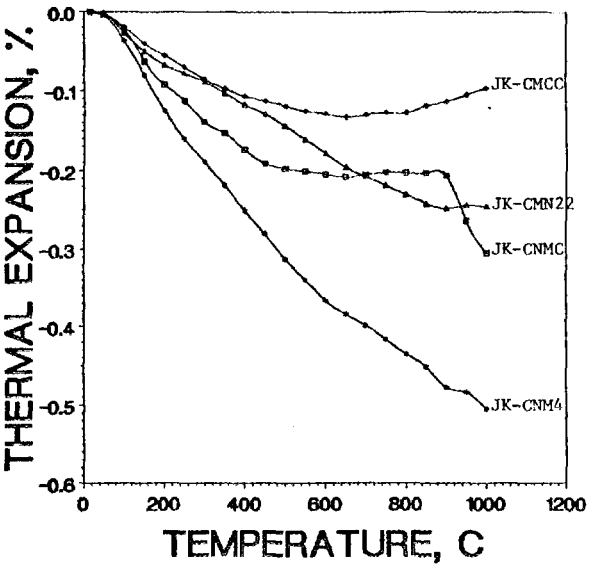

Figure 6. Linear thermal expansion behavior of NZP-type compounds modified by Ca^{+}, Mg^{+}, and Na^{+} ions.

Summary

From the initial screening results, some of the modified NZP-type structures, i.e. $RbZr_2(PO_4)_3$, $CsZr_2(PO_4)_3$, solid solution of (Rb-Cs) zirconium phosphate, and $Ca_{0.25}Mg_{0.25}Zr_2(PO_4)_3$, show promising low CTE values. We feel that $Ca_{0.25}Mg_{0.25}Zr_2(PO_4)_3$ is much more promising than any other systems considered at this stage, especially considering economic factors.

Status of Milestones

Status of milestones is presented in Table 10 and Figure 7. The x-ray diffraction lab is being upgraded and the thermal analysis system is due to be delivered in May 1988.

Publications

None this period.

Table 10. Key to major milestones

VPI 1.1	Process selection for phosphate- and silicate-based systems (Oct. 31, 1986)
VPI 1.2	Process selection for mullite- and zircon-based systems (Oct. 31, 1986)
VPI 2.1	Complete literature review (Oct. 31, 1986)
VPI 3.1	Complete upgrade of characterization facility (Dec. 31, 1986)
VPI 3.2	Complete upgrade of specimen fabrication, processing facilities (June 30, 1987)
VPI 4.1	Complete initial screening of phosphate-based systems (Dec. 31, 1987)
VPI 4.2	Complete initial screening of silicate-based systems (Dec. 31, 1987)
VPI 4.3	Complete initial screening of zircon-based systems (Dec. 31, 1987)
VPI 4.4	Complete initial screening of mullite-based systems (Dec. 31, 1987)
VPI 5.1	Complete second-stage property and characterization evaluation of phosphate-based systems (Sept. 30, 1988)
VPI 5.2	Complete second-stage property and characterization evaluation of silicate-based systems (Oct. 31, 1988)
VPI 5.3	Complete second-stage property and characterization evaluation of mullite-based systems (Nov. 30, 1988)
VPI 5.4	Complete second-stage property and characterization evaluation of zircon-based systems (Dec. 31, 1988)
VPI 6.0	Complete scale-up specimen fabrication of most promising low-expansion ceramics (Feb. 28, 1989)

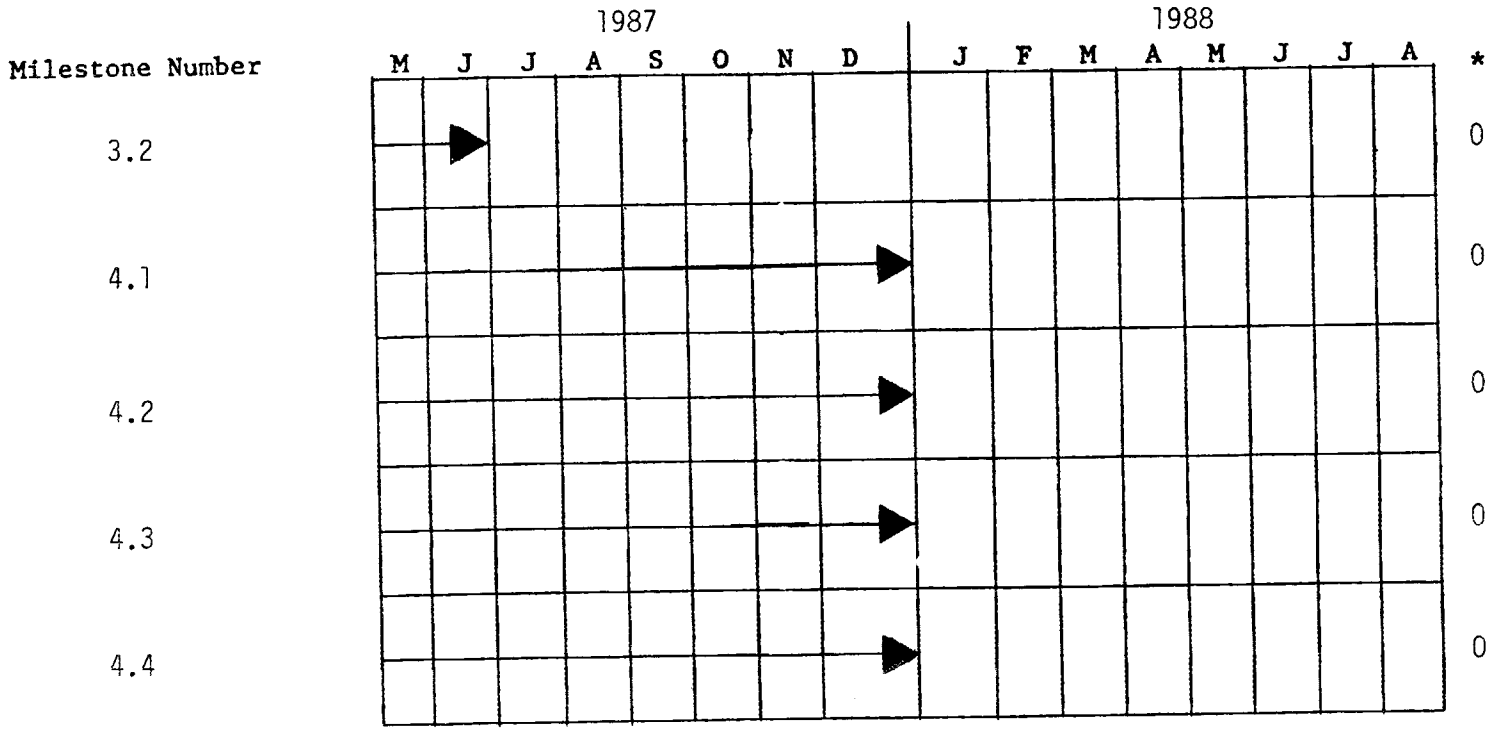

*On, Ahead of, or Behind Schedule.

Figure 7. Milestone status.

References

1. W. F. Horn and F. A. Hummel, "The System BPO_4-$AlPO_4$," *Trans. J. Brit. Ceram. Soc.*, 77 [5], 158-62 (1978).
2. A. J. Perrotta, "Low Thermal Expansion Ceramic Material Comprising a Single-Phase Solid Solution of Beta-Eucryptite and Aluminum Phosphate," *U. S. Patent 2,549,394*, 22 Dec. 1970, Appl. 18 Dec. 1957.
3. J. S. Moay, A. G. Verduch, and M. Hortal, "Thermal Expansion of Beta-Eucryptite Solid Solutions, " *Trans. J. Brit. Ceram. Soc.,* 73 [6], 177-78 (1974).
4. W. D. Kingery, *Introduction to Ceramics*, John Wiley & Sons, Inc., New York, London, Sydney, 125 (1960).
5. J. J. Brown, Jr., R. E. Swanson, and F. A. Hummel (Consultant), "Semiannual Progress Report for the Period April 1, 1987 - September 30, 1987," Dept. of Materials Eng., VPI & SU, October 1987.
6. J. E. Fenstermacher and F. A. Hummel, "High-Temperature Mechanical Properties of Ceramic Materials: IV Sintered Mullite Bodies," *J. Am. Ceram. Soc.*, Vol. 44, No. 6, 185-7 (1961).
7. Zhdanov, *Crystal Physics*, Academic Press, New York, (1965).
8. T. Oota and I. Yamai, "Thermal Expansion Behavior of $NaZr_2(PO_4)_3$-Type Compounds," *J. Am. Ceram. Soc.*, 69 [1], 1-6 (1986).
9. H. A. McKinstry, D. K. Agrawal, G. E. Lenain, C. S. Vikram, S. Y. Limaye, and A. Patankar, "Ultra-low Thermal Expansion Ceramics," Final scientific report submitted to Dept. of Air Force, AFOSR/NC Contract No. AFOSR-83-0291, August 1986.

1.3 THERMAL AND WEAR COATINGS

1.3.1 ZrO_2 Base Coatings

Development of Adherent Ceramic Coatings to Reduce Contact Stress Damage of Ceramics

V. K. Sarin (GTE Laboratories)

Objective/Scope

The objective of this program is to develop oxidation-resistant, high toughness, adherent coatings for silicon based ceramic substrates, namely, reaction bonded Si_3N_4, sintered SiC, and hip'ed Si_3N_4 for use in an advanced gas turbine engine. The program will utilize a singular coating technique, chemical vapor deposition (CVD), to develop appropriate coating configurations to accommodate as many of the mechanical, thermal and chemical requirements demanded of the application as possible.

Technical Highlights

Thermodynamic Modeling.

Thermodynamic modeling has been used to analyze the formation of interfacial phases between the AlN coating layer and each of the substrates which may take place during CVD of AlN. The results indicated that no new phases should form at the interface in the SSC and RBSN systems at temperatures of interest. However, in the case of AY6(H), the model predicts formation of AlN and Si_2N_2O. Figure 1 shows each phase present at equilibrium in the AY6(H) system and its amount as a function of temperature. These results are relative to 1.0 mole of substrate and 1.0 mole of gas initially present. Also, they are for one initial gas composition and pressure, but similar results are obtained at other conditions. The source of oxygen for the Si_2N_2O is Al_2O_3 which in added to AY6(H) during processing to promote densification. Since Si_2N_2O is the basis for some SiAlON-type compounds, it is possible that a SiAlON interface will form between AlN and AY6(H). This is expected to be beneficial to adherence since it promotes chemical bonding between coating and substrate and since it provides an interfacial zone across which thermal expansion and lattice parameter mismatch can be gradually accomodated. Formation of a SiAlON-type interface by a post-deposition anneal was proposed as part of the work because it was expected that this would improve adherence. In the case of AY6(H), it is possible that the post-deposition anneal may not be necessary. Experimental results support the model prediction, as discussed below.

Finite Element Analysis.

Additional modeling of residual stresses in the coating configuration has been done using finite element analysis. The goal was to develop a model which could predict optimum thickness of the interfaces and coating layers so that the residual stress would be minimized. At first, conventional finite element analysis was used, and this gave stresses which oscillated. This was attributed to the large aspect ratios of the finite elements since the substrate is much thicker than the coating. To overcome this problem without resorting to unrealistic coating and substrate dimensions, a technique referred to as a hybrid-stress model was used to allow the finite element mesh size to be varied. Using this method, the mesh size is made pro-

gressively smaller in going from the substrate to the coating (see Fig. 2). Very thin mesh sizes are used within the coating (see detail of corner in Fig. 2). At the corners, four sections of mesh with varying lengths are used to simulate the rounded edge. This hybrid-stress technique was successful in eliminating oscillatory behavior. In addition, it gave calculated stresses which are similar in magnitude to those measured for some ceramic coatings on various substrates (1,2).

Selected model results are given in Tables 1-5. Two cases were considered for each system - a 10μm thick Al_2O_3 layer with a 4μm thick AlN layer (case a) and a 4μm thick Al_2O_3 layer with a 10μm thick AlN layer (case b). In addition, each coating/substrate system was modeled with and without interfaces. The interface between the outer coating layer and AlN was assumed to be $Al_xO_yN_z$, and the interface between AlN and substrate was assumed to be a SiAlON. When an interface was included, its mechanical properties were obtained by averaging the properties of the layers it connected. Finally, the outer layer of the coating was treated as pure Al_2O_3 and the inner layer as pure AlN.

Table 1: Residual stresses calculated for the AY6(H) substrate system. The assumed temperature drop is 1000°C. Case a is for a 10μm thick Al_2O_3 layer and a 4μm thick AlN layer and case b is for the reverse.

	Young's Modulus (GPa)	Poisson's Ratio	Thermal Exp. Coeff. (°C)	Residual Stress (MPa)	
				case a	case b
Al_2O_3	390	0.22	7.8×10^{-6}	2475	2482
AlN	340	0.24	4.9×10^{-6}	937	943
AY6(H)	296.5	0.27	2.7×10^{-6}	-16	-11

Table 2: Residual stresses calculated for the AY6(H) substrate system with the interface between the coating and substrate included. The assumed temperature drop is 1000°C. Case a is for a 10μm thick Al_2O_3 layer and a 4μm thick AlN layer and case b is for the reverse.

	Young's Modulus (GPa)	Poisson's Ratio	Thermal Exp. Coeff. (°C)	Residual Stress (MPa)	
				case a	case b
Al_2O_3	390	0.22	7.8×10^{-6}	2475	2482
AlN	340	0.24	4.9×10^{-6}	938	943
Interface	320	0.255	3.8×10^{-6}	442	448
AY6(H)	296.5	0.27	2.7×10^{-6}	-16	-11

Tables 1-3 list residual stress values for the AY6(H) substrate system, and Tables 4-5 give the corresponding results for the SSC substrate system. The calculated stresses are tensile (>0) in the coating and compressive (<0) in the substrate, as expected since the coating has a larger thermal expansion coefficient than the substrate. Furthermore, the magnitude of the stress increases as the mismatch between coating and substrate increases. However, the model was found to be insensitive to differences in the thicknesses of the various coating layers. The distribution of stress in the coating is shown in Fig. 3 for SSC and AY6(H) substrates. As the edge is approached (e.g., large distances from the axis of symmetry), the stress decreases, indicating that failure of the coating due to internal stress should originate at the center.

Experimental verification of the predicted stress values using x-ray diffraction has been attempted but has thus far been unsuccessful. Since several of the diffraction peaks for AlN are very close to those for Si_3N_4 and SiC, extremely high resolution capabilities are necessary to measure residual stress.

Table 3: Residual stresses calculated for the AY6(H) substrate system with the interfaces between the coating and substrate and between the coating layers included. The assumed temperature drop is 1000°C. Case a is for a 10μm thick Al_2O_3 layer and a 4μm thick AlN layer and case b is for the reverse.

	Young's Modulus (GPa)	Poisson's Ratio	Thermal Exp. Coeff. (°C)	Residual Stress (MPa)	
				case a	case b
Al_2O_3	390	0.22	7.8×10^{-6}	2476	2482
Interface	365	0.23	6.35×10^{-6}	1671	1677
AlN	340	0.24	4.9×10^{-6}	938	944
Interface	320	0.255	3.8×10^{-6}	443	448
AY6(H)	296.5	0.27	2.7×10^{-6}	-15	-10

The results of the finite element analysis show that use of the hybrid-stress model improves accuracy over what could be obtained with conventional finite element analysis. However, the predictive capability of the model is not satisfactory, and, hence, it has limited utility in designing new coating configurations. In particular, the effects of varying the thickness of the coating and interface layers cannot be assessed. This is believed to be due to the use of linear elastic theory. It has been concluded that this theory is not suitable for simulating coating/substrate systems since the thickness of the substrate is so much greater than that of the coating. A model which is based on non-linear theory should overcome this problem. In addition, inclusion of compositional variations and plastic deformation in the coating should give more accurate predictions.

Table 4: Residual stresses calculated for the SSC substrate system. The assumed temperature drop is 1000°C. Case a is for a 10μm thick Al_2O_3 layer and a 4μm thick AlN layer and case b is for the reverse.

	Young's Modulus (GPa)	Poisson's Ratio	Thermal Exp. Coeff. (°C)	Residual Stress (MPa)	
				case a	case b
Al_2O_3	390	0.22	7.8×10^{-6}	1731	1740
AlN	340	0.24	4.9×10^{-6}	282	290
SSC	207	0.22	4.3×10^{-6}	-11	-6

Table 5: Residual stresses calculated for the SSC substrate system with the interface between the coating layers included. The assumed temperature drop is 1000°C. Case a is for a 10μm thick Al_2O_3 layer and a 4μm thick AlN layer and case b is for the reverse.

	Young's Modulus (GPa)	Poisson's Ratio	Thermal Exp. Coeff. (°C)	Residual Stress (MPa)	
				case a	case b
Al_2O_3	390	0.22	7.8×10^{-6}	1732	1741
Interface	365	0.23	6.35×10^{-6}	971	980
AlN	340	0.24	4.9×10^{-6}	283	291
SSC	207	0.22	4.3×10^{-6}	-10	-5

No additional finite element analysis will be conducted in this phase of the work. Optimization of coating layer and interface thicknesses is being done empirically. It is suggested that modification of the model to include non-linear theory be incorporated in the next phase of this program.

Experimental Results.

A CVD process for depositing the full coating configuration on all three substrates has been developed. Coatings on all substrates have excellent adherence, as determined using a conventional scratch test. The critical load measured for the AlN layer on AY6(H) is 50% higher than for AlN on SSC and RBSN (see October 19, 1987 Semi-Annual Report), although all systems have critical loads which are at least as good as that reported for TiC on WC-Co. The latter system is considered to have excellent adherence since it is extensively used in machining applications. Coating of 2 inch MOR bars of each substrate has begun. In addition, pieces of MOR bars are being coated and used for long term oxidation and thermal shock tests.

Characterization.

Evaluation of fully coated substrates has begun. Coated pieces of MOR bars are being tested for long term oxidation resistance and thermal shock resistance. Preliminary results are described below.

The rapid thermal anneal technique (RTA) is being used to conduct thermal shock tests. Samples are cycled from 150°C to 1000°C in 30 seconds with a 10 second soak at 1000°C using a HEATPULSE 210 apparatus. The HEATPULSE system contains an annealing chamber with upper and lower banks of high-intensity, tungsten-halogen lamps and reflective walls. The sample to be heated is placed on a silicon tray, which is in turn heated by radiation from the lamps. Although the sample is heated primarily by radiation from the lamps, some conduction from the silicon wafer also takes place. The temperature of the silicon is measured with a chromel/alumel thermocouple embedded in the surface of the silicon wafer, and the thermocouple signal is fed to a controller.

Samples tested include uncoated AY6(H) (for reference), AlN-coated AY6(H), composite-coated AY6(H), and composite/AlN-coated AY6(H). After 50 cycles, no changes were observed when viewed in an optical microscope at 1000x magnification. The samples are currently being evaluated for changes in mechanical and chemical properties.

Long term oxidation studies at 1000°C have also been initiated. Fully coated pieces as well as uncoated substrates are heated in stagnant air in a 4″ diameter tube furnace. All three substrates are being tested simultaneously. After 50, 100, 250, and 500 hour tests, the AY6(H) and SSC samples showed no weight gain, while the RBSN samples gained a small amount of weight (approximately 1% of their original weight). All samples have been examined in an optical microscope for cracks. No damage was observed. Each sample will be evaluated for changes in mechanical and chemical properties.

References

1. A. J. Perry and L. Chollet, J. Vac. Sci. Technol. A 4(6), 1986.

2. L. Chollet, H. Boving, and H. E. Hintermann, J. Mat. Energy Sys., 6(4), 1986.

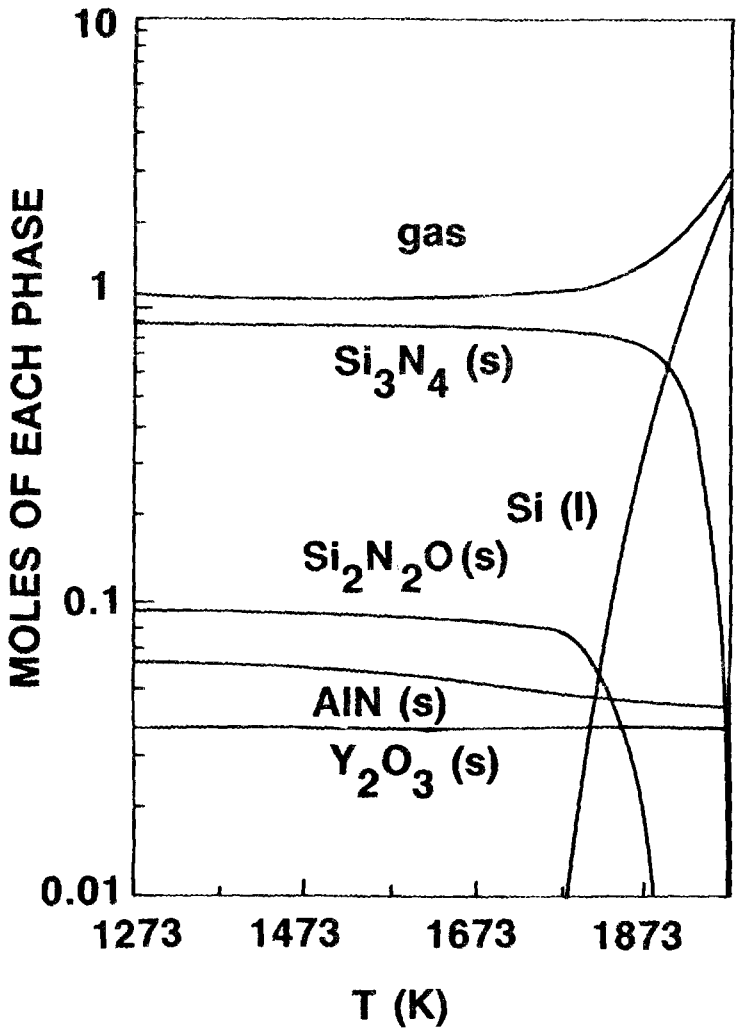

Figure 1: Equilibrium amounts of the various phases present in the AY6(H)/CVD gas mixture system for a range of temperatures. Operating conditions: P = 100 torr, x^{o}_{AlCl3} = 0.006, x^{o}_{NH3} = 0.090, x^{o}_{H2} = 0.542, x^{o}_{Ar} = 0.361. The subscripts "s" and "l" refer to solid and liquid phases, respectively.

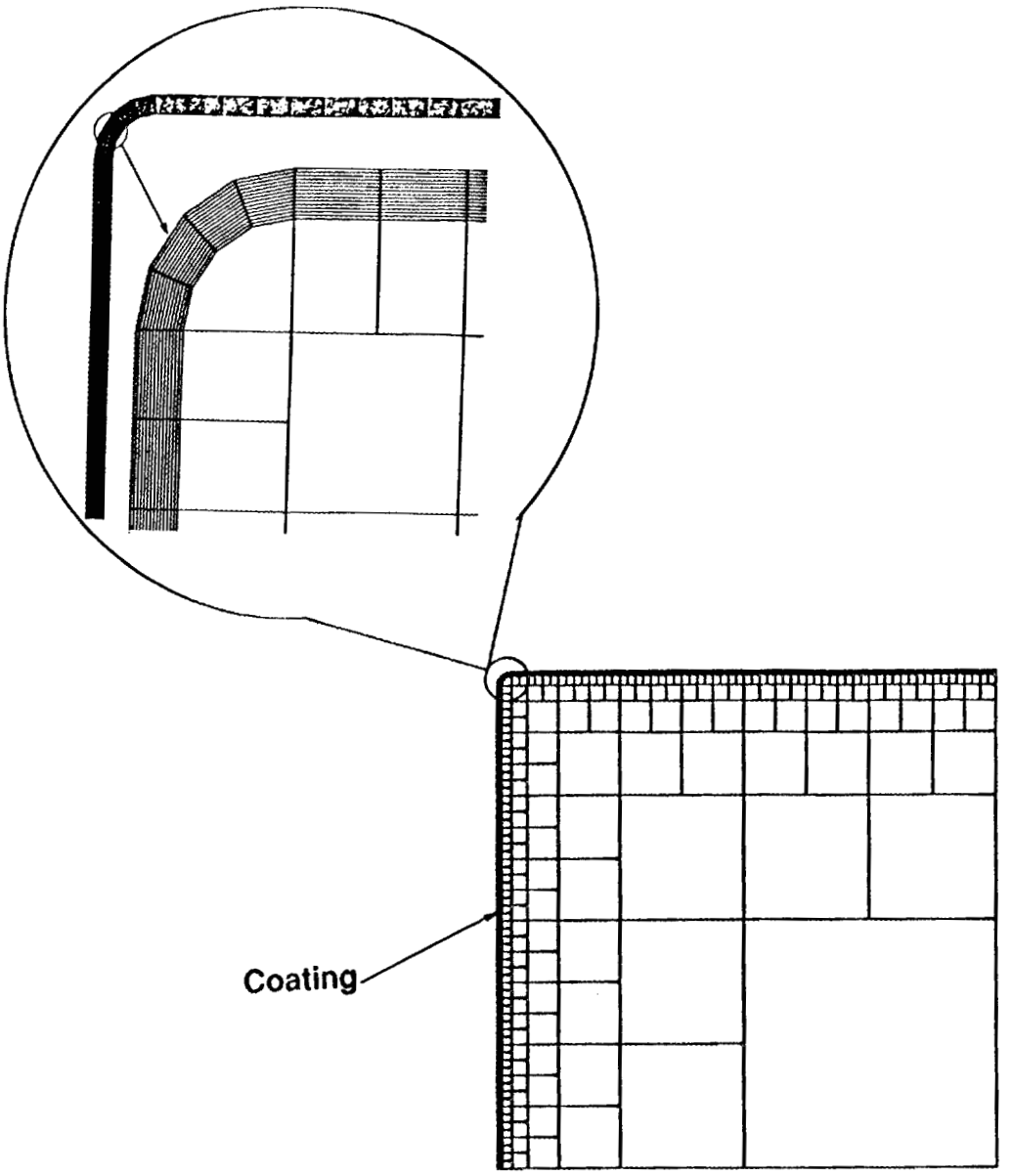

Figure 2: Schematic of the finite element mesh obtained using the hybrid-stress model.

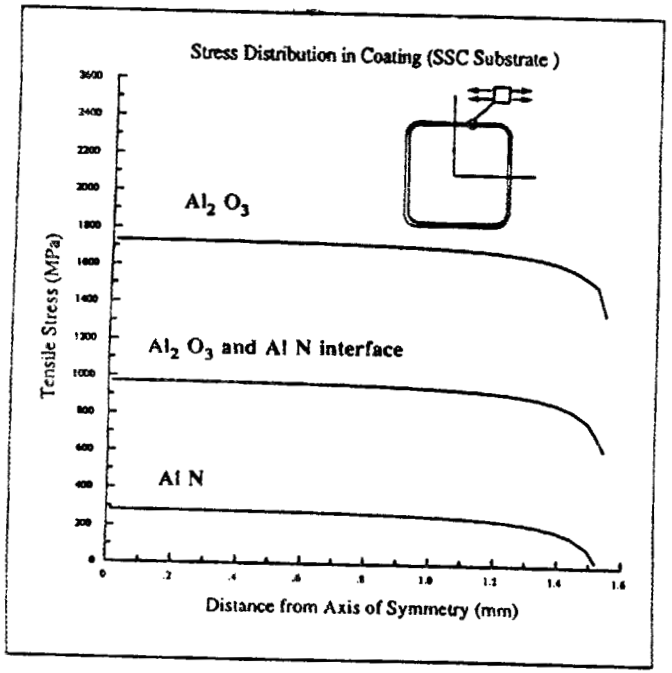

(a)

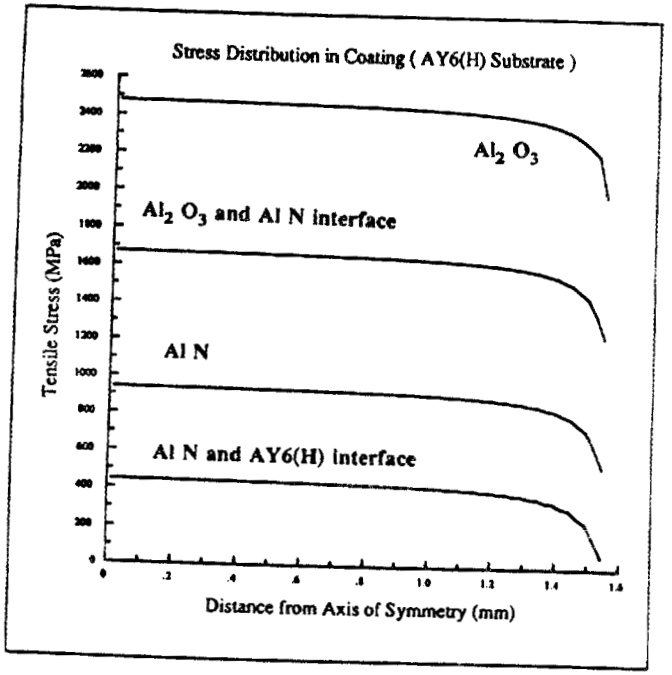

(b)

Figure 3: Stress distribution in each coating layer and at each interface. a)substrate = SSC, b) substrate = AY6(H).

Status of Milestones

Second milestone due in December 1987 was completed on time. Third milestone due in June 1988 is on schedule.

Publications

V. K. Sarin, "Design Criteria for a Coating to Reduce Contact Stress Damage," to be published in the Proc. of the DOE Workshop on Coatings for Advanced Heat Engines.

H. E. Rebenne and V. K. Sarin, "Ceramic Coatings to Reduce Contact Stress Damage of Ceramics - Thermodynamic Modeling," to be published in the Proc. of the 25th Automotive Technology Development Contractors' Coordination Meeting.

T.-L. Sham and V. K. Sarin, "Residual Stress Calculations in Coating Configurations using Finite Element Analysis," to be published in Proc. 12th Annual Conf. on Composites and Advanced Ceramics.

Advanced Coating Technology

D. P. Stinton, C. S. Yust, and P. J. Blau (Oak Ridge National Laboratory)

Objective/scope

Contact stress damage at ceramic-ceramic interfaces in gas turbine engines has been identified as a major source of ceramic component failure in experimental engine tests. Therefore, the objective of this program is to reduce or eliminate the contact stress damage at these interfaces. Contact stresses will be reduced by chemically vapor depositing a coating that consists of Al_2O_3 and a solid lubricant to minimize the coefficient of sliding friction. This work supports a larger contract with GTE Laboratories where chemically vapor deposited zirconia-toughened alumina coatings are being developed to reduce contact stress damage to silicon carbide and silicon nitride components. After satisfactory Al_2O_3-lubricant cotings have been produced at ORNL, tribological testing will identify the optimum composition and concentration of lubricant to minimize the coefficient of friction.

Technical progress

Contact stress coatings are being developed at GTE Laboratories with a composition of Al_2O_3 and small additions of ZrO_2. Since the final composition and coating conditions have not yet been determined, Al_2O_3 will be deposited at ORNL to simulate zirconia-toughened Al_2O_3. A simple horizontal tube furnace system was installed for the deposition of Al_2O_3-solid lubricant coatings. The furnace system consisted of a 7.5-cm-diam Inconel reaction tube surrounded by a resistance heating element. A second smaller furnace for the chlorination of aluminum was located just upstream from the first heating element.

Aluminum oxide coatings were produced by reacting $AlCl_3$ and CO_2 with hydrogen carrier gas. Unfortunately, homogeneous nucleation of particulates in the gas phase resulted in large quantities of Al_2O_3 powder and low-density, friable deposits. The morphologies of the coatings were very similar for all deposition conditions investigated. Therefore, it appeared that the geometry of the system or contaminants present were responsible for the homogeneous nucleation. The residence time of reactants within the furnace was quite long, thus providing ample time for nucleation. The capacity of the vacuum system is limited, however, and the volume of gas cannot be increased sufficiently to significantly reduce the residence time without a substantial increase in system pressure. Therefore, the entire coating system was modified to address both of these problems. The cylindrical 7.5-cm-diam Inconel tube was replaced with a rectangular fused silica tube (2 cm by 6 cm). The cross-sectional area of the tube was reduced by a factor of 4 and should allow much greater variation in residence time without a significant change in system pressure. Coating conditions will be explored in order to identify appropriate concentrations for the deposition of high-quality coatings.

Thermodynamic calculations were performed on systems identified in Table 1. The simple reaction of $AlCl_3$, CO_2, and H_2 to form Al_2O_3 was examined initially. The composition of the gaseous phase within the reaction at 1300 K is shown in Table 2 for appropriate amounts of $AlCl_3$ and CO_3. The calculations were limited to 1300 K and 0.01 MPa (0.1 atm) because the zirconia-toughened alumina coatings are being produced at GTE under these conditions. The composition of the gas phase must, of course, remain approximately the same for systems where reactants are introduced to also deposit the lubricant phases. Therefore, the concentrations of the reactants were systematically varied in the calculations to identify regions where Al_2O_3 and about 10 wt % lubricant would codeposit.

The system Al_2O_3 plus 10 wt % Mo was examined first, where Mo was deposited from MoF_6. No gaseous species of significant vapor pressure containing either Al or Mo were formed, so essentially all the $AlCl_3$ and MoF_7 reacted to form Al_2O_3 and Mo metal, respectively. The partial pressure of oxygen remained at a level of about 10^{-12} Pa. The system Al_2O_3 plus 10 wt % Co behaved very much like the system with Mo. No significant gaseous species were formed containing either Al or Co, so the efficiencies remained near 100%. The partial pressure of oxygen was also unchanged.

Table 1. Systems of interest investigated by thermodynamic calculations

Reactants	Desired coating
$AlCl_3$, CO_2, H_2	Al_2O_3
$AlCl_3$, CO_2, H_2, MoF_6	Al_2O_3 plus 10 wt % Mo
$AlCl_3$, CO_2, H_2, CoI_2	Al_2O_3 plus 10 wt % Co
$AlCl_3$, CO_2, H_2, H_2S, MoF_6	Al_2O_3 plus 10 wt % MoS_2
$AlCl_3$, CO_2, H_2, BCl_3, NH_3	Al_2O_3 plus 10 wt % BN
$AlCl_3$, CO_2, H_2, $CaBr_2$, F_2	Al_2O_3 plus 10 wt % CaF_2
$AlCl_3$, CO_2, H_2, CH_4	Al_2O_3 plus 10 wt % C

Table 2. Composition of gaseous phase during deposition of pure Al_2O_3 coatings

Gaseous phase	Concentration (%)
H_2	90.16
CO	4.18
HCl	2.83
H_2O	2.76
CO_2	0.07
O_2	10^{-8} [a]

[a]Partial pressure of oxygen is 1×10^{-12} Pa.

Examination of the system Al_2O_3 plus 10 wt % MoS_2 was considerably more complicated than the previous systems. Molybdenum hexafluoride and H_2S were used as the sources of Mo and S. Metallic Mo, however, was predicted to form instead of MoS_2. Fourteen times the stoichiometric amounts of H_2S had to be added to produce MoS_2 because numerous gaseos sulfur-containing species were formed.

Thermodynamic calculations for the system to deposit Al_2O_3 plus C were also quite involved. The Ellingham diagram from Darken and Gurry[1] showed that Al_2O_3 and carbon should coexist at 1300 K for oxygen partial pressures between 10-13 Pa and 10^{-23} Pa. Therefore, the fraction of methane in the reactants was increased until Al_2O_3 and 10 wt % C were produced. Approximately 10 times the stoichiometric amounts of methane was required because of the formation of numerous gaseous carbon-containing species. The partial pressure of oxygen for these conditions was 10-17 Pa.

Conditions could not be identified where Al_2O_3 codeposits with either BN or GaF_2. Calculations for the BN system showed that B_2O_3 was more likely to form than BN for a partial pressure of oxygen of 10^{-11} Pa. Addition of methane to reduce the partial pressure of oxygen failed to change these results. Methane was added until free carbon was produced. Calculations for the CaF_2 system were very similar because CaO was always more likely to form that CaF_2. Reduction of the partial pressure of oxygen by the addition of methane failed to change these results.

After the quality of the coatings has been improved, the codeposition of Al_2O_3 and a solid lubricant will be initiated. From thermodynamic calculations reported above, it appears that Al_2O_3 plus Mo, Al_2O_3 plus MoS_2, and Al_2O_3 plus C would be the simplest systems to prepare and will be investigated first. Therefore, MoF_6, H_2S, and CH_4 gases have been purchased to supply the Mo, S, and C during the codeposition.

The pin-on-disk wear test system has been modified to provide reciprocating linear motion and to permit the measurement of the friction coefficient as a function of time and position during a sliding cycle. The rotational motion of the original system has been converted to linear motion by use of an eccentric pin which drives a specimen stage which moves on linear support rods. The sliding motion of the stage is accomplished at low frictoin by use of linear ballbearings. The tangential force generated at the sliding interface between the surfaces in contact is measured by the deflection of a cantilever beam. The beam is the only restraint on the motion of the pin member of the sliding couple; hence, the magnitude of the restraining force is equal to the tangential force. The force magnitude is determined by the use of calibrated strain gauges affixed to the cantilever beam. The beam provides a reading for sliding in both directions of the reciprocating motion. The tangential force data are recorded by a computer-controlled data acquisition system at the rate of 1000 readings per second, which permits the determination of friction coefficient as a function of position in the sliding cycle. The data can be recorded at preselected time intervals, permitting the determination of friction as a function of sliding time.

References

1. L. S. Darken and R. W. Gurry, p. 349 in *Physical Chemistry of Metals*, ed. R. F. Mehl and M. B. Bever, McGraw-Hill Book Company, Inc., New York, 1953.

Status of milestones

The milestone, "Complete modification to the pin on disk system and demonstrate that friction coefficients can be measured as a function of time and position during a sliding cycle," was completed on schedule.

Publications

None.

Wear-Resistant Coatings

C. D. Weiss (Caterpillar, Inc.)

Objective/Scope

The goal of this technical program is to develop wear-resistant coatings for piston ring and cylinder liner components for low heat-loss diesel engines.

Wear resistant coatings will be applied to metallic substrates utilizing plasma spraying, vapor deposition (CVD-PVD) and enameling coating processes. This program will begin by optimizing the adherence of each coating for each process to the metallic substrates. Methods which can be utilized for improving the adherence of these coatings includes development of unique substrate preparation methods before application of the coating, grading coating compositions to match the thermal expansion of the metallic substrate, compositional changes, laser or electron beam fusing and/or optimizing coating thickness. Once the adherence of each coating is optimized, each will be screened for wear and friction at 350°C under lubricated conditions. Coatings which show promise after this initial screening will be further optimized by adjustments to chemistry and hard particle content to meet the program's wear and friction requirements. Finally, the optimized coating systems will be fully characterized for oxidation resistance, adherence, uniformity, thermal shock resistance, wear and friction.

Selection of the most promising coatings and coating processes will be made after completion of the characterization task. Criteria for selection will include not only performance (i.e. wear, adhesion, friction coefficient, thermal shock resistance and thermal stability) but manufacturability/cost factors, as well. Utilizing both criteria, a coating/system having acceptable cost/benefit relationships will be selected.

Technical Progress - Development of Adherent Coatings

Plasma Spraying

All the cast iron, H13 tool steel and SAE 1010 mild steel substrate materials have been received and evaluated as acceptable with respect to microstructure and chemistry. All the adherence specimens have been cut and are available for coating. The ceramic pins for the pin-on-disk wear testing have been ordered.

Review and selection of the initial plasma spray coatings have been completed. Table 1 contains a list of the plasma coatings, bond coatings and solid lubricants to be evaluated as part of this program. Graded plasma coatings will be evaluated to attempt to reduce the thermal stresses which develop in the coatings because of differences in the thermal expansion between the plasma spray coatings and the metallic substrate. In addition, laser glazing will be evaluated as a method for increasing the density of the plasma spray coatings as well as providing a smooth surface after plasma spraying.

Two methods will be utilized to add the solid lubricants to the plasma coatings. The first involves co-spraying the solid lubricant into the plasma spray coatings. The second will apply the solid lubricants as a post-treatment after plasma spraying.

Spire Corporation will perform all the pre-deposition treatments of ion implantation of boron, carbon, and nitrogen.

Enamel Coating

Slip Technique

Solar Turbines, Inc utilizing their experience in vitreous phase coating technology used for gas turbine applications, selected three frits designated S5-8A, A-I and B-1 as potential candidates as wear resistant coatings. Solar also designated frits A-2 and B-2 as potential candidates for bond coats to provide coatings with improved adherence. Both frits have the same compositions of A-1 and B-1 except that these compositions also contain a small amount of Ni0, Co_3O_4 and MnO_2. These additions were incorporated to improve the bonding of the frits to the substrate.

All three frit compositions were smelted in a SiO_2 crucible at 1343°C using either oxides and/or carbonates as raw materials. After smelting, the coefficient of thermal expansion for each frit composition was determined using a Bocckler dilatometer (cylindrical 25mm specimens with a 3.25mm radius). The results of the thermal expansion data indicated the thermal expansion of frits B-1 and B-2 closely match that of the SAE 1010 steel to which they will be applied. For this reason they were chosen as the initial frit composition to be evaluated.

The firing temperature for the B-1 and B-2 frit compositions were determined next by placing a small amount of the frit on a Hastelloy X coupon and noting the physical appearance of the frit after firing for various times and temperatures. Using this criteria, a firing cycle of 871°C for 10 minutes was chosen.

Coating trials were initiated with the B-1 and B-2 frits on 50mm x 50mm SAE 1010 steel substrates. In general, all the B-1 and B-2 coated specimens were heavily oxidized after the coating was fired. To prevent oxidation of the base metal during the firing of the B-1 or B-2 frits, probably a lower firing temperature or firing the enamel frits in a neutral or non-oxidizing atmosphere will be required.

Hot Substrate Method

The University of Illinois selected two cast iron porcelain enamel frits from the composition tables in A. I Andrews, Porcelain Enamels, Garrard Press, Champaign, IL 1961, (Second Edition) as well as obtaining commercial frits from the Ferro Corporation and Pemco Products Group of the Mobay Corporation.

A dry spray coating technique was developed. This method consists of milling the frit in the following volumetric proportions:

40% Solids
36% Reagent grade isopropanol
24% Distilled Water

In addition a substrate preparation method was developed. The procedure developed consists of first sand blasting the substrate with silica beads. Next the surface is degreased, pickled in 6% H_2SO_4 for 60 seconds, rinsed in distilled water and finally treated with reagent grade acetone. Finally, the approximate firing schedules (time, temperature) for the six (6) frits available were determined.

A preliminary composite coating was prepared by mixing a distribution of SiC particle sizes with an A. I Andrews Co–based enamel. The amount of enamel added was equivalent to the theoretical volume of the voids between the packed SiC particles. Photomicrographs of the substrate, unfired and fired coatings are contained in Figure 1.

Table 1 Plasma Sprayed Coatings and Solid Lubricants

Plasma Applied Wear Coating	Bond Coat/ Grading Material	Solid Lubricants
PS 212	Ni-Cr	CaF_2
MoFeB	Ni-Cr-Al-Y	Intercolloidal Graphite
Cr_3C_2	MoFe	
Al_2O_3		Mix-metal sulfide
Al_2TiO_5		
ZrO_2		
ZrO_2-TiO_2-Y_2O_3		
MgO-Al_2O_3 Spinel		
62%Co-28%Mo-8%Cr-2%Si alloy		

CVD/PVD Coating

A visit was made to Sylvester and Company, Beachwood, OH and Spire Corporation, Bedford, MA. Sylvester is one of the CVD sources while Spire is the source for ion implantation. The CVD coatings to be evaluated and the supplier for each are listed in Table 2.

The Ti(C,N) CVD coating will be applied to the 17-4 PH stainless steel substrate. The CVD coating composition was chosen because it can be applied at a lower temperature than the other CVD coatings chosen enabling a lower temperature heat treatment to be utilized on the 17-4 PH stainless.

Table 2 also contains the PVD coatings to be evaluated along with the supplier for each coating composition.

Table 2 Chemical and Physical Deposition Coatings

Coating Type	Composition	Supplier
PVD-Electron Beam	TiN	Balzers
PVD-Arc evaporation	TiN	Caterpillar Inc
PVD-Hollow Cathode	TiN	Richter Precision
CVD	TiC/TiN Layered	Sylvester & Co
CVD	Cr_3C_2	Sylvester & Co
CVD-Mid-Temp	Ti(C,N) Mixed	Sylvester & Co
CVD	WC	San Fernando Laboratories

Cast Iron Surface
"As-Machined"

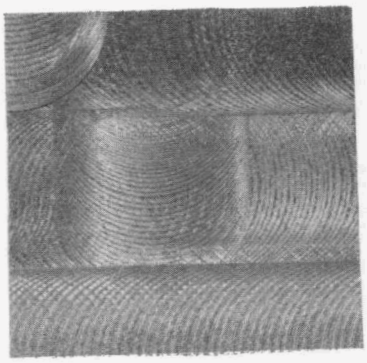

Porcelain Enamel
Coating (unfired)

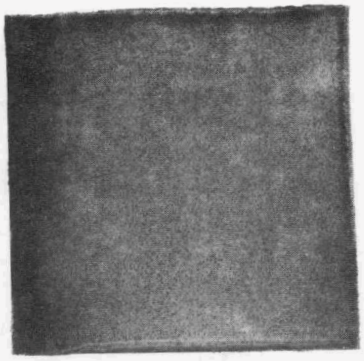

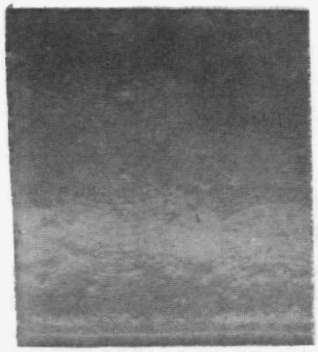

Porcelain Enamel
Coating on Cast
Iron-Fired

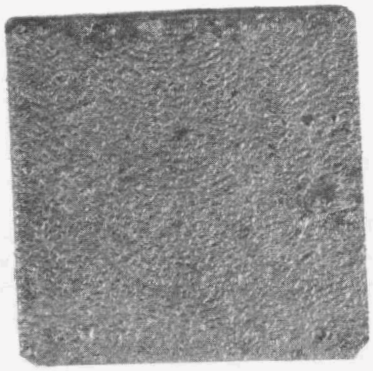

Composite SiC Particle
Enamel Coating
on Cast Iron-Fired

Figure 1 Photomicrograph of Machined Substrate, Unfired and Fired SiC Loaded Enamel Coating

Status of Milestone

MS1 is complete.

Publications

None.

Development of Wear-Resistant Ceramic Coatings for Diesel Engine Components

M.G.S. Naylor (Cummins Engine Company, Inc.)

Objective/scope

The objective of this program is to develop advanced wear resistant coatings for in-cylinder components for future, low heat rejection diesel engines. Coatings and substrates (for piston rings and cylinder liners) are to be developed to meet the following requirements.

- Low wear (as measured in laboratory rig tests at ambient and 350°C). Wear coefficients in the range 5×10^{-12} to 5×10^{-11} $mm^3/mm/N$ are targeted (at 350°C).
- Low friction coefficients when tested under boundary lubricated conditions (target 0.1) and unlubricated conditions (target 0.2) at ambient temperature and 350°C.
- Good thermal shock resistance.
- High adherence and compatibility with the substrate materials up to 650°C.
- High uniformity and reproducibility.

Technical Progress

Introduction

Future trends for heavy duty diesel (HDD) engines are driving us towards a) higher top ring reversal temperatures (through the use of in-cylinder insulation and higher top ring positions), b) decreased oil supply to the compression rings (to meet emissions requirements), c) extended durability goals (e.g. 1 million miles mean time before overhaul).

The effect of these requirements will be to place much greater stress on the in-cylinder tribology system, which in a conventional HDD engine typically comprised of Cr electroplated rings, grey cast iron cylinder liners and a mineral oil based lubricant.

In order to meet future durability goals, it will be necessary to develop more advanced tribology systems, which provide greater wear resistance than conventional materials under more marginally lubricated conditions, and at higher operating temperatures.

To illustrate these requirements, Figure 1 shows a plot of wear rate against temperature for segments of Cr plated piston rings sliding on pieces cut from a grey iron cylinder liner with a conventional 15W40 CE/SF mineral oil based lubricant (fresh). The tests were performed on a Cameron Plint TE77 wear tester. Wear rates are expressed as the volume of wear divided by the product of sliding distance and normal force. Wear rates for the ring were found to double for every 48 K rise in temperature for the lubricant tested in Figure 1, liner wear rates doubled every 87 K.

Typical TRR temperatures for conventional heavy duty diesel engines are in the range 250 300°C, for which ring wear rates are predicted from Figure 1 to be in the range 5×10^{-12} to 10^{-11} $mm^3/mm/N$. Top ring wear rates calculated from engine test data (field and dynamometer tests) agree very well with these numbers. Thus, ring wear coefficients in this range are target figures for acceptable engine durability in LHR engines operating at higher TRR temperatures (eg. 400-500°C).

In conventional engines, the wear rate of the rings is usually designed to be much lower than that of the liner (for the materials in Fig. 1, the rings were found to be 10-100 times more wear resistant than the liners). The reason for this is that sophisticated piston ring profiles (eg. barrel face, taper face, etc) are required to provide the necessary gas sealing pressures and to minimize blowby and oil consumption. When original ring profiles are lost due to wear, oil consumption increases dramatically, and the engine has to be overhauled. Thus, for the ring & liner tribology system, very low ring wear rates are important in addition to low total wear rate (ring & liner). Unfortunately, increasing the wear resistance of one of the sliding surfaces often causes an increase in the wear rate of the counterface

In previous experiments, Cummins has found that using plasma sprayed ceramic coatings on the rings and the liners can sometimes have the result of improving the liner wear rate without improving the ring wear rate (see Figure 2). The best candidate identified in these previous studies was plasma sprayed chromium oxide (self-mated). In summary, the wear properties of the ring and liner surfaces must be matched very carefully.

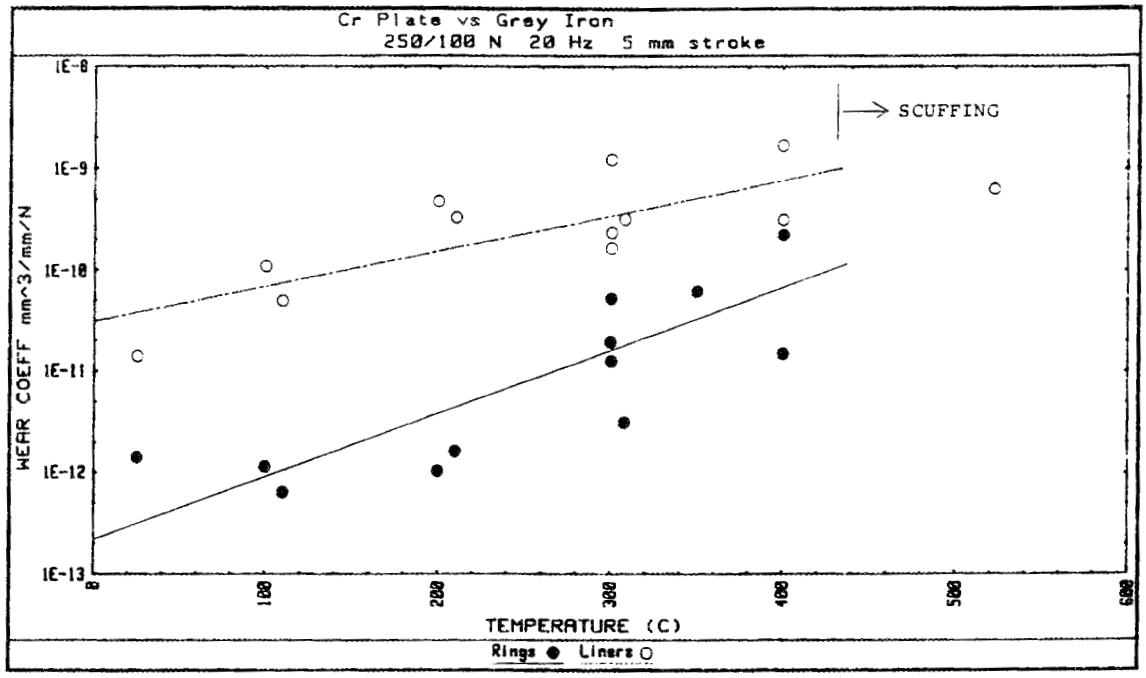

Figure 1 Wear coefficient as a function of temperature for Cr plated piston rings sliding against grey iron liners with a fresh CE/SF 15W40 mineral oil based lubricant, supplied at one drop every 10 seconds.

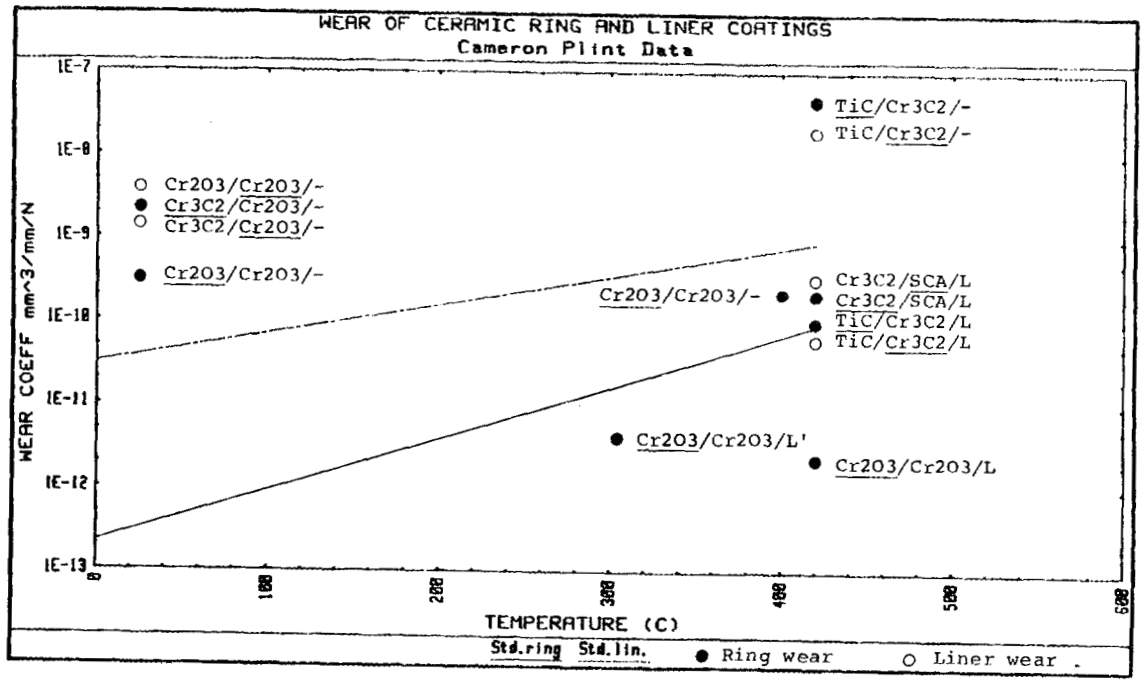

Figure 2 Piston ring and cylinder liner wear coefficients measured for various Cameron Plint tests. Solid and dashed lines show variation of ring and liner wear with temperature for conventional materials (Cr plated ring, grey iron liner) with a commercial CE/SF 15W40 mineral oil based lubricant. Data points show wear coefficients for various ceramic coatings. The captions refer to the ring material/liner material/lubricant: - = unlubricated, L = commercial polyol ester based lubricant, L' = CE/SF 15W40 mineral oil based lubricant. Cr_2O_3 = plasma sprayed chromium oxide, CR_3C_2 plasma sprayed chromium carbide, TiC = plasma sprayed titanium carbide with CaF_2, Ni, Cr, Fe. SCA = silica-chromia alumina dipped coating.

Coating and Substrate Material Selection and Sample Procurement

Table 1 shows the candidate ring and liner materials selected for this program. Piston ring substrates (HK40 castable stainless steel, 422 martensitic stainless and Inconel 625) were selected on the basis of handbook data for tempering temperature (steels), high temperature UTS and yield strength and creep rupture data. In addition, the diffusion alloying process entails some further requirements on a substrate chemistry and we have been guided by advice from our diffusion alloying subcontractor (Turbine Metal Technology, Tujunga, CA.). Estimates of the maximum operating temperature capabilities of each material are listed in Table 2.

Table 1 Candidate Ring and Liner Materials
APS = air plasma spray
VPS = Vacuum plasma spray

Piston Ring Coating/Thickness	Piston Ring Substrate
1 Plasma Spray	
APS Cr_2O_3-SiO_2-Al_2O_3 (4 compositions) (100-250 um)	
VPS B_4C (100-250 um)	HK40 steel
VPS borides (100-250 um) (eg TiB_2, SiB_6, etc) (4 compositions)	HK40 steel
2 High Velocity Thermal Spray	
Cr_3C_2-Ni-Cr (100-250 um) (2 suppliers)	HK40 Steel
88% WC - 12% Co (100-250 um)	HK40 Steel
3 Electro-Spark Deposition	
Cr_3C_2 - Ni (25-50 um)	422 Steel
4 Diffusion Alloys	
Nickel Aluminide (50-100 um)	422 steel Inco 625
Boride (50-100 um)	422 steel Inco 625
5 Physical Vapor Deposition	
ZrN (20 um)	HK40 steel

Table 1 Continued

Cylinder Liner Coating/Thickness	Cylinder Liner Substrate
1 Uncoated	
None	High P grey iron
None	Hardened grey iron
None	PM Nitronic 20
2 Nitrided	
Ion Nitrided (200-250 um)	Type 1 Niresist
3 Slurry Coating	
SCA (50 um) (SiO_2-Cr_2O_3-Al_2O_3	Grey Iron
4 Diffusion Alloys	
Nickel Aluminide (50-100 um) Boride (50-100 um)	H13 Tool Steel

Table 2 Estimated maximum operating temperature of piston ring substrate materials.

* Inconel 718 will only be considered if other candidates fail.

Material	Approx. Composition	Max Service Temperature
HK40 Castable Stainless	Fe,26Cr,20Ni,0.2-0.6C	600°C if 30ksi yield strength is sufficient
422 Martensitic Stainless	Fe,13Cr,1Ni,1Mo,1W,0.3V,0.2C	480°C
Inconel 625 Nickel base superalloy	Ni,22Cr,9Mo,5maxFe,4Nb,0.06C	650°C
Inconel 718 Nickel base superalloy	* Ni,19Cr,29Fe,0.08maxC	700°C

Our two major coating subcontractors are APS Materials, Dayton, OH and Turbine Metal Technology, Tujunga, CA. The work plans for coating development by these subcontractors are summarized below.

APS Materials Inc.

APS Materials will develop air plasma spray and inert atmosphere plasma spray coatings, concentrating on three materials systems.

a) Air Plasma Sprayed Cr_2O_3-Al_2O_3-SiO_2
May 1988 - August 1988

The material systems to be studied in this phase are chromia, chromia alumina and chromia with minor alloying additions such as silica. APS Materials has much experience in spraying chromia-based materials, and Cummins has achieved very favorable results in both engine tests and bench wear tests with plasma sprayed chromia. The objective of this phase will be to determine the optimum chemistry and microstructure for piston ring applications. It is thought that alloying with Al_2O_3 may improve thermal shock performance, but possibly at the expense of wear resistance.

b) Inert Chamber Spraying of Boron Carbide
September 1988 - December 1988

APS Materials has developed proprietary processes for spraying boron carbide. Further development of these processes may result in exceptionally wear-resistant coatings.

c) Inert Chamber Spraying of Hard Metal Borides
Jan 1989 - June 1989

The third project will involve forming hard (>2800kg./mm2) metal boride coatings. These materials can be compared to chromia and alumina hardnesses of roughly 1000 kg/mm2 and pure tungsten carbide at 2500 kg/mm2. Candidates for sprayability tests include borides of silicon, molybdenum, cerium, titanium, and yttrium. Silicon hexaboride has a hardness approaching 2800 kg/mm2, good sprayability, suspected low coefficient of friction, but the lowest hardness of the borides to be tested. Titanium diboride, on the other hand, has the highest hardness of the metal boride candidates (3480 kg/mm2) but thus far has been unsprayable in compound form. Should the sprayability of metal borides prove difficult, the co-spraying and exoergic reaction of individual components will be attempted. For instance, APS has co-sprayed

titanium and boron in the inert chamber to form titanium diboride. APS has proven this technology in the past in work with the DOE Mound lab. The major problem in producing this coating as highly reacted titanium diboride is depositing a stoichiometric mix of sufficient density. We will try mixing, milling, binding and co-feeding techniques to obtain fully reacted coatings of titanium diboride or possibly other metal borides.

Turbine Metal Technology (TMT)

TMT will concentrate on three coating methods: diffusion alloying, electrospark deposition (ESD) and high velocity thermal sprays.

Diffusion Alloys

A diffusion alloy is a layer of intermatallic compound formed by the addition of elements to the surface of the part, and the simultaneous reaction of those elements with that surface. Thus, elements from the part and the elements added comingle to form the new material. In reality it is not a true "coating", but a modification of the surface chemistry and structure.

Surface alloys are formed by chemical and physical reactions that are caused to take place at and in the surface of a part. These high temperature processes are carefully controlled to produce smooth, uniform systems of desired physical properties. Basically, the part is heated to a temperature in the 760° to 1100°C range, and at that temperature, elements are deposited on the surface by chemical vapor deposition techniques or simply by the vapor pressure of the desired element. Once deposited on the surface, the elements react with the surface of the part to form compounds. At the reaction temperature, the concentration gradient and the physics of diffusion cause the reaction layer to grow. Elements from the substrate diffuse into the surface layer, and elements added at the surface diffuse toward the substrate. Since the entire surface and all elements present are involved, the resultant layer has no residual grain boundaries, is essentially uniform in composition, and most importantly has the desirable monolithic nature.

By selecting the elements and matching them with the elements in the part, characteristics can be produced at the surface which are very different from the base metal. In addition, unlike plating or plasma spray, there is no sharp interface to separate under mechanical or thermal stress, nor are there pinholes and the like to weaken the system. Thus, a method of producing desirable surface

characteristics on common structural materials is achieved.

Since the process involves high temperatures, the part to be alloyed is in a thermally stable condition and is subsequently heat treated. With some simple precautions, the heat treating can be carried out in the normal manner.

The investigation will focus on hard aluminides and borides, formed on substrates of 422 martensitic stainless steel, Inconel 625 nickel base superalloy and H-13 tool steel. Aluminides will be based on Ni_3Al and borides on iron or mixed iron/chrominum boride compositions.

Electro-Spark Deposition

Electro-spark deposition (ESD) is a coating process using short duration, high current electrical pulses to deposit an electrode material on a metallic subsrate. A principal attribute of the process is its ability to apply metallurgically bonded coatings with such a low total heat input that the bulk substrate material remains at or near ambient temperature.

Electro-spark deposition (ESD) coatings are produced by discharging stored energy from a capacitor bank through an electrode of the materials to be deposited. In the resulting spark, electrode material is both vaporized and melted and under correct conditions the molten material is welded to the substrate. Coatings of nearly any electrically conductive metal, alloy or cermet can thus be deposited on electrically conductive substrates. Some diffusion between the coating and substrate occurs and a true metallurgical bond results without significantly changing the bulk material temperature or properties.

Cr_3C_2-Ni materials will be investigated by means of this process. Comparisons are to be made with Cr_3C_2-metal systems applied by other methods (eg. high velocity thermal sprays).

High Velocity Thermal Coatings

High velocity thermal coating is a new technique in which coating particles are projected at hypersonic speeds by injecting powder into the nozzle of an oxy/fuel gas spray gun based on a rocket motor design. The advantages of the process are twofold: extremely high particle impact speeds result in high bond strengths, and relatively low combustion temperatures (compared to arc-plasma spraying) cause less solution of carbide particles in the matrix. In addition, compressive

residual stresses are often generated, resulting in higher coating strength and allowing thicker coating build-up to be achieved without cracking. Coating porosity is generally very low. The new TMT HV system offers significant improvement over other line of sight thermal coating systems, including D-gun, with respect to bond strength, hardness, surface finish and cost effectiveness.

The Cr_3C_2-Ni-Cr system has been selected for development for piston ring applications.

Other Suppliers

In addition to the subcontractors described above, other suppliers may be selected for promising coating systems. Such suppliers include Boyd Machine and Repair Co., Kimmell, IN (plasma spray and high velocity thermal spray), Vac Tec, St. Paul, MN (thick PVD zirconium nitride) and the University of Stony Brook, NY (laser glazing technology).

Status of Sample Procurement

HK40, 422, Inco 625 and H-13 substrate materials have been ordered from Wiscon Centrifugal, Inc. in the form of centrifugally cast pipes (4 1/2" o.d., 2 1/2" id, 30" length). To date, we have received two HK40 pipes and one each of the other alloys. A further three HK40, two H13 and one each 422 and Inco 625 castings should be received within the next month. One of the HK40 pipes has been sent to Boyd Machine and Repair Co. Kimmell, IN for surface grinding and coating with Cr_2O_3 (plasma spray), Cr_3C_2-Ni-Cr and 88% WC 12% Co (high velocity thermal sprays). The coated samples have not yet been received. The remaining cast pipes are being subjected to metallurgical examination and will be sent to our coating subcontractors. Liner samples of grey cast iron and type 1 Niresist have been machined and the Niresist samples sent out for ion nitriding. H-13 tool steel liner samples are to be machined from the centrifugally cast pipes. Two potential suppliers of powder metal steel products have been identified: CIPS and Avesta Nyby Powder AB (both Swedish), and quotations for PM Nitronic 20 and other potential liner substrate materials are being sought.

Wear Test Conditions

Further modelling work has been performed to identify the test conditions which best simulate the piston ring: cylinder liner environment. Particular attention has been paid to the loading of the ring against the liner at top ring reversal. Calculations of the gas loading force per

unit circumferential distance have been made as a function of ring geometry, peak cylinder pressure and the coefficient of friction between the ring side walls and the piston groove. Figure 3 shows a typical plot for a commerical top ring for a pressure drop of 2300 psi across the ring. The model takes into account the gas pressures acting inwards on the top half of the barrel face ring, above the line contact with the liner. As the ring wears, the area of contact with the liner increases, resulting in a decrease in this inward force and a net increase in the outward loading of the ring against the liner. The side wall friction is not known, but if we assume that, for boundary lubrication, the value is in the range 0.1 to 0.2, we can obtain an estimate of the range of values for the ring loading (in this case 10-45 Nmm^{-1}). For wear testing, we have selected a value of 30 Nmm^{-1} as being representative of TRR conditions. A cylinder - on - flat test configuration will be used (simulating a barrel face ring on liner contact), with a barrel radius of 50.8mm, which is within the range of values found for typical production rings. This geometry allows for easy sample preparation, since test specimens can be machined from coated 4" OD cylinders. Contact stresses may be calculated for the above values for loading and radius of curvature: for Cr plate in contact with grey iron, a value of 131 MPa (18.0 ksi) is obtained.

The conditions to be used for Cameron Plint wear tests have been determined. The "ring" sample will oscillate against the 'liner' at 20 Hz using a 5 mm stroke. The normal load will be 225 N on a 7.49 mm sample (30 Nmm^{-1} loading). For lubricated tests, oil will be supplied at a rate of one drop every 10 seconds. These test conditions have previously been found to provide good correlations between wear rig and engine test data. The test duration will be 6 hrs for lubricated tests and 1 hr for unlubricated tests. The wear volumes for the ring

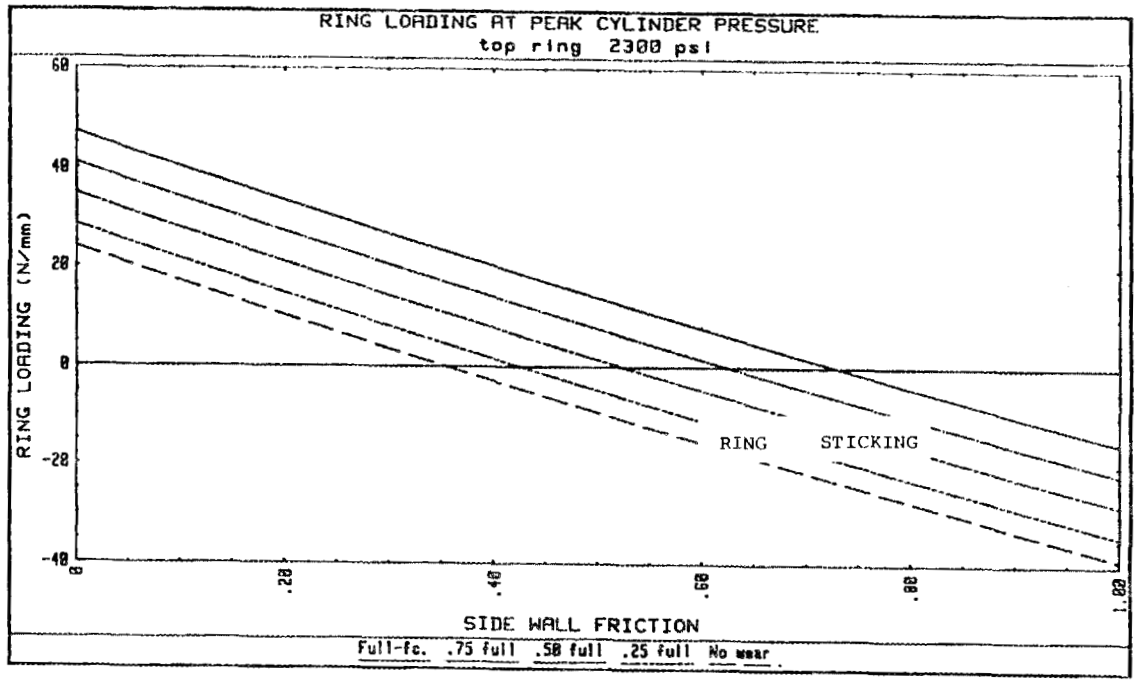

Figure 3 Example of a theoretical prediction of top ring loading at peak cylinder pressure as a function of ring side wall friction and amount of wear of the (barrel-faced) ring.

will be calculated from measurements of the scar width (see Figure 4) and for the liner from stylus profilometry measurements.

Test Matrix

For each coating system the following tests will be performed:

- microstructural characterization (including flaw detection)
- microhardness (at elevated temperature, if possible)
- friction and wear tests
- adherence tests (Revetest and/or tensile tests)
- thermal fatigue tests
- oxidation tests

Wear tests will be performed unlubricated (2 tests at 350°C) and under boundary lubrication (2 tests per lubricant at 350°C). Since the project is primarily a materials development effort, we will limit our choice of lubricant to one mineral oil based fluid for the initial screening tests. More advanced synthetic fluids will be utilized in the latter stages of the program when the number of materials will be greatly reduced. From the list of initial candidates described in Table 1, it may be seen that we have approximately 18 ring materials x 7 liner materials x 4 tests = 504 tests for a full-factorial analysis. This test matrix will need to be reduced to about 300 tests for the scope of this project. This will be achieved by continually discarding obviously poor candidates and possibly by using the Hohman A9 wear tester which can be used to test two (identical) ring and liner samples simultaneously. This tester is currently undergoing modifications, and should be available for use within the next two months. Obviously, we will need to confirm that the Hohman A9 tester produces identical results to the Cameron Plint tester, when operated under the same conditions with the same samples, before committing ourselves to this course of action.

Friction Test Results

Although the coated samples described in Table 1 were not available for testing in this reporting period, we have made use of plasma sprayed ceramic samples from a previous program to investigate the effects of temperature on friction under boundary lubricated conditions, as a function of sliding materials. Samples were available as

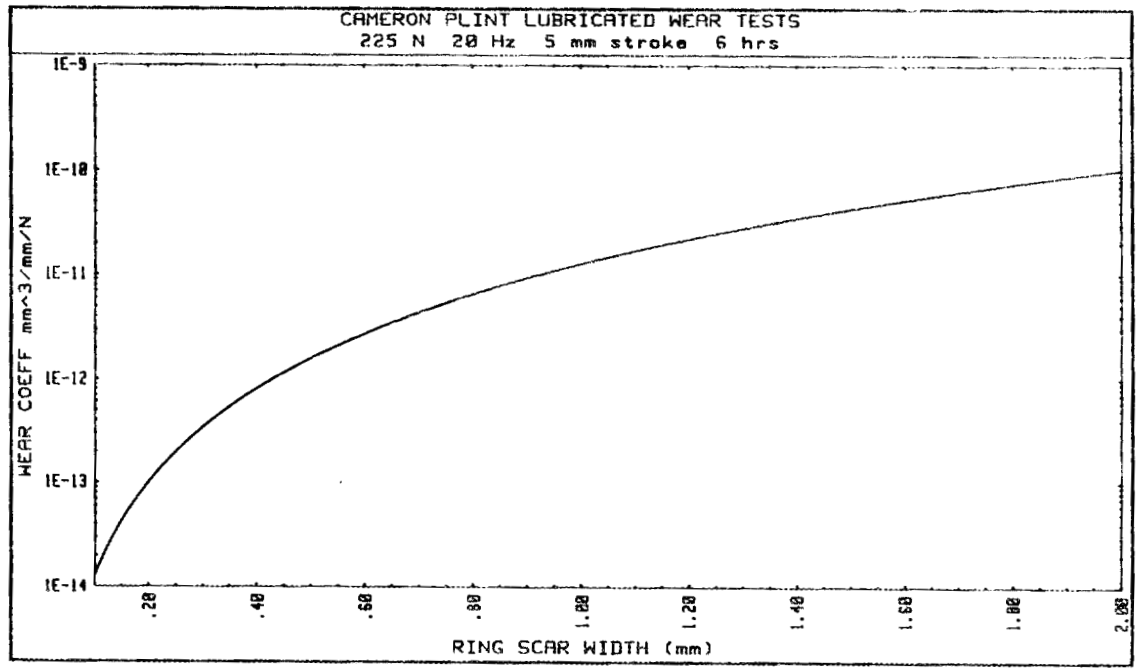

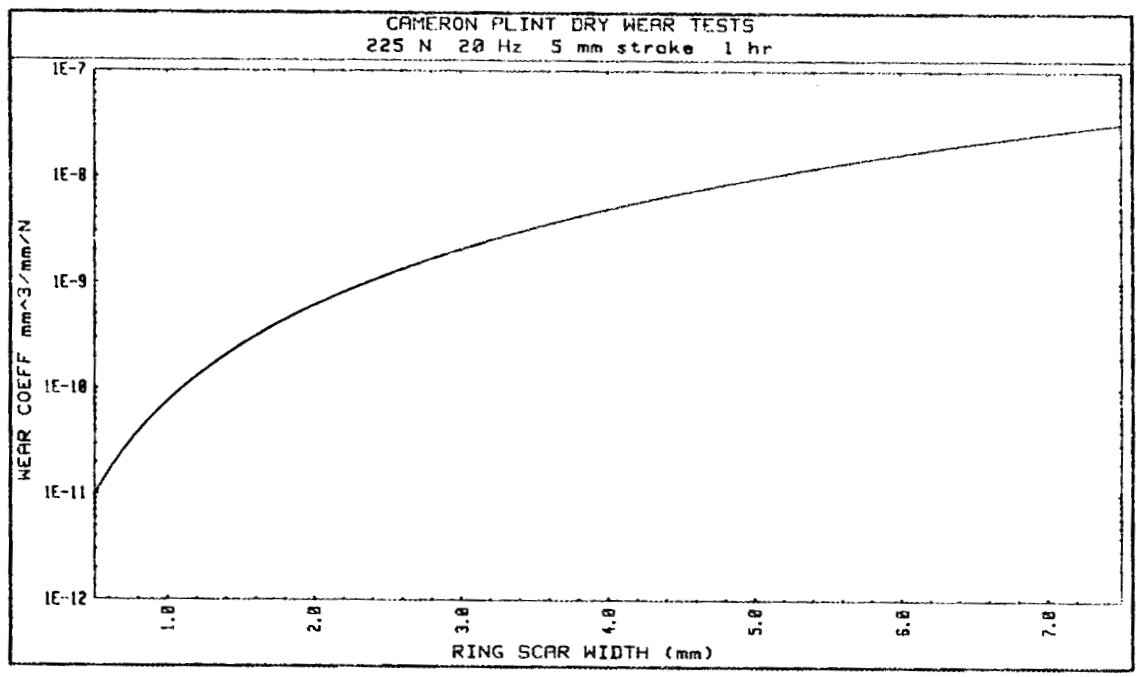

Figure 4 Wear coefficient as a function of wear scar width on the ring sample for the test conditions described in the text. (a) lubricated tests, (b) unlubricated tests.

inlaid piston ring coatings and coated cylinder liners. The materials combinations investigated were:

Piston Ring	Cylinder Liner
Cr electroplate	Grey cast iron
Cr_2O_3 plasma spray	Grey cast iron
Cr_2O_3 plasma spray	Cr_2O_3 plasma spray
TiC-CaF_2-Ni-Cr plasma spray	Grey cast iron
TiC-CaF_2-Ni-Cr plasma spray	Cr_3C_2 plasma spray

Tests were performed on a Cameron Plint oscillating wear tester using 250N load on a 12.5 mm ring segment, 20 Hz frequency, 5 mm stroke and using a lubricant feed of one drop every 10 seconds. The lubricant was the same commercial premium quality CE/SF 15W40 mineral oil based fluid in all cases.

After a 60 minute run-in period at room temperature, the samples were heated at 3°C per minute up to 600°C, continously monitoring the friction coefficient. The plots of friction against temperature are shown in Figure 5.

Discussion of Test Results

This test provides useful information regarding the maximum temperature capability of a tribological system. Typically, the friction coefficient is in the range 0.1-0.25 up to some critical temperature, above which the oil film is either absent or ineffective, and scuffing of the sliding materials occurs. The 'scuff temperature' is a function of the lubricant and the rate of oil supply: the lower the rate of supply, the lower the 'scuff temperature'.

The data shown in Figure 5 shows that the 'scuff temperature' was constant (430 $\pm$ 10°C) for all the materials combination studied, which is an important result. Two possible interpretations of the transition from low to high friction are:

a) loss of oil film due to evaporation
b) thermal and oxidative decomposition of the lubricant film

In the second case, the concern would be that a ceramic surface may act catalytically to decrease the 'scuff temperature'. The present results suggest that this was not a factor for the materials: lubricant combinations studied.

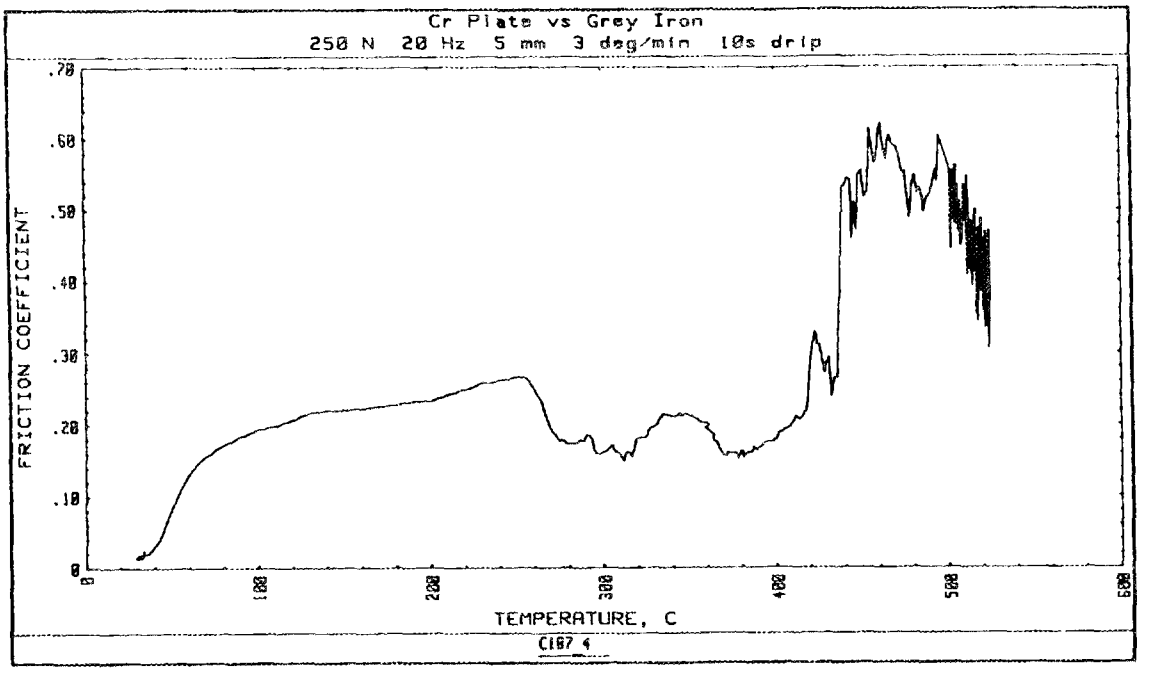

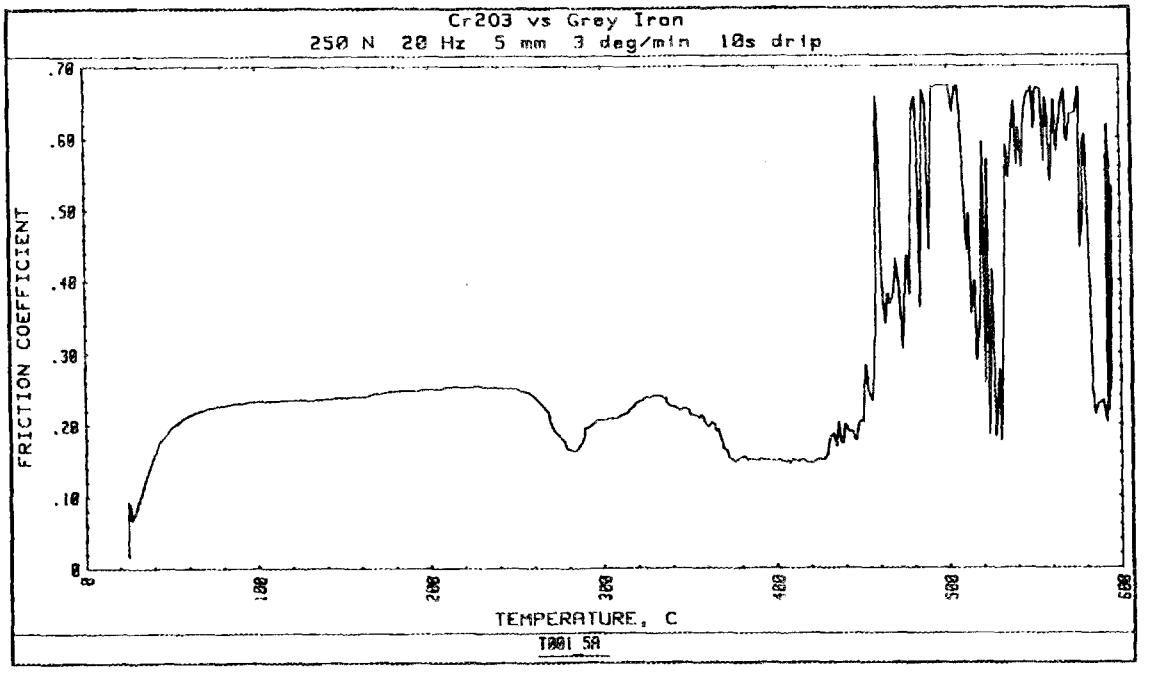

Figure 5 Plots of friction coefficient as a function of temperature for various material combinations using the same lubricant. (a) Cr plate vs grey iron, (b) Cr_2O_3 vs grey iron.

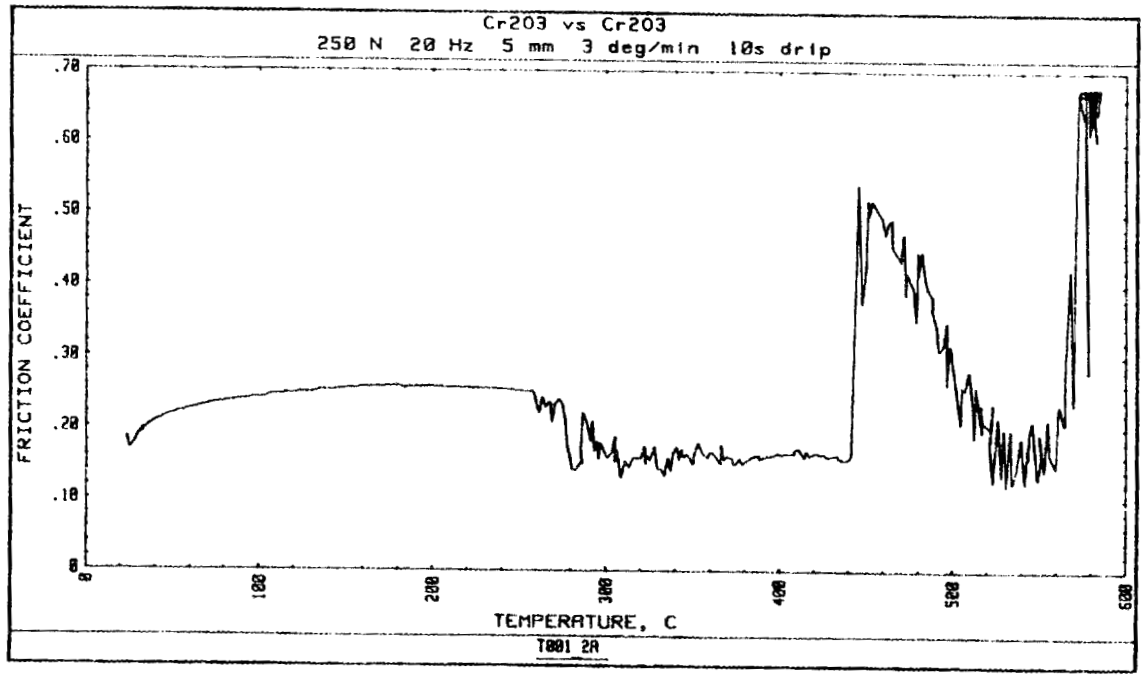

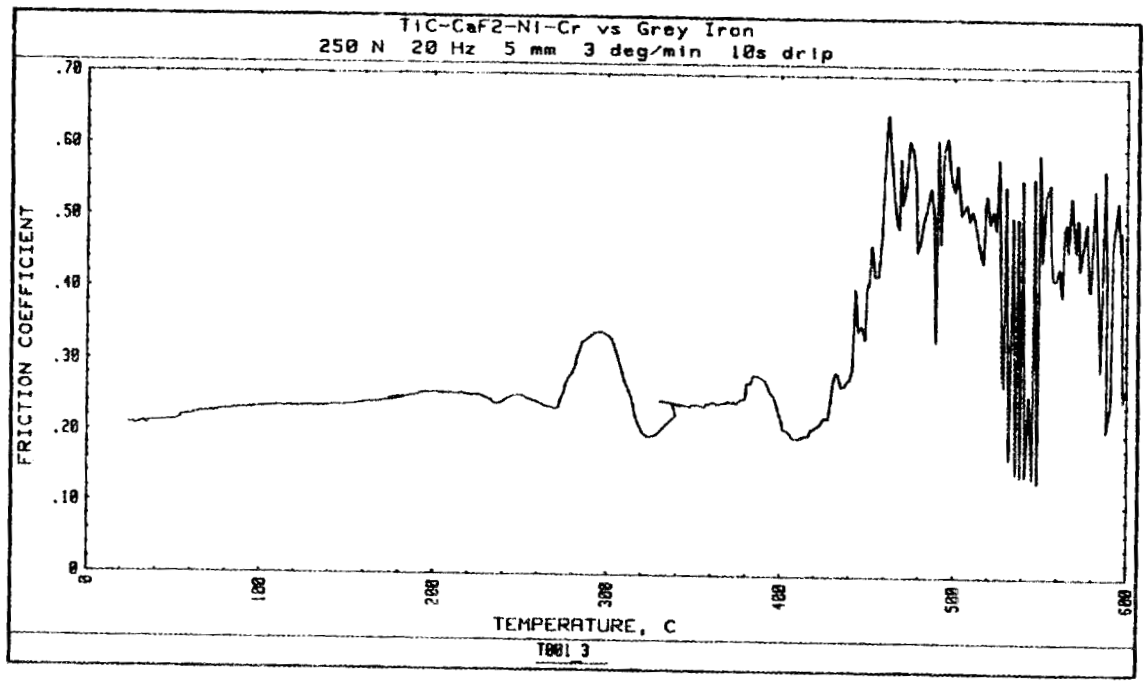

Figure 5 cont'd. Plots of friction coefficient as a function of temperature for various materials combination using the same lubricant. (c) Cr_2O_3 vs Cr_2O_3, (d) TiC-CaF_2-Ni-Cr vs grey iron.

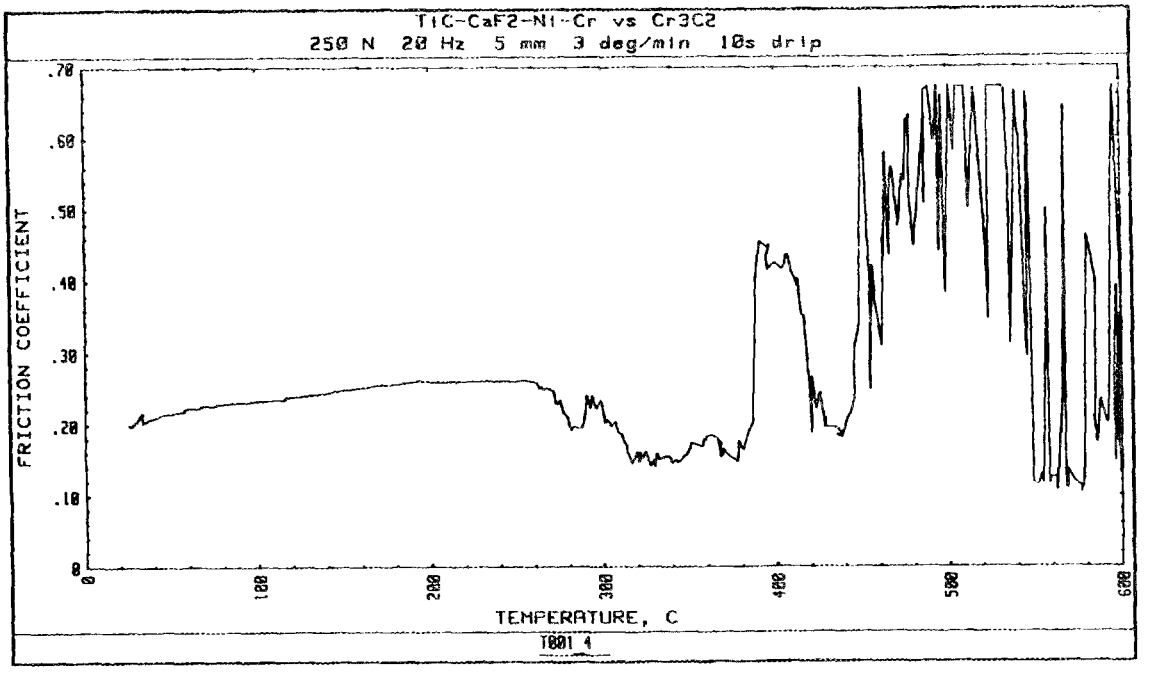

Figure 5 cont'd. Plots of friction coefficient as a function of temperature for various materials combinations using the same lubricant (e) TiC-CaF_2-Ni-Cr vs Cr_3C_2.

Other features of the friction temperature plots were repeatable for all the materials studied: the friction coefficent was generally stable at about 0.2 from 25 to 260°C, followed by a sudden drop (except for the TiC vs Grey Iron combination). The cause of this decrease is not known, but decomposition of the anti-wear additive is suspected. It is thus interesting that the effect is manifested with both ceramic and metallic wear surfaces. Clearly, more detailed study of the surface chemical interactions between lubricant additives and sliding surfaces are required to understand this effect.

Status of Milestones

The first milestone: Task 1, Experimental Plan and Coating Disposition is in progress and on schedule. Task 2, sample characterization will start on schedule (beginning of month 7).

Publications

None.

1.4 JOINING

1.4.1 Ceramic-Metal Joints

Joining of Ceramics for Heat Engine Applications
M. L. Santella (Oak Ridge National Laboratory)

Objective/scope

The objective of this task is to develop strong reliable joints containing ceramic components for applications in advanced heat engines. Presently, this work is focused on the joining of partially stabilized zirconia to nodular cast iron by brazing. Joints of this arrangement will be required for attaching monolithic pieces of partially stabilized zirconia to cast iron piston caps in order for the ceramic to provide the insulation necessary for use in low-heat-rejection diesel engines. A novel method for brazing zirconia to cast iron has already been established. The emphasis of this activity during FY 1988 will be on investigating: (1) the effects of testing temperature and zirconia surface finish on the flexure strength of zirconia-to-zirconia, and zirconia-to-cast iron joints; (2) correlating zirconia braze joint microstructures with strength data to identify any factors that may limit joint strength; (3) flexure testing of silicon nitride braze joints; and (4) developing a method of calibrating the indentation fracture technique to determine the accuracy of residual stress measurements in ceramic-to-metal joints.

Technical progress

The purpose of this report is to summarize the initial results of our assessment of the brazing of partially stabilized zirconia to nodular cast iron for uncooled diesel engine applications which was the main objective of this program at its inception. The focus of the report is mainly on braze process selection and development, as well as mechanical properties of zirconia braze joints. Also, results from a preliminary metallographic analysis of fractured joint specimens are discussed. One of the specific anticipated applications of this brazing technology was attachment of insulation pieces to the tops of cast iron pistons. This particular application defined two important boundary conditions for brazing: (1) the brazing thermal cycle should not significantly alter the mechanical properties of the cast iron, for instance, by overaging or inducing transformation of the cast iron microstructure; and (2) the braze joints should have reasonably good strength (100 MPa) at the expected service temperature (300 to 400°C). These two constraints meant that it would be necessary to restrict the brazing temperature to between about 500°C and 750°C.

Another important consideration in the brazing of zirconia is the need to produce wetting of the oxide by the braze filler metal. Brazing is essentially a liquid phase bonding process that uses metallic alloys as bonding agents. Generally, liquid alloys do not readily wet oxide surfaces so that producing strong oxide braze joints is difficult unless special precautions are taken. Wetting of oxide surfaces by metal alloys can be obtained by two general methods: (1) alloying braze filler metals with

certain elements like titanium, and (2) applying coatings that promote wetting to the oxide surfaces prior to brazing.

The two brazing approaches considered in this work embody both methods of promoting the wetting of oxides, and are shown schematically in Fig. 1. On the left in Fig. 1 is the process known as active filler metal or direct brazing; on the right is the process known as active substrate or indirect brazing. Active filler metal brazing takes its name from the alloying of the braze filler metal with titanium, an element that "activates" wetting of oxide surfaces. The titanium-alloyed filler metals are known as active filler metals or ABA alloys. A drawback of active filler metal brazing for the applications of interest on this program is that alloy additions such as titanium tend to increase the melting temperatures of the relatively low temperature braze alloys required. The range of active braze filler metals in terms of composition is limited and, until recent developments, the brazing temperatures for these alloys were typically in the range of 800 to 1000°C, high enough to cause undesirable phase transformations in the cast iron components of zirconia-to-cast iron braze joints. Presently, lower temperature active braze filler metals are commercially available. The reported brazing temperature range for one particular alloy, Incusil-15 ABA (manufactured by GTE-Wesgo), is 750 to 770°C, although our investigation of this alloy indicated that a temperature of at least 770°C was required for producing acceptable braze joints. Some evaluation of Incusil-15 ABA was done and will be discussed throughout this report.

The active substrate brazing process employs a coating on the oxide surface to promote wetting and bonding. The coating material selected in this work was titanium and it was applied by vapor deposition techniques. A disadvantage of this approach is the need to coat the oxide surfaces prior to brazing. However, active substrate brazing allows for a much wider range of candidates from which to select a brazing filler metal. The alloy chosen for brazing zirconia to nodular cast iron permitted brazing temperatures to be limited to 735°C, and it was readily available on a commercial basis. Because lower brazing temperatures could be achieved with the active substrate brazing process, our efforts to braze zirconia to cast iron have emphasized the use of this method.

The success of vapor coatings as a means of promoting the wetting of oxide surfaces by liquid metals was demonstrated some time ago,[1,2] but was not exploited for producing strong oxide braze joints until it was selected for consideration on this program. The viability of the active substrate process was demonstrated by producing several zirconia-to-cast iron braze joints in which the mating surfaces were over 11 cm in diameter. One of these joints is shown in Fig. 2. The thickness of the zirconia disk is 5 mm and the thickness of the cast iron is 19 mm. A 0.65-mm-thick disk of titanium was sandwiched between the zirconia and cast iron to accommodate some of the residual stresses induced in the joint by the mismatch in thermal expansion coefficients between the zirconia and the iron. Titanium was selected for this because its thermal expansion coefficient is nearly the same as that of the zirconia, and it has very good ductility up to the brazing temperature.

The effect of brazing thermal cycles on the microstructure and hardness is presented in Fig. 3, where the as-received iron (grade 8003, courtesy of Cummins Engine Co.) is on the left, a specimen of iron from an

ORNL-DWG 87-17186

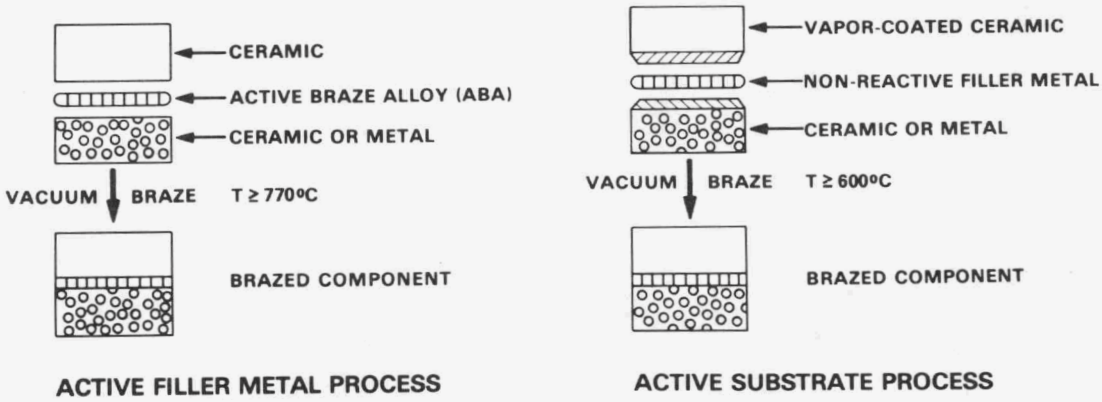

Fig. 1. Schematic representation of the two brazing approaches being used in this work. Active filler metal provess (left); active substrate process (right).

PHOTO 6268-85

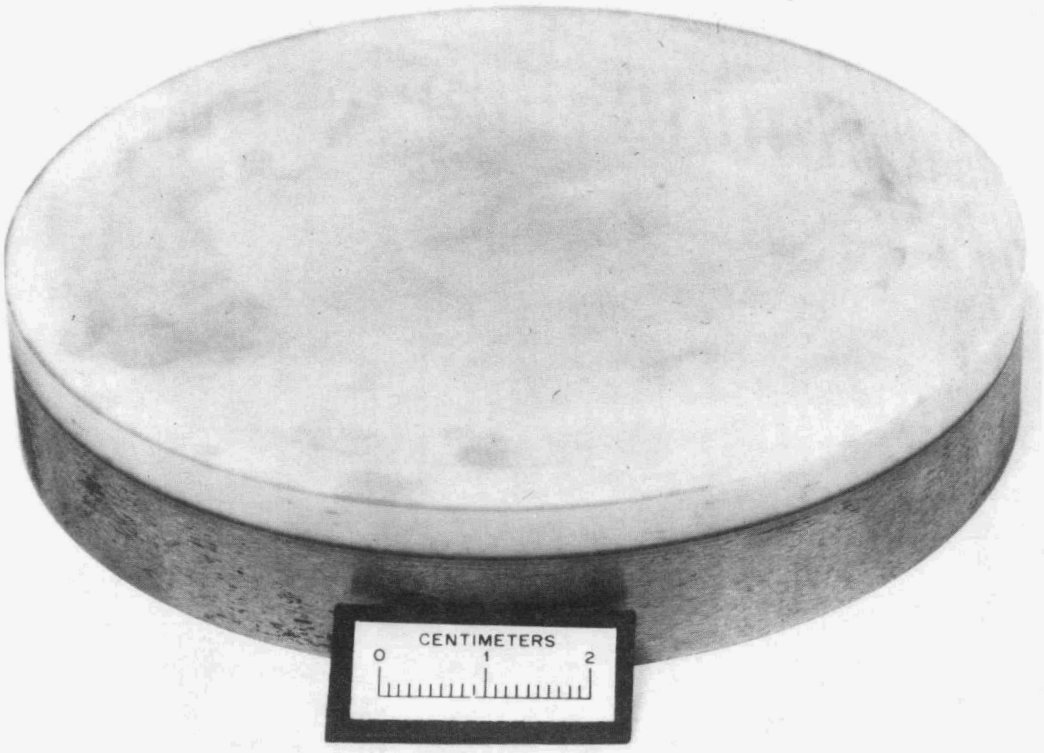

Fig. 2. Demonstration braze of 11.2 cm disks of partially stabilized zirconia to nodular cast iron. Zirconia thickness is 5 mm; cast iron thickness is 19 mm.

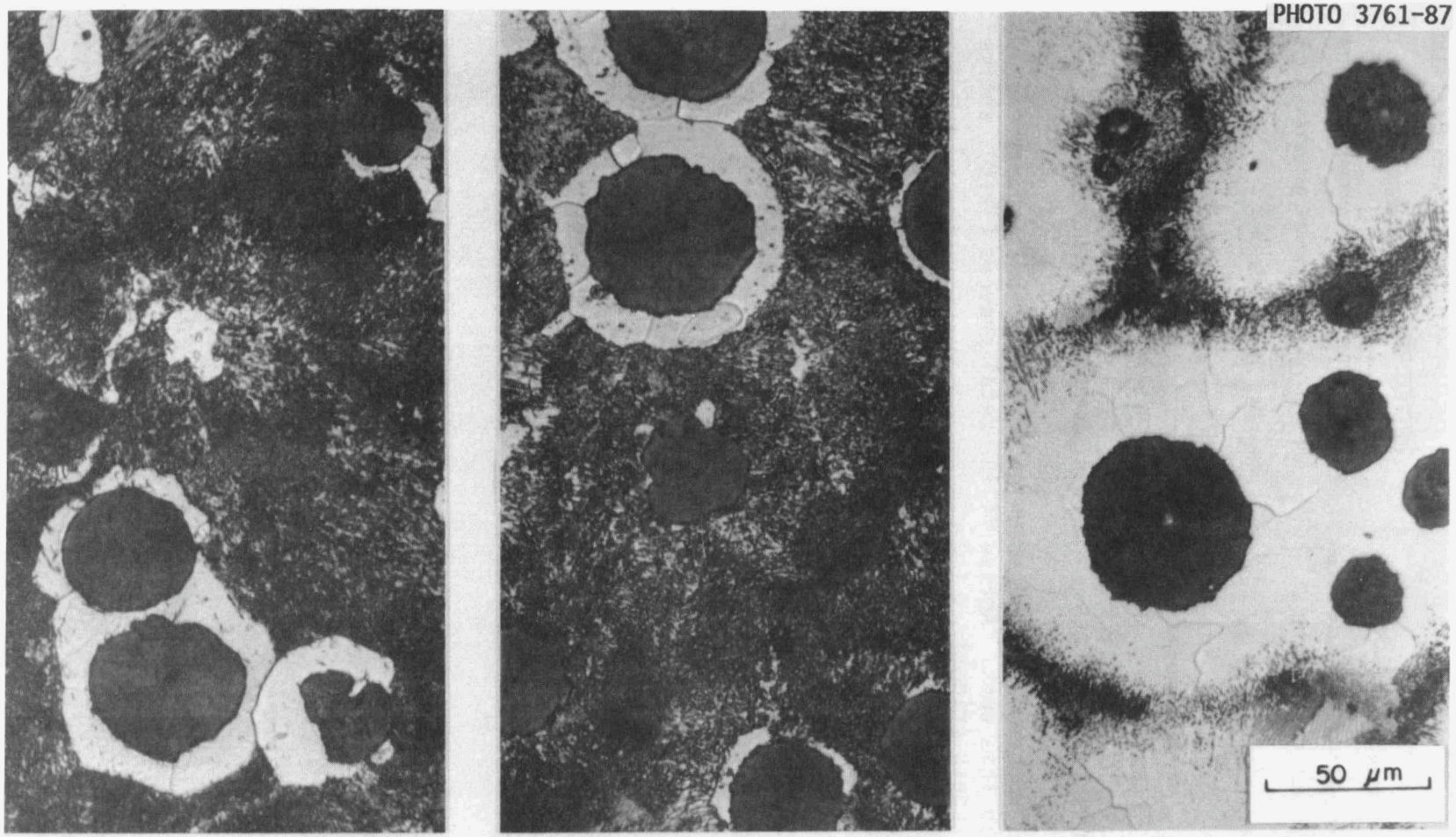

AS-RECEIVED
$R_c = 32$

$T_p = 735°C$
$R_c = 32$

$T_p = 770°C$
$R_c = 10$

Fig. 3. Effect of peak brazing temperature on the microstructure and hardness of nodular cast iron. As-received (left); peak temperature used for active substrate brazing (center); peak temperature used for active filler metal brazing with Incusil-15 ABA.

11 cm diameter demonstration braze is in the center, and a specimen heat treated to simulate the thermal cycle that would be required for producing a similarly sized demonstration piece with Incusil-15 ABA is on the right. The peak temperatures for the thermally cycled specimens and the Rockwell C hardness for all three specimens is also shown. Cycling to a temperature of 735°C for the active substrate process did not significantly alter the microstructure or the hardness of the nodular cast iron. On the other hand, slow heating and cooling to the peak temperature of 775°C required of Incusil transformed the matrix of the iron from pearlite to ferrite containing only remnants of the pearlite colonies. The change of microstructure was accompanied by a significant loss in hardness. Based on the ferritic microstructure a significant decrease of strength and increase of ductility would also be expected. This experiment serves to emphasize the need to maintain the lowest possible temperature when brazing zirconia-to-nodular cast iron joints if overaging of the iron is undesirable, and indicates that the active substrate process has a clear advantage in this regard.

The remainder of this report will discuss mainly the mechanical testing of zirconia braze joints.

Materials and experimental details

The materials used for this work were: Nilsen grade MS partially-stabilized zirconia, grade 8003 nodular cast iron, and commercially pure titanium (ASTM B265 grade 1). The zirconia was brazed to the metals by either active filler metal or active substrate brazing. The braze filler metal used for the active filler metal process was Incusil-15 ABA which has a nominal composition of Ag-23.5Cu-14.5In-1.3Ti, wt %. Handy & Harmon Braze 604 (BVAg-18) was used for the active substrate process. The nominal composition of the 604 alloy is Ag-30Cu-10Sn, wt %. The zirconia surfaces used for brazing were typically ground to a 180 to 220 grit finish by machining. No further treatments of the zirconia surfaces were used except for vapor coating where applicable.

The initial development of the active substrate process used RF-sputtering to deposit layers of titanium metal up to thicknesses of 2.0 μm on the zirconia surfaces. Prior to vapor coating, the surfaces were ion etched in an argon plasma for 10 min to aid adhesion. In later experiments the zirconia was vapor coated with a 0.6-μm-thick layer of titanium by vacuum evaporation. For evaporation coating a titanium vapor was produced in the vacuum chamber by melting a pure titanium source with an electron beam melting system operating at 7 kV and 100 mA. Typically, the pressure inside the chamber at the time melting of the titanium began was 400 μPa and dropped to 50 μPa during evaporation. A shutter shielded the zirconia from the titanium vapor until the pressure inside the chamber stabilized. A standard quartz oscillation technique was used to monitor coating thickness during evaporation, and thickness was verified by reference weighing tabs. A typical evaporation time to produce a 0.6-μm-thick layer using this procedure was 20 min. The zirconia specimens were not preheated prior to coating. All specimens were ultrasonically cleaned with acetone followed by ethyl alcohol and then air dried before being placed in the evaporation chamber.

The nodular cast iron was also coated prior to brazing because carbon from the graphite nodules was believed to dissolve in the both of the

braze filler metals and restrict wetting. To overcome this problem, all nodular cast iron braze joint components were cleaned in a hot bath of commercial caustic solution and electroplated with a 50-μm-thick layer of pure copper prior to brazing.

All brazing was done in vacuum. Joint assemblies were placed in an alumina tube which was subsequently sealed and evacuated to a pressure of about 130 μPa. After evacuation, the tube was inserted into an air muffle furnace preset to the desired brazing temperature, and heating commenced. A thermocouple positioned near each assembly was used to continuously monitor temperature during the brazing thermal cycle. The brazing temperatures used were 735°C for the 604 braze filler metal, and 770°C for the Incusil-15 ABA. The holding time at each brazing temperature was 10 min, after which the alumina tube was backfilled with argon to a pressure of about 20 kPa, and the tube was withdrawn from the furnace and cooled to room temperature.

The shear strength of joints between zirconia and either the nodular cast iron or titanium was measured using a device modeled after a similar one used by Ritter and Burton[3] to measure the adherence of droplets formed by sessile drop experiments. Shear test specimens are shown in Fig. 4. The shear test device is shown in Fig. 5 where Part B fits concentrically into assembly A, while Part C (shown in an inverted position) bolts to Part B to constrain the shearing action of the claw (marked by the arrow in A) against the bar of the brazed test specimen. The claw engages the bar adjacent to the braze interface just above the braze fillet. The pad is held secure against the surface of Part C by a set screw in the back of Part B. The only contact the bar makes with this assembly is the point where it is engaged by the claw. The bar is pushed off the pad in the direction of the arrow in Fig. 4. The dimensions of the specimen pad and bar are 12.7 × 12.7 × 5 mm and 12.7 × 5 × 3.4 mm, respectively, and the contact area between the brazed bar and the pad is typically 43 mm^2. Shear testing was done at test temperatures of 25°C and 400°C. Although this approach does not permit the determination of true shear strength values, it does provide a relatively fast and economical means of evaluating joint strength, and therefore is valuable as a screening tool.

Because of the difficulty of interpreting shear strength data and of performing the shear strength tests at elevated temperature flexure, testing was also used to test the strength of brazed joints. Braze joints for our initial flexure tests were made by the approach shown schematically in Fig. 6. Individual plates with dimensions of 25 × 14 × 3 mm were joined along the 25 × 3-mm edge. Afterward the brazed specimens were surface ground on both faces, polished to a 1 μm diamond finish on their tensile faces, and cut into flexure test bars with dimensions of 28 × 2.5 × 2 mm and having a brazed joint in the center of each bar. Testing was done by four point bending at a loading rate of 22.7 kg/s. The flexure test fixture had an outer span of 19.05 mm and an inner span of 6.35 mm. Flexure testing was done at temperatures of 25°C, 200°C, 400°C and 575°C. The test bars were heated to the test temperature and equilibrated for 30 min prior to fracture.

PHOTO 6265-85

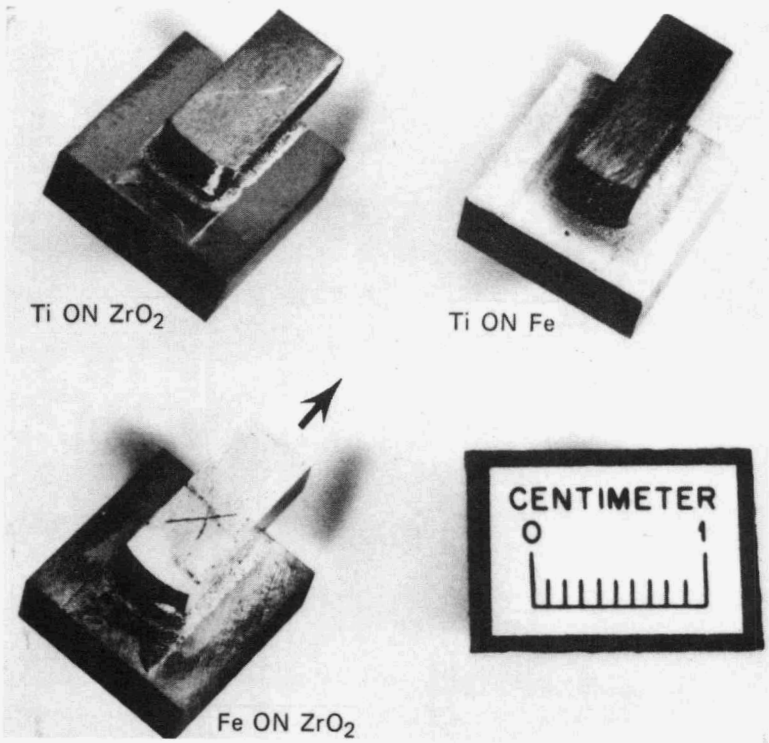

Fig. 4. Configuration of specimens used for shear testing. Arrow indicates direction of shear straining.

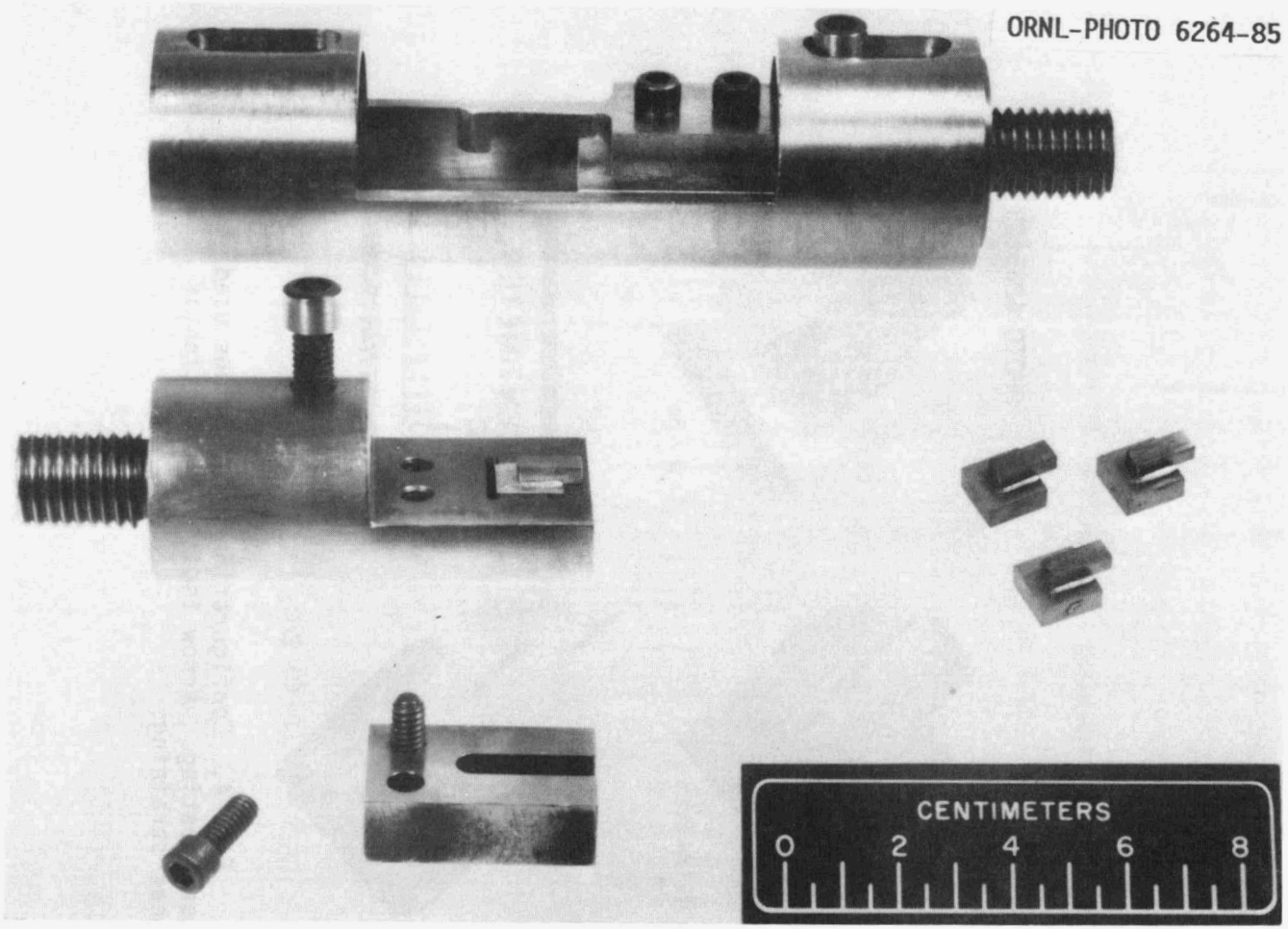

Fig. 5. Apparatus used for shear testing of braze interfaces.

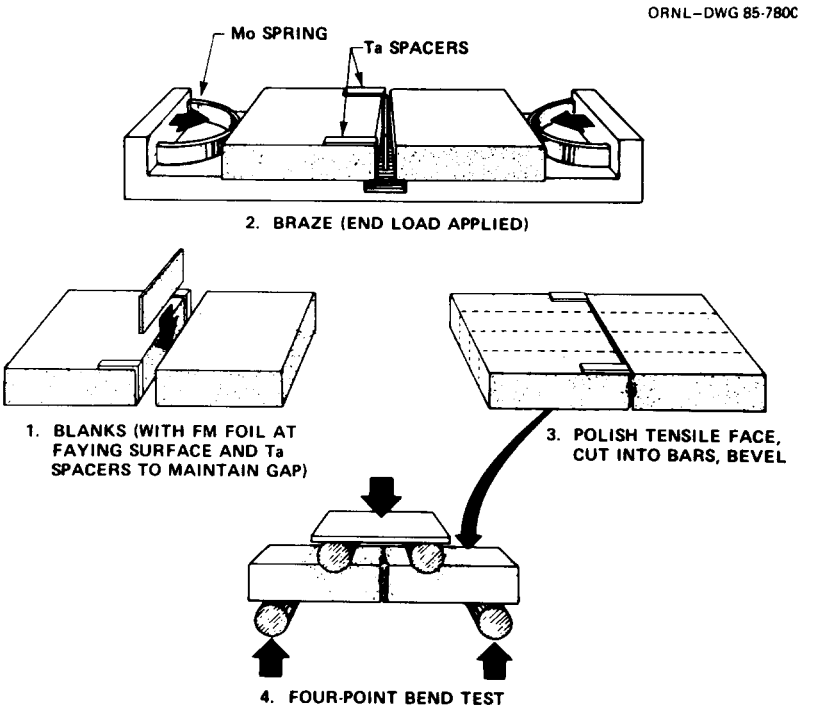

Fig. 6. Schematic representation of technique used to produce specimens for four-point flexure testing of zirconia braze joints.

Results and discussion

Shear testing of sputter-coated zirconia braze joints

Initial braze process development and joint strength evaluation was done using zirconia specimens that were sputter coated with titanium prior to brazing. Shear test results for braze joints between titanium-sputter-coated ZrO_2 and either nodular cast iron or titanium are given in Table 1. Four specimens of each combination were tested at 25°C, and the joint strengths were excellent. At 400°C, three ZrO_2-Ti joints were tested. As Table 1 shows, the shear strength of the ZrO_2-Ti joints was only about 20% of their room temperature value. A decrease of shear strength at elevated temperature was expected, but the very low strength of the ZrO_2-Ti joints prompted a careful microstructural evaluation.

Table 1. Shear strength of active substrate braze joints made with sputter-coated zirconia

Interface	Test temperature (°C)	Shear strength (MPa)
ZrO_2-Fe	25	137
ZrO_2-Ti	25	140
ZrO_2-Ti	400	28

All of the ZrO_2-Fe and ZrO_2-Ti joints, whether tested at 25°C or 400°C, fractured at the interface between the zirconia and the braze filler metal, so these surfaces were examined in detail in a scanning electron microscope (SEM). Figure 7(a) shows the typical appearance of a sputter-coated zirconia surface after joint fracture. Small fragments of braze filler metal remained bonded to the zirconia, but the surface appeared to have been relatively unaffected by brazing and shear testing. Figure 7(b) shows the appearance of the braze filler metal surface that mated to the zirconia surface shown in Fig. 7(a). It is obvious from Fig. 7(b) that a considerable amount of porosity formed at the interface between the zirconia and the braze filler metal during brazing. This condition was observed over the entire area of contact for all of the ZrO_2-604 braze filler metal interfaces regardless of whether the zirconia was brazed to nodular cast iron or titanium. In some cases the contact area of the braze alloy on the zirconia was reduced by as much as 60%. This situation would undoubtedly reduce joint strength at room temperature as well as at 400°C.

A major effort was directed toward the elimination of the porosity in these joints by varying the sputter coating conditions and the plasma ion etching time. These attempts were unsuccessful, and the alternative coating process of evaporation coating was selected. The optical micrographs

M21884

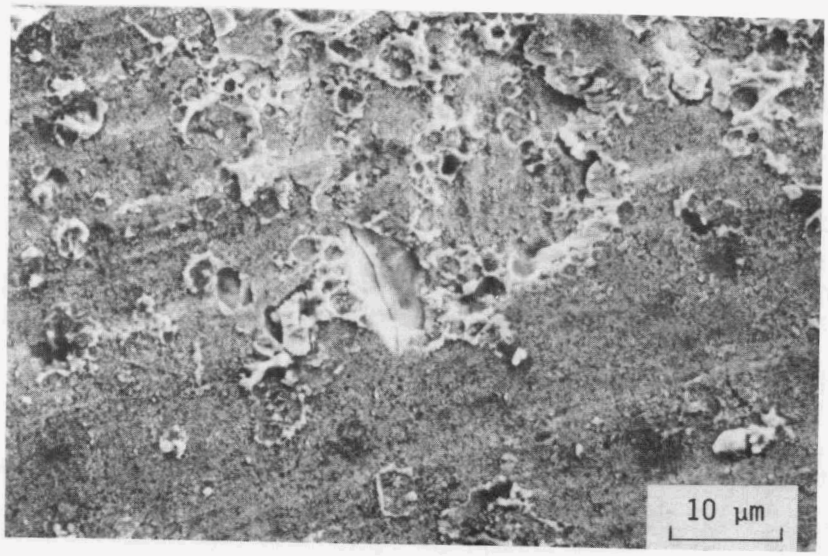

(*a*)

M21879

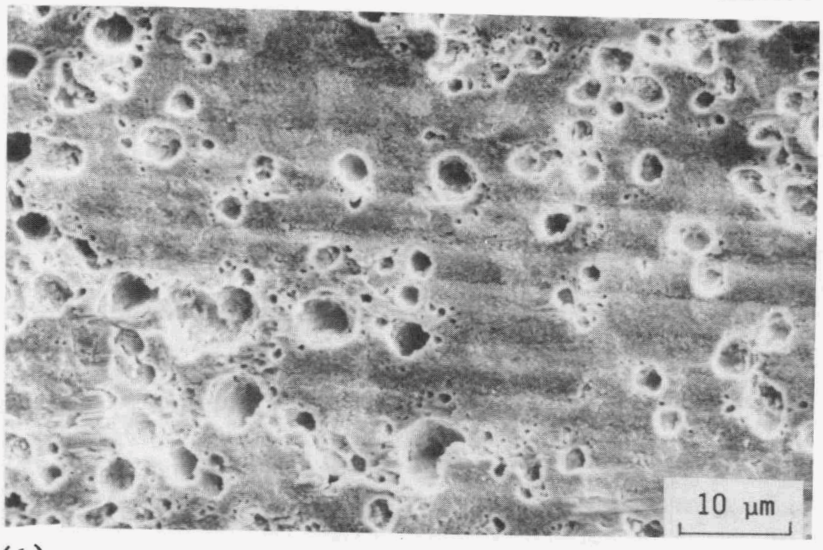

(*b*)

Fig. 7. SEM micrographs of (*a*) zirconia surface and (*b*) braze filler metal surface after fracture at the interface between the zirconia and braze filler metal.

presented in Fig. 8 show the reduction of porosity obtained by making this process modification. The joint made with zirconia that was coated with titanium by evaporation is essentially porosity-free. The source of the porosity in the joints of sputter-coated zirconia was not established experimentally. However, published reports[4,5] indicate that the inert gases used in the sputtering and ion etching processes can become entrapped in the deposited coating or etched surface. If this were the case it would be expected that the application of a sufficient amount of heat to these deposits would provide the thermal activation necessary to allow the escape of the gas. Based on this theory it is proposed that the porosity in the joints of sputter-coated zirconia was produced by the evolution of argon from the sputter-coated surfaces during brazing.

Shear testing of evaporation coated zirconia braze joints

Joints between titanium-vapor-coated zirconia and either nodular cast iron or titanium were subjected to shear testing at temperatures of 25°C and 400°C. The specimens were tested in the unaged condition or after aging at 400°C. Both the aging and testing of specimens at 400°C was done in air. The temperature of 400°C was selected because it is in the range where the brazed interface between zirconia and cast iron is expected to be under steady state operating conditions for a piston top that is thermally insulated from the combustion chamber by a zirconia cap in an uncooled diesel engine. Test results are given in Table 2 for ZrO_2-Fe joints and in Table 3 for ZrO_2-Ti joints. The room temperature strengths of the unaged joints are higher than those of the joints made with sputter-coated zirconia, Table 1, indicating the extent of improvement obtained by elimination of porosity in the braze layer. For both sets of data the shear strength of the joints at 400°C is only about half of the strength at 25°C. At both temperatures the strength of the ZrO_2-Ti joints was significantly higher than for the ZrO_2-Fe joints. The ZrO_2-Fe joints contain a higher level of residual stress, especially in the unaged condition and this situation is undoubtedly responsible for the lower measured strength of these joints.

Similar shear test specimens were aged at 400°C for times of 100 h, 120 h, and for ZrO_2-Ti joints, 500 h. Those specimens held for 120 h were a second set of joints that were unintentionally held at the aging temperature for 120 rather than 100 h. The second set of aged specimens was made because it was suspected that the scatter in the data from the first set was due to some difficulties that arose in assembling the joints before brazing. The scatter was reduced considerably for both types of joints in the second set of data. Aging improved the strength of the ZrO_2-Fe joints for testing at 25°C. The reason for this may be that the aging treatment relieved some of the residual stresses that resulted from the bonding. Only one shear test was done at 400°C on an aged ZrO_2-Fe specimen and it indicated that aging drastically reduced the joint strength. For the ZrO_2-Ti joints, aging had little effect on joint strength at either test temperature. Specimens of the ZrO_2-Ti joints that were aged at 400°C for 500 h had the same strength as joints that were tested in the unaged condition. Also, the specimens tested at 400°C had similar strengths before and after aging.

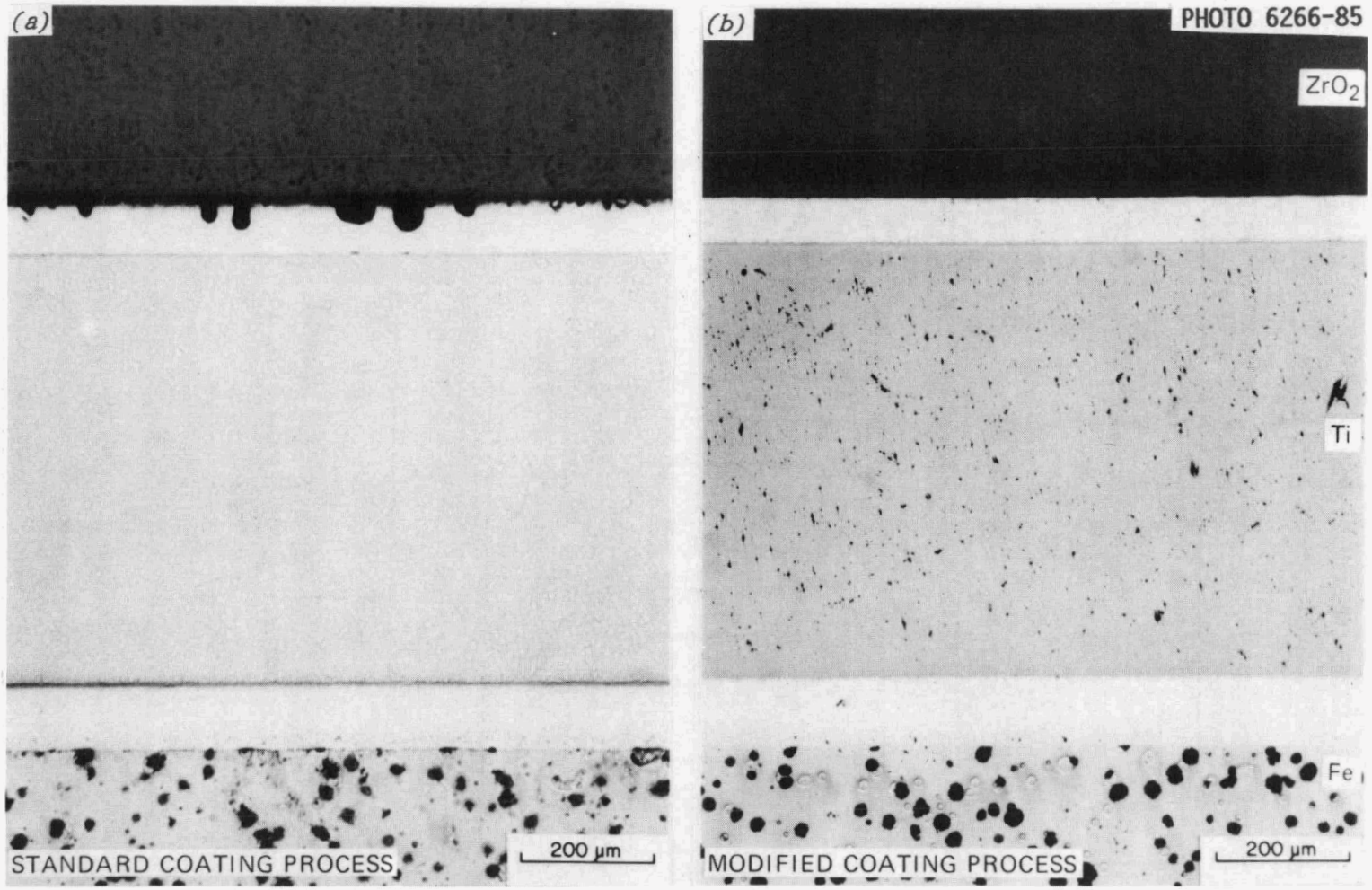

Fig. 8. Optical micrographs showing (*a*) porosity at surface of sputter-coated zirconia and (*b*) elimination of the porosity by use of evaporative coating process.

Table 2. Shear strength of joints of evaporation coated zirconia brazed to nodular cast iron by active substrate process

Specimen	Interface	Aging	Test temperature (°C)	Shear strength (MPa)
MCB-64	ZrO_2-Fe	None	25	188
MCB-65				194
MCB-66				191
			Average =	191
MCB-70	ZrO_2-Fe	None	400	85
MCB-71				96
MCB-72	ZrO_2-Fe	400°C/100 h	25	114
MCB-178				202
MCB-179				43
			Average =	120
MCB-244	ZrO_2-Fe	400°C/120 h	25	229
MCB-245				246
MCB-246				261
MCB-247				213
MCB-248				251
			Average =	240
MCB-73	ZrO_2-Fe	400°C/100 h	400	30

Table 3. Shear strength of joints of evaporation coated zirconia brazed to titanium by active substrate process

Specimen	Interface	Aging	Test temperature (°C)	Shear strength (MPa)
MCB-97	ZrO_2-Ti	None	25	262
MCB-98	ZrO_2-Ti	None	400	133
MCB-99	ZrO_2-Ti	400°C/100 h	25	123
MCB-169				210
MCB-170				117
			Average =	150
MCB-249	ZrO_2-Ti	400°C/120 h	25	216
MCB-250				299
MCB-251				267
MCB-252				255
MCB-253				332
			Average =	274
MCB-171	ZrO_2-Ti	400°C/500 h	25	291
MCB-172				259
MCB-100	ZrO_2-Ti	400°C/100 h	400	123

Shear testing of active filler metal braze joints

Our initial tests of zirconia brazed with Incusil filler metal were aimed at optimizing the braze process parameters for this alloy. The manufacturer (GTE-Wesgo) advised that the brazing temperature range was 750 to 770°C, that the alloy would wet both uncoated ceramics and cast iron, and that ceramic surfaces should be polished before brazing. Our evaluation of Incusil-15 indicated that 770°C was the lowest temperature at which good bonding to zirconia could be obtained. Once this was established several braze joints were made and shear tested at room temperature. These results are given in Table 4, and indicate that the stronger joints are possible with unpolished zirconia. Also, it was found that copper coating the nodular cast iron prior to brazing improved joint strength. All subsequent testing with Incusil was done with unpolished zirconia and copper coated iron, and these results are presented in Table 5 for ZrO_2-Fe joints and in Table 6 for ZrO_2-Ti joints.

Table 4. Shear strength of joints of zirconia brazed to nodular cast iron with Incusil-15 ABA filler metal

Specimen	Pad	Bar	Shear Strength, MPa
MCB-60	Unpolished ZrO_2	Uncoated Fe	127
MCB-61	Unpolished ZrO_2	Cu-coated Fe	165
MCB-62	Polished ZrO_2	Uncoated Fe	77
MCB-63	Polished ZrO_2	Cu-coated Fe	11

The data shown in Table 5 indicates that the unaged ZrO_2-Fe joints had very good strength and retained their strength at 400°C. Comparison with data in Table 2 indicates that the joints made with Incusil had much better strength at 400°C than those made with the 604 alloy. Aging had no significant effect on the shear strength of the joints at 25°C, but caused a substantial drop in the joint strength at 400°C. A drawback of the Incusil-15 was reproducibility. Difficulties were encountered in obtaining consistent behavior of the alloy during brazing and this is reflected in the scatter of the shear strength data. Data for the ZrO_2-Ti joints brazed with Incusil-15 were even more erratic than that for the ZrO_2-Fe joints. Overall, these data indicate that brazing zirconia to titanium with this alloy will not produce joints with consistently high strength.

Flexure testing of zirconia active substrate braze joints

Three types of joints were made for flexure testing: ZrO_2-ZrO_2, ZrO_2-Fe, and ZrO_2-Ti. The fracture strength data for the joints are

Table 5. Shear strength of joints of zirconia brazed to nodular cast iron by the active filler metal process

Specimen	Interface	Aging	Test temperature (°C)	Shear strength (MPa)
MCB-61	ZrO_2-Fe	None	25	165
MCB-79	ZrO_2-Fe	None	400	140
MCB-95	ZrO_2-Fe	400°C/100 h	25	61
MCB-182				180
MCB-183				150
			Average =	130
MCB-234	ZrO_2-Fe	400°C/120 h	25	57
MCB-235				226
MCB-236				123
MCB-237				252
MCB-238				190
			Average =	170
MCB-96	ZrO_2-Fe	400°C/100 h	400	28

Table 6. Shear strength of joints of zirconia brazed to titanium by the active filler metal process

Specimen	Interface	Aging	Test temperature (°C)	Shear strength (MPa)
MCB-108	ZrO_2-Ti	None	25	289
MCB-109	ZrO_2-Ti	None	400	123
MCB-110	ZrO_2-Ti	400°C/100 h	25	103
MCB-184				118
MCB-185				87
			Average =	103
MCB-239	ZrO_2-Ti	400°C/120 h	25	150
MCB-240				19
MCB-241				24
MCB-242				50
MCB-243				71
			Average =	63
MCB-187	ZrO_2-Ti	400°C/500 h	25	39
MCB-188				111
MCB-111	ZrO_2-Ti	400°C/100 h	400	67

given, respectively, in Table 7, Table 8, and Table 9. The average strength of the ZrO_2-ZrO_2 and ZrO_2-Fe joints decreased moderately with increasing temperature up to 400°C, and then showed a more marked decrease at 575°C. It should be noted that the solidus temperature of the 604 braze filler metal is about 620°C so that the low joint strengths at 575°C are reasonable. The average strength of the ZrO_2-Ti joints decreased linearly with increasing temperature. The average strength of the three types of joints is plotted against test temperature in Fig. 9, which shows that the highest strengths were obtained for the ZrO_2-ZrO_2 joints. Figure 9 also shows that the ZrO_2-Ti joints had higher strength at room temperature than the ZrO_2-Fe joints but that the strength of the ZrO_2-Ti joints decreased more rapidly with temperature so that at 200°C and above the strengths of the ZrO_2-Ti and ZrO_2-Fe joints were about the same.

There was considerable scatter in the strength data for all three types of joints and this is illustrated in Fig. 10 for the ZrO_2-ZrO_2 joints, Fig. 11 for the ZrO_2-Fe joints, and Fig. 12 for the ZrO_2-Ti joints. The largest variations were found for the ZrO_2-Fe joints. In all three cases there was a slight tendency for the scatter to decrease with increasing temperature.

The maximum strength values of the three types of joints are plotted against temperature in Fig. 13. The trends of these data are similar to those of Fig. 9, and they suggest that the highest strengths can be expected for the ZrO_2-ZrO_2 joints. Figure 13 indicates that the room temperature strength of the ZrO_2-Ti joints is higher than that of the ZrO_2-Fe joints but that it decreases more rapidly with increasing temperature. Both Fig. 9 and Fig. 13 indicate that the strength of the ZrO_2-Fe joints is fairly constant with temperatures up to 400°C. Furthermore, Fig. 13 suggests that the strength of the ZrO_2-Fe joints approaches that of the ZrO_2-ZrO_2 joints at high temperatures. It should be noted that the fracture strength of the zirconia was never exceeded in any of the tests. In all three types of joints fracture always occurred at or near one of the brazed surfaces, indicating the possibility of a strong influence of bond zone microstructure on joint strength.

A Weibull plot of the strength of ZrO_2-ZrO_2 active substrate braze joints is shown in Fig. 14. At room temperature, the strength of some of the strongest specimens approached that of the monolithic MS-ZrO_2 (~600 MPa), but joint strengths were typically much lower, and decreased chacteristic of the joint strength data was the low values of the Weibull modulii. Between 25°C and 400°C the Weibull modulus of the strength data was in the range of 4 to 4.5, and it decreased to 2.5 for testing at 575°C. The Weibull modulus of the monolithic MS-ZrO_2 is typically about 20. The lower values obtained for the braze joint specimens are indicative of a large amount of scatter in the test results. The source of this scatter, and ways of reducing it as well as increasing joint strength, is the subject of continuing analysis. Metallographic analysis of the test bars is in progress. Initial observations on the highest strength joint tested at 25°C indicated that fracture initiated and propagated along the interface between the titanium vapor coating and the 604 braze filler metal. Some subsurface cracking of the zirconia and pull-out of zirconia fragments was also observed. In contrast, observations of the lowest strength joint tested at 25°C indicated that the fracture path was mainly along the interface between the zirconia and the original titanium vapor coating. This result suggests that poor adhesion of the titanium coating

Table 7. Flexure strength of zirconia brazed to zirconia by the active substrate process

Specimen	Test temperature, °C	Fracture strength, MPa
MCB-175	25	365
		493
		508
		462
		483
MCB-299		571
		532
		493
MCB-346		327
MCB-347		269
MCB-348		314
MCB-361		332
MCB-362		432
MCB-363		312
	Average =	421
	Standard deviation =	95
MCB-299	200	459
MCB-346		444
MCB-347		323
		293
MCB-348		383
MCB-362		239
MCB-363		342
	Average =	355
	Standard deviation =	74
MCB-299	400	356
MCB-346		370
MCB-347		228
MCB-348		325
MCB-361		242
MCB-362		319
		299
MCB-363		199
		296
	Average =	292
	Standard deviation =	55
MCB-299	575	61
MCB-346		149
MCB-347		124
MCB-348		127
		94
MCB-362		125
		71
MCB-363		109
		48
	Average =	101
	Standard deviation =	32

Table 8. Flexure strength of zirconia brazed to nodular cast iron by the active substrate process

Specimen	Test temperature, °C	Fracture strength, MPa
MCB-300	25	380
		356
		399
		354
		370
MCB-350		149
MCB-351		25
MCB-367		36
MCB-369		102
	Average =	241
	Standard deviation =	150
MCB-300	200	363
MCB-349		58
MCB-350		237
MCB-367		326
	Average =	241
	Standard deviation =	118
MCB-300	400	364
MCB-349		80
MCB-350		249
MCB-367		358
MCB-369		111
		53
	Average =	203
	Standard deviation =	128
MCB-300	575	39
MCB-349		28
MCB-350		101
MCB-367		70
		28
MCB-369		27
		16
	Average =	51
	Standard deviation =	28

Table 9. Flexure strength of zirconia brazed to titanium by the active substrate process

Specimen	Test temperature, °C	Fracture strength, MPa
MCB-298	25	375
		470
		343
MCB-343		435
MCB-344		309
MCB-345		351
MCB-364		345
MCB-365		307
MCB-366		399
	Average =	370
	Standard deviation =	52
MCB-298	200	353
MCB-344		287
MCB-345		319
MCB-364		280
MCB-365		106
		142
MCB-366		332
		309
	Average =	266
	Standard deviation =	85
MCB-298	400	182
MCB-344		180
		168
MCB-345		212
MCB-364		173
		166
MCB-365		197
MCB-366		189
		137
	Average =	178
	Standard deviation =	20
MCB-298	575	118
MCB-344		100
MCB-345		128
		107
MCB-364		109
		103
MCB-365		49
	Average =	102
	Standard deviation =	23

ORNL-DWG 88-2244

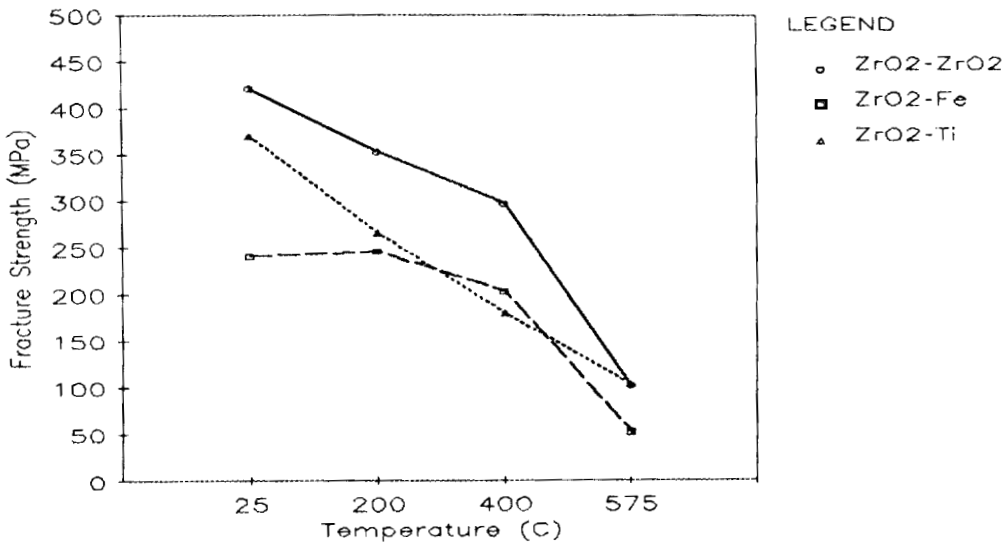

Fig. 9. Average flexural fracture strength plotted against test temperature for joints of ZrO_2-ZrO_2, ZrO_2-Fe, and ZrO_2-Ti made by active substrate brazing.

ORNL-DWG 88-2245

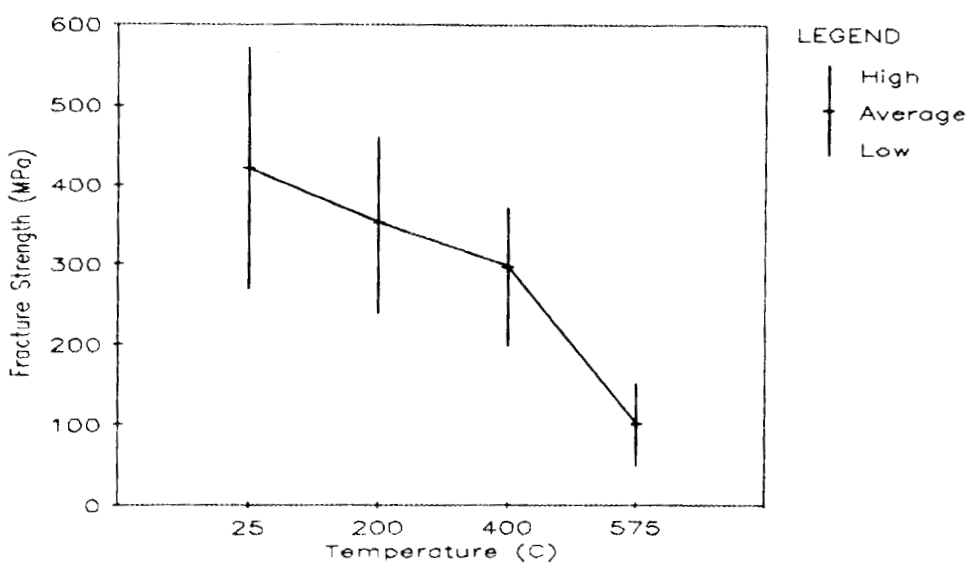

Fig. 10. Fracture strength plotted against test temperature for ZrO_2-ZrO_2 joints made by active substrate brazing. Vertical lines indicate extent of scatter in strength values.

ORNL-DWG 88-2246

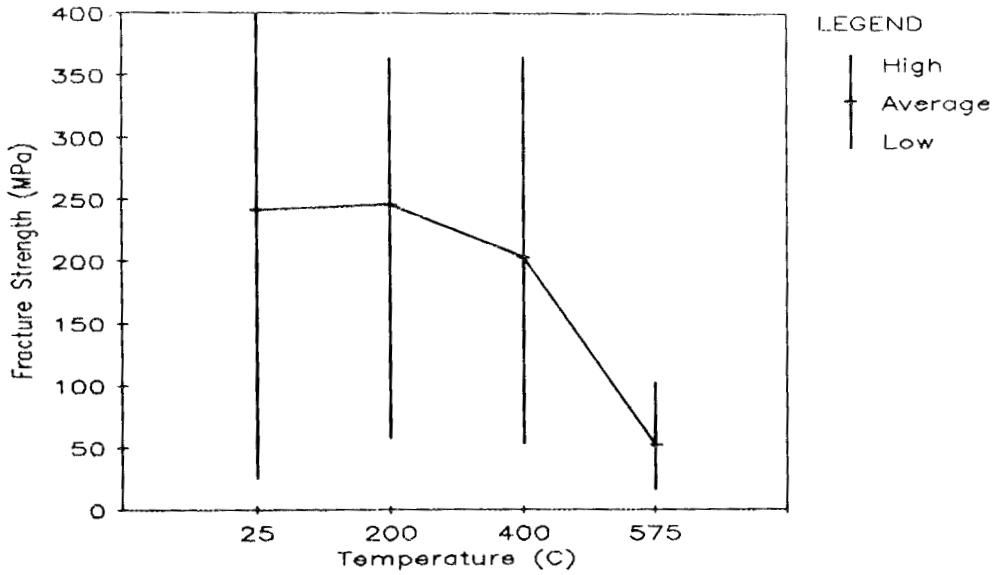

Fig. 11. Fracture strength plotted against test temperature for ZrO_2-Fe joints made by active substrate brazing. Vertical lines indicate extent of scatter in strength values.

ORNL-DWG 88-2247

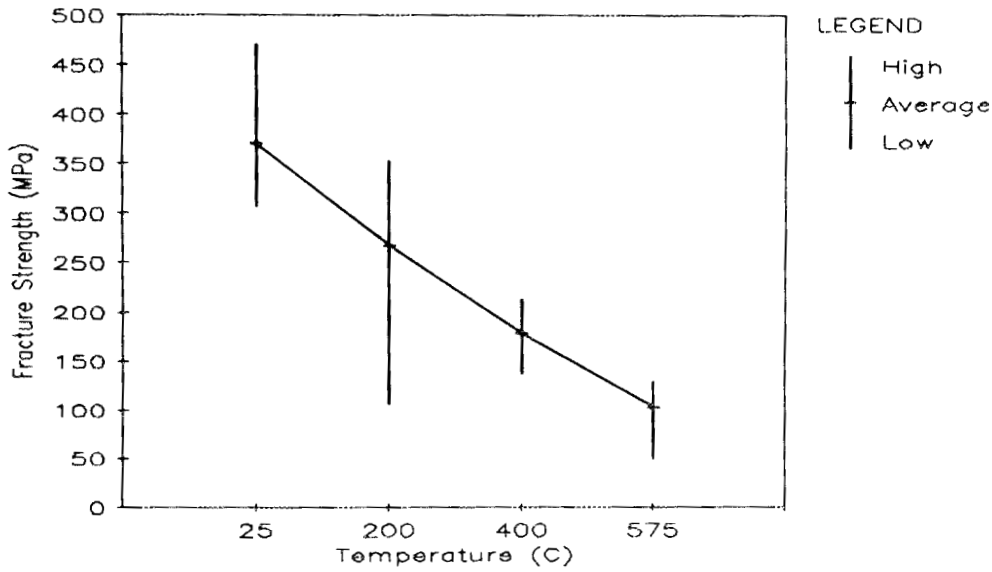

Fig. 12. Fracture strength plotted against test temperature for ZrO_2-Ti joints made by active substrate brazing. Vertical lines indicate extent of scatter in strength values.

ORNL-DWG 88-2248

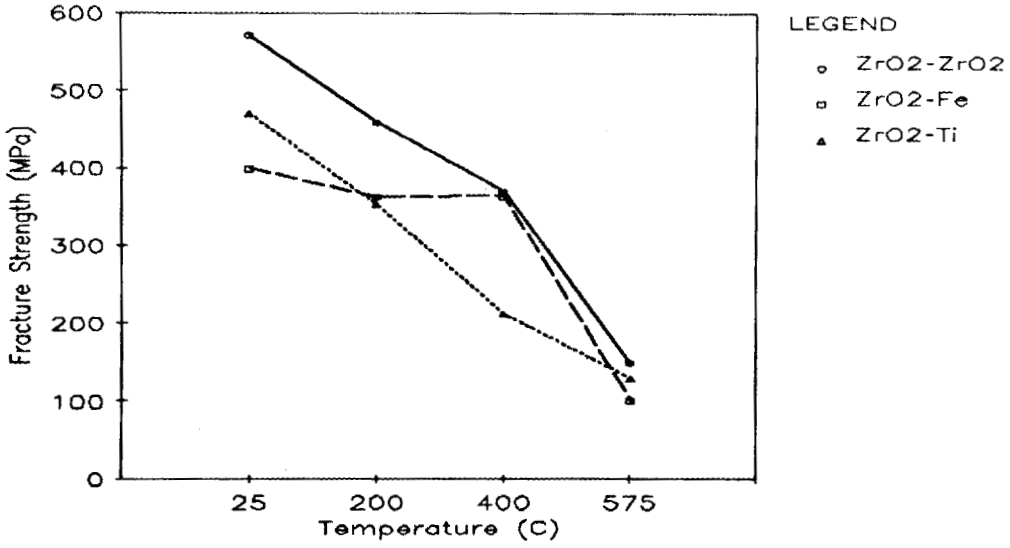

Fig. 13. Maximum flexural fracture strength plotted against test temperature for joints of ZrO_2-ZrO_2, ZrO_2-Fe, and ZrO_2-Ti made by active substrate brazing.

ORNL-DWG 88-2249

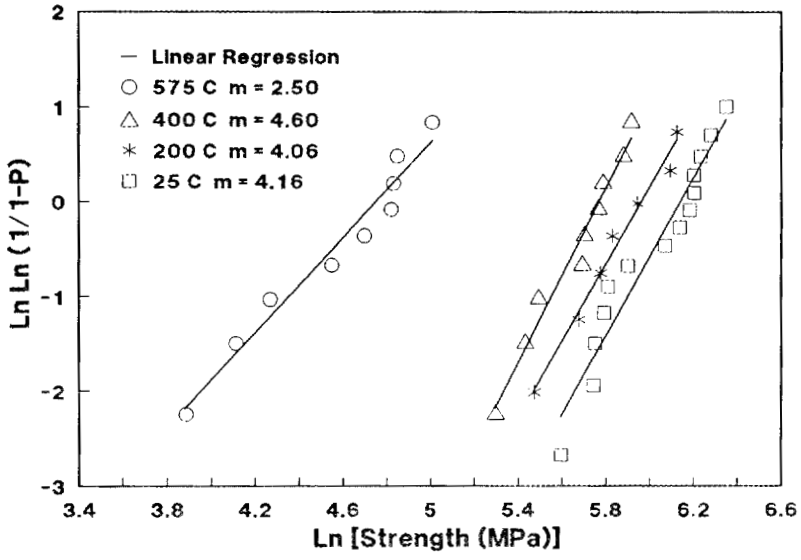

Fig. 14. Weibull plots of the strength data of zirconia-to-zirconia braze joint flexure specimens tested at 25°C, 200°C, 400°C, and 575°C.

to the zirconia may have been responsible for the low strength of this joint. Poor adhesion of the titanium coating would contribute to increased scatter in the data as well.

A Weibull plot of the strength of ZrO_2-cast iron active substrate joints tested at room temperature is shown in Fig. 15. The Weibull modulus is very low, but Fig. 15 shows that there are actually two frequency distributions for the data. The strengths of the four weakest specimens were 25, 36, 102 and 149 MPa. Examination of the fractured zirconia-to-cast iron specimens indicated that the layer composed of the copper electroplating used to coat the cast iron and the filler metal did not adhere to either iron or the zirconia part of the joint. The fracture surface of the cast iron half of the lowest strength specimen is shown in Fig. 16. Microanalysis in a scanning electron microscope indicated that levels of silicon much higher than that of the iron (about 3.0 wt %) were present on this surface. Relatively high levels of potassium were found on some of the other low-strength specimens. These observations suggest that a likely explanation for the low strength of these specimens was contamination of the copper coating during the electroplating operation.

The strengths of remaining specimens were relatively high, 354 to 399 MPa, but still below that of the monolithic zirconia. A fracture surface representative of all of the high strength specimens is shown in Fig. 17. The fracture initiated near the ZrO_2/Ti-vapor coating interface and eventually led to the pull-out of a large piece of the zirconia adjacent to the brazed surface. Examination of the fracture surface near the tensile face of the specimen at higher magnification showed that areas of the titanium coating were still adhering to the zirconia after fracture, Fig. 18. Flakes of the Ti (possibly TiO_x) coating are also visible. The average strength of these five specimens, 372 MPa, was also lower than the average strength of the ZrO_2-ZrO_2 joints, 421 MPa, and undoubtedly this is due to the residual stresses present in the ZrO_2-cast iron joints.

The preliminary results of metallographic examination of the ZrO_2-ZrO_2 and ZrO_2-cast iron flexure test specimens indicate that if coatings are used to enhance the brazing characteristics of a ceramic or metallic material, then obtaining good coating adherence is a prerequisite to obtaining high strength joints. The metallographic examination of the fractured high strength zirconia-to-cast iron joints also suggests that excellent bonding to the Ti-vapor-coated zirconia surface occurred during brazing, and that microstructural features near the brazed surface in the zirconia and the reaction layers that result from brazing may control joint strength.

Status of Milestones

On schedule.

Publications

A paper entitled, "Brazing of Titanium-Vapor-Coated Silicon Nitride," by M. L. Santella, was accepted for publication in the journal *Advanced Ceramic Materials*.

ORNL-DWG 88-2250

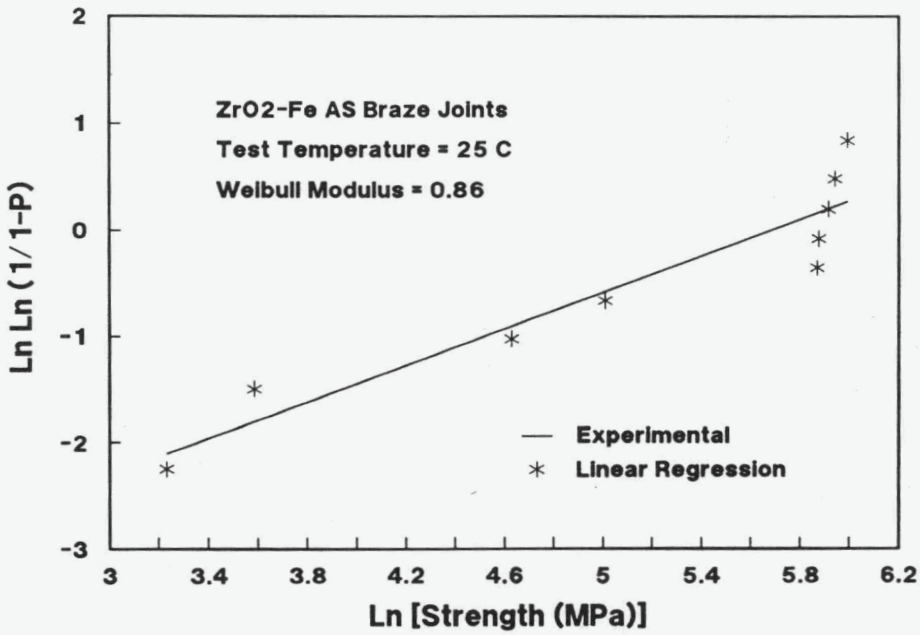

Fig. 15. Weibull plot of the strength data of zirconia-to-cast iron braze joint flexure specimens tested at 25°C.

M26884

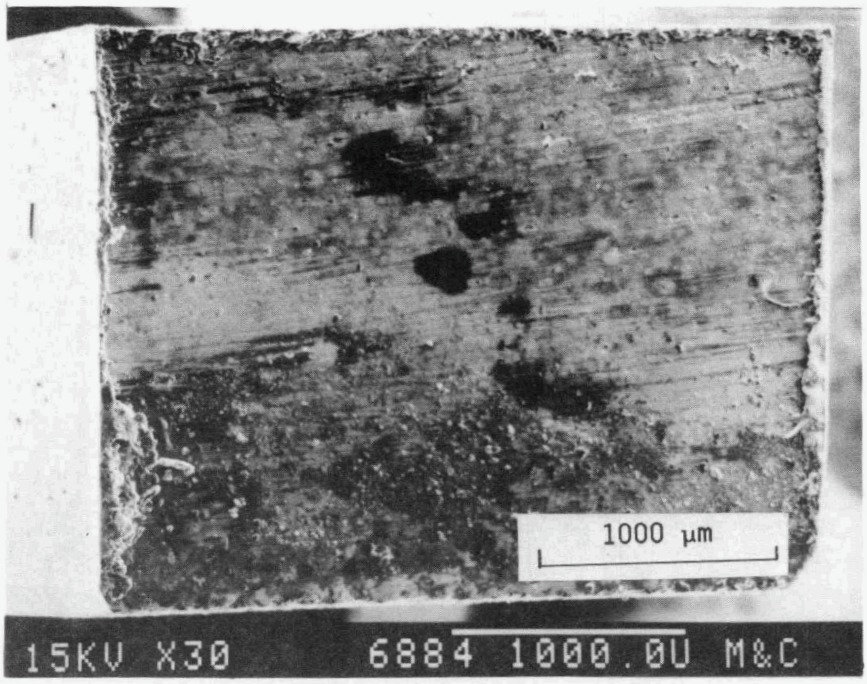

Fig. 16. Fracture surface of cast iron half of ZrO_2-cast iron flexure test specimen with four-point bend strength of 25 MPa. Electroplated coating of copper did not adhere to cast iron surface.

M27548

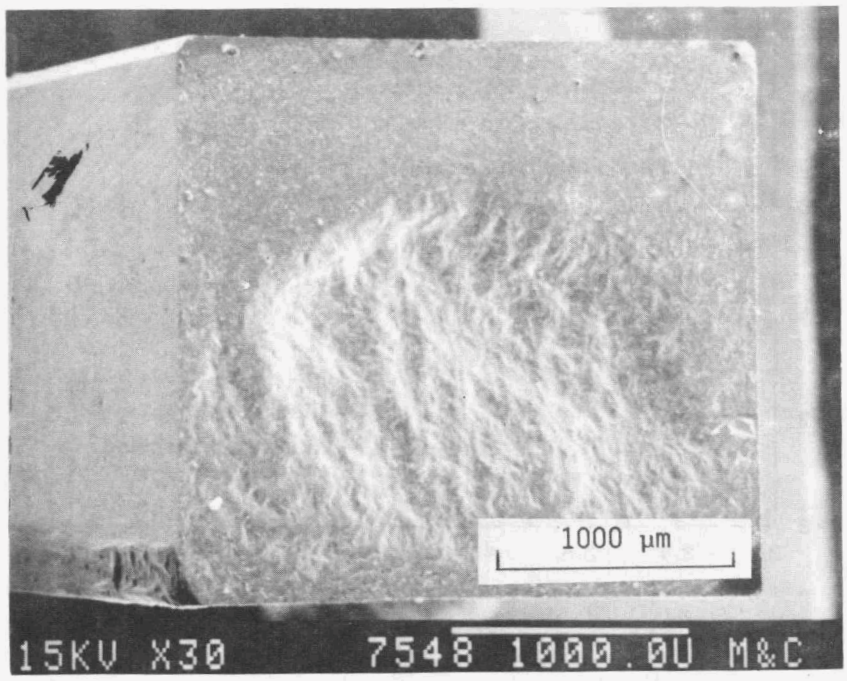

Fig. 17. Fracture surface of cast iron half of ZrO_2-cast iron flexure test specimen with four-point bend strength of 354 MPa. A large fragment of the zirconia was pulled-out during testing.

M27549

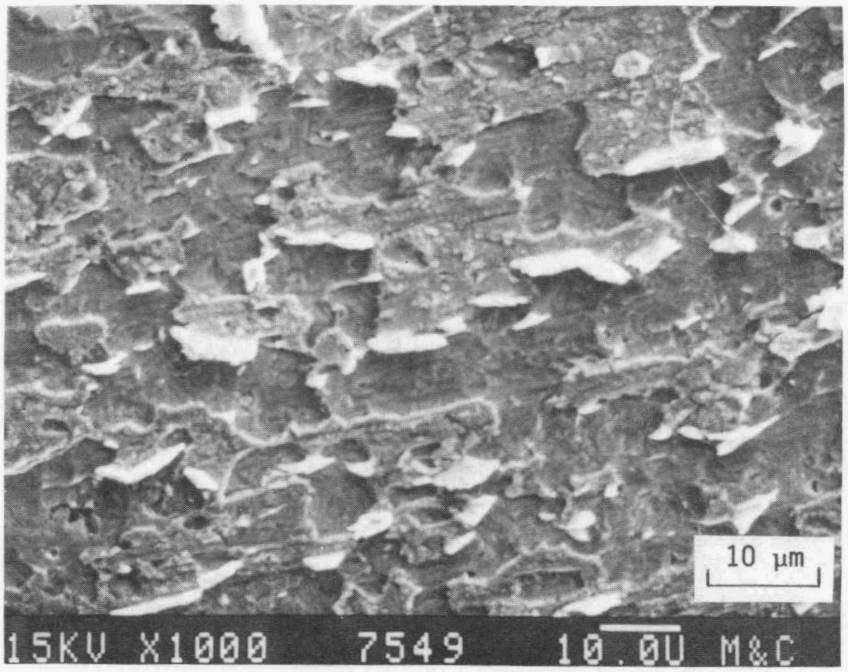

Fig. 18. Higher magnification view of Fig. 3 showing adherene of Ti vapor-coating to zirconia surface.

Unpublished work

A talk entitled, "Brazing of Ceramics for Heat Applications," was presented at the 25th Automotive Technology Development Contractors' Coordination Meeting, Dearborn, MI.

References

1. S. Weiss and C. M. Adams, "The Promotion of Wetting and Brazing," *Weld. J.* 46, 49-s-57-s (1967).
2. E. F. Brush and C. M. Adams, "Vapor Coated Surfaces for Brazing Ceramics," *Weld. J.* 47, 106-s-114-s (1968).
3. J. E. Ritter, Jr. and M. S. Burton, "Adherence and Wettability of Nickel, Nickel-Titanium Alloys, and Nickel-Chromium Alloys to Sapphire," *Trans. AIME* 239, 21-26 (1967).
4. H. F. Winters and E. Kay, "Gas Incorporation into Sputtered Films," *J. Appl. Phys.* 38, 3928-34 (1967).
5. W. W. Y. Lee and D. Oblas, "Argon Entrapment in Metal Films by dc triode Sputtering," *J. Appl. Phys.* 46, 1728-32 (1975).

Analytical and Experimental Evaluation of Joining Silicon Nitride to Metal and Silicon Carbide to Metal for Advanced Heat Engine Applications

E. M. Dunn (GTE Laboratories Incorporated)

Objective/Scope

The goal of this work is to demonstrate analytical tools for use in designing ceramic-to-metal joints including the strain response of joints as a function of the mechanical and physical properties of the ceramic and metal, the materials used in producing the joint, the geometry of the joint, externally imposed stresses both of a mechanical and thermal nature, temperature, and the effects of joints exposed for long times at high temperature in an oxidizing (heat engine) atmosphere. The maximum temperature of interest for application of silicon carbide to metal and silicon nitride to metal containing joints is 950°C. The initial joint fabrication work shall include "experimental" joints whose interfacial area is not less than two square centimeters. The work shall also include demonstration of the potential for scale-up of the joint size to interfacial areas of commercial significance, applicability of the analytical joint modeling tools and the ability to use these tools to design and predict the mechanical and thermal stability of the larger joints. These joints, referred to as "scale-up" joints, shall have an interfacial area of at least twenty square centimeters.

Technical Highlights

The mechanics aspects of ceramic-to-metal brazing have been analyzed. A set of criteria for reliable braze joining has been derived. A criterion for preventing ductile rupture of the braze, the β criterion has been derived. This determines the size and geometry of the braze joint. Strain localization has been predicted at the braze edge from finite element analysis of the braze plastic deformation. Another criterion, γ, characterizes the conditions for brazing without causing brittle fracture of the ceramic. Both of these criteria refer to survival of the components under a single brazing-process cycle for butt joints. This analysis was extended to axi-symmetric joints which are prototypical of those planned for Task II. Demo-calculations have been made with FEM for analysis of Task II-type axi-symmetric joints.

Materials system development was divided between bulk braze alloy development, coatings to enhance braze-ceramic bonding, and selection of interlayer materials. The wetting behavior of Nioro (82 wt. % Au-18 wt. % Ni) braze on coated silicon nitride and silicon carbide was measured. Good wetting behavior was observed with Ti, Zr, Hf, and Ta coatings. A new methodology to quantify the effect of such coatings on ceramic strength was developed and applied to silicon nitride. Based on this series of tests, it was observed that Zr coatings offer good wetting with less reduction in mechanical

strength than other candidates. Reaction products on the ceramic surfaces were evaluated using scanning electron microscopy.

Braze alloy development work centered around the screening of 59 melts of Au-base alloys. Tests involved rolling for ductility, DTA and wettability. Investigation of the Au-Ni-Ti braze alloy system continued with emphasis on Au-3 wt. % Ni-0.6 wt. % Ti. Ductile material was produced and brazed at 1030°C. Dissolution of the structural alloy components into the braze was noted.

Rectangular coupon specimens of candidate materials were shear tested after brazing with Nioro. Materials included Incoloy 909 to SNW1000, Mo to SNW1000, and SNW1000 to SNW1000. Large differences in expansion coefficient were associated with low shear strengths. Mo has a low expansion coefficient making it a candidate interlayer material.

Design/Criteria/Stress Analysis

A. Analysis of Braze Damage (β criterion)

In the braze joint between a ceramic and a metal component, plastic deformation is substantial because of thermal mismatch strain. A criterion which predicts the size of sound braze is:

$$\beta \leq 1, \tag{1}$$

where

$$\beta = \frac{T_s - T}{\sqrt{3}\varepsilon_e} [(\alpha_M - \alpha_c - \frac{\varepsilon^{EA}}{T_s - T})^2 (\frac{r}{t})^2 + 3(\alpha_M + \alpha_C - 2\alpha_B)^2]^{1/2} \tag{2}$$

Here, α_M, α_C, and α_B are the thermal expansion coefficients of the metal, ceramic and braze, respectively. T_s is the solidus temperature of the braze. T is the temperature of interest, t is the braze thickness and r is the radial distance from the centroid of the braze area on the braze plane. ϵ^{EA} is the elastic accommodation strain between the ceramic and metal. ϵ_e is the braze rupture strain.

This criterion was derived from the assumption that the braze plastic deformation is, locally, simple shear. However, detailed analysis shows that shear localization occurs in the braze. The shear localization changes its pattern, depending on the geometry of the braze edge. Different patterns of shear localization alter the stress distribution near the braze edge. A typical shear localization is illustrated by the slip line field near the braze edge in Figure 1. As shown in the figure, only 74% of the braze thickness undergoes plastic deformation. In addition, severe shear localization occurs along the slip line field. Figure 2 shows the deformation pattern of the braze. Figure 3 shows

the equivalent total plastic strain contour near the edge of the braze. As shown in these figures, strain localization occurs near the edge of the braze. This localization is likely to cause localized damage accumulation so that the β criterion requires an adjustment factor according to this analysis. Figure 4 shows the stress distribution at the interface near the edge. As shown, σ_{yy} (normal stress) and σ_{xx} (transverse stress) are highly concentrated near the edge, despite the plastic deformation of the braze. Therefore, the ceramic failure can be easily initiated near the edge of the braze. Figure 5 shows the amplitude of shear strain localization across the thickness of the braze. The finite element calculation of the elastic-plastic braze predicts the location of the localization very close to the prediction of slip line field of rigid plastic material. Figure 6 shows the strain distribution near the edge of the braze. Figure 7 shows the stress distribution near the edge of the braze. For the above analysis, ABAQUS general finite element code was employed. For better understanding of braze damage, a thermomechanical damage rule should be developed. Also, the damage accumulation should be calculated for general fatigue loading. An investigation on the effect of braze geometry and external loading for braze damage is in process.

B. Analysis of Ceramic Fracture (γ criterion)

As discussed in the previous section, stress concentration occurs near the edge of the braze. This stress concentration often is the cause of brittle failure of ceramic components. In order to prevent ceramic failure, the γ criterion was formulated, based on fracture mechanics:

$$\gamma_l \leq \gamma_t \leq 1 \tag{3}$$

where

$$\gamma_t \equiv \frac{4t\tau_o^2 g_l f_l}{K_{IC}^2} \tag{4}$$

$$\gamma_l \equiv \frac{4l\tau_o^2 g_l^2}{K_{IC}^2}$$

Here, τ_o is the shear yield stress of the braze. K_{IC} is the fracture toughness of the ceramic, l is the initial flaw size, t is the thickness of the braze. g_l and f_l are functions of the angle (θ) between the braze plane and the crack initiated near the edge of the braze. These functions must be determined by analytic methods.

This criteria can also be written in the form:

$$\frac{lg_l}{f_l} < t < \frac{K_{IC}^2}{4\tau_o^2 g_l f_l} \tag{5}$$

As shown in this inequality, there is an acceptable range of braze thicknesses. Therefore, if $\frac{K_{IC}^2}{4\tau_o^2 g_l f_l} < \frac{lg_l}{f_l}$, brazing will cause fracture of the ceramic component for any thickness. Using a conservation integral, $f_l(\theta)$ has been obtained in closed form

$$f_l(\theta) = \cos\psi \sqrt{\frac{1}{\pi} - \frac{\sin^2\frac{\theta}{2}}{\theta + \sin\theta} - \frac{\cos^2\frac{\theta}{2}}{\theta - \sin\theta}} \tag{6}$$

where $\tan\psi = K_{II}^P/K_I^P$. Numerical methods such as the finite element method or the boundary integral method must be used to determine $f_{l(\theta)}$ and $g_l(\theta)$. This effort is in progress.

If the brazing geometry is finite but the ceramic component is large, then the energy release rate (or J integral) for the micro crack can be obtained from the conservation law of M integral. M integral is defined as $M = \int_\Gamma (Wn_i - t_j \frac{\delta u_j}{\delta x_i}) x_i ds$ where Γ is the contour of integration, W is the strain energy density, n_i is the component of normal vector to the contour Γ, t_j is the component of the traction vector, u_j is the component of displacement vector, x_i is the component of position vector and s is the arc length along the contour Γ

If we consider a crack initiating near the edge of the braze, it can be schematically illustrated as shown in Figure 8. In the figure, l indicates the crack length, 2L is the braze size and P is the concentrated force equivalent to $\tau_o t$ where τ_o is the shear flow stress of the braze. Then the conservation of M integral states that

$$\Sigma M = Jl - \frac{(1-\nu^2)P^2}{E}\left\{\frac{\sin^2\theta/2}{\theta+\sin\theta} + \frac{\cos^2\theta/2}{\theta-\sin\theta}\right\}$$

$$- \frac{3(1-\nu^2)P^2}{\pi E} + J_B x_B + J_C x_C + J_D x_D$$

$$- \int_0^L \tau_o \frac{\delta u}{\delta x}\, x\, dx + \int_L^{2L} \tau_o \frac{\delta u}{\delta x}\, x\, dx = 0$$

$$Jl = \frac{(1-\nu^2)P^2}{E}\left\{\frac{\sin^2\theta/2}{\theta+\sin\theta} + \frac{\cos^2\theta/2}{\theta-\sin\theta}\right\}$$

$$+ \frac{3(1-\nu^2)P^2}{\pi E} - P(\omega_B x_B + \omega_C x_C - \omega_D x_D)$$

$$- 2\tau_o L(u_D - u_o) - \tau_o \int_0^L u dx + \int_L^{2L} u dx$$

where u is the displacement and ω is the rigid body rotation of the material point. Although the expression given above shows physical meanings clearly, the calculation of the exact J requires the full solution of the boundary value problem. This is because of u and ω involved in the above equation.

C. Analysis of Axi-Symmetric Task II-Type Specimens

In order to apply the β and α criteria to joints planned for Task II, the mechanics of socket-joint brazing have been analyzed. The geometry of the joint includes the curvature of the braze surface so that it produces normal stress during the cooling process. This normal stress is believed to help in maintaining the high ductility of the braze during cooling. However, it also produces an unnecessarily high hydrostatic pressure in the ceramic component. Unlike ductile metals, ceramics are vulnerable to cracking caused by hydrostatic pressure if some microflaws are present. The hydrostatic pressure is a function of the thickness of the metal socket. In order to avoid ceramic cracking as a result of hydrostatic crushing, a thin metal socket is preferred. However, good joint stiffness requires thick sections. These two considerations must be analyzed to find the optimum thickness of the metal. The addition of an interlayer that has intermediate thermal expansion coefficient must be included to improve the strength of the joint.

Figure 9 shows the geometry of the socket joint which was analyzed; the boundary condition and the FEM meshes are shown in Figure 10. All the components are treated as elastic-plastic with the appropriate elastic modulus and yield stress shown in Figure

9. The loading is 800°C temperature differential loading. Figure 11 shows the deformation of the meshes, and Figure 12 shows the distribution of equivalent plastic strain. Von Mises equivalent stress distribution is shown in Figure 13. Figure 14 and 15 show the stress distribution at the interface of braze and metal, and braze and ceramic. As expected, plastic strain is concentrated near the braze edge, which could be reduced by making the metal end have a taper. Von Mises equivalent stress contours show that a substantial amount of strain energy is stored in the ceramic component. A level of 5 or higher in the ceramic is taken as a large relative strain.

Future analysis will address the effect of geometric changes such as tapering the socket and the inclusion of interlayers on ceramic loading.

Materials System Development

In order to screen coating materials for brazing, a series of experiments were performed with some metal elements and compounds. The primary purpose of coating is to enhance bond strength and wettability of braze on ceramic substrates. Selection of candidate materials was based on the thermodynamic driving force and kinetic response. Data on standard free energy changes of the reactions was obtained from the JANAF table.

The work on braze alloy development has been divided between the bulk alloys and coatings screening. In order to be of interest, the filler material must meet the following requirements.

1. The alloy must wet the ceramic, but not necessarily have to flow.

2. Melting temperature should be from 950°C to 1100°C for the 650°C application.

3. The alloying element should be selected from material with low vapor pressure at brazing temperature.

4. The alloy must resist oxidation up to 1000 hours at 650°C in air.

5. The alloy must be capable of forming slight fillet between ceramic-metal joint.

6. The alloy must be sufficiently ductile, and be capable of some plastic flow at elevated temperatures, but meet the mechanical stress requirement at application temperature of 650°C.

Al-995 alumina, 1-1/4″ x 1-1/4″ thick with ground face and refired at 1600°C to heal grinding damage, was selected as a substrate in these tests. The metal member will be Kovar strip, 10 mil thick by 0.250″ wide by 3″ long in annealed condition.

The filler metal will be an alloy of mainly gold with minimum quantity of reactive metal selected from Ti, Zr, V, Nb, Ta, etc. To adjust the melting point, a third and possibly fourth element will be selected from Pd, Ni, Co, Cu, In, Sn, Si, Ga, B, etc. The experimental alloys were prepared by weighing 5 gram samples to 0.01 accuracy, and melting in a skull melter under Argon atmosphere. The buttons were remelted about 4 times by turning over to homogenize.

Preliminary examination of various alloy systems was evaluated and are listed below:

Au-Ti
Au-Cu-Ti
Au-In-Ti
Au-Ni-Ti
Au-Si-Ti
Au-Ni-Si-Ti
Au-Ni-Sn-Ti

59 alloys were prepared as 5-gram buttons
56 alloys were melted on alumina for wettability tests
59 alloys were tested for ductility by rolling
48 DTA's were carried out mostly on ductile alloys
43 alloys studied were based on the most favorable Au-Ni-Si-Ti alloy compositions. The liquidus is about 1025°C, and the solidus is about 950°C of the alloys in the desirable composition range.

Evaluation of gold-rich brazes in the Au-Ni-Ti, Au-Ni-Si-Ti, and Au-Cu-Pd-Ti systems were conducted. Test showed that the above alloys wet alumina well; however, some dewetting was noted when high brazing temperatures were used. The hardening effect of 1 wt. % titanium is very pronounced. The effect of titanium on the melting temperature of the alloy is slight. Nickel has a hardening effect on the alloy, but much less than titanium (by wt. percent). The addition of nickel decreases the melting temperature. The addition of Si decreases the contact angle and assists wetting of the ceramic. The melting temperature is very slightly affected by the addition of 1 wt. % silicon.

Coatings to be applied to ceramic surfaces must promote wetting of the ceramic by the braze in order to be useful. Wetting behavior was studied using the sessile drop method with a video camera recording the drop shape for contact angle measurements. Coatings investigated included Hf, Ta, Ti, and Zr. Substrate materials were SNW1000 silicon nitride and SiC. The results of the wetting tests on SNW1000 are given in Figure 16. Hf, Ti, and Zr performed comparably, reaching a contact angle of about 0 degrees in over 200 seconds. Ta exhibited wetting behavior of 20° at the end of the test. On SiC (Figure 17), Ti coatings reached a 0 degree contact angle in 60 seconds. The other coatings

showed contact angles of about 15 degrees, with Nioro at the termination of the test. In terms of wetting behavior, the coatings were roughly comparable. Choices between these must therefore be based on other considerations such as mechanical properties and chemical interactions at the interface.

As a part of the coating materials screening portion of the program, the effect of coating materials (Ti, Zr, Hf and Ta) on the mechanical properties of ceramic materials was investigated using MOR (Modulus of Rupture) tests. One side of the MOR bar surfaces, to be under tension, was polished to 3 μm optical grade and coated with one of the candidate coating materials (Figure 18). Coating was done by e-beam evaporator (K.H. Frederick Co.) at 300°C in 10^{-6} torr. vacuum. Final coating thickness obtained was in the range of 3 - 6 μm. Coated MOR bars were exposed to 940°C for 3 - 4 min. (a brazing cycle) and tested at R.T. with a 4-point bend. As shown in Figure 19, Ti coating resulted in a noticeable drop in MOR strength of SNW1000 after the coated MOR bars were exposed to 940°c for 3 - 4 min. in vacuum. Since the MOR strength of SNW1000, which was treated at 940°C for 4 hours in vacuum, is equivalent to or slightly better than that of as-polished SNW1000, the strength drop is attributed to the existence of "reactive" coating materials, rather than to the thermal cycle. Results from separate experiments support this conclusion, in that nonreactive coating like Ni coating improved the MOR strength of SNW1000 significantly. This result also ruled out the thermal expansion mismatch between metal coating and ceramic as a possible cause of the damage ($\alpha_{Ti} < \alpha_{Ni}$). In order to isolate the effect of the oxide formation (TiO_2 or ZrO_2) on the mechanical property of ceramic, the same experiments were carried out with samples which had Ni coating on the top of Ti coating. It was found that (Ti,Ni) coating also reduced the MOR strength significantly compared with as-polished SNW1000. This implies that the reduction in MOR strength is not directly related to the presence of oxides. Figure 19 shows that the property levels from Ta-coated SNW1000 are not significantly better than those of Ti-coated SNW1000. Tantalum also showed poor adhesion on 3-μm polished SNW1000, while reasonable adhesion was obtained from a 9-μm polished surface. This was attributed to the high melting point of Ta (3020°C) and to relatively cool substrate (300°C) during coating. The scanning electron microscope was used to study the reaction products between Ta and SNW1000. Figure 20(a-b) shows that the Ta coating has cracked and spalled off without bonding. The bright area in Figure 20-c was always associated with cracks. It appears that Ta started reacting with the bulk ceramic, resulting in the bright phase. The reaction stopped due to buckling and subsequent cracking of the coating layer. Light polishing or scraping of the ceramic surface with a sharp object did not remove the bright phase. Figure 21 shows the element maps using wavelength dispersive equipment, revealing clearly that the bright phase is a reaction product of Ta (i.e., TaN). This indicates that the change in MOR strength of coated samples is closely related to the reaction, which is thermodynamically driven with a moderate kinetic rate at a 940°C brazing temperature. Continued studies with other reactive coatings are needed to understand the effect of coating on properties.

Work was initiated to characterize the behavior of combinations of materials in the candidate system through the use of shear testing of rectangular brazed coupon specimens as shown in Figure 22. In this fashion, it will be possible to observe the effect on properties of the structures generated in dissimilar material brazing.

Various ceramic-metal joints were prepared and tested to evaluate the strength of the joints. All substrate materials were polished to a 3 μm finish, and the polished surfaces of SNW1000 were coated with one of the coating materials to promote the wetting of braze alloy. Joints were brazed with Nioro (Au-18% Ni) at 980°C for 10 min. and subjected to testing using the shear fixture reported previously. For consistency of the testing, the same joint area, i.e., 0.15 in^2, was employeo throughout the test. Failure loads were recorded when the drop in load was noted to avoid inflated strength values due to scraping during shear tests. Most of the strength values are an average of two or three tests.

As shown in Table 1, three different systems were examined, i.e., Incoloy 909-SNW1000, Mo-SNW1000 and SNW1000-SNW1000. As expected, the strength of joints decreases as the mismatch in thermal expansion coefficient increases. Incoloy 909 is a known Fe-based superalloy with a low thermal expansion coefficient (α = 8-10 x 10^{-6}/C, up to 650°C). However, the difference in α between SNW1000 and Incoloy 909 is large enough to crack the ceramic surface after a brazing cycle; α of SNW1000 is 2.0 - 4.0 x 10^{-6} in the temperature range of 25 - 1000°C. The Incoloy 909-SNW1000 system with Zr coating was less sensitive to cracking after a brazing run compared to the same system with other coating materials. Failure (or crack path) of this system is almost always associated with ceramic or "ceramic-metal interface." The failure at ceramic-metal interface is due to inadequate bonding, rather than to braze failure.

Table 1: Materials systems development
Rectangular Coupon Shear Test Data

System	Average Strength (ksi)	Number of Samples
Incoloy 909-Nioro-Hf-SNW1000	3.8	2
Incoloy 909-Nioro-Ti-SNW1000	0.7	1
Incoloy 909-Nioro-Zr-SNW1000	3.0	2
Mo-Nioro-Hf-SNW1000	7.7	3
Mo-Nioro-Ti-SNW1000	7.1	2
Mo-Nioro-Zr-SNW1000	11.5	3
SNW1000-Ta-Nioro-Ta-SNW1000	27.5	2
SNW1000-Ti-Nioro-Ti-SNW1000	42.3	2
SNW1000-Zr-Nioro-Zr-SNW1000	45.1	1

The Mo-SNW1000 system showed no signs of cracking or partial bonding after a brazing run. Pure molybdenum is often used as a buffer layer to prevent premature cracking of ceramic. The thermal expansion coefficient of pure molybdenum is 4.8 - 6.7 x 10^{-6} in the temperature range of 25 - 900°C. The strength level of the joint is 2 - 10 times higher than that of the Incoloy-SNW1000 system. it was interesting to note that the crack path developed in this system is associated not only with ceramic bulk, but with molybdenum substrate, indicating good compatibility of molybdenum with the ceramic substrate. Cracks were initiated at SNW1000 and diverted to the molybdenum substrate. This is due to the brittle nature of the molybdenum substrate.

The strength of the SNW1000-SNW1000 joint can be referenced to reveal the damage due to the α mismatch; the level of SNW-SNW joint strength implied that Incoloy 909-SNW1000 and Mo-SNW1000 joints retain residual stress, which can be represented by 30 - 45 ksi shear stress. Another significant finding from this study is that the joint strength level obtained from Zr coating is equivalent or better than that of Ti coating. This is consistent with the results seen from coating study with MOR bars. These experiments confirm the previous work with coated MOR bars in selecting Zr as a coating material for the wetting of Si_3N_4-based ceramic substrates. It is to be noted that the low strength of Ta-coated SNW1000-SNW1000 joints is primarily due to the poor adhesion of Ta (T_m of Ta = 3000°C) on SNW1000 substrate.

Status of Milestones

The program is on schedule.

Communications/Visits/Travel

Frequent discussions with Professor K-S. Kim, University of Illinois, on mechanics modeling. On 3/16/88, E.M. Dunn, S. Kang and H.J. Kim visited Oak Ridge National Laboratory to discuss progress to date and future plans with M.L. Santella of ORNL and the other subcontractors from Battelle and Norton.

Problems Encountered

None.

Publications

None.

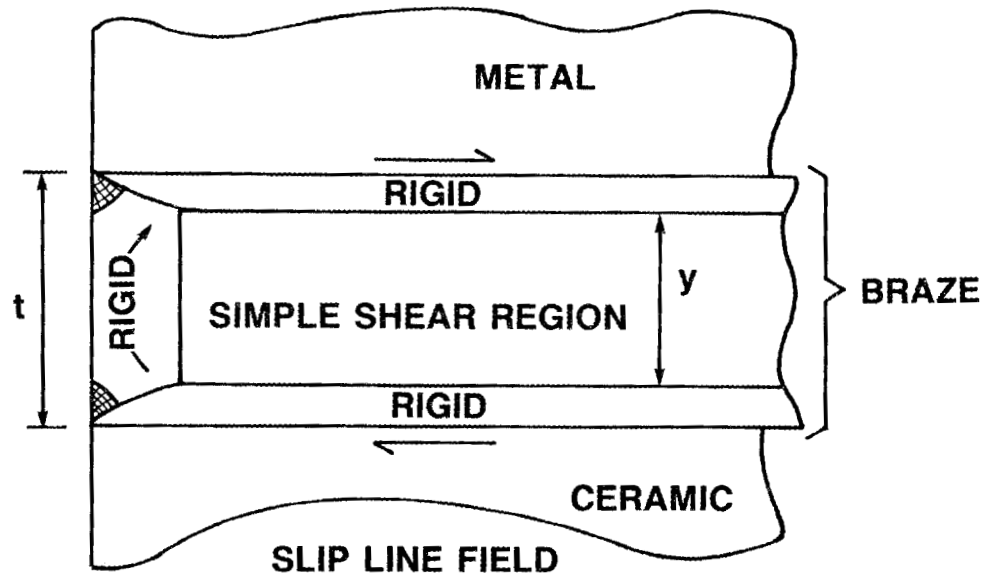

$y/t \sim 0.736$

Figure 1: Schematic illustrating shear localization near braze edge

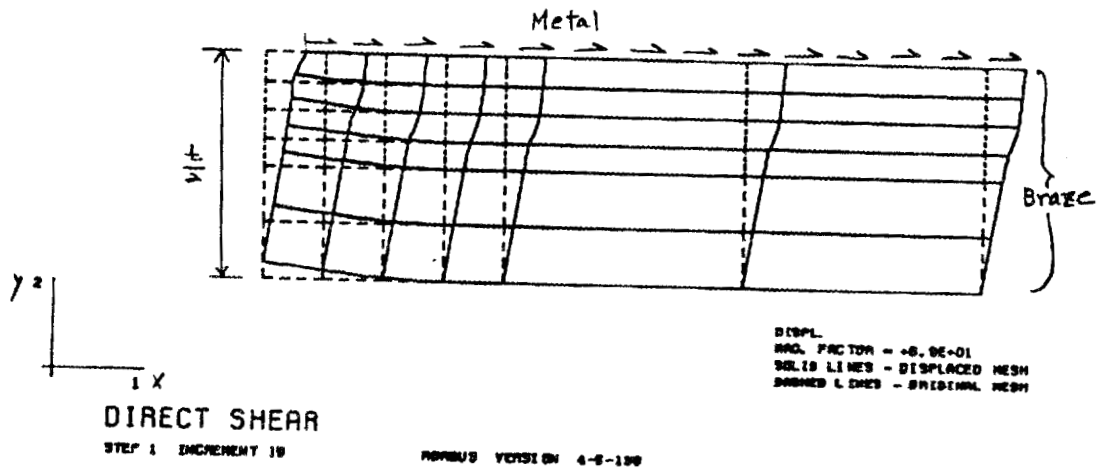

Figure 2: Deformation of braze (half of the thickness) near the braze edge

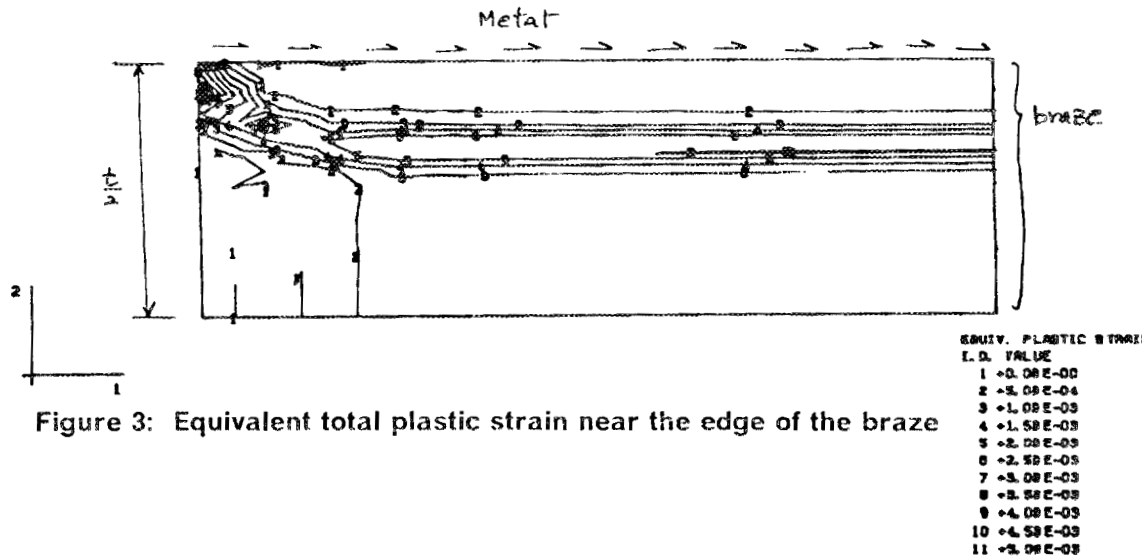

Figure 3: Equivalent total plastic strain near the edge of the braze

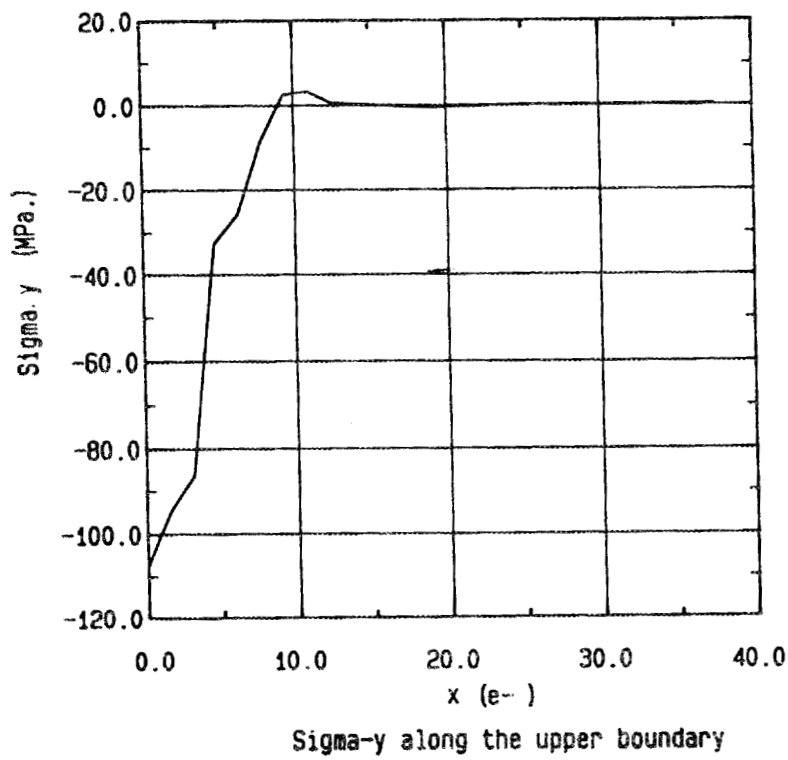

Figure 4: (a) σ_{yy} (normal stress) at the braze-metal interface

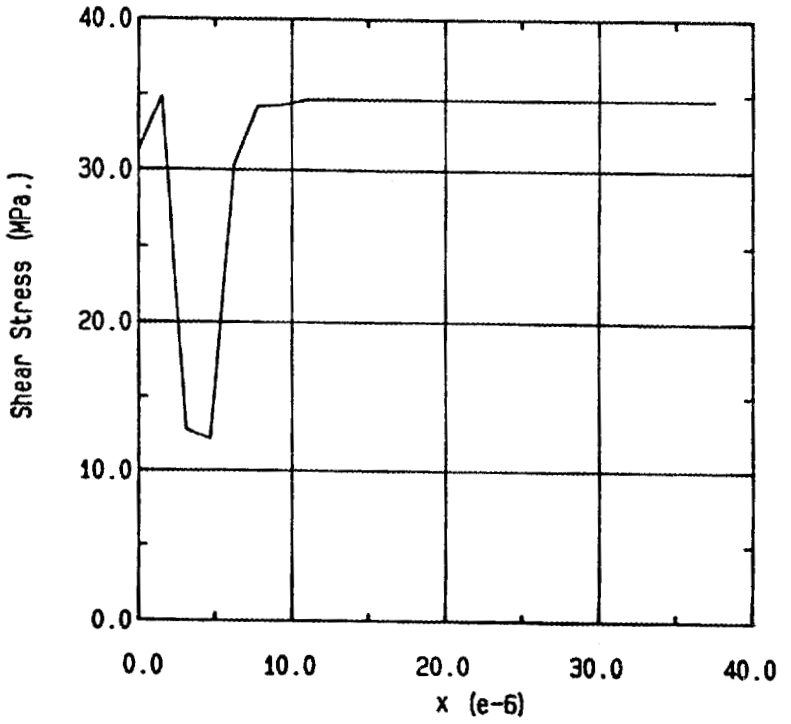

Figure 4: (b) Shear stress along the interface

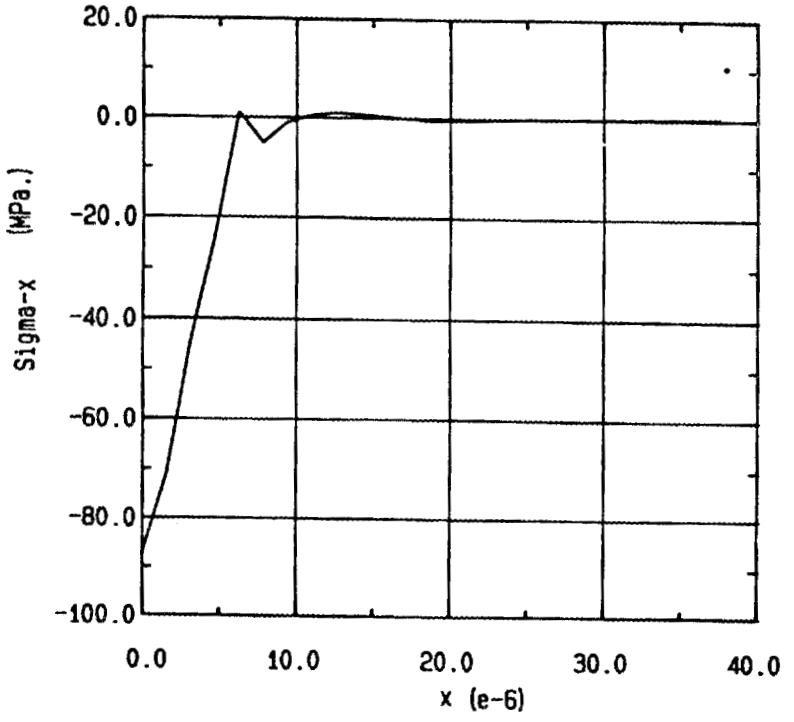

Figure 4: (c) Transverse stress σ_{xx} along the interface

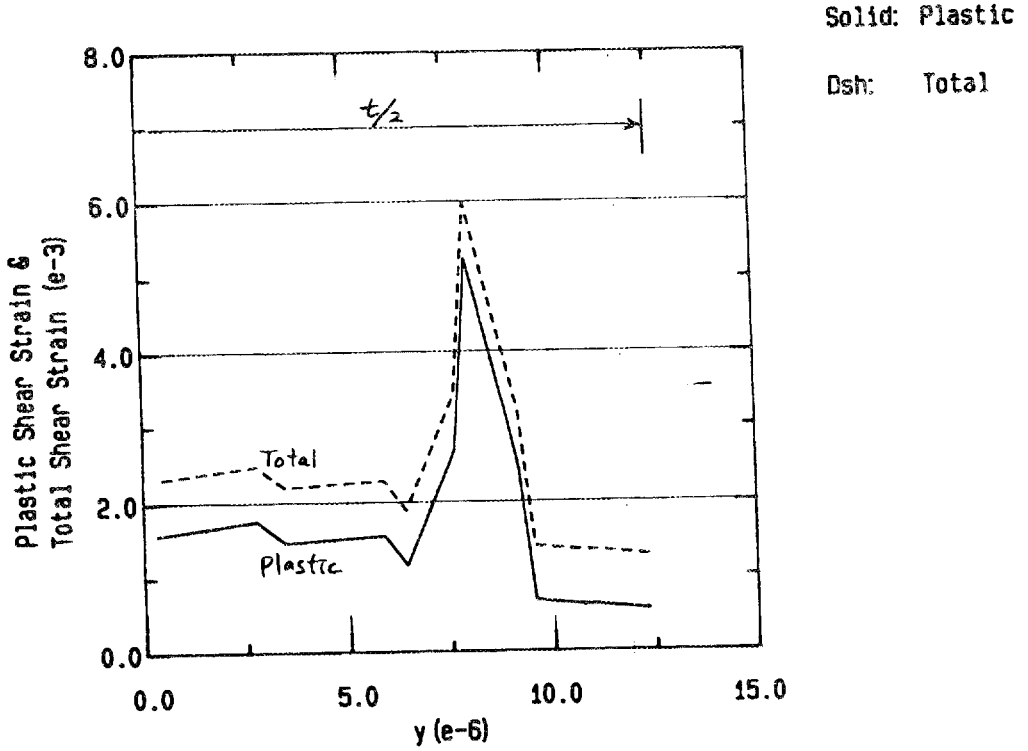

Figure 5: (a) Plastic shear strain & total shear strain at x - 18.75 e-6 m

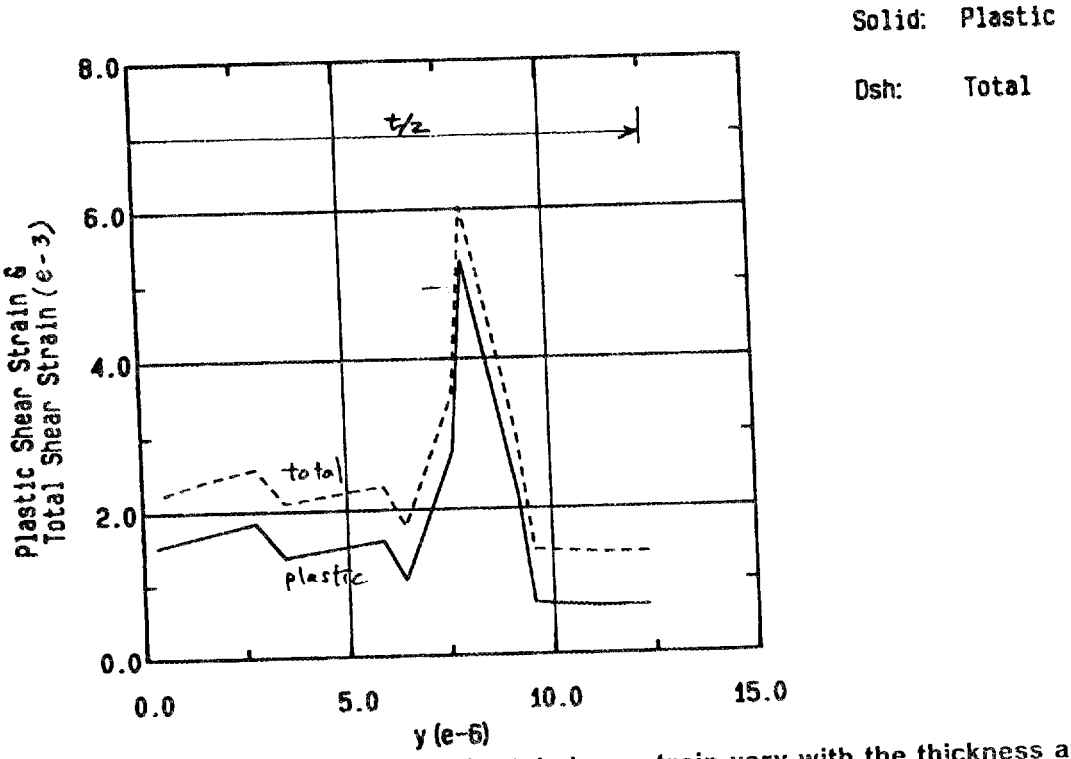

Figure 5:(b) Plastic shear strain and total shear strain vary with the thickness at x - 26 4088e-6

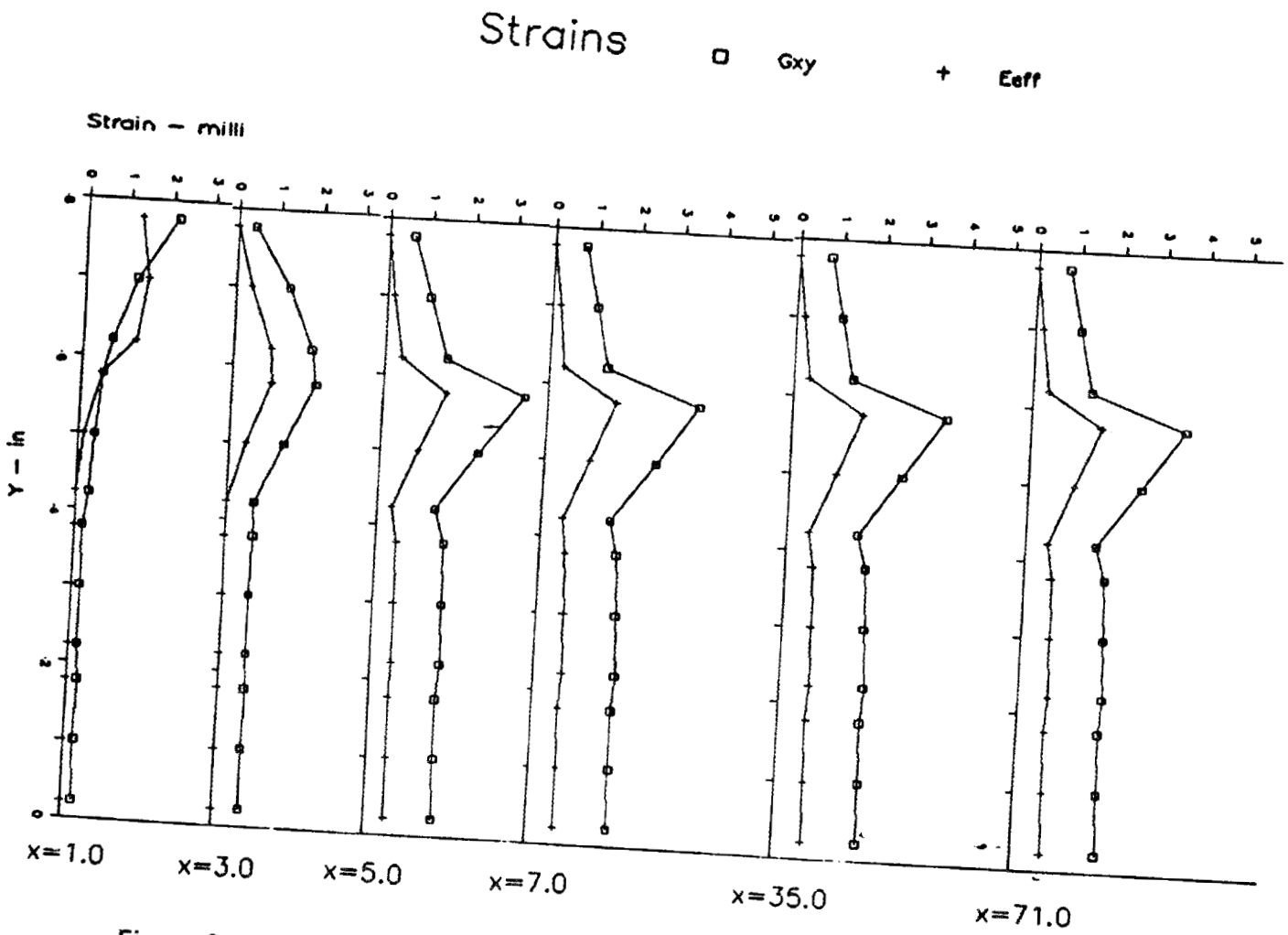

Figure 6: Shear strain and effective strain near the edge of the braze

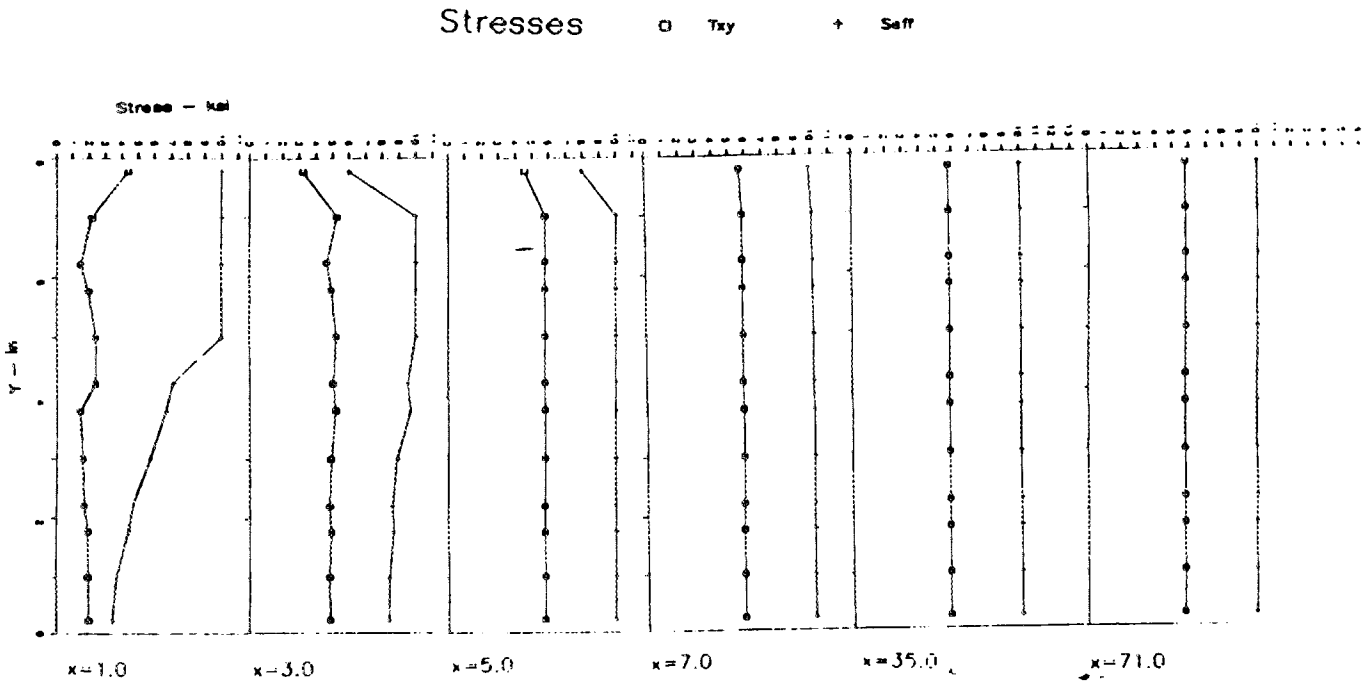

Figure 7: Shear stress and effective stress near the edge of the braze

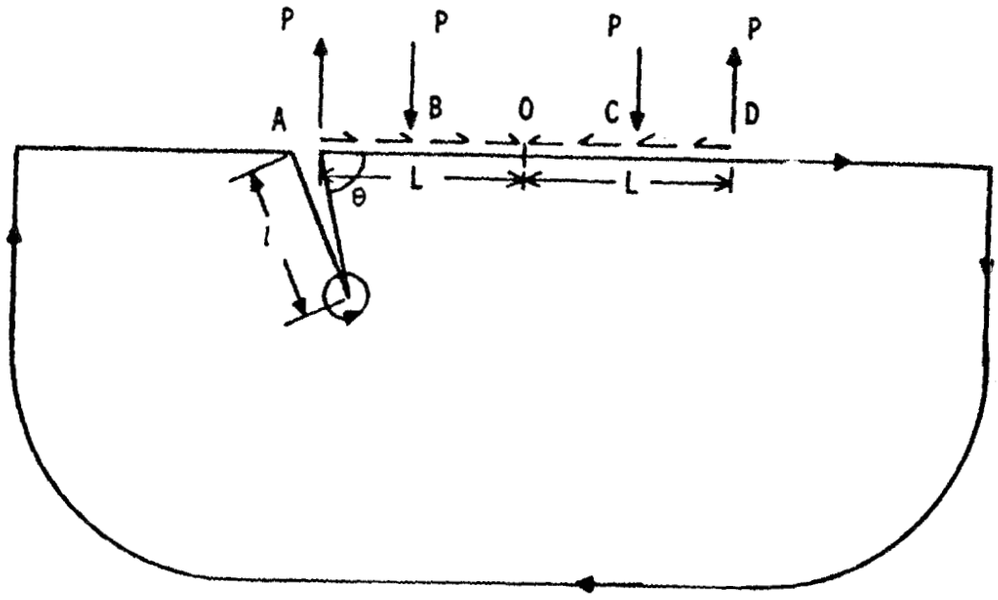

Figure 8: Schematic illustrating ceramic-metal interface of length 2L with a crack length of l

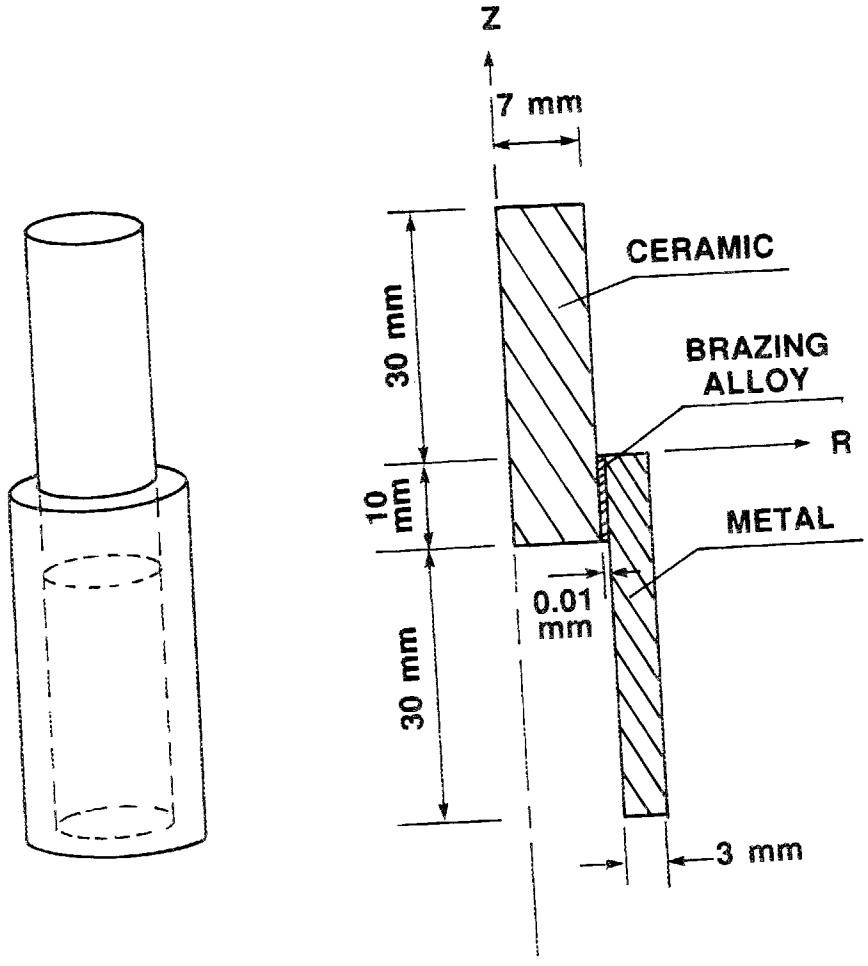

MATERIAL PROPERTIES

Metal:

$E = 210 \times 10^9$ Pa
$\nu = 0.29$
$\sigma_y = 400 \times 10^6$ Pa
$\alpha = 12 \times 10^{-6}$ Pa

Ceramic:

$E = 380 \times 10^9$ Pa
$\nu = 0$
$\alpha = 8 \times 10^{-6}$ Pa

Brazing alloy:

$E = 124 \times 10^9$ Pa
$\nu = 0.31$
$\sigma_y = 60 \times 10^6$ Pa
$\alpha = 19 \times 10^{-6}$ Pa

Figure 9: Geometry of socket joint of ceramic and metal using brazing method and material properties

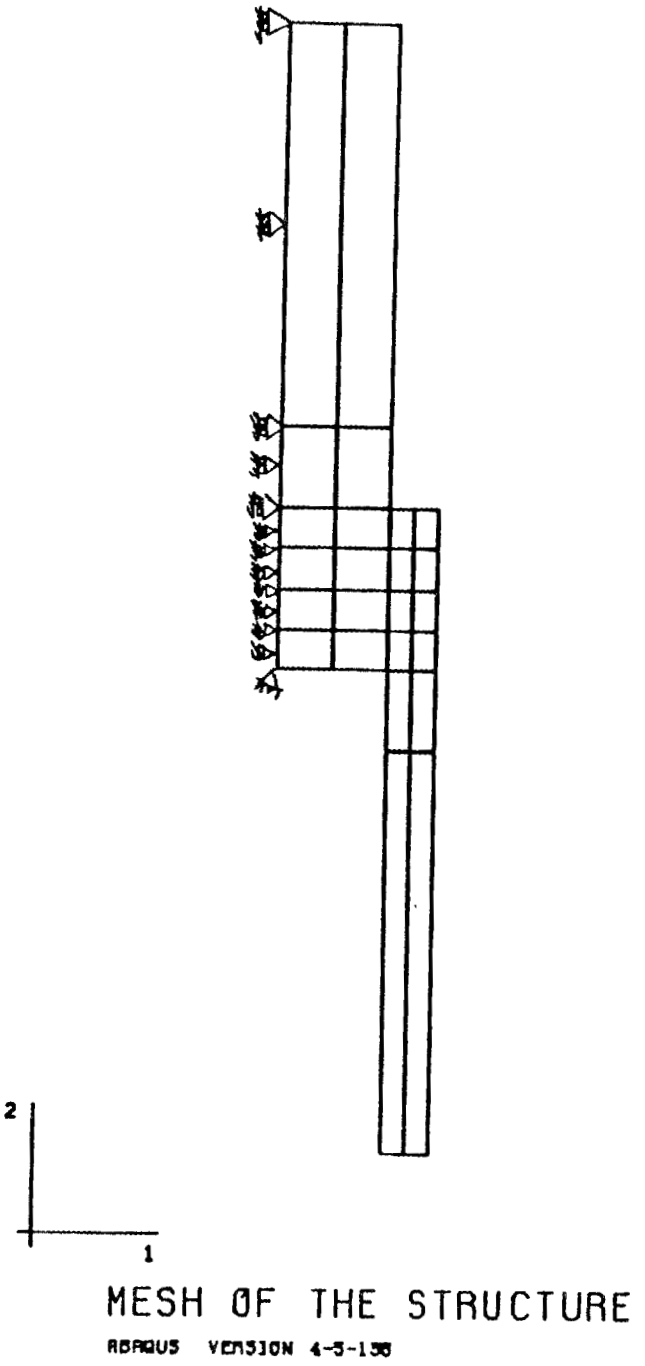

Figure 10: **Boundary conditions**
1 is R direction; 2 is Z direction

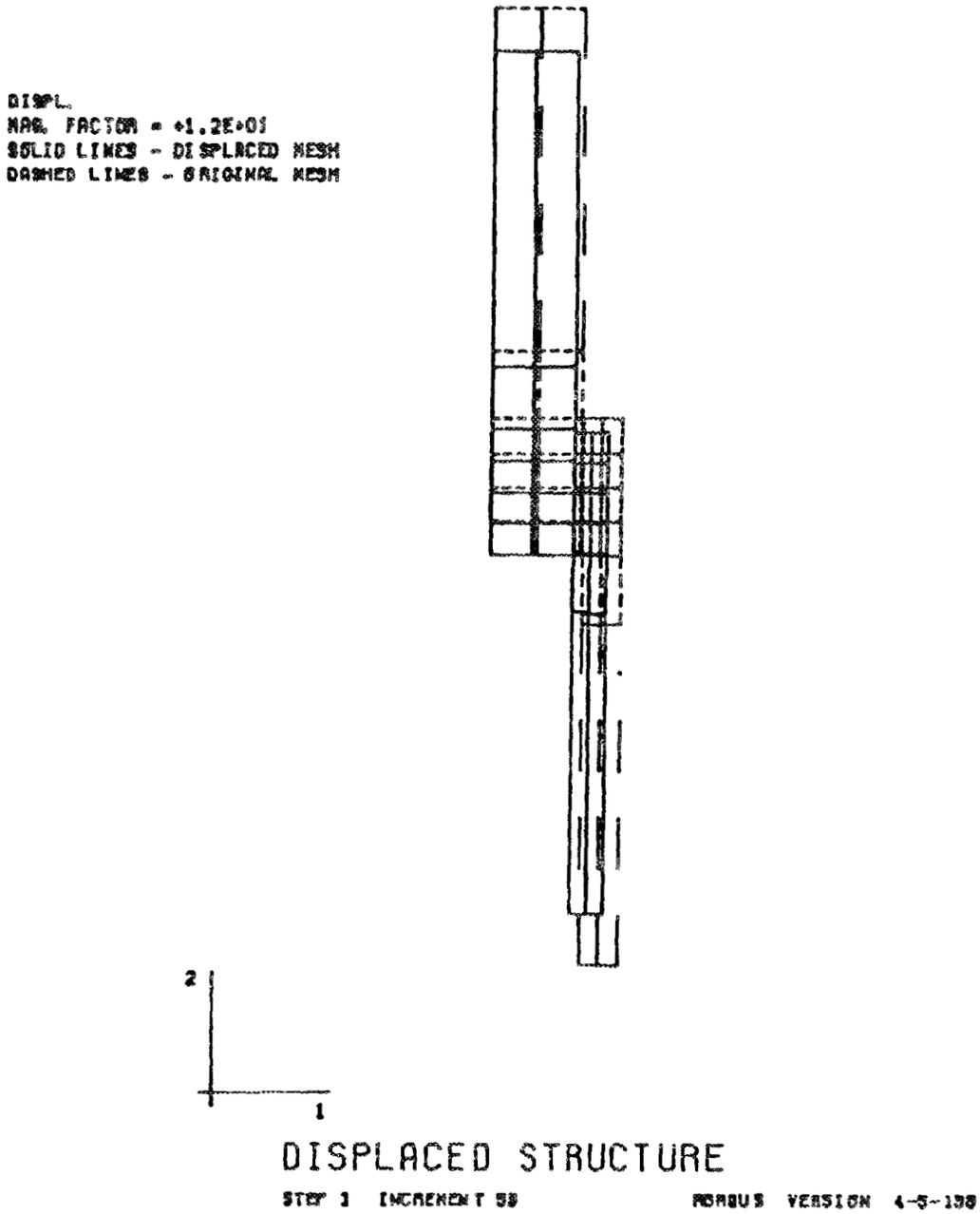

Figure 11: Deformation of the elements

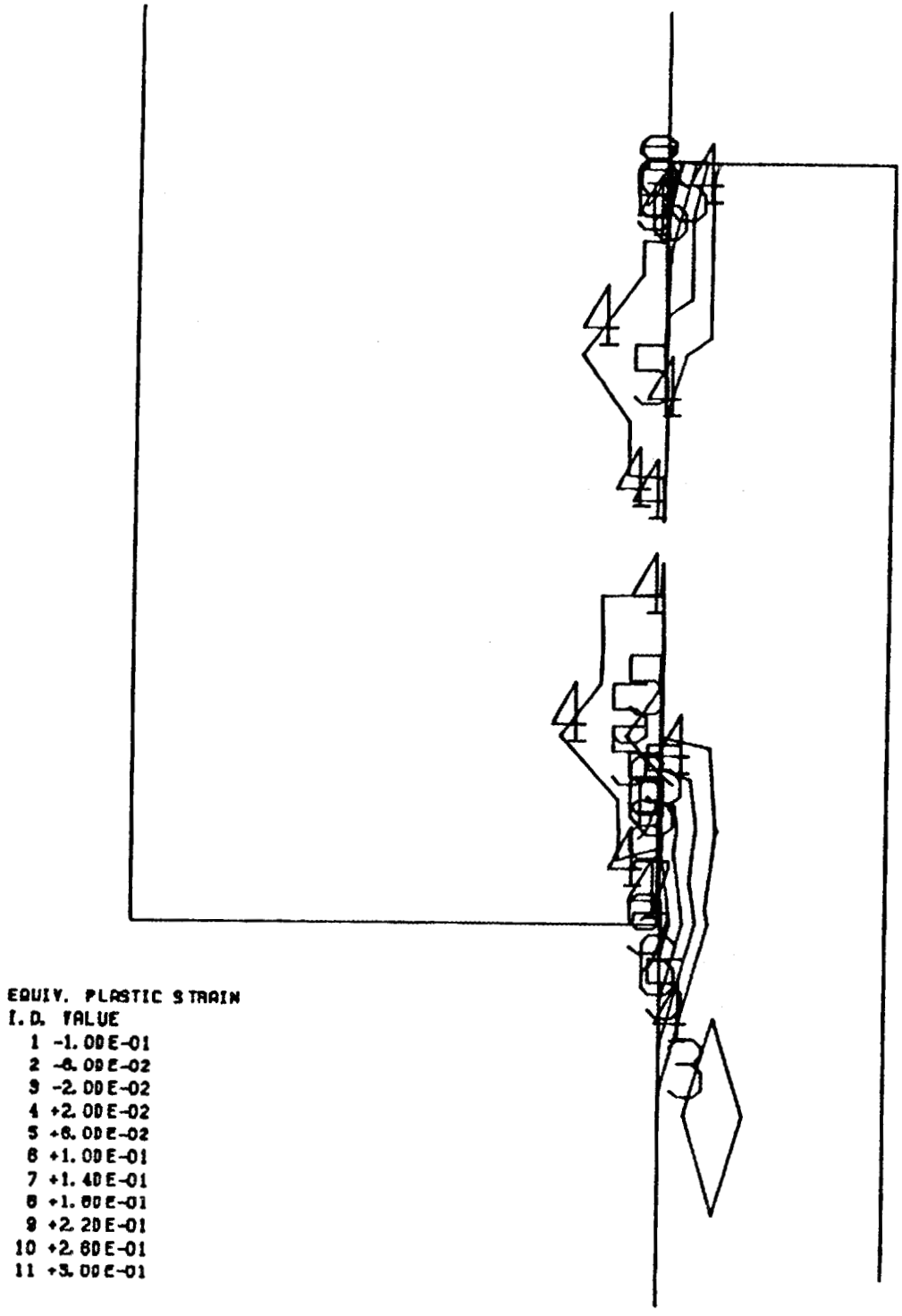

Figure 12: Plastic strain distribution

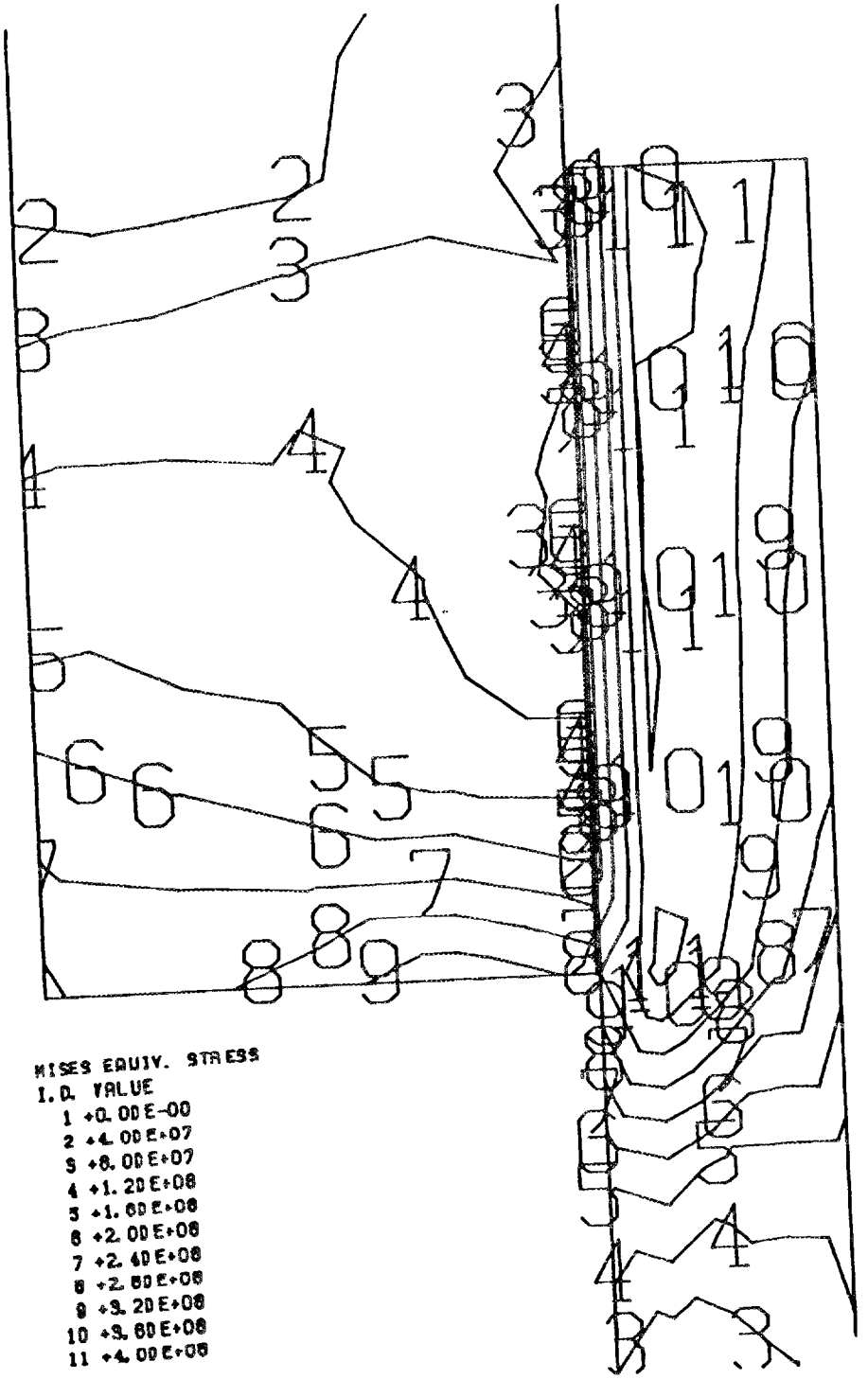

Figure 13: Enlarged view of the von Mises equivalent stress

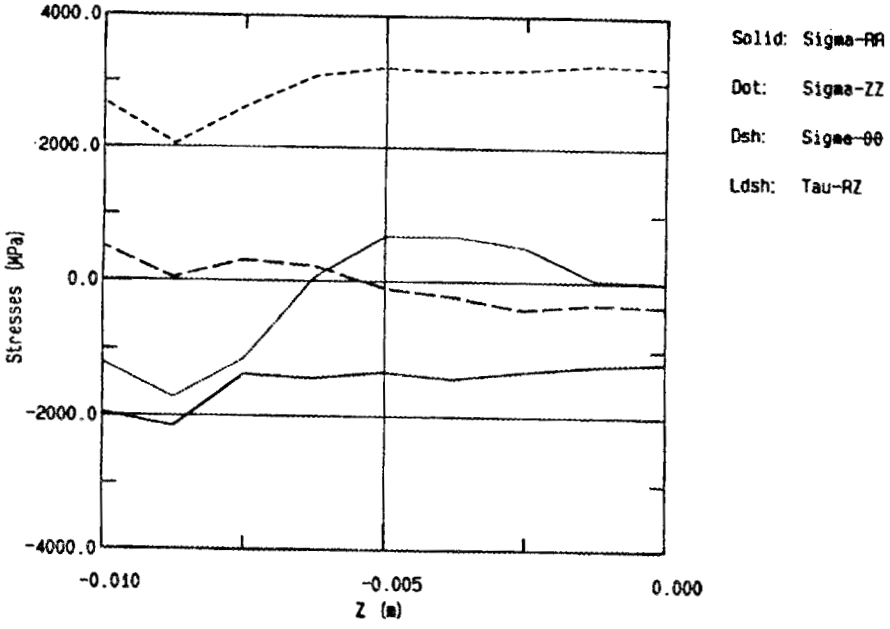

Figure 14: Stresses along the interface of the metal and brazing alloy, i.e., stresses vs Z

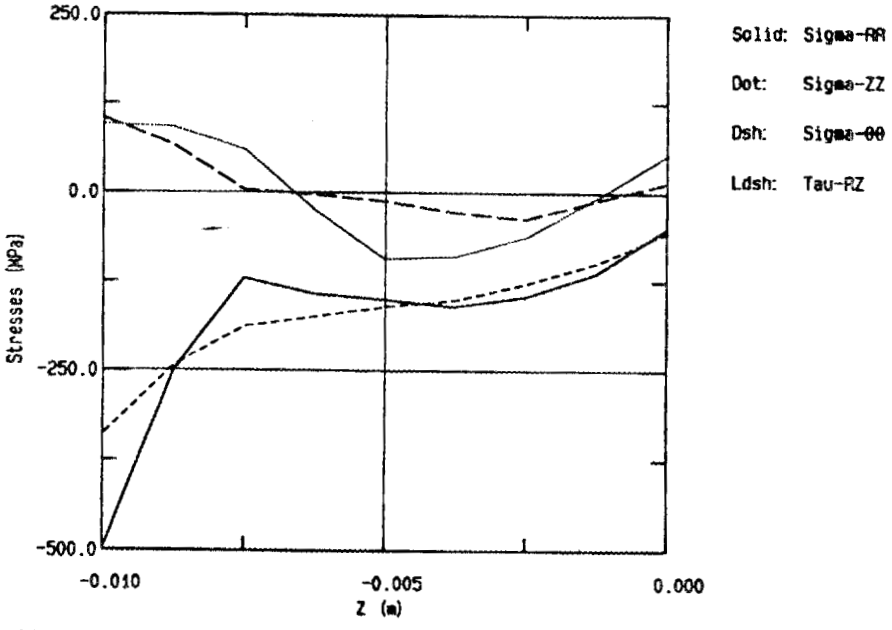

Figure 15: Stresses along the interface of the ceramic and brazing alloy, i.e., stresses vs Z

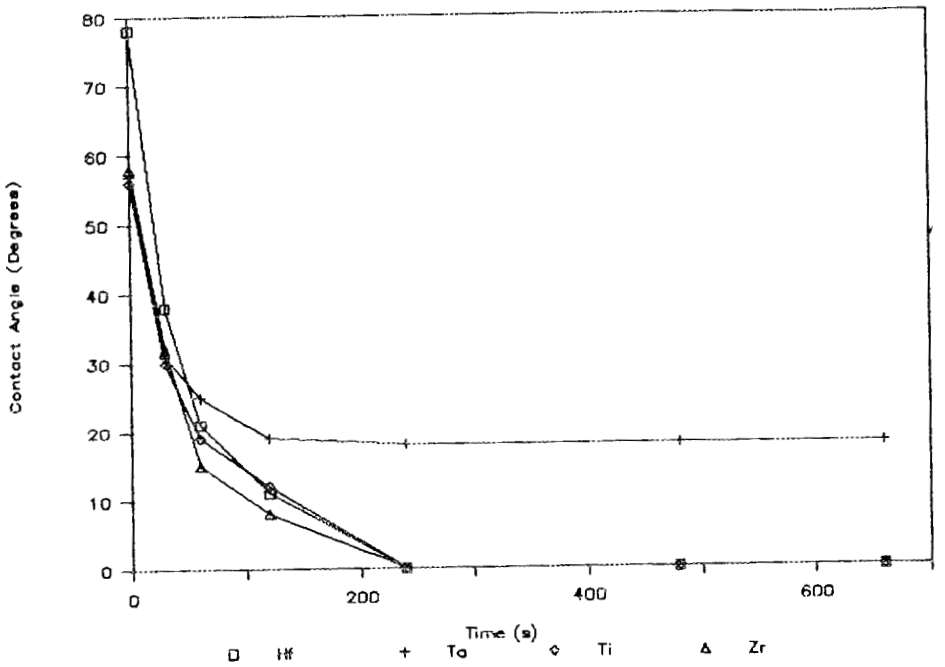

Figure 16: Contact angle vs time for Nioro braze on coated SNW1000

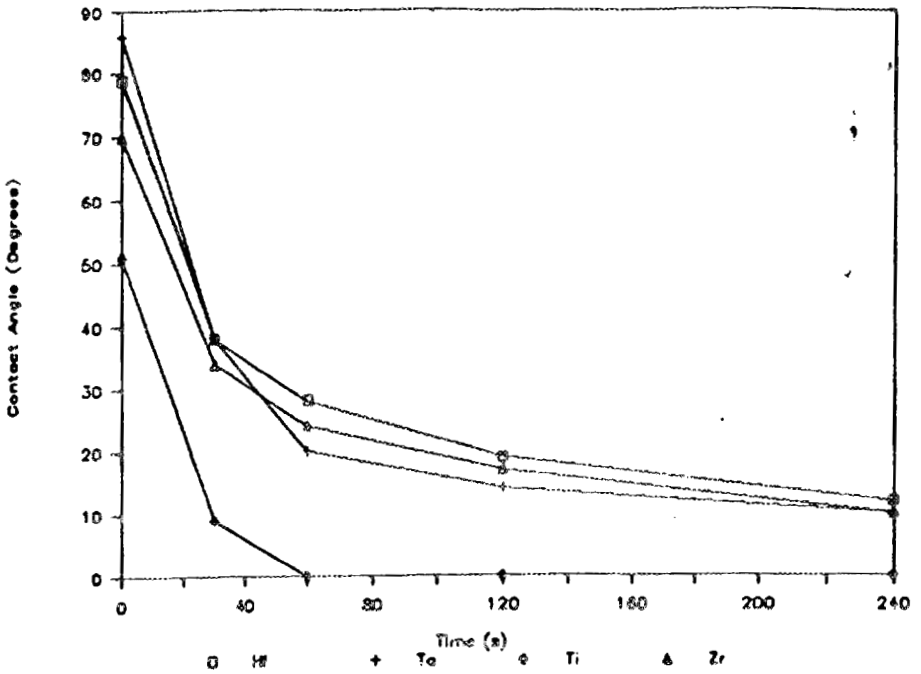

Figure 17: Contact angle vs time for Nioro braze on coated SiC

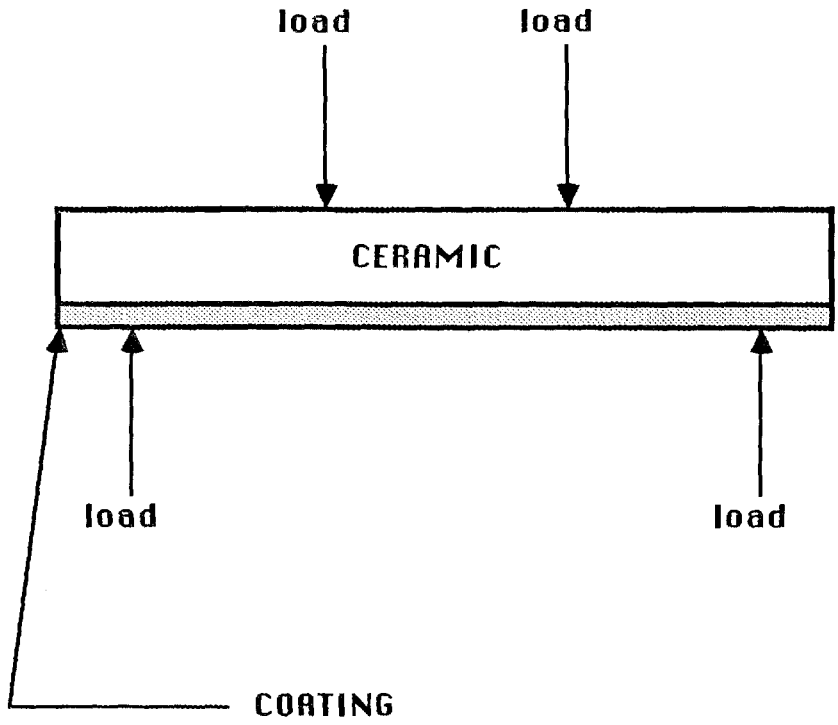

Figure 18: Schematic illustrating ceramic-coating interaction MOR test

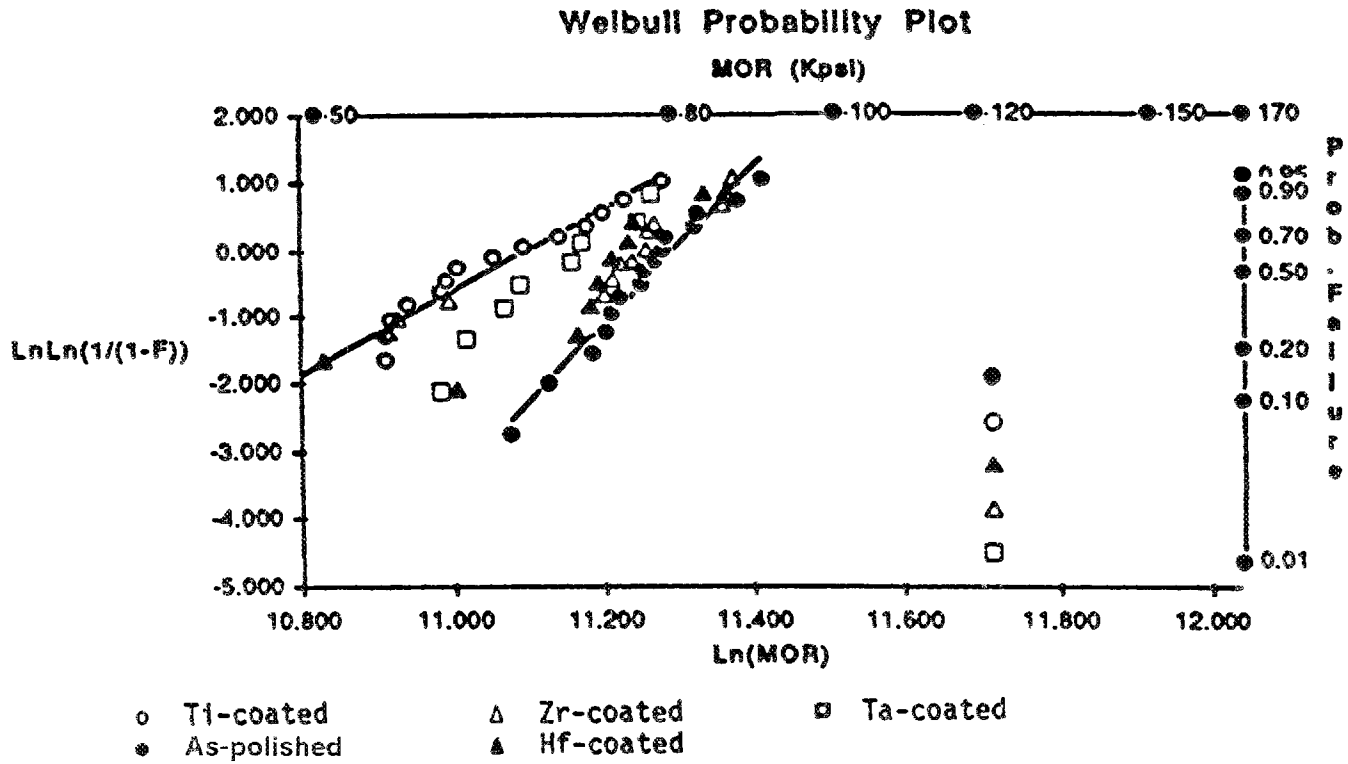

Figure 19: The effect of coating on the mechanical properties of SNW1000

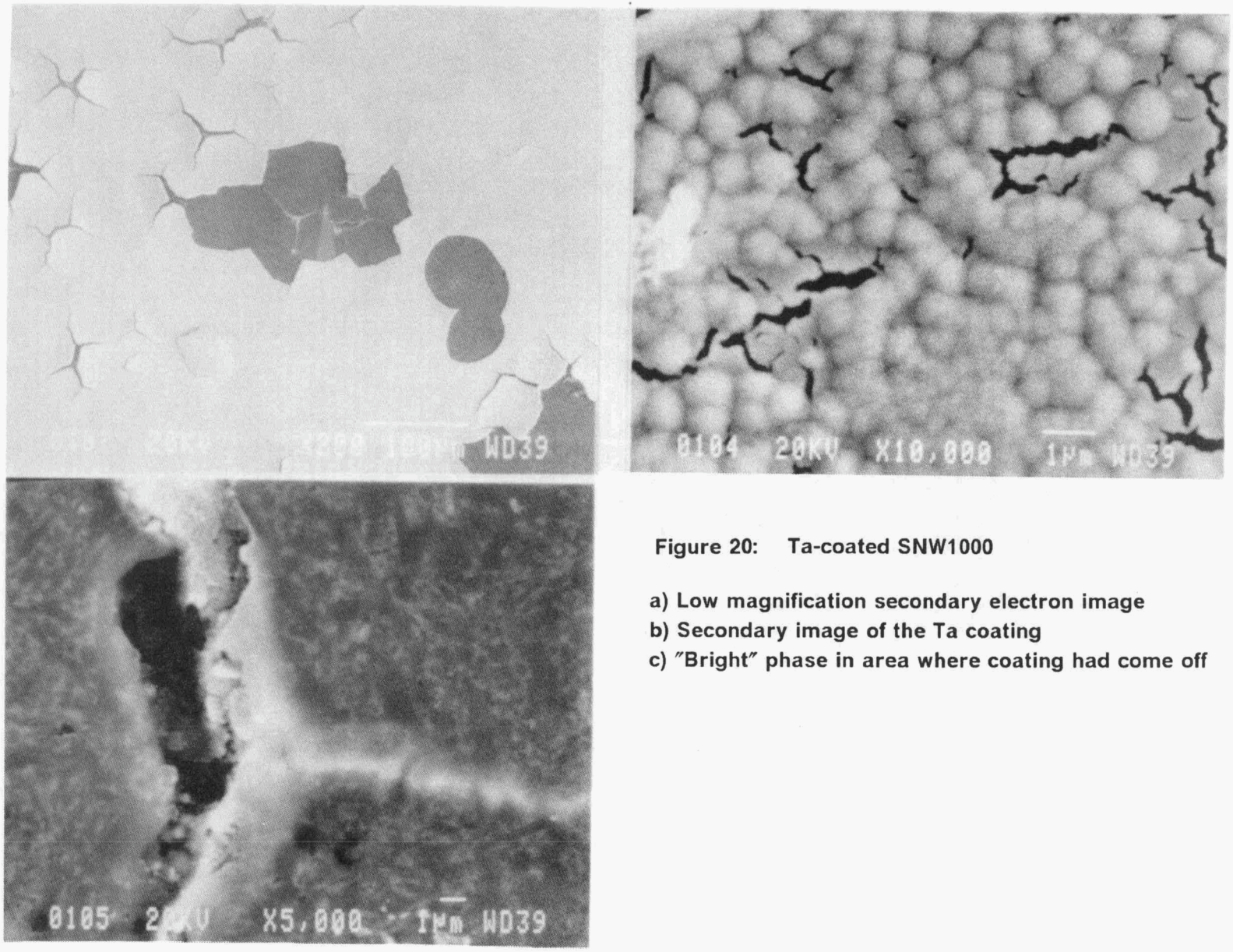

Figure 20: Ta-coated SNW1000

a) Low magnification secondary electron image
b) Secondary image of the Ta coating
c) "Bright" phase in area where coating had come off

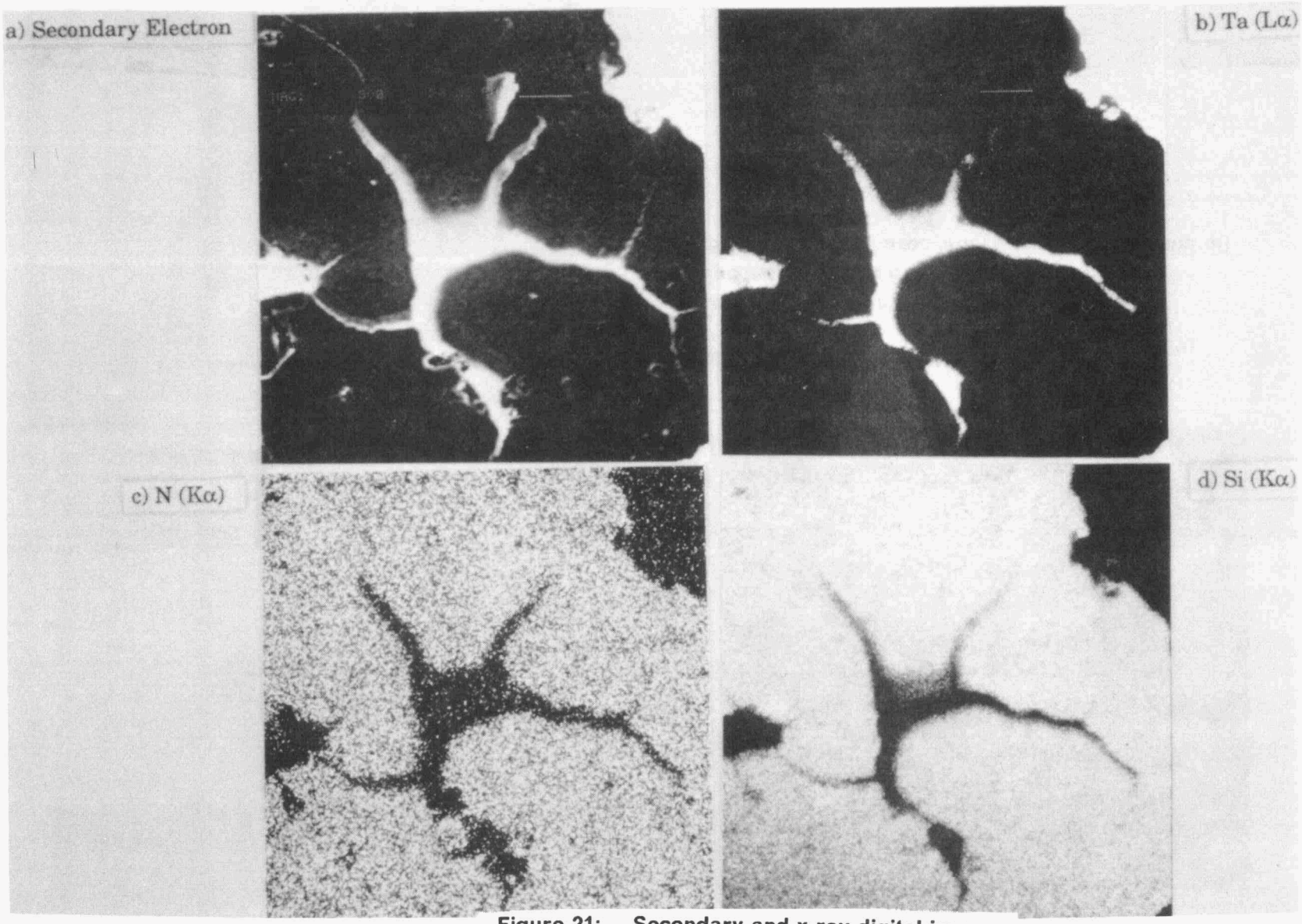

Figure 21: Secondary and x-ray digital images

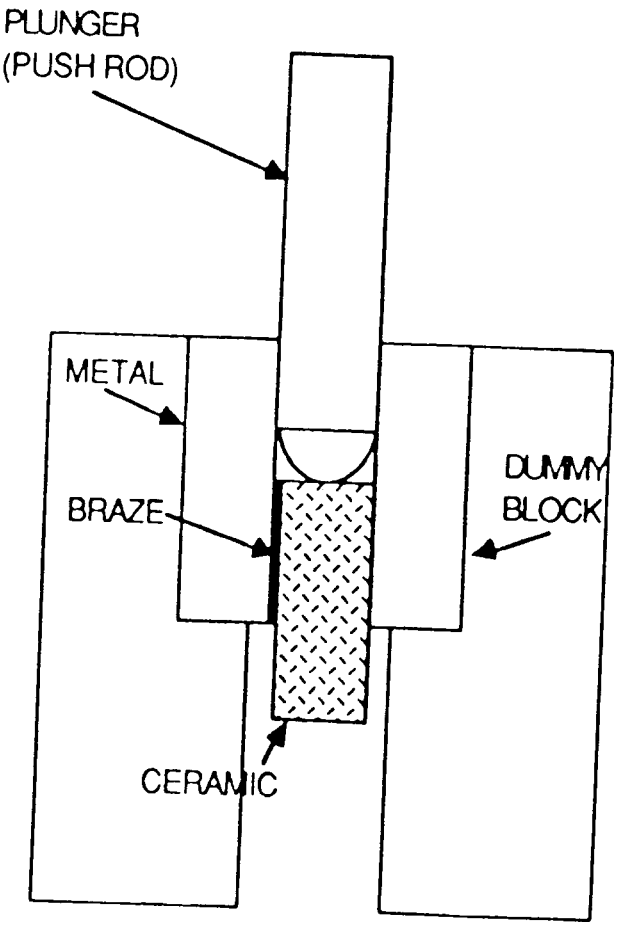

Figure 22: **Schematic illustrating coupon sample, shear sample, and text fixture**

Analytical and Experimental Evaluation of Joining Ceramic Oxides to Ceramic Oxides and Ceramic Oxides to Metal for Advanced Heat Engine Applications

R. A. Schmidt, J. Ahmad, and A. Rosenfield
(Battelle Columbus Division)

Objective/Scope

The objective of this project is the development of the analytical tools necessary to design reliable, high strength ceramic oxide-to-ceramic oxide and ceramic oxide-to-metal joints. The technical work consists of analytical and experimental tasks.

The goal of the analytical work is a predictive model that can be used in engineering design of ceramic joints. This work consists of several subtasks involving residual stress modeling, deterministic stress and fracture mechanics modeling, engineering design modeling, probablistic modeling, and model validation. Inputs to these models come from the experimental efforts.

The experimental work will involve the fabrication and testing of first, small scale, and later, scale-up sized joints to determine the mechanical behavior of these ceramic joints. Experiments will be performed to determine elastic constants and stress-strain curves as a function of temperature, tensile strength, shear strength, Mode I and Mode II fracture toughness, creep deformation, time dependent strength, and strength degradation from hot oxidizing gases and from thermo-mechanical cycles.

Technical Progress

1.0 Analytical Efforts

The main analytical and numerical effort in the present project involves detailed analyses of zirconia-to-zirconia and zirconia-to-nodular cast iron joint experiments. These experiments will involve specimens with known initial crack (debond) lengths. While preparations for these specimens are underway, the analysis effort has thus far been focused on (a) review of the literature on bimaterial interface cracks, and (b) preliminary finite element analyses to compute residual stress fields in bimaterial specimens without a crack. These are briefly discussed in the following.

For a crack along a bimaterial interface (see Figure 1), the stress and deformation fields close to the crack tip are remarkably different than for a crack in a monolithic material. For example, even under a remote stress σ^{∞}_{22} normal to the crack plane, the normal and shear stresses along the interface ($\theta = 0$) and close to the crack tip can be expressed as follows:

$$\sigma_{11} = \frac{K_I}{\sqrt{2\pi r}}\left[(\cos\beta - 2\alpha\sin\beta)\ \frac{3e^{-\alpha\pi} - e^{\alpha\pi}}{2\cosh\alpha\pi}\right] \qquad (1)$$

$$\sigma_{22} = \frac{K_I}{\sqrt{2\pi r}} (\cos\beta - 2\alpha\sin\beta) \tag{2}$$

$$\sigma_{22} = \frac{K_I}{\sqrt{2\pi r}} (\sin\beta + 2\alpha\cos\beta) \tag{3}$$

$$\beta = \alpha \ln(r/2a)$$

$$\alpha = \frac{1}{2\pi} \ln[(\lambda_A/\mu_A + 1/\mu_B)/(\lambda_B/\mu_B + 1/\mu_A)]$$

where,

μ = shear modulus
ν = Poisson's ratio
λ = $3-4\nu$ for plane strain
$(3-\nu)/(1+\nu)$ for plane stress

and subscripts A and B indicate the two materials as shown in Figure 1. For the monolithic case, the bimaterial constant (α) is zero. Then, the terms within the brackets in Equations (1) and (2) become unity and the term within the brackets in Equation (3) becomes zero. Thus, one recovers the classical asymptotic stress fields for a crack in a monolithic material.

For $\alpha \neq 0$, there are two features of the stress field which are worth noting. First, the shear stress is singular. Therefore, even under opening mode loading, the crack tip experiences combined Mode I and Mode II. The second feature is the oscillatory nature of the stresses because of the parenthetical terms in Equations (1), (2), and (3). The oscillatory nature of crack tip stresses has been the subject of debate in the literature for over two decades. The present consensus seems to be that the oscillatory nature is an artifact of the use of linear elasticity theory.

Based on the literature review, it appears that an unambiguous and a practically useful fracture mechanics approach to the interface crack problem may be possible by using the combined mode energy release rate as the crack tip characterizing parameter. Anticipating future consideration of crack-tip plasticity effects, we have decided to do so using the path independent integral J to determine the energy release rate. It has been demonstrated that J retains its path independent property for cracks along bimaterial interfaces. Thus, it provides a useful computational means to determine energy release rate.

Preliminary finite element analyses of bimaterial beam specimens have indicated high residual stresses normal to the bond line in a small region close to the specimen edge. The finite element mesh used

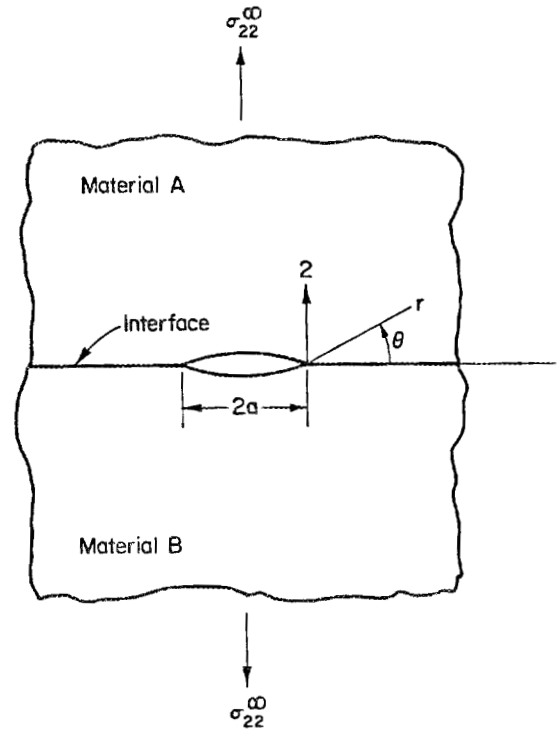

FIGURE 1. CRACK AT THE INTERFACE OF TWO SEMI-INFINITE PLATES OF DIFFERENT MATERIALS

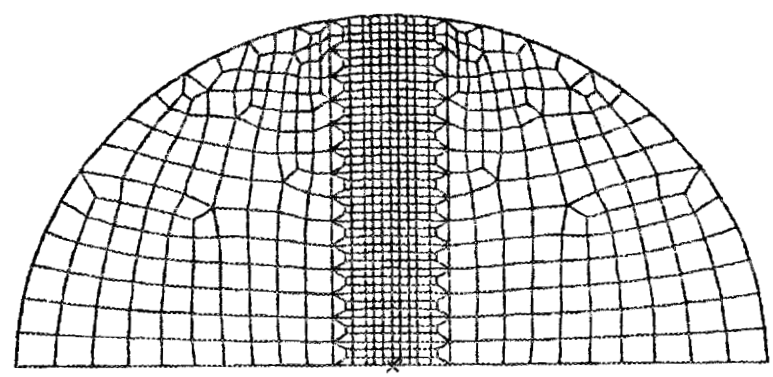

FIGURE 2. FINITE ELEMENT MESH OF THE BIMATERIAL DISK SPECIMEN WITHOUT A CRACK

in this preliminary assessment of the disk specimen is shown in Figure 2. For the center-crack disk to be used in the experiments, the residual stresses are not expected to have significant effect if the crack length is kept small compared to the disk diameter.

2.0 Experimental Efforts

The objective of this task is to design, fabricate, and test small-area ceramic oxide-to-ceramic oxide and ceramic oxide-to-metal joints. Statistically significant numbers of experimental-sized joints in which the interfacial area is a minimum of two-square centimeters will first be fabricated and both physical and mechanical properties needed for model inputs will be evaluated. This task will result in validated joining procedures and, in combination with analytical efforts, validated analysis procedures.

2.1 Joint Fabrication

2.1.1 Oxide/Oxide Joints. Initial experiments have been performed in joining partially stabilized zirconia (Corning Zycron L Mg-PSZ) billets (14.1 mm diameter) to each other using sol-gel derived Mg-PSZ as the interlayer. The best results so far have been achieved using the following method: a fine-grained sol-gel Mg-ZrO_2 powder was prepared by hydrolysis of a solution of magnesium methoxide and zirconium n-propoxide in methoxyethanol, followed by gelation, drying, and calcination at 800 C for four hours. The interlayer material was prepared by mixing the ZrO_2 powder with a similarly prepared sol-gel mixture (prior to gellation). The surfaces of the zirconia billets were roughened by sandblasting and etching with dilute hydrofluoric acid prior to application of the sol-gel interlayer. The sol-gel interlayer material was applied to both roughened faces of the zirconia billets, the sandwich was joined by heating the sandwich under a slight weight (300 grams) of alumina plates to a temperature of 1550 C. Successful joints have been fabricated by this technique, but the strengths of the joints need to be improved using more optimized joining heat treatment conditions (i.e., higher temperatures). Future experiments will address the effect of higher joining temperatures (1700 C) on the strength of the sol-gel zirconia/zirconia joints. An important reason for increasing the joining temperature is that performing the joining heat treatment below 1700 C can degrade the base PSZ material. It is hoped that simple sintering will be sufficient to achieve sufficient joint strengths, although the capability to hot press the zirconia billets in air to form the joint, if necessary, will be available within the next two months.

Controlled cooling from the joining temperature is crucial to obtaining optimum strength and toughness of Mg-PSZ. Since the Mg-PSZ billets will be essentially re-sintered during the joining process, a cooling cycle that does not totally degrade the Mg-PSZ will have to be developed. The manufacturer has suggested cooling from the sintering temperature (1700 C) at a rate of 200 C/hour and holding at some

temperature between 1000 and 1100 C before continuing the cool-down cycle.

The 50.8-mm diameter by 19-mm length zirconia billets for the final joining experiments have been received recently. One of these billets will be cut into bend-test and fracture toughness specimens. These specimens will be given various heat-treatments at 1700 C, followed by cooling at 200 C/hour and two-hour holds at various temperatures between 1000 and 1100 C. Mechanical property measurements will be performed, and the best (but not optimum) cool-down cycle will be selected. After this cycle is determined, joining experiments on the billets will proceed.

2.1.2 Ceramic/Metal Joints. Activities to date have focused on the acquisition, manufacture, and characterization of materials. The experimental plan initially called for the zirconia-to-metal joints to be fabricated using yttria partially stabilized zirconia (Y-PSZ) in order to closely match the thermal expansion coefficient of the cast iron. Therefore, Y-PSZ powders were obtained and dense polycrystals were prepared by hot pressing. It has since been decided that Mg-PSZ will be used. This decision is principally the result of the selection of Mg-PSZ for the oxide-oxide joints. In order to most effectively use the available resources for baseline material characterization, the same oxide composition will be used in both types of experiments. It is anticipated that the behavior of the zirconia-metal joint will not be substantially altered by the zirconia selection since the braze layer will provide some degree of accommodation.

The source of cast iron has also been changed. Initial efforts have been directed at characterizing a cast iron sample obtained from the Iron Casting Research Institute. However, the availability of a large block of a well characterized cast iron from Sandia National Labs has resulted in a change to this material for production experiments.

Based upon considerations of thermal expansion coefficient mismatch, a composition of six-weight- percent Y-PSZ was selected. Two types of powders were obtained from Toyo Soda Co.; TZ-8Y (13.54 wt-% Y_2O_3) and TZ-0 (unstabilized zirconia). Mixing various ratios of these powders allows the stabilizer level to be tailored. A 150 gram sample of 6 wt-% Y-PSZ was prepared using 83.53 grams of TZ-0 and 66.47 grams of TZ-8Y. The powder was ball milled for 18 hours in a polyethylene jar with Y_2O_3 media. It was then hot pressed at 1500 C for 1.5 hours under 34.5 MPa pressure. The material prepared in this way was 94 percent of theoretical density. The resultant disc (44.5 mm x 8 mm) was cut into nine bars yielding eight bars with dimensions 2.5 mm x 5.1 mm x 12.7 mm and one bar with dimensions 2.5 mm x 5.1 mm x 38.1 mm. The long specimen was for use in baseline characterization testing; the others were intended to form one half of a joint sample. These bars were annealed in air at 1450 C for one hour in order to restore stoichiometry.

A cylinder (25.4 mm x 31.8 mm) of nodular cast iron was obtained from the Iron Casting Research Institute (ICRI #6834-3). This material is supplied with the following property data: ultimate tensile strength

= 714 MPa, yield strength = 448 MPa, elongation = 9.5 percent, and Brinell hardness = 229. The microstructure of the cast iron was investigated using optical microscopy and was found to be 60% pearlite with about 85 percent nodularity of graphite. No evidence of spherical carbides was found.

Braze 603/604 filler metal has been purchased from Lveas Milhaupt Co. (55 pieces, 38 mm diameter x 0.08 mm thick). The brazing procedure to be used requires Cu-electroplating onto the surface of the cast iron and Ti-sputtering onto the surface of the oxide. A simple electroplating bath has been set up to carry out the Cu plating. A bath composition of 190 gm/l of $CuSO_4 \cdot 5H_2O$ and 74 gm/l of H_2SO_4 is being employed. The bath is at room temperature and a 6 V potential is applied. Trials have been carried out to demonstrate the setup.

The sputtering at Ti will be carried out using a standard Pelco Model 3 Sputter Coater 91000. A Ti target has been purchased and is currently being set up.

2.2 Physical Property Determination

Published values for physical properties of both Zycron-L zirconia and nodular cast iron were obtained in order to make preliminary calculations of bond characteristics and to use as a reference for the data to be obtained on this task. These properties are listed in Tables 1 and 2. Unless otherwise specified, the zirconia data are from the manufacturer. The nodular iron data were measured by Takaku, et al (Ref. 1) and are for a ferritic microstructure corresponding both to SAE D4018 (equivalent to ASTM A536, Grade 60-40-18) and to the Sandia material.

2.3 Mechanical Property Evaluation

2.3.1 Base-Material Properties. The specimen designs for testing the base materials were finalized. The tensile strength will be evaluated by using the 4-point bend bar. The Mode I fracture toughness will be measured by using both the chevron-notched bend bar, and the cracked disk specimen (Ref. 3). Two geometries have been chosen to assure that the measurements and analysis procedure provide toughness values which are independent of the geometry. As discussed below, the cracked-disk has advantages for bond-strength measurement. However, the chevron-notched bend bar requires less material and machining and, hence, is a more attractive specimen for evaluating the Mode I fracture toughness.

The base material properties necessary for the stress analysis have not yet been determined because the temperature cycle for fabricating the zirconia-zirconia joints has yet to be finalized. The effects of heat treatment are currently being evaluated by hardness measurements and X-ray diffraction techniques. Some representative data are indicated in Table 3.

TABLE 1. PHYSICAL PROPERTIES OF ZIRCONIA

Property	Value
Elastic Modulus, Tension (20 C)	200 GPa
Poisson's Ratio *	0.22 **
Specific Gravity	5.5 g/cc
Specific Heat (25 C, 1000 C) *	450, 640 J/kg-deg. C
Thermal Conductivity	2 W/m-deg. C.
Thermal Expansion (20 - 540 C)	9.9 X 10^{-6} /deg. C

* Data from Creyke, et al (Ref. 2)
** Typical value for ceramics.

TABLE 2. PHYSICAL PROPERTIES OF NODULAR CAST IRON

Property	Value
Elastic Modulus, Tension (20 C)	171 GPa
Poisson's Ratio	0.28
Specific Gravity	7.1 g/cc
Specific Heat (20 C, 400 C)	460, 630 J/kg-deg. C *
Thermal Conductivity (25 - 400 C) **	37 W/m-deg. C.
Thermal Expansion (20 - 400 C)	13 - 13.2 X 10^{-6} /deg. C *

* Values at 800 C are higher due to the phase transformation.
** Depends on Ni + Si content; tabulated value is typical.

TABLE 3. EFFECT OF HEAT CYCLING ON HARDNESS OF ZIRCONIA*

Exposure	Diamond Pyramid Hardness**
As-Received	950
1500 C in air	790
1500 C in vacuum	780

* Catalog value : 1100 kgf/mm^2 diamond pyramid hardness (DPH)
** 500 gm. load, Vickers indenter

The material under the indenter cracked slightly after the 1500 C exposure, indicating that the ceramic was degraded. Accordingly, careful attention is being focused on the processing parameters, in an attempt to reduce degradation of the base material by the joining process. Once the parameters are selected, tests will start on the base material, which will undergo a heat treatment cycle similar to the joints.

Table 4 reports typical mechanical properties of a nodular cast iron similar to the one to be used on this program (Ref. 4).

TABLE 4. MECHANICAL PROPERTIES OF NODULAR CAST IRON

Property	Value
Yield Strength	258 MPa
Tensile Strength	~ 620 MPa
Fracture Toughness	75-95 MPa-m$^{1/2}$

2.3.2 Shear Strength Measurement. Trials of the bond-strength measurement technique were made using the diametrally-compressed disk specimen and were based on a design used to obtain fracture-toughness data in both the opening and longitudinal shear loading modes (Ref. 5).

When loaded in compression, a tensile stress is generated normal to the loading axis. At the center of the specimen its value is one-third that of the compressive stress. Inclined planes are also subjected to shear stresses. At an angle of 30 degrees to the loading axis, the center stresses are pure shear and equal to $1/\sqrt{3}$ times the maximum compressive stress. Typically, a notch of length equal to 1/4 or 1/3 of the diameter is cut into the specimen in order to measure fracture toughness. Testing specimens with the notch at different angles to the loading axis allows the failure envelope for combined Mode-I/Mode-II (tension/longitudinal-shear) to be measured.

To measure bond strength for similar-material joining, two D-shaped pieces are bonded together and compressed with the bond line at 0 deg. (opening mode) or 30 deg. (shear mode) to the compression direction. The angles for dissimilar-material joining will be different because of the interface shear stresses arising from the elastic modulus mismatch. It is anticipated that tests will be performed at two angles giving two distinct K_I/K_{II} ratios.

Feasibility of the diametral compression system was demonstrated using specimens made by gluing together pieces of electrical porcelain. Two different glues were used, one of relatively low strength and one of relatively high strength. Figure 3 shows the fracture behavior.

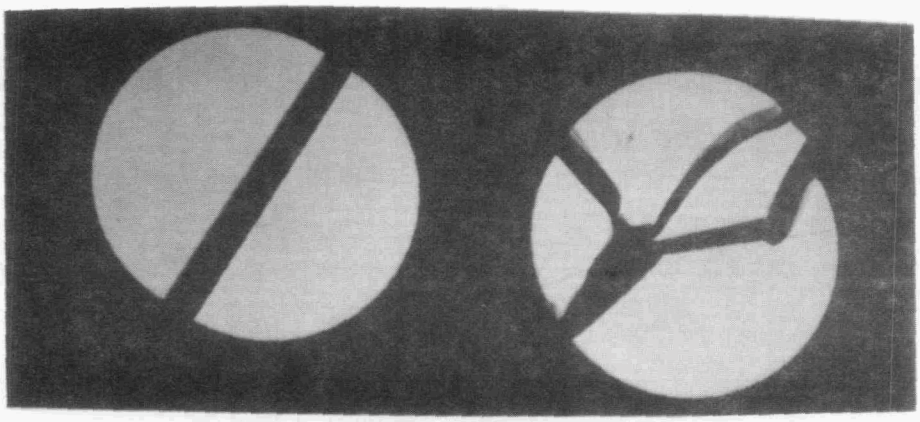

(a) Weak Bond (b) Strong Bond; some fragments missing

FIGURE 3. BROKEN BOND-STRENGTH SPECIMENS OF PORCELAIN
(Photograph slightly larger than actual size.)

The weak specimen sheared completely along the interface, while the strong bond behaved like a precracked monolithic specimen. In that case, it appears that a crack formed in the bond at the center of the specimen and grew about halfway through it. The crack plane then diverted to align itself with the maximum tension. Subsidiary shattering is also observed, as has been observed in fracture-toughness specimens (Ref. 6).

Mixed Mode fracture toughness (Mode I - Mode II) of joints will be evaluated by using the disk specimen, modified to incorporate a chevron notch along the bond line, with the joint lying at various angles to the loading axis.

References

1. H. Takaku, et al, "Properties of Core Materials Cut from Castor Type Cast Iron Model Cask", CRIEPI Report E286001, April, 1987.

2. W. E. C. Creyke, I. E. J. Sainsbury, and R. Morrell, Design with Non-Ductile Materials, Applied Science, London, 1982.

3. D. K. Shetty, A. R. Rosenfield, and W. H. Duckworth, "Fracture Toughness of Ceramics Measured by a Chevron-Notch Diametral-Compression Test", J. Amer. Ceram. Soc., Vol. 68, 1985, C325-C327.

4. A. R. Rosenfield, et al, "Crack Arrest Toughness of Nodular Iron", Final Report on EPRI Project RP2813-12, Battelle Memorial Institute, January 29, 1988.

5. D. K. Shetty, A. R. Rosenfield, and W. H. Duckworth, "Mixed-Mode Fracture in Biaxial Stress State: Application of the Diametral-Compression (Brazilian Disk) Test", Engg. Fracture Mech., Vol. 26, 1987, 825-840.

6. A. R. Rosenfield, "Fracture of Brittle Materials Under a Simulated Wear Stress System", Proceedings of the Fifteenth Annual Automotive Materials Symposium, Detroit, April 26, 1988 (to be published).

Analytical and Experimental Evaluation of Joining Silicon Carbide to Silicon Carbide and Silicon Nitride to Silicon Nitride for Advanced Heat Engine Applications

Donald O. Patten, Jr., Carl H. Bates, Guilio A. Rossi, and Glenn J. Sundberg (Norton Company)

Objective/Scope

The purpose of this program is to develop techniques for producing reliable ceramic-ceramic joints and analytical modeling to predict the performance of the joints under a variety of environmental and mechanical loading conditions including high temperature, oxidizing atmospheres. The ceramic materials under consideration are silicon nitride and silicon carbide. The joining approach for silicon nitride is based on the ASEA hot isostatic pressing process while the plan is to co-sinter silicon carbide green forms together. These joining methods were selected to produce joints which exhibit the minimum possible deviation in properties from those of the parent ceramic materials. Analytical models will be experimentally verified by measurements on experimental size and scale-up joints produced as part of this work.

Background

Because of their strength, oxidation resistance, and other desirable high temperature properties, silicon nitride and silicon carbide are under extensive study for use in advanced gas turbine and internal combustion engines. In both engine types there are requirements for joining the ceramics to themselves, other ceramics, and various engineering alloys. Existing bonding methods lack the high temperature capabilities required for use in advanced heat engines. Further, analytical modeling techniques to predict joint reliability and performance have not yet been developed. These technical needs have prevented consideration of economically fabricating large, complex ceramic engine components from smaller, less complicated segments. The current program will address these issues for silicon nitride to silicon nitride and silicon carbide to silicon carbide joints.

Technical Progress

Joining Approach and Material Selection

The initial thrust of the program is to develop reproducible techniques for joining silicon nitride and silicon carbide to themselves. The ideal joint is one which

exhibits the minimum possible property deviations from the adherend materials. This is particularly true for demanding applications such as the high temperature oxidizing atmospheres which exist in advanced heat engines. For this reason we are pursuing methods of joining green bodies with the goal of producing joints with the same physical and chemical properties as the adherend materials; an increased defect population is likely to be the principal difference between bond and bulk material.

The material choices were strongly influenced by the joint strength goals of 140 MPa at 1300 and 1530°C. The silicon nitride is Norton Company's NCX5100, a 4 w/o Y_2O_3 material developed specifically for high temperature applications. As NCX5100 is a hot isostatically pressed material, joining will be performed using a glass encapsulated (ASEA process) co-HIPping approach. The silicon carbide is a new Norton material, NCX4500, a sintered silicon carbide produced from beta powder using boron and carbon as sintering aids under a license from General Electric. A co-sintering approach is planned for silicon carbide.

Silicon Nitride Joint Development

Silicon nitride joining trials are underway, forming butt joints between green die-pressed cylinders, 33mm in diameter and 30mm long. Three methods of joining have been attempted: bare green bodies butted together, application of a 4% Y_2O_3 silicon nitride slip at the joint interface, and application of an injection molding compound of the 4% Y_2O_3 composition as an interlayer. Although all joint surfaces were finished in the green state, it is difficult to achieve a flatness tolerance below 0.026mm. The use of the previously mentioned plastically deformable interlayers may be helpful in filling the voids between the two imperfectly flat faces as even the large isostatic pressure applied during sintering may be insufficient to close them through deformation. A continuous bead of 4% Y_2O_3 silicon nitride was applied as a slip to the external seam of all joints to maintain joint integrity during firing.

Finished joint quality has been evaluated by bulk density and sectioning for obvious signs of bond voids, porosity, and intrusion of the encapsulant material. 3 X 4 X 50mm flexure specimens were machined from the joints and four-point quarter-point flexural strength was measured at room temperature and 1300°C, employing test fixtures with 40mm outer spans. Joint strength was compared with NCX5100 control tiles fired in the same run.

Two bare (no interlayer) joints have been HIPped. One of the joints had a discontinuous bead at the external seam which did not adequately protect the joint from intrusion of the encapsulant material during firing. The result was a complete destruction of joint integrity. The second specimen, with a

continuous bead, attained 98.6% of theoretical bulk density as determined by the boiling water method (ASTM C 20-80a). After sectioning half of the joint surface was observed to be incompletely closed and was filled with the encapsulant material. The other half exhibited a seam that appeared to be completely "healed" with no gross porosity detected visually. Flexure specimens were machined from the joined specimen for evaluation by optical microscopy and then strength testing.

Regions of the joint that were completely closed (FIGURE 1) were difficult to detect optically, in sharp contrast with those which experienced encapsulant intrusion (FIGURE 2). Microfocus X-radiography was performed on the flexure specimens through the 3mm dimension at varying film exposure time, tube current and voltage. The closed joints could not be detected at the lowest resolution limit of 100 microns confirming the absence of large regions of porosity and phases of dissimilar density. Joints which were not completely closed could be easily detected.

The flexural strength of the NCX5100 bare butt joint specimens were evaluated at room temperature and 1300°C and compared with the control tile from the same HIP cycle (see table).

(standard deviations in parenthesis)

Sample	Mean RT Flexural Strength - MPa	#	Mean 1300°C Flexural Strength - MPa	#
Joint 30-5,6	663 (229)	7	534 (30.6)	5
Control	814 (114)	5	701 (29.1)	5

Of the 12 joined bars tested, only one of the 1300°C breaks occurred at the bond itself. Although the joints fared well in this testing, the strengths are substandard for the NCX5100 silicon nitride. The strengths of the control specimens may be considered typical for the material. A high percentage of the room temperature joined test bar breaks occurred under one or both of the inner span loading pins. The most likely cause of the low strengths and pin region failures is reduced density in the area away from the joint, due to the unusually long die pressed green forms required to make the test specimens. We will attempt to avoid this in the future by cold isostatic pressing and then machining the green bodies to the desired geometry.

Two additional joints have been prepared and HIPped, both using a 4% Y_2O_3 silicon nitride interlayer. One is a standard butt joint while the other employs a machined tongue and groove to improve green strength and joint integrity during firing. Twelve joints are scheduled for HIPping in the near future including bare, injection molding mix, and slip interlayer variations.

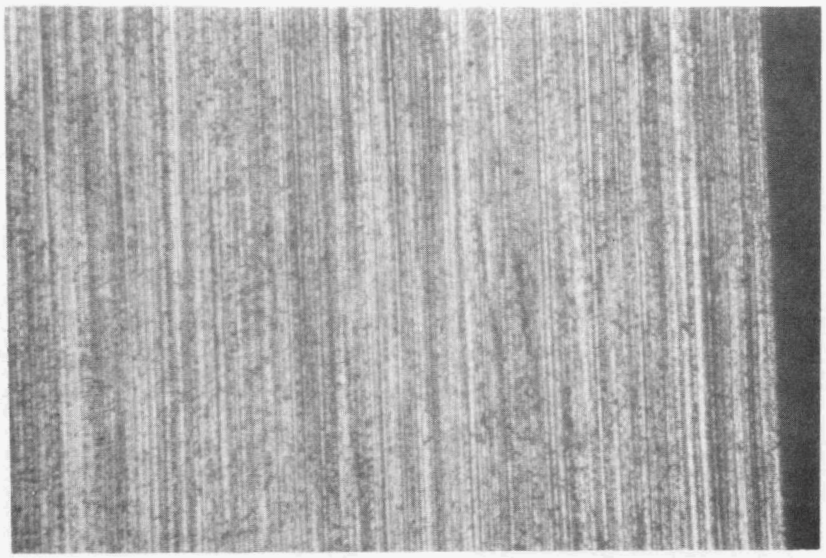

a.) Bright Field

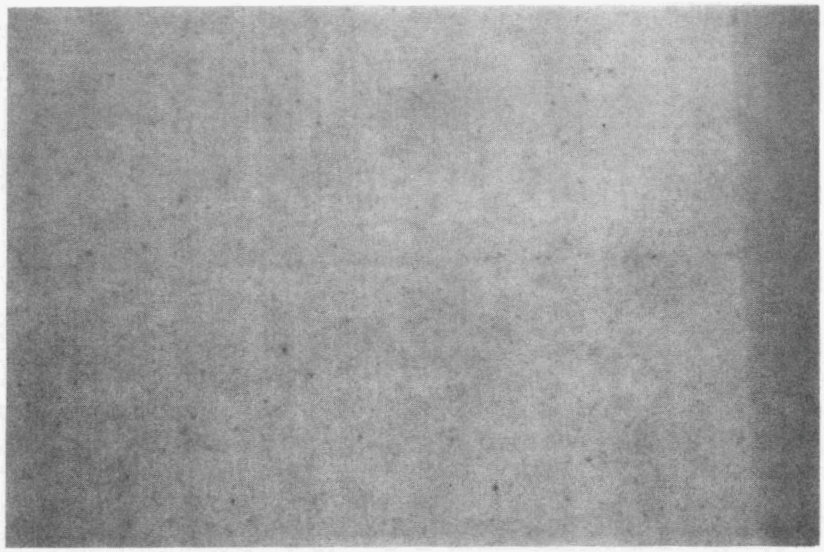

b.) Crossed Polars

FIGURE 1: Optical Metallograph of Closed Si_3N_4 Joint at 100X.

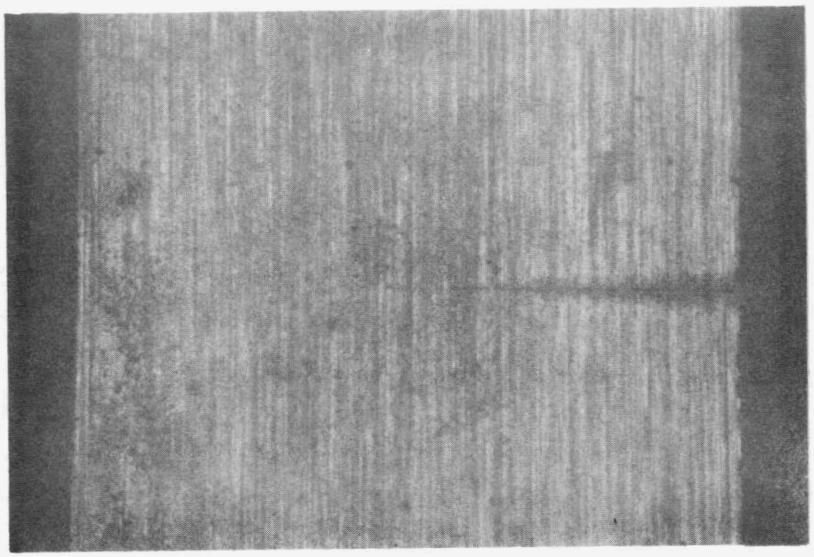

a.) Bright Field

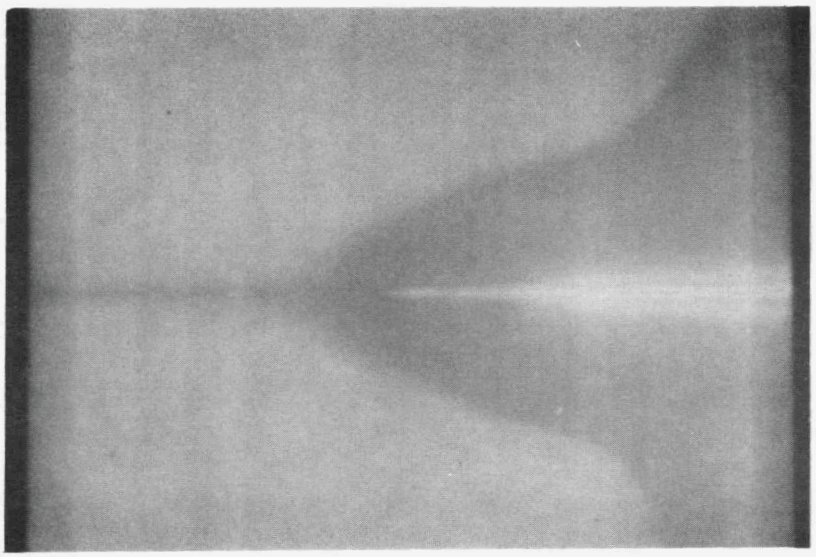

b.) Crossed Polars

FIGURE 2: Optical Metallograph of Si_3N_4 Joint with Encapsulant Intrusion at 32X.

Silicon Carbide Joint Development

Silicon carbide joint development efforts are in progress, based on a co-sintering approach. As in the case of silicon nitride, the challenge is expected to be the closing of bond voids. Although pressureless sintering eliminates some concerns about maintaining joint integrity during firing, the closing of joint line defects is expected to be more difficult without the pressure driving force.

Attempts have been made at producing co-sintered joints using a variety of slip and binderized interlayers. For aqueous slip interlayers, a zero shrinkage pre-sinter was found to be necessary to provide adequate joint green strength. The best results obtained by this method were four 13mm diameter butt joints, three of which were shear tested giving an average nominal shear strength of 5.9 MPa. The fourth specimen was sectioned and optical microscopy revealed the existence of porosity along the joint line. The fracture surfaces of the sheared specimens showed evidence of "mud cracking" in the interlayer, attributed to the drying of the slip. FIGURE 3a shows the mud crack phenomenon on a sheared specimen in which the crack initiated in the joint and deflected into the bulk silicon carbide. FIGURE 3b shows a close-up view of the interface region. Non-aqueous slips and surfactants are being considered to reduce the liquid surface tension and thus minimize this problem.

Several joints were attempted using interlayers of clean burning binders in the form of aqueous and non-aqueous suspensions of SiC powder. The resulting joints exhibited large scale porosity in the bond region. Only two of these joints survived diamond sawing. One was made with an experimental binder, mixed with an aqueous beta SiC slip. The entire specimen sintered to only 88% of theoretical density, attributed to contamination of the furnace. The joint was very porous as shown in FIGURE 4. A screening test bar gave a flexural strength of 13.9 MPa. The second surviving joint, from the same run and again only 88% dense, was made from a suspension of SiC powder in acetone and a reactive carrier which yields 50 w/o beta SiC on firing. This joint was also quite porous and a screening test bar gave 12.8 MPa flexural strength. Future attempts using this approach will focus on maximizing the interlayer solids loading and minimizing its thickness.

A final co-sintering attempt was made using a patented joining method* employing a liquid phase interlayer of Mo_2B_5. Of three specimens fired, two did not join. The bond surfaces exhibited large alpha platelets, apparently due to excessive reaction between the bond and adherend materials. The third joint will be shear tested.

* Kennecott Corp. - U.S. Patent 4,419,161

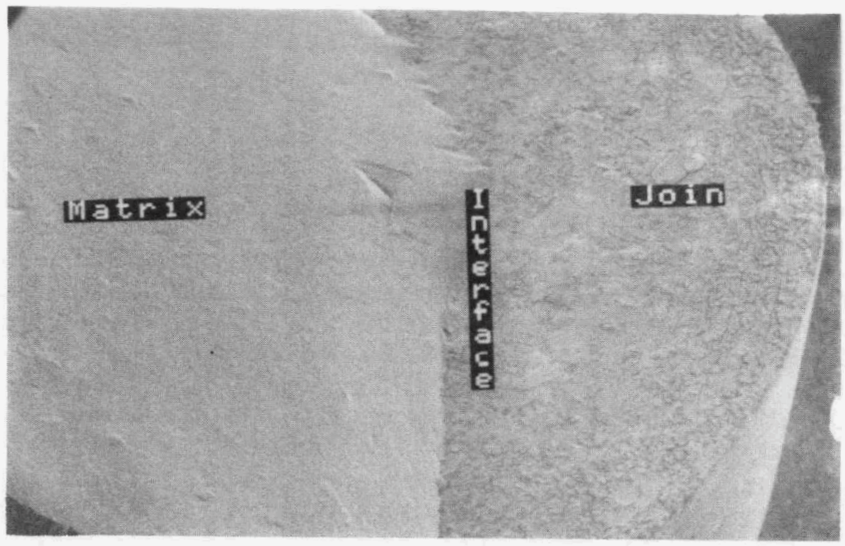

a.) 12.7X

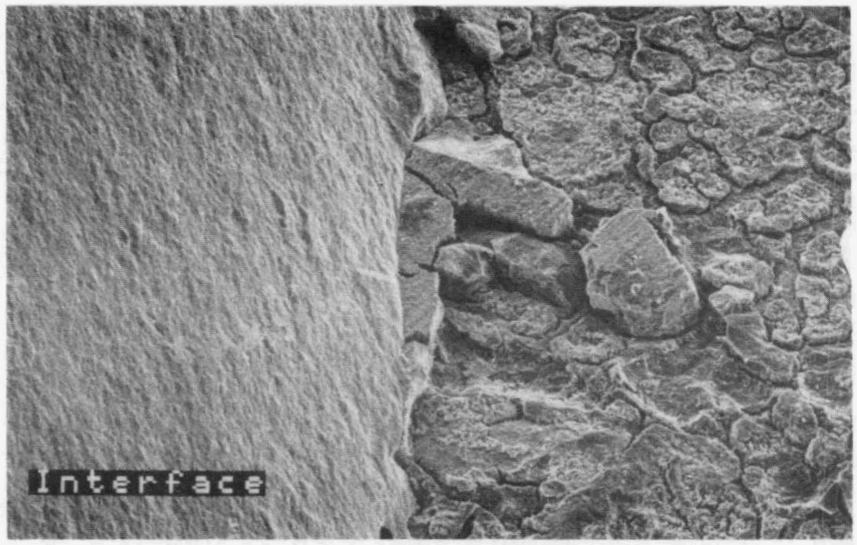

b.) 100X

FIGURE 3: Sheared SiC Joint Fracture Surface Showing Plane of "Mud Cracked" Interlayer and Crack Deflecting into Bulk Material.

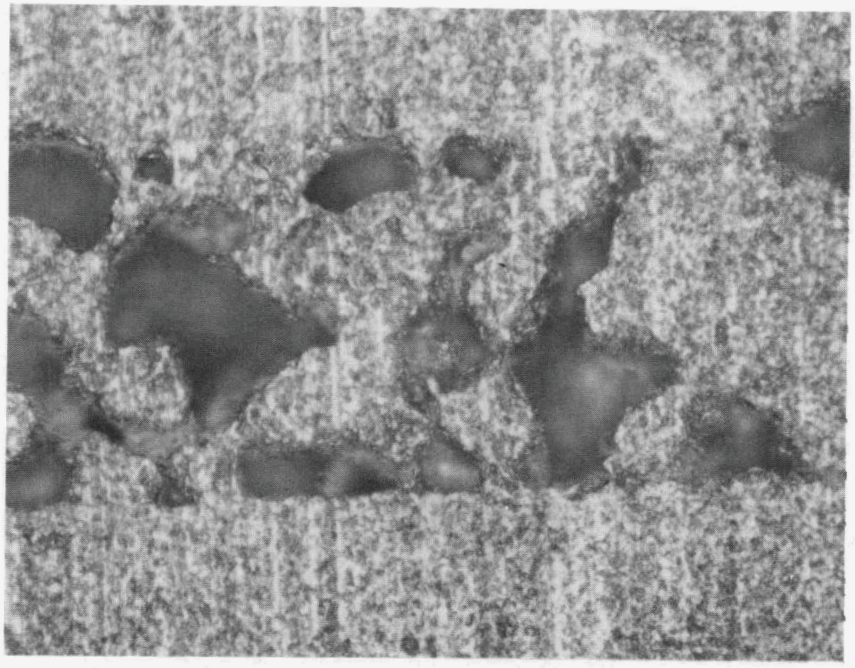

FIGURE 4: Porous SiC Joint Made with Binderized Aqueous Slip Interlayer (200X).

Exploratory attempts were made to join fired pieces of SiC using several different interlayers. These included silicon metal, silicon plus SiC powders, silicon plus carbon plus SiC powders, as well as the reactive liquid carrier described above, both with and without SiC powder in suspension. None of these joints were strong enough to survive diamond sawing.

Microstructural evaluation of the bonds made to date will guide future joining trials. An injection molding mix of the NCX4500 SiC powder is being prepared for future interlayer use. Additional methods for joining fired bodies are being evaluated and materials are on order to test some of these.

Analytical Modeling

Our efforts to date in the area of analytical modeling have centered on a literature search investigating ceramic failure mechanisms and corresponding modeling approaches. Although exact bond constituents and properties will not be known until the completion of the joint development phase of the program, we have for the purposes of the literature search made the assumption that the physical and chemical properties of the joints will not differ significantly from the bulk ceramic materials. The literature search, therefore, was based on the premise that the ceramic-ceramic joints will differ from the adherends due only to an increased defect population. Failure mechanisms anticipated to require modeling work include: fast fracture, creep, oxidation, cyclic fatigue, thermal cycling, and slow crack growth. Models will be developed employing finite element analysis to allow extension to arbitrary geometry and loading conditions.

Fast fracture

Fast fracture strength in brittle materials is understood to be controlled by the flaws which are present. Although fracture mechanics allows a deterministic prediction of strength for a known flaw, the random size and orientation of defects normally necessitates a statistical approach to failure prediction. Weibull's weakest link theory[1] is widely employed for probabilistic failure analysis. The probability of failure is calculated:

$$P_f = 1 - e^{-\int_V \left(\frac{\sigma-\sigma_u}{\sigma_0}\right)^m dV} \qquad (1)$$

where:
- σ is the local maximum principal stress
- σ_0 is a normalizing stress, characteristic of the material
- σ_u is a stress below which failure is not expected
- m is the Weibull modulus

For dealing with more complex stress states the principle of independent action[2] and Batdorf's model for polyaxial stress states[3,4,5] including shear sensitivity can be employed.

In practice, finite element analysis (FEA) is used to determine the complete stress distribution throughout the component of interest. Equation (1) is then numerically integrated over the entire volume. SCARE (Structural Ceramics Analysis Reliability Evaluation), developed by John Gyekenyesi at NASA-Lewis[6,7] is an available software which postprocesses FEA results using either Weibull or Batdorf models to calculate probability of failure. As the surface and volume flaw populations are usually different in ceramic materials, SCARE was written to allow calculation of the probability of concurrent surface and volume flaw induced failure. As joined specimens will have a third flaw population in the bond area, joint strength distributions will be experimentally measured and included in our models as a separate material type with the appropriate Weibull parameters.

Creep Modeling

At high temperatures, creep is an important deformation and failure mechanism in ceramic materials. Creep and creep rupture are controlled by the physical structure of the material grain boundaries[8]. If the structure has little or no amorphous phase, creep is normally determined by a combination of grain boundary sliding and, predominantly, diffusion-controlled plastic deformation of the individual ceramic grains. If a glassy grain boundary phase is present, creep is controlled by the physical properties of this second phase. Grain boundary sliding is the dominant mechanism but cavitation can occur at high stresses or large deformations. At high stress levels, failure is controlled by slow crack growth whereas at lower levels, failure occurs by creep rupture.[9]

Evans and Rana[10] developed a statistical creep cavitation model of high temperature failure in ceramic materials. They formulated an analytical model of creep rate by combining statistical methods with micro-mechanics of deformation. The theory states that high temperature failure of ceramics involves the nucleation, growth, and coalescence of microcracks or cavities located at the grain boundaries. The results give a non-linear stress-strain relationship, in accord with experimental observations, and predictions of rupture time are also consistent with available data. However, substantial model development and extensive experimental observations of microscopic structural composition are needed to establish an acceptable model.

For practical purposes, our modeling will be based on experimentally measured macroscopic deformation of the joints and bulk material rather than focusing on the detailed microscopic mechanisms of deformation. Experimentally determined time-dependent constituitive relations will be employed in FEA creep models, providing independent material properties for the joints and bulk ceramic.

Generic uniaxial creep behavior is described by the following relationship[11]:

$$\epsilon(t) = \epsilon_0 + \epsilon_p + \epsilon_s + \epsilon_t \qquad (2)$$

where: ϵ_0 is the instantaneous deformation
ϵ_p is primary or transient creep strain
ϵ_s is secondary or steady state creep
ϵ_t is tertiary or unstable creep

Primary and secondary creep are the most studied behaviors[12] and exist as preset routines in the general purpose FEA software, ANSYS. Primary creep can be modeled as a function of the local applied stress, the absolute temperature, and time. ANSYS provides several combinations of these three variables. The generic incremental equation for primary creep can be written:

$$(\Delta\epsilon_{cr})_p = C1\sigma^{C2}t^{C3}\epsilon^{C4}e^{-C5}\Delta t \qquad (3)$$

where C1, C2, C3, and C4 are empirically determined constants and C5 is a function of time, temperature, and stress.

Steady state or secondary creep can be described by combining Norton's law with Arrhenius' law[13,14]:

$$\dot{\epsilon} = A\sigma^n \qquad (4)$$

where: $\dot{\epsilon}$ is the creep strain rate
σ is the applied stress
n is the stress exponent
A is the pre-exponent constant depending only on test temperature and material properties. A can be empirically written:

$$A = \dot{\epsilon}_0 e^{-(Q/RT)} \qquad (5)$$

where: $\dot{\epsilon}_0$ is the initial creep rate
Q is the activation energy
R is Boltzmann's constant
T is the absolute temperature

ANSYS provides several secondary creep modeling options. The finite element program models macroscopic creep behavior by an incremental technique. Uniaxial creep relations are applied to the discrete elements within the model in an iterative scheme to equilibrate internal stresses.

Oxidation Modeling

Oxidation of silicon nitride and silicon carbide at high temperatures can have significant influence on their strength[15-17]. Oxidation effects on indented cracks in hot pressed silicon nitride can result in the blunting of crack tips, reducing stress intensity factors and initially strengthening the material, followed by a substantial reduction in strength[18,19].

Siebels[19] conducted oxidation tests with both Si_3N_4 and SiC. These experiments showed a rapid formation of a protective SiO_2 layer which then reduced the oxidation rate. RBSN showed a drop in strength beginning at 900°C while HPSN displayed the effects of oxidation at temperatures above 1260°C. McLean et al.[20] studied the effect of oxidation on the strength of HPSN and SiC flexure specimens. Test results showed a rapid drop in strength during the first 1000 hours due to an increasing oxidation layer, followed by a slower oxide reaction causing less degradation in strength. Oxidation reactions in SiC occurred at a higher temperature than for Si_3N_4 by the formation of a smooth SiO_2 layer. This layer did not cause a surface degradation and the flexural strength remained fairly constant.

Doremus and Szewczyk[21] proposed modeling oxidation of silicon by the use of the molecular diffusion based relation:

$$L^2 + AL - AC\ln\left(1+\frac{L}{C}\right) = Bt \qquad (6)$$

where A, B, and C are parameters found by fitting experimental data, L is the oxidation layer thickness, and t is time. Equation (6) was derived by assuming that there are two processes involved in oxidation, diffusion through the oxide film and a chemical reaction at an oxide interface. The parameters are functions of microscopic composition and diffusion mechanisms.

Modeling of the mechanical property changes in ceramic materials by an oxide layer thickness approach is not very practical. Silicon nitride, for example, frequently experiences a strength reduction due to oxidation from random surface pits. A more effective approach consists of characterizing the strength of the ceramic using Weibull parameters[22]. These parameters are modified from their fast fracture values by the effects of the oxidizing environment. Since the strength of ceramics is sensitive to surface flaws

which are in turn affected by oxidation, Weibull parameters expressed as functions of oxidation time and temperature would constitute a complete set of equations to predict strength in oxidizing environments. Experiments will characterize the changes in mechanical properties of the joint and bulk materials with oxidation. The resulting statistical parameters will be applied to FEA results as previously discussed for fast fracture.

Cyclic Fatigue Modeling

As brittle materials, ceramics do not possess the plastic deformation systems, except at high temperatures, which are responsible for the cycle dependent fatigue of metals. The failure mechanism considered responsible for the fatigue of ceramics is slow crack growth, a cycle independent phenomenon. Thus, fatigue in ceramics can occur under a constant applied load and is frequently termed static fatigue[23-31]. Slow crack growth crack velocity is usually expressed:

$$v = AK_I^n \qquad (7)$$

where K_I is the crack tip stress intensity factor and A and n are experimentally determined slow crack growth parameters. Hamanaka et al.[27] have attempted to combine Weibull theory with slow crack growth data to predict probability of static fatique failure at a given time.

Evans and Fuller[32], Kawakubo and Goto[33], and Fett et al.[34] have attempted to model cyclic fatigue using slow crack growth data. None of this work has conclusively defined the significance of the cycling component of load in delayed ceramic failure.

Silicon nitride and silicon carbide are quite resistant to slow crack growth at room temperature. Thus, one would expect them to be insensitive to cyclic loading until they reach temperatures at which slow crack growth becomes significant. Our modeling work will focus on extending the probabilistic approach to lifetime prediction for static fatigue. Cyclic service life will also be predicted from slow crack growth data, using time under load correction factors.

Thermal Cycling

Thermal cycling has not been identified as a failure mechanism in ceramics except when heat transfer rates are high enough to develop significant thermal shock stresses. Hasselman et al.[35,36] used slow crack growth data to predict the thermal fatigue (thermal shock) life of silicon nitride by numerically calculating the extent of slow crack growth for each individual cycle. Predictions agreed reasonably with experimental data. Singh et al.[37] also studied subcritical

crack growth as the mechanism of thermal fatigue failure. An analytical method was developed for estimating thermal fatigue life allowing simultaneous changes in T_{max} and ΔT. No experiments were done to verify their model.

If modeling is required in the thermal shock regime, the temperature distributions and and stresses would be calculated using FEA. These would become inputs to the cyclic fatigue modeling discussed above.

Characterization Experimental Plan

Work is underway on the experimental plan which will specify the characterization testing to be performed on the joints developed under this program. The plan will provide the data required for the above described models to address the failure mechanisms anticipated in the ceramic-ceramic joints. This plan will include details such as test specimen geometries, numbers of specimens, test temperatures, fixturing, and measurement methods.

STATUS OF MILESTONES

1. Complete Modeling Literature - 3/31/88 - Complete.

2. Complete Characterization Experimental Plan - 4/30/88 - Some risk of over-run due to personnel change.

3. Complete Joint Development Work - 10/31/88 - On schedule.

4. Complete 2 cm^2 Joint Experimental Plan - 12/31/88 - On schedule.

PUBLICATIONS

None

REFERENCES

1. W. Weibull, "A Statistical Theory of the Strength of Materials," Ingeniors Vetenskaps Akademien, Handlingar, no. 151, pp.1-45 (1939).

2. A.M. Freudenthal, "Statistical Approach to Brittle Fracture," Fracture vol.2, ch.6, H. Liebowitz, Academic Press, New York, 1968.

3. S.B. Batdorf, "Fundamentals of the Statistical Theory of Fracture," Fracture Mechanics of Ceramics vol.3, pp.1-31, Bradt, Evans, Hasselman, and Lange, Plenum Press, New York, 1977.

4. S.B. Batdorf and J.G. Crose, "A Statistical Theory for the Fracture of Brittle Structures Subjected to Non-Uniform Polyaxial Stresses," J. Appl. Mech. vol.41, 459-464 (June 1974).

5. J. Lamon, "Statistical Approaches to Failure for Ceramic Reliability Assesment," Battelle, Centres de Recherche de Geneve, 7 Route de Drize, 1227 Carouge-Geneva, Switzerland.

6. J.P. Gyekenyesi and N.N. Nemeth, "Surface Flaw Reliability Analysis for Ceramic Components with the SCARE Finite Element Postprocessor Program," NASA Tech. Memo. 88901

7. J.P. Gyekenyesi, "SCARE: A Postprocessor Program to MSC/NASTRAN for Reliability Analysis of Structural Ceramic Components," Trans. ASME, vol.108, 540-6 (July 1986).

8. J. Lankford, K.S. Chan, and R.A. Page "Creep Cavitation Behavior in Polycrystaline Ceramics," Fracture Mechanics of Ceramics vol.7, pp.327-347, Bradt, Evans, Hasselman, and Lange., Plenum Press, New York, 1977.

9. S. M. Wiederhorn and E. R. Fuller, Jr. "Structural Reliability of Ceramic Materials," Presented at the International Symposium on Engineering Ceramics, Jerusalem, Israel, pp.169-86, Dec. 16-20, 1984.

10. A.G. Evans and A. Rana, "High Temperature Failure Mechanisms in Ceramics," Acta Metall., vol.28, 129-141 (1980).

11. R.F. Pabst, "Creep in Si_3N_4 and SiC Materials," Max-Planck-Institut fur Metallforschung. Institut fur Werkstoffwissenchaften, Stuttgart, FRG.

12. S.M. Wiederhorn, T.J. Chuang, D.F. Carroll, and B.J. Hockey, "Tensile Creep Studies of SiC," Proc. 25th Aut. Tech. Der. Contractor's Coord. Meeting, Dearborn, Mich., Oct. 29, 1987.

13. H. Riedel, "Fracture at High Temperatures", Mat. Res. and Eng., Edited by B. Ilschner and N.J. Grant, Springer-Verlag, NY., 1987.

14. J.P. Poirier, "Creep of Crystals, High Temperature Deformation Process Metals, Ceramics, and Minerals," Cambridge Earth Sci. Series, Cambr. Univ. Press., Cambridge, England, 1985.

15. J.A. Rubin, "Probable Causes of Pitting in Hot Pressed Si_3N_4 Ceramics," Proc. DARPA/NAVSEA Ceramic Gas Turb. Demo. Engine Prog. Review, MCIC 78-36, pp.739-746 (August 1977).

16. D. Dubiccioti and K.H. Lau, "Kinetics of Oxidation of Hot Pressed Silicon Nitride Containing Magnesia," J. Am. Ceram. Soc. 61(11-12) 512-7 (1978)

17. S.W. Freiman, C.Cm. Wu, K.R. McKinney, and W.J. McDonough, "Effect of Oxidation on the Room Temperature Strength of Si_3N_4 Hot Pressed with MgO or ZrO_2," Proc. DARPA/NAVSEA Ceramic Gas Turb. Demo. Engine Prog. Review, MCIC 78-36, pp.655-663 (August 1977).

18. N.J. Tighe and S.M. Wiederhorn, "Effects of Oxidation on the Reliability of Silicon Nitride," Fracture Mechanics of Ceramics , vol.5, pp.403-424, Bradt, Evans, Hasselman, and Lange., Plenum Press, New York, 1977

19. J.E. Siebels, "Oxidation and Strength of Silicon Nitride and Silicon Carbide," Proc. 6th Army Materials Tech. Conf., Ceramics for High Performance Applications 3: Reliability, pp.793-804 (July 1979).

20. A.F. McLean, E.A. Fisher, R.J. Bratton, and D.E. Miller, "Effect of Long-Term Oxidation on the Strength of Hot-Pressed Silicon Nitride and Silicon Carbide," in Brittle Materials Design, High Temperature Gas Turbine, Tech. Rep. AMMRC-CTR-75-28 pp.133-137 (October 1975).

21. R.H. Doremus and A. Szewczyk, "Oxidation of Silicon by Oxygen: a Rate Equation," J. Matl. Sci. 22, 2887-2892 (1987).

22. S.M. Wiederhorn, "A Probabilistic Framework for Structural Design," Fracture Mechanics of Ceramics Vol. 5 pp. 197-226,Bradt, Evans, Hasselman, and Lange, Plenum Press, New York, 1977.

23. A.G. Evans, "A Method for Evaluating the Time-Dependent Failure Characteristics of Brittle Materials - and its Application to Polycrystalline Alumina," J. Mat. Sci., vol. 7, 1136-1146 (1972).

24. S.M. Wiederhorn, "Prevention of Failure in Glass by Proof-Testing," J. Am. Ceram. Soc., Discussions and Notes, pp.227-8 (April 1973).

25. J.E. Ritter, Jr. and K. Jakus, "Overview of Lifetime Predictions for Silicon Nitride," Proc. DARPA/NAVSEA Ceramic Gas Turb. Demo. Engine Prog. Review, MCIC 78-36, pp.701-713 (August 1977).

26. M. Matsui, Y. Ishida, T. Soma, and I. Oda, "Ceramic Turbocharger Rotor Design Considering Long Term Durability," Proc. Cer. Mat. and Components for Engines, Lubeck-Travemunde, FRG, pp.1043-1050, April 14-17, 1986

27. J. Hamanaka, Y. Hashimoto, A. Ookoshi, N. Watanabe, "A Reliability Evaluation System for Ceramic Gas Turbines," JSME Int. J. 30(261), 408-13, (1987).

28. J.L. Henshall, "The Mechanisms and Mechanics of Subcritical Crack Propagation in Hot-Pressed SiC Above 1000°C," Adv. in Frac. Res., Proc. 5th Int. Conf. on Fracture, vol 4. pp.1541-9, Pergamon Press, New York, (1982).

29. J.L. Henshall, "High Temperature Slow Crack Growth in Hot Pressed Silicon Carbide," Res. Mech. vol.1 pp.229-48, (1980).

30. R.W. Rice, S.W. Freiman, and J.J. Mecholsky, Jr., "Fracture Sources in Si_3N_4 and SiC," Proc. DARPA/NAVSEA Ceramic Gas Turb. Demo. Engine Prog. Review, MCIC 78-36, pp.665-88 (August 1977).

31. R.N. Katz, G.D. Quinn, and E.M. Lenoe, "High Temperature Static Fatigue in Ceramics," Fatigue Environment and Temperature Effects, 14-18 July 1980, Bolton Landing, Lake George, New York, pp.221-30, Plenum Publishing, New York, 1983.

32. A.G. Evans and E.R. Fuller, "Crack Propagation in Ceramic Materials Under Cyclic Loading Conditions," Met. Trans. vol.5, pp.27-33 (January 1984).

33. T. Kawakubo and A. Goto, "Fatigue Strength Analysis of Silicon Nitride," Toshiba Rev. No.158 pp.39-42, Winter 1986.

34. T. Fett, G. Himsolt, and D. Munz, "Cyclic Fatigue of Hot Pressed Silicon Nitride at High Temperatures," Adv. Cer. Matls. 1(2), 179-84 (1986).

35. D.P.H. Hasselman, E.P. Chen, C.L. Ammann, J.E. Doherthy, and C.G. Nessler, "Failure Prediction of the Thermal Fatigue of Silicon Nitride," J. Am. Ceram. Soc. 58(11-12), 513-6 (1975).

36. R. Badaliance, D.A. Krohn, and D.P.H. Hasselman, "Effect of Slow Crack Growth on the Thermal-Stress Resistance of an Na_2O-CaO-SiO_2 Glass," J. Am. Ceram. Soc. 57(10), 432-6 (1974).

37. J.P. Singh, K. Niihara, and D.P.H. Hasselman, "Analysis of Thermal Fatigue Behavior of Brittle Structural Materials," J. Mat. Sci. vol.16, 2789-97 (1981)

2.0 MATERIALS DESIGN METHODOLOGY

INTRODUCTION

This portion of the project is identified as project element 2 within the work breakdown structure (WBS). It contains three subelements: (1) Three-Dimensional Modeling, (2) Contact Interfaces, and (3) New Concepts. The subelements include macromodeling and micromodeling of ceramic microstructures, properties of static and dynamic interfaces between ceramics and between ceramics and alloys, and advanced statistical and design approaches for describing mechanical behavior and for employing ceramics in structural design.

The major objectives of research in Materials Design Methodology elements include determining analytical techniques for predicting structural ceramic mechanical behavior from mechanical properties and microstructure, tribological behavior at high temperatures, and improved methods for describing the fracture statistics of structural ceramics. Success in meeting these objectives will provide U.S. companies with methods for optimizing mechanical properties through microstructural control, for predicting and controlling interfacial bonding and minimizing interfacial friction, and for developing a properly descriptive statistical data base for their structural ceramics.

2.1 MODELING

2.1.1 Modeling

Microstructural Modeling of Cracks
J.A.M. Boulet (University of Tennessee, Knoxville)

Objective/Scope

The goal of the study is to investigate and develop mathematical models for fracture of cracks with realistic geometry under arbitrary stress states. For brittle fracture of such cracks, interference between surface irregularities (bumps) on opposing crack faces may significantly influence fracture initiation. A sequence of elasticity problems leading to the rough-faced crack in an infinite body under arbitrary loads will be defined and solved. Application of fracture criteria to the stress field around the crack will lead to predictions of fracture-initiating loads, which will then be compared with those cited in the literature for cracks of simpler geometry subjected to the same loads.

Technical Highlights

We have considered a numerical solution of the rough-faced crack under arbitrarily oriented stresses by the boundary element method (BEM). This method is preferred over the finite element method (FEM) because of the need to do parameter studies and the greater expense of FEM versus BEM. But because the time required to develop a BEM computer simulation is prohibitive, this year's work will stop short of considering BEM solutions. Furthermore, we restrict ourselves to the two-dimensional case (an irregular "line" crack under arbitrarily oriented biaxial stress). (The three-dimensional case is a "planar" crack under arbitrarily oriented triaxial stress.) In the mathematical model under development, we represent protrusions on the crack faces as wedge-shaped bumps, and we assume them to be of various heights. If the wedges abut each other (so as to form "saw-toothed" crack faces), then they interact directly with each other and the crack tip. (For direct interaction, the stresses in one wedge cannot be calculated independently of those in neighboring wedges. Likewise, the stress field at the crack tip cannot be calculated independently of those in the neighboring wedges.) In this case, stresses can only be calculated from a solution that treats the entire crack at once. If, however, the wedges are sufficiently separated (isolated bumps on an otherwise smooth crack face), they do not interact directly with each other, nor with the crack tip. In this case, the effect of each interference site can be calculated independently and the results superimposed. The influence of the interference on the stresses at the crack tip can be closely approximated by replacing the wedges with the concentrated loads -- shear force, normal force, and moment -- acting at their bases.

For our initial investigation, we assume that the crack is opened enough so that the faces are in contact at only one point on the crack (the site of the tallest bump), and the interference is far enough away from the crack ends (tips) so that its influence on the stresses there can be accurately predicted by superposition. Our model of the interference region is pictured in Figs. 1 and 2. Far from this region, the effect of the interference is the same as if the bumps were represented by the concentrated loads shown in Fig. 3. The solution of this problem can serve as a benchmark for a numerical model of a saw-tooth-faced crack. The details of the benchmark solution should be reproduced by the numerical solution in the vicinity of the wedge-wedge contact.

As indicated above, the problem at hand is that of a line (Griffith) crack subjected to uniform biaxial stress and with interference (due to roughness) between the opposing crack faces. Depending on their signs and orientation, the applied stresses tend either to open or to close the crack. Also, when the crack is aligned with neither stress, the stresses tend to shear the crack (slide the opposing faces parallel

to themselves, but in opposite directions). Unless the crack is opened enough so that protrusions on the opposing faces are not interleaved, shearing may cause the protrusions to interfere with each other.

When protrusions on opposing crack faces come into contact with each other, they deform elastically. For wedge-shaped bumps, the deformation is essentially bending, as is illustrated qualitatively in Fig. 4. Consequently, contact occurs over a finite region, the contact patch, whose size is small relative to other dimensions of the problem. In general, the contact pressure is not uniform over the patch. A much simpler problem is obtained if we assume that the contact patch is essentially a point, so that the pressure distributed over the patch is replaced by a point load (concentrated force), P, as shown in Fig. 2. Except for a small region in the immediate vicinity of the point where the force is applied, the stress field associated with this simpler problem will be the same as that for the more realistic problem. The difference near the force is not important for the present study, because the stresses that produce fracture are those at the crack tip, which is outside the wedge.

The contact force P arising from shearing of the crack can be found by iteration. Consider the problem illustrated in Fig. 5, which shows a line crack subjected simultaneously to uniform biaxial stress and the concentrated loads shown in Fig. 3. Solution of the equations of elasticity for this problem gives a certain shearing displacement, u, at the location of the concentrated loads. But with interference like that shown in Fig. 1, each value of u implies a certain amount of bending of the wedges. The bending, in turn, implies a certain contact force, P. Again, the equations of elasticity allow us to calculate the value of P corresponding to a given value of u. Given the biaxial stress field and the wedge geometry, only one value of P and one value of u can simultaneously satisfy the equations of elasticity for the two problems pictured in Figs. 2 and 4. Thus, the two steps in our iteration procedure are step A, calculation of u for a given value of P, and step B, calculation of P for a given value of u. We begin with step A and P equal to zero. The procedure consists of alternating between steps A and B until convergence is achieved. Once the correct value of P is found, its influence on the stress fields at the crack tips can be calculated.

From the discussion above, it is clear that two elasticity problems must be solved before the iteration procedure can be used. The solutions we use are based on the well-known complex variable formalism of Kolosov and Muskhelishvili (see [1, 2]). In this approach, the partial differential equations of elasticity are exchanged for integral equations from whose solutions stresses and displacements can be derived. We have derived the solution required for step A, which corresponds to Fig. 5, from results given in [3]. The solution for step B, which corresponds to Fig. 2, is not available from the literature. Using the techniques of conformal mapping and analytic continuation, we have produced an original solution for the system of Fig. 2 (a concentrated normal force applied to one side of a wedge-shaped bump on a half-space). (Reference [4] was essential to our success in this effort.) Details of these solutions and results of the computer-based iteration procedure will be presented in subsequent interim reports.

In the immediate future, the simulation referred to above will be used to answer several questions, among which are the following.

1. How far apart must the wedges be so that replacing them by concentrated loads is valid? (The answer comes from comparing the solution for Step B with the solution for concentrated loads on a half-space.)

2. For what ranges of the various parameters (wedge half-angle, ratio of wedge height to crack length, ratio of principal stresses, orientation of crack relative to principal axes, and stress level) does crack-face interaction significantly affect the stress intensity factors K_I and K_{II} at the crack tips?

3. When crack-face interaction is important, what happens to predictions of the level of stress required to initiate fracture?

4. For biaxial tests, does this model give better predictions of fracture-initiating stress levels than

those given by the usual methods (which neglect crack-face interference)?

References

[1] Muskhelishvili, N.I.
Some Basic Problems from the Mathematical Theory of Elasticity.
P. Noordhoff, 1953.

[2] Muskhelishvili, N.I.
Singular Integral Equations.
P. Noordhoff, 1953.

[3] Erdogan, F.
On the stress distribution in plates with collinear cuts under arbitrary loads.
In R. M. Rosenberg (editor), *Proceedings of the Fourth U.S. National Congress of Applied Mechanics, Vol. 1*, pages 547-553. ASME, 1962.

[4] England, A.H.
Complex Variable Methods in Elasticity.
Wiley-Interscience, 1971.

Status of Milestones

The milestone schedule is as follows:

2111001	Jun-15-88
2111002	Aug-15-88
2111003	Aug-15-88

Publications

None.

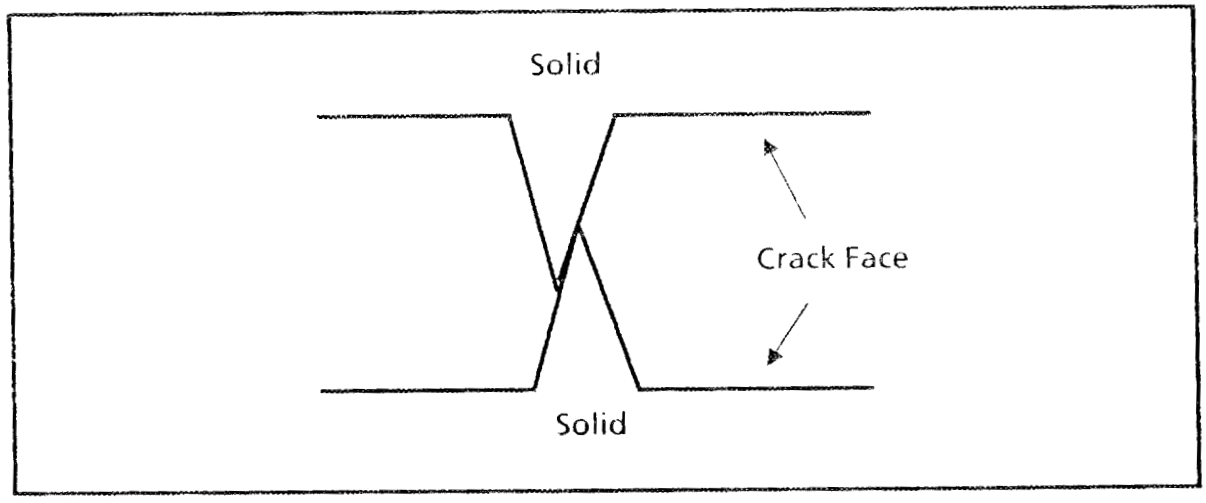

Figure 1. Interference between wedge-shaped bumps on crack faces.

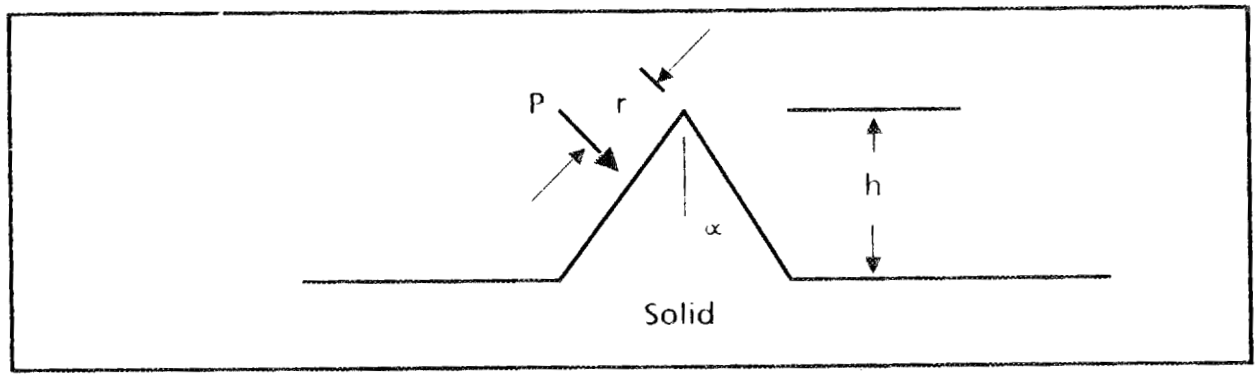

Figure 2. Concentrated normal force on one face of a wedge-shaped bump on a half-space

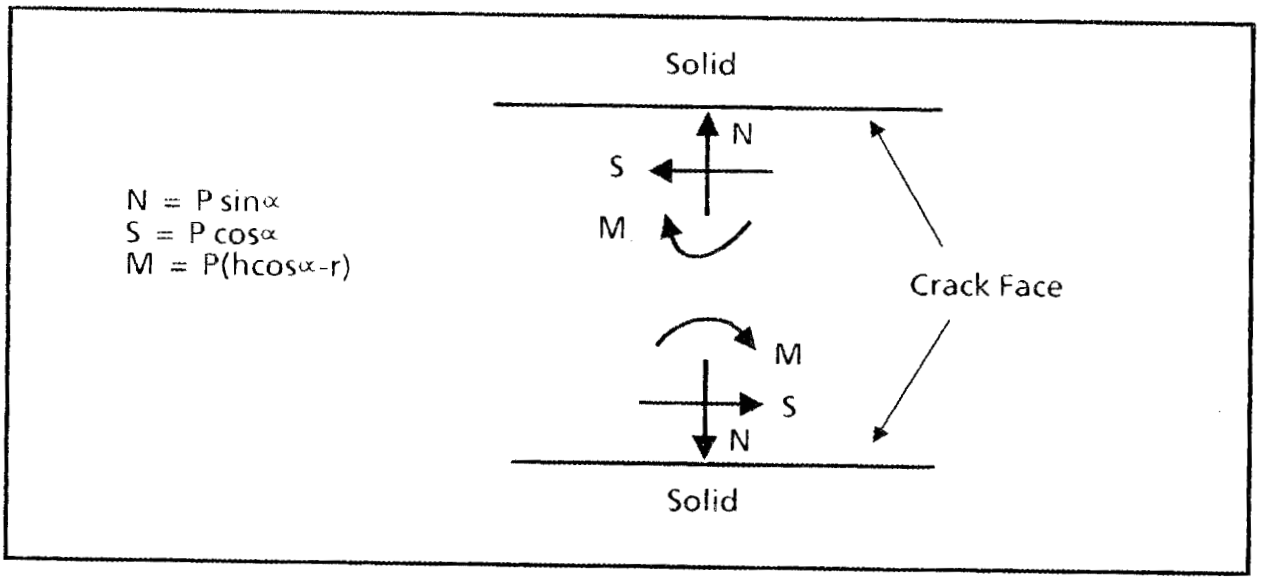

Figure 3. Line crack with concentrated loads representing wedge bump interference.

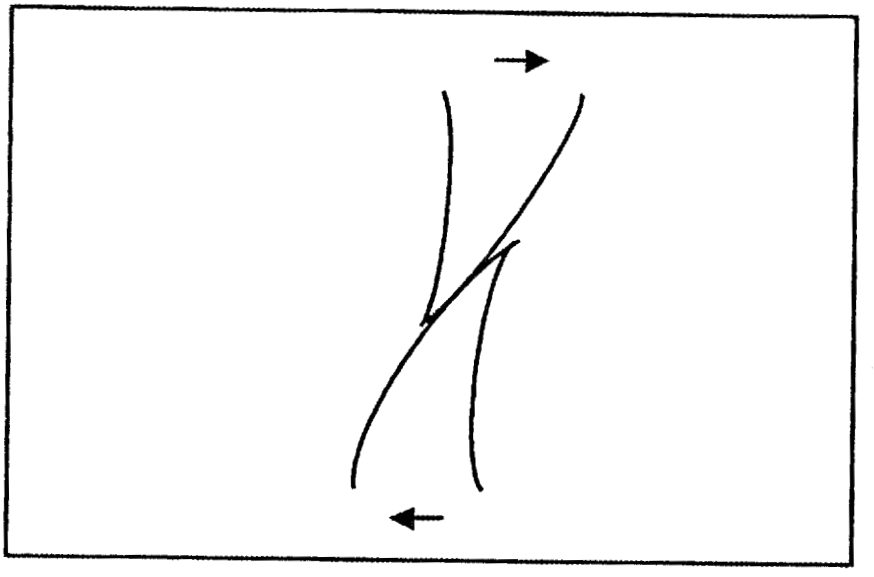

Figure 4. Wedge-wedge contact.

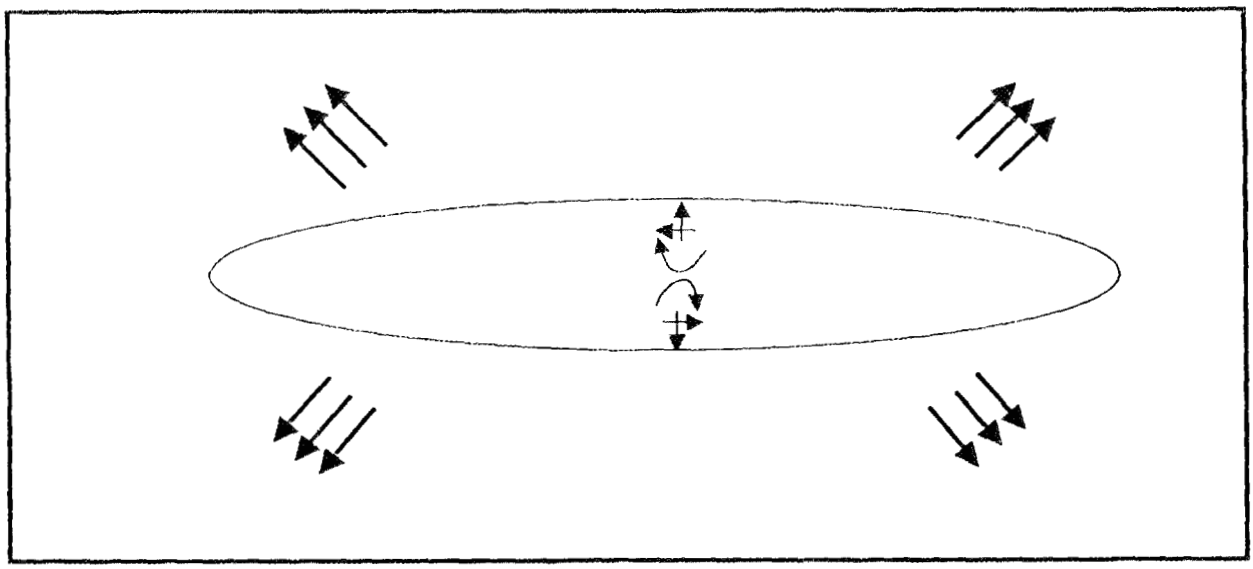

Figure 5. Line crack subjected simultaneously to arbitrarily oriented uniform biaxial stress at infinity and concentrated loads on the crack faces.

2.2 CONTACT INTERFACES

2.2.2 Dynamic Interfaces

Studies of Dynamic Contact of Ceramics and Alloys for Advanced Heat Engines

K. F. Dufrane and W. A. Glaeser (Battelle Columbus Division)

Objective/scope

The objective of the program is to develop an understanding of the friction and wear processes of ceramic interfaces based on experimental data. The supporting experiments are to be conducted at temperatures to 650 C under reciprocating sliding conditions reproducing the loads, speeds, and environment of the ring/cylinder interface of advanced low heat rejection engines. The test specimens are to be carefully characterized before and after testing to provide detailed input to the model. The results are intended to provide the basis for identifying solutions to the tribology problems limiting the development of these engines. The original three-year program was completed in September 1987, and a two-year follow-on was initiated in October 1987 to consider additional materials, ion implantation and high temperature lubricants.

Technical progress

Apparatus

The apparatus developed for this program uses specimens of a simple flat-on-flat geometry, which facilitates specimen procurement, finishing, and testing. The apparatus reproduces the important operating conditions of the piston/ring interface of advanced engines. The specimen configuration and loading is shown in Figure 1. The contact surface of the ring specimen is 3.2 x 19 mm. A crown with a 32 mm radius is ground on the ring specimen to ensure uniform contact. The ring specimen holders are pivoted at their centers to provide self-alignment. A chamber surrounding the specimens is used to control the atmosphere and contains heating elements to control the temperature. The exhaust from a 4500 watt diesel engine is heated to the specimen temperature and passed through the chamber to provide an atmosphere similar to that of actual diesel engine service. A summary of the testing conditions is presented in Table 1.

Materials

The materials to be procured and evaluated in the current phase will include advanced toughened ceramics, such as silicon carbide whisker-reinforced alumina, silicon carbide whisker-reinforced silicon nitride, and nickel aluminide bonded tungsten carbide. Coating methods will include plasma spray, electro spark alloying, and ion implantation.

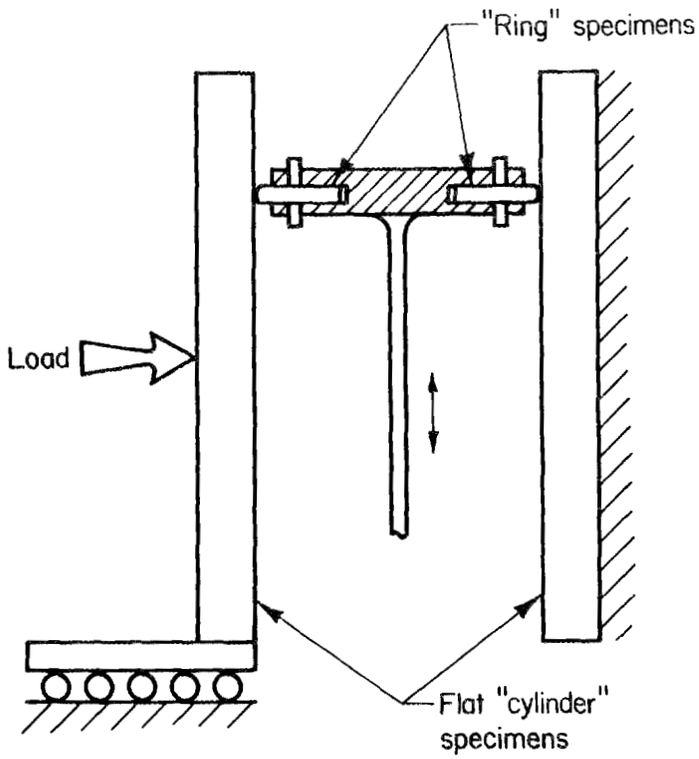

Figure 1. Test specimen configuration and loading

TABLE 1. SUMMARY OF TESTING CONDITIONS

Sliding Contact:	Dual flat-on-flat
"Cylinder" Specimens:	12.7 x 32 x 127 mm
"Ring" Specimens:	3.2 x 19 x 19 mm
"Ring" crown radius:	32 mm
Motion:	Reciprocating, 108 mm stroke
Reciprocating Speed:	500 to 1500 rpm
Average Specimen Speed:	1.8 to 5.4 m/s
Load:	to 950 N
Ring Loading:	to 50 N/mm
Atmosphere:	Diesel exhaust or other gases
Measurements:	Friction and wear (after test)

Cylinder specimens of four different compositions have been received for evaluation in the program. The materials represent either different basic compositions from those evaluated previously or represent different bonding approaches.

Cylinder Material	Source
K 162B (TiC-Ni/Mo)	Kennametal, Inc.
Sialon	Kennametal, Inc.
Sialon - SiC	Kennametal, Inc.
Si_3N_4 (sinterable)	Cercom, Inc.

Coated ring specimens were also received from Wear Technology for evaluation. The coatings were applied to AISI 410 stainless steel by an electrospark alloying (ESA) process. The coating identifications were:

VR73	WC/TaC/TiC/Co,
VA 20	WC/TaC/TiC/Ni,
CA 815	Cr_3C_2/Ni, and
Moly	Mo.

Ring specimens were also prepared at Battelle with a plasma sprayed Cr_2O_3 coating on a mild steel substrate.

The lubricant used in the experiments has been SDL-1, a polyalphaolefin synthetic oil. This oil is subject to rapid oxidation at temperatures above approximately 250 C and produces tenacious decomposition products. While lubricant development efforts are being conducted in other contracts to formulate suitable lubricants for higher operating temperatures, the results are not likely to be available for use in this study. Therefore, future experiments will evaluate the suitability of polyalkyleneglycol. This fluid also decomposes at temperatures above 260 C, but does not leave a residue as part of the oxidation process. Therefore, operating at higher temperatures, such as 350 to 400 C, should be possible without forming undesirable deposits.

Wear Experiments

In the first phase of the study the need for lubrication at the ring/cylinder interface was established by the high friction coefficients and wear rates measured during dry sliding of a variety of monolithic ceramics and ceramic coatings. With lubrication, the wear rates of ceramic coatings such as Cr_2O_3 and WC tested at 260 C were found to approach those measured in heavy duty truck engines with conventional ring/cylinder materials. With the need for lubrication, the maximum operating temperature with ceramics was found to be limited by the availability of suitable lubricants.

Experiments were conducted to determine the potential benefit of a proprietary surface preparation, Ceratek, applied by PCK Technology on Si_3N_4 cylinder specimens. The preparation produces an Au/Co/Ni alloy coating bonded to the Si_3N_4 surface. Mating ring specimens of cobalt-bonded tungsten carbide were used in both a control experiment (as-ground

Si_3N_4) and with the Ceratek specimens. The experiments were conducted at 260 C using SDL-1 polyalphaolefin lubricant after break-in at room temperature and 100 C. The calculated wear coefficient for the ring specimens operating against as-ground Si_3N_4 was 6×10^{-7}, whereas the wear coefficient for the ring specimens operating against the Ceratek-treated Si_3N_4 was 1×10^{-6}. In both cases the friction coefficient was in the range of 0.03 to 0.06. On the basis of these single experiments, the Ceratek treatment on Si_3N_4 produced no apparent advantage over the as-ground Si_3N_4 specimens.

A wear experiment was initiated using the K 162 B (TiC-Ni/Mo) cylinder specimens and Cr_2O_3-coated ring specimens and SDL-1 (polyalphaolefin) as the lubricant. The initial surface finish of the cylinder specimens was 6 to 8 microinches cla. After one hour of running at room temperature at 500 rpm and a light load of 12.3 N/mm, the ring wear coefficient was calculated to be a relatively high 3×10^{-6}. Examination of the profilometer traces showed that although the initial surface finish was quite low, the texture consisted of numerous small peaks, presumably from edges of the TiC grains standing in relief. After the initial running period at room temperature, the ring wear coefficient decreased to 6×10^{-7} during 4 hours of running at 100 C. Operation at 260 C for 4 hours resulted in an increase in the average wear coefficient to 1×10^{-6}. Although one ring specimen had a relatively low wear rate, the wear rate on the other remained high. The surface finish on the cylinder specimens improved to 1.7 microinches cla after the nine hours of running. The experiment will be continued to determine whether the wear rate on the second ring specimen will decrease also as result of the improved surface finish.

While the initially high wear coefficient experienced by the ring specimens operating against the TiC cylinder specimens would be undesirable if it were to continue, it may provide a means for ring seating in an actual engine. While the Cr_2O_3-coated rings provide much improved wear resistance relative to that of metallic rings, practical engines will require the rings to "seat", or wear preferentially to accommodate geometric imperfections. Therefore, a high initial wear rate to enhance seating may be desirable.

Status of Milestones

The study is progressing in accordance with the overall milestone schedule.

Publications

A paper titled "Wear Performance of Ceramics in Ring/Cylinder Applications" has been submitted to the American Ceramics Society for publication.

2.3 NEW CONCEPTS

Advanced Statistical Concepts of Fracture in Brittle Materials

C. A. Johnson and W. T. Tucker (General Electric Corporate Research and Development)

Objective/Scope

The design and application of reliable load-bearing structural components from ceramic materials requires a detailed understanding of the statistical nature of fracture in brittle materials. The overall objective of this program is to advance the current understanding of fracture statistics, especially in the following three areas:

- Optimum testing plans and data analysis techniques.
- Consequences of time-dependent crack growth on the evolution of initial flaw distributions.
- Confidence and tolerance bounds on predictions that use the Weibull distribution function.

The studies are being carried out largely by analytical and computer simulation techniques. Actual fracture data are then used as appropriate to confirm and demonstrate the resulting data analysis techniques.

Technical Highlights

During the previous six month reporting period, work concentrated on the last of three milestones for this year. This milestone is an effort to develop methods for generating tolerance bounds on estimates of strengths. The following describes the results of these efforts toward the third milestone.

Numerical simulation studies for conformation testing of previously developed methods, likelihood ratio and exact conditional integration, for determining confidence/tolerance bounds in Class III problems have been completed. It turns out, at least for location-scale and certain other families, that there is a relationship (Hinkley (1), Barndorff-Nielsen (2)) between the two methodologies; the likelihood ratio method just gives a numerical approximation to the integration approach. Moreover, when there are only a single test volume condition and a single component volume condition, conditional integration methods (going back to Fisher (3) and employed by Lawless (4)) are exact (Barndorff-Nielsen (5,2)). This situation falls into what is called a group transformation model, for which the location-scale models are special cases. Also, preliminary theoretical results indicate that for other Class III problems the integration method is again exact; these simulation studies should help to resolve

this issue.

Indeed, initial runs indicate that when testing and estimating the Weibull modulus and inherent strength at three distinct sizes and computing tolerance bounds at various other conditions, that the integration method is exact. Also these preliminary results indicate that the likelihood ratio method (which only gives approximate limits) may be more precise for the same number of total observations when this total is spread out over more than a single size of test specimens. Finally, the methodology to obtain confidence and tolerance bounds for Class IV problems is yet to be developed and is, among other things, to be studied in the follow-on effort.

In all simulation trials a Weibull distribution with $m = 1$ and $\sigma_0 = 1$ (e.g., a standard exponential) was employed. This is proper and adequate since $\hat{m}$ and $\hat{\sigma}_0$ have a form of equivariance (Lawless (6)). This then implies, among other things, that the distributions of $\hat{m}/m$ and $\hat{m}\ln(\hat{\sigma}_p/\sigma_p)$ are independent of m and σ_0. In this setup $\sigma_p = [(1/kV)\ln(1/(1-p))]^{1/m}$ and gives the quantile at proportion p. (A confidence interval on σ_p is then a type of tolerance interval, and these confidence intervals were the subject of the simulation study.) These results could be employed to develop unconditional confidence limits in the same manner as do Thoman, Bain, and Antle (7). However, this would require simulation to determine the percentage points of the required distributions for each sample size (number of specimens) and combination of specimen sizes (the problem is not analytically tractable). This is essentially an undoable task; one does not know ahead just what combination of specimen sizes and numbers that might be employed in future experimental schemes.

However, the previous results can be employed to show that the $a_i = (x_i/\hat{\sigma}_p)^{\hat{m}}$ are ancillary statistics. Then these results imply that the conditional integration method is exact for the general Class III problem. And, in any event, if the conditional method is not exact the likelihood ratio method can be employed. It only suffers the drawback of not being exact for finite sample sizes ("small" in practice). It is, however, asymptotically exact and, therefore, the approximation improves as the sample size is increased.

Moreover, the estimators and confidence limits only depend on the relative sizes. That is, the ratio of the test specimen sizes to the component size is all that is relevant for analysis purposes. Thus, for example, employing a total of 15 specimens equally allocated at sizes of 1.0, 10.0, and 100.0 and a component size of 1000.0 is equivalent to 15 specimens equally allocated at sizes of, say, 10.0, 100.0, and 1000.0 and a component size of 10000.0. This fact and the invariance with respect to the true parameter values can be employed to reduce the coverage

of the simulation study. Even so, the results presented herein should be augmented in the future with additional simulation studies.

The simulation studies consist of two major investigations: miscellaneous runs to verify the procedure, and a specific study carried out at three distinct sizes. Each simulation run consists of 500 individual trials and in all cases the confidence coefficient was 0.95. For this setup the standard error for the estimated coverage probability is 0.00698212 for an individual limit and 0.00979796 for a two sided interval. These values can be used as guides in checking the veracity of the procedures investigated in the simulation studies. Also for all trials only a single quantile, 0.05, was investigated. Unless otherwise stated the runs were begun with a different random number seed, generally, the ending seed of the previous run.

For the verification studies only a single testing condition was employed. The first suite investigated relative sizes and a common seed was employed for two separate runs. The first consisted of 15 observations at a size of 1.0 with a component at 10.0 while the second consisted of 15 observations at a size of 10.0 with a component at 100.0. The results are presented in Table 1 where are shown the number of covers of the respective confidence intervals on a given run. Also shown for comparison purposes are the respective proportions of coverage. As can be seen, the coverage results are identical for the two size setups. Furthermore, a record was kept of any trial in which at least one miss was observed. These records were identical for each of the simulation runs, and in each case both $\hat{m}$'s agreed and, to within the proper scale factor, the confidence intervals also agreed. All of this is consistent with the fact that only relative size is important in the calculations. Note that while the interval coverage of the likelihood ratio (lr) method was adequate, the lower limit under covered and the upper limit somewhat over covered. This general pattern persists for the lr method, but the effect diminishes as the total sample size is increased.

Shown in Table 2 are the results of a replication study: three runs with 15 observations at a size of 1.0 and a component size of 10.0 in each. And shown in Table 3 are the results of a sample size comparison: three runs with 10, 20, and 30 observations each at a size of 1.0 with a component at 10.0. All in all the simulation results agree with known results concerning the two methods. That is, the integration method is exact and the lr method is an approximation. In this regard much work has been done in obtaining corrections for the bias in the lr method. For example, see Barndorff-Nielsen and Cox (8). Also the lr approach is probably adequate with a suitably allocated total sample size of approximately 30 observations.

With this verification study as background, a larger study investigating the effects of more than one specimen size was performed. In all runs, observations were allocated to the sizes 10.0, 100.0, and 1000.0 with various component sizes. The sample sizes were 3, 4, 3 and 5, 5, 5 with the stated specimen sizes. Thus total sample sizes of 10 and 15 were studied. The results are shown in Tables 4 and 5. The first, second, and fifth entries in Table 4 were carried out with the same starting seed so that a direct comparison could be made when predicting to various component sizes. Inspection of these results reveals that for this seed the integration method suffers less bias with respect to coverage across the various component sizes than does the lr method. Also the lr method appears to perform better at the intermediate and largest component sizes than at the smallest component size. Comparing, in a general sense, the results for the integration method to the previous results indicates that there is no reason to doubt that the integration method is also exact in the differing specimen size situation.

As noted, the runs in Table 5 were started with seeds from earlier runs in Tables 1 and 2. This was done so as to allow a more or less direct comparison on the effect of spreading out the observations over differing specimen sizes. Inspection of the corresponding Table entries indicates that the integration method performed about the same irrespective of the specimen allocation. However, the lr method results are very much improved when the specimen observations are spread among the three sizes. This phenomenon needs to be investigated further (recall the results of Table 4 concerning the lr method). For example, does it hold when the component size is at an extreme in the size range, say, at 1.0 or 10000.0 in the simulation study? Finally, overall inspection of the results indicates that the integration method may well be exact in the general Class III problem.

REFERENCES

1. Hinkley, D. V. (1978), "Likelihood inference about location and scale parameters," Biometrika, **65**, 253-261.

2. Barndorff-Nielson, O. E. (1983), "On a formula for the distribution of the maximum likelihood estimator," Biometrika, **70**, 343-365.

3. Fisher, R. A. (1934), "Two new properties of mathematical likelihood," Proc. Royal Society A, **144**, 285-307.

4. Lawless, J. F. (1975), "Construction of tolerance bounds for the extreme-value and Weibull distributions," Technometrics, **17**, 255-61.

5. Barndorff-Nielson, O. E. (1980), "Conditionality Resolutions," Biometrika, 67, 293-310.

6. Lawless, J. F. (1982), Statistical Models and Methods for Lifetime Data, John Wiley and Sons, New York.

7. Thoman, D. R., L. J. Bain, and C. E. Antle (1969), "Inferences on the Parameters of the Weibull Distribution," Technometrics, 2, 445-60.

8. Barndorff-Nielson, O. E. and D. R. Cox (1984) "Bartlett Adjustments to the Likelihood Ratio Statistic and the Distribution of the Maximum Likelihood Estimator," J. R. Statist. Soc., 46, 483-495.

Status of Milestones

The three milestones for the third year of the program have been completed.

Table 1

RELATIVE SIZE COMPARISON
n = 15

Size	Method					
	Integration			Likelihood Ratio		
	Interval	Lower	Upper	Interval	Lower	Upper
1.0/10.0	478 .956	489 .978	489 .978	468 .936	475 .950	493 .986
10.0/100.0	478 .956	489 .978	489 .978	468 .936	475 .950	493 .986

Table 2

REPLICATION TRIALS
n = 15

Size	Method					
	Integration			Likelihood Ratio		
	Interval	Lower	Upper	Interval	Lower	Upper
1.0/10.0	479 .958	491 .982	488 .976	469 .938	475 .950	494 .988
1.0/10.0	480 .960	492 .984	488 .976	473 .946	479 .958	494 .988
1.0/10.0	476 .952	484 .968	492 .984	471 .942	473 .946	498 .996

Table 3

SAMPLE SIZE COMPARISON
Size: 1.0/10.0

n	Method					
	Integration			Likelihood Ratio		
	Interval	Lower	Upper	Interval	Lower	Upper
10	474 .948	487 .974	487 .974	466 .932	472 .944	494 .988
20	476 .952	488 .976	488 .976	473 .946	481 .962	492 .984
30	480 .960	493 .986	487 .974	472 .944	483 .966	489 .978

Table 4

DIFFERING SPECIMEN SIZES
n=3 at 10.0, n=4 at 100.0, n=3 at 1000.0
Total n=10

Component Size	Method					
	Integration			Likelihood Ratio		
	Interval	Lower	Upper	Interval	Lower	Upper
1.0*	473 .946	487 .974	486 .972	464 .928	492 .984	472 .944
100.0*	471 .942	485 .970	486 .972	471 .942	483 .966	488 .976
100.0	469 .938	481 .962	488 .976	468 .936	478 .956	490 .980
100.0	473 .946	488 .976	485 .970	465 .930	479 .958	486 .972
10000.0*	473 .946	488 .976	485 .970	470 .940	482 .964	488 .970

*Same starting seed

Table 5

DIFFERING SPECIMEN SIZES
n=5 at 10.0, n=5 at 100.0, n=5 at 1000.0
Total n=15

Component Size	Method					
	Integration			Likelihood Ratio		
	Interval	Lower	Upper	Interval	Lower	Upper
100.0[1]	484 .968	493 .986	491 .982	482 .964	490 .980	492 .984
100.0[2]	472 .944	484 .968	488 .976	467 .934	476 .952	491 .982
100.0[3]	475 .950	491 .982	484 .968	471 .942	486 .972	485 .970

[1]Same starting seed as Table 1 runs
[2]Same starting seed as 1st run in Table 2
[3]Same starting seed as 3rd run in Table 2

3.0 DATA BASE AND LIFE PREDICTION

INTRODUCTION

This portion of the project is identified as project element 3 within the work breakdown structure (WBS). It contains five subelements, including (1) Structural Qualification, (2) Time-Dependent Behavior, (3) Environmental Effects, (4) Fracture Mechanics, and (5) Nondestructive Evaluation (NDE) Development. Research conducted during this period includes activities in subelements (1), (2), and (3). Work in the Structural Qualification subelement includes proof testing, correlations with NDE results and microstructure, and application to components. Work in the Time-Dependent Behavior subelement includes studies of fatigue and creep in structural ceramics at high temperatures. Research in the Environmental Effects subelement includes study of the long-term effects of oxidation, corrosion, and erosion on the mechanical properties and microstructures of structural ceramics.

The research content of the Data Base and Life Prediction project element includes (1) experimental life testing and microstructural analysis of Si_3N_4 and SiC ceramics, (2) time-temperature strength dependence of Si_3N_4 ceramics, and (3) static fatigue behavior of PSZ ceramics.

Major objectives of research in the Data Base and Life Prediction project element are understanding and application of predictive models for structural ceramic mechanical reliability, measurement techniques for long-term mechanical property behavior in structural ceramics, and physical understanding of time-dependent mechanical failure. Success in meeting these objectives will provide U.S. companies with the tools needed for accurately predicting the mechanical reliability of ceramic heat engine components, including the effects of applied stress, time, temperature, and atmosphere on the critical ceramic properties.

3.1 STRUCTURAL QUALIFICATION

Failure Analysis

B.J. Hockey, Jr. and S.M. Wiederhorn (National Bureau of Standards)

Objective/Scope:

The objective of this part of the program is to identify the mechanisms of failure in structural ceramics subjected to mechanical loads in various test temperatures and environments. Of particular interest is the damage that accumulates in structural ceramics as a consequence of high temperature exposure to environments and stresses normally present in heat engines.

Design criteria for the use of ceramics at low temperature differ from those at high temperature. At low temperature ceramics are elastic and brittle; failure is controlled by a distribution of flaws arising from processing or machining operations, and the largest flaw determines the strength or lifetime of a component. By contrast, at high temperature where ceramics are viscoelastic, failure occurs as a consequence of accumulated, or distributed damage in the form of small cavities that are generated by the creep process. This damage effectively reduces the cross-section of the component and increases the stress that must be supported. Such increase in stress is in a sense autocatalytic, since it increases the rate of damage and eventually leads to failure as a consequence of loss in cross section. When this happens, the individual flaw loses its importance as a determinant of component lifetime. Lifetime now depends on the total amount of damage that has occurred as a consequence of the creep process. The total damage is now the important factor controlling lifetime.

Recent studies of high temperature failure of the non-oxide ceramics intended for use for heat engines indicates that for long term usage, damage accumulation will be the primary cause of specimen failure. Mechanical defects, even if present in these materials, are healed or removed by high temperature exposure so that they have little influence on long term lifetime at elevated temperature. In this situation, lifetime can be determined by characterizing the nature of the damage and rate of damage accumulation in the material at elevated temperatures. In ceramic materials such as silicon nitride and the sialons, such characterization requires the use of high resolution techniques of analysis because of the fine grain size of these materials: hence the need for transmission electron microscopy as an adjunct to the mechanical testing of ceramics for high temperature applications is apparent.

In this project, the creep and creep-rupture behavior of several ceramic materials will be correlated with microstructural damage that occurs as a function of creep strain and rupture time. Materials to be studied include: sialons; hot-pressed silicon nitride; and sintered silicon carbide. This project will be coordinated with WBS 3.4.1.3, Tensile Creep Testing, with the ultimate goal of developing a test methodology for assuring the reliability of structural ceramics for high temperature applications.

Technical Highlights:

During the past six months an analysis of the microstructure of siliconized silicon carbide (SOHIO KX01) in both the as received and deformed condition was completed and a technical publication describing the results completed and submitted for publication. The principle findings of this work is relevant to mechanisms of deformation and failure of two phase materials. Microstructural data obtained on both deformed and as-received materials suggest that the material deforms like an assembly of unequal spheres which tend to form clustered elements that slide past one-another during deformation. Within each element, the spheres have relatively fixed positions; sliding and damage resulting from sliding occurs primarily at the boundary of each element. Deformation is inhomogeneous and tends to occur in increments. Reorientation of stresses within the solid and transfer of stress to the second phase occurs when contact asperities between elements are broken or slide past one another. The model adopted is identical to that used by geologists to explain the deformation of particle aggregates.

The model agrees with microscopic observations made to date. Contact damage is observed to occur within the SiC grains at isolated points throughout the solid, figure 1. More damage occurs in compression than in tension, as would be expected if creep occurred primarily by the sliding of particles of the material over one another. In compression, the net pressure resulting from the applied stress pushes the particles together increasing the difficulty of deformation. In tension, the particles are pulled apart and can slide over one another more easily. This not only leads to less damage at the contact asperities in tension than in compression, but also requires a greater force for deformation in compression than in tension, which is actually observed in materials tested, figure 2.

The model can also be used to rationalize the increase in creep rate exponent in both tension and compression when the applied stress increases beyond a critical stress for each mode of loading. The fact that compressive specimens support creep loads above the melting point of silicon suggests that creep in compression is controlled by deformation of the SiC particles of the composite. This suggestion is supported by evidence from TEM studies, which indicate that the composite creeps in compression primarily by plastic deformation of the contact points between SiC grains. By itself, this kind of deformation would result in a creep exponent of 3 to 5 as is observed for most other dislocation mechanisms of creep and would not explain the high creep exponent observed at high stresses in compression. If, however, accelerated slip were to occur at some of the contact points between grains so that the contact points ruptured, then a rapid redistribution of load would occur as the contact point ruptured, resulting in an increment of strain in the vicinity of the contact point. The load that was supported by the ruptured contact point would then be picked up by other contact points in the material, and the deformation would continue. This is the same sort of deformation model that is responsible for the generation of earthquakes, and is referred to as stick-slip-deformation. Since cavities are not observed in compression, the increment of strain envisioned at the rupture of a contact asperity

would have to be a shear strain. When such "stick-slip" occurs, the creep rate depends not on the rate of deformation of contact points between elements, but on the rate at which the contact points rupture, so that rupture kinetics determine the rate of creep, and the stress exponent of the creep rate is not necessarily equal to that of the basic creep mechanism. The same model can also be applied to explain the abrupt change creep exponent with increasing stress. In tension, however, rupture of the contact points results in an abrupt transfer of addition stress to the silicon phase which results in cavitation.

Status of Milestones:

To date, all milestones have been met or are on schedule. We will be presenting a talk on the subject at the Annual Meeting of the American Ceramic Society this spring (Milestone 311101) and have already written a technical paper on this work (Milestone 311102).

Publications:

"Effect of Creep on the Microstructure of Reaction Bonded Silicon Carbide," B.J. Hockey and S.M. Wiederhorn, J. Amer. Ceram. Soc. submitted.

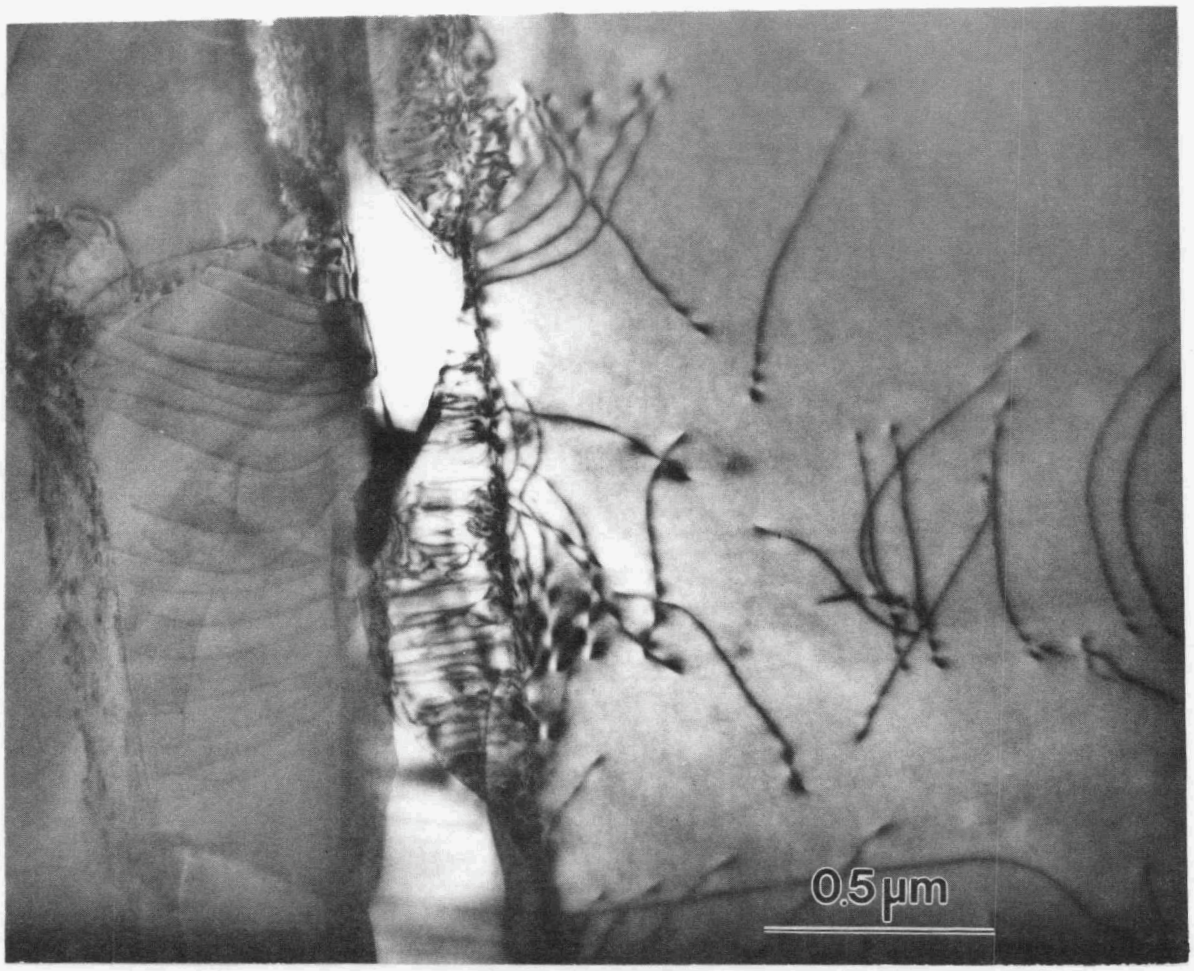

1. Contact damage in silicon carbide resulting from deformation in which the grains of SiC tend to slide over one another. The same type of deformation is observed in both tension and compression, however, much less occurs in tension. This damage lends qualitative support to a model that describes the flow as a granular assembly of particles.

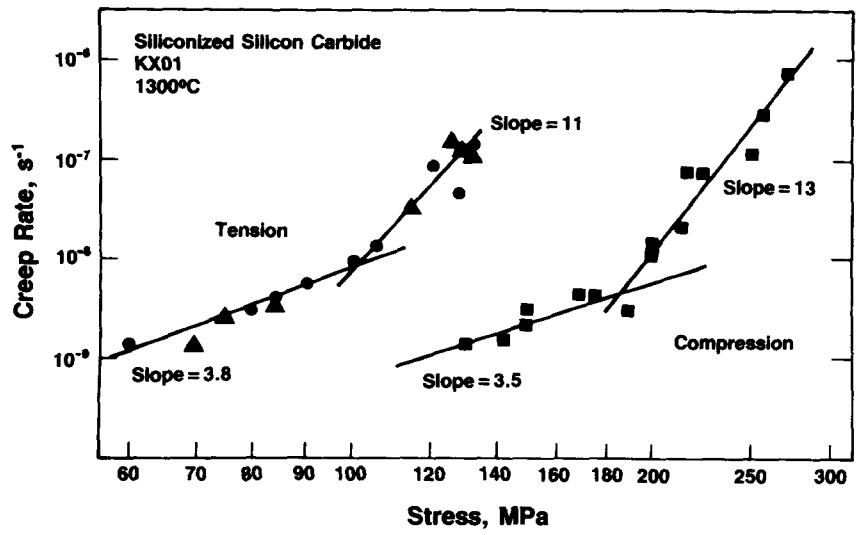

2. A comparison of creep rates in tension and in compression. The material creeps much more readily in tension than in compression. Tensile and compressive creep both follow a bimodal behavior in which the creep rate accelerates as the stress increases above a critical stress.

Physical Properties of Structural Ceramics

R. K. Williams, J. B. Bates, R. S. Graves, D. L. McElroy, and
F. J. Weaver (Oak Ridge National Laboratory)

Objective/scope

The structural ceramics which will be used in the combustor chambers of advanced heat engines must also thermally isolate the metallic parts of the engine from the high temperature combustion gases. The ceramics being considered for this application are complex materials which are toughened by the presence of a second phase. The purpose of this task is to develop an improved understanding of the factors which determine the thermal conductivities of these structural materials at high temperatures. This study is required because the thermal conductivities of the ceramics of interest are generally not known at high temperatures, and the theory has not yet been sufficiently developed to yield reliable predictions. The influences of second phase type, content, shape and of parallel energy transport by photons are of particular importance. At present our understanding of these variables is at best only qualitative. The two areas which will be investigated are the role of photon transport at high temperatures and the influence of second phase additions.

Technical progress

At high temperatures, both phonons and photons make significant contributions to energy transport in translucent ceramics.[1] The contributions of the two carriers are inferred from the observed effect of temperature on the thermal conductivity: phonons yield a contribution which decreases about as T^{-1}, while, in the absence of direct radiant transmission, photons produce a contribution which is roughly proportional to T^3 (ref. 2).

At present, thermal conductivities, are usually determined from thermal diffusivity, α, and specific heat data. The main purpose of this study was to make a comparison of results obtained in this way with data obtained by direct measurements of λ. This comparison was required because the data are used to design various advanced ceramic components which may be used in insulated heat engines,[3] and studies of fibrous insulating materials[4] suggest that the two methods for determining λ do not always yield identical results.

Experimental methods

The thermal diffusivity was obtained by the laser flash method,[5] and a differential scanning calorimeter was used to measure the specific heat. The thermal diffusivity apparatus had been highly developed over several years[6] and a Perkin Elmer Model DSC-2 (ref. 7) was used to make the specific heat measurements. Thermal diffusivity values were measured in vacuum over the temperature range 300-1473 K, and repeat measurements indicated that heating the samples to 1473 K did not cause significant changes in the measured α values. Specific heat data were obtained up to 873 K and linearly extrapolated to higher temperatures. Generally, λ values obtained in this way are thought to have absolute uncertainties of about ±10%.

The thermal conductivity was directly measured by two methods. A comparative longitudinal heat flow apparatus[8] was used to make preliminary measurements over the temperature range 305-365 K. The uncertainty of these data is about ±3% (ref. 9) and the 2-3% corrections used for metals[10] were not applied because tests with a Pyroceram standard[9] indicated that they are not appropriate for low λ materials.

Higher temperature λ measurements were made by the absolute radial heat flow method.[11] The data, which span the temperature range 320-1273 K, have an absolute uncertainty of about ±2% (ref. 12). These measurements were made in a helium atmosphere, which is required to produce satisfactory thermal contacts between the sample and the Pt-Pt10%Rh thermocouples.

Sample characteristics

The partially stabilized zirconia (PSZ) material was MS grade produced by Nilcra.[13] All of the stock was obtained in the form of 51-mm-diam, 25.4-mm-tall discs; the samples were machined with diamond tools. Two 12.7-mm-diam, 1.5-mm-thick samples were produced for the α measurements and the axes of these samples were oriented parallel and perpendicular to the axis of the starting stock. The material had a bulk density of 4.78 Mg/m^3. A quantitative electron microprobe measurement showed that 8.4% of the metallic ions were Mg^{++}.

The microstructure of the material is shown in Figs. 1, 2, and 3. These three figures show that the grain size and pore size distributions of the samples were not altered by high temperature anneals associated with the thermal property measurements. Also, X-ray diffraction measurements on specimens with metallographically polished surfaces showed that the ratio of monoclinic (grain boundary) to cubic plus tetragonal (matrix) zirconia remained at about 3% after all of the thermal treatments. The tetragonal phase is present as a finely divided precipitate in the cubic matrix of the ZrO_2 grains, and the MS grade generally contains about 35 vol % of tetragonal ZrO_2 (ref. 14).

The appearance of the samples did change during the α and λ measurements. Figure 4 shows that a darkened layer formed on the surface of the thermal conductivity samples, affecting about 10% of the sample volume. The change was more severe for the α samples, which turned from white to light brown during the measurements. This change appeared to alter the opacity of the material, since it was noted that the α sample was much easier to examine with a light microscope. The absorption coefficients of the samples are compared in Fig. 5. These data were obtained in a Cary 17D spectrophotometer,[15] and the results were experimentally corrected for reflective losses. The data show that heating PSZ increases its absorption coefficient by about a factor of two. This is presumably due to microstructural coarsening, which has no effect on the energy transport. The results also show that the darkened region of Fig. 4 transmits about as well as the α sample, and the central region of the radial heat flow samples is significantly (~25%) less opaque than either the darkened case or the α sample.

Y210447

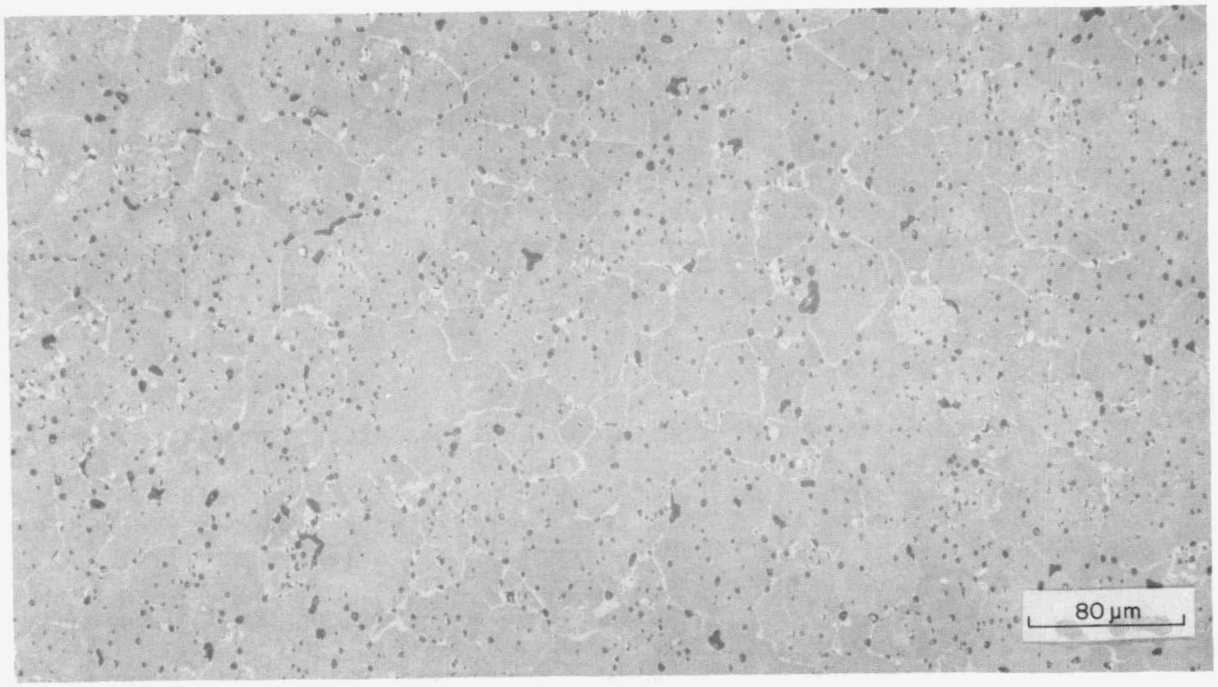

Fig. 1. As-received MS grade partially stabilized zirconia. Etched in water-10% HF.

Y210451

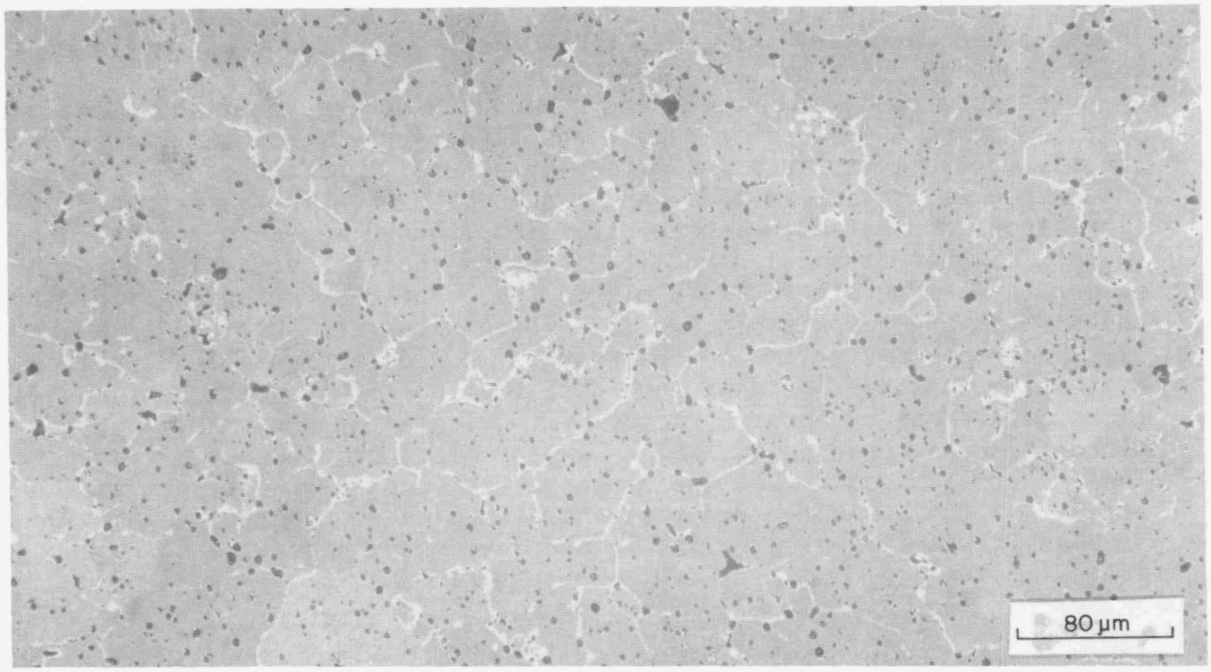

Fig. 2. MS grade partially stabilized zirconia after the radial heat flow thermal conductivity experiments. Sample was at 1273 K for about 48 h. Etched in water-10% HF.

Y210449

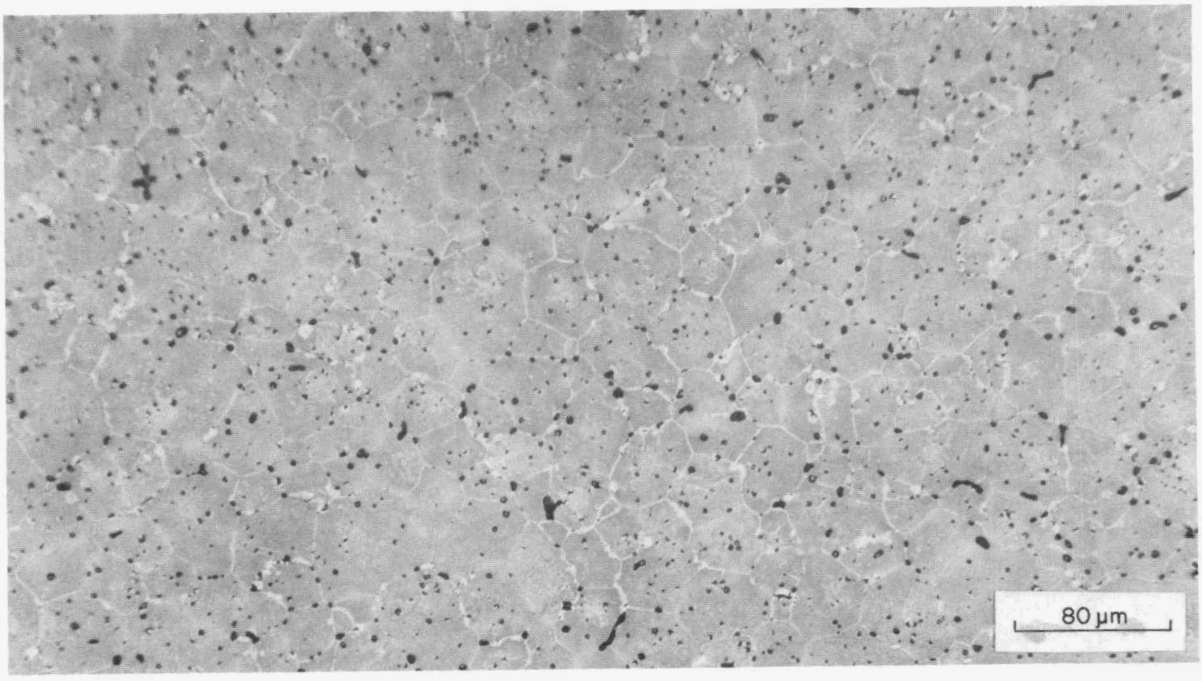

Fig. 3. MS grade partially stabilized zirconia after thermal diffusivity measurements. Sample was at 1473 K in vacuum for about 30 min. Etched in water-10% HF.

YP5188

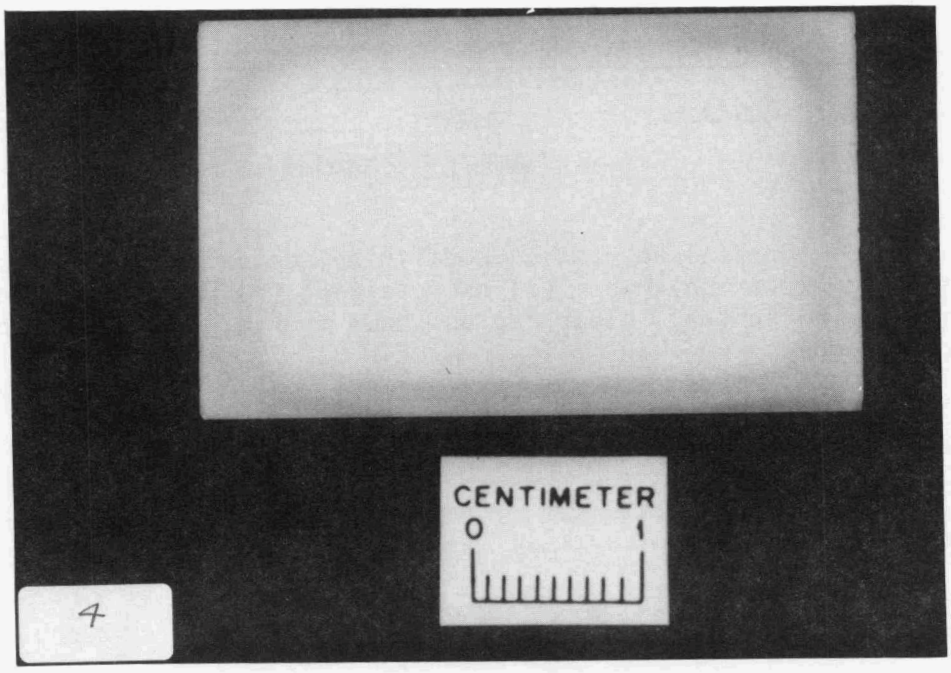

Fig. 4. Section through one of the radial heat flow samples after the measurements were completed. Darkened layer on surface affects about 10% of the sample.

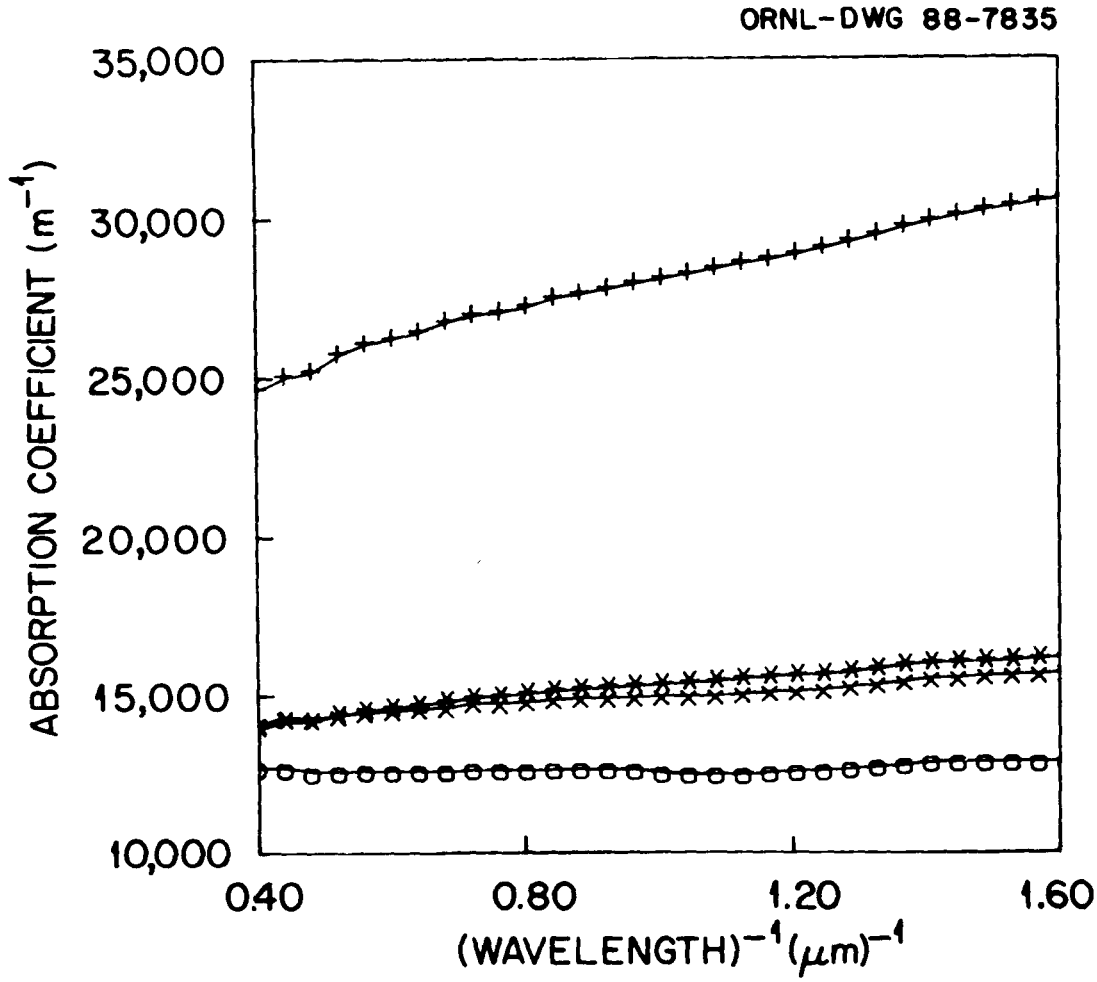

Fig. 5. Optical absorption coefficient data for the PSZ samples. The symbols are as follows: (+) as received; (*) dark, core region shown in Fig. 4; (○) central, clear region shown in Fig. 4; and (X) thermal diffusivity sample.

Experimental data

The λ data are shown in Fig. 6. The two sets of λ data derived from α values for samples with different orientations differed by only 1-2%, and the results shown in Fig. 6 are their average. At ambient temperatures, the two directly measured λ values differ by only about 0.9%, while the value derived from the α measurements[16] is about 7% lower. The difference between the two λ determinations reaches a minimum of about 4% at ~650 K, and the two curves diverge at higher temperatures. At 1273 K, the difference amounts to about 14% and exceeds the combined experimental uncertainties. The checkpoint (#19) shows that this difference cannot be attributed to shifts in sample characteristics during the radial heat flow measurements of λ, which require about 48 h for each determination.

The two sets of thermal conductivity values are adequately described by the empirical equations:

$$\text{(steady-state)}\ \lambda = 3.818 - 0.00278T + 25.5/T + 0.130 \times 10^{-5}T^2 \quad (T \text{ in K}, \lambda \text{ in W/m·K})\ ; \tag{1}$$

$$\text{(thermal diffusivity)}\ \lambda = 3.586 - 0.00228T + 0.232/T + 0.883 \times 10^{-6}T^2 \quad (T \text{ in K}, \lambda \text{ in W/m·K})\ . \tag{2}$$

The average deviations for Eqs. (1) and (2) are 0.82 and 0.67%.

Discussion

The two sets of results shown in Fig. 6 are similar in that λ^{-1}, the thermal resistivity, initially increases approximately linearly with temperature and then passes through a maximum at a higher temperature. The differences are in the positions of the two maxima and a vertical offset between the two curves. At lower temperatures, the vertical offset is within the combined experimental uncertainties. Since the direct λ measurements are more accurate, the vertical offset between the two curves was eliminated by simply shifting the upper curve downward by 0.0185 m·K/W.

The maxima are generally thought to arise from the different temperature variations of the contributions of two types of energy carriers:

$$\lambda = \lambda_g + \lambda_p\ . \tag{3}$$

In this equation, λ_g is the contribution from phonons or lattice vibrations and λ_p is a photon contribution. This can be expected if the sample is optically thick.[2] In the following, λ_p is experimentally estimated and compared with calculated[2] values. The experimental estimate is based on identifying λ_g from lower-temperature data and extrapolating to higher temperatures to yield values for $(\lambda - \lambda_g)$.

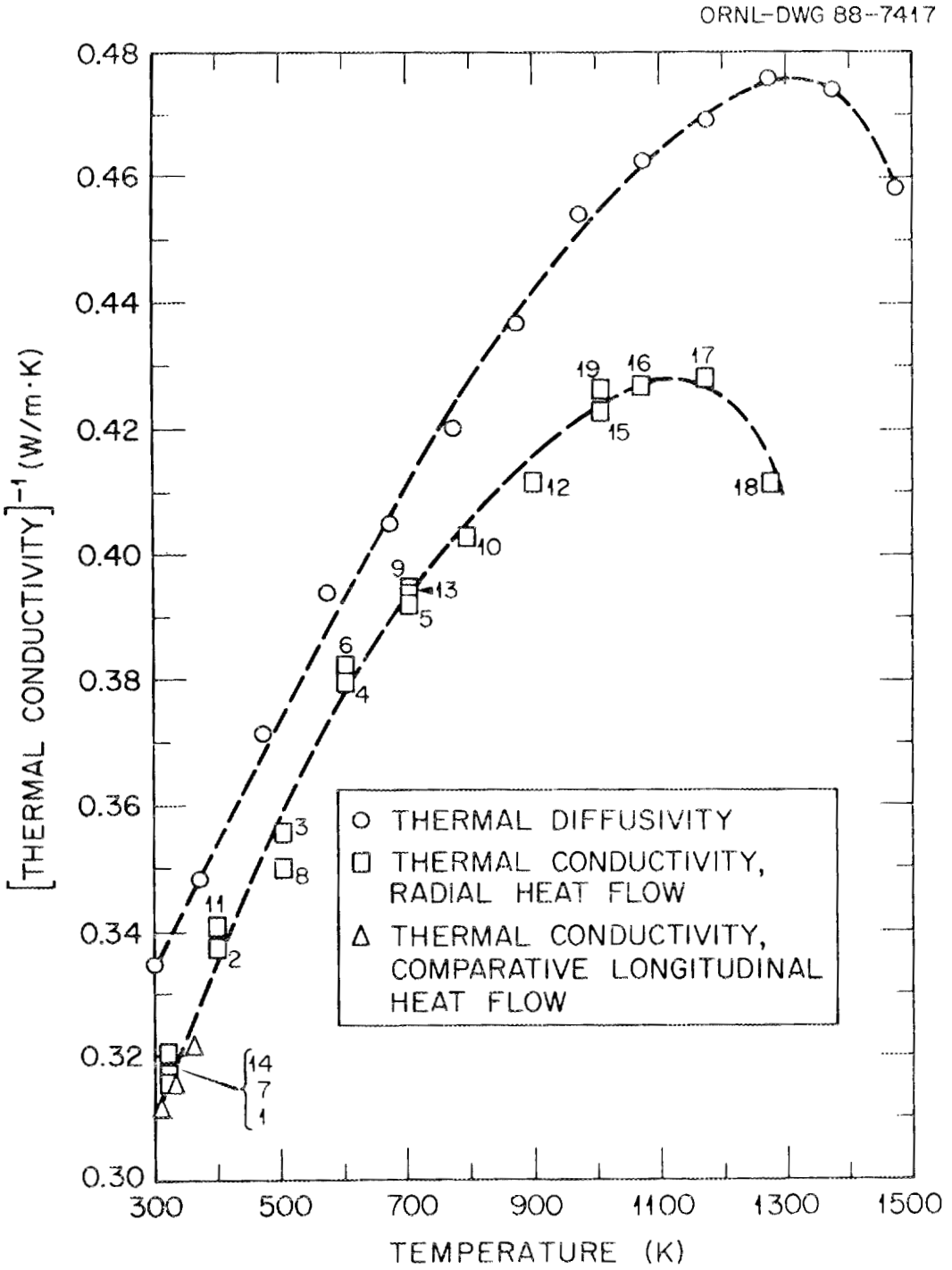

Fig. 6. Experimental thermal conductivity values for partially stabilized zirconia. The radial heat flow data points are numbered in the order they were obtained.

This material contains all three polymorphs of ZrO_2, and the net temperature variation of λ_g must depend on the three individual variations. A semicontinuous grain boundary network of monoclinic ZrO_2 and MgO pipes[14] is present, and the grains consist of a cubic matrix containing about 35 vol % of very finely divided, rod shaped tetragonal precipitates. Presumably, both the monoclinic and tetragonal phases are highly depleted in Mg.

The most direct method to estimate the behavior would be to use measured λ values for each phase in an appropriate mixing formula. However, no data are available for the monoclinic polymorph[17] and only one study[18] of tetragonal ZrO_2 is available. In this study,[18] it was shown that very fine grained ZrO_2–2.4 wt % Y_2O_3 exhibits glass-like behavior at low temperatures and that λ reaches a roughly constant value at about 40 K. This λ value (~2 W/m·K) is similar to values reported for the cubic phase,[17] but both the fine grain size and the presence of oxygen vacancies would probably greatly reduce λ relative to values for a defect-free tetragonal single crystal.

Some λ values have been inferred from α data.[19,20] Swain et al.[19] state that the λ values for monoclinic, tetragonal, and cubic ZrO_2 are 5.2, 4.8, and 1.8 W/m·K, but do not specify the temperature. Buykx and Swain[20] derived room temperature values for α of monoclinic and tetragonal ZrO_2 from data on PSZ. With literature data for the cubic form,[21] their results indicate that the λ values for the monoclinic, tetragonal, and cubic polymorphs should fall in the order 1:1.35:0.5. The difference between these two[19,20] results show that the experimental situation is not clear enough to provide useful guidance for an extrapolation of the data (Fig. 6) for MS-PSZ.

Figure 7 shows an attempt at a theoretical calculation. Callaway's model[22] was used in the calculation and the U-process scattering strength was estimated by following the procedure given by Slack.[23] The Debye temperature, 322 K, was based on reducing the elastic constant value[24] to account for dispersion. The Grüneisen constant, 1.75, was obtained from elastic constant[24] and high temperature expansion[25] data. The phonon-point defect scattering, which is almost entirely due to the effect of oxygen vacancies, was calculated from the prediction of Ratsifaritana and Klemens[26] and N-processes were estimated to occur twice as frequently as U-processes.

These estimates show that the λ values for the three polymorphs should tend to merge at higher temperatures, and this is a favorable situation because microstructural effects should be least important at high temperatures, where identification of the photon component is required. For the three phases, estimates are in better agreement with the Swain et al.[19] suggestion than with values from Buykx and Swain.[20] The calculated curve for the cubic phase is too low[17] and approaches the amorphous limit[1] at high temperatures. For this material, λ is almost entirely fixed by point-defect scattering, so the result suggests that the theoretical calculation of the scattering rate[26] is too large.

Since neither experimental data for the three polymorphs nor theory can give a satisfactory extrapolation, a more empirical approach was adopted. For an insulator, thermal resistivity can often be approximated by:

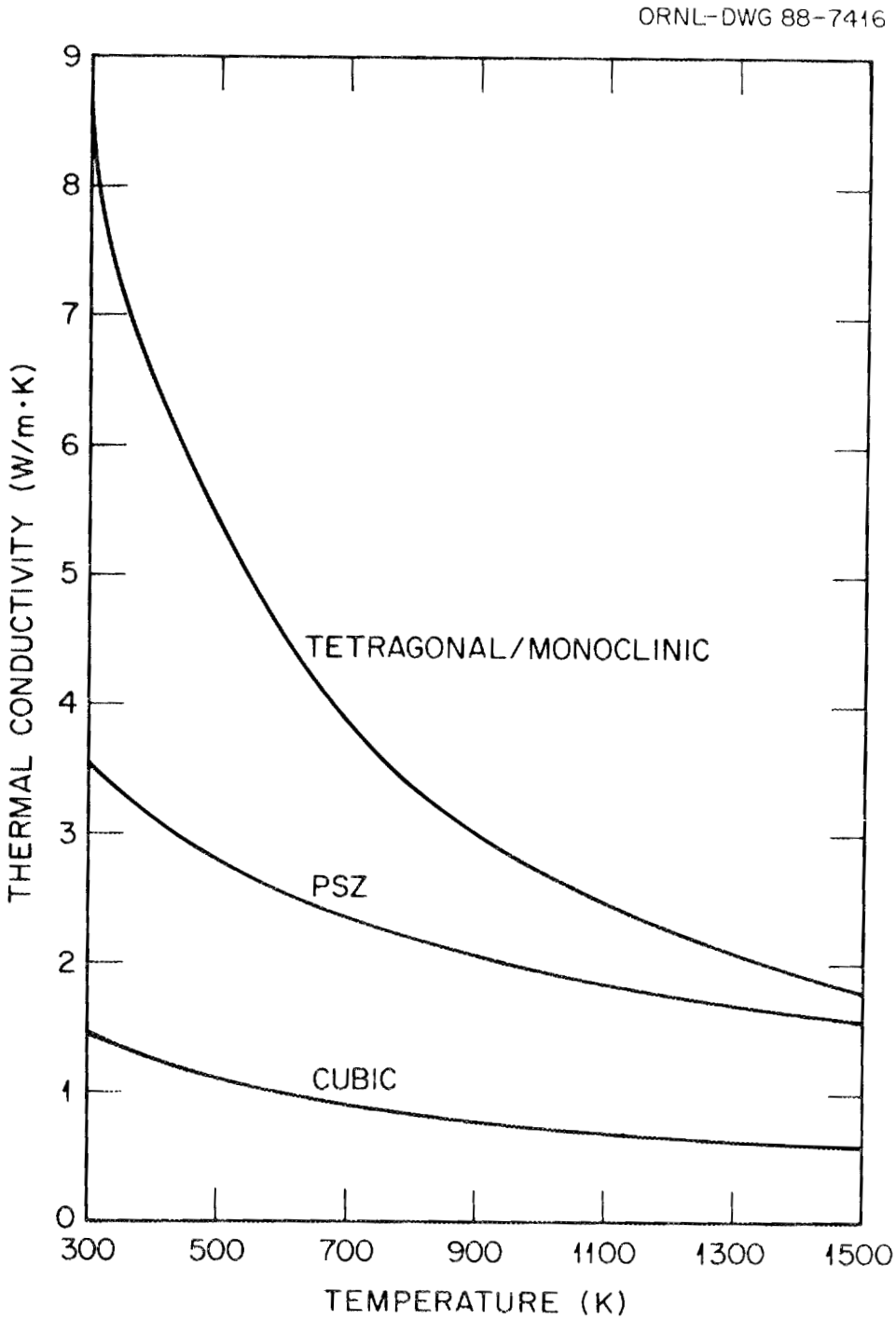

Fig. 7. Estimated thermal conductivity curves for monoclinic, tetragonal, and cubic zirconia. The model does not distinguish between monoclinic and tetragonal, and the curve for the cubic form includes point defect scattering from oxygen vacancies. The curve labeled PSZ is described in the text.

$$\lambda^{-1}_{g} = A + BT \ . \qquad (4)$$

This equation usually describes data when the scattering is dominated by U-processes. However, when point-defect scattering is very strong, the linear term in Eq. (4) should be replaced by a slower variation.[27] Estimates of the U-process and point-defect relaxation times show that this is the case for PSZ, even at high temperatures. Also, at the highest temperatures, λ is only about a factor of 4 greater than typical, temperature independent, values for amorphous solids. The approach adopted was to use Callaway's equation to fit the lower temperature data. This was accomplished by reducing the point defect scattering rate until a reasonable description of the lower temperature (≤700 K) data was obtained. This result is also shown in Fig. 7, and the point defect scattering was reduced to about 50% of the theoretical value.[26]

The derived $(\lambda-\lambda_g)$ photon contributions are shown in Fig. 8. At the highest temperatures, the contribution varies about as T^3 and this is as expected theoretically.[2] This is also the regime of minimum uncertainty since the component makes a larger percentage contribution and the calculation of the phonon part is least sensitive to microstructural effects. The difference between the two λ_p curves is also about what would be expected from the optical characteristics shown in Fig. 5. The λ_p curve derived from the direct λ measurements exceeds the other curve by an average of about 30%, while the ratio of the two absorption coefficients averages about 1.25. The magnitude of λ_p can also be calculated from the theory.[2] Using literature data[28] for the index of refraction of cubic zirconia with the absorption coefficients shown in Fig. 5 yields λ_p values which average about one-third of values shown in Fig. 8. The agreement improves as the temperature increases.

This analysis shows that photon transport is probably responsible for the upturn in the thermal conductivity at high temperatures. There is no evidence that thermal diffusivity and steady-state measurements yield different results,[4] but the data do show that environmentally produced changes in optical properties can alter the energy transport characteristics of translucent materials at high temperatures.

Status of milestones

311202	Complete initial analysis of thermal transport in PSZ ceramics. Submit technical paper for publication (Feb. 29, 1988)	On schedule

Publications

R. K. Williams, R. S. Graves, and D. W. Yarbrough, "The Thermal Conductivity of Oxide Ceramics," accepted for publication in the Proceedings of the 25th Automotive Technology Development Contractors Coordination Meeting.

R. K. Williams, J. B. Bates, R. S. Graves, D. L. McElroy, and F. J. Weaver, "Comparison Of Thermal Conducitivity Data For Partially Stabilized Zirconia With Values Derived From Thermal Diffusivity Results," submitted to *Int. J. Thermophysics*.

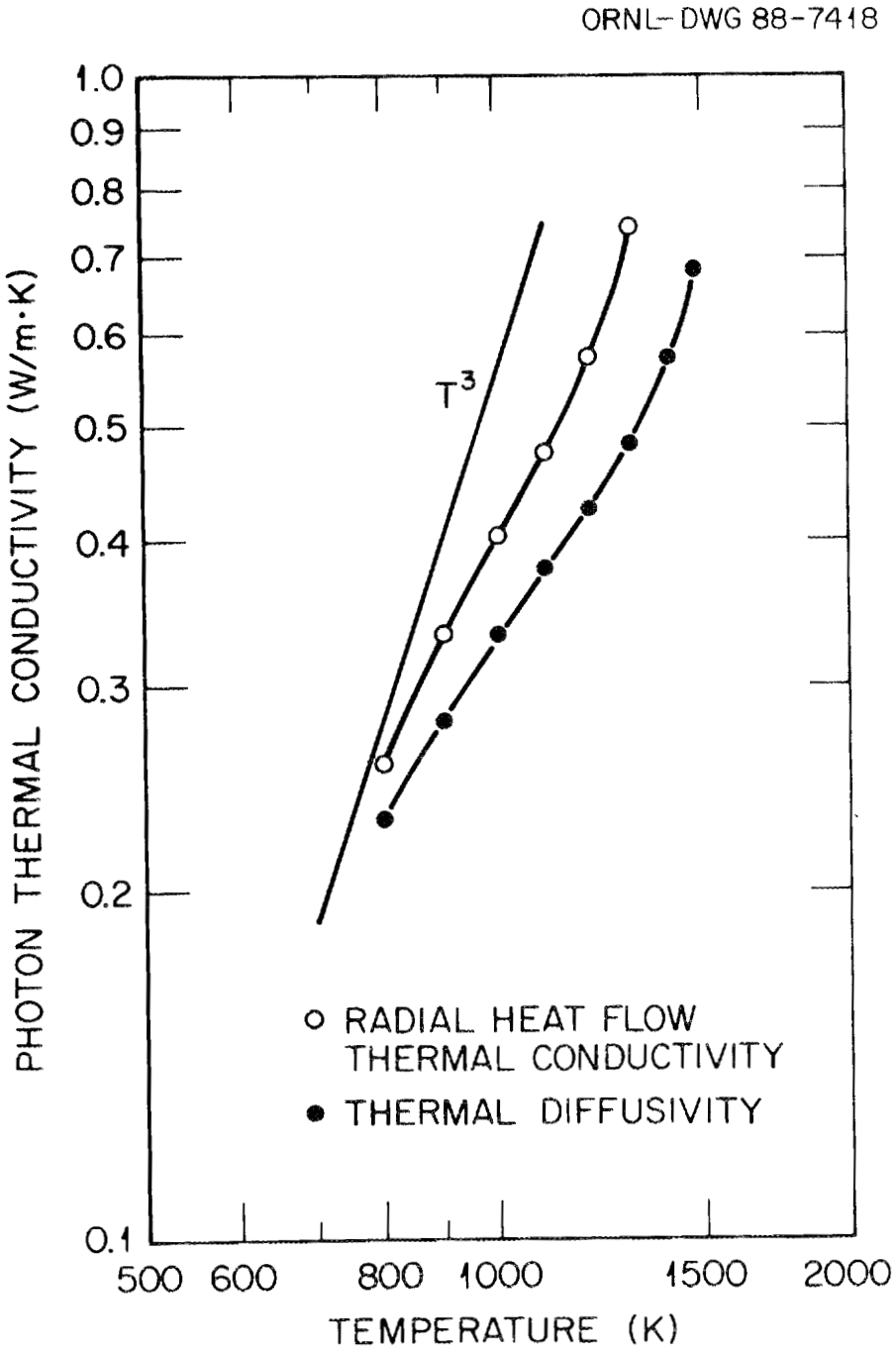

Fig. 8. Photon thermal conductivity curves derived for the PSZ samples used for the thermal conductivity and diffusivity measurements.

References

1. R. Berman, *Thermal Conduction in Solids*, p. 106, Clarendon Press, Oxford (1976).

2. L. Genzel, *Z. Phys.* 135, 177 (1953).

3. S. Wahiduzzaman and T. Morel, *Effect of Translucence of Engineering Ceramics on Heat Transfer in Diesel Engines*, ORNL/Sub/86-22042/1 (October 1987).

4. D. L. McElroy, R. S. Graves, D. W. Yarbrough, and T. W. Tong, *High Temp. High Pressures* 17, 395 (1985).

5. W. J. Parker, R. J. Jenkins, C. P. Butler, and G. L. Abbott, *J. Appl. Phys.* 32, 1679 (1961).

6. R. E. Taylor, *High Temp. High Pressures* 11, 43 (1979).

7. The Perkin Elmer Corp., 761 Main Avenue, Norwalk, CT 06859.

8. R. K. Williams, R. K. Nanstad, R. S. Graves, and R. G. Berggren, *J. Nucl. Mater.* 115, 211 (1983).

9. R. K. Williams, R. S. Graves, and J. P. Moore, *A Study of the Effects of Several Variables on the Thermal Conductivity of 2-1/4 Cr-1 Mo Steel*, ORNL-5313 (1978).

10. R. K. Williams, R. S. Graves, and F. J. Weaver, and D. W. Yarbrough, *J. Appl. Phys.* 62, 2778 (1987).

11. J. P. Moore, "Analysis of Apparatus with Radial Symmetry for Steady-State Measurements of Thermal Conductivity," p. 61 in *Compendium of Thermophysical Property Measurement Methods, Vol. 1: Survey of Measurement Techniques*, eds. K. D. Maglic, A. Cezairliyan, and V. E. Peletsky, Plenum Press, New York (1984).

12. W. Fulkerson, J. P. Moore, R. K. Williams, R. S. Graves, and D. L. McElroy, *Phys. Rev.* 167, 765 (1968).

13. Nilcra Ceramics Pty. Ltd., 239 Separation St., Northcote, Victoria 3070 Australia.

14. P. F. Becher, M. V. Swain, and M. K. Ferber, *J. Mater. Sci.* 22, 76 (1987).

15. Varian Instruments Div./Cary Products, Palo Alto, CA 94303.

16. R. E. Taylor, H. Groot, and J. Larimore, Purdue University, West Lafayette, Indiana, private communication (1987).

17. Y. S. Touloukian, R. W. Powell, C. Y. Ho, and P. G. Klemens, *Thermal Conductivity, Nonmetallic Solids*, IFI/Plenum, New York, pp. 246, 442, (1970).

18. W. N. Lawless and T. K. Gupta, *Phys. Rev. B* 28, 5507 (1983).

19. M. V. Swain, L. F. Johnson, R. Syed, and D. P. H. Hasselman, *J. Mater. Sci. Lett. (GB)* 5, 799 (1986).

20. W. J. Buykx and M. V. Swain, "Thermal Diffusivity of Zirconia Partially and Fully Stabalized with Magnesia," p. 518 in *Advances in Ceramics*, Vol. 12, N. Claussen, M. Ruhle, and A. Heuer, eds., The American Ceramic Society, Inc., Columbus, Ohio (1984).

21. Y. S. Touloukian, R. W. Powell, C. Y. Ho, and M. C. Nicolau, *Thermal Diffusivity*, IFI/Plenum, New York, p. 409 (1970).

22. J. Callaway, *Phys. Rev.* 113, 1046 (1959).

23. G. A. Slack, p. 1 in *Solid State Physics*, ed. F. Seitz and D. Turnbull Academic, New York, Vol. 34 (1979).

24. H. M. Kandil, J. D. Greiner, and J. F. Smith, *J. Am. Ceram. Soc.* 67, 341 (1984).

25. Y. S. Touloukian, R. K. Kirby, R. E. Taylor, and T. Y. R. Lee, *Thermal Expansion, Nonmetallic Solids*, IFI/Plenum, New York, p. 603 (1977).

26. C. A. Ratsifaritana and P. G. Klemens, *Int. J. Thermophys.* 8, 737 (1987).

27. B. Abeles, *Phys. Rev.* 131, 1906 (1963).

28. D. L. Wood and K. Nassau, *Appl. Opt.* 21, 2978 (1982).

Effect of Translucence of Engineering Ceramics on Heat Transfer in Diesel Engines

Syed Wahiduzzaman and Thomas Morel (Integral Technologies Incorporated)

Objective/scope

Ceramic materials are being used as thermal barrier materials, separating the engine metal substructure from the convective and radiative heat fluxes originating in the combustion gases. The heat transfer through the ceramic layer to the substructure will be increased by any translucence, which would allow a part of the radiation heat flux to pass through the barrier material. To quantify the effect of translucence of engineering ceramics on the heat transfer in diesel engines, Integral Technologies has conducted analytical studies using detailed computer codes which describe a realistic engine thermal environment including gas-to-wall heat fluxes, as well as the combined radiation/ conduction heat transfer through a thermal barrier layer. A detailed parametric study was carried out in which the following parameters were varied, and their effect on heat barrier effectiveness was studied: 1) material absorption coefficient, 2) material conductivity, and 3) material thickness. An analysis of the results yielded bounds on critical properties, beyond which there is a reason for concern about this effect. Also, suggestions were made for methods to control any adverse effects.

In the experimental portion of this work, data were acquired describing the radiation properties of several engineering ceramics. The objective is to obtain the specific information needed for the analytical part of this work. This includes the absorption coefficient, scattering albedo and surface reflectivities of the materials. In order to obtain the data, specialized samples of the materials were fabricated. Measurements of reflectance and transmittance were obtained, and from these the desired radiation properties will be deduced using an analytical data reduction technique.

Technical progress

During this reporting period ceramic samples were sent to two laboratories, at Willey Corporation and at the National Bureau of Standards, for reflectance and transmittance measurements. These samples include ceramic coupons for four different ceramic materials. These were obtained from Plasma Technics (PSZ, 13% Yttria Stabilized), Caterpillar (PSZ, 24% Ceria Stabilized) and two from Oak Ridge National Laboratory (PSZ and Tridiagonal Zirconia Polycrystals (TZP)). A total of thirteen samples were sent for thirteen reflectance and nine transmittance measurements. The results of the first set of these measurements made over a wavelength band spanning 2.0 μm to 20.0 μm were received from the Willey Corporation Laboratories in November. Partial results for the shorter wavelength band (up to 2.5 μm) were received recently.

Analysis at Longer Wavelengths

The analytical model developed for inversion of radiative properties was applied to this experimental data. It was found that the current model has sufficient sensitivity to resolve radiative properties in the infrared spectral region where thermal radiation is important if sufficient number of consistent and independent measurements are available. However, preliminary analysis of data revealed that additional measurements, especially for smaller sample thicknesses (equivalently at smaller optical depths), are required for optimization of most important radiative properties. It became evident that with only three different sample thicknesses, it was impossible to obtain sufficiently separated or linearly independent measurements for successful optimization of three parameters (refractive index, scattering coefficient and absorption coefficient). It was, therefore, decided that optimization of only two most important properties: absorption coefficient and scattering coefficient be carried out, with a fixed refractive index value imposed. This value of refractive index will be chosen either from full optimization at lower wavelengths or from literature values. It was observed in previous investigations (Makino and Kunitomo, 1984)[1] for similar materials that refractive index remains nearly constant from 0.5 to 5.0 μm, and its value typically ranged from 1.7 to 2.2.

Figures 1 and 2 show typical reflectance and transmittance measurements of partially stabilized zirconia. Figures 3 and 4 show computed scattering and absorption for this material. The scattering coefficient decreases as the wavelength is increased, whereas the absorption coefficient remains relatively constant up to wavelengths around 4.0 μm where it starts to increase very sharply. These qualitative trends are similar to those observed by Makino and Kunitomo (1984).

However, some difficulties were noted in the data analysis:

(1) TZP and PSZ samples from Oak Ridge exhibited very similar spectrum despite different composition. This behavior was unexpected, and we are investigating the possibility that the laboratory tested twice the same sample or that ORNL supplied two sets of samples of same material.

(2) At lower wavelengths the sum of reflectance and transmittance values was in some cases greater than unity for TZP samples. This indicates a certain level of inaccuracy in the data, which will introduce uncertainty in the results.

(3) Reflection spectrum for PSZ samples from Caterpillar exhibited inconsistent trend with thickness. The highest and lowest thicknesses possess spectrum remarkably different spectrum than those of middle two thicknesses. Again, we are investigating a

---

[1]Toshiro Makino and Takeshi Kunitomo (1984), "Thermal Radiation Properties of Ceramic Materials," Heat Transfer-Japanese Research, Vol. 13, No. 4.

possibility that the samples are not what they should be or that the data were recorded incorrectly to make sure that the data trends are real.

Upon review of these observations with Dr. Willey of Willey Corporation, it was understood that reflectance measured by a Fourier Reflectometer is less accurate at lower wavelengths and could be the cause of the second problem. It was suggested that reflectance values be appropriately reduced keeping transmittance values unchanged, since the transmittance is the more reliable of the two measurements. As far as the first and third discrepancies, we will be looking carefully at the NBS results when they will be complete.

Analysis at Shorter Wavelengths

The first batch of the reflectance data at short wavelengths (up to 2.5 μm) has arrived from NBS. Corresponding transmittance data are yet to be received and NBS has reported difficulties arising out of low signal-to-noise ratio for some of the samples. Additional samples are being readied and will be shipped if it is requested by NBS. In the meantime the newest data are being carefully scrutinized for possible inconsistencies within itself and with the data at longer wavelengths (2 to 20 μm) measured at Wiley Corporation.

As mentioned above, the TZP and PSZ samples from Oak Ridge exhibited very similar spectrum at long wavelengths (2 to 20 μm) despite different compositions. This was not expected and results of the short wavelength data were awaited from NBS to see if similar observations could be made for the short wavelength spectrum. Except for the overlap region (2-2.5 μm), where Wiley data are unreliable due to excessive noise inherent in their method of measurements (Fourier Reflectometer), the same conclusion was drawn for the short wavelength region, i.e., two Oak Ridge samples are radiatively identical within the resolution of the present method. Figures 5 and 6 show the reflectance data for these samples for both regions.

In addition, spectrum for the thickest samples (No. 6 and No. 9) are somewhat different in nature than the rest of the samples. This implies differences in composition and/or surface preparation. Similar inconsistencies exist in the PSZ sample from Caterpillar (Figure 7). Under the circumstances, some of the inconsistent data are required to be excluded from the data analysis set.

The partial data obtained from NBS allowed us to look into the issue of the larger than unity sum of reflectance and transmittance observed in the Willey measurements of the TZP samples. The possibility that the measured reflectances are biased to a higher value at short wavelengths was supported by the NBS data. Specifically, in Figure 5 it may be observed that in the overlap region (2 to 2.5 μm) Wiley data is always higher than NBS data.

Need for a Four-Flux Model

A further analysis of the data identified a weakness in the original radiative parameter inversion model. It showed that for the ceramics under study the scattering coefficient decreased to low values at longer wavelengths. The radiative transfer process was represented in this model by two diffuse fluxes. This involves an implicit assumption that once the collimated radiation enters the scattering medium, it is quickly transformed into diffused flux by multiple scattering. However, this assumption is not valid if scattering level is low which was found to be the case in long infrared region. At small optical depths, since the incident beam is collimated, the contribution of internal collimated flux to total transmittance and reflectance will be comparable to the contribution from the internal diffuse flux. In addition, Fourier reflectivities at the interfaces are quite different for diffuse and collimated fluxes. Hence,it is necessary to solve for both collimated and diffuse fluxes simultaneously with boundary conditions that are consistent with the method used in the reflectance and transmittance measurements. To accomplish this goal, the previous two flux model was extended to a four flux model which is better capable to address the problem at hand. In the four flux model the incident collimated beam penetrates the scattering medium and decays into diffuse flux due to multiple scattering as it travels into the medium. There are two conservation equations (forward and backward) each for collimated and diffuse flux components. Boundary conditions are provided by separately calculating the interfacial reflectivities for collimated and diffuse fluxes.

Reexamination of the data under the present model revealed that the old model underestimated the scattering coefficient by as much as a factor of two at higher wavelengths, while the absorption coefficient changed only slightly.

Status of Milestones

Milestone 11a, model formulation, was reached in March, 1986. Milestone 11b, model development, was completed in August, 1986. Milestone 11c, material property search, was completed in December, 1986. Milestone 11e, definition of material samples, was completed in October, 1986. A report was completed and delivered to ORNL in May, 1987.

Publications

None.

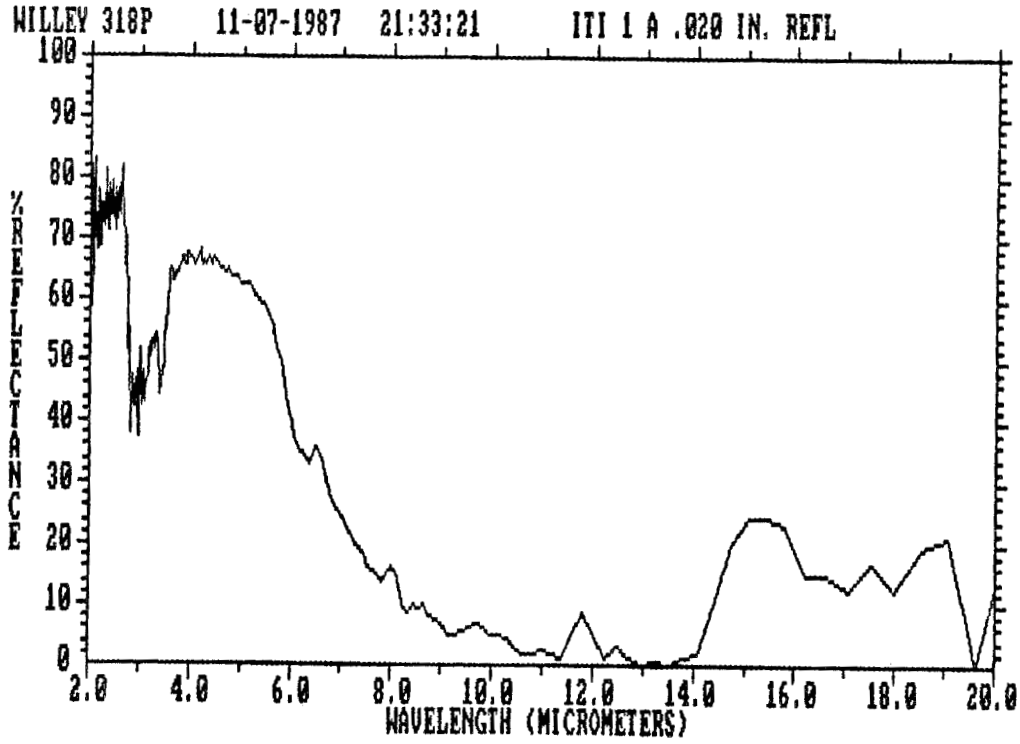

Figure 1. Reflectance spectrum of Plasma Technics 0.020 inch PSZ sample.

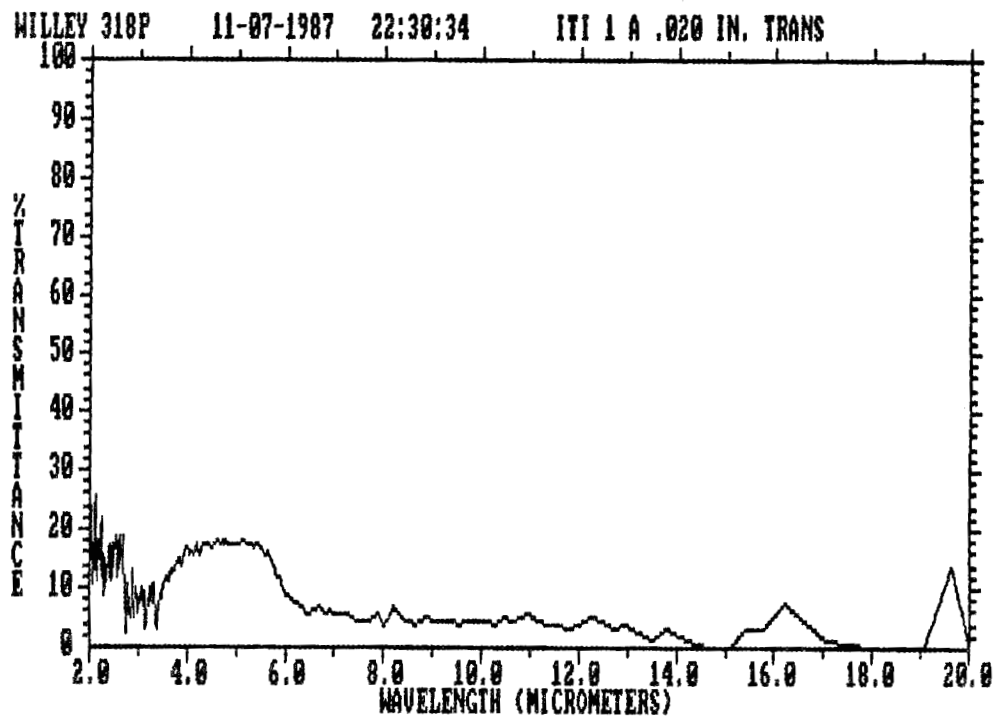

Figure 2. Transmittance spectrum of Plasma Technics 0.020 inch PSZ sample.

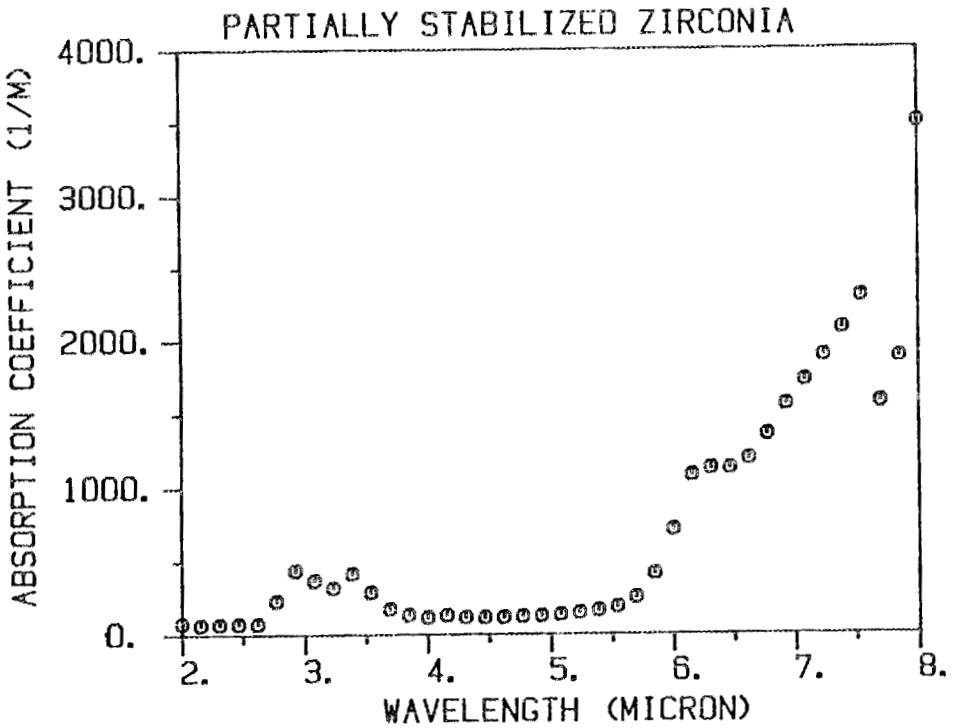

Figure 3. Absorption coefficient of Plasma Technics PSZ.

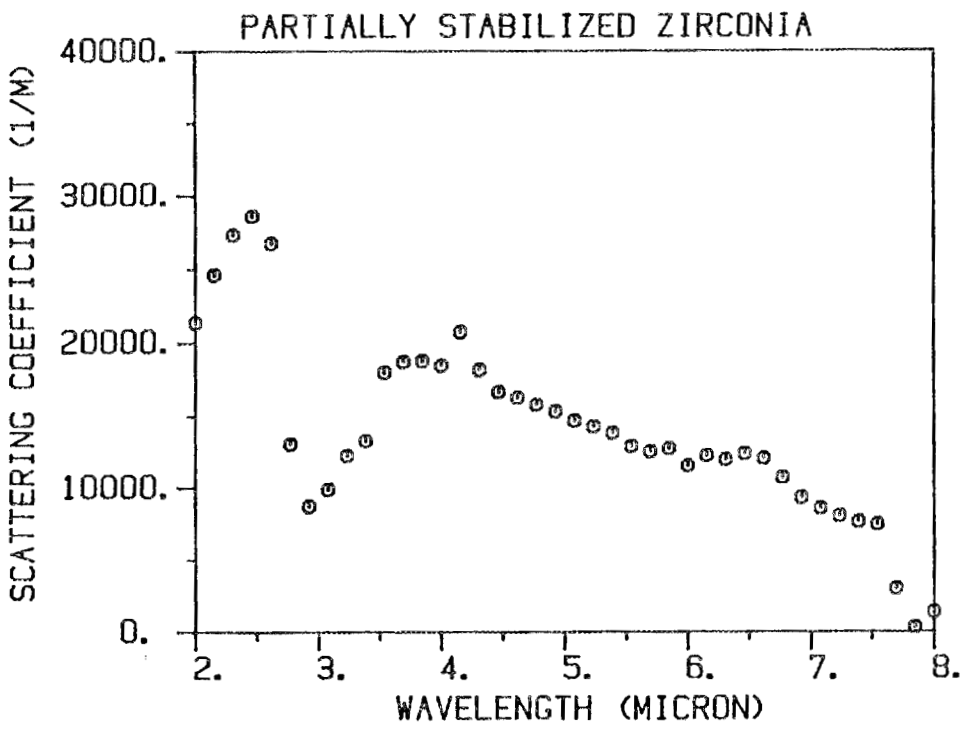

Figure 4. Scattering coefficient of Plasma Technics PSZ.

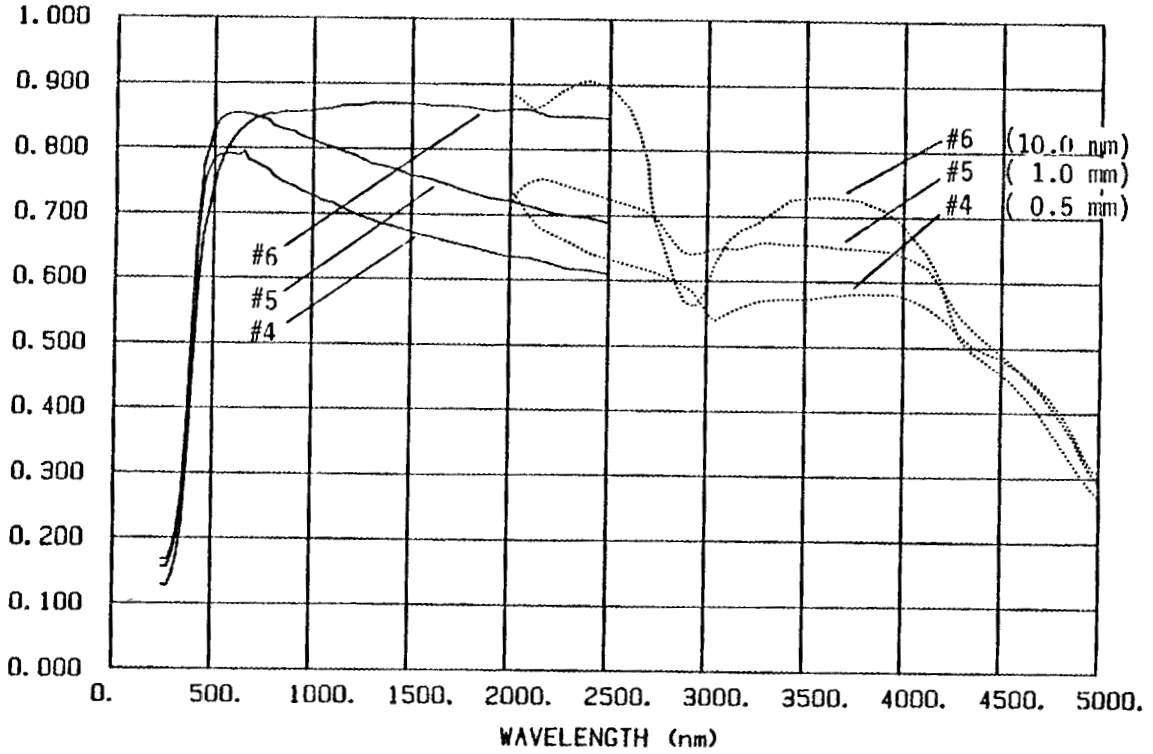

Figure 5. Reflectance Data for TZP Samples Supplied by Oak Ridge National Laboratory. ——— NBS Data; ····· Wiley Data.

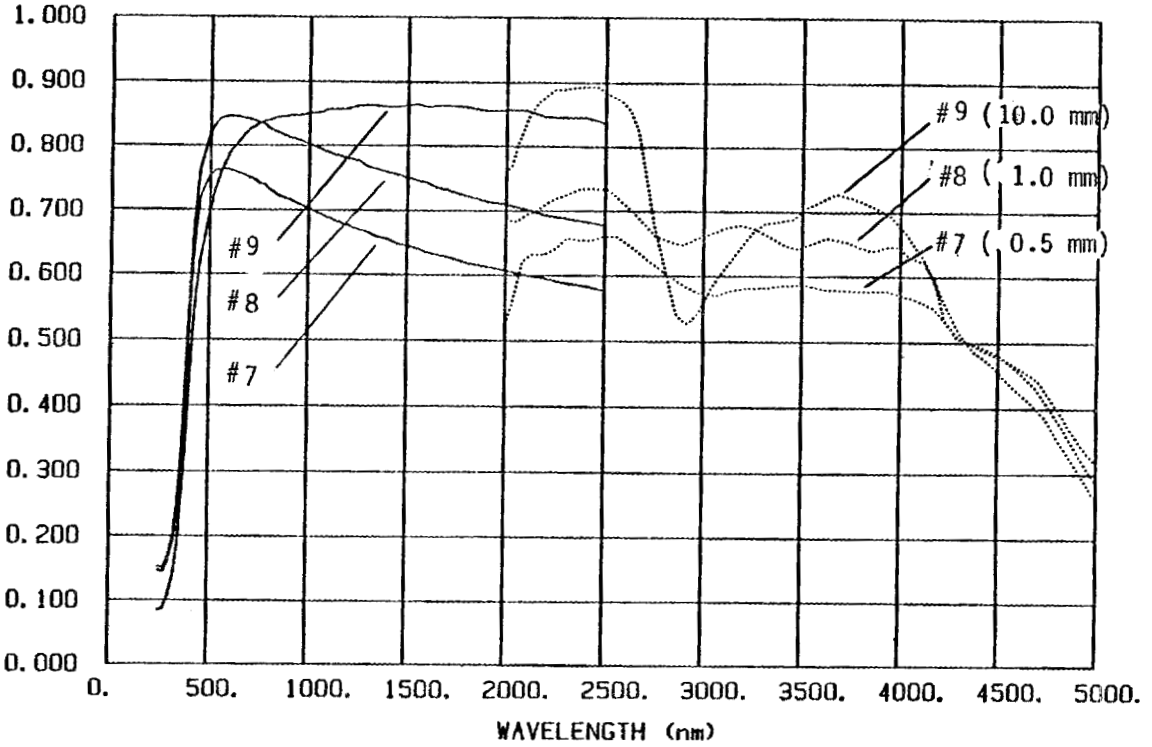

Figure 6. Reflectance Data for PSZ Samples Supplied by Oak Ridge National Laboratory. ——— NBS Data; ····· Wiley Data.

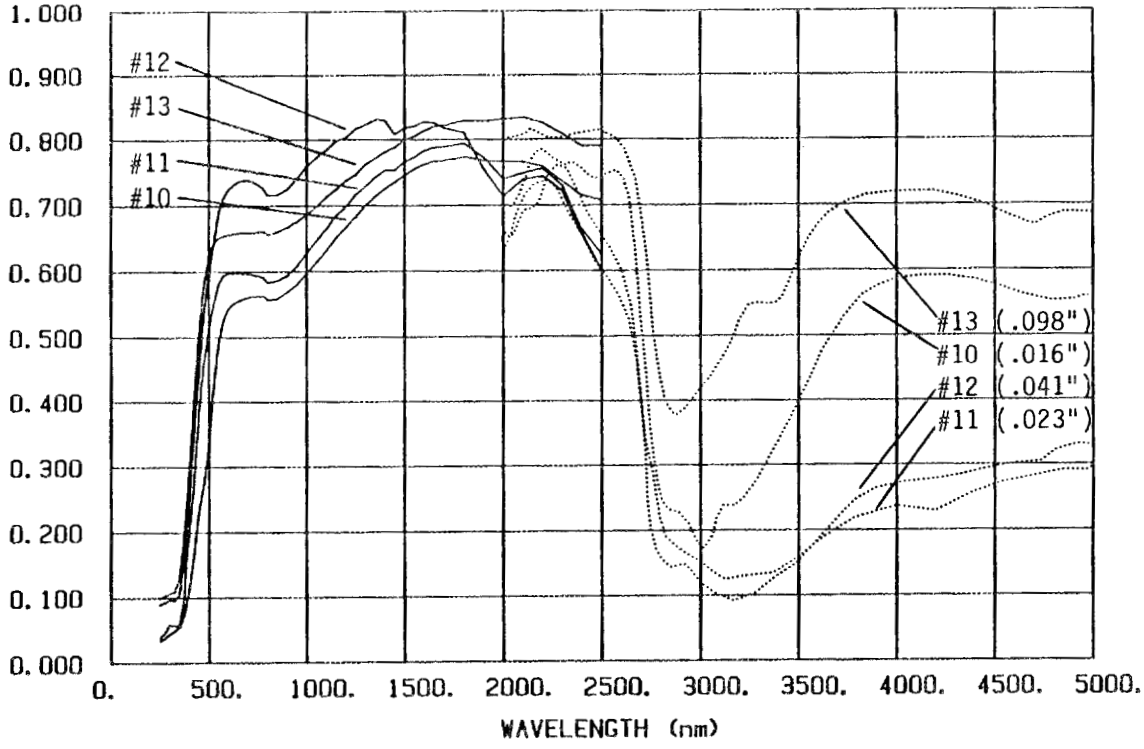

Figure 7. Reflectance Data for PSZ Samples Supplied by Caterpillar Tractor Company. ——— NBS Data; ..... Wiley Data.

3.2 TIME-DEPENDENT BEHAVIOR

Characterization of Advanced Transformation Toughened Zirconias
J. J. Swab (Army Materials Technology Laboratory)

OBJECTIVE/SCOPE

Because of their unusual combination of properties, transformation toughened zirconias (TTZ), specifically yttria tetragonal zirconia polycrystal (Y-TZP), are leading candidates for cylinder liners, piston caps, head plates, value seats and other components for the adiabatic diesel engine. These materials are age-hardened ceramic alloy systems and as such, they are likely to be susceptible to overaging and loss of strength after long times at high temperatures). Accordingly, a task was initiated to define the extent and magnitude of the overaging (if any) at engine operating temperatures (1000-1200C) and the resulting impact on material performance.

It is also well known the Y-TZP's undergo a phenomenon at low temperatures (200-400C) which leads to decreases in strength and fracture toughness and that this phenomenon is accelerated by the presence of water. As a result, a preliminary study to try and determine the effects of this phenomenon has been included in this task.

TECHNICAL PROGRESS

None/No Funding

STATUS OF MILESONES

Stress Rupture testing has been completed and the data is now being analyzed.

Room temperature MOR of "NEW" TZP materials has been completed and the data is now being analyzed.

The completion date for the preliminary study of the effects of oxidation state on the properties of a HIP'ed has been moved to 30 May from 15 March.

COMMUNICATIONS/VISITORS/TRAVEL

Attended the 12th Annual Conference on Composites and Advanced Ceramic Materials. Presented a paper entitled "Effects of Oxygen Non-Stoichiometry on the High Temperature Performance of a Yttria-Tetragonal Zirconia Polycrystal Material". J.J. Swab, R.N. Katz and C.J. Starita.

PROBLEMS ENCOUNTERED

No Funding during this period. Funds were received 1 April 1988.

PUBLICATIONS

None

Fracture Behavior of Toughened Ceramics

P. F. Becher, T. N. Tiegs, and W. H. Warwick (Oak Ridge National Laboratory)

Objective/scope

Because of their excellent toughness, oxide ceramics such as partially stabilized zirconia (PSZ), dispersion-toughened alumina (DTA), and whisker-reinforced ceramics are prime candidates for many diesel engine components. The enhanced toughness of the PSZ and DTA materials is due to a stress-induced transformation (of the dispersed tetragonal ZrO_2 phase) which requires additional energy in order for catastrophic fracture to occur. However, these materials are still susceptible to slow crack growth, creep, and thus strength degradation with increase in temperature. Also, there is evidence that, at temperatures above 700°C, time-dependent aging effects can reduce the concentration of the phase involved in the transformation process, leading to significant losses in toughness and strength. Again, it is essential that mechanisms responsible for both the slow crack growth, creep, and aging behavior be well understood. Similarly, the toughening behavior in whisker-reinforced ceramics and their high-temperature performance must be evaluated to develop materials for particular applications.

In response to these needs, studies have been initiated to examine toughening and fatigue properties of transformation-toughened and whisker-reinforced materials. Particular emphasis has been placed on understanding the effect of microstructure upon processes responsible for time-dependent variations in toughness and high-temperature strength. In addition, fundamental insight into the slow crack growth and creep behavior associated with these materials is being obtained.

Technical progress

Studies of the static fatigue behavior (time to failure as a function of applied stress) of various SiC whisker-reinforced alumina composites in four-point flexure at temperatures of 800 to 1400°C in air were started. The installation of this equipment in the High Temperature Materials Laboratory has been completed. The focus of these latest tests is on the failure behavior of composites at 800 to 1400°C. Previous studies indicated that at a temperature of 1100°C crack blunting and associated increasing strength occur when samples were subjected to applied stresses of approximately two-thirds of the fast fracture strength at 1100°C. The current studies are addressing which stress levels can be applied to these composites while avoiding time-dependent failure at temperatures where thermally activated crack growth may occur. Note that at room temperature, crack growth behavior is such that stresses approaching approximately 90% of the fast fracture strength can be applied without initiating time-dependent failure.[1]

In order to determine the processes limiting the mechanical reliability of these composites at temperatures above 1000°C in air, four-point flexural creep apparatus which include a high-temperature

multiple-probe dilatometer have been assembled and modified to obtain creep strains as a function of applied stress and temperature (for temperatures up to 1600°C). Considerable effort was expended to obtain reliable and accurate measurements of the creep deflection. Preliminary creep results of the alumina composites containing 20 vol % of the SiC whiskers have been obtained at 1200, 1300, and 1400°C in air. The dependence of the steady-state creep rates as a function of applied stress for this composite are shown in Fig. 1. At 1200 and 1300°C, the stress exponent of the creep rate is approximately 2 over the stress range of 100 to 250 MPa. In comparison, alumina with the same grain size (~1-1.5 mm) exhibits a creep rate that is 1000 times higher than that of the composite at 100 MPa at 1200°C. Thus, whisker reinforcement has substantially increased the creep resistance of the alumina. At 1400°C, the stress dependence of the creep rate appears to exhibit a transition from a stress exponent of approximately 2 at stresses below 100 MPa to approximately 5 at stresses above 100 MPa. Studies are under way to extend this data and to examine the microstructural changes (e.g., grain growth, cavity nucleation, and growth) that occur during the various stages of creep.

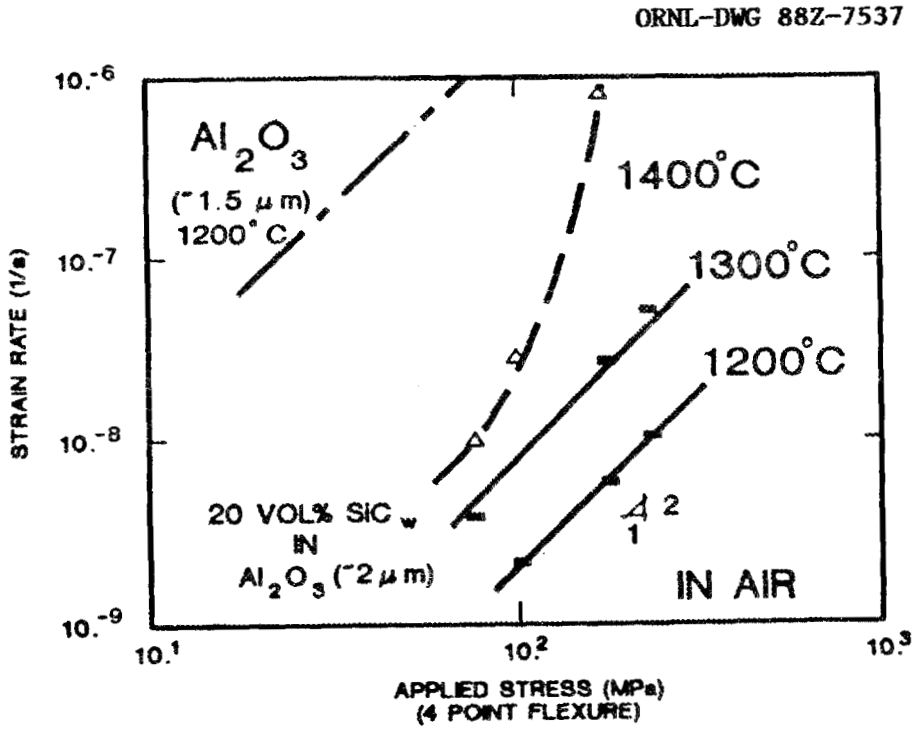

Fig. 1. Steady-state creep rates of alumina-20 vol % SiC whisker-reinforced composite show transition in behavior at 1400°C at higher applied stress levels. Below 1400°C, the stress exponent of the creep rate is approximately 2. At 1400°C, the creep rates in four-point flexure are much more sensitive to the applied stress level.

Recent studies have resulted in analytical descriptions of toughening behavior in whisker-reinforced ceramics based on whisker bridging in the crack tip region accompanied by whisker pullout. The theoretical models, developed in research sponsored by the BES Materials Sciences Program, are briefly described here as they provide insight into whisker-toughening behavior which is pertinent to the various efforts in this project.

First, increased toughness is derived by strong whiskers which bridge the crack in the region behind the crack tip. In addition, whiskers further behind the crack tip fracture and/or are pulled out of the matrix. Such processes are documented by microscopy studies by Angelini et al.[2,3] The result is that over a distance DB behind the crack tip, bridging whiskers exert a closure stress σ^c that must be overcome to advance the crack. The toughness increase due to whisker bridging is

$$dK^{wr} = 2\ \sigma^c\ (2\ D_B/\pi)^{1/2}\ , \tag{1}$$

and the toughness of the composite $K_{IC}{}^c$ is

$$K_{IC}{}^c = K_{IC}{}^m + dK^{wr}\ . \tag{2}$$

where $K_{IC}{}^m$ is the matrix toughness.[4,5] In the case of aligned whiskers, the closure stress exerted by the bridging whiskers is

$$\sigma^c = V_f\ \sigma_f{}^w\ , \tag{3}$$

where V_f is the volume fraction of whiskers and $\sigma_f{}^w$ is the tensile strength of the whiskers. The length of the bridging zone behind the crack tip can be derived from the crack opening displacements and is a function of the whisker interface debonding conditions, the whisker strength, and elastic properties.[4,5] The toughness increase due to whisker bridging is then

$$dK^{wr} = \sigma_f{}^w\ [V_f\ r(E^c\ \gamma^m/E^w\ \gamma^i)/3(1-\nu^2)]^{1/2}\ , \tag{4}$$

where E^c and E^w are the Young's moduli of the composite and whisker, respectively, γ^m and γ^i are the fracture energies of the matrix and the whisker-matrix interface, and ν is the Poisson's ratio of the composite. The additional toughening effects due to whisker pullout involving high interfacial shear strengths, as is the case with many SiC whisker-reinforced ceramics, exhibit the same behavior shown in Eq. (4) with only the numerical constant being altered.

These analytical descriptions are found to accurately predict the toughening behavior observed in several SiC whisker reinforced ceramics.[4,5] The results also show that whisker strength and diameter, as well as the matrix-whisker interface strength, have a significant impact on the degree of toughening obtained. Furthermore, with matrices like alumina, the toughness of the composite can be strongly influenced by the matrix microstructure. SiC whisker-reinforced alumina composites exhibit an increase in toughness with increase in matrix grain size due to matrix microcracking and matrix bridging effects.[4,5]

Status of milestones

Milestone 321305 dealing with the influence of whisker characteristics on mechanical behavior has been completed. The results are included in two technical papers which have been submitted for publication.

Publications

None.

References

1. P. F. Becher, T. N. Tiegs, J. C. Ogle, and W. H. Warwick, "Toughening of Ceramics by Whisker Reinforcement," pp. 61-73 in *Fracture Mechanics of Ceramics*, Vol. 7, R. C. Bradt, A. G. Evans, D. P. H. Hasselman, and F. F. Lange, ed., Plenum Press, New York (1986).

2. P. Angelini, W. Mader, and P. F. Becher, "Strain and Fracture in Whisker Reinforced Ceramics," pp. 241-57 in MRS Proceedings: Advanced Structural Ceramics, Vol. 78, P. F. Becher, M. V. Swain, and S. Somiya, ed., Materials Research Society, Pittsburgh, Pa. (1987).

3. P. Angelini and P. F. Becher, "In Situ Fracture of SiC Whisker Reinforced Al_2O_3, pp. 148-49 in *Proc. Electron Microscopy Society of America*, G. W. Bailey, ed., San Francisco Press, San Francisco (1987).

4. P. F. Becher, C. H. Hsueh, P. Angelini, and T. N. Tiegs, "Toughening Behavior in Whisker Reinforced Ceramic Matrix Composites," submitted to *Am. Ceram. Soc.* (1987).

5. P. F. Becher, T. N. Tiegs, and P. Angelini, "Whisker Toughened Ceramic Composites," in *Fiber Reinforced Ceramics*, K. S. Mazdiyasni, ed., Noyes Publications, Park Ridge, N.J., in press.

Cyclic Fatigue of Toughened Ceramics

K. C. Liu and C. R. Brinkman (Oak Ridge National Laboratory)

Objective/scope

The objective of this task is to develop, design, fabricate, and demonstrate the capability to perform tension-tension dynamic fatigue testing on a uniaxially loaded ceramic specimen at elevated temperatures.

Three areas of research have been identified as the main thrust of this task: (1) design, fabrication, and demonstration of a load train column which truly aligns with the line of specimen loading; (2) development of a simple specimen grip that can effectively link the load train and test specimen without complicating the specimen geometry and, hence, minimize the cost of the test specimen; and (3) design and analysis of a specimen for tensile cyclic fatigue testing.

Technical progress

Tensile fatigue testing Of Nilcra's MgO-PSZ

Tensile fatigue testing of Nilcra's MgO-PSZ resumed after a new batch of 20 buttonhead tensile specimens was received. These specimens were made from another grade of rod samples designated as "MS" for maximum strength with reference to the first batch as "TS" grade for maximum thermal shock resistance. The finished specimen has a uniform gage section of 6.3 mm (0.25 in.) in diameter by 25.4 mm (1 in.) gage length. Details of specimen preparation can be found in previous reports.

Seven specimens were used to determine the tensile strength of this material at room and elevated temperatures. Test results are tabulated in Table 1 and data are plotted in Figs. 1 and 2. The four-point bend flexural strength data reported by the material supplier are also plotted in Fig. 1 to facilitate comparison with the ORNL tensile data. The broken curve represents the average tensile strength obtained previously for the TS grade PSZ and the solid one for the MS grade PSZ. Both curves clearly indicate that the tensile strength of this material is a function of temperature. At temperatures below 700°C, the MS grade PSZ is apparently superior in tensile strength compared with the TS grade PSZ. However, the situation is reversed at high temperatures above 700°C. The tensile strength of the MS grade PSZ falls consistently below the flexural strength by about 40% over the temperature range tested.

A cyclic fatigue test was performed at 1000°C. To avoid rupture by excessive loading, the specimen was cycled initially to a level equivalent to about two-thirds of the tensile strength determined previously. Subsequently, the cyclic load was increased in steps of about 14 MPa (2,000 psi) each until failure occurred. A detailed account of the test conditions can be found in Table 1 and the test data are shown in Fig. 2. The closed symbols indicate failure which occurred at the test condition, whereas the open symbols indicate intermediate loading steps with no specimen failure occurring at the indicated test condition. A cursory examination of stress-strain plots indicated a hint of strain ratchetting resulting from the cyclic loading. However, the total accumulation appeared to be much less severe than that observed in the test for the TS grade PSZ. Similarly, the "coaxing" effects which were evident in the case of the TS grade were also less obvious in this material.

Table 1. Results of tensile and cyclic fatigue tests of NILCRA's MgO-PSZ at elevated temperatures (MS grade)

Specimen	Temperature (°C)	Tensile strength [MPa (ksi)]	Cyclic stress to failure [MPa (ksi)]	Intermediate cyclic stress [MPa (ksi)]	Number of cycles at intermediate cyclic loading	Number of cycles to failure
26	RT	468 (67.9)				1
28	400	341 (49.5)				1
29	400	440 (63.7)				1
30	800	265 (38.5)				1
31	300	258 (37.5)				1
32	1000	222 (32.3)				1
33	1000	194 (28.1)				1
34	1000			140 (20.4)	45,100	(45,100)[a]
	1000			154 (22.4)	44,850	(89,950)
	1000			168 (24.4)	43,938	(133,888)
	1000		183 (26.5)		96,657	230,545

[a]Number of cycles accumulated at the end of intermediate loading.

ORNL-DWG 88-2242

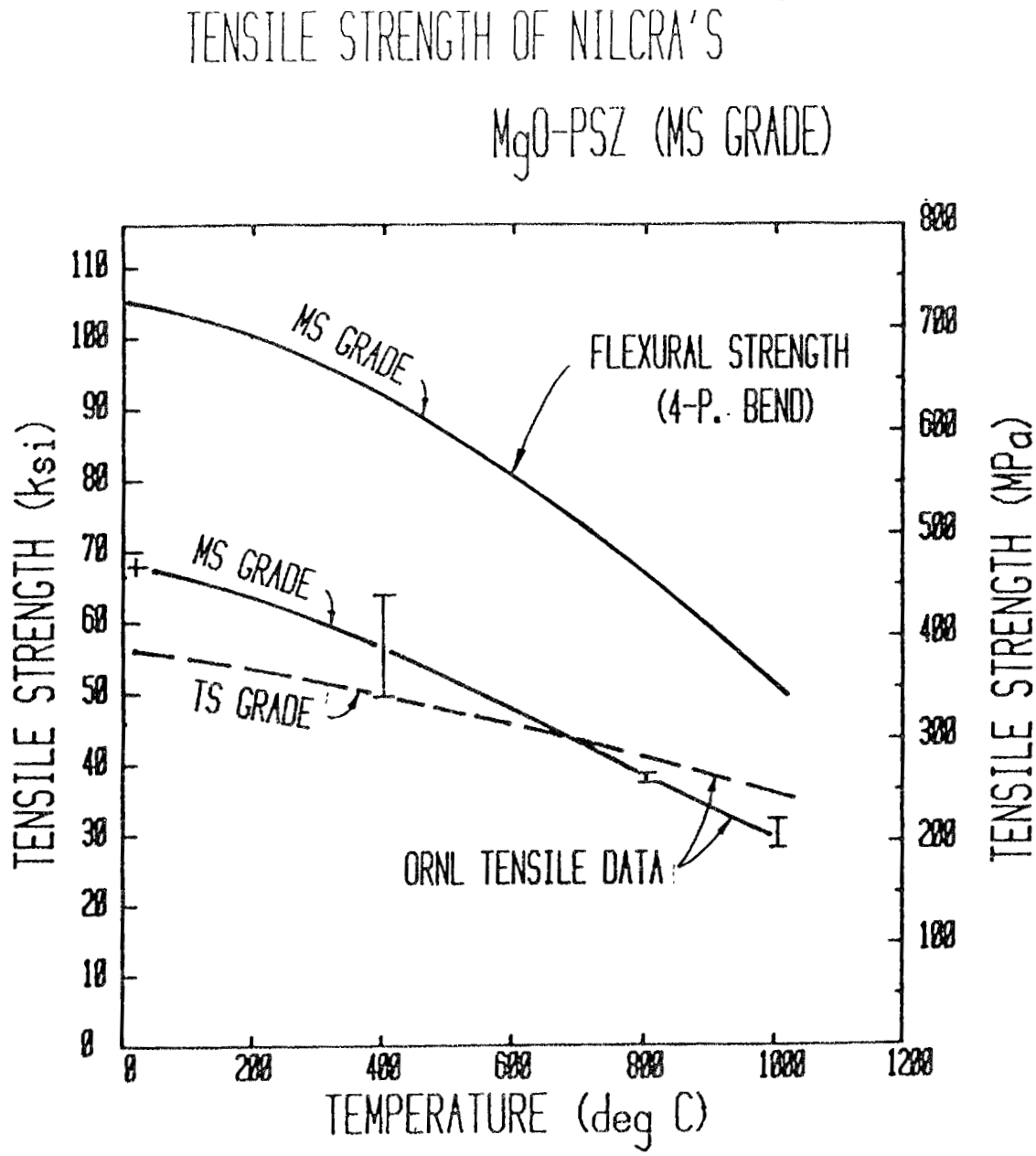

Fig. 1. Comparison of four-point bend flexural strength and uniaxially determined tensile strength of MgO-PSZ at room and elevated temperatures.

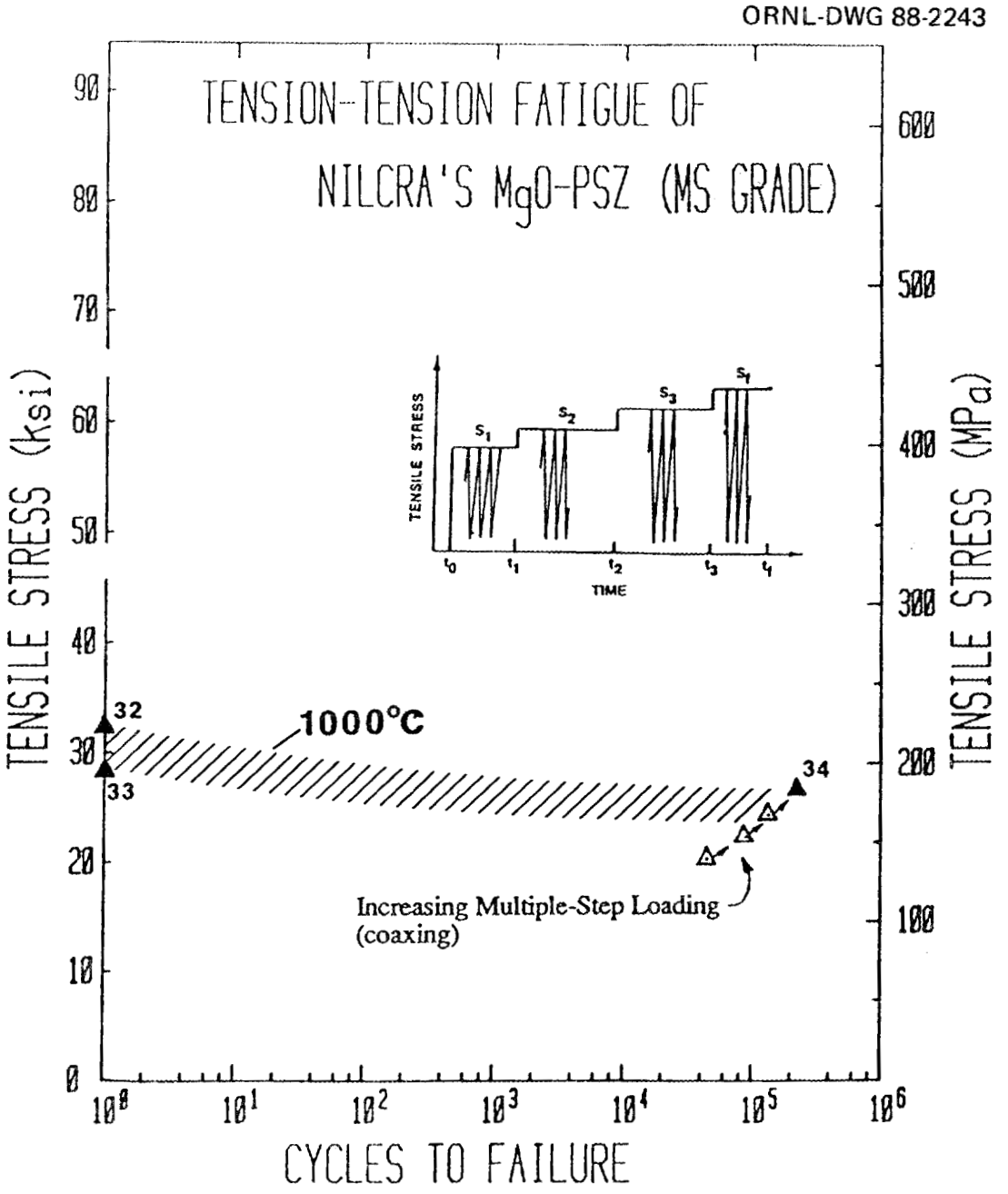

Fig. 2. Tensile strength and fatigue behavior of MgO-PSZ (MS grade) tested at 1000°C.

Tensile testing of silicon nitride

A set of five hot isostatically pressed (HIPed) and eight hot-pressed Si_3N_4 tensile specimens was received from Norton Company. The specimens are made from an experimental Si_3N_4 referred to as sample No. 3205. All the five HIPed specimens have been tested in uniaxial tension at 1200°C. Test results are summarized in Table 2. Note that two specimens (Nos. 2 and 5) ruptured outside the uniform gage section. Therefore, the fracture strengths (column 2 of Table 2) are calculated based on the actual area of the fracture surface, whereas the ultimate tensile strength (UTS) (column 3) is based on the minimum area of the gage section. The average value of the fracture strength is 305.5 MPa (44.3 ksi) with a standard deviation of 60.9 MPa (8.8 ksi) and the coefficient of variation of about 20%. The statistics for the UTS are slightly better compared to the above. The average value of the UTS is 329.3 MPa (47.8 ksi) with a standard deviation of 55.3 MPa (8.0 ksi) and the coefficient of variation of 16.8%.

Four specimens from the batch of eight hot-pressed specimens were tested in tensile fast fracture mode at room temperature. Remaining specimens were returned to Norton to be tested on their newly acquired testing machine for comparison with the ORNL data which are summarized in Table 3.

Table 2. Results of tensile tests of HIPed Si_3N_4 (Norton No. 3205) at 1200°C

Specimen	Fracture strength		Maximum tensile strength		Fracture location
	(MPa)	(ksi)	(MPa)	(ksi)	
1	251.63	36.5	251.63	36.5	Within gage section
2	342.24	49.6	396.94	57.6	6.3-mm (0.25-in.) off gage section
3	341.36	49.5	341.36	49.6	Within gage section
4	376.04	54.5	376.04	54.5	Within gage section
5	216.16	31.41	280.7	40.7	7.9-mm (5/16-in.) off gage section
Average	305.49	44.31	329.33	47.76	
Standard deviation	60.87	8.79	55.32	8.02	
Percent of variance	19.9	19.9	16.8	16.8	

Table 3. Results of tensile tests of hot-pressed Si_3N_4 (Norton No. 3205) at room temperature

Specimen	Young's modulus		Fracture strength	
	(GPa)	(ksi)	(MPa)	(ksi)
1	254	36.8	516	74.9
2	265	38.4	418	60.6
4	263	38.1	421	61.1
7	282	40.9	484	70.3
Average	266	38.6	460	66.7
Standard deviation	10.1	1.5	41.8	6.1
Percent of variance	3.8	3.8	9.1	9.1

The average value of the UTS is 460 MPa (66.7 ksi) with a standard deviation of 41.8 MPa (6.1 ksi) and the coefficient of variance of 9.1%. According to Norton, the strength values fall closely on the predicted values of a Weibull distribution. A more detailed analysis of the data will be deferred until the testing of the remaining specimens is completed by Norton. The average value of the Young's moduli obtained from these tests is 266 GPa (38.6×10^6 psi) with a standard deviation of 10.1 GPa (1.5×10^6 psi) and the variance of 3.8%.

Fracture surfaces were examined by optical microscopy which showed that all specimens failed from inclusions which acted as fracture initiation sites. This observation clearly indicates that these inclusions, believed to be iron, are detrimental to the UTS of this material.

Flat plate specimen testing

Ceramic materials used for research purposes are often available only in limited shape, size, and volume. Because of the availability and specimen fabrication costs considerations, there is high interest in performing tensile testing using small flat plate specimens instead of relatively large cylindrical rod specimens. A dog-bone-shaped flat plate specimen, as shown in Fig. 3, will be used. The plate specimen with a 6.3 by 6.3 mm (0.25 by 0.25 in.) cross section as shown contains more material in the gage section than our standard cylindrical rod specimen having a 6.3 mm gage diameter by about 25%, while the plate specimen uses substantially less material than the rod specimen by about 66%. Clevis holes usually employed in each end of the plate specimen are not used in this

ORNL-DWG 88-2241

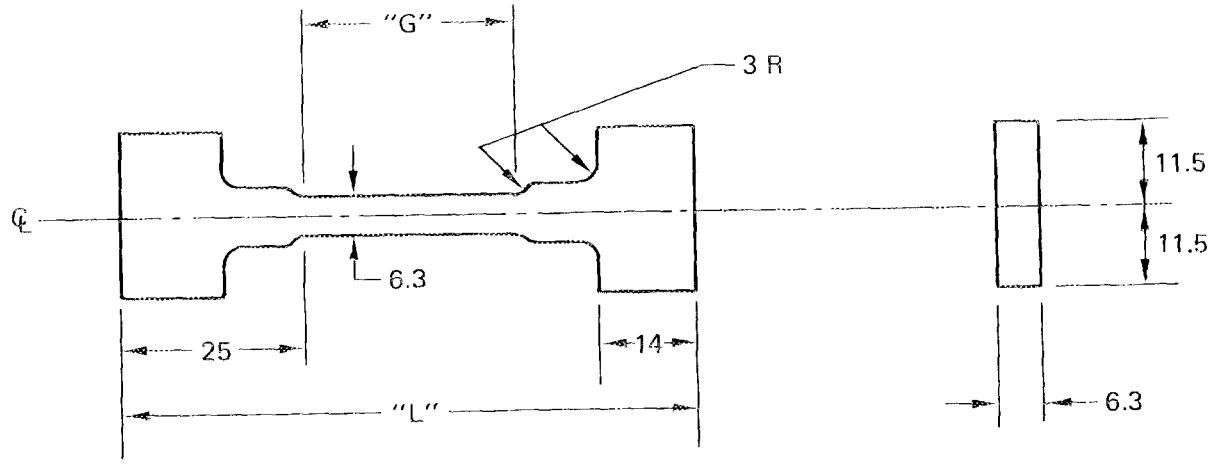

"L" = TOTAL LENGTH
"G" = L - 50 = GAGE LENGTH

ALL DIMENSIONS IN mm

Fig. 3. Details of flat tensile specimen.

design to reduce the machining cost. However, the holeless plate specimen is not without some drawbacks, namely, that it is more difficult to grip and achieve good alignment.

Significant progress has been made to overcome these problems and the flat plate specimen can now be tested with a newly developed pull-rod assembly in conjunction with the self-aligning grip to achieve uniform stress loading. Results of preliminary tests using a dummy aluminum specimen instrumented with strain gages showed that the new pull-rod assembly could perform bend-free tensile loading equally well, as in the case of the standard rod specimen.

A set of 12 flat plate ceramic tensile specimens were fabricated from a billet of Norton XL 144H silicon nitride. The specimens are now being subject to nondestructive examination analysis.

Publications

Liu, K. C., and Brinkman, C. R., "Dynamic Cyclic Fatigue of Si_3N_4," to be published in proceedings of 25th ATD-CCM, Dearborn, Michigan, October 26-29, 1987.

Liu, K. C., Pih, H., and Voorhes, D. W., "Uniaxial Tensile Strain Measurement for Ceramic Testing at Elevated Temperature – Requirements, Problems, and Solutions," invited for presentation at the Conference on Mechanical Testing of Engineering Ceramics at High Temperatures, to be held in London, England, April 11-12, 1988.

Liu, K. C., "Ceramic Specimen Heating by Induction Power," invited for presentation at the Conference on Mechanical Testing of Engineering Ceramics at High Temperatures, to be held in London, England, April 11-12, 1988.

Liu, K. C., and Brinkman, C. R., "High Temperature Fatigue Behavior of Commercial MgO-PSZ," abstract for a paper to be presented at the Third International Symposium, Ceramic Materials and Components for Engines, Las Vegas, Nevada, November 28-30, 1988.

Rotor Data Base Generation

M. K. Ferber (Oak Ridge National Laboratory)

Objective/scope

The goal of the proposed research program is to systematically study the tensile strength of a silicon nitride and a silicon carbide ceramic as a function of temperature and time in an air environment. Initial tests will be aimed at measuring the statistical parameters characterizing the strength distribution of three samples types (two tensile specimens and one flexure specimen). The resulting data will be used to examine the applicability of current statistical models as well as sample geometries for determining the strength distribution.

In the second phase of testing, stress rupture data will be generated by measuring fatigue life at a constant stress. The time-dependent deformation will also be monitored during testing so that the extent of high-temperature creep may be ascertained. Tested samples will be thoroughly characterized using established ceramographic, SEM, and TEM techniques. A major goal of this effort will be to better understand the microstructural aspects of high-temperature failure including:

(1) extent of slow crack growth;
(2) evolution of cavitation-induced damage and fracture;
(3) transition between brittle crack extension and cavitation-induced growth; and
(4) crack blunting.

The resulting stress rupture data will be used to examine the applicability of a generalized fatigue-life (slow crack growth) model. If necessary, model refinements will be implemented to account for both crack blunting and creep damage effects. Insights obtained from the characterization studies will be crucial for this modification process. Once a satisfactory model is developed, separate stress-rupture (confirmatory) experiments will be performed to examine the model's predictive capability. Consequently, the data generated in this program will not only provide a critically needed base for component utilization in automotive gas turbines, but also facilitate the development of a design methodology for high-temperature structural ceramics.

Technical progress

The equipment required for the flexure testing phase of this program was made operational. This equipment (Fig. 1) consists of two specially designed Flexure Test Systems (F.T.S.) each capable of holding up to three bend samples. The Test Frame contains the hardware for applying

mechanical forces to each of three samples which are supported by aluminum oxide (Al_2O_3) four-point bend fixtures. The loads are generated by pneumatically driven air cylinders located at the top of the support frame. In order to minimize impact problems normally encountered during fracture, a hydraulic fluid is used as the working medium in the cylinder. The mechanical loads are transmitted into the hot zone of the furnace through Al_2O_3 rods. Each of the bottom three Al_2O_3 rods are also attached to a load cell which monitors the applied force as a function of time. Water-cooled adapters connect the aluminum oxide rams to both the load cells and the air cylinders. During a test, an LVDT tracks the downward displacement of the load ram. The computer monitors this displacement as well as the load on each specimen and provides necessary adjustments in the air pressure (via the electro-pneumatic transducer) such that the desired stress level is maintained.

ORNL-DWG 88-2266

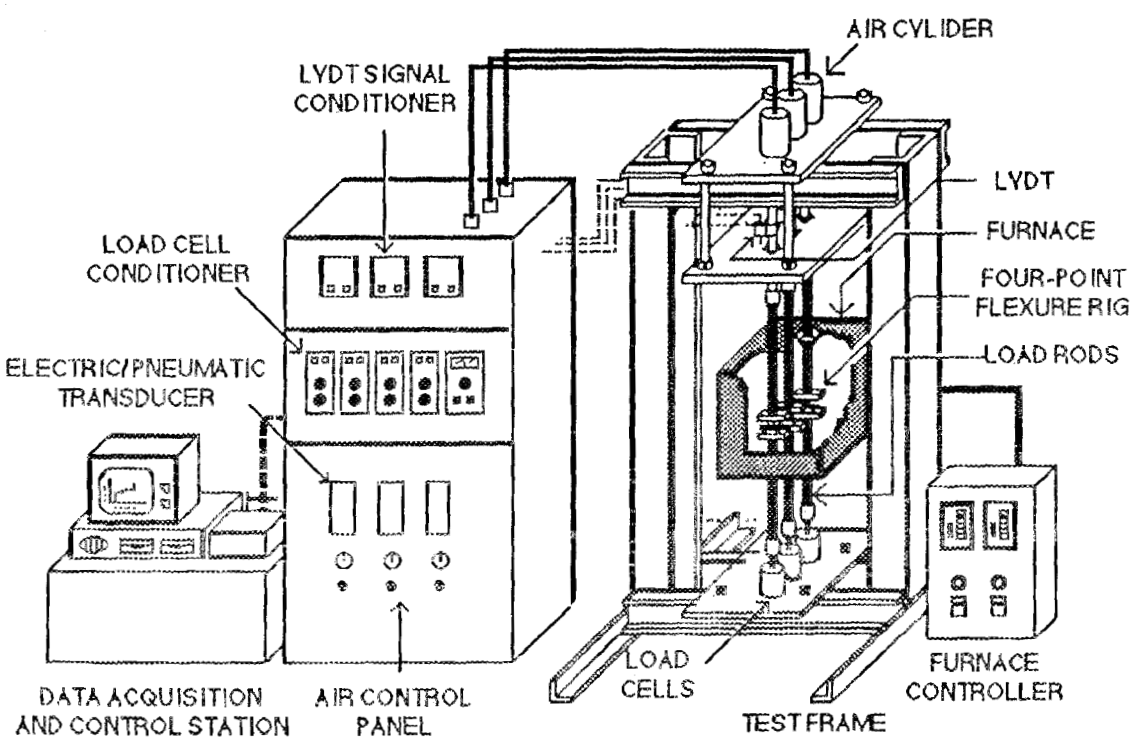

Fig. 1. A pneumatic load train system is used to generate the high-temperature flexure data in the present study.

The performance of F.T.S. was evaluated by testing an experimental dispersion toughened alumina (DTA). Initially, the four-point bend strength (Sf) was measured at 25 and 1000°C. The results indicated a substantial temperature dependence with Sf decreasing from 838+/-70 MPa (121+/-10 ksi) at 25°C to 430+/-63 MPa (62+/-9 ksi) at 1000°C. Subsequent static load tests conducted at 1000°C revealed a significant fatigue effect for this DTA. As shown in Fig. 2, the fatigue life was less than 20 h when the stress level was maintained at approximately 50% of the

short-term breaking stress. The associated slow crack growth exponent (N) was estimated as 16. This number should only be taken as a rough approximation due to the limited nature of the fatigue data.

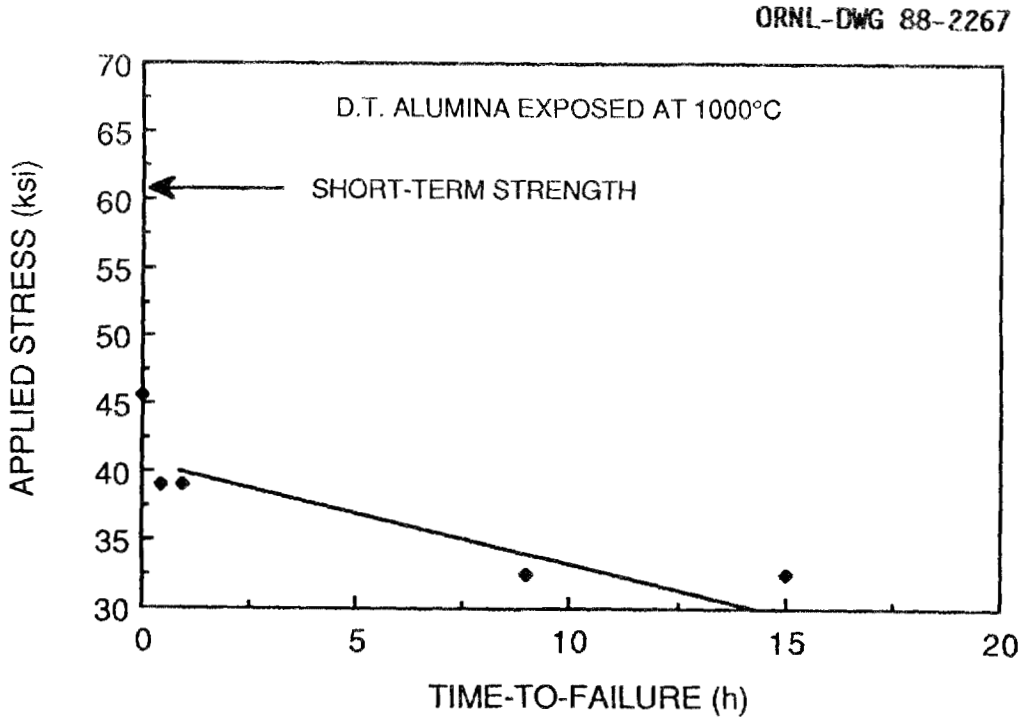

Fig. 2. A significant fatigue effect was observed in the DTA material exposed at 1000°C.

The observed fatigue behavior may have resulted from a creep rupture process. For example, evidence of a time-dependent deformation mechanism was provided by the LVDT displacement measurements. Figure 3 illustrates the displacement-time curves for two DTA samples subjected to a stress level of 214 MPa (31 ksi). A third sample, which was also exposed at 1000°C but not stressed, was used to measure the effects of background thermal fluctuations. As shown in Fig. 3, these fluctuations were significantly smaller than the deformation occurring in the stressed specimens. Finally, it is interesting to note that the unstressed sample was loaded to failure following the premature failures of the stressed specimens. The resulting strength was 544 MPa (78.9 ksi) which is greater than the value obtained from short-term testing. This result indicates the importance of applied stress in the fatigue process.

Equipment required for the measurement of fracture toughness was also made operational. This equipment consists of a computer-controlled pneumatic loading system which contains a standard Vickers indenter mounted in the load train. The toughness, K_{IC}, can be determined using one of two techniques. First, the length of the cracks produced from the indentation of a polished sample can be used in conjunction with well established equations to calculate K_{IC}, which is often designated as

ORNL-DWG 88-2268

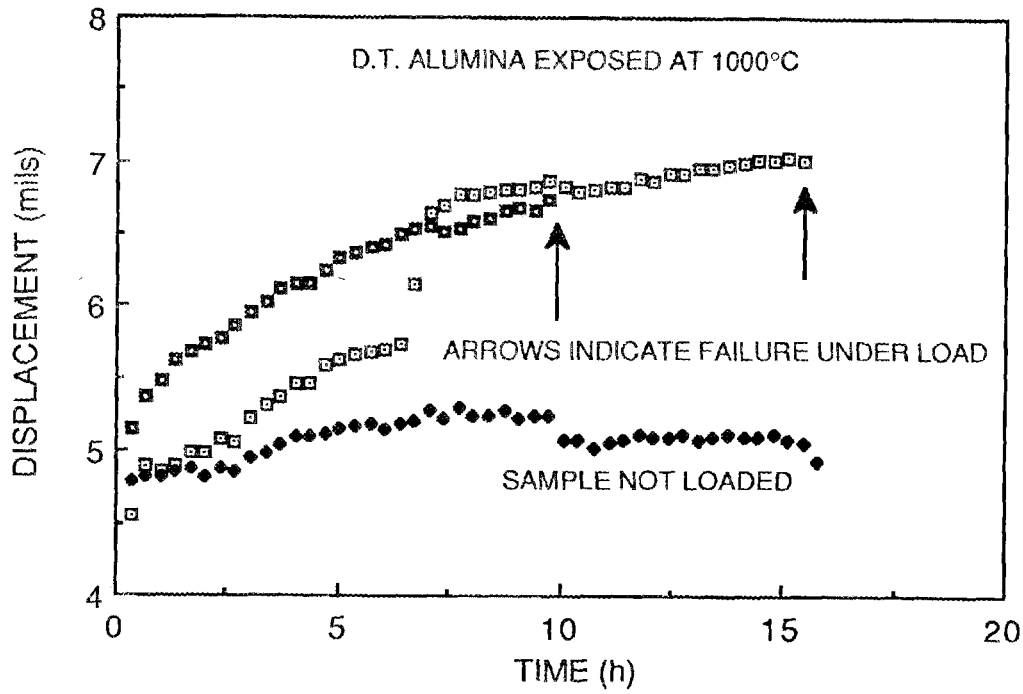

Fig. 3. DTA samples stressed at 1000°C experienced a time-dependent deformation.

indention fracture toughness. This approach requires values of the hardness and Youngs modulus. The second method involves introducing 3 to 4 indent cracks into the gauge section of a polished flexure specimen. The sample is then loaded until failure occurs from one of the indent cracks. The length of cracks associated with the surviving indents and the value of the fracture stress is then used to calculate K_{IC}, which is generally designated as controlled flaw fracture toughness. The primary advantage of the latter technique is that measurements can be made at elevated temperatures.

The performance of the indentation system was evaluated by testing an experimental dispersion toughened alumina (DTA). The results are summarized in Table 1. The fracture toughness typically ranged from 5.7 to 6.9 and was relatively insensitive to temperature.

Table 1. Summary of fracture toughness measurements for DTA

Method	Temperature (°C)	No. of samples	K_{IC} [MPa(m)$^{1/2}$]	Standard deviation
I.F.T.	25	9	5.7	0.6
C.F.T.	25	1	6.9	---
C.F.T.	1000	2	5.8	0.5

I.F.T. - indention crack length method; C.F.T. - controlled flaw method.

The silicon nitride flexure and tensile samples required for the Phase 1 of this study were ordered during this reporting period. The tensile specimens will consist of both button head samples (circular cross section) and flat samples. All test samples will be provided by the vendor in near net shape geometries. A four axis grinding machine, which is to be installed by April, will be used for the final machining of the tensile specimens.

The tensile test machines to be utilized in this study were installed in March. These machines have a maximum temperature capability of 1500°C. Specimen bending during loading is minimized by employing hydraulic couplers in the load train.

Status of milestones

No activity.

Publications

No publications.

3.3 ENVIRONMENTAL EFFECTS

Environmental Effects in Toughened Ceramics

N. L. Hecht (University of Dayton)

Objectives/scope

Effective September 1987, the ORNL sponsored project at the UDRI investigating SiC and Si_3N_4 ceramics which are candidates for heat engine applications was extended. The primary focus of this project is to extend the mechanical property data base for SiC and Si_3N_4 ceramics and increase the degree of confidence for using these materials in designing heat engine components. The specific objectives of this project are to develop a more comprehensive understanding of fatigue behavior and to obtain tensile strength data for the various commercial compositions from 25° to 1400°C. We have selected these objectives to aid us in attaining our goal of providing reliable engineering data for heat engine design.

Background

The problems associated with non-uniform stress, due to eccentric loading during tensile testing or longitudinal friction during flexure testing, can be detected by monitoring specimen strain during strength measurements with holographic interferometry and laser speckle interferometry.

Holography is a two-stage lensless laser photography process, yielding a virtual three-dimensional image which is an extremely accurate reproduction of the original object. The technique is based on the natural phenomenon of light wave interference. The hologram is formed by recording the complex interference pattern produced by the superposition of a beam of light from a monochromatic, coherent source (laser) and light from the same source which has been diffusely reflected from a three-dimensional object. The laser beam is split into two beams; an object beam and a reference beam. These two wavefronts (the complex optical wave reflected from the object and the reference wave) combine to form a complex series of interference patterns (see Figure 1).

In the second stage of the process the hologram (the interference pattern) is re-illuminated by laser light originating from the same relative position as the original reference beam. The interference pattern on the photographic plate acts as a diffraction grating which recreates the object wave front. By looking through the hologram, the viewer observes a true three-dimensional virtual image which is an exact replica of the object in size and position, and displays both depth of field and parallax. The view seen through the hologram is exactly what would be seen by looking at the original object (see Figure 2). The light arriving at the

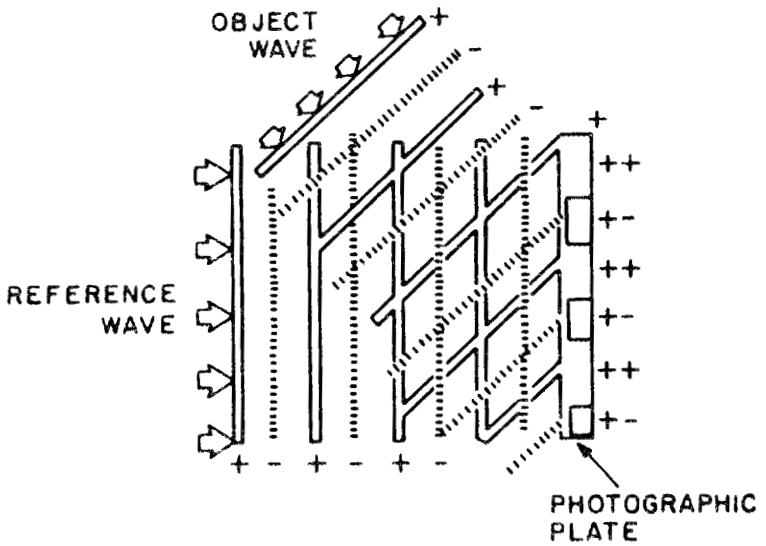

Figure 1. Interaction of reference wave and object wave to form a hologram.

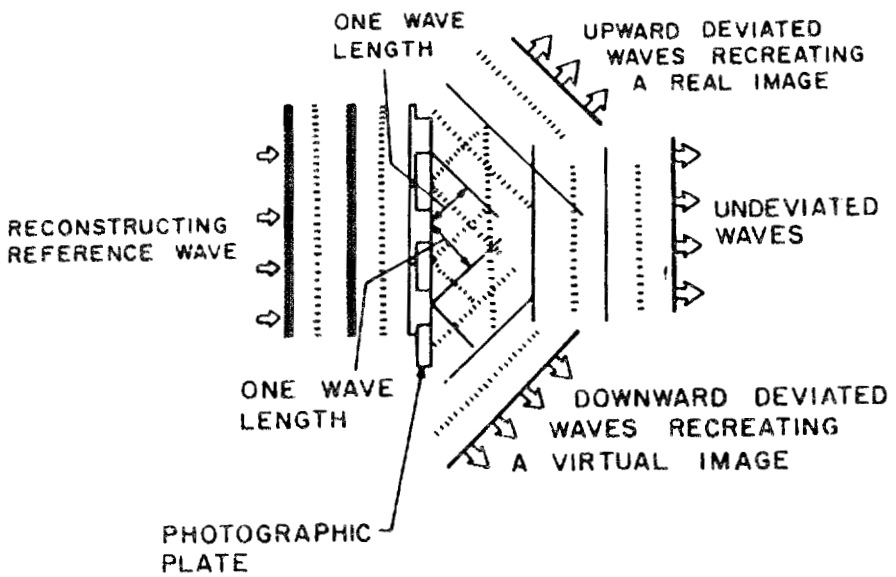

Figure 2. Diffraction of the reference wave to recreate the object wave front.

observer's eye from the holographic reconstruction is exactly the same as the light reflected from the surface of the original project and for all practical purposes can be optically treated as the original object.

If the holographic image is reconstructed and the object is left in place and illuminated, then the viewer will observe two images of the object that exactly overlap. If the object undergoes some positional change (displacement) as a result of the application of stress or vibration, such that the relative distances of the object and image from the viewer are not the same, the coherent light reaching the viewer from the two sources will not have the same phase and interference fringes characteristic of the displacement pattern will result. This technique is termed holographic interferometry [1-8]. It is usually employed either in real time, as described above, or in a time lapse mode (double exposure method). In the time lapse mode, the reconstructed image of the object at rest is superimposed on the image of the displaced object and both holograms are recorded on the same photographic plate. The resulting hologram reconstructs both object wavefronts simultaneously on re-illumination. Interference fringes, due to the shift of surface points, are observed in this recreation.

An alternate method for measuring small displacements is laser speckle interferometry. Laser speckle is the term applied to the graininess observed when viewing laser light illuminated objects whose surface has random irregularities with dimension of half the wavelength of light (10 μm) or larger. The speckle size observed is a function of the observation system,

$$\phi = 1.2\ \lambda F \qquad (1)$$

where ϕ is the mean speckle diameter, λ is the wavelength of the laser, and F is the f-number of the observation system lens in use. The speckle pattern is related to the surface structure scattering the light. If the surface shifts laterally, due to vibration or strain, the speckle pattern will shift. If the shift is comparable to the size of the speckle grains or larger, overlayed images captured "before" and "after" will demonstrate an "interference" effect. The effect is a moiré pattern and the moiré fringes are a map of the surface motion. This system has been used with fast optics (small F) to record motions of 0.4 μm [9]. Recently much interest has been shown in a system in which the speckles can be viewed by a TV camera so that the speckle pattern can be captured electronically and the speckle "interferograms" processed directly in video and computer systems.

Work plan

The research plan developed for this project is outlined in Table 1. During the past six months, Task I was initiated and completed. Eleven companies which are suppliers of SiC and Si_3N_4

Table 1. Research Plan

Task I Project Initiation

Phase I - Candidate Material Selection

A. Review Candidate Material Options
B. Select Two Candidate Materials for Investigation and Evaluation and Establish Procedures for Specimen Preparation and Specifications for Surface Finish
C. Place Order for Flexure and Tensile Specimens

Phase II - Re-evaluate and Finalization of Testing Protocol

A. Review of Testing Protocol Technology
B. Re-evaluation of Flexure Testing Facility

Phase III - Establish Protocol for Data Storage

A. Investigate Computer Data Storage Systems
B. Establish the Data Storage Protocol to be Used

Task II Investigation of Fatigue at Elevated Temperatures

Phase I - Dynamic Fatigue -- Four Point Flexure Testing @ 1000°C/1200°C/1400°C in Air at Three Loading Rates

Phase II - Tensile Stress Rupture (static fatigue) @ 1000°C/1200°C/1400°C in Air at 2/3 the measured fast fracture tensile strength

Phase III - Analysis of Results

A. Statistical Analysis of Test Data
B. Fracture Analysis - Visual Inspection/ Microscope Examination/SEM and EDXA Examination/TEM/Auger

Task III Tensile Strength Measurements

Phase I - Measurement of Tensile Strength @ 25°C/500°C/750°C/1000°C/1200°C/1400°C

Phase II - Analysis of Test Results

A. Statistical Analysis of Tensile Test Data
B. Fracture Analysis - Visual Inspection/ Microscope Examination/SEM and EDXA/TEM

Table 1. Research Plan (Concluded)

Task IV Material Characterization

A. Microstructure and Chemistry - Optical Microscopy/SEM and EDXA/XRD/Raman and IR Spectroscopy/Auger
B. Density (immersion)/Hardness (Vickers microhardness)/Coefficient of Thermal Expansion
C. Fracture Toughness - Controlled Flaw Method at 25°C/1000°C/1400°C (alternate methods of measuring K_{Ic} will be investigated)
D. Elastic Modulus - By Sonic Methods and Also Interferometry at 25°C/1000°C/1400°C
E. Flexural Strength - Measurement of Flexural Strength in Air @ 25°C/500°C/750°C (analysis of MOR results - statistical analysis/fracture analysis)

Task V Data Base Extension

Phase I - Review and Finalize Data Storage System to be Used

Phase II - Establish Data Storage Protocol and Format

Phase III - Initiate Data Storage Program

Task VI Project Addendum - Limited Characterization of Additional Si_3N_4 and SiC Ceramics

Phase I - Candidate Material Identification and Selection

Phase II - Materials Evaluation - High Temperature Dynamic Fatigue Evaluation (1000°C/1200°C/1400°C)

Phase III - Extended Material Analysis - Tensile Strength Measurement @ 25°C/500°C/1000°C/1400°C Data, Fracture Toughness @ 25°C and 1400°C, Flexural Strength Measurements at 25°C and 500°C, Analysis - Weibull analysis/Fracture Analysis

ceramics were contacted about this materials evaluation project and our interest in obtaining test specimens of their product. Based on the information received and with concurrence of our contract monitor, a materials testing plan was developed and orders submitted for the required test specimens. Two materials (sintered α-SiC and Si_3N_4) were selected for detailed tensile strength measurements and high temperature fatigue evaluation. Six materials [one SiC (cvd) and five sintered Si_3N_4 ceramics)] were selected for limited high temperature (1000°, 1200°, and 1400°C) fatigue analysis. In addition, one material (a sintered Si_3N_4) was selected for limited tensile and fatigue evaluation.

Activities for Phase III to establish the protocol for data collection and storage have also been completed. As part of this activity a data collection format was developed using d Base III software. A comprehensive file of literature (about SiC and Si_3N_4 property measurements) has been accumulated for incorporation into the data base.

Efforts were also initiated for the investigation of holographic interferometry for monitoring mechanical strength measurements. A tentative arrangement for using double exposure holographic interferometry to evaluate the displacement of tensile and flexure specimens was developed (see Figures 3 and 4).

During the initial months of this project, the characterization of GTE-PY6 Si_3N_4, Sohio Hexoloy SA SiC, and Norton/TRW XL144 Si_3N_4 was extended.[3] Flexural strength measurements were made at 1300° and 1450°C. In addition, the room temperature (25°C) flexural strength of Norton/TRW XL144 specimens was also measured. At 1450°C the flexural strength of ten specimens of each of the three materials was measured at the slow loading machine crosshead speed of 0.0025 cm/min (.001 in/min). The results obtained were compared to the flexural strengths measured for these three materials at 1450°C for the fast loading machine crosshead speed of 0.38 cm/min (.15 in/min). At 1300°C the flexural strengths of the Hexoloy SA and the XL144 ceramics were measured at both the fast and slow loading machine crosshead speeds (0.0025 and 0.38 cm/min).

All of the flexural strength measurements were made using an Instron Universal Testing machine (Model 1123). The high temperature tests were conducted in an ATS #3320 furnace. All of the test specimens measured were 5.1 x 0.64 x 0.32 cm (2 x 0.25 x 0.125 in). The tensile surface of all test specimens was ground and the long edges were rounded and polished. Strength was measured using a four point flexure fixture which has an outer span of 3.81 cm (1.5 in) and an inner span of 1.91 cm (0.75 in). For room temperature flexural strength measurements a hardened steel fixture was used and for elevated temperature measurements a hot pressed SiC fixture was used. Fracture origins were determined by optical microscope (Nikon Epiphot Metallograph) and SEM (JEOL/SM-840). The flexural strength values obtained were evaluated to determine the fatigue and Weibull parameters.

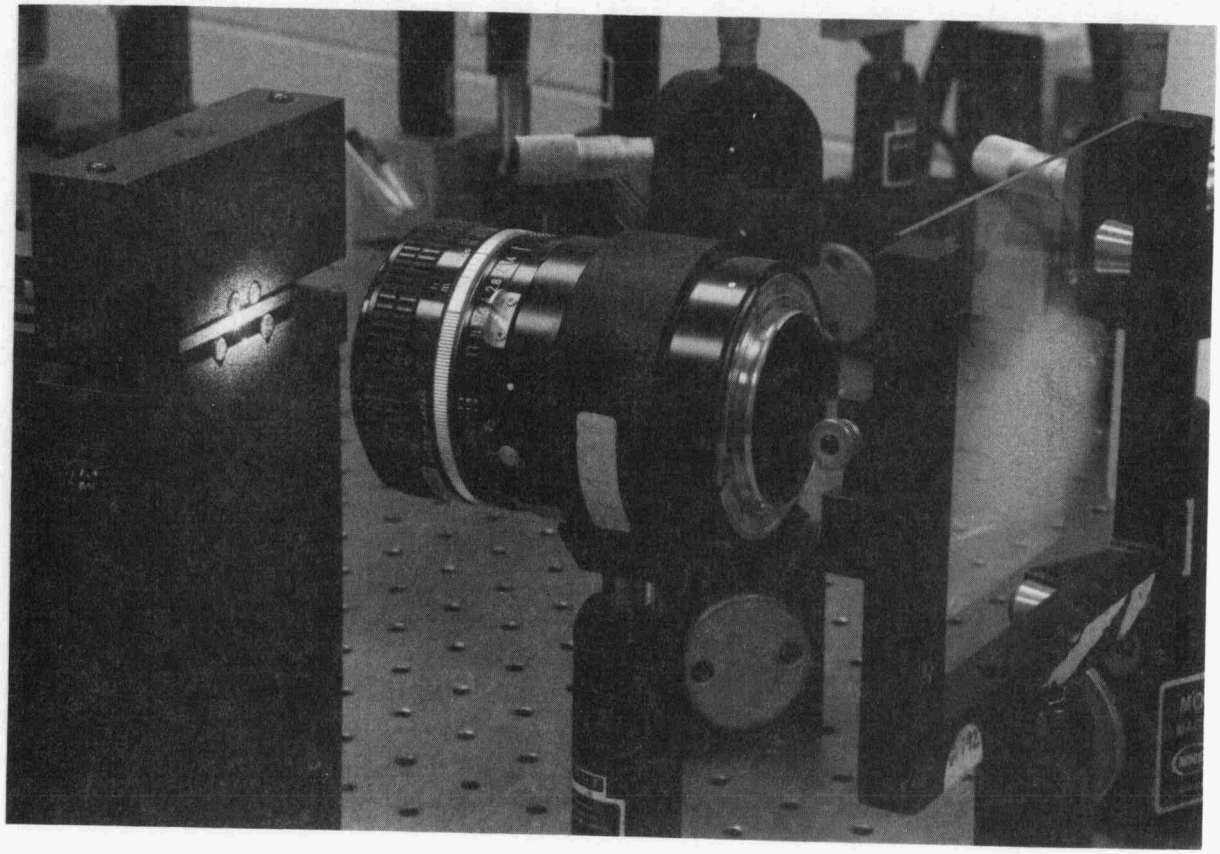

Figure 3. Arrangement for the holographic evaluation of flexure specimens.

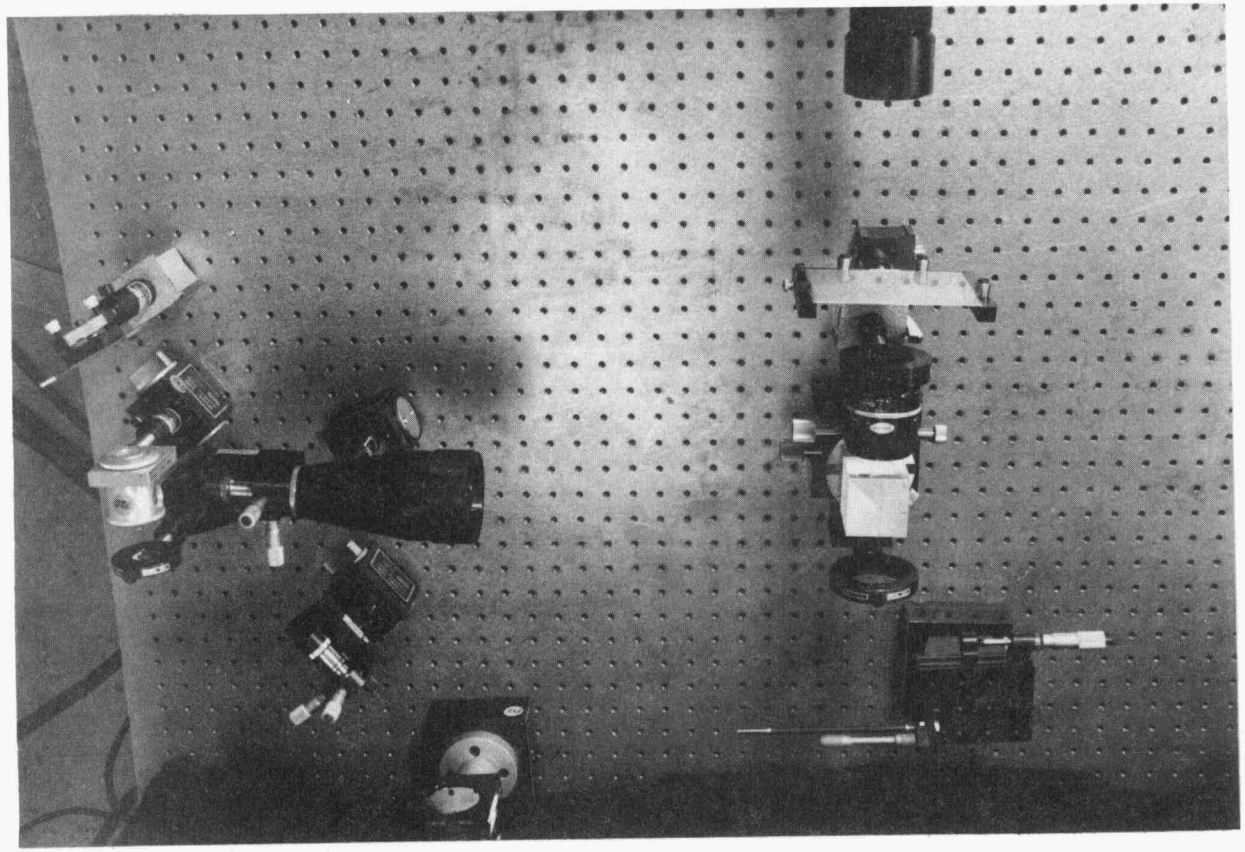

Figure 4. Arrangement for the holographic evaluation of tensile specimens.

It has been observed for many ceramics that higher strengths are observed at higher stressing rates because there is less time for subcritical crack growth to occur. This effect, known as dynamic fatigue, is best characterized by a ln-ln plot of fracture strength versus stressing rate. The relationship between fracture strength and stressing rate is:

$$\sigma_f = A'\dot{\sigma}^{(\frac{1}{n+1})} \qquad (2)$$

where σ_f = fracture strength

$\dot{\sigma}$ = stressing rate

A',n = constants.

The constant n, the stress intensity factor exponent, gives a measure of the stress corrosion susceptibility of the material. Large n values are synonymous with lower stress corrosion or fatigue susceptibility. Thus the plot of log $\dot{\sigma}_f$ versus log σ yields a straight line with a slope of: $\frac{1}{n+1}$.

For the Weibull analysis maximum likelihood estimates of the shape parameter, m (modulus), and the scale parameter, S_0 (the 63rd percentile distribution of breaking strength for a unit surface area) were determined.

During this reporting period the thermal expansion coefficient was measured on one Hexoloy SA and one XL144 specimens. Each specimen was tested three times from 25° to 1450°C using a Theta Industries Dilatronic II (Model 6024). Specimen weight change was determined after each run.

Technical progress and discussion of results

Holographic interferometry

The holographic development effort has concentrated on the development of the software for computer analysis of the interferometric fringe patterns. This software will be needed to measure fractions of fringe displacement anticipated. This software is also needed to qualify the optical systems used to make the interferograms. The evaluations of optical configurations have only been limited pending the availability of software. Using the holographic configurations developed tensile and flexure specimen displacement test patterns were obtained for use in the software development.

The problems in computer analysis of fringe patterns deal with determining the local edge of the fringe based on the local variation in gray level of the signal, connection of the local edges to form a global edge, and shifting the global edge population to eliminate connected edges whose total length does

not exceed the threshold set to differentiate signal from noise. Once the fringe edges have been determined, the fringe center line is determined as the geometric mean of the edges which form the boundary of the fringe. The locus of midpoints forms the "fringe location," usually fixed with sub-pixel accuracy. These fringe centers will be the basis of the interferogram analysis.

The fringes will be fit, by least squares adjustment, to straight lines so that their linearity (or curvature) can be evaluated. This will provide a measurement of any bending introduced during tensile testing. The fringe separations will be measured along the specimen to determine the uniformity of the elongation.

The current state of the development of the computer software can be seen in the following figures. Figures 5a and 5b show photographs of typical interferograms obtained when a tensile specimen is translated several microns in plane and rotated out of plane, respectively. The computer software must deal with the granularity of the image, i.e., the image is not smooth and this leads to false edges being assigned to the dark areas in the middle of fringes. The intensity varies across the image so that the edge threshold must be dynamically adjusted to compensate for the intensity variation. Figure 6 shows the results of the computer's first pass assigning edges. The edges are connected into global fringe edges (some of the information is difficult to discern in this black and white photograph of information that is color encoded for presentation to the programmer). Problems with local intensity variation and "islands" resulting from noise can be seen in the lower right corner. Figure 7 is an example of the output of the software after the program has filtered out the "islands" and adjusted the intensity to provide a uniform variation across the image. The algorithm for determining fringe centers is now being implemented.

Flexural strength measurements

The results of the flexural strength measurements at 1450°C for Hexoloy SA, XL144, and PY6 are summarized in Table 2. These results are graphically displayed in Figure 8. The results of the flexural strength measurements at 1300°C for Hexoloy SA and XL144 are summarized in Table 3 and graphically displayed in Figure 9. As shown in Figure 8, the flexural strength of the PY6 and XL144 ceramics is considerably lower for the slow loading rate than for the fast loading rate. These results would suggest that these two materials are subject to time delayed failure (fatigue) at 1450°C.

The room temperature (25°c) flexural strength measured for ten XL144 specimens is compiled in Table 4. These specimens were provided by Norton/TRW and were ground and polished to our test specifications. As shown in Table 4, the average flexural

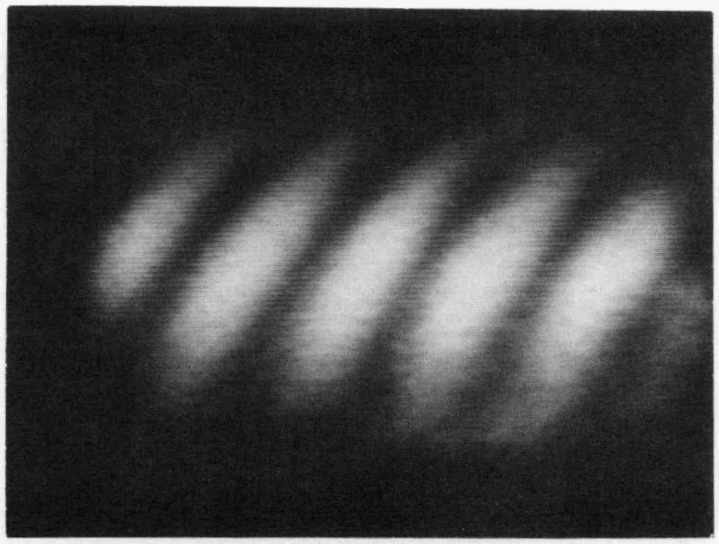

Figure 5a. Holographic fringe pattern for in plane translation of a tensile test specimen.

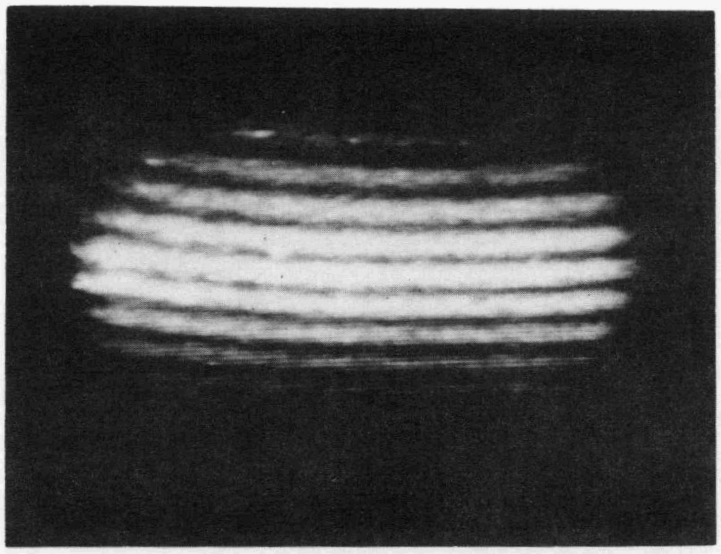

Figure 5b. Holographic fringe pattern for out of plane rotation of a tensile test specimen.

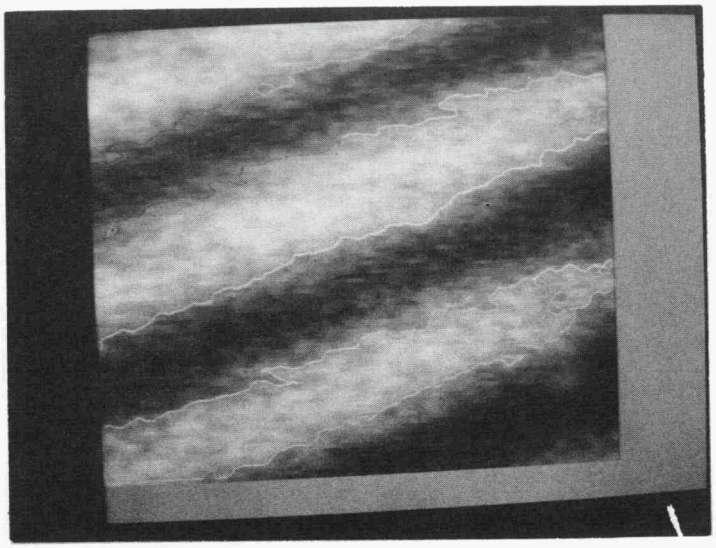

Figure 6. Initial computer generated fringe pattern.

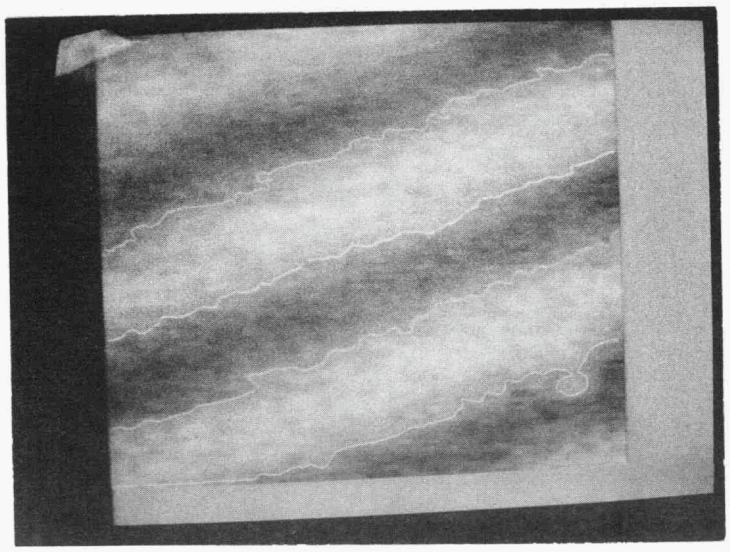

Figure 7. Improved computer generated fringe pattern.

Table 2. Comparison of Flexural Strength Measurements for Hexoloy SA, XL144, and PY6 Ceramics at 1450°C[+]

Material	Strength Fast Loading (MPa)	Standard Deviation (MPa)	Strength Slow Loading (MPa)	Standard Deviation (MPa)	Fracture Mode
PY6	393	69	214	36	For the fast loaded specimens fracture originated at tensile surface and edge flaws, some failures at subsurface flaws and inclusions. The slow loaded specimens fractured at inclusions on or just below the tensile surface and appeared to be subject to SCG.
XL144	453	53	213	12	For the fast loaded specimens fracture originated at tensile surface and edge flaws. The specimens appeared to be subject to SCG.
SA-SiC	500	52	455	59	Both the fast and slow loaded specimens fractured at flaws located on the tensile surface and edges.

[+]Data based on the strength measurement of 10 specimens of each material and test condition.

Table 3. Comparison of Flexural Strength Measurements for Hexoloy SA and XL144 at 1300°C[+]

Material	Standard Fast Loading (MPa)	Standard Deviation (MPa)	Strength Slow Loading (MPa)	Standard Deviation (MPa)	Fracture Mode
SA-SiC	494	90	500	77	Fracture was initiated at flaws on the tensile surface for both the fast and slow loaded specimens.
XL144	604	44	546	93	For the fast loaded specimens fracture originated at tensile surface flaws and in a few cases at subsurface inclusions. For the slow loaded specimens fracture originated at tensile surface flaws.

[+]Data based on the strength measurements for 10 specimens of each material and test condition except for the XL144 slow loaded which is based on 7 specimens tested to date.

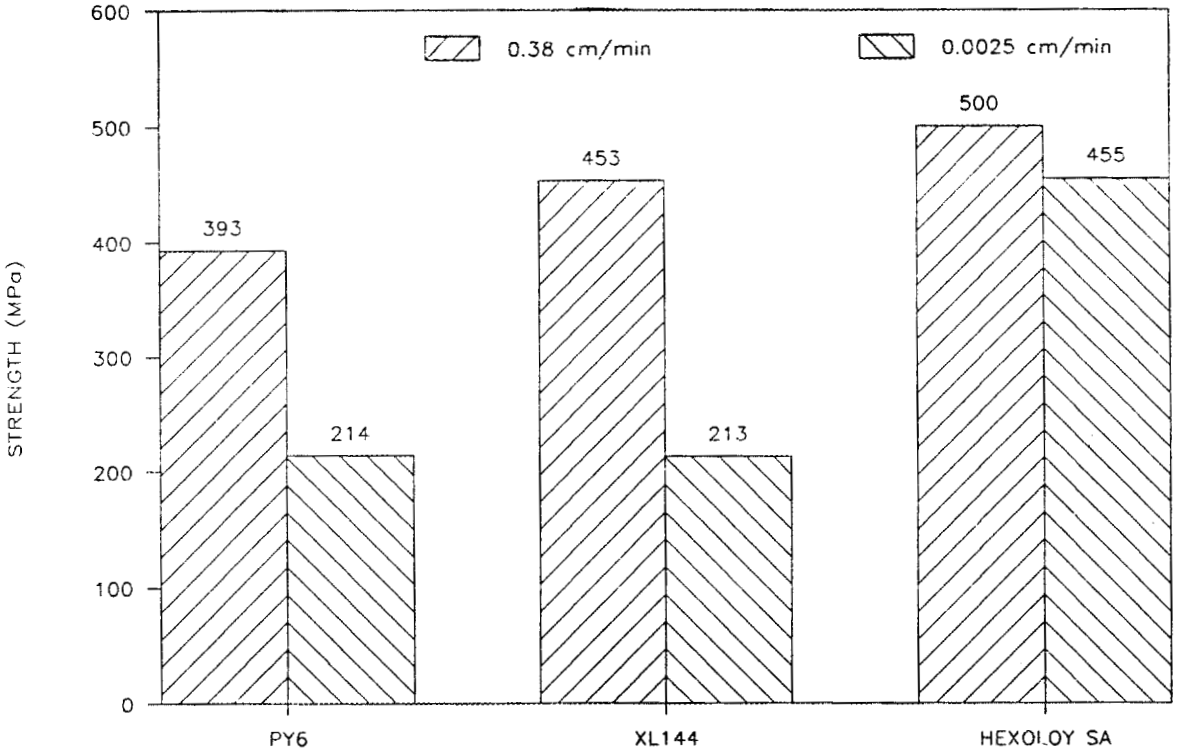

Figure 8. Comparison of flexural strength of GTE PY6, Norton XL144, and Sohio Hexoloy SA at 1450°C for fast and slow stressing rates.

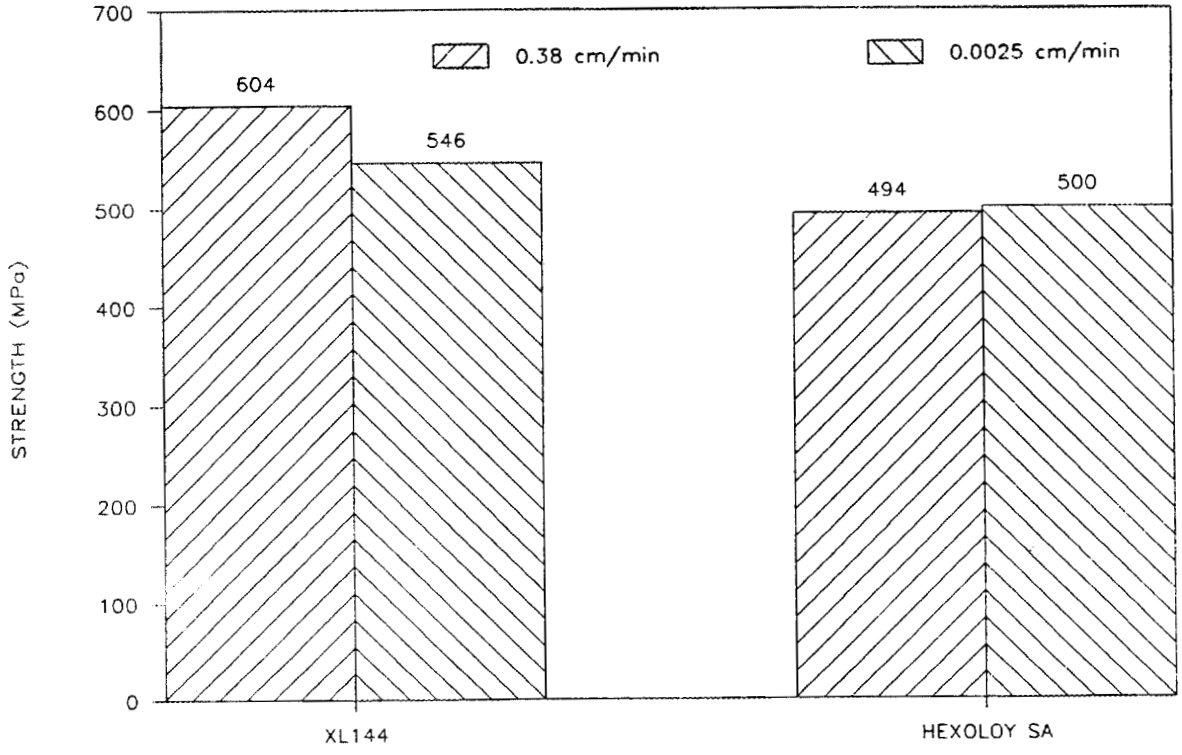

Figure 9. Comparison of flexural strength of Norton/TRW XL144 and Sohio Hexoloy SA at 1300°C for fast and slow stressing rates.

Table 4. Flexural Strengths Measured for Norton/TRW-XL144 at 25°C Using a Machine Crosshead Speed of 0.38 cm/min*

Specimen Number		Flexure Strength (MPa)
1		741
2		772
3		844
4		838
5		811
6		779
7		762
8		833
9		758
10		731
	Average	787
	St. Dev.	41

*For this material earlier flexural strength measurements gave an average of 538 MPa with a standard deviation of 97 MPa.

strength was 787 MPa (114 ksi) for these specimens. This value is considerably higher than the average value obtained from flexural strength measurements obtained earlier in our project. The average room temperature flexural strength measured for ten specimens prepared at the University of Dayton from a hot pressed block of XL144 provided by Norton/TRW was 538 MPa (78 ksi). This variation in strength measurement may be due to batch variations or to the differences in specimen preparation procedures.

Using the data obtained from the flexural strength measurements, the value of n was determined from equation (2) (see Table 5). Computer generated graphs of $\ln\sigma_f$ vs. $\ln\dot{\sigma}$ for each of the materials investigated were prepared and are presented in Figures 10-14. As seen from Table 5 and Figures 10-14, both the PY6 and XL144 materials are subject to time delayed failure at 1450°C. This suggests the susceptibility of these two materials to slow crack growth.

The flexural strength data was also characterized by a Weibull analysis of each of the materials and temperature conditions. The 95% confidence bounds, the Weibull modulus or shape parameter (m) and the scale parameter (the 63rd percentile distribution of breaking strength for a unit surface area) (S_0) were determined using a maximum likelihood analysis. The results of these analyses are summarized in Table 6 and displayed in a series of Ln Ln $(\frac{1}{1-PF})$ vs. Ln Strength graphs (see Figures 15 through 24).

As described in Tables 2 and 3, the Hexoloy SA material failed primarily at tensile surface edge flaws (see Figures 25 and 26 and did not show evidence of slow crack growth. The XL144 and PY6 materials failed at tensile surface and edge flaws or inclusions or subsurface inclusions (see Figures 27 and 28). In an earlier part of this project the inclusions at the fracture site were analyzed and found to contain Fe, Cr, Cu, and Mo contaminates. At 1450°C both Si_3N_4 materials also showed considerable evidence of slow crack growth. The effects of slow crack growth were not as evident in the XL144 material tested at 1300°C at both fast and slow stressing rates (see Figures 29 and 30). At 1300°C the XL144 material failed primarily at tensile surface and edge flaws.

Thermal expansion measurements

The results of the thermal expansion measurements are presented in Table 7. The coefficient values obtained for XL144 are similar to those values obtained in our earlier measurements and in good agreement with the values reported in the literature. The coefficient values obtained for the Hexoloy SA are somewhat lower than the values obtained in our earlier measurements. However, the more recent measurements have provided values more consistent with the values reported in the literature. The difference in values measured may be due to

Table 5. Calculated n Values

Material	Temperature (°C)	n Values
Hexoloy SA	1450	not significantly different from zero
Hexoloy SA	1300	not significantly different from zero
XL144	1450	5.8
XL144	1300	not significantly different from zero
PY6	1450	7.5

Table 6. Summary of Weibull Analysis Results for Hexoloy SA, XL144, and PY6

Material	Temperature (°C)	Loading Rate ($\frac{MPa}{sec}$)	Mean Strength (MPa)	95% Confidence Bounds (MPa)	Weibull Modulus (m)	Scale Parameter (S_0) (MPa)
Hexoloy SA	1450	294	500	(463-538)	10	251
Hexoloy SA	1450	1.8	455	(413-498)	9	214
Hexoloy SA	1300	295	494	(429-558)	8	211
Hexoloy SA	1300	1.9	500	(445-555)	8	217
XL144	1450	168	453	(415-491)	12	259
XL144	1450	1	213	(204-222)	16	140
XL144	1300	168	604	(573-635)	13	356
XL144	1300	1	546	(466-626)	9	267
PY6	1450	168	393	(343-442)	8	169
PY6	1450	1	214	(187-242)	7	81

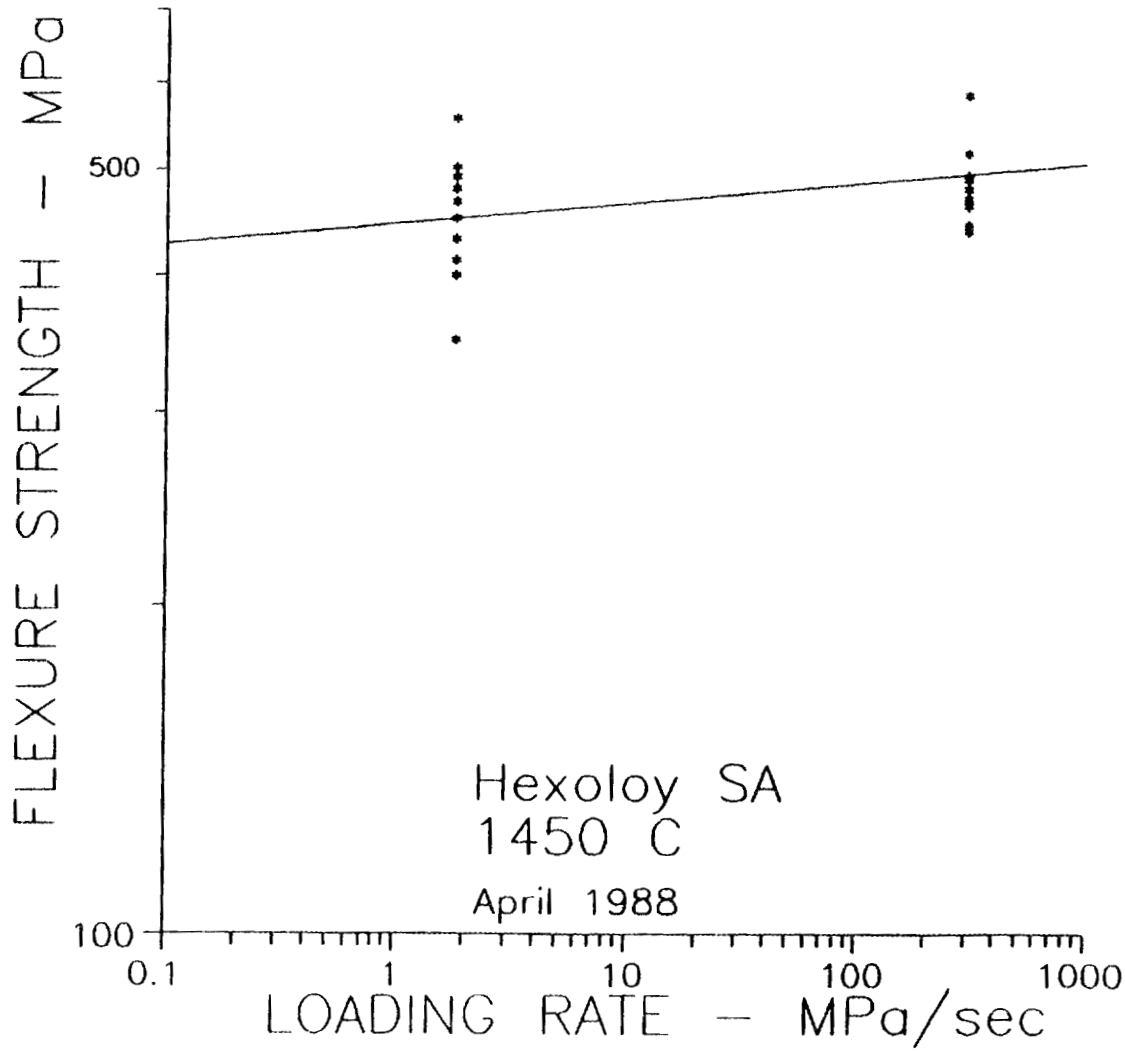

Figure 10. Flexural strength as a function of loading rate Hexoloy SA.

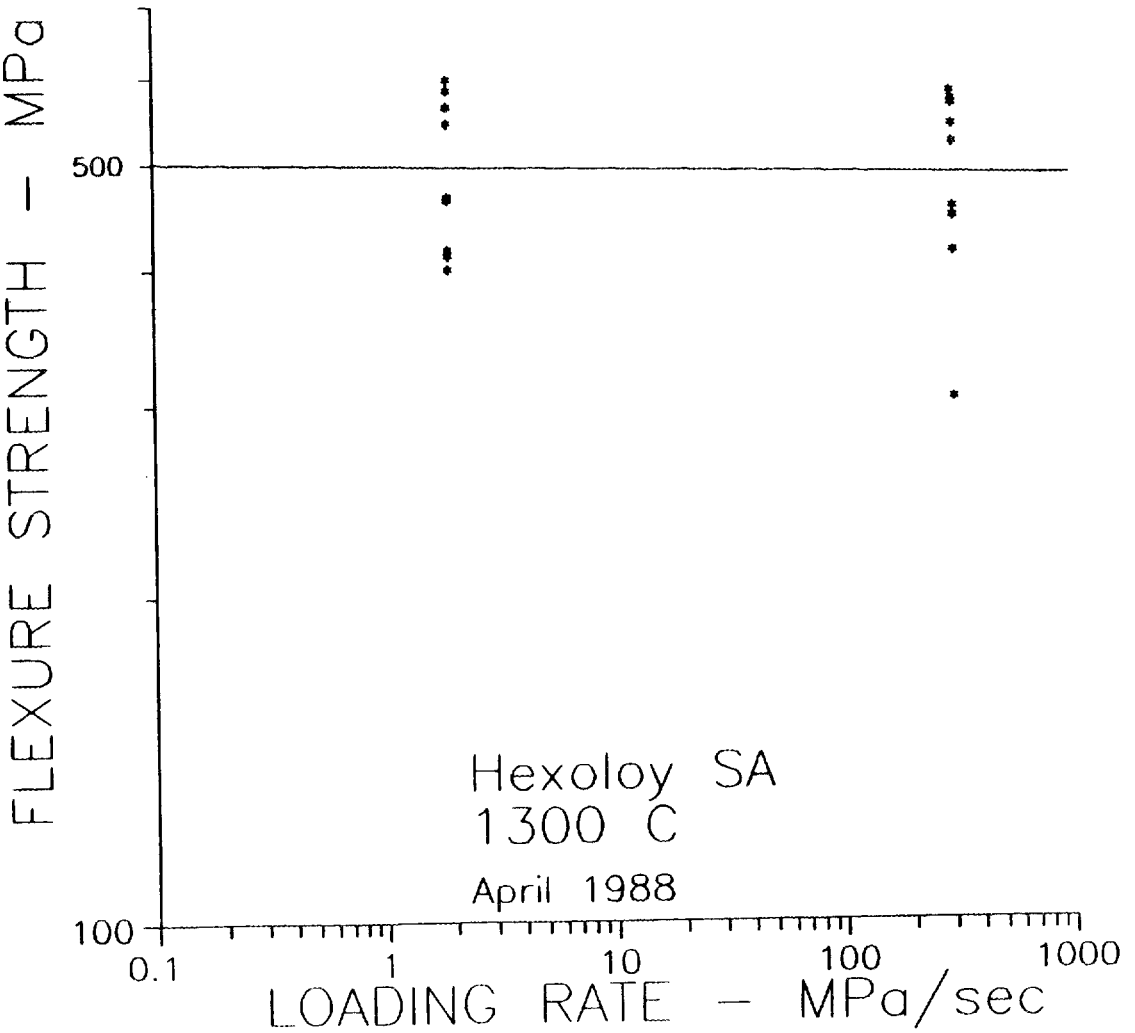

Figure 11. Flexural strength as a function of loading rate Hexoloy SA.

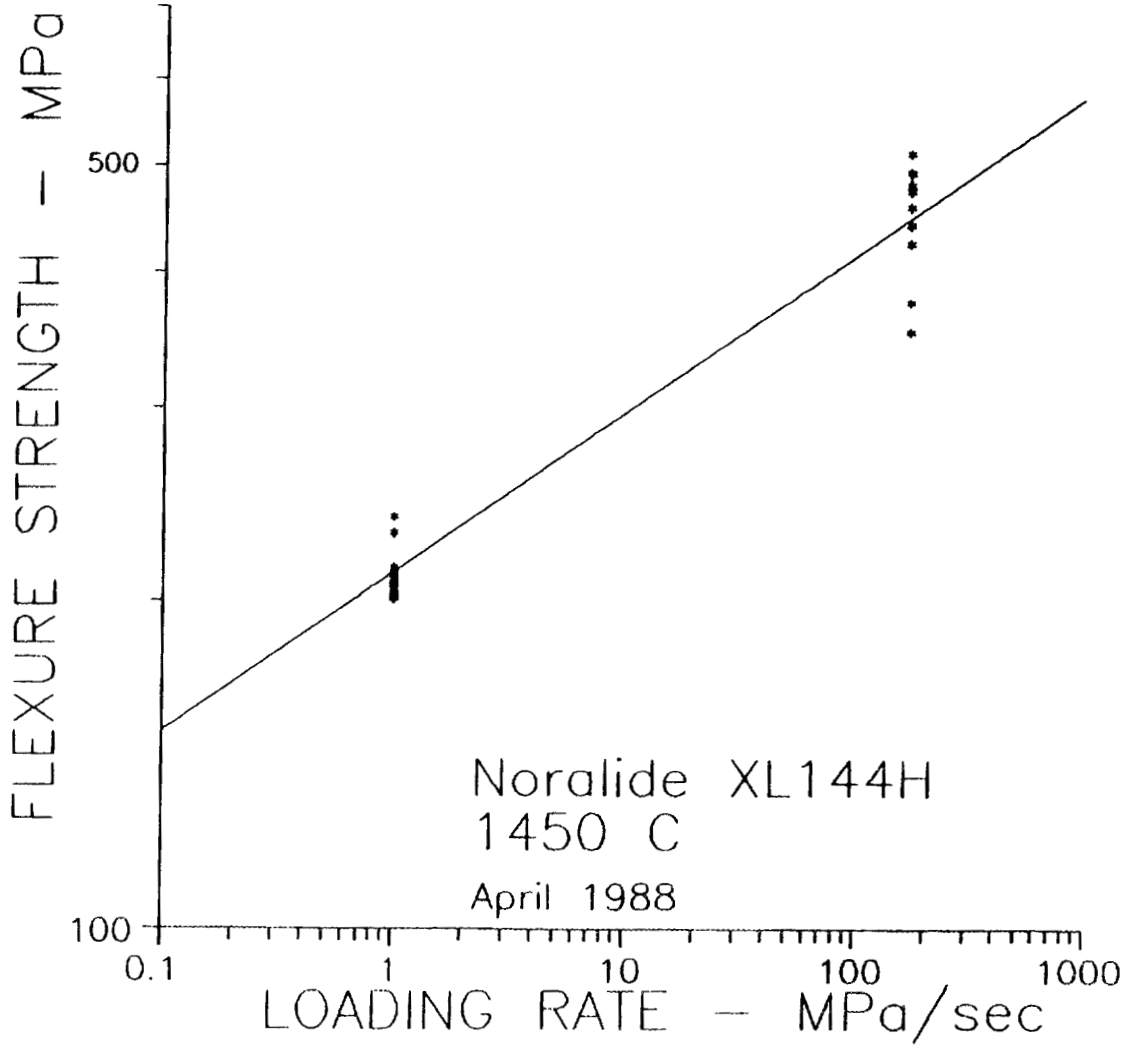

Figure 12. Flexural strength as a function of loading rate Noralide XL144H.

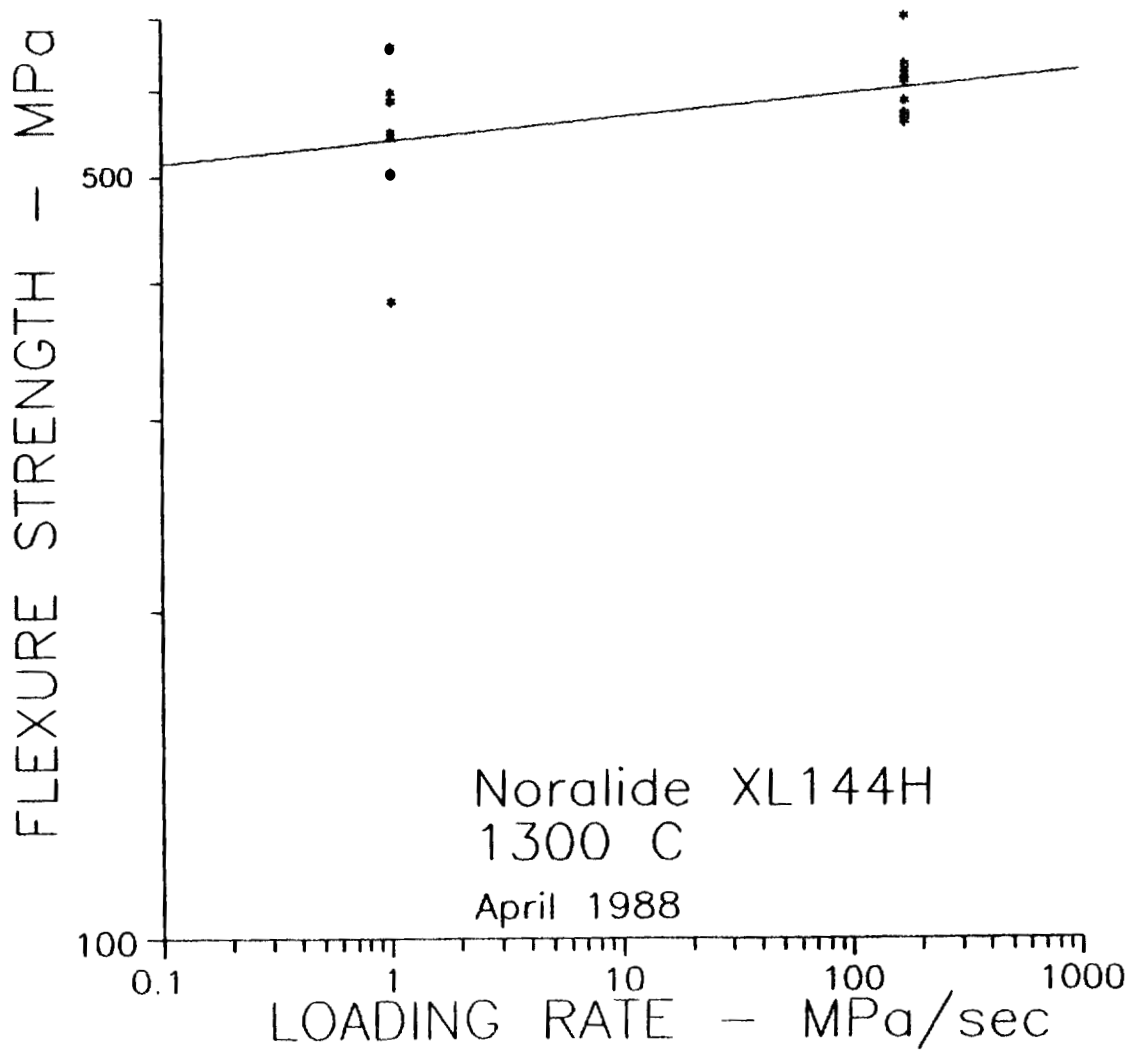

Figure 13. Flexural strength as a function of loading rate Noralide XL144H.

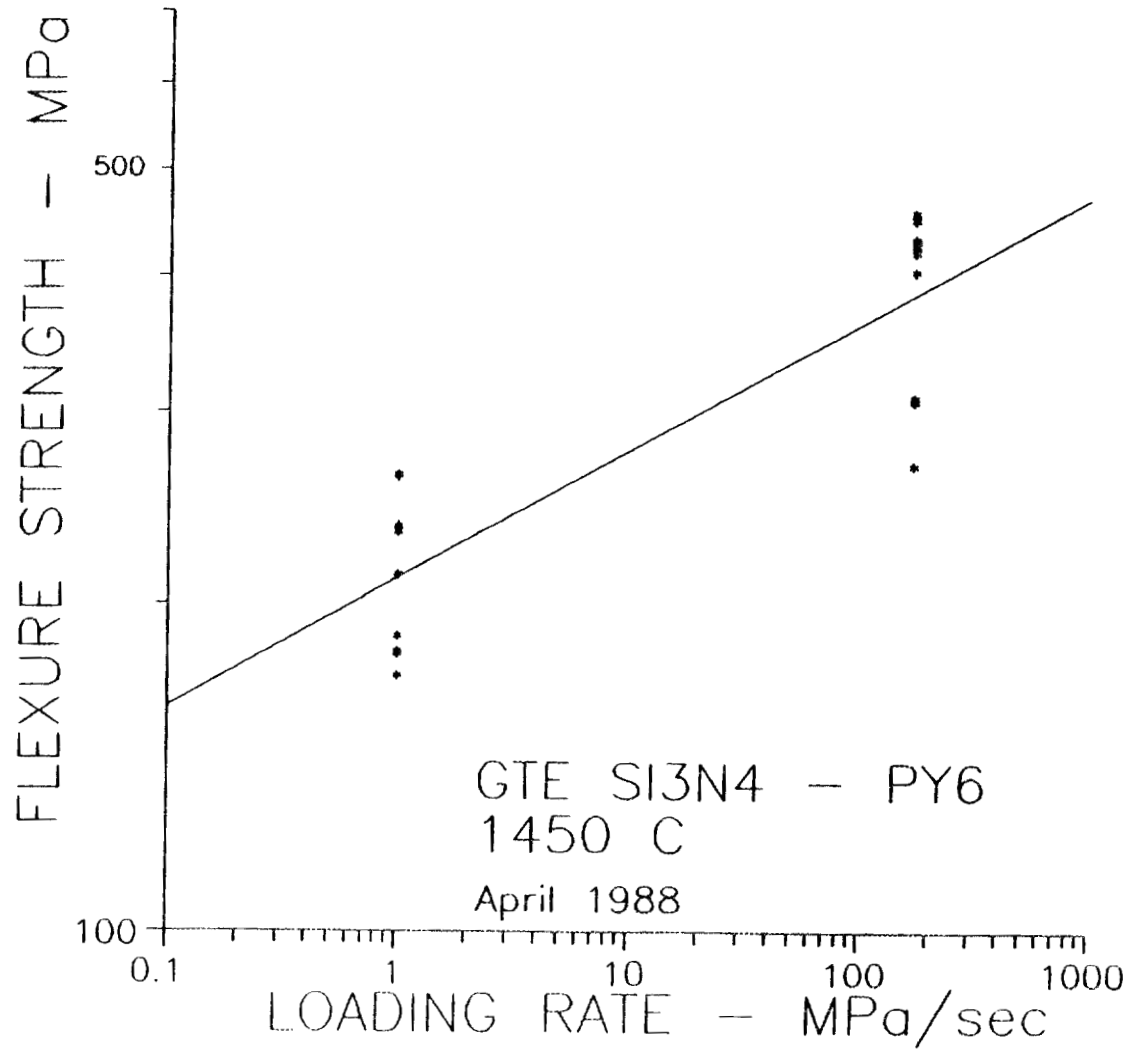

Figure 14. Flexural strength as a function of loading rate GTE Si_3N_4, PY6.

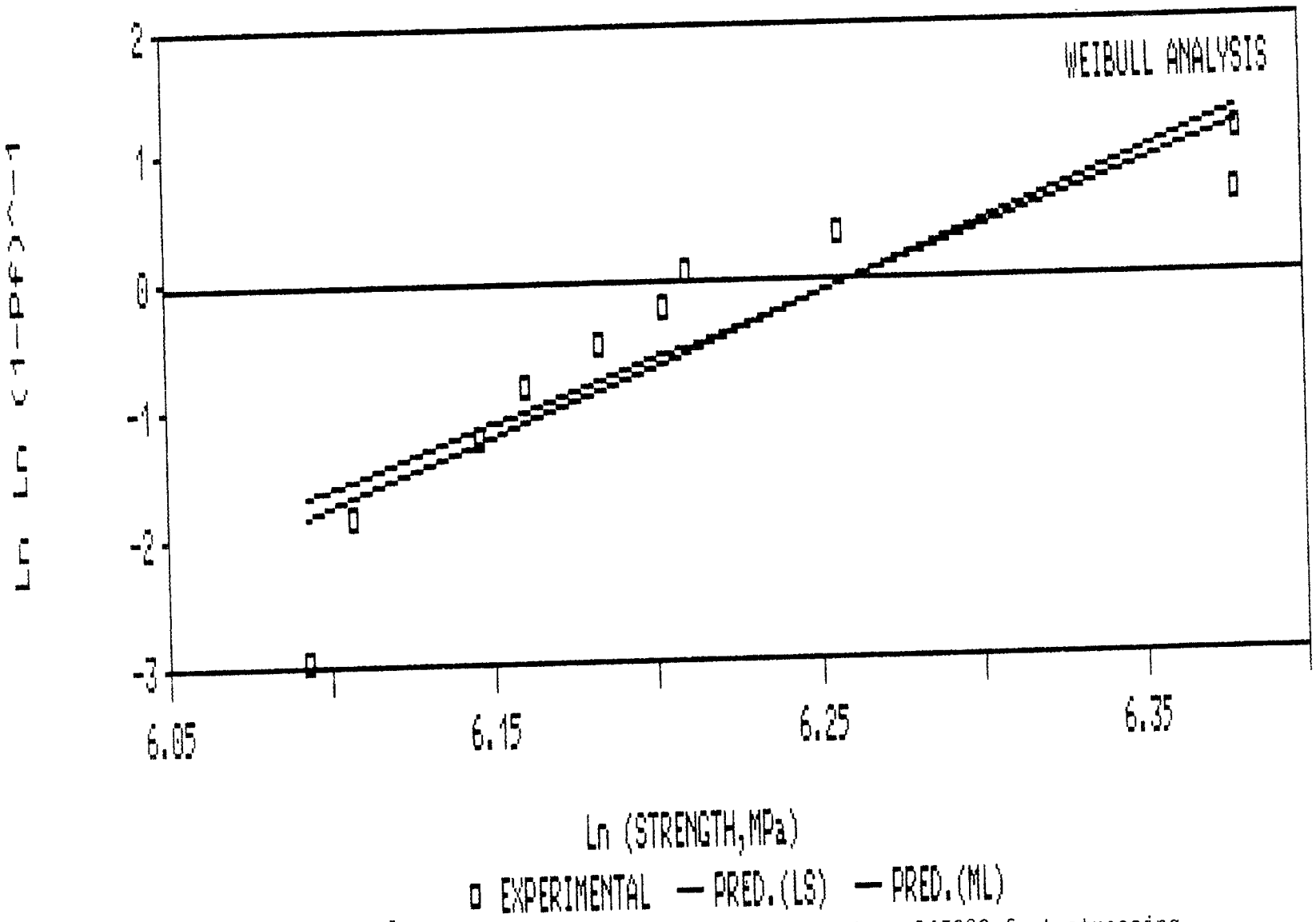

Figure 15. Graph of $\mathrm{LnLn}(\frac{1}{1-PF})$ versus Ln strength for Hexoloy SA at 1450°C fast stressing.

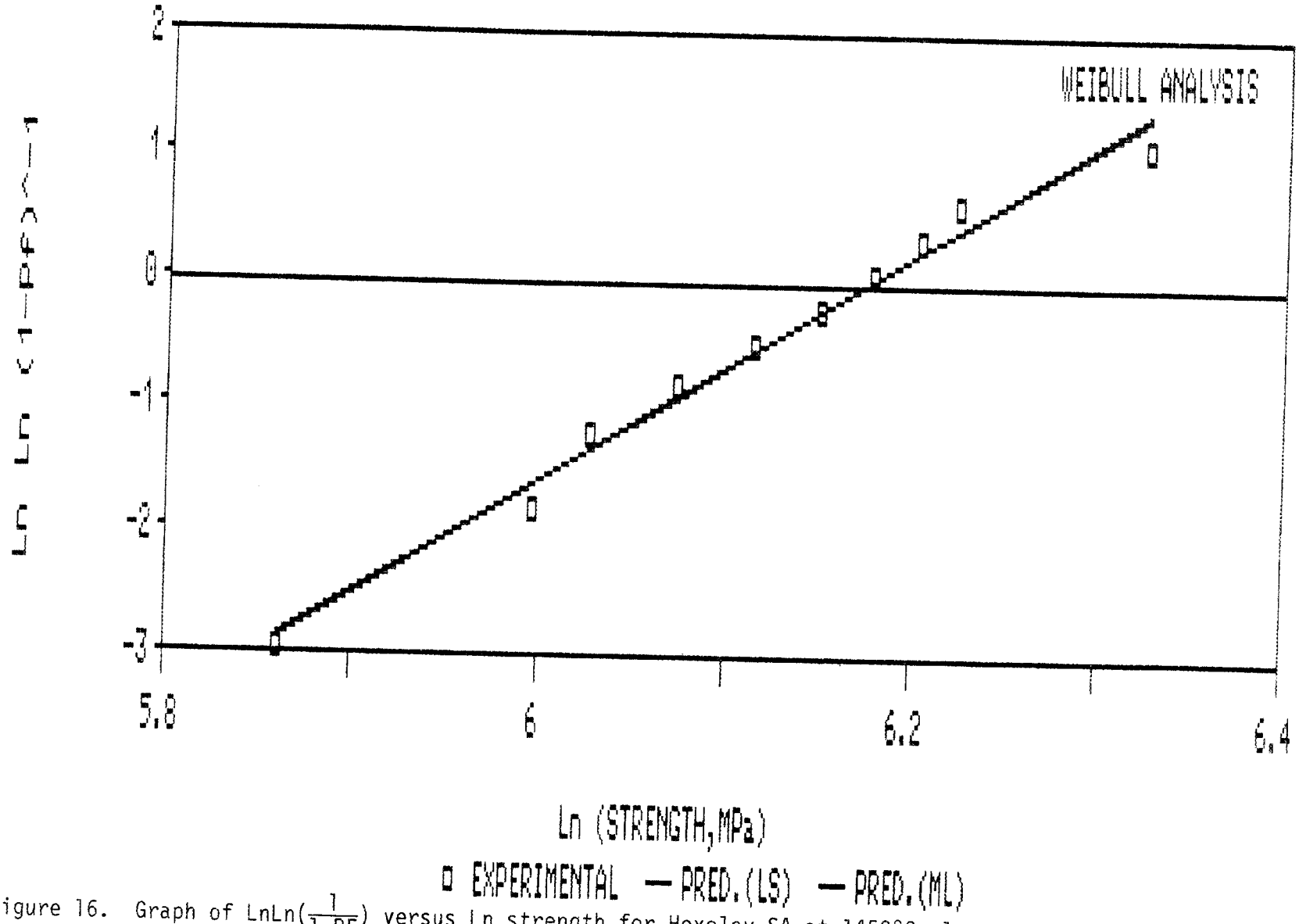

Figure 16. Graph of $\mathrm{LnLn}(\frac{1}{1-PF})$ versus Ln strength for Hexoloy SA at 1450°C slow stressing.

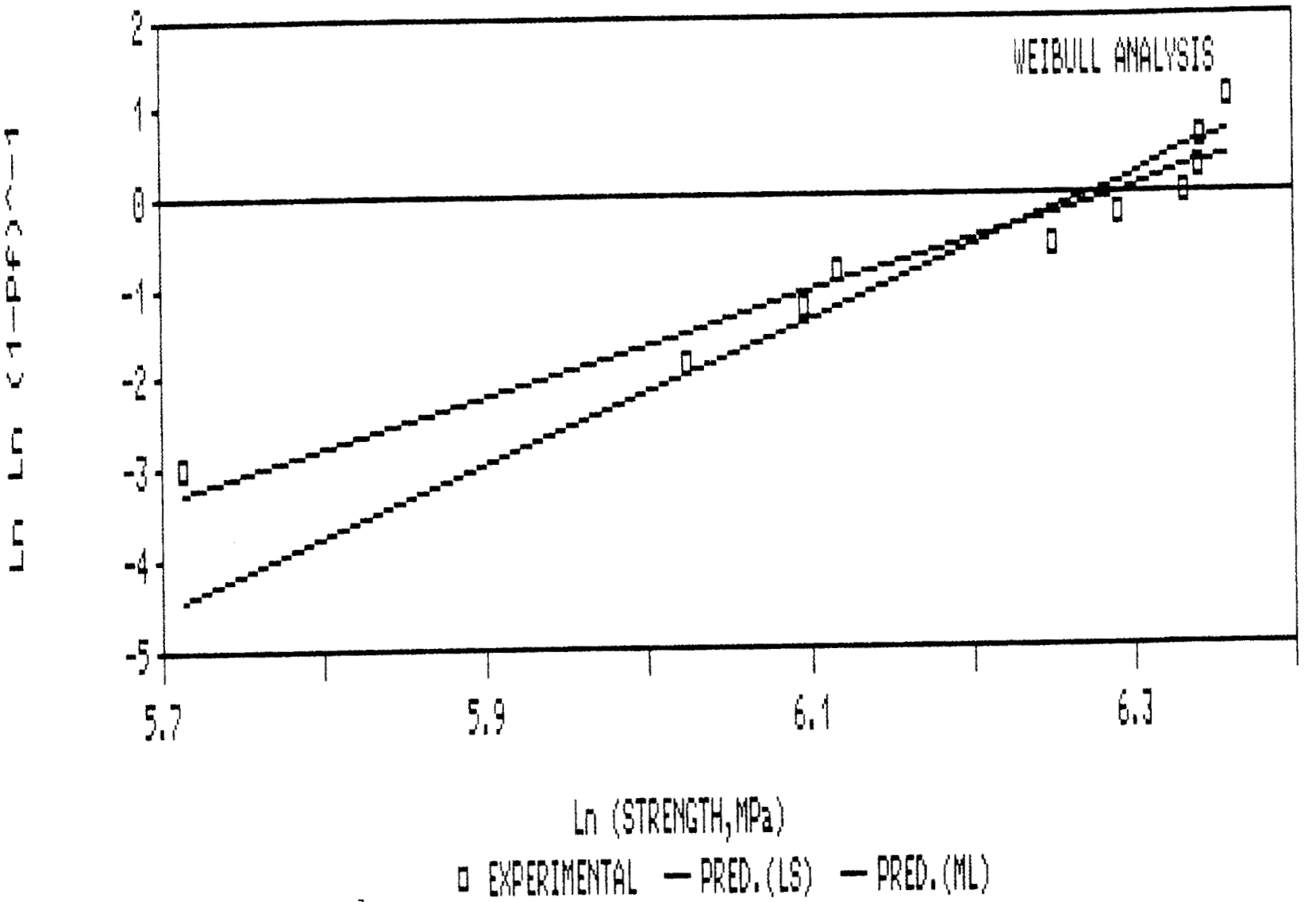

Figure 17. Graph of $\mathrm{LnLn}(\frac{1}{1-PF})$ versus Ln strength for Hexoloy SA at 1300°C fast stressing.

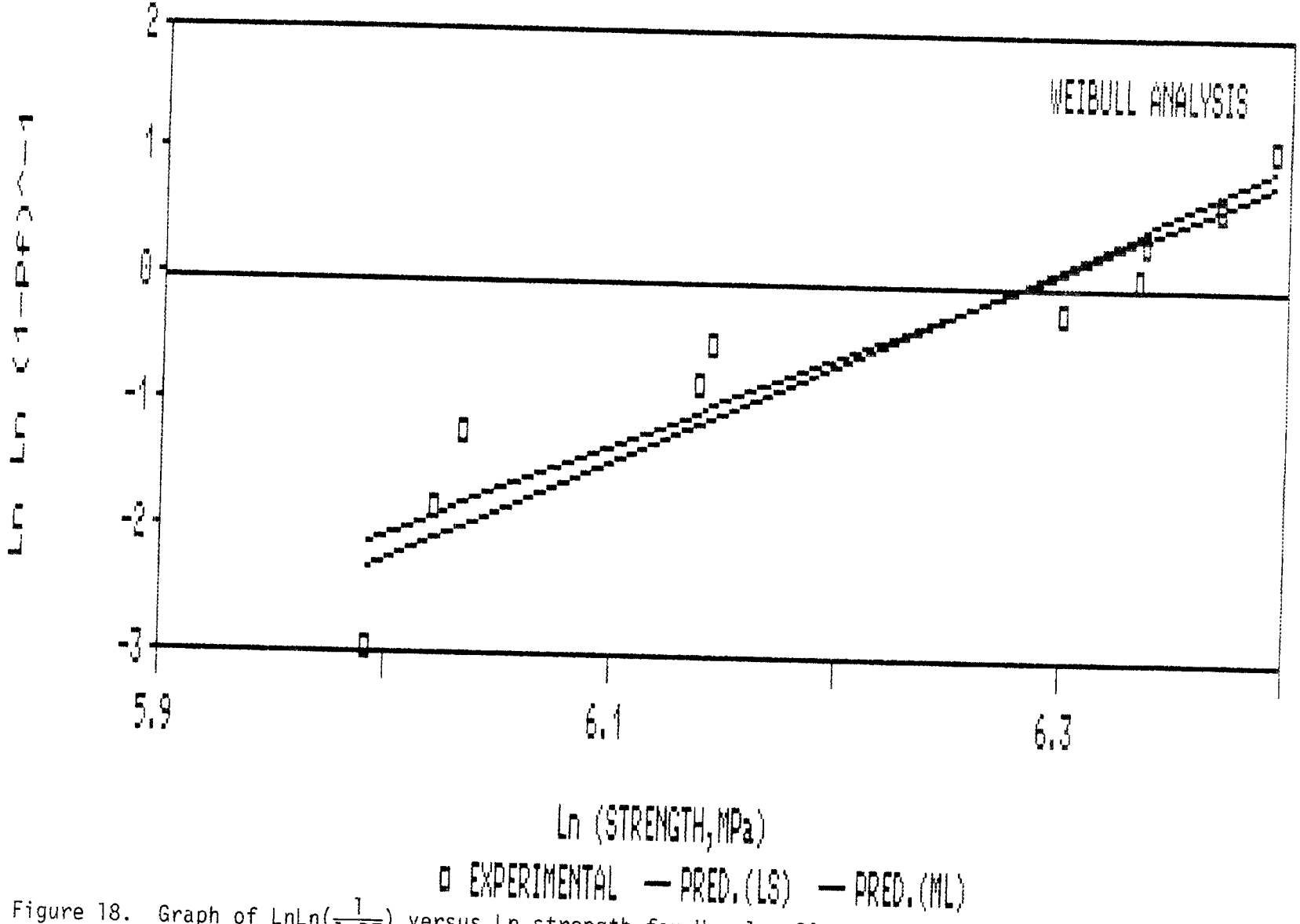

Figure 18. Graph of $\mathrm{Ln}\mathrm{Ln}(\frac{1}{1-PF})$ versus Ln strength for Hexoloy SA at 1300°C slow stressing.

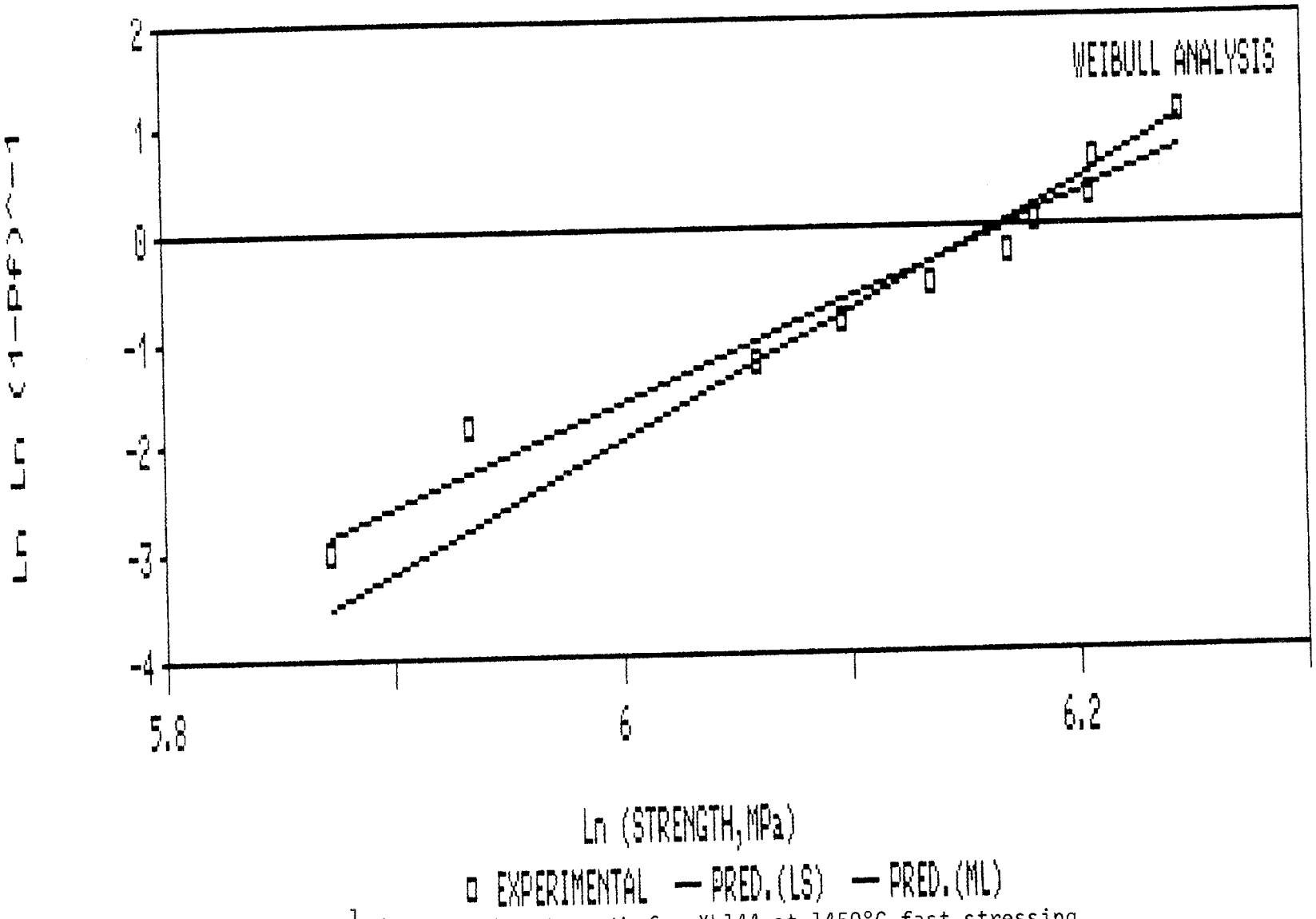

Figure 19. Graph of $\mathrm{LnLn}(\frac{1}{1-PF})$ versus Ln strength for XL144 at 1450°C fast stressing.

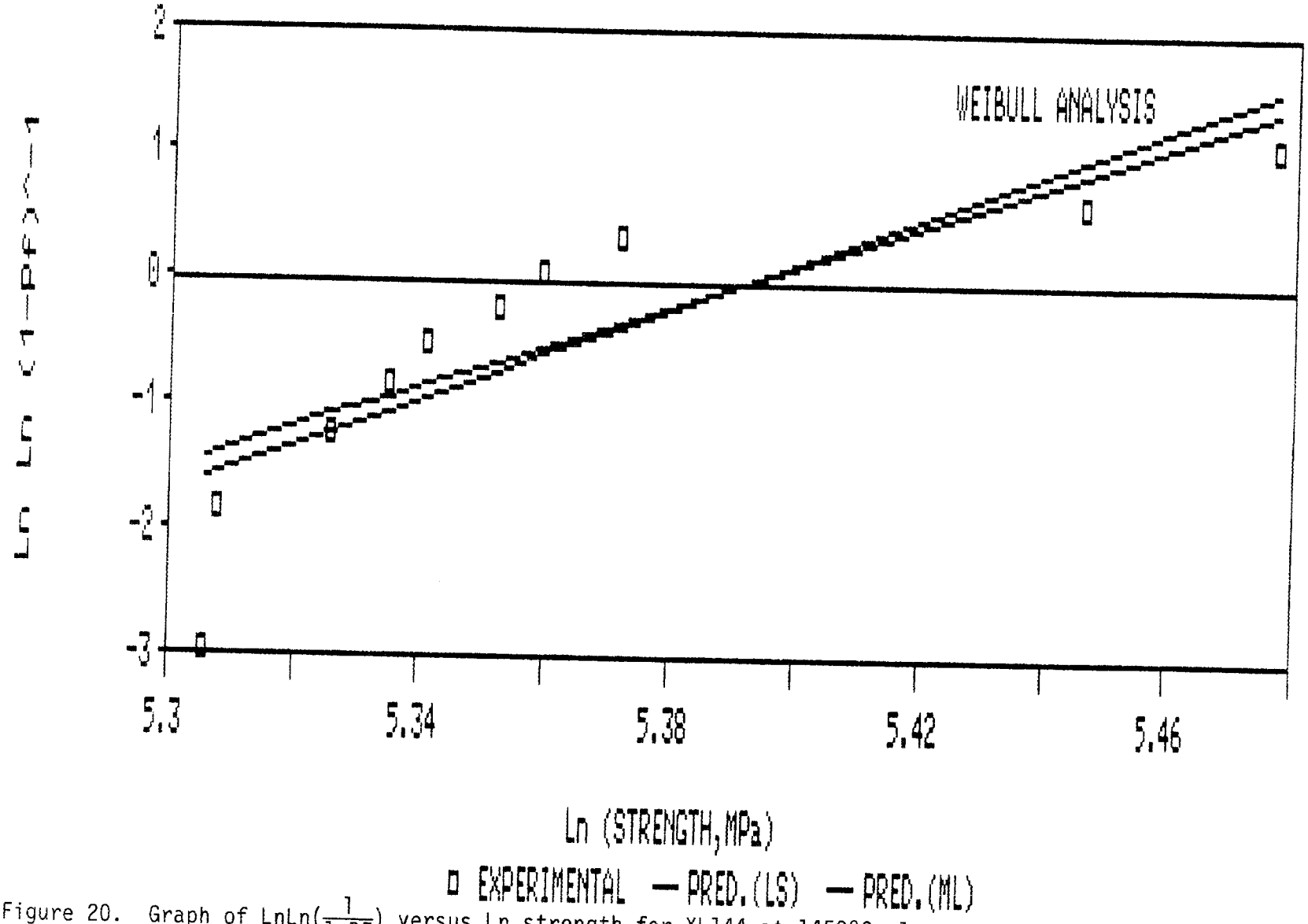

Figure 20. Graph of $\mathrm{Ln}\mathrm{Ln}(\frac{1}{1-PF})$ versus Ln strength for XL144 at 1450°C slow stressing.

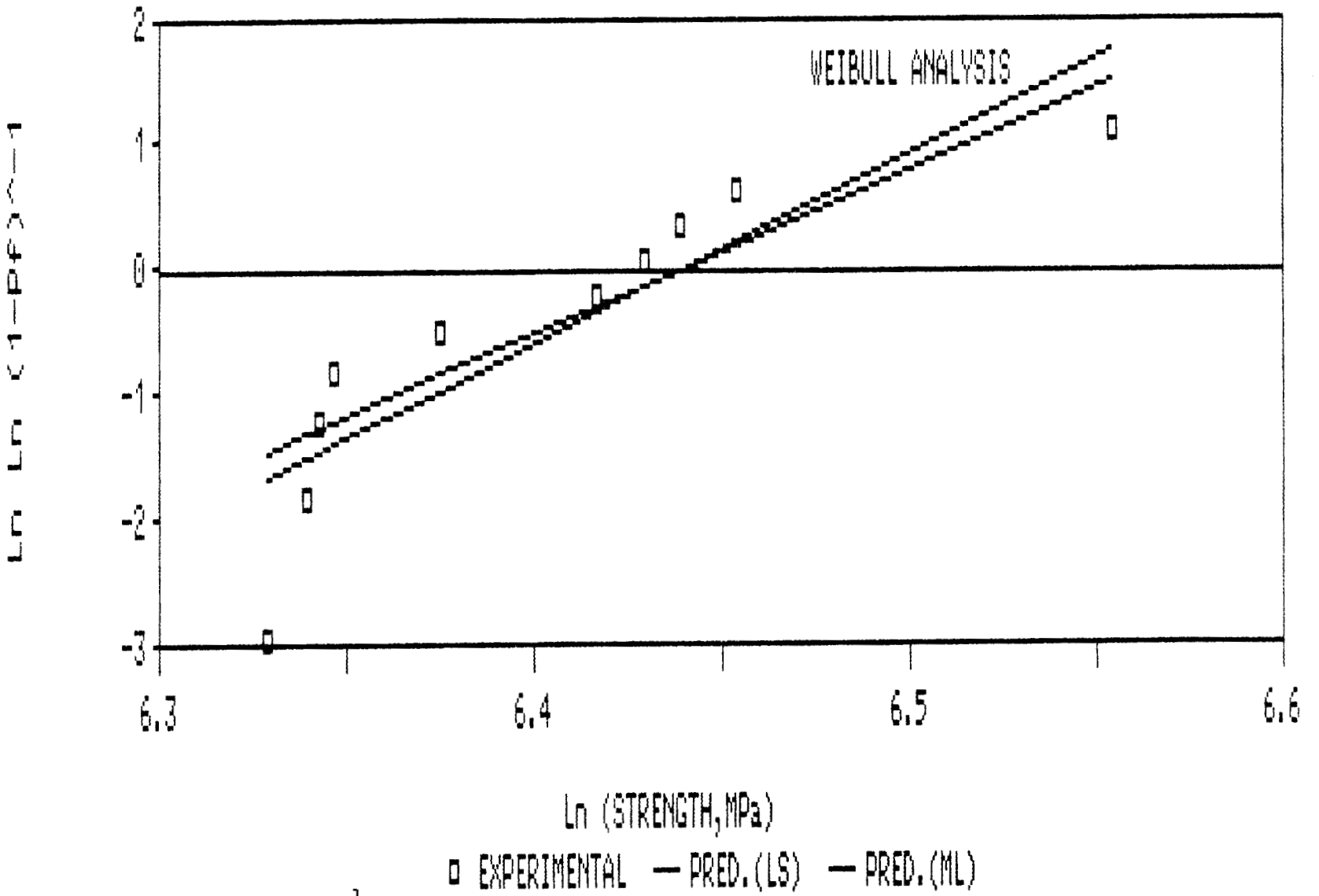

Figure 21. Graph of $\mathrm{Ln}\mathrm{Ln}(\frac{1}{1-PF})$ versus Ln strength for XL144 at 1300°C fast stressing.

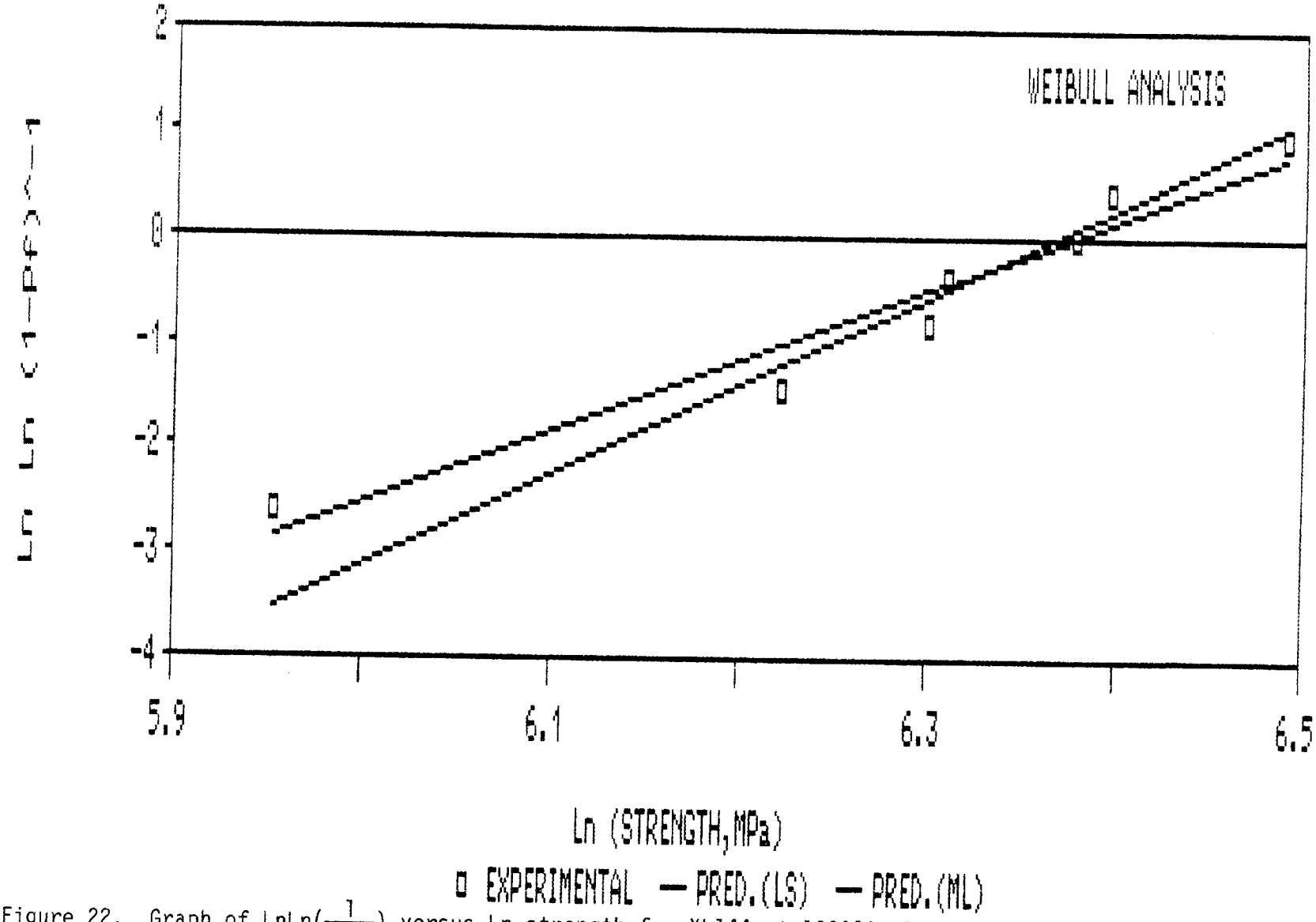

Figure 22. Graph of $\mathrm{LnLn}(\frac{1}{1-PF})$ versus Ln strength for XL144 at 1300°C slow stressing.

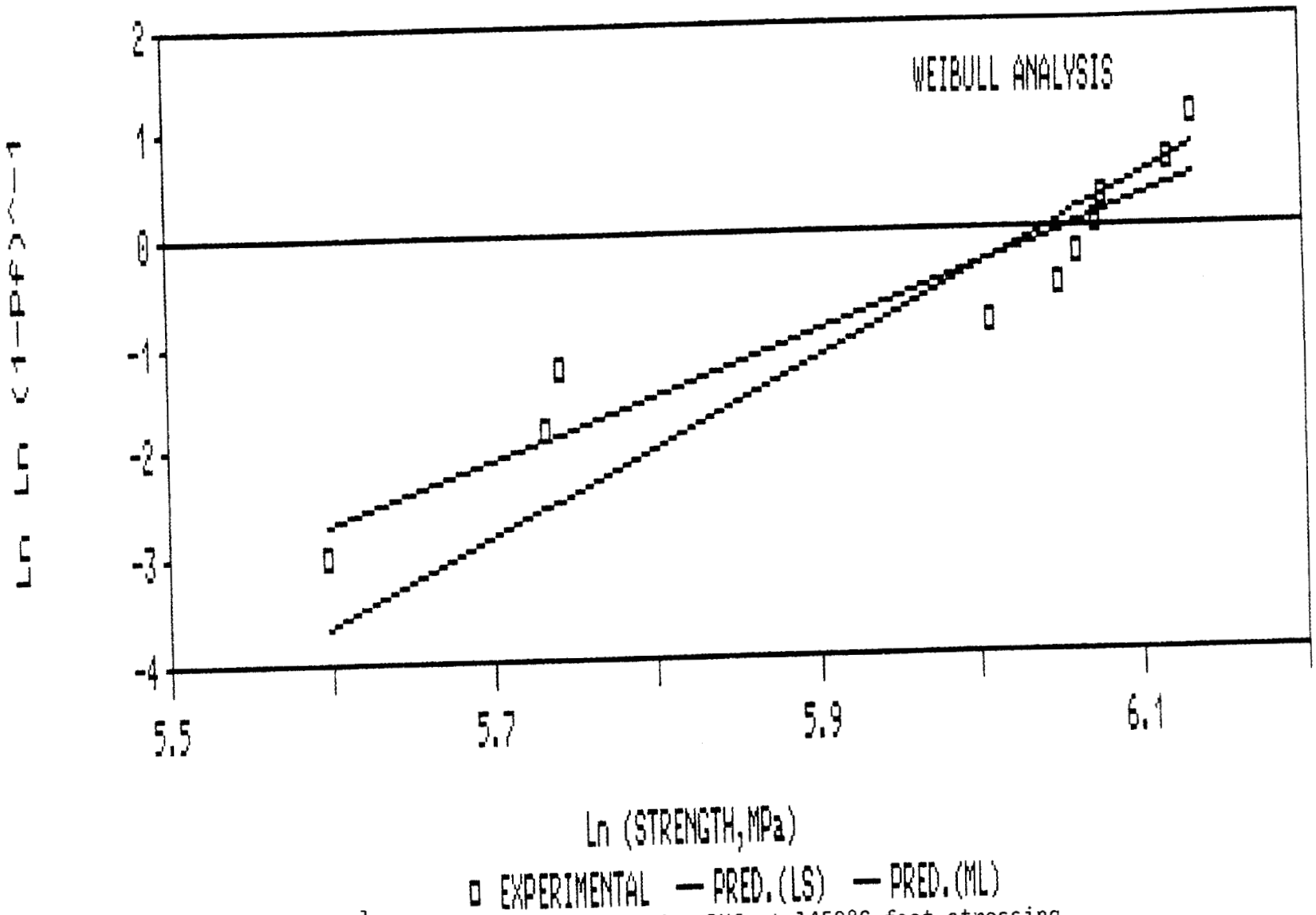

Figure 23. Graph of $\mathrm{LnLn}(\frac{1}{1-PF})$ versus Ln strength for PY6 at 1450°C fast stressing.

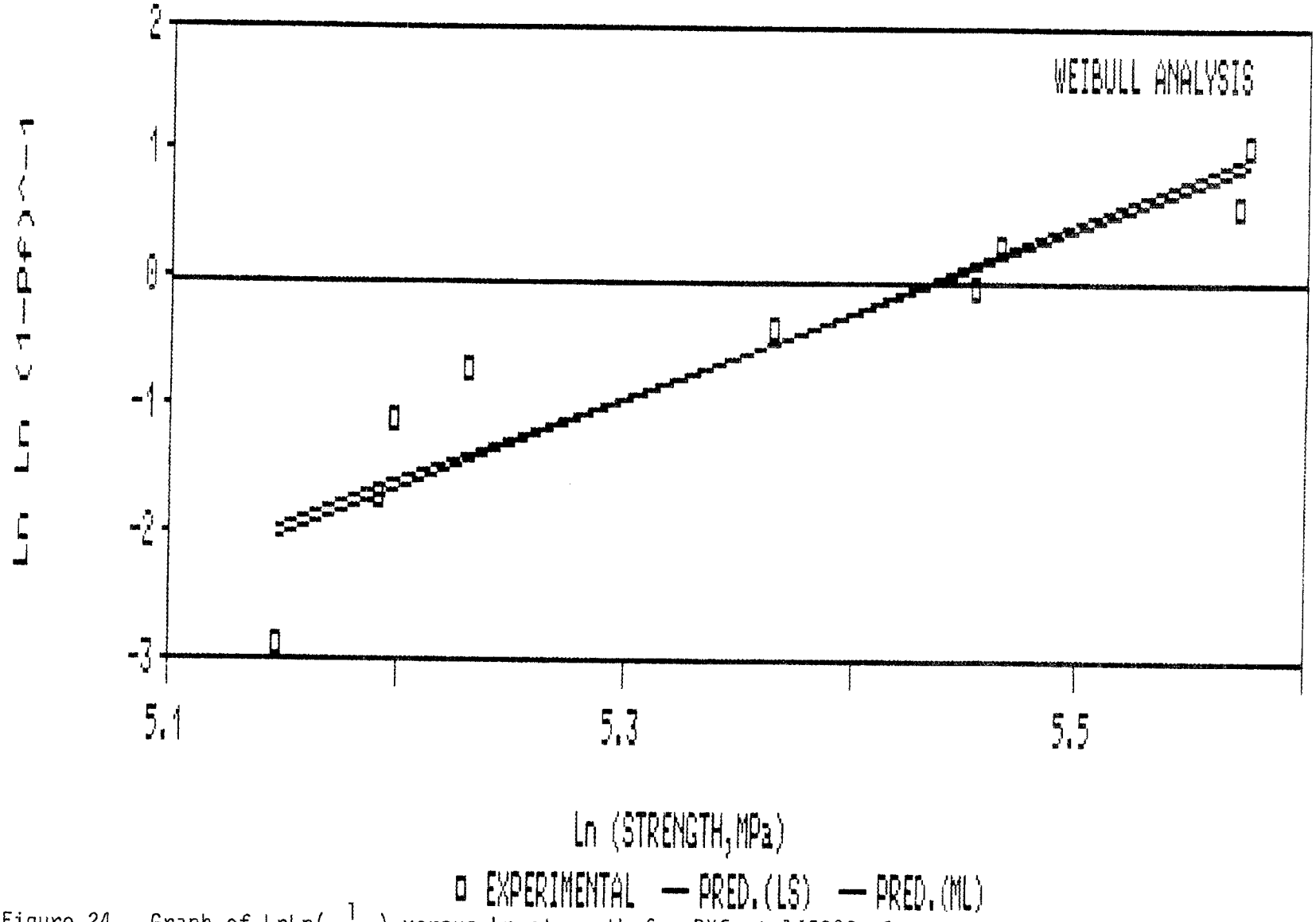

Figure 24. Graph of $\mathrm{LnLn}(\frac{1}{1-PF})$ versus Ln strength for PY6 at 1450°C slow stressing.

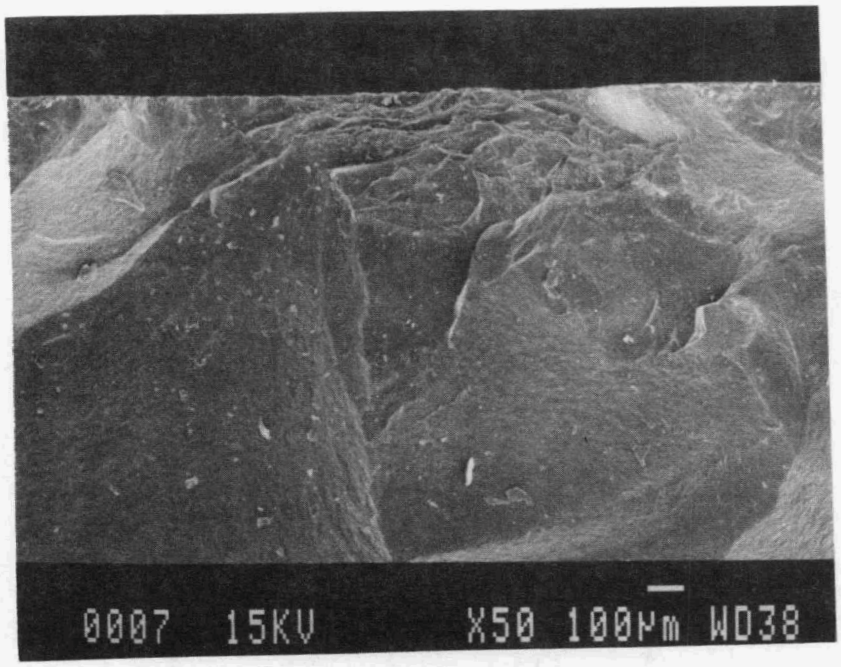

Figure 25. Typical tensile surface fracture for Hexoloy SA tested at 1450°C.

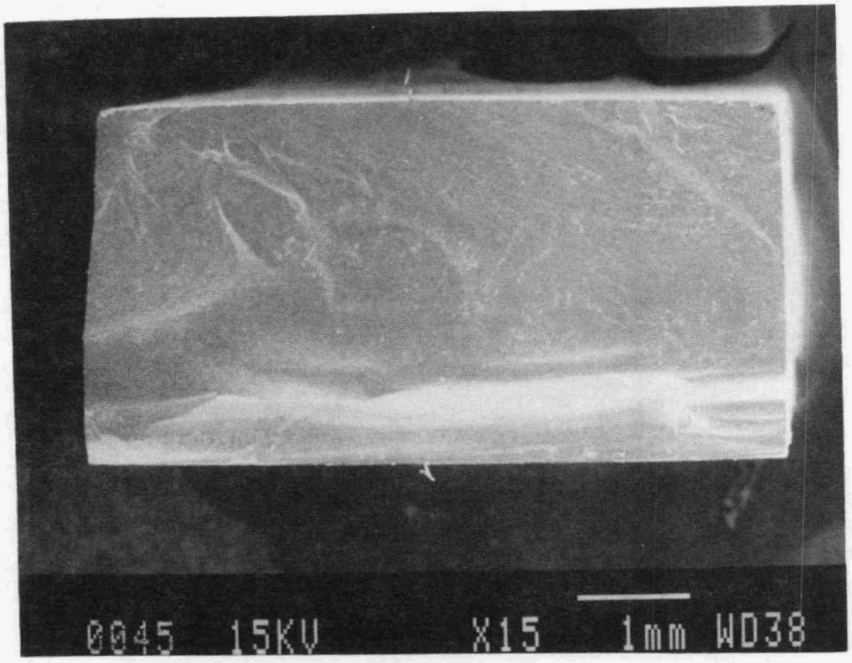

Figure 26. Typical tensile edge fracture for Hexoloy SA tested at 1450°C.

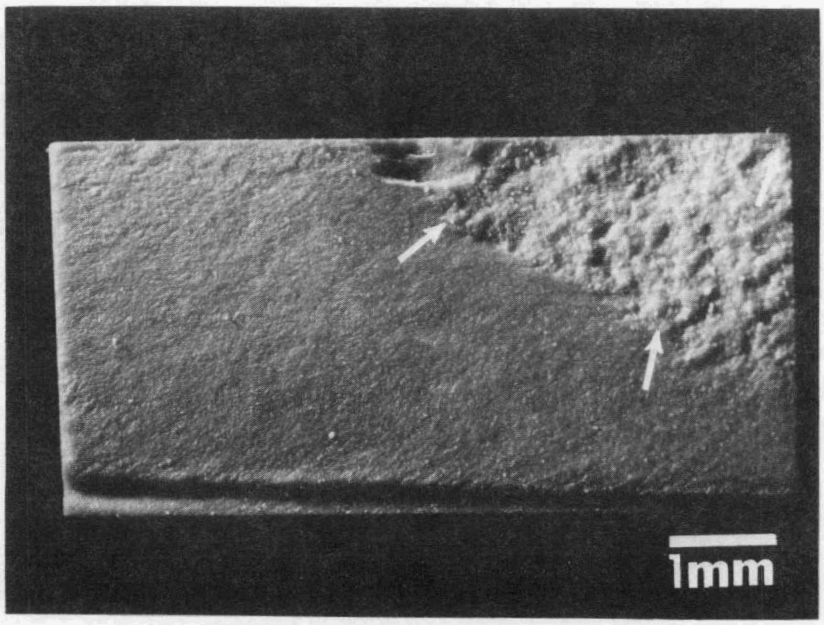

Figure 27. Typical tensile edge fracture for XL144 tested at 1450°C.

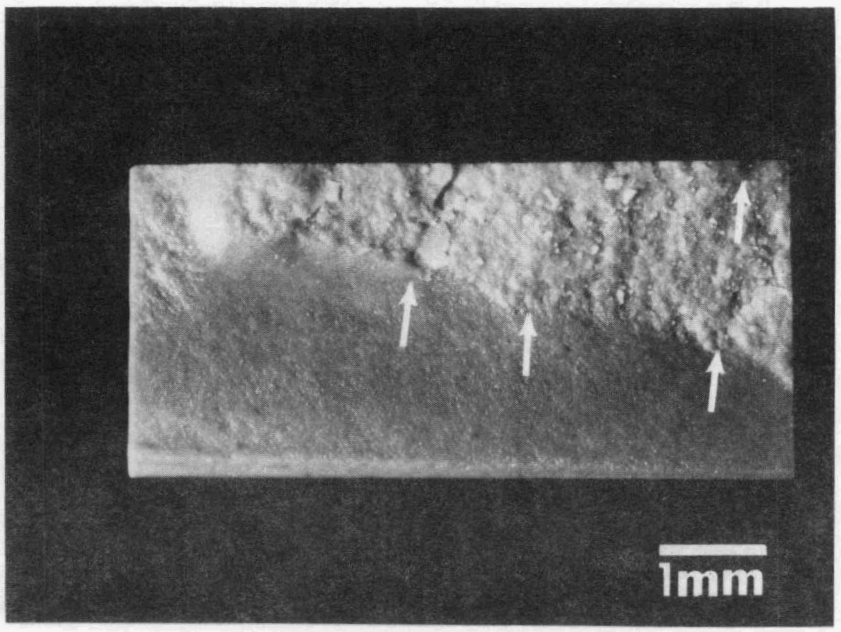

Figure 28. Inclusion initiated fracture surface for PY6 tested at 1450°C.

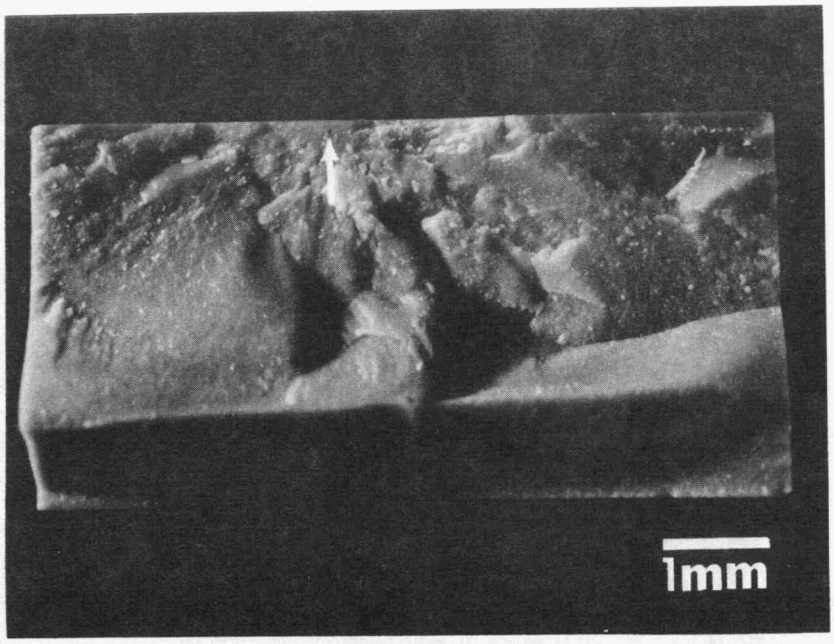

Figure 29. Typical tensile surface fracture for XL144 tested at 1300°C fast stressing rate.

Figure 30. Typical tensile surface fracture for XL144 tested at 1300°C slow stressing rate.

Table 7. Coefficient of Thermal Expansion Measurement for Hexoloy SA and XL144 Ceramics

Heating Cycle #	Coefficient of Thermal Expansion ($x10^{-6}$ °C^{-1}) 500°C	1000°C	1400°C	Weight Change (%)
		For Hexoloy SA		
1	3.97	4.62	4.50	+0.013
2	4.17	4.70	4.97	+0.010
3	4.20	4.77	5.05	+0.006
		For XL 144		
1	2.54	3.09	3.47	-0.003
2	2.67	3.10	3.39	+0.003
3	2.72	3.01	3.27	+0.006

specimen variations or machine accuracy. In the last several months we have improved the reliability of our Theta Dilatronic II Unit, and this may account for the differences obtained.

Conclusions

As a result of the limited evaluations conducted, we have found that at 1450°C the Si_3N_4 ceramics investigated exhibited considerable susceptibility to slow crack growth (fatigue). The α-SiC ceramic did not show any susceptibility to slow crack growth at this temperature. At 1300°C slow crack growth was not observed for any of the materials evaluated. The measured flexural strength of the two Si_3N_4 ceramics at 1450°C was between 35-40% lower than the strengths measured at 25°C. The measured flexural strength of the α-SiC increased at 1450°C. At 1300°C the flexural strength of the XL144 Si_3N_4 ceramic decreased only 22% from its room temperature value. Although the α-SiC had lower room temperature strength than the Si_3N_4 ceramics, it maintains significantly higher strength values at 1450°C than the values measured for the Si_3N_4 ceramics. At 1300°C the α-SiC and the XL144 Si_3N_4 were more equivalent, and in fact, the XL144 had somewhat higher strength. The XL144 Si_3N_4 ceramic also appears to have greater reliability with its higher Weibull modulus values.

References

1. Abramson, N. Appl. Opt., 10, p. 2155, 1971.

2. Dudderar, t. D. and R. O'Regan. "Holographic Interferometry in Materials Research and fracture Mechanics," in Symposium on Advanced Experimental Techniques in the Mechanism of Materials, Texas, September 1970, preprint.

3. Hecht, N. L., J. E. Minardi, D. Lewis, and R. L. Fusek. "Quantitative Theory for Predicting Fringe Pattern Formation in Holographic Interferometry, Applied Optics, Vol. 12, p. 2665, November 1973.

4. Holeman, J. M., F. A. Passanti, and J. Wallach. "Holographic Strain Measurement on a Tensile Specimen," General Electric Company, Schenectady, New York, August 1971.

5. Molin, N. E. and K. A. Stetson, Optik, 33, 399, 1971.

6. Vest, C. M. "Holographic Interferometry in Material Testing," in Symposium on Advanced Experimental Techniques in the Mechanics of Materials, Texas, September 1970, preprint.

7. Vest, C. M. "Holographic Interferometry," John Wiley & Sons, 1979.

8. Vienot, J. C., et al. "Hologram Interferometry: Surface Displacement Fringe Analysis as an Approach to the Study of Mechanical Strains and Other Applications to the Determination of Anisotropy in Transparent Objects," in Proceedings of the Symposium on the Engineering Uses of Holography, ed. E. R. Robertson and J. M. Harvey (University of Strathclyde, Glasgow, September 1968).

9. Wykes, C. Opt. Eng. 21, 400, 1982.

3.4 FRACTURE MECHANICS

Improved Methods for Measuring the Fracture Resistance of Structural Ceramics

R. C. Bradt and A. S. Kobayashi (University of Washington)

Objective/Scope

The long-term goals of this study are to develop and demonstrate a technique for the determination of the fracture resistance of monolithic ceramics and ceramic matrix composites that is applicable over the temperature range from 20° C to 1400° C.

Technical Progress

Testing of the monolithic silicon nitride material is now complete. Fracture toughness of the sintered silicon nitride was found to be dependent on temperature for all of the measurement techniques. As is expected for this material, the two sharp-notch specimen types, the chevron-notch and the controlled microflaw specimens showed toughness values that are less than the blunt crack of the straight-notch specimen. This is consistent with the results that were reported previously for silicon carbide. There also is excellent agreement between the two sharp-notch techniques. The R-curves were observed to be flat at all temperatures except at 1400°C. The value of the crack growth resistance, however, decreases with temperature. The modulus of rupture values were found to be dependent on temperature, as suggested by the toughness measurements.

Testing of the dense transparent spinel using all the techniques is nearly complete. Samples for the controlled flaw Knoop indented technique for measuring fracture toughness of SiC whiskers reinforced Al_2O_3 is under preparation. Testing of this composite by chevron and straight notches is already complete.

Status of Milestones

Although the present status is still lagging the originally projected milestones, elevated temperature fracture testing and a significant portion of the MOR and controlled micro-flaw testing is now complete.

Problems Encountered

No significant new problems have been encountered during this reporting period.

Publications

The following papers have been submitted for publication :

1. Indentation Fracture Toughness of Sintered SiC in the Palmquist Crack Regime.

(Submitted to the American Ceramic Society)

2. Elevated Temperature Fracture Resistance of a Sintered Silicon Carbide.

(Submitted to the American Ceramic Society)

The following papers are under preparation for publication:

1. Elevated Temperature Fracture Resistamce of a Sintered Silicon Nitride.

2. R-Curves of Monolithic Ceramics at Elevated Temperatures.

3. Indentation Fracture Toughness of a Sintered Silicon Carbide in the Median Crack Regime.

Testing and Evaluation of Advanced Ceramics at High Temperature in Uniaxial Tension

J. Sankar, V. S. Avva, and A. Sinha (North Carolina A&T State University)

Objectives/Scope

The purpose of this effort will be to test and evaluate advanced ceramic materials at temperatures up to 1500 deg. C in uniaxial tension. Testing may include fast fracture strength, stepped static fatigue strength, along with analysis of fracture surfaces by Scanning electron microscopy. This effort will comprise the following tasks:

Task 1. Specifications for Testing Machine and controls + (Procurement)
Task 2. Identification of Test Materials (s) + (Procurement of specimens)
Task 3. Identification of Test Specimen Configuration
Task 4. Specifications for Testing grips and Extensometer + (Procurement)
Task 5. Specifications for Testing furnace (Procurement) and Controls
Task 6. Developement of Test Plan
Task 7. High Temperature Tensile Testing
Task 8. Reporting (Periodic)
Task 9. Final Report

It is anticipated that this program will help in understanding the behavior of Ceramic materials at very high temperatures in uniaxial tension.

Technical Progress

Fractography and X-Ray microanalysis of the fracture surfaces of the GTE SNW-1000 silicon nitride samples tested at room temperature was completed. Figure 1 shows the fracture surface of the typical silicon nitride sample tested at a stressing rate of 450 MPa/min. High magnification image analysis of this area indicated that the fracture origin is an inclusion. Figures 2-3 are the X-Ray energy spectrums obtained from the fracture initiation site and from the matrix area away from the fracture initiation site, respectively, of the sample in Figure 1. Figure 2, the spectrum from the fracture initiation site of the sample in Figure 1 (marked (X)) indicated the presence of impurity elements such as Fe, Cl, Ca, K, C, O, and Na. Pasto et al [1] have reported the presence of trace elements such as Fe, Mg, Cl, and Ca in inclusions in sintered silicon nitride materials. Figure 3, the

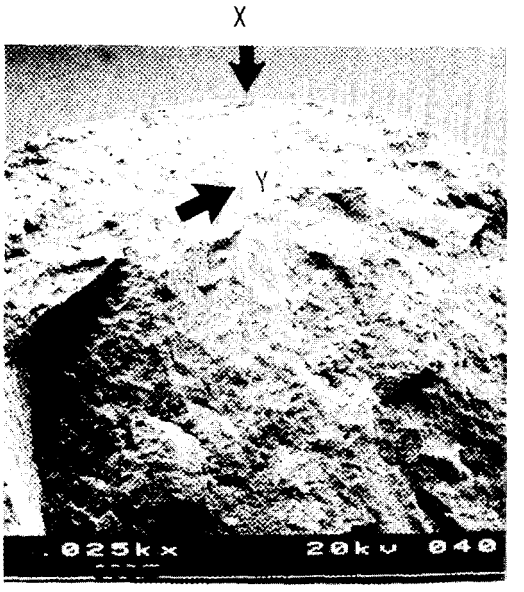

Figure 1. A typical silicon nitride fracture surface, sample tested at a stressing rate of 450 MPa/min

the X-Ray spectrum obtained from the matrix area of the sample in Figure 1 (marked (Y)) indicated the presence of Si, Al and Y as the major elements. Fractography analysis of all the room temperature tests (test done at different stressing rates) samples indicated that the fracture origin is normally from pores and occasionally from inclusions. The SEM investigation of the polished virgin sample indicated that the spectrum from the inclusion is similar to the spectrum (Figure 2) obtained from the inclusion in the fractured sample in Figure 1. and the pore area was similar to Figure 3. All the spectrums were obtained using the thin window detector at an accelerating voltage of 30 KV.

During this reporting period two additional stressing rates of 3.75 MPa/min and 7.5 MPa/min were also used to contrast the test results obtained earlier using higher stressing rates of 450, 900, 2100 MPa/min. Table 1. shows the tensile strength and strain values obtained at stressing rate of 3.75 and 7.5 MPa/min. It was observed that the range of strength values obtained for the slow stressing rates were of the same order as that obtained for the higher stressing rates.

Figure 4 shows the fracture surface of a sample tesyed at a stressing rate of 7.5 MPa/min. Figure 5 shows the magnified image of the fracture initiation site in Figure 4. It may be observed from Figure 4, as expected that the size of the fracture mirror is quite large. It was observed that the fracture mirror sizes were generally larger for the slow stressing rates than the high stressing rates, though this fact is not reflected in the tensile strength values. Figure 6 is a plot of the log stressing rate versus log tensile strength of the SNW-1000 samples

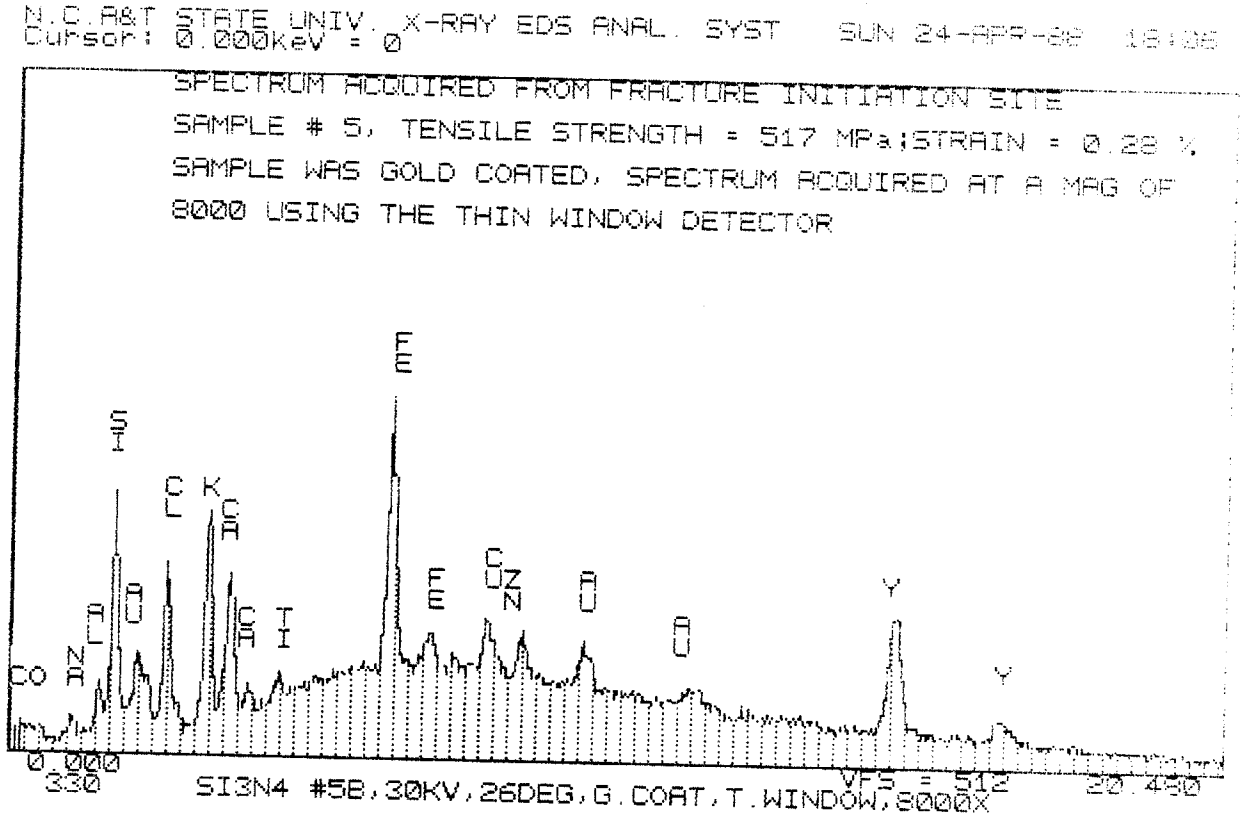

Figure 2. X-Ray spectrum acquired from the fracture initiation site (marked 'X')

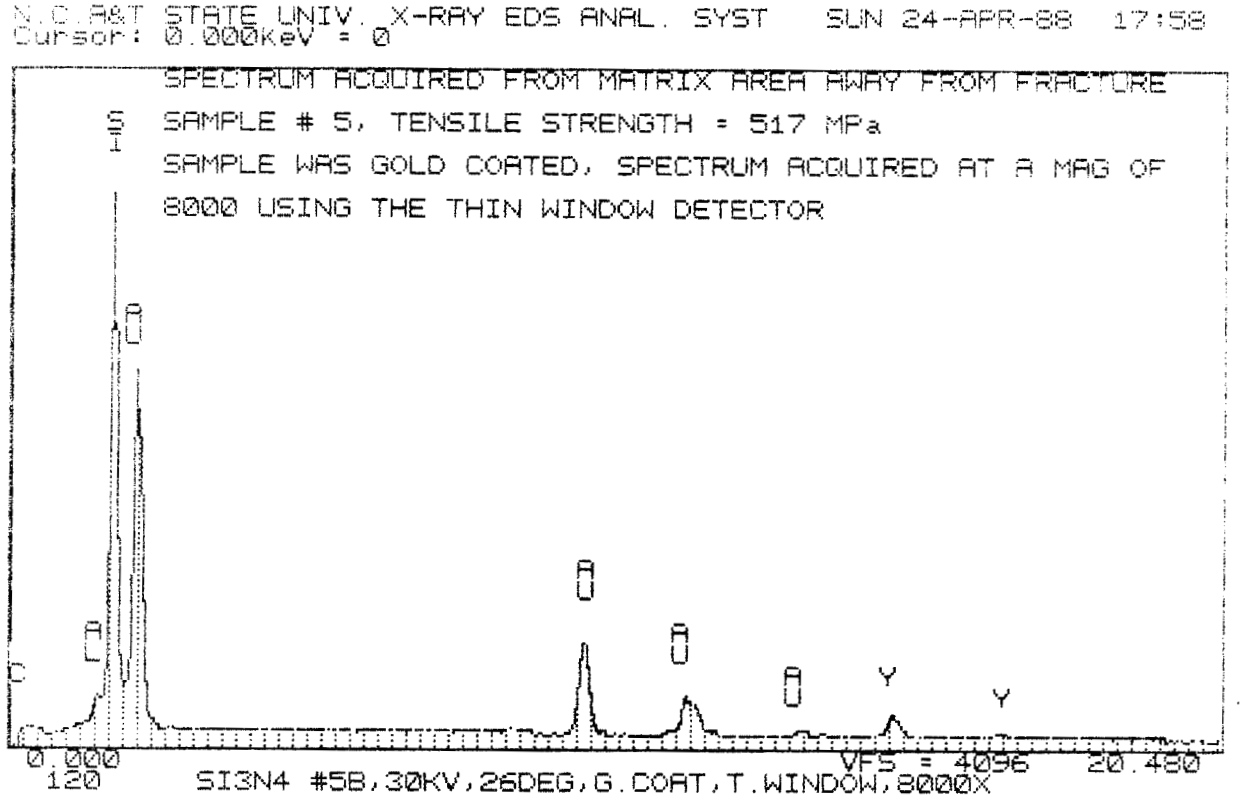

Figure 3. X-Ray spectrum acquired from the matrix area away from the fracture initiation site (marked 'Y')

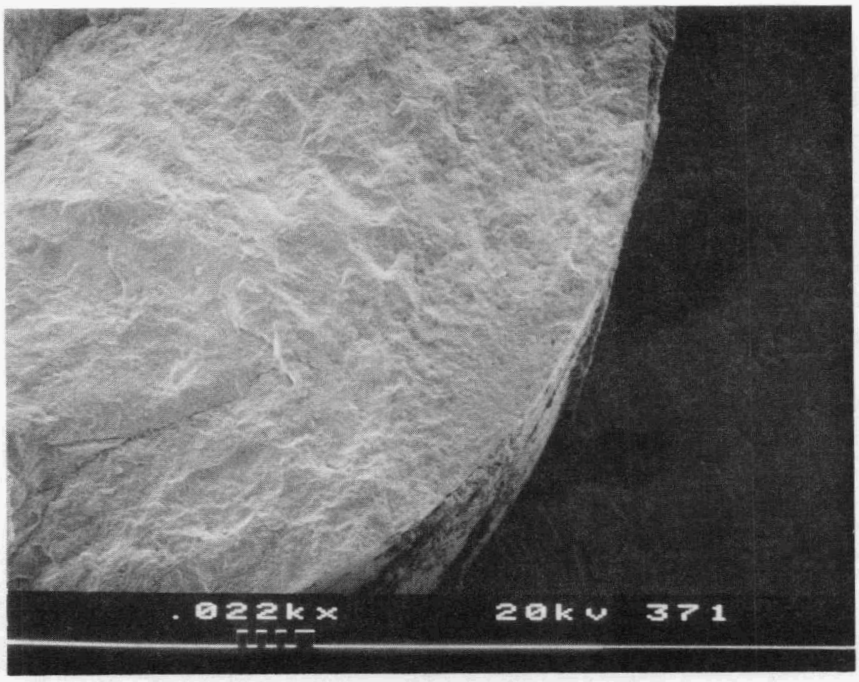

Figure 4. Fracture surface of a typical sample tested at a slow stressing rate of 7.5 MPa/Min

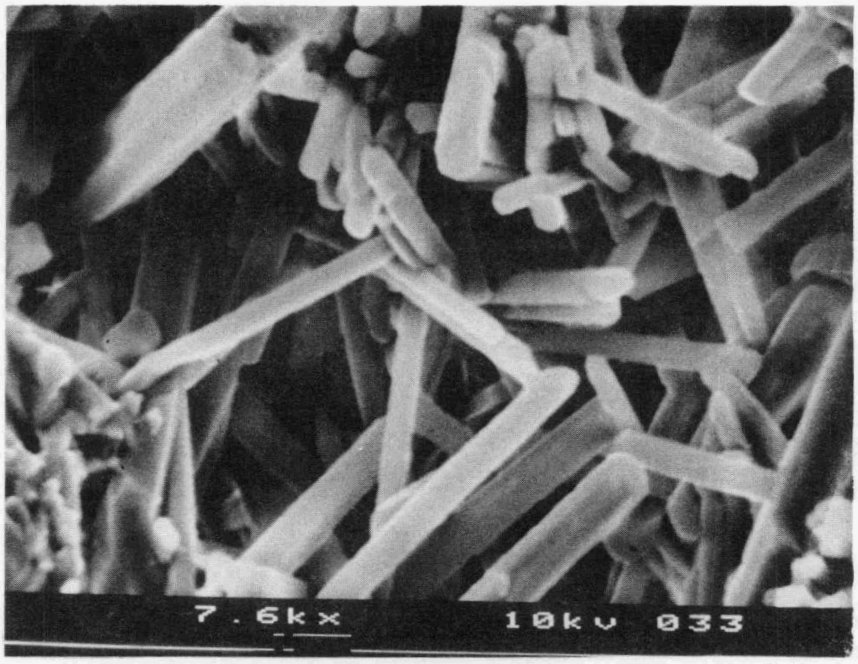

Figure 5. High magnification image of the fracture initiation site in Figure 4

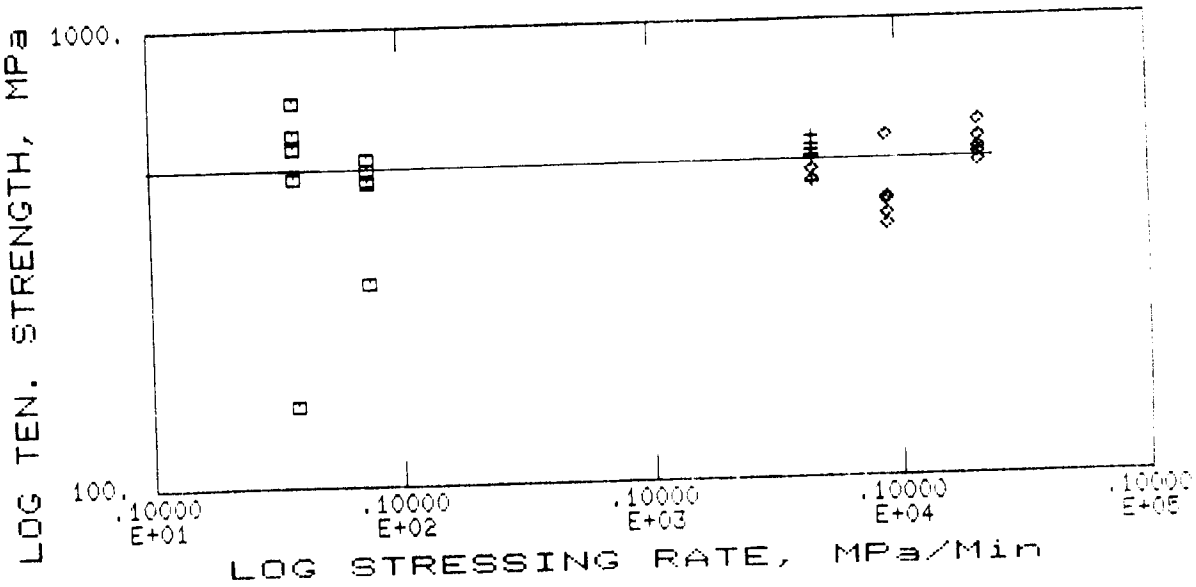

Batch # 1 □ ; Batch # 2 + ; Batch # 3 ◊

Figure 6. Plot of log stressing rate versus log tensile strength of the SNW-1000 samples tested at room temperature

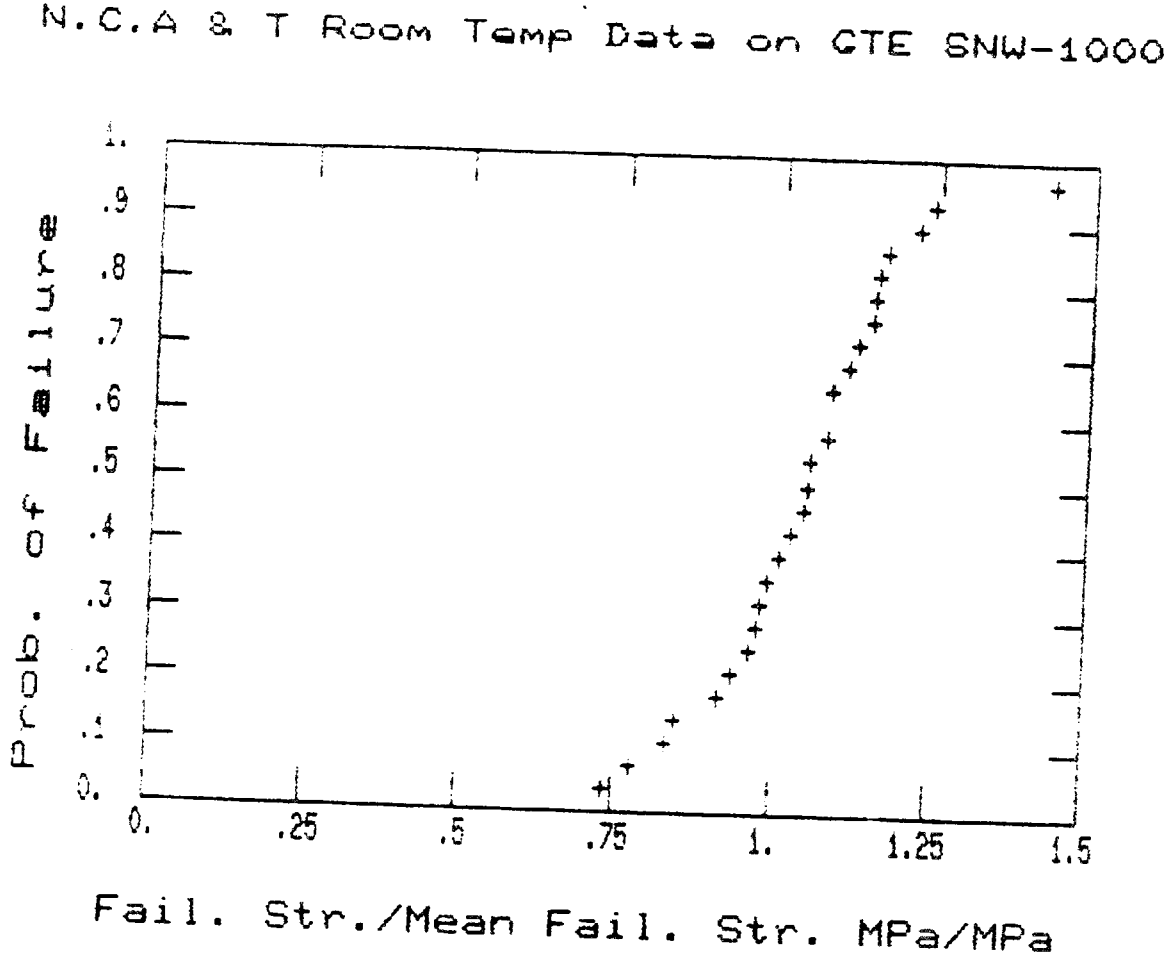

Figure 7. Probability of failure data curve

tested at room temperature. This indicates that the tensile strength at room temperature for this material is independent of the stressing rate. Using regression analysis a probability of failure data curve was obtained for the room temperature tests. Figure 7 shows this probability failure data curve.

Figure 8a and 8b shows the set up used for the high temperature tests. The "Zygo" laser telemetric system for the high temperature extensometry, the control panel for the furnace, data recorder, and the furnace along with the test sample with attached flags (Platinum) for the strain measurements at room temperature are shown by arrows in the figure.

During the reporting period the high temperature set up was also completed. A special box series furnace with SiC heating coil, heating just the gage section of the sample was designed and procured from the Applied Test Systems, Inc. During this reporting period much time was spent on firing and calibrating both the furnace and the laser system. Temperature profile along the sample was also optimized. The temperature variation from the center to the top of the sample was found to be between 20 - 25 deg. C.

Since, tensile tests of silicon nitride at room temperature showed very low strains (0.15% - 0.21%), it was necessary to obtain maximum resolution through the Zygo system to measure such low strains. Optimum window size for the laser was established for the maximum resolution. Maximum resolution was obtained by adjusting the window (nominal dimension) in such a way that for a minimum gap between the flags responded to maximum voltage. In this case it was found that for a flag gap of 0.1 inches (2.54 mm) the voltage range was -10 to +10 volts. This gave the maximum resolution obtainable in Zygo 121 model.

Tensile tests at high temperature were run using the program supplied by MTS. The tensile testing software provided by the MTS Corporation was suitable only for the room temperature tests, since the software could not accept tha data from the Zygo system directly. This called for certain modification in the software and hardware. The hardware was modified by taking the analog output from the " BNC Connector " of the Zygo system and introducing the same into a seperate A/D board on the MTS 880 machine. The software supplied by the MTS Corporation was modified to acquire the online continuous data on an external disk and use the same to plot the stress versus strain curves.

Tensile tests were also carried out to calibrate the laser extensometer and to check the deviation if any, against the MTS extensometer. Table 2. shows the deviation of laser and the MTS extensometer. A stressing rate of 7.5 MPa/min was used for the calibration check. Table2. shows a maximum deviation of 0.01% between the two systems.

During this reporting period tensile tests were also carried out

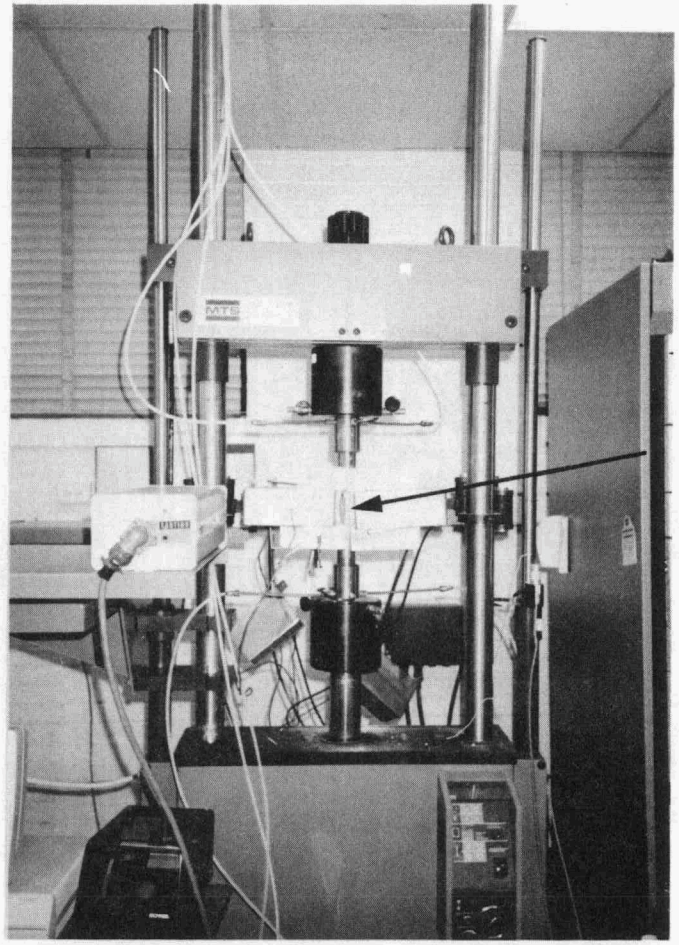

Figure 8a. High temperature set up with slightly opened furnace showing test sample with attached Platinum flags

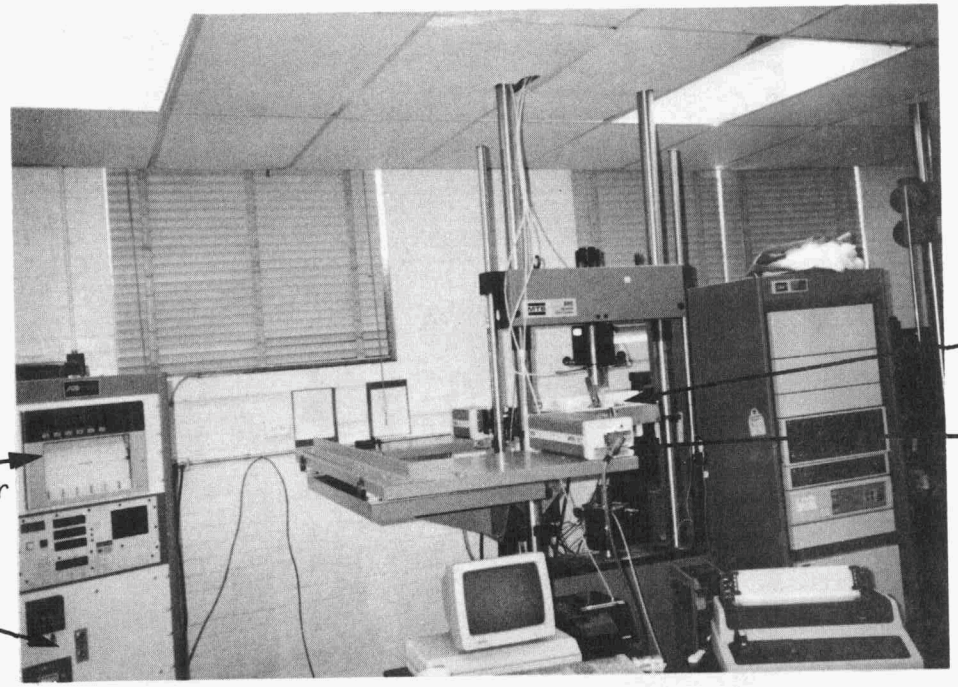

Figure 8b. High temperature set up

Table 1. Tension test results for silicon nitride SNW-1000 tested at room temperature, at stressing rates of 3.75 MPa/Min and 7.5 MPa/Min.(Batch #3).

Sample #	Tensile Strength MPa(Ksi)	Strain at Fracture %	Duration of Test Hr:Min:Sec	Stressing Rate MPa/Min
22	276.97(40.17)	0.080	0:35:06	7.50
23	519.50(75.34)	0.150	1:06:03	7.50
24	490.29(71.11)	0.164	1:02:21	7.50
25	461.10(66.88)	0.132	0:58:36	7.50
26	465.99(67.58)	0.172	0:59:12	7.50
27	539.00(78.18)	0.210	1:08:51	7.50
28	582.74(84.52)	0.186	2:29:21	3.75
29	150.69(21.86)	0.057	0:38:06	3.75
30	473.91(68.73)	0.125	1:59:28	3.75
31	685.58(95.52)	0.211	2:57:09	3.75
32	549.52(79.70)	0.194	2:10:06	3.75

Table 2. Calibration of laser extensomrtry at room temperature, at stressing rate of 7.5 MPa/Min.(Batch #3)

Sample #	Strength MPa(Ksi)	Strain %		Stressing Rate MPa/Min
		Laser	MTS	
33	539.0(78.18)*	0.21	--	7.5
34	244.0(35.38)	0.07	0.07	7.5
35	114.0(16.53)	0.04	0.038	7.5

* --- Test carried out till fracture.

Table 3. Tension test results for silicon nitride SNW-1000 tested at 900 ± 20 DEG C, at stressing rates of 7.5 MPa/Min

Sample #	Tensile Strength MPa(Ksi)	Strain at Fracture %	Duration of Test Hr:Min:Sec	Stressing Rate MPa/Min
36	286.74(41.59)	0.38	0:36:28	7.5
37	514.52(74.62)	0.37	1:05:19	7.5
38	427.51(62.01)	0.35	0:54:04	7.5

at 900 deg. C. Table 3. gives the stress and strain values at 900 deg. C. Itmay be observed that the fracture strength varied between 428.0 to 515.0 MPa (60 to 75 Ksi) which is in the same range obtained at room temperature tests. Tha strain values showed a comparatively higher value of 0.38%.

Status of Milestones

Task 1-6 are complete. Presently, the high temperature testing is being carried out. The next report will include the detailed SEM and EDS analysis of the samples tested at high temperature and further tests at 900 and 1100 deg. C.

Communications/Visitors/Travel

1. Dr. K. C. Liu (Oak Ridge National Lab.)
2. Dr. Ray Johnson (Oak Ridge National Lab.), and
3. Dr. R. B. Shultz (Department of Energy)

visited the A&T facility and technical discussions were carried out about the high temperature set up.

Problems Encountered

1. Laser Beam Alignment: Before the furnace was fired to the required temperature, the laser beam was aligned with the laser port in the furnace and the flag. As the furnace reached the required temperature, it was held at that temperature for 15-20 minutes to get a uniform temperature gradient, which was measured through the thermocouples attached to the top and bottom of the sample. It was found that during certain arbitary time the Zygo system did not scan gap between the flags. This resulted in zero strain reading in that duration and to correct this, data points during this scan period were deleted to get an accurate stress versus strain curve.

2. Extension Rod: It was observed that the extension rod threads were jamming up during the high temperature experiments. A coating of "Boron Nitride" lubricoat was applied on the top of the sample and also inside and the outside threads of the extension rod, to prevent this from occuring. This did not solve the problem completely.

3. Temperature Control: Calibration of the temperature profile along the sample indicated a variation of ± 20 deg. C between the top and center of the sample.

Publications & Presentations

1. R. Vaidyanathan, J. Sankar, V. S. Avva, "Testing and Evaluation of Silicon Nitride in uniaxial tension at room temperature", paper presented at the 25th Automotive Technology Developement Contractor's Coordination meeting, Dearborn, Michigan, October 1987. Proceedings of the 25th Automotive Development Contractor's Coordination meeting, to be published by Society of Automotive Engineers, Inc.

2. R. Vaidyanathan, J. Sankar, V. S. Avva, "Uniaxial tensile characteristics of silicon nitride at room temperature",paper presented at the 12th Annual conference on Composites and Advanced Ceramics, Engineering Ceramics Division meeting of the American Ceramic Society, Inc., 85-C-88F, Cocoa Beach, Florida, January 1988.

References

1. A. E. Pasto, J. T. Neil, and C. L. Quackenbush, "Microstructural effects influencing strength of silicon nitride", Proceedings of the International Conference on Ultrastructure Processing of Ceramics, Glass and Composites, 1983.

Standard Tensile Test Development

S. M. Wiederhorn, D.F. Carroll, T.-J. Chuang and D. E. Roberts
(National Bureau of Standards)

Objective/Scope:

This project is concerned with the development of test equipment and test procedures for measuring the tensile strength and creep resistance of ceramic materials at elevated temperatures. Inexpensive techniques of measuring the creep and strength of ceramics at elevated temperatures are being developed and are being used to characterize the mechanical behavior of structural ceramics. The test methods use self aligning fixtures, and simple grinding techniques for specimen preparation. Creep data obtained with tensile test techniques will be compared with data obtained using flexure and compressive creep techniques. The ultimate goal of the project is to assist in the development of a reliable data base and methodology that can be used for structural design of heat engines for vehicular applications.

Technical Highlights

During the past 6 months, work has concentrated on using the creep and creep rupture data obtained to date to develop a general methodology for predicting the lifetime of ceramic components that are subject to creep at elevated temperatures. This need is based on the fact that lifetime at elevated temperatures is often determined by mechanical damage generated as a consequence of creep [1]. In tensile test specimens, damage is in the form of small cracks or cavities that form at grain boundaries or interfaces within the material [2-5]. For small amounts of deformation, cavitation occurs at random through out the gauge section. As deformation increases, the damage accumulates into cracks, or crack-like cavities that are the ultimate cause of failure. As in the case of metals, which also fail by cavitation [6], the creep rupture time can be expressed as a power law function of the steady state creep rate, regardless of load or test temperature. The rupture time is usually found to be an inverse function of the steady state creep rate, a relationship that is known as the Monkman-Grant equation [7].

Relationships such as the Monkman-Grant equation have been used for practical purposes to predict the lifetime of structural materials that fail by creep rupture. Provided creep and creep rupture data obtained in tension and compression are applicable to other modes of loading, such relationships can be used for the prediction of lifetime in complex loading states. Unfortunately, recent data on the creep of ceramic materials suggest that creep in tension and in compression may be quite different for ceramic materials [2, 3, 5, 8]. Glass ceramics [2], siliconized silicon carbide [5, 8] and reaction bonded silicon nitride [3] have all been shown to creep considerably faster in tension than in compression. For these materials, the creep rate in tension is at least 20 times greater than that in compression. Therefore, portions of a

component that are subjected to tensile stresses will always creep faster, in complex modes of loading, than portions subjected to compressive stresses. The net effect of this behavior is a time dependent stress distribution in the component [9-12], so that the initial applied stress distribution, calculated from elasticity theory, cannot be used as an estimate of the driving force for crack growth and component failure. This time dependence of the stress distribution is also modified when cavitation accompanies creep. Because cavitation leads to a breakdown in the power laws that describe creep, the analysis required for specimens subjected to complex modes of loading must also reflect the possibility of power-law breakdown [12]. As a consequence, additional analyses are needed before data obtained in uniaxial tensile tests can be applied to other geometries and loading states.

To date, the detailed analyses needed to understand these conditions of creep have been achieved only for four-point flexural loading, in which case, the effect of asymmetric creep is reasonably well understood [9-12]. For materials that creep faster in tension than in compression, quantitative analyses are available to describe the stress and strain distributions as a function of time. The role of cavities has been factored into the analysis, and the time dependence of the stress distribution has been determined. In this report, the earlier work on flexural testing is extended to include creep rupture of flexural bars. Creep data in tension and compression are combined with creep rupture data obtained in tension to obtain the creep rupture behavior in flexure. Experimental and theoretical results are summarized here; detailed accounts of the research are presented elsewhere [5, 13, 14].

Creep and Creep Rupture Data

Creep and creep rupture studies were conducted on a grade of reaction bonded silicon carbide (SOHIO KX01)[1] that cavitates only in tension. The material contained ≈33% silicon and 67% SiC, in the form of 2 to 5 μm SiC grains distributed at random within the silicon matrix, figure 1. In tension, the material fails by cavity formation. Cavities are nucleated at interfaces between the silicon and silicon carbide, generally between closely spaced silicon carbide particles [4, 5]. At first, cavities nucleate at random throughout the gauge section, but later accumulate in planar patterns to form the crack-like cavities that lead to structural failure. An effective threshold for cavity formation is observed, below which creep occurs primarily by deformation of the silicon matrix. Above the threshold, cavity formation contributes significantly to the creep process [4]. As indicated by optical and transmission electron microscopy, cavitation does not occur when this material is subjected to compressive creep [14].

A comparison of the steady state creep rate of the reaction bonded silicon carbide in both tension and compression is given in figure 2. As can be seen, the material creeps much more easily in tension than in

---

[1] This brand name is supplied for purposes of identification only and does not imply endorsement by the National Bureau of Standards.

compression. The creep data in tension and in compression both can be represented by two straight lines, which suggests that the creep rate is more sensitive to stress at higher stresses. In tension, the increase in the slope of the creep rate curve has been attributed to cavities that nucleate and grow rapidly enough above a stress of 100 MPa to enhance the creep rate. This apparent threshold for cavitation is temperature sensitive, and at 1100°C occurs at 132 MPa [4]. In compression, the increase in the slope of the creep rate curve cannot be attributed to cavitation, since no cavities are observed in this material, even at the highest creep rates. Investigations of this material by transmission electron microscopy indicate an enhancement of dislocation activity within the silicon carbide grains for high creep rates and large degrees of strain, suggesting a role of plastic deformation in the creep rate at high compressive stresses [14].

As illustrated in figure 3, the creep rupture behavior of this material in tension can be approximated by a straight line on logarithmic plot of steady state creep rate, $\dot{\epsilon}_s$, versus creep rupture time, t_r, regardless of test temperature or applied load. The magnitude of the slope of the line, ≈0.71, is less than the value of 1 usually obtained from creep rupture studies on metals [7]. Creep rupture curves for this material indicate that for ≈80 to 90 % of the test period, deformation can be characterized by steady state creep. As a consequence, the rupture strain, ϵ_r, can be determined, to a good approximation, from the steady state creep rate and the rupture time: $\dot{\epsilon}_s \cdot t_r \approx \epsilon_r$. Thus, each point on the curve in figure 3 represents a unique strain to failure, a finding that is used in this study to predict the lifetime in flexure from creep-rupture data in tension. Also, since the magnitude of the slope of the curve in figure 3 is less than 1, the strain to failure in tension for this material is greater for low strain rates and long failure times than for rapid strain rates and short failure times.

Creep-Rupture Time in Flexure

In flexure, the rupture time is calculated from the creep data in figure 2, and the rupture data in figure 3. The creep data give the constitutive laws that describe the creep behavior in each section of the flexure bar, which permits the stresses and strains to be calculated in the cross section of the bend bar. The bimodal creep curve of figure 2 was used for the tensile data; however, to simplify the calculation, the creep in compression was represented by the lower portion of the compressive creep curve. Local failure in the flexure beam was assumed to occur when the creep strain exceeded the creep strain for failure in tension at the same creep rate. The creep strain in a four-point flexure bar varies linearly through the cross-section of the bar as a consequence of the uniform bending moment within the inner span. Thus, local failure (as indicated by a critical density of cavities or by creep cracks) occurs when the material near the surface exceeds the critical creep strain. The damage zone slowly spreads into the bend bar as deformation proceeds, until it finally reaches a critical size at which time the test beam no longer supports the imposed load, figure 4. In the calculation, the critical damage zone size is assumed to be

calculable from a linear elastic analysis of a crack in a bent beam; measured values of the critical stress intensity factor for chevron notched flexure specimens are used in the calculation, figure 5.

Using the constitutive equations for creep, figure 2, the creep rupture data, figure 3, and the assumptions for damage accumulation and critical damage zone size, figure 4, the estimated lifetime for flexural loading was calculated and compared with experimental test data, figure 6. For a given applied stress the calculated failure time is in excellent agreement with the measured value of the failure time. These results support the model proposed to predict flexural creep and creep rupture behavior of materials from uniaxial tensile and compressive creep data. The assumptions of critical strain for cavity coalescence and equal failure strain in tension and bending appear to be applicable to flexural bars of reaction bonded silicon carbide. A full evaluation of the model, however, awaits further research on other materials and test geometries.

References

1. A.G. Evans, "Engineering Property Requirements for High Performance Ceramics," Mater. Sci. and Eng., 71, 3-21 (1985).

2. R. Morrell and K.H.G. Ashbee, "High Temperature Creep of Lithium Zinc Silicate Glass-Ceramics, Part 1, General Behavior and Creep Mechanisms," J. Mater. Sci. 8, 1253-1270 (1973).

3. J.M. Birch, B. Wilshire and D.J. Godfrey, "Deformation and Fracture Processes During Creep of Reaction Bonded and Hot Pressed Silicon Nitride," Proc. Brit. Ceram. Soc. 26, 141-54 (1978).

4. D.F. Carroll and R.E. Tressler, "Effect of Creep Damage on the Tensile Creep Behavior of a Siliconized Silicon Carbide," J. Am Ceram. Soc. to be published.

5. S.M. Wiederhorn, "Damage Enhanced Creep in a Siliconized Silicon Carbide: Phenomenology," J. Am. Ceram. Soc. to be published.

6. H.E. Evans, "Mechanisms of Creep Fracture," Elsevier Applied Science Publishers, London (1984).

7. F.C. Monkman and N.J. Grant, "An Empirical Relationship Between Rupture Life and Minimum Creep Rate in Creep Rupture Tests," Proc. ASTM 56, 593-620 (1956).

8. S.M Wiederhorn, L. Chuck, E.R. Fuller, Jr. and N.J. Tighe, "Creep Rupture of Siliconized Silicon Carbide," pp 755-773 in Tailoring Multiphase and Composite Ceramics, R.E. Tressler, G.L. Messing, C.G. Pantano and R.E. Newnham eds. Materials Science Research, Vol. 20, Plenum Press, New York (1986).

9. H. Cohrt, G. Grathwohl and F. Thümmler, "Non-Stationary Stress Distribution in a Ceramic Bending Beam During Constant Load Creep," Res. Mechanica, 10, 55-71 (1984).

10. T.-J. Chuang, S.M. Wiederhorn and C.F. Chen, "Transient Behavior of Structural Ceramics under Flexural Creep," pp. 957-73 in The Proceedings of the Third International Conference on Creep and Fracture of Engineering Materials and Structures, B. Wilshire and R.W. Evans eds., The Institute of Metals, London (1987).

11. H. Cohrt, G. Grathwohl and F. Thümmler, "Strengthening after Creep of Reaction-Bonded Siliconized Silicon Carbide," pp.515-26 in The Proceedings of the Second International Conference on Creep and Fracture of Engineering Materials and Structures, B. Wilshire and R. Owen eds., Pineridge Press Limited, Swansea, U.K. (1984).

12. T.-J. Chuang and S.M. Wiederhorn, "Damage-Enhanced Creep in a Siliconized Silicon Carbide: Mechanics of Deformation," to be published.

13. T.-J. Chuang, D.F. Carroll and S.M. Wiederhorn, "Creep Rupture Behavior of a Metal-Ceramic Particulate Composite," to be published in the 7th Int. Conf. on Fract., Houston, TX, (1989).

14. B.J. Hockey and S.M. Wiederhorn, "Creep Deformation of Siliconized Silicon Carbide," to be published.

15. K. Kromp, T. Haug, R.F. Pabst, and V. Gerold, "C^* for Ceramic Materials? Creep Crack Growth at Extremely Low Loading Rates at High Temperatures using Two-Phase Ceramic Materials," pp. 1021 to 1032 in ref. 10.

Status of Milestones

341302 Dogbone specimen has been improved to give approximately 1% or less strain in bending during tensile tests. A paper has been written and will be published on the subject of specimen development (paper 5 below). The alignment achieved to date is deemed satisfactory; there will be no further work on this milestone.

341303 Creep and creep rupture data have been collected in tension and compression on a grade of reaction bonded silicon carbide. The data has been used to analyze failure mechanisms in the flexure configuration. Lifetime predictions have been made, and found to be in good agreement with experimental data. The results of this milestone are found in paper 6 listed below.

Publications

1. T.-J. Chuang and S.M. Wiederhorn, "Damage-Enhanced Creep in a Siliconized Silicon Carbide: Mechanics of Deformation," J. Am. Ceram. Soc. accepted for publication.

2. S.M. Wiederhorn, D.E. Roberts, T.-J. Chuang and L Chuck, "Damage Enhanced Creep in a Siliconized Silicon Carbide:Phenomenology," J. Am. Ceram. Soc. Accepted for publication.

3. "High Temperature Mechanical Properties of Sialon Ceramic: Creep Characterization," C.F. Chen and T.-J. Chuang, Ceram. Eng. and Sci. Proc. 8, 796-804 (1987).

4. "Creep and Reliability of Ceramic Materials at Elevated Temperatures," S.M. Wiederhorn, T.-J. Chuang and D.F. Carroll, pp. 117 to 130 in the Proceedings of the International Symposium on Fine Ceramics, Arita '87, Held in Arita, Saga Prefecture. Nov. 17 to 18, 1987.

5. D.F. Carroll and S.M. Wiederhorn, "High Temperature Creep Testing of Ceramics," To be published in the Proceedings of the Conference on Mechanical Testing of Engineering Ceramics at High Temperatures, held in London, England. April 11 - 12, 1988.

6. F. Carroll, T.-J. Chuang and S.M. Wiederhorn, "A comparison of Creep Rupture Behavior in Tension and Bending," To be published in Ceramic Engineering and Science Proceedings, Presented at the 12th Annual Conference open Composites and Advanced Ceramic Materials, Sponsored by the Engineering Ceramics Division of the American Society, January 17 - 20, 1988, Cocoa Beach, FL.

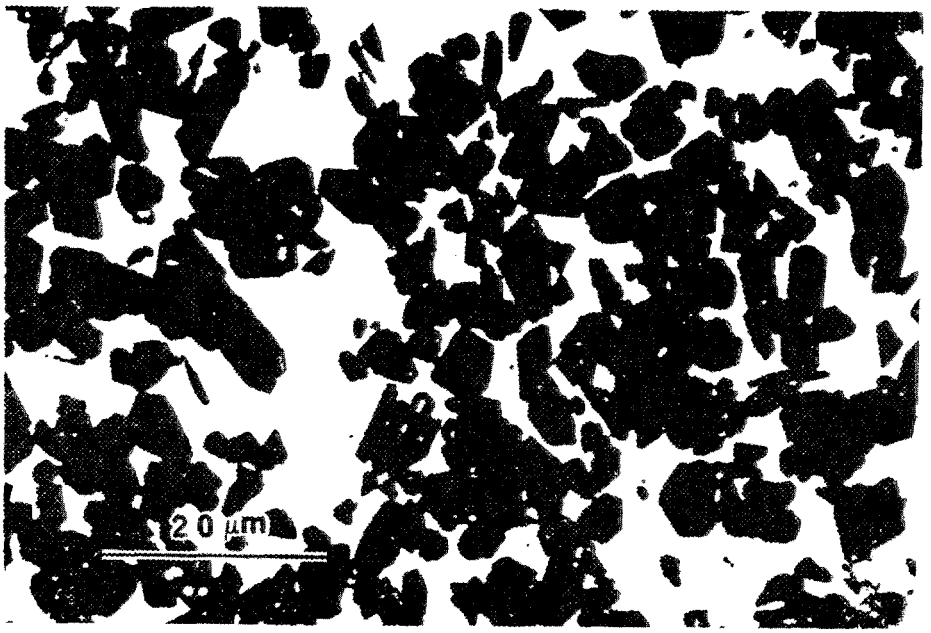

1. Optical micrograph of reaction bonded silicon carbide, SOHIO KX01. The silicon carbide grains (dark grey) are completely surrounded by silicon (white). As can be seen from the pockets of silicon and the agglomerates of silicon carbide, the material is not homogeneous, from ref. 5.

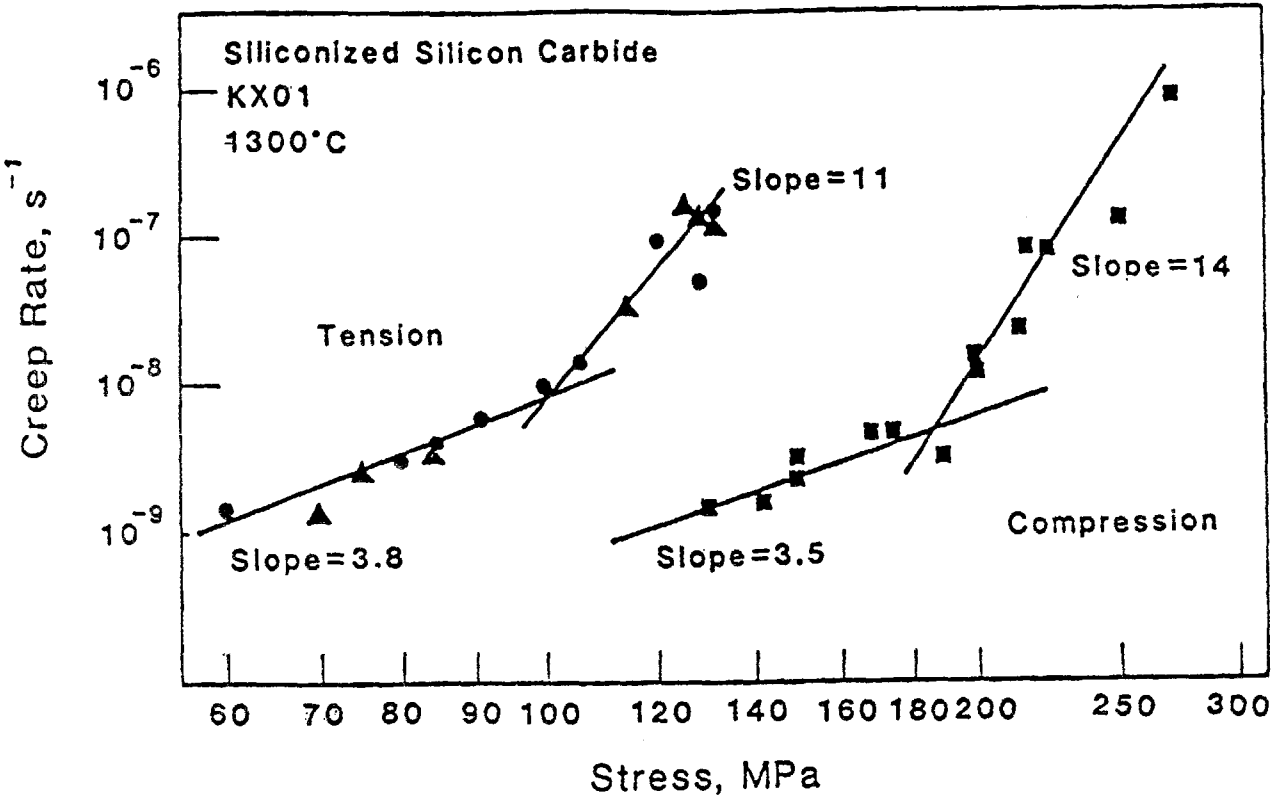

2. A comparison of creep rates in tension and compression. The material creeps much more readily in tension than in compression. Tensile and compressive creep both follow a bimodal behavior in which the creep rate accelerates as the stress increases above a critical stress, from ref. 5.

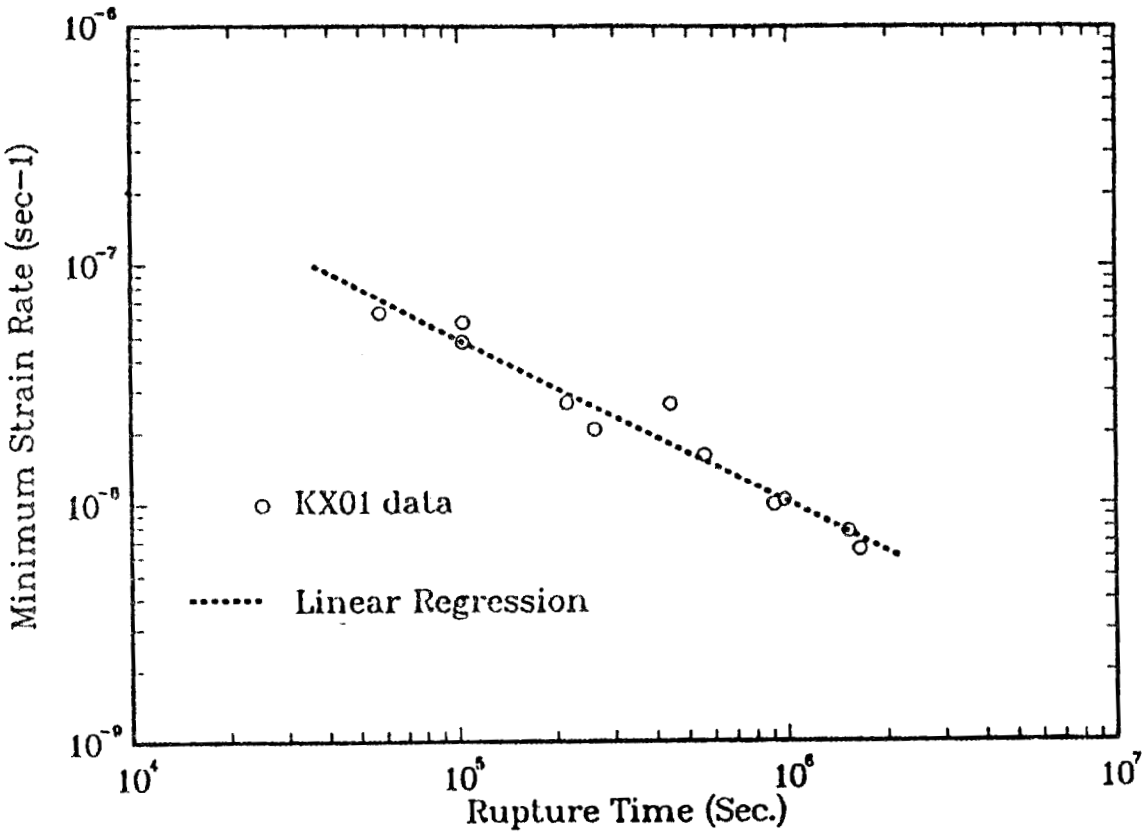

3. Creep rupture behavior of reaction bonded silicon carbide in tension. All of the data follow a linear plot of log $\dot{\epsilon}_s$ versus log t_r, regardless of test temperature or test stress. The temperatures and stresses used to obtain the above data ranged from 75 MPa and 1400°C to 125 MPa and 1225°C.

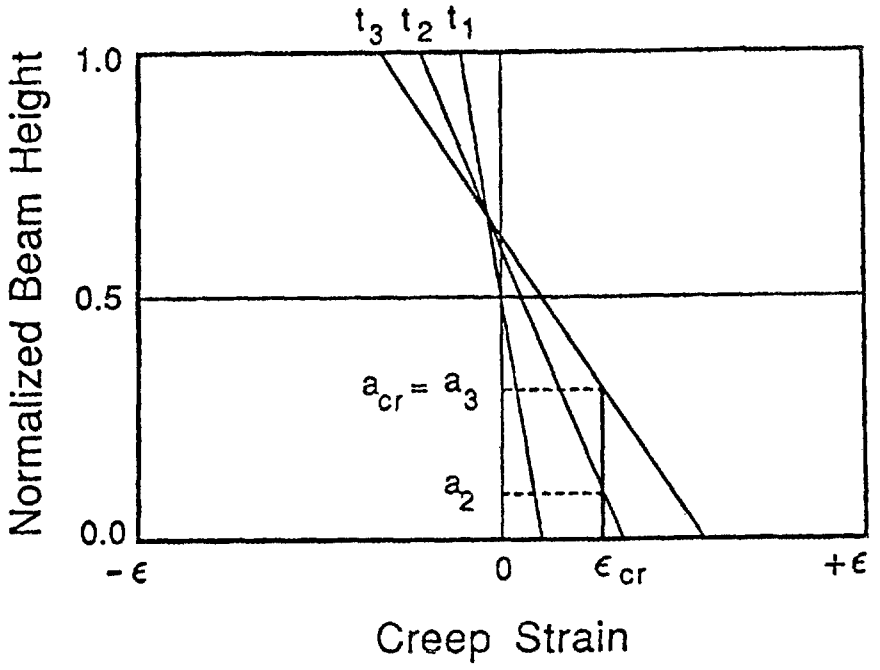

4. Schematic diagram of the progression of a critical damage zone in a bend bar, as it progresses from the tensile to the compressive surface of the bar. Once the critical strain is achieved at a distance, a, from the tensile surface, the flexure beam is assumed to be effectively broken up to position a. Failure is assumed to occur when the effective crack size equals the critical crack size as calculated from a linear elastic fracture mechanics analysis of a crack in a bent beam [13]. In the above figure, at time, t_1, there is no effective crack in the flexure bar, because the maximum strain at the tensile surface is smaller than the critical strain; at time, t_2, the depth of the effective crack is a_2; while, at time, t_3, the crack size, a_3, has reached the critical size, and failure occurs.

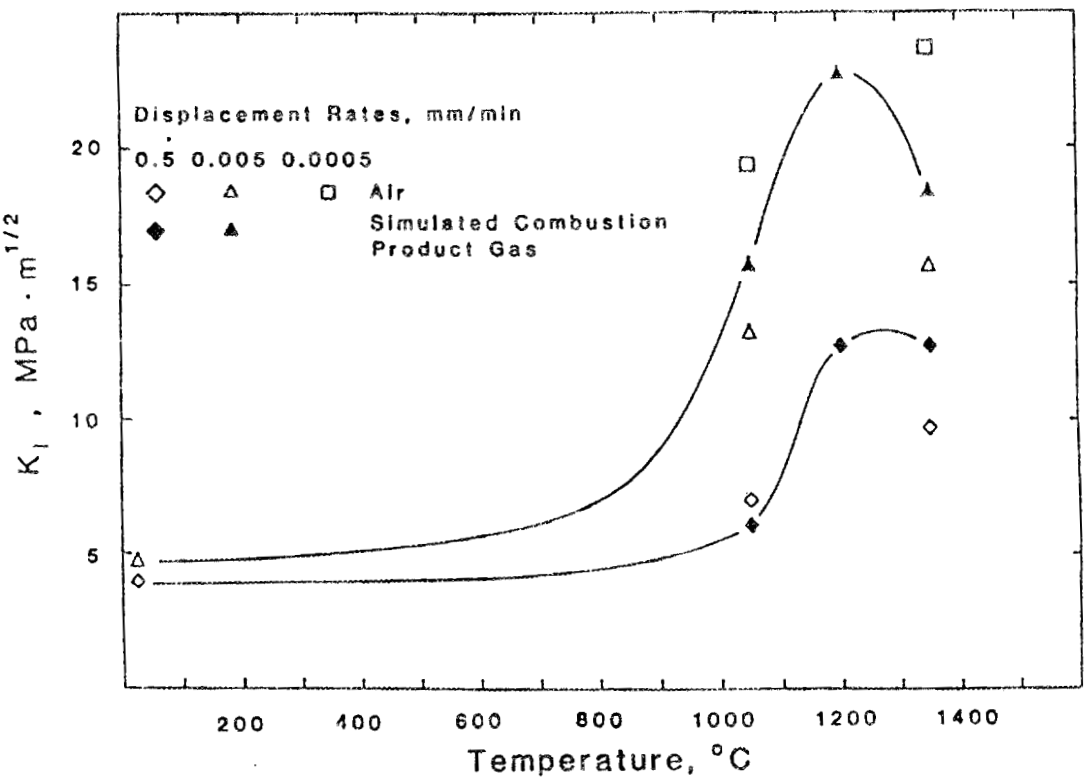

5. Fracture toughness of reaction bonded silicon carbide as a function of temperature and test environment. For the slow loading rates, a toughness of >20 MPa-$m^{½}$ can be achieved. Courtesy of L. Chuck and R. Krause. Data similar to these were obtained by Kromp, et al. [15]. In the present study a K_{Ic} of 20 MPam^{½} was assumed.

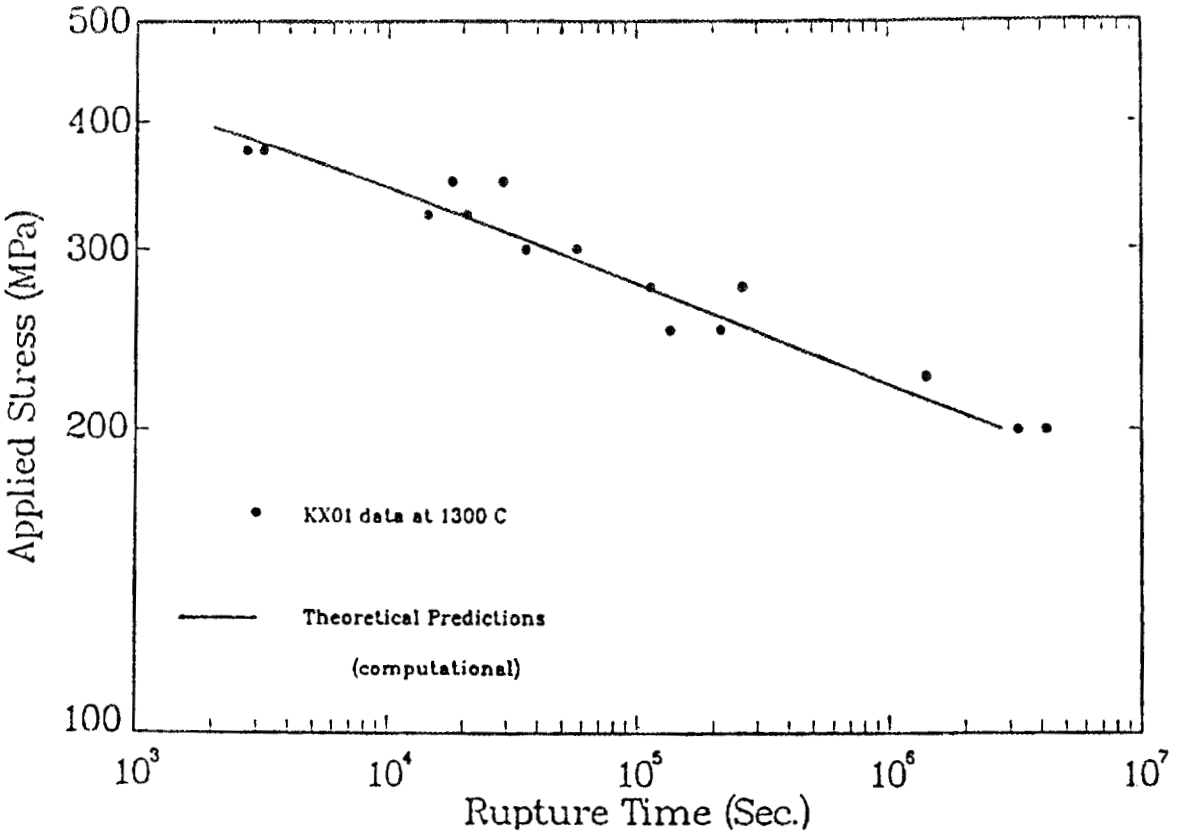

6. Creep rupture behavior of reaction bonded silicon carbide in 4-point flexure. The theoretical prediction (solid line) falls very close to the data points (closed circles). Test temperature 1300°C.

3.5 NONDESTRUCTIVE EVALUATION DEVELOPMENT

Nondestructive Characterization
R. W. McClung (Oak Ridge National Laboratory)

Objective/scope

The purpose of this program is to conduct nondestructive evaluation (NDE) development directed at identifying approaches for quantitative determination of conditions (including both properties and flaws) in ceramics that affect the structural performance. Those materials that have been seriously considered for application in advanced heat engines are all brittle materials whose fracture is affected by structural features with dimensions on the order of the dimensions of their microstructures. This work seeks to characterize those features using high-frequency ultrasonics and radiography to detect, size, and locate critical flaws and to measure nondestructively the elastic properties of the host material.

Technical progress

Ultrasonics – W. A. Simpson, Jr., and K. V. Cook

We have developed a model for the beam distribution of an ultrasonic field inside a ceramic. This model allows for propagation of the beam through a liquid-solid interface (i.e., typical noncontact immersion testing) and determines the relative field amplitude at any point within the solid. Previous models developed by others could handle the beam distribution for a transducer radiating into a single medium, but to our knowledge this is the first such model which is applicable to the configurations occurring in actual ceramic inspection. In addition, complex ceramic shapes can be treated by this model as well as aspherical transducer lenses. The latter capability is particularly important, since it is known that nonspherical lens configurations can provide considerable improvement in transducer sensitivity in some instances of metals evaluation. The cost of an empirical study in ceramics would be prohibitive, however, since high-frequency transducers are typically several thousand dollars each.

The significance of the new model is that it allows a priori evaluation of the performance of a given transducer in ceramic inspection. In other words, the lateral and depth resolution and sensitivity of a transducer can be calculated and optimized for a given test configuration. Since the sensitivity for detection of a given flaw size at various depths in a ceramic determines how coarsely one must scan the part in depth (and hence how rapidly the part can be inspected), a technique for optimizing, or at least estimating, this quantity would be of considerable importance. Previously, we have had to determine the lateral and depth sensitivity empirically, which necessitates actually buying the transducer, which is untenable for the reasons given above.

We have completed computation of the beam distribution inside typical ceramics for a number of transducer designs. The initial calculations were performed at low frequencies, since the computations required less

time. The designs studied included spherically and parabolically focused elements as well as axicons (conically "focused" transducers). A further design, termed the optimally point-focused element, whose shape was determined by back-propagating a diffraction-free cone of rays through the ceramic surface, was also included.

Figure 1 shows the results obtained on a spherically focused transducer, which is the most common design. The figure depicts the beam amplitude as a function of depth and transverse position in the solid. Each grid line represents a quarter-wavelength in the sample. The figure is centered on the geometric focus of the transducer lens, i.e., it is located at the point where the transducer would focus neglecting aberration. The point of maximum amplitude is seen to lie near the geometric focus, although it is slightly closer to the transducer. This is to be expected, since the marginal rays from the transducer will focus closer to the surface of the sample because of aberration.

The figure indicates that the full width of the transducer response at half-maximum amplitude is about 1 wavelength. More important is the fact that the sensitivity to depth variations of the flaw can also be determined from the figure. If we define the useful depth of focus for a given transducer as the distance over which the beam amplitude is within 6 dB of maximum, then Fig. 1 shows that the depth of focus for the transducer studied is about 5 wavelengths. This represents a distance of only

ORNL-DWG 88-6996

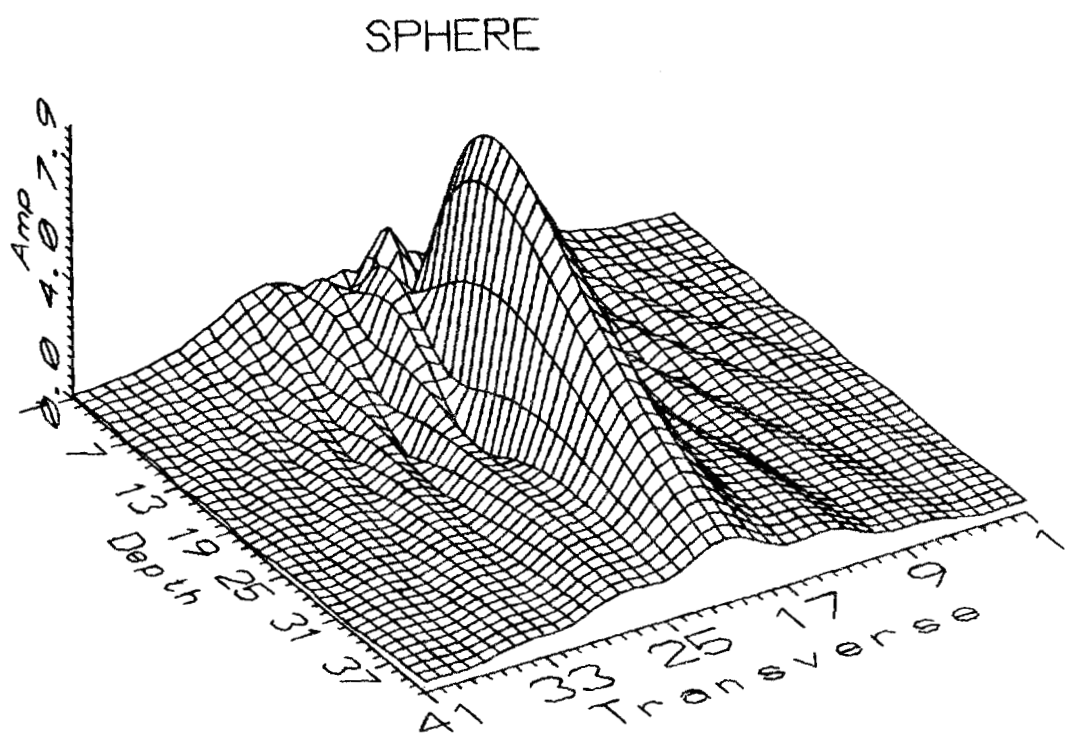

Fig. 1. Low-frequency beam distribution of a spherically focused ultrasonic transducer.

about 1 mm for a 50-MHz transducer in alumina, if these results hold for higher frequencies. Furthermore, the figure indicates that the sensitivity decreases more slowly below focus than above.

Figure 2 shows the results obtained for a low-frequency axicon (i.e., conically focused) transducer. This design is well known for its long depth of "focus" when radiating into a single medium. The figure shows that, while the peak amplitude is about 9 dB below that obtained with a spherically focused transducer, the depth of focus is indeed larger than for the spherical unit, particularly in the zone below focus. In the present case the depth of focus is about 9 wavelengths as compared to 5 wavelengths for the spherical transducer. The improvement is not as dramatic as in the case of a single medium, but it is nonetheless significant. If a lower overall sensitivity can be tolerated, the axicon transducer appears to be capable of reducing total inspection time because of its greater depth of focus.

We next computed the distribution produced in alumina by a 50-MHz, 12.7-mm focus spherical transducer, which is perhaps the most common design for high-frequency transducers. The results are shown in Fig. 3 and indicate that the -6 dB focal spot diameter is about 0.75 wavelengths, or about 160 μm at the center frequency. The -6-dB depth of focus is again about 5 wavelengths, or 1.1 mm. This result indicates that if the transducer is positioned to focus at its maximum depth (~1.75 mm) in alumina, then flaws lying in a band from about 0.64 mm above to about 0.42 mm below the focal plane will be detected with a sensitivity within 6 dB of maximum.

ORNL-DWG 88-6995

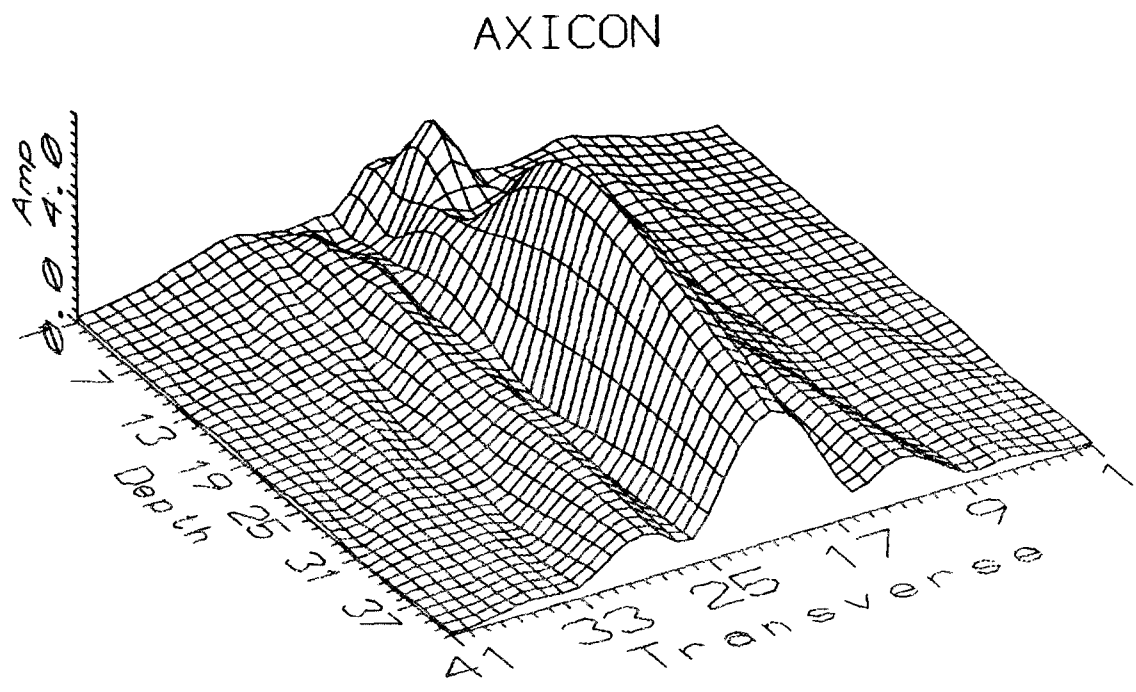

Fig. 2. Low-frequency beam distribution of an ultrasonic axicon transducer.

ORNL-DWG 88-6934

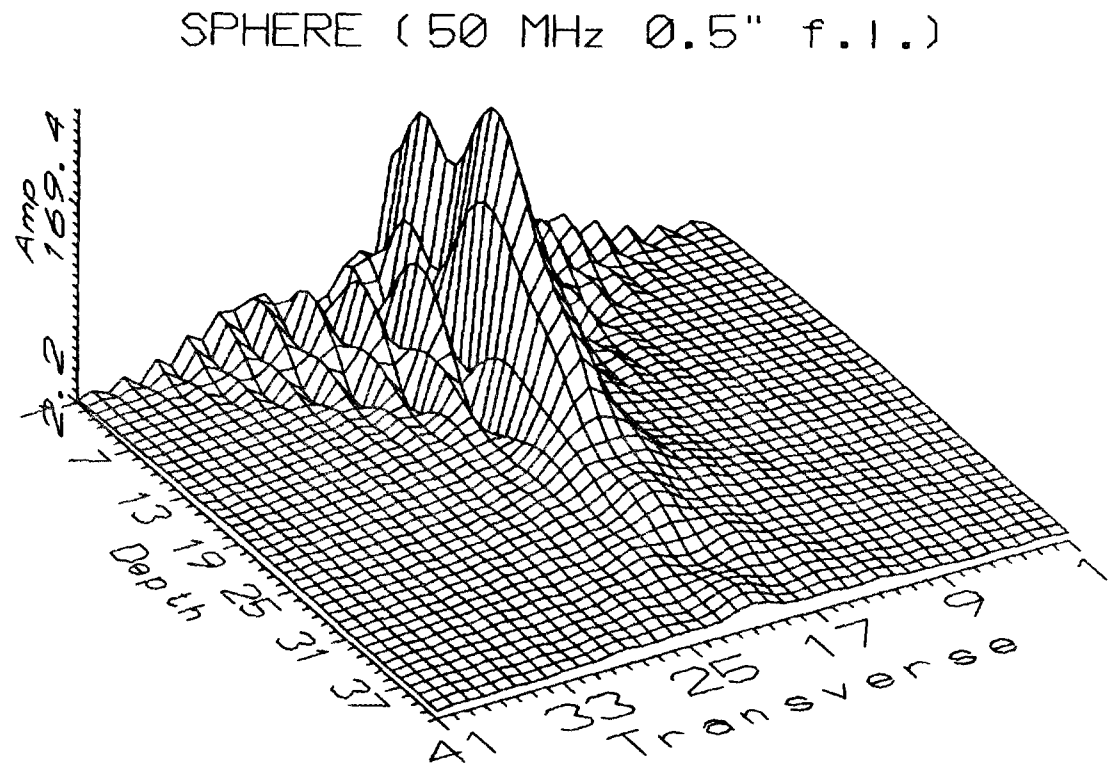

Fig. 3. Beam distribution of a high-frequency spherical transducer in alumina.

We also note that the near-field oscillations of the high-frequency transducer are more pronounced than for its low-frequency counterpart, but this is attributable to the fact that the sample is necessarily in the transducer near field, since the water column must be reduced to the smallest distance possible because of losses in the coupling fluid.

The distribution produced by a 50-MHz axicon transducer having the same nominal focal length of 12.7 mm is shown in Fig. 4. The total -6-dB depth of focus is about 1.7 mm, or about 50% greater than for the spherical transducer. The focal spot diameter is the same as for the sphere.

For the low-frequency axicon transducer, the maximum amplitude at focus was about 9 dB below that for a spherical transducer, while it is about 6 dB larger at 50 MHz (this is probably attributable to the difference in materials selected rather than the difference in frequency). Thus the axicon design appears to have considerable potential for inspection of ceramics.

We have also examined the beam distribution produced by a toroid transducer in alumina. This design is characterized by a refracting surface whose cross section is defined by two identical circles with offset centers and has been touted for its great depth of field (in a single medium) and suppression of the near-field oscillations characteristic of most transducers. However, as Figs. 5 and 6 indicate, this design appears to be decidedly inferior to either the spherical or axicon transducers for

ORNL-DWG 88-6937

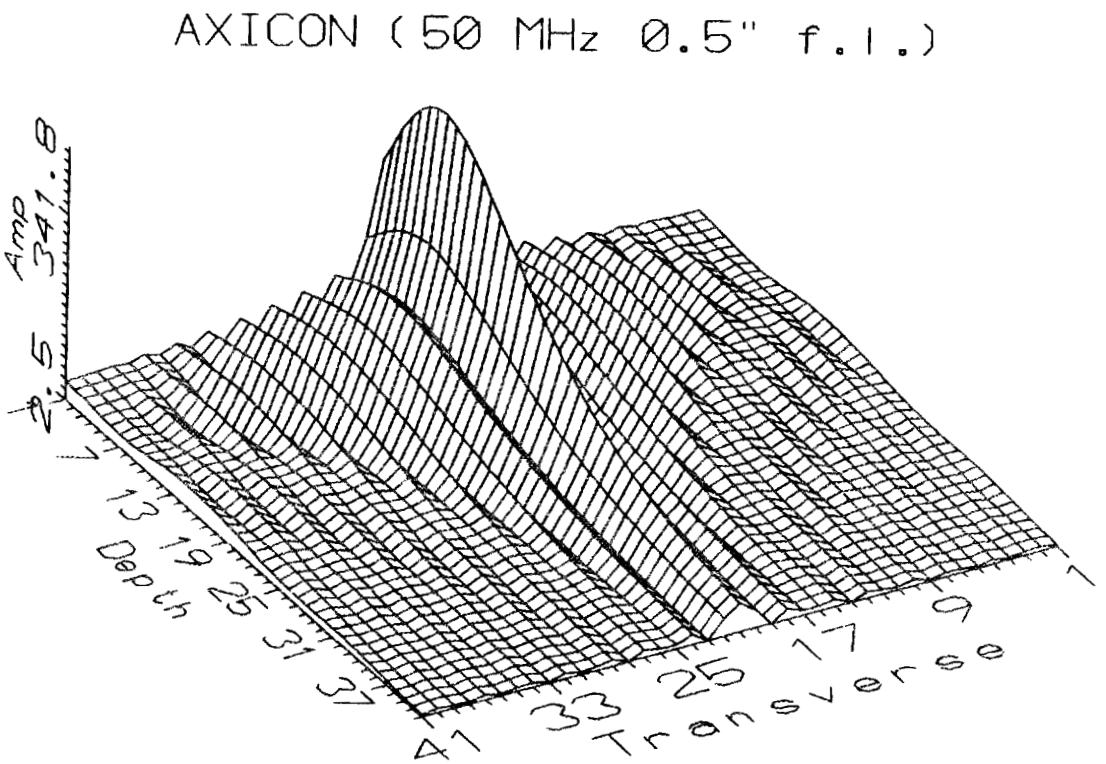

Fig. 4. Beam distribution of a high-frequency axicon transducer in alumina.

ORNL-DWG 88-6936

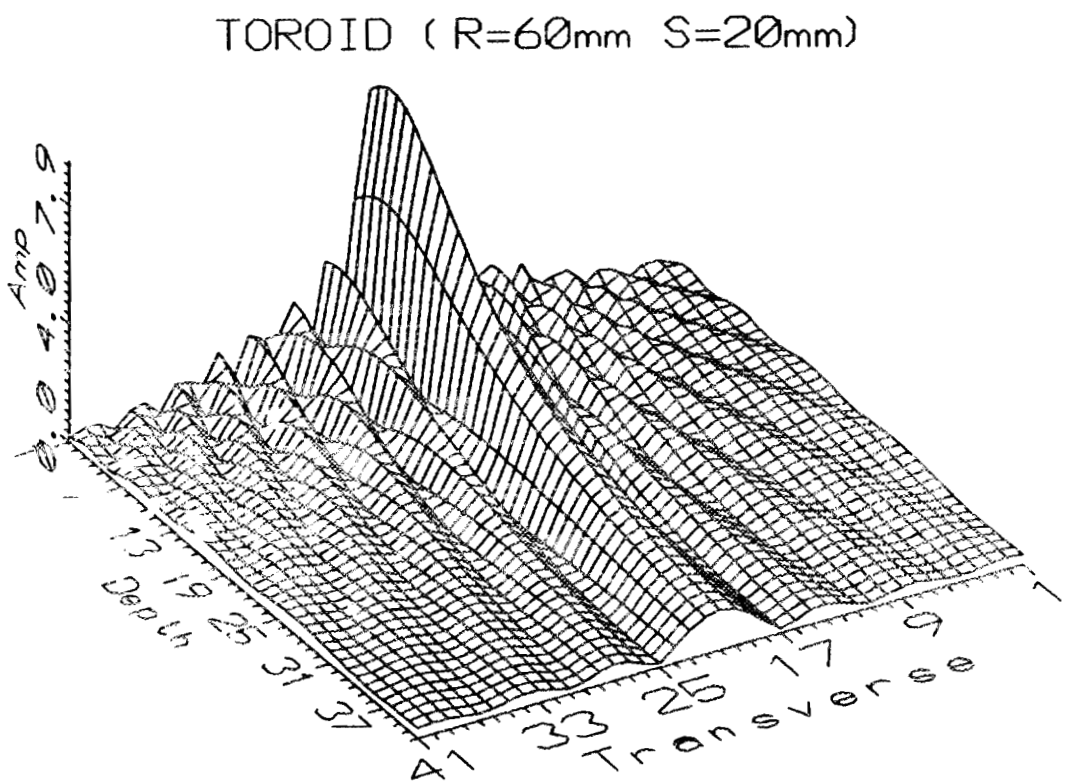

Fig. 5. Beam distribution of a toroidal transducer of relatively short focus.

ORNL-DWG 88-6935

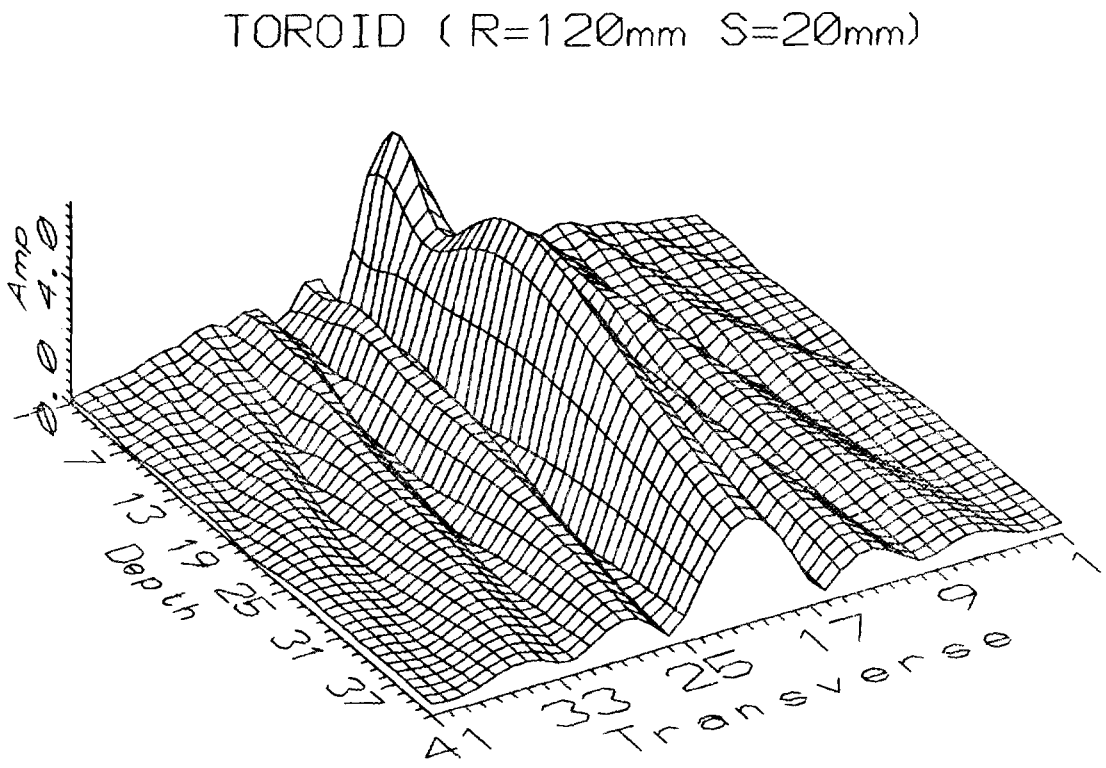

Fig. 6. Beam distribution of a toroidal transducer of relatively long focus.

ceramic immersion inspection. While a smooth near field and high amplitude could be obtained with this design (Fig. 5), the focal depth was much less in alumina for a given lens curvature that for the other transducers. When the lens curvature was flattened to produce a greater focal depth (Fig. 6), there were severe near-field oscillations and greatly reduced focal amplitude.

Although a plane-wave transducer would not be used for critical flaw detection in ceramics, we nevertheless computed the field in alumina of such a design for completeness and as a check on our model. The results indicated that the field produced by a 50-MHz, 12.7-mm-diam element exhibited very severe near-field oscillations at all practical depths in the ceramic and produced a very low maximum axial amplitude relative to any of the focused transducer designs. The diffraction (beam spread) of the incident field was easily seen, however.

A number of other low-frequency transducer designs have also been studied, including a paraboloid and an "optimum focus" design whose surface figure was defined by back-propagating a diffraction-free, perfectly focused beam through the ceramic-water interface. Not surprisingly, to the first order this surface is defined by a paraboloid. The results yielded a slight improvement over the spherical transducer at focus, but the depth of focus was virtually identical. The use of either of these designs is therefore not indicated, since the fabrication cost would be greater.

The model can handle the shear wave produced by mode conversion at the water-ceramic interface as well as the longitudinal wave. We have not yet computed the shear wave field distribution, but a computer program to evaluate this function has been written.

As part of our effect to make available the technology which we have developed for ceramics evaluation, we have examined a number of samples of alumina recently obtained from an outside vendor. This material was scheduled to be cut into MOR bars and consisted of both rectangular and cylindrical billets of sintered material. However, evaluation of the billets using 50-MHz ultrasonic surface waves revealed that 40% of the samples were severely cracked. In addition, the surface waves also revealed the presence of numerous surface pits. Visual microscopy of these pits indicated that they were almost perfectly circular with sizes ranging from 25 to 250 μm. Evaluation of the interior of the billets was also performed using 75-MHz elastic waves. As expected, numerous voids were found throughout the volume of the samples. No attempt was made to determine the diameter of these voids, but previous experience with this material suggests that they ranged from 25 μm to perhaps as large as 200 μm in a few instances.

We also began examination of nonplanar ceramic samples consisting of rods of magnesia-stabilized zirconia. As expected, the surface curvature of these samples greatly reduced the sensitivity of the ultrasonic evaluation, but we have designed an aspheric transducer lens which our calculations show should correct for the sample curvature. We are investigating the possibility of having such a transducer fabricated by a commercial vendor.

Software has been written to permit a high-speed ram disk to be used to acquire data from our ultrasonic scan system. This modification should greatly decrease the time required to evaluate ceramic parts using this system, which has previously been limited to a linear scan rate of about 25 mm/s by the requirement for storing the data on magnetic tape. This modification should permit scan rates of about 250 mm/s with our present pulser, or even higher rates if the pulser can be modified to operate at higher repetition rates. The ultimate limit of this system is about 500 mm/s, which is imposed by the mechanical scanner.

Radiography – B. E. Foster

Five samples of dispersion-toughened alumina were received for radiography. The samples were approximately 25 by 50 mm (1 by 2 in.) with thicknesses ranging from 3.3 to 4 mm (0.131–0.158 in.). Surface roughness, thickness variations within a sample, and cracks in the edges of the samples were noted.

Twelve rectangular-shaped samples with widths of 36.3 mm (1.45 in.) and with thicknesses of 8.1 mm (0.325 in.) were radiographed. Eight of these samples with lengths of 66.3 mm (2.65 in.) contained numerous surface pits with diameters ranging from 0.1 to 0.4 mm (0.004–0.016 in.) and depths from 0.05 to 0.3 mm (0.002–0.012 in.) and several internal voids with similar dimensions. In addition, cracking was detected in one of the samples. The other four samples with lengths of 26.3 mm (1.05 in.) contained similar pits and internal voids. Three of these samples contained cracks.

Three alumina disks with diameters of 152 mm (6 in.) and thicknesses of 9.8 mm (0.390 in.) were radiographed. Several surface pits and internal voids were noted in addition to surface gouges and scratches. One of the scratches that appears quite shallow visually gives a very strong indication on the radiograph. The true depth is obviously greater than can be seen from the surface.

The procurement of a computerized X-ray tomography system is in progress but awaiting administrative approval.

Status of milestones

None.

Publications

D. R. Johnson, M. A. Janney, and R. W. McClung, "Needs Assessment for NDT and Characterization of Ceramics: I. Approach to Reliability and Assessment of Inspection and Characterization Technology for Raw Materials," pp. 19-32 in *Nondestructive Testing of High-Performance Ceramics*, Conference Proceedings, August 25-27, 1987, Boston, The American Ceramic Society, Westerville, Ohio, 1987.

R. W. McClung and D. R. Johnson, "Needs Assessment for NDT and Characterization of Ceramics: Assessment of Inspection Technology for Green State and Sintered Ceramics," pp. 33-51 in *Nondestructive Testing of High-Performance Ceramics*, Conference Proceedings, August 25-27, 1987, Boston, The American Ceramic Society, Westerville, Ohio, 1987.

W. A. Simpson, Jr., and R. W. McClung, "NDE of Advanced Structural Ceramics," pp. 290–303 in *Conference Proceedings, Nondestructive Testing of High-Performance Ceramics, August 25–27, 1987, Boston*, American Ceramic Society, Westerville, Ohio.

R. W. McClung, "Nondestructive Examination and Characterization of Advanced Ceramics," presented at CERAMTEC '88, Dearborn, Michigan, February 3, 1988.

R. W. McClung, "Cooperative NDT Development for Ceramics," presented at the WATTec '88, 15th Annual Technical Conference and Exhibition, Knoxville, Tennessee, February 16-19, 1988.

W. A. Simpson, Jr., and R. W. McClung, "Quantitative Ultrasonic Attenuation Technique for Materials Characterization," presented at the Spring Conference of the American Society for Nondestructive Testing, Orlando, Florida, April 11–15, 1988.

Computed Tomography

W. A. Ellingson, M. W. Vannier, and H. C. Yeh (Argonne National Laboratory)

Objective/scope

The purpose of this program is to develop X-ray computed tomographic (CT) imaging for application to structural ceramic materials. This technique has the potential for mapping short-range (<5 mm) and long-range (>5 mm) density variations, detecting and sizing high- and low-density inclusions, and detecting and sizing (within limits) cracks in green-state and densified ceramics. CT imaging is capable of interrogating the full volume of a component, and is non-contacting. It is also relatively insensitive to part shape and thus can be used to inspect components with complex shapes such as turbocharger rotors, rotor shrouds, and large individual turbine blades.

Technical progress

Technical effort in this program has centered on two main activities: (1) developing and implementing corrections for beam hardening (BH) and (2) development of calibration phantoms. During the current reporting period, we focused exclusively on applying dual-energy techniques[1-7] to prototype turbocharger rotors. In particular, we concentrated on studying how well the dual-energy software package would work without additional calibration on two different types of turbocharger rotors. All work was done with a medical CT imager (a Siemens DR-H) equipped with a dual-energy software package and modified software allowing extension of the dynamic range.

The first specimen studied was a densified, injection-molded, and sintered SiC rotor produced and loaned to us by B-P America (formerly SOHIO Engineered Materials) of Cleveland, OH. This rotor is fairly large: 12.5 cm in diameter with a shaft about 2.5 cm in diameter and about 7.5 cm long. (It is important to note that until now, we have had limited success in obtaining images of reasonable quality with a medical scanner X-ray head for dense ceramic pieces of this size. Dual-energy images were taken along the axial plane shown by the dashed line in Fig. 1, with X-ray head accelerating voltages of 85 and 125 kVp. Figures 2 and 3 show, respectively, the 85- and 125-kVp uncorrected CT images. Figure 2 shows that at 85 kVp, even though the object was penetrated, the detected signal strength for that calibration was "out of range." This simply means that the detected energy was out of the normal calibration range; it does not mean that the data were invalid. In addition, Fig. 2 shows the expected BH, which is evident from the densitometer trace. Figure 3 shows the 125-kVp image obtained at exactly the same table position (TP=93) used to obtain Fig. 2. Extensive BH is still present at 125 kVp, but the signal level obtained is within the detector calibration range.

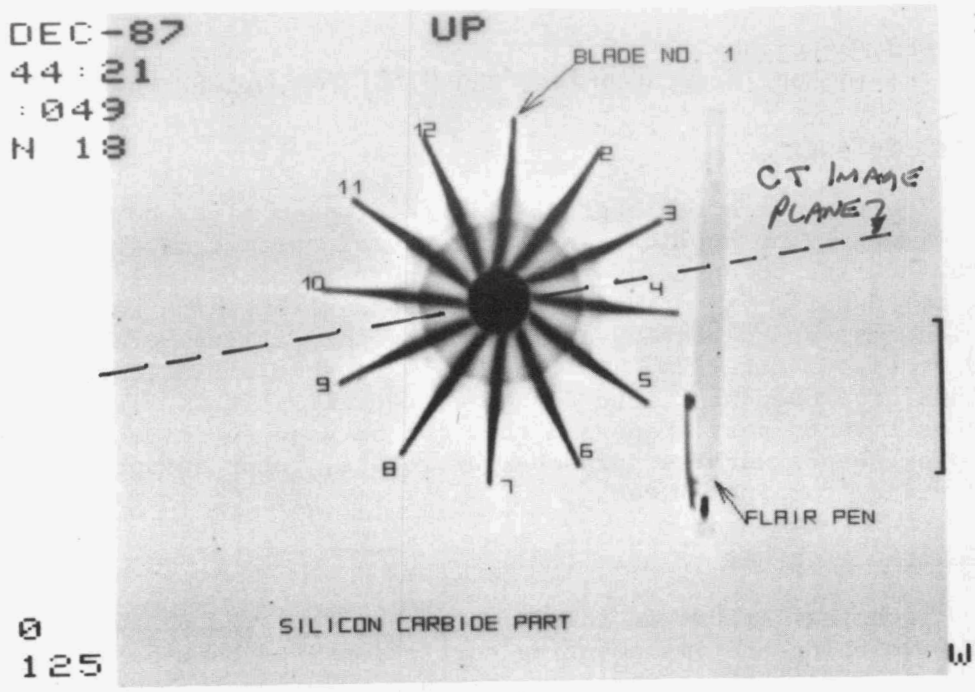

Fig. 1. Transaxial CT Image Showing Rotor Blade Identification and Location of Axial Images for SiC Turbocharger Rotor.

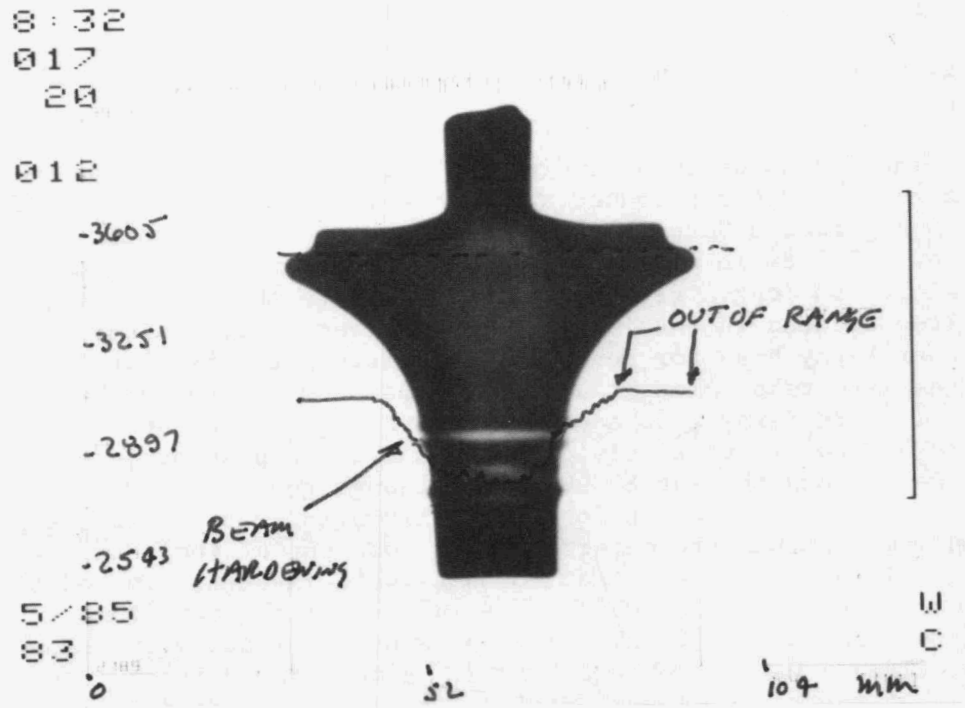

Fig. 2. Axial CT Image of SiC Turbocharger Rotor, Taken with X-Ray Head Accelerating Voltage of 85 kVp. Slice thickness is 4 mm; kernel-head SP. In this and subsequent images, the densitometer trace corresponds to the location shown by the dotted line.

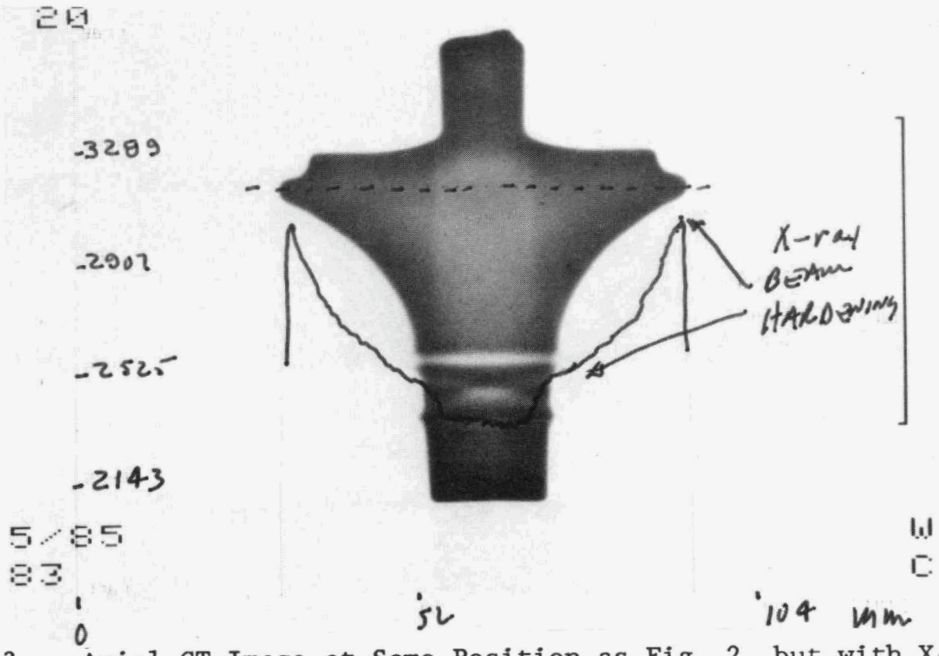

Fig. 3. Axial CT Image at Same Position as Fig. 2, but with X-Ray Head Accelerating Voltage of 125 kVp. Slice thickness is 4 mm.

Application of the dual-energy software package to the individual 85- and 125-kVp data sets produced the images shown in Figs. 4 and 5. Figure 4 includes a densitometer trace at the same posiions as those of Figs. 2 and 3. A comparison of the densitometer traces in Figs. 3 and 4 shows the significant reduction in BH that results from the use of the dual-energy software package. Figure 5 is the same dual-energy image as Fig. 4, but with an axial densitometer trace. As was previously discussed,[8-9] the application of the dual-energy approach to polychromatic X-ray CT imaging yields equivalent monochromatic images. Use of this aspect of the dual-energy package yielded an equivalent 120-keV monochromatic image, as shown in Fig. 6. It is important to note that a series of such images could be generated for different keV levels, as presented previously.[9]

Fig. 4

Axial CT Image Resulting from Application of Dual-Energy Software Package to Data Shown in Figs. 2 and 3.

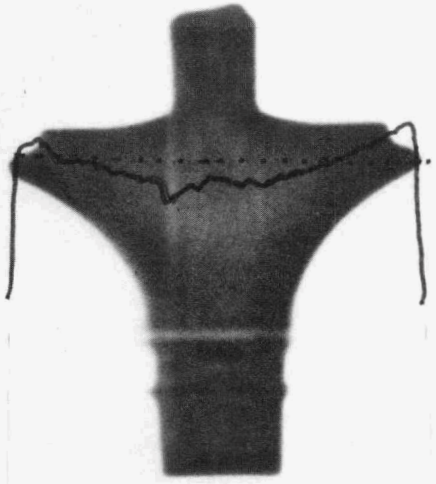

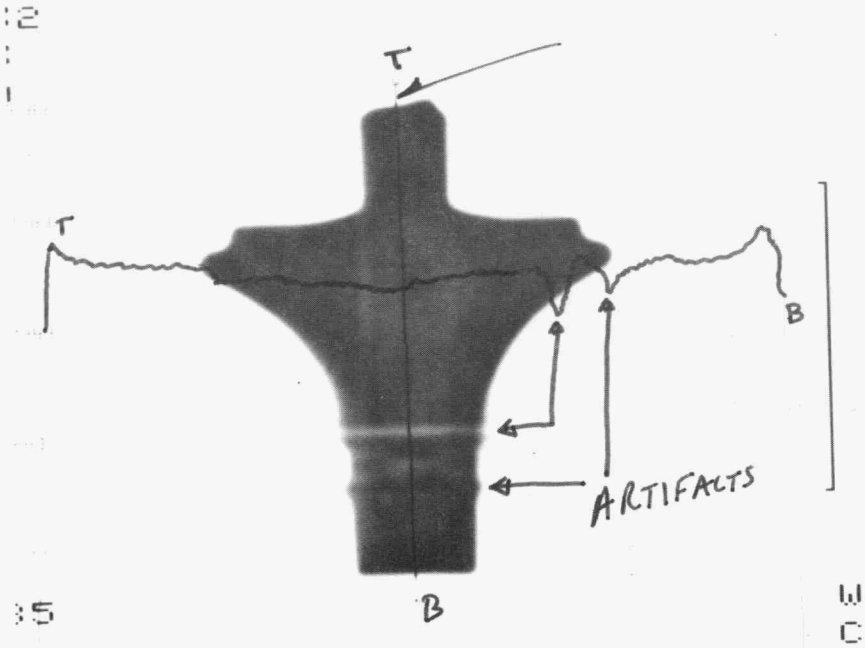

Fig. 5. Same CT Image as Shown in Fig. 4, with Axial Densitometer Trace The axial trace detects two artifacts associated with edge effects (i.e., sharp high-density contrasts with sharp cutoffs).

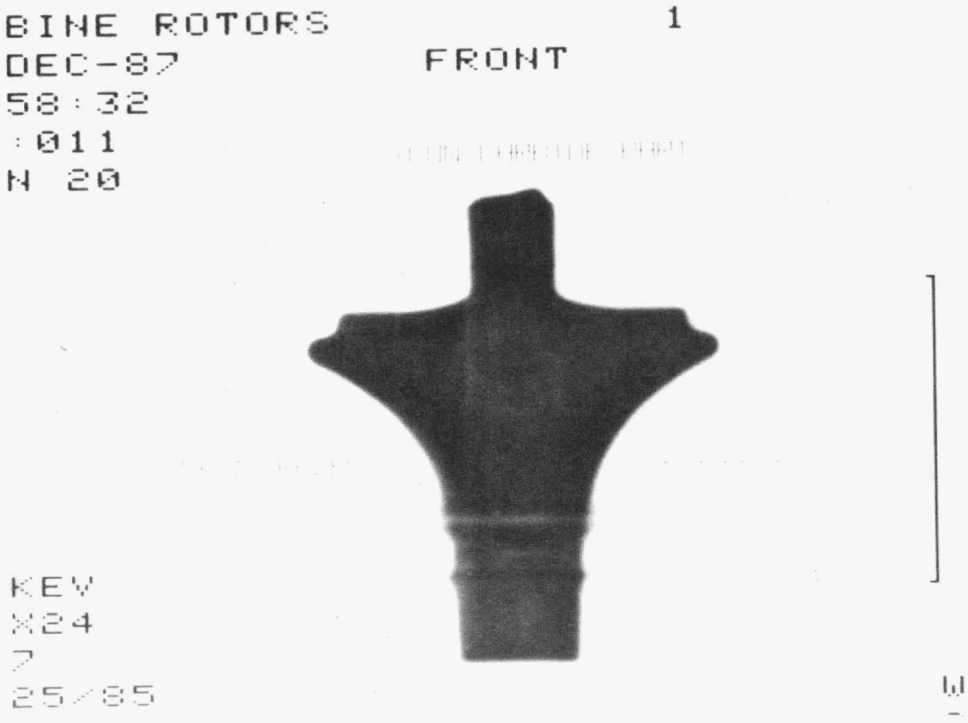

Fig. 6. CT Image Reconstructed at 120-keV Equivalent Monochromatic Energy from Data Shown in Figs. 2 and 3.

During the current period, we also used CT imaging to examine two small injection-molded Si_3N_4 turbo rotors, densified by the reaction bonding process. These two rotors were nominally 5 cm in diameter, with shafts 1.4 cm in diameter and 15 cm long. Significant differences in the defect contents of these two rotors are apparent from the X-ray images of Figs. 7 and 8. The images shown in Fig. 7 were obtained with a new X-ray image receptor called photostimulable phosphors.[10] Figure 8 shows a digital radiographic image of the two rotors and the plane of the transaxial CT images in Fig. 9. Figure 7 illustrates a common problem with ordinary X-ray contact or projection radiography: detailed diagnostic information cannot be obtained in regions where the superposition of data occurs, such as the blade hub region in a turbo rotor.

Rotor A

Rotor B

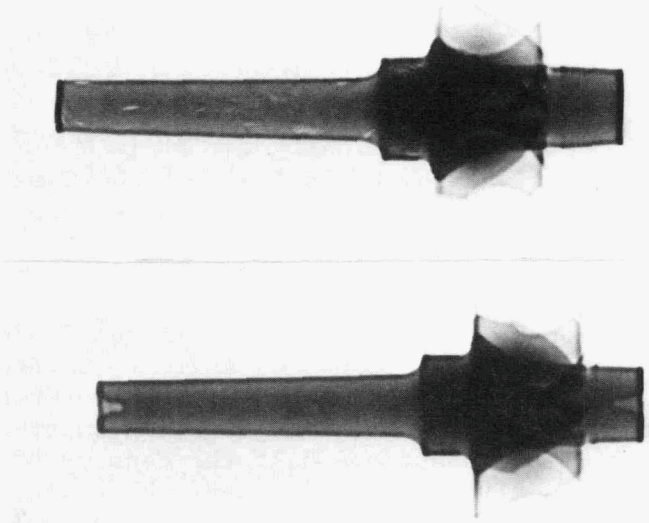

Fig. 7. Contact X-Ray Images of Two Reaction-bonded Si_3N_4 Rotors. Rotor A shows extensive internal cracking; Rotor B appears to be free of defects.

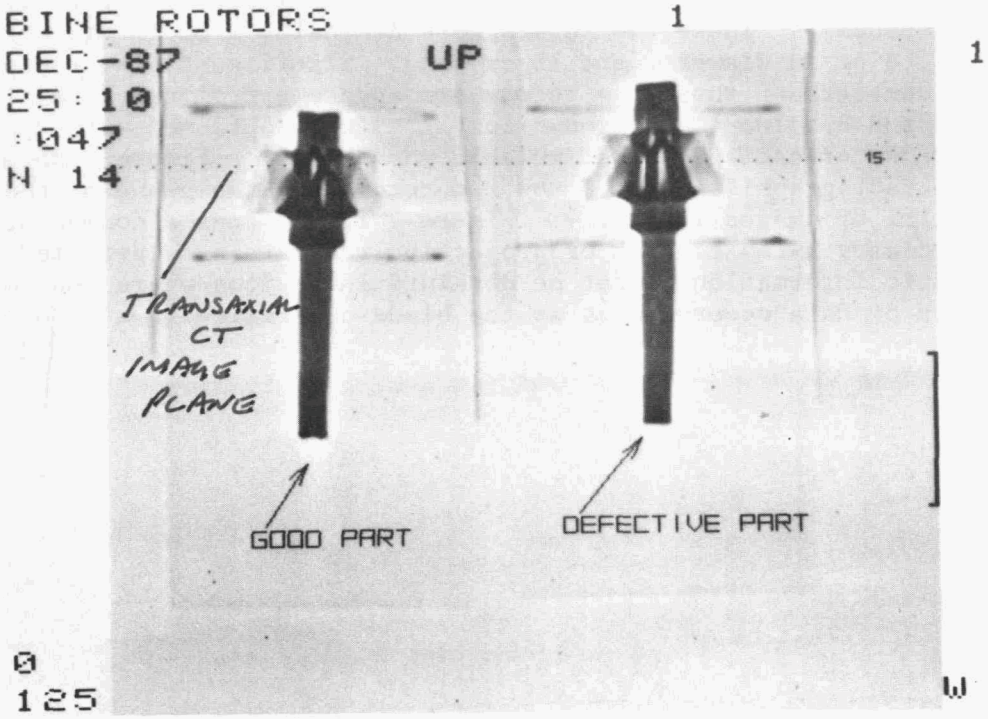

Fig. 8. Digital Radiographic Image of The Same Si_3N_4 Turbo Rotors Shown in Fig. 7. Transaxial CT images were obtained in the plane shown by the dotted line.

The 120-keV monochromatic equivalent image of Fig. 9 was obtained by using data at 85 and 125 kVp, as noted earlier. Careful observation of Fig. 9 reveals several interesting features. In rotor A, the light-colored region at 7 o'clock could likely be a region of unreacted metallic silicon, which has about one-half the density of reaction-bonded Si_3N_4. Rotor B shows a circular annulus near the shaft, which also suggests a lower density region. Destructive analysis will be conducted to establish whether this is an artifact or a real low-density region. More extensive results of these CT image tests will be discussed in the next reporting period.

Status of milestones

All milestones are on schedule.

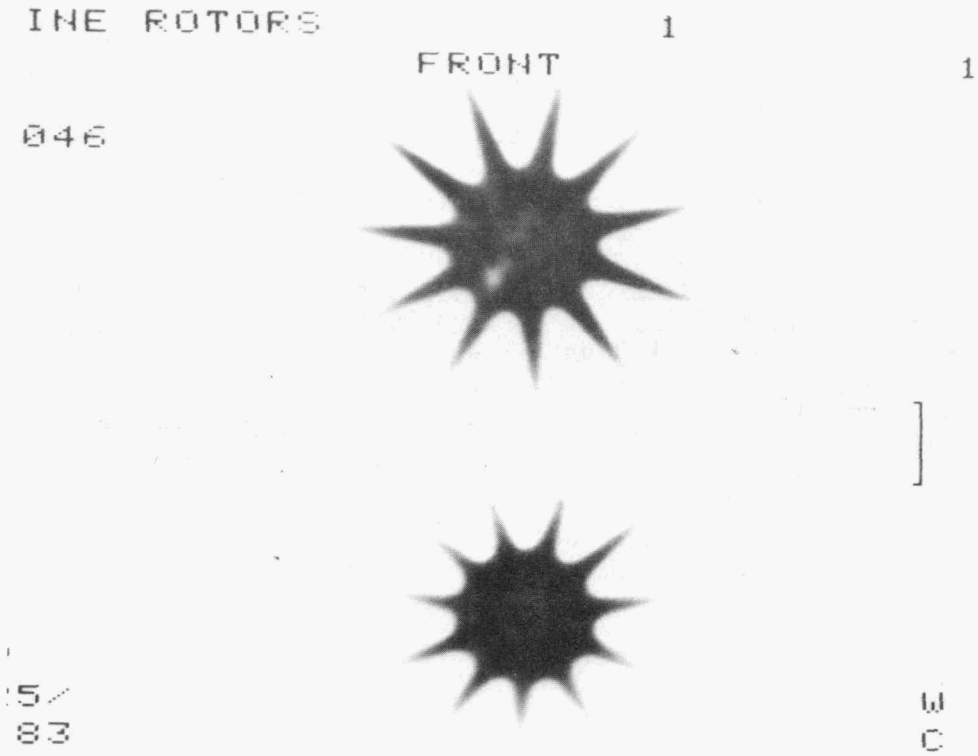

Fig. 9. Transaxial CT Image (4-mm Slice Thickness) of Si_3N_4 Turbo Rotors, Taken at the Position Shown in Fig. 8. Rotor A shows a light-colored (low-density) region near the center, which could be either a crack or unreacted metallic silicon. Rotor B (bottom) shows a low-density annulus.

References

1. E. Segal and W. A. Ellingson, "Beam-Hardening Correction Methods for Polychromatic X-Ray CT Scanners Used to Characterize Structural Ceramics," in Nondestructive Characterization of Materials, II, Proceedings of the 2nd Intl. Symposium (Montreal, Canada, July 21-23, 1986), J. F. Bussiere et al., eds., Plenum Press, New York, 1987, pp. 169-178.

2. E. Segal, W. A. Ellingson, Y. Segal, and I. Zmora, "A Linearization Beam-Hardening Correction Method for X-Ray Computed Tomographic Imaging of Structural Ceramics," in Review of Progress in Quantitative NDE (La Jolla, CA, August 3-8, 1986), D. O. Thompson and D. E. Chimenti, eds., Plenum Press, New York, 1987, Vol. 6A, pp. 411-419.

3. M. W. Vannier and W. A. Ellingson, "Quantitative Computed Tomography," to be published in Review of Progress in Quantitative NDE, Williamsburg, Va., June 21-26, 1987.

4. W. A. Kalendar, W. H. Perlman, J. R. Vetter, and E. Klotz, "Evaluation of a Prototype Dual-Energy Computed Tomographic Apparatus: I. Phantom Studies," Med. Phys. 13(6), 334-339 (May-June 1986).

5. L. A. Lehmann, R. E. Alvarez, A. Macovski, and W. R. Brody, "Generalized Image Combinations in Dual kVp Digital Radiography," Med. Phys. 8, 659-667 (1981).

6. R. E. Alvarez and A. Macovski, "Energy-Selective Reconstruction X-Ray Computerized Tomography," Phys. Med. Biol. 21, 733-744 (1976).

7. A. J. Coleman and M. Sinclair, "A Beam Hardening Correction Using Dual-Energy Computed Tomography," Phys. Med. Biol. 30(11), 1251-1256 (1985).

8. W. A. Ellingson, M. W. Vannier, and H. C. Yeh, "Computed Tomography," in Ceramic Technology for Advanced Heat Engines Project Semiannual Progress Report for Period October 1986-March 1987, Oak Ridge National Laboratory, Oak Ridge, Tenn., in press.

9. Ibid., for the Period April 1987 to September 1987.

10. K. Takahashi, K. Kohda, and J. Miyahara, "Mechanism of Photostimulated Luminescence in BaFx:Eu^{2+} (x=Cl,Br) Phosphors," J. Lumin. 31 and 32, 266-268 (1984).

11. W. A. Ellingson, P. Vandiver, and J. J. Lubick, "Radiographic Imaging Technology for Archaeological and Advanced Ceramics," to be published in Proceedings of the Spring 1988 MRS Conference, Reno, Nev., April 5-8, 1988.

Nuclear Magnetic Resonance Imaging

W. A. Ellingson, P. S. Wong, and H. C. Yeh (Argonne National Laboratory)

Objective/scope

The objectives of this program are to (1) establish the feasibility of using NMR imaging systems to map distributions of organic binder/plasticizer (B/P) in injection-molded green ceramics, with emphasis on Si_3N_4; (2) examine the potential of NMR spectroscopy to determine if there are chemical variations within and/or between batches of organic binder which impact process reliability; and (3) determine the sensitivity of NMR imaging methods to injection-molding process variables as manifested in B/P distribution.

Technical progress

Specimen and phantom preparation

During this reporting period, two blocks of organic B/P (blocks nos. 5-9734 and 5-7643) from different parts of a standard B/P lot (lot no. 205-208), were supplied by Garrett Ceramic Components Division (GCCD), Allied-Signal Aerospace Company, Torrance, CA. This standard lot of commercially supplied B/P will be used for the entire program. These samples were prepared to determine the homogeneity of the as-received B/P. In addition, samples from two injection-mix[a] batches (batch nos. 113-149B and 113-169C) were prepared by the standard Sigma mixer blending procedure at GCCD. Five injection-molded test bars (bar nos. 7959, 7963, 7966, 8125, and 8126) were also received. These samples will be used to conduct initial NMR imaging studies.

Two types of test phantoms (special imaging test specimens) ~25 mm (1 in.) in diameter and 25 mm in height are in preparation. Figure 1 is a schematic showing the designs of the phantoms. In both types of phantoms, the base cylinder is the standard as-molded GN-10 Si_3N_4 material containing 15.5 wt.% binder. A set consisting of two Type I phantoms (A and B) and one Type II phantom, plus unseeded base cylinders, will be supplied by GCCD. Each test phantom will be inspected by X-ray film radiography and examined visually prior to NMR experiments.

Eight batches of GN-10 Si_3N_4 powders were also milled during this reporting period. Six of these batches were blended with the standard B/P lot (lot no. 205-208) by means of the established Sigma mixer blending procedure. This sigma mixer blended material (15.5 wt.% binder) will be used to fabricate the base cylinders for the phantoms. The other two batches will be used to prepare the small (¼-in.-diam) inserts for the Type I phantoms, with the binder loadings shown in Fig. 1.

[a] Injection-mix is a term used to describe the complete mixture of ceramic powder, B/P, sintering aids, etc., recovered from the blender and after pelletizing.

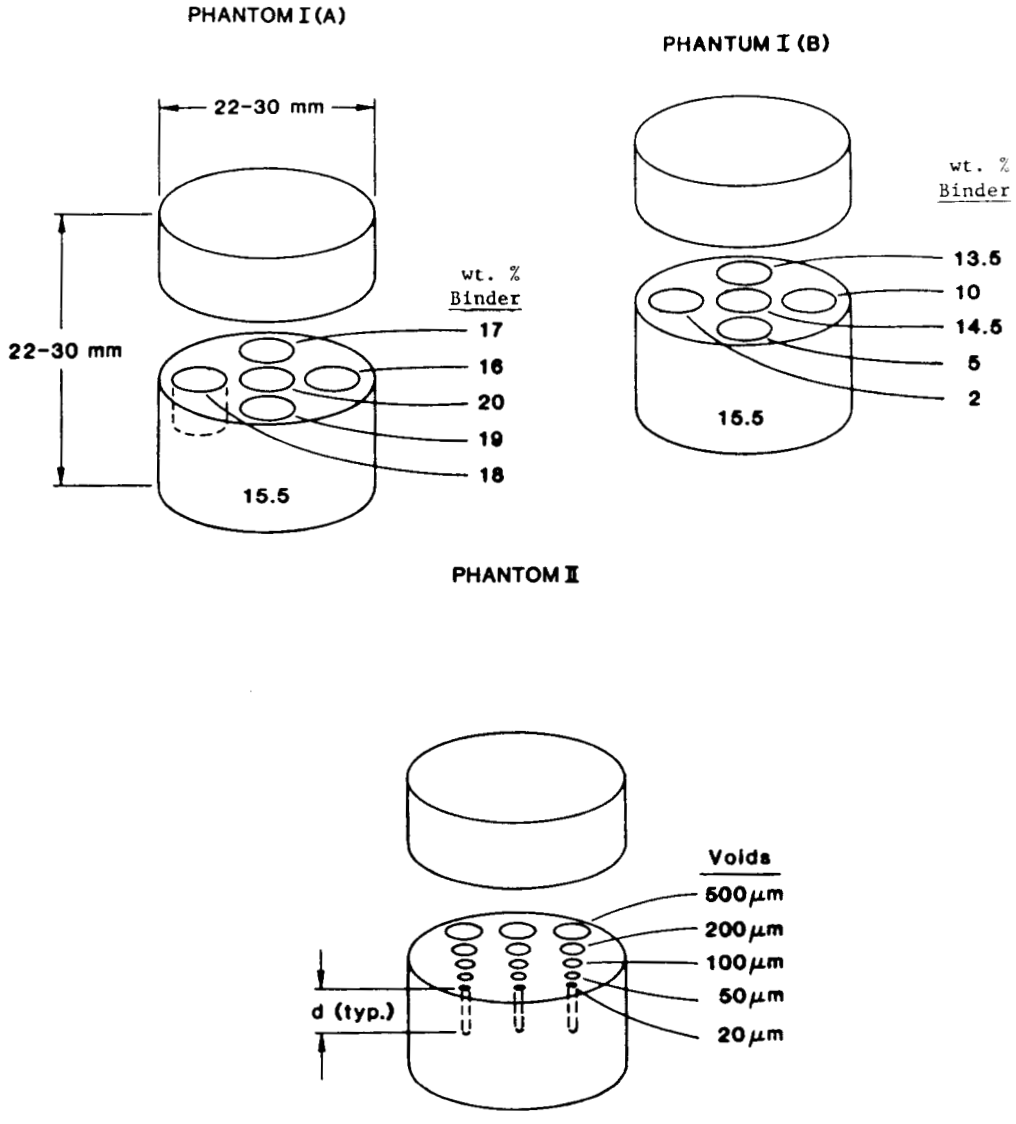

Fig. 1. Schematic Diagram of Special NMR Imaging Test Specimens (Injection-Molded Si_3N_4) Prepared by GCCD.

Injection-molding and compression-molding techniques are being investigated to fabricate good-quality, 1-in.-diam base cylinders. Several experimental cylinders were obtained and further experimentation is in progress. To blend the mixes for the small inserts with various binder contents (Fig. 1), a small 100-g-capacity Haake rheometer mixer is being used. Mixes with 10 to 17% binder were successfully blended with the Haake mixer. However, mixes with the two lowest binder contents, 2 and 5%, could not be uniformly blended with the Haake mixer and will require special procedures. Experiments involving liquid solvent blending will be investigated. Mixes containing different binder contents will then be compression-molded into ¼-in.-diam cylinders to be inserted into the base cylinders to form the Type I phantoms (Fig. 1).

^{1}H NMR spectroscopy studies

During this period, we conducted a series of variable-temperature and room-temperature NMR spectrometer tests to establish the T_2 (spin-spin) values of a typical "wax-like" organic B/P. We also wanted to understand the effect of elevated temperature on NMR signal strength from a typical wax-like B/P, both alone and mixed with Si_3N_4 powder.

The NMR spectral linewidth and T_2 tests were conducted in a 7.1-T Bruker model 300 AM variable-temperature NMR spectrometer. We first conducted an NMR spectral linewidth experiment (using a simple 90° pulse sequence) to detect any difference between B/P with and without Si_3N_4. The relation

$$\Delta_{1/2} \simeq 1/\pi T_2^* \qquad (1)$$

was used to correlate T_2^*, where $\Delta_{1/2}$ is the full width at half maximum (FWHM) of the amplitude vs frequency trace and T_2^* is the estimated (denoted by *) characteristic time constant for loss of phase coherence among spins oriented at an angle to the vector of the main magnetic field, B_o. The results are shown in Table 1. It should be noted that the T_2^* values for B/P alone and the Si_3N_4+B/P (15 wt.%) mixture are well below 1 msec even at elevated temperature (except for B/P alone at 60 and 100°C), i.e., nearly 2 orders of magnitude smaller than those necessary for a reasonable S/N ratio on most commercial medical imagers.

In general, the NMR spectral linewidth in a normal, solid state is likely to be quite broad owing to dipole-dipole interactions between the nuclei of interest.[1-4] Since the size of a coupling is proportional to the magnetogyric ratio, γ, of each spin of a coupling pair and inversely proportional to the cube of the separation between the pair,[5-7] increases in molecular motion (and hence separation) due to elevated temperature will narrow the NMR linewidth. This behavior was confirmed by the spectroscopy tests on the 7.1-T Bruker NMR spectrometer at 100°C. A relatively sharp NMR peak (FWHM of ~11 Hz) was obtained for the B/P, as shown in Fig. 2. The chemical shift (ξ) is calculated as follows:

$$\xi \text{ (in ppm)} = \frac{\text{observed shift (in Hz)} \times 10^6}{B_o \text{ (in Hz)}} , \qquad (2)$$

Table 1. Effect of Temperature on T_2* (Spin-Spin) for B/P Alone and Si_3N_4 + 15 wt.% B/P

Temperature (°C)	FWHM (Hz)	T_2* (ms)
	B/P Alone	
23	1000	0.32
42	1000	0.32
47	800	0.40
49	700	0.45
51	640	0.50
53	580	0.55
55	550	0.58
60	313	1.02
100	11	29.00
	Si_3N_4 + 15 wt.% Binder	
20	3700	0.09
30	3700	0.09
45	2840	0.11
60	1490	0.21
70	1420	0.22
100	1400	0.23

where B_o = 300 MHz in a 7.1-T field and ξ = 0 ppm for tetramethylsilane, which is used as a reference.

We also conducted a series of "real" T_2 measurements (i.e., not estimated, as in the spectral linewidth studies) on the B/P itself and on the Si_3N_4+B/P mixture. We used a Hahn spin-echo pulse sequence, which is represented by

$$D_1\text{-}t(90°)\text{-}\tau\text{-}t(180°)\text{-}\tau\text{-FID} \quad ,$$

where D_1 is the time required to relax to equilibrium (~$5T_1$ for complete relaxation; a value of 2 sec was used), τ is the variable delay time, and t(90°) and t(180°) are pulse durations. The results as a function of temperature are shown in Table 2, and the T_2 values for the B/P alone are plotted as a smooth curve in Fig. 3. The increase in T_2 with temperature indicates that the mobility of H protons in the wax-like B/P increases with temperature.

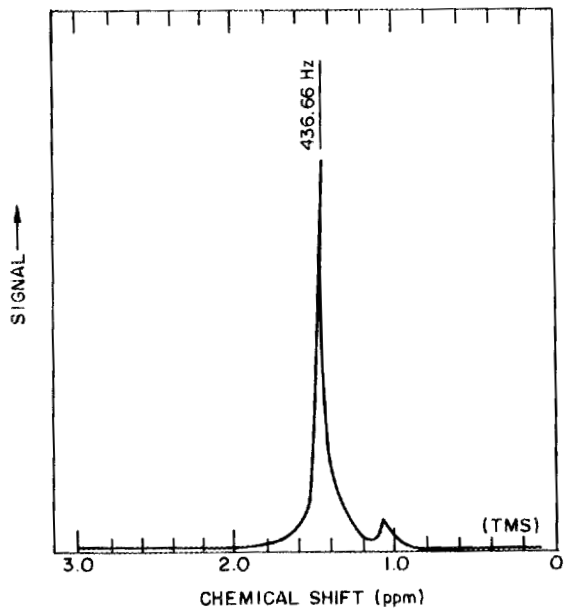

Fig. 2

NMR Spectral Linewidth of Organic B/P at 100°C, as Determined with a 7.1-T Bruker Spectrometer (No Magic Angle Spinning).

Table 2. Effect of Temperature on T_2[(a)] for B/P Alone and Si_3N_4+B/P Mixture

Temperature (°C)	T_2 (msec) B/P	T_2 (msec) Si_3N_4+B/P
22	0.26	0.24
40	0.52	0.35
60	12.35	0.69
80	43.00	N/A
100	69.00	N/A

[a]T_2 was measured with a 7.1-T Bruker spectrometer and a Hahn pulse sequence.

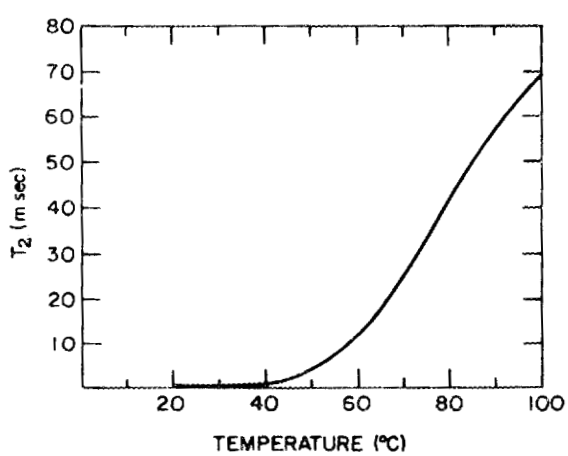

Fig. 3

T_2 as a Function of Temperature for Organic B/P, Measured with 7.1-T Bruker Spectrometer and Hahn Pulse Sequence

Comparison of T_2 Measurements made with different instruments

In order to understand the impact of static magnetic field and magnetic gradient on T_2 values, we also measured the T_2 of the B/P at room temperature (22°C) with a 2-T GE Chemical Shift Imager (GE CSI-II), shown schematically in Fig. 4. A Hahn spin-echo pulse sequence was again used. In Fig. 5, the results of this measurement are compared with the T_2 values obtained with the 7.1-T Bruker NMR spectrometer at the same temperature.

Because of the narrower linewidth (better resolution) and higher T_2 value (closer to the level required by the medical imager) obtained for the B/P in elevated-temperature experiments, we plan to implement direct NMR imaging of B/P and Si_3N_4+B/P mixture at elevated temperature.

Fig. 4

Schematic of GE Chemical Shift Imager.

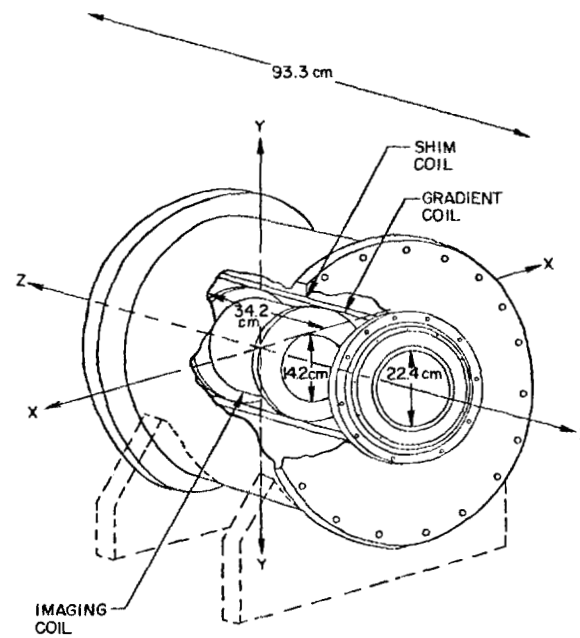

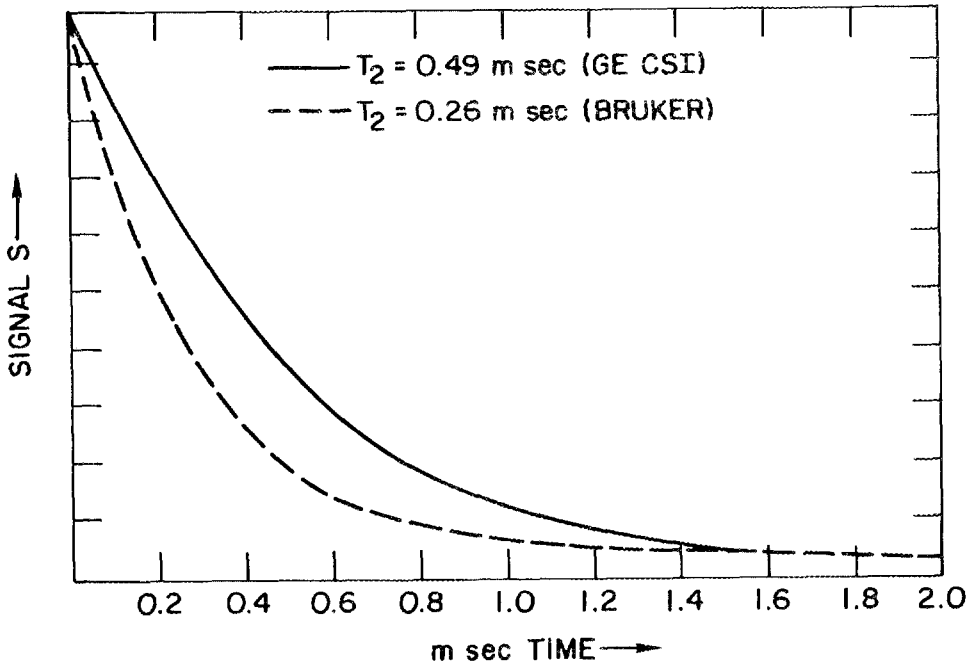

Fig. 5. Comparison of Room-Temperature T_2 Measurements of Organic B/P Obtained with the Bruker Spectrometer (7.1 T) and with the Spectrometer Mode of the GE Chemical Shift Imager (2 T).

NMR data transfer, process, and analysis

During this reporting period, we have explored some software solutions for NMR data transfer, processing, and analysis. All of the experimental data acquired will be processed and analyzed on the Argonne National Laboratory Materials Science Division (ANL/MSD) VAX 11/785 minicomputer with the FTNMR 4.5 software package. The major steps involved are shown schematically below. First, the raw data must be acquired on a disk drive and downloaded onto magnetic tape. A file transfer software program must be implemented to reformat the GE data into a VAX-compatible format. These reformatted data must then be used as the raw data in the FTNMR 4.5 analysis. The final data must be displayed and printed.

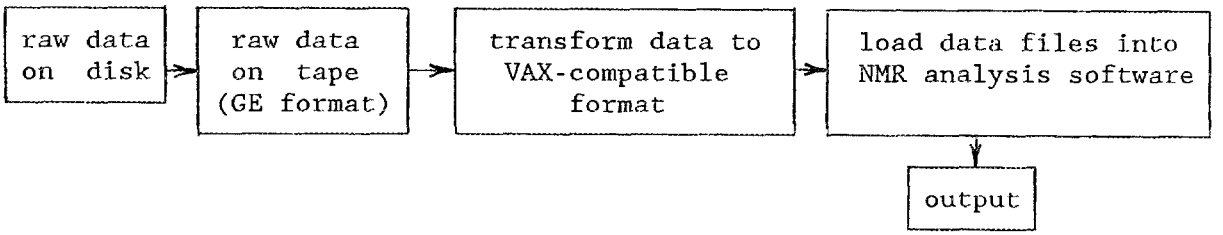

Step 1: Downloading the data from GE CSI disk onto magnetic tape. The original raw NMR data files (from NMR spectroscopic and NMR imaging experiments) on the 1204 Phoenix removable magnetic disk in the GE CSI-II were successfully transferred to BASF 2000 A.D. magnetic tape by use of the GETAPE software program.

Step 2: Acquisition of software for processing one and two-dimensional NMR data. A software program, FTNMR 4.5, was acquired from Hare Research, Inc., in Woodinville, Washington. FTNMR 4.5 is a program for efficient processing of complex vectors and contains a variety of standard vector processing capabilities, plus other specialized capabilities used in Fourier transform NMR spectroscopy. FTNMR supports processing of very large matrices, and will allow users to access any matrix row or column without a transpose. Matrices may be displayed in various formats, including stacked, contour, and intensity plots. FTNMR includes features which allow efficient assignment of peaks in two-dimensional matrices and automatic generation of crosspeak maps, volume integrals, and listings.

The FTNMR 4.5 program was successfully downloaded from the magnetic tape onto the ANL/MSD VAX 11/785 successfully.

Step 3: Acquisition of software program to convert data from GE CSI-II to a common format readable by FTNMR. The software program GETAPE, which is needed to convert the GE data format to the readable FTNMR format on the VAX 11/785, was transmitted from Hare Research, Inc., to Argonne. GETAPE, which is written entirely in FORTRAN-77, was then compiled and downloaded onto the VAX system. This step concluded the data transmission process. We are now able to analyze all of the experimental NMR data obtained from the GE CSI-II (which is located at the University of Illinois) on the ANL/MSD VAX 11/785 computer system.

Additional activities

Some difficulties may be encountered in imaging at elevated temperature with spin-echo techniques, so we are currently exploring the possibility of using back-projection as an alternative method for two-dimensional NMR image reconstruction. Although this method of data processing and analysis is not normally part of conventional two-dimensional spectroscopic analysis, it has been associated with NMR imaging from the very beginning for two reasons. First, if one is willing to rotate the test sample mechanically, only one gradient channel is required, and the complexity of the pulse programmer is reduced. Secondly, this technique is quite familiar in medical imaging, and has found application in X-ray computed tomography and in cross-sectional imaging in nuclear medicine. Conceptually, the theory amounts to writing the two-dimensional Fourier transform in polar coordinates.

Status of milestones

All milestones are on schedule.

References

1. S. Emid and J. H. N. Creyghton, "High Resolution NMR Imaging in Solids," Physica 128B, 81-83 (1985).

2. S. Emid, "Ultra High Resolution Multiple Quantum Spectroscopy in Solids," Physica 128B, 79-80 (1985).

3. M. Mehring, High Resolution NMR Spectroscopy in Solids, Springer-Verlag, Berlin, 1976.

4. E. R. Andrew, "The Narrowing of NMR Spectra of Solids by High-Speed Specimen Rotation and the Resolution of Chemical Shift and Spin Multiplet Structures for Solids," Prog. in Nucl. Magn. Reson. Spectros. 8, 1-39 (1971).

5. E. Fukushima and S. B. W. Roeder, "Experimental Pulse NMR: A Nut and Bolts Approach," pp. 2217-2295 in NMR of Solids, Addison-Wesley Publishing Company (London, Amsterdam, Sydney, Tokyo), 1981.

6. G. E. Maciel, "High Resolution Nuclear Magnetic Resonance of Solids," Science 226, 282-288 (1984).

7. C. P. Slichter, Principles of Magnetic Resonance, 2nd ed., Springer-Verlag, New York, 1978.

Powder Characterization

M. A. Janney and A. C. Young (Oak Ridge National Laboratory)

Objective/scope

The objectives of this research element are threefold: (1) to identify and characterize those aspects of the chemistry and physics of a ceramic powder (or whisker)/solvent interface that control processing; (2) to develop standard methods of analysis for item 1; and, (3) to develop procedures for writing specifications for ceramic powders, to include any methods of analysis developed in this project.

Technical progress

This project is a new start for FY 1988. It is a natural outgrowth of a study of needs and requirements for ceramic materials characterization that was conducted by ORNL staff.[1] Two quotes from that study are appropriate starting points to describe this project:

1. Inspection and qualification of raw materials is the most important step in manufacturing a high-quality ceramic part. The established goal is to identify the material parameters and characterization techniques for process control that can be used in the fabrication process to achieve and ensure a high percentage of fully acceptable parts.

2. The object of processing R&D is to understand the physics and chemistry of a ceramic particulate system. The benefits to be derived from such an understanding include (1) the ability to cure and anticipate processing problems, (2) the ability to determine how sensitive a process is to changes in procedures or raw materials, and (3) the potential to improve current processes and to develop new processes.

Some of the critical questions that we expect to answer during the course of this investigation are:

(1) Can a critical set of parameters be specified for a given powder that will truly qualify that powder for a particular process?
(2) Can standard electrophoresis test procedures be developed that will allow two or more independent laboratories to obtain the same set of values on the same powder for a given set of conditions?
(3) Can we determine the scientific basis to describe the chemical and physical nature of the ceramic powder/solvent interface?
(4) Can that scientific basis be translated into a set of QA tests that are meaningful to the practicing ceramic engineer?

Our approach is a combination of basic materials science and applied materials engineering. The project is comprised of three distinct elements:

(1) a round-robin characterization of electrophoretic mobility and mobility distribution, acid-base character, and perhaps other aspects of the powder to be conducted by ORNL and three university partners (industrial participation in the round robin, by both ceramics firms and instrument manufacturers, will be sought on a voluntary basis);
(2) special projects at each laboratory to include such investigations as determining the nature of the powder/solvent interface in both aqueous and nonaqueous solvents, adsorption onto powder surfaces, acid/base characteristics of powders in nonaqueous solvents, and controlled chemical doping of powder surfaces; and
(3) adaptation and verification of analytical procedures developed during the course of these investigations to determine their usefulness in the research laboratory or in industrial practice.

Silicon nitride has been selected as the powder for investigation.

The principal investigators for this project at ORNL have responsibility for both the administration of the subcontract work and for in-house investigations. These two responsibilities are reported separately below.

Subcontracts - A Request for Proposal for three university subcontracts has been written and submitted to program management. The work to be performed under the subcontracts includes (1) participation in a round-robin characterization of electrophoretic mobility by the microelectrophoresis method and (2) special projects at each university, specifically, characterization of the silicon nitride-aqueous solution interface, characterization of the silicon nitride-nonaqueous solution interface, and surface modification of silicon nitride by controlled doping with sintering aids in the 0.1 to 5.0 wt % range.

For the round robin on electrophoresis measurements to be a success, as many parameters as possible in the test (as well as in the preparation of the samples) must be defined and controlled. A working document that addresses the procedures to be followed in conducting the round robin has been drafted. Some of the concerns that are raised in the document are absolute electrophoretic mobility standards, kinds of container materials, mixing procedures, aging times and conditions, pH range and buffers, types and concentrations of centurions, and specific methods of slurry preparation. Review of the document by recognized experts in the field is in progress. Their comments will be included in drafting the first set of round-robin guidelines.

In-house - An assessment of various characterization techniques, entitled "Physicochemical Characterization of Ceramic Powders," by John F. Fellers, Mark A. Janney, and Albert C. Young, was drafted during the first two months of the project. The findings in that report strongly recommend the use of gas-solid chromatography (GSC) as a tool for characterizing ceramic powders. It further points toward the eventual use of GSC to predict the interactions of solid surfaces with solvents and solutes such as binders, dispersants, or other processing aids. A final version of the report should be ready in the third quarter of FY 1988.

We have set up a gas chromatograph, which is on loan to us from the Analytical Chemistry Division at ORNL. A personal computing system and the necessary data analysis software and interfaces have been specified and ordered; installation should occur in April or May.

We have initiated our experiments in characterizing ceramic powders using GSC. Actually, we are using a technique known as inverse gas chromatography (I-GSC). In conventional GSC, a column of known character is used to separate a series of unknown chemical compounds. In I-GSC, it is the column that is the unknown and the probe molecules are of known character. By characterizing the interactions of various probe molecules having well-characterized properties (such as Lewis acids, Lewis bases, polarizable molecules, or nonpolar molecules) with the surface of a powder, one can infer the chemistry of that surface.

Procedures for making columns using standard ceramic powders are being developed with help from staff in the Analytical Chemistry Division. It is our desire to test the powders in as close to the as-received condition as possible. However, typical as-received ceramic powders are too fluffy to be easily packed into a GC column. Therefore, we have chosen to granulate the powders by isopressing at 2000 to 8000 psi, then screening through 40 to 200 mesh sieves to produce a powder that can be handled. This procedure should introduce very little in the way of contaminants to the powder surface. We have been successful in packing columns with granules made from Reynolds RCHPDBM alumina and UBE E10 silicon nitride. The granulation process also keeps the permeability of the column from being so low as to prevent easy passage of the gases through the column.

Our initial studies will be on alumina or silica. These adsorbents are commonly used in GSC and a large data base exits regarding the interaction of probe molecules with their surfaces. The use of silica and alumina will help us to establish appropriate experimental procedures. After we demonstrate that our experimental techniques are valid, we will start to examine powders that are of interest to the Ceramic Technology Project, such as silicon nitride, zirconia, and silicon carbide.

Reference

1. D. R. Johnson et al., *Needs Assessment for NDE and Materials Characterization for Improved Reliability in Structural Ceramics for Heat Engines*, ORNL/TM-10345.

4.0 TECHNOLOGY TRANSFER

4.1 TECHNOLOGY TRANSFER

4.1.1 Technology Transfer

Technology Transfer
D. R. Johnson (Oak Ridge National Laboratory)

Technology transfer in the Ceramic Technology Project is accomplished by a number of mechanisms including the following:

Trade shows. A portable display describing the program has been built and used at several trade shows and technical meetings, most recently at the Annual Meeting of the American Ceramic Society, April 26-30, 1987, in Cincinnati, Ohio.

Newsletter. A Ceramic Technology Newsletter is published regularly and sent to a large distribution.

Reports. Semiannual technical reports, which include contributions by all participants in the program, are published and sent to a large distribution. Informal bimonthly management and technical reports are distributed to the participants in the program. Open-literature reports are required of all research and development participants.

Direct Assistance. Direct assistance is provided to subcontractors in the program via access to unique characterization and testing facilities at the Oak Ridge National Laboratory.

Workshops. Topical workshops are held on subjects of vital concern to our community.

International Cooperation. Our program is actively involved in and supportive of the cooperative work being done by researchers in West Germany, Sweden, and the United States under an agreement with the International Energy Agency. That work, ultimately aimed at development of international standards, includes physical, morphological, and microstructural characterization of ceramic powders and dense ceramic bodies, and mechanical characterization of dense ceramics. Detailed planning and procurement of ceramic powders and flexural test bars have been accomplished. Exchange of preliminary data on ceramic and powder characterization results has been started by those laboratories participating.

IEA ANNEX II Management
V. J. Tennery (Oak Ridge National Laboratory)

Objective/scope

The IEA Annex II agreement between the United States, the Federal Republic of Germany, and Sweden on structural ceramics is directed to cooperative research and development oriented to the identification and adoption of standardized methods for characterizing these materials. This agreement includes four subtasks: (1) information exchange, (2) ceramic powder characterization, (3) ceramic chemistry and structural characterization, and (4) ceramic mechanical property characterization. Each country is providing selected ceramic powders and sintered structural ceramics for use in the research work in Subtasks 2, 3, and 4 in all three participating countries. Participating laboratories in all three countries have agreed to share all resulting data with the purpose of using the knowledge gained from work for developing standard measurement methods for characterizing ceramic powders and sintered structural ceramics.

The lack of such standard measurement methods has been an impediment to the evolution and development of structural ceramics, from the point of view of both the manufacturer and the user. This Annex II agreement was conceived to accelerate the development of standard methods for determining important properties of these evolving materials.

In the United States, many companies and their research staffs have agreed to contribute significant resources in performing the required measurements. For example, in Subtask 2, 12 laboratories are participating; in Subtask 3, 7 laboratories are participating; and in Subtask 4, 8 laboratories are participating.

The research in Subtask 2 includes five ceramic powders which are being studied in the initial phase of this subtask. For Subtasks 3 and 4, three sintered ceramics are being studied, including one from each of the three countries. The ceramic from the United States is a silicon nitride, SNW-1000 from GTE-Wesgo; that from Germany is a hipped SiC from ESK Kempton; and that from Sweden is a silicon nitride from ASEA Cerama.

Technical progress

The major technical status changes since the last semi-annual report will be reviewed briefly:

Subtask 2, Ceramic Powder Characterization

The remaining three ceramic powders were distributed by the U.S. National Bureau of Standards (NBS) during this period to the laboratories participating in this Subtask in the United States, Sweden, and the Federal Republic of Germany. The U.S. working group met in Orlando on November 4 to review the U.S. results prior to meeting with the Swedish and German participants on November 5 and 6. Dr. Steve Hsu of the NBS is now responsible for the U.S. activities in this subtask. At

the Orlando meeting, there was considerable discussion regarding the status of measurements on the two powders which have now been distributed, and a date by which the NBS will complete the distribution of the remaining three powders to participants in all three countries. In addition, based upon the results reported in Orlando, there was intense discussion regarding the pros and cons of changing some of the measurement strategy for the remaining three powders, based upon what had been learned from the first two powders. The first two powders included the Toya Soda zirconia and the L. C. Stark silicon nitride. It was agreed that some or all participants in Subtask 2 would consider performing zeta potential (electrophoretic mobility) measurements on all five powders. Finalizing details of this procedure, identifying those participating institutions in the U.S. who have the instrumentation in place to do these measurements, and identifying those who are willing to do these measurements in a timely fashion was the responsibility of a subcommittee chaired by Dr. P. H. Tewari of Norton Company. Due to the necessary schedule for completion of all measurements in Subtask 2, details for these measurements had to be resolved very soon after the Orlando meeting if the United States was to have a unified position in this matter and our participating laboratories were to have time to complete the measurements.

The procedures to be used in the United States for the zeta potential measurements and obtaining agreements from the laboratories that would be making the measurements was to be finalized by March 15,1988, or this plan was to be abandoned. These agreements could not be finalized in the short time available, and therefore it was determined that the zeta potential measurements would not be made on the scale anticipated from the Orlando working group meeting.

The following is the agreed to time schedule for the remainder of the research to be conducted in Subtask 2:

February 29, 1988	NBS completes all powder distribution.
March 15, 1988	Finalize details for zeta potential measurements (U.S. laboratories) and decide if there is sufficient interest to actually do these measurements.
August 15, 1988	All powder analyses completed and results submitted to NBS.
October 10-11, 1988	Data reported and reviewed at Working Group meeting in FRG.
January 16, 1989	All data analysis completed.
March 15, 1989	NBS final report draft completed and distributed to all U.S. participants for review and comment.
May 31, 1989	First draft of international report completed and distributed for review and comment.
October 24, 1989	IEA final draft action by Executive Committee.

The NBS agreed to complete distribution of the remaining three powders to all participating laboratories by February 29, 1988. This schedule

with a standard deviation of 0.023. The number of determinations representing the Swedish values were not provided at the meeting. These values have a maximum spread of about 1%, even though the standard deviations for a given group of specimens may indicate a much smaller variation. Analyses for Si have been received from only two U.S. laboratories with an average of 68.10 wt % and a standard deviation of 1.697. Three U.S. carbon analyses were received, and the average was 29.45 wt % with a standard deviation of 0.1947.

For the ASEA silicon nitride, density values were obtained from both U.S. laboratories and from Sweden. The water immersion density from four U.S. laboratories had an average value of 3.199 g/cm^3 with a standard deviation of 0.0035. The toluene density from the same four laboratories was 3.2078 g/cm^3 with a standard deviation of 0.0075. Sweden provided a density value of 3.202 g/cm^3, with a standard deviation of 0.0032. The greatest spread for these values was therefore about 0.1%. Sweden provided analyses results for Fe, Al, Ca, and Y. We have to date received no data for these elements from U.S. participants with which to compare the Swedish results. For these four elements, the results with their standard deviations, based upon duplicate analyses for each element from a given specimen and analyses of three specimens (N generally = 6); 0.025 wt % Fe, S.D. = 0.0032; 0.057 wt % Al, S.D. = 0.0006; 0.00025 wt % Ca, S.D. = 0.0001; 1.967 wt % Y, S.D. = 0.1155. The U.S. results for these four elements include two results for Al and two for Fe. The average U.S. Fe value was 0.02 wt %, the Al value was 0.0550 wt %, and the Ca value was 0.005 wt %. The one U.S. result for a Si analysis gave a value of 56.62 wt %. No major element analyses were obtained from Sweden at the time. The average values for the U.S. results for Fe and Al compared well with the Swedish results, while the one U.S. analysis value for Ca was twice that of the Swedish average.

During the Dearborn meeting, Dr. Michael Hatcher of KemaNord in Sweden agreed to be responsible for drafting the final report on the research in this subtask. All chemical analysis data from U.S. participants was due to Dr. Arvid Pasto of GTE Laboratories by February 12, 1988. We are committed to providing Dr. Hatcher all of the U.S. data no later than February 29. He, in turn, is responsible for having the first draft of the final report for this research distributed and for it to be an item for discussion and first-level review at the time of the next IEA Executive Meeting to be held in Amsterdam during the first full week of June 1988.

On March 1, the compilation of U.S. data for this subtask was sent to Dr. Hatcher by Dr. Pasto. Results were obtained from a total of eight U.S. laboratories. Some reported extensive results, while some reported only sketchy results. In general, density was determined by two and in some cases three methods by all but one of the U.S. laboratories. Very little major element analyses were reported by any of the U.S. participants.

For example, for the ESK silicon carbide, only two participants reported a quantitative value for the Si content, and one of these values was 0.8% below the theoretical value, while the other was 3.2% under this value. The carbon results from these two laboratories varied from 1% to

3% below the theoretical value for SiC. These results show that, in general, the determination of the major elements in silicon carbide cannot be analyzed easily so as to obtain values for carbon and silicon which are reasonably close to the theoretical values. The major phase reported included the 6H or 12H polytypes of α silicon carbide, while the minor phases were reported as being the 4H, 8H, or 15R polytypes of SiC, as well as graphite.

For the ASEA silicon nitride, only one participant provided a quantitative silicon value, which was 56.62 wt %. This value is 3.45 wt % below the theoretical value, which may be reasonable when the sintering aid contribution to the composition is taken into account. No determinations for the nitrogen content were reported. The analyzed yttrium content varied from 2% to 3%, while the aluminum concentration varied from 0.05 to 0.08 wt %. The ß silicon nitride phase was reported as the major phase, with a number of secondary phases.

For the GTE silicon nitride, no quantitative determinations were reported for either of the major elements Si and N. The yttrium concentration varied from 10 to about 11 wt %, while the aluminum concentration varied from 1.1 to about 1.2 wt %. The major phase reported was ß silicon nitride, and a number of minor phases were reported.

Subtask 4, Mechanical Properties of Ceramics

Dr. Dietrich Munz of the KFK presented at the October meeting results from the German laboratories for flexure strength and fractography results for not only the ESK silicon carbide, but also presented preliminary data from the laboratories fracturing the ASEA and GTE silicon nitrides. We had exchanged for ESK flexure strength data with both FRG and Sweden sometime earlier. Three German laboratories had reported data to Dr. Munz for the ASEA nitride. These had a Weibull modulus of about 14 based upon N = 60, while the average value for the modulus based upon the U.S. data from five laboratories was 14.25 (ML method) based upon data sets having a nominal N value of 80. The calculated value of the modulus for all U.S. data is 1.75. The average value of the modulus from the three Swedish data sets with N = 60 was 14.22. Therefore, based only upon average values, the data sets presently available from all three countries for the ASEA silicon nitride provided averages which were very similar. Results for the GTE nitride from FRG for four data sets having N = 60 gave an average Weibull modulus of 11.6, while the average of the modulus from three Swedish data sets was 11.4, and the average of the modulus from seven U.S. data sets having N ≈ 80 had an average of 11.1. The similarity of these values indicates that the Weibull modulus α (m in the ceramic literature), can be measured for a given structural ceramic material so as to obtain reasonable agreement between data sets obtained in different laboratories and in various countries. The U.S. and FRG, at least, have tentatively agreed to use Kolmogorov-Smirnov statistics for evaluating the goodness-of-fit of the data sets to the Weibull distribution function described by the maximum likelihood estimators for the α and the β Weibull parameters.

The flexure strength results obtained from all participating laboratories for both the ASEA Cerama and GTE silicon nitride ceramics, including the maximum likelihood and the least squares values for the Weibull parameter α, are given in Tables 1 through 3.

Table 1. Weibull parameter α, strengths (MPa), and number of specimens for ASEA silicon nitride

Participating laboratories	α (ML)	α (LS)	Standard average	Standard deviation	N[a]
		United States			
GTE	17.0	16.5	634.6	46.2	80
Sohio	13.1	9.4	603.2	68.1	80
Allison	15.4	13.3	688.7	56.2	78
NASA	13.4	12.1	661.2	61.4	80
GTEC	12.3	10.1	673.8	71.4	80
All	11.75	10.89	651.38	68.32	398
		German			
Bosch	14.1	11.3	690.6	68.7	60
ESK	15.1	14.1	602.2	50.3	60
HCT	14.4	15.3	650.6	51.5	60
IWM	18.2	19.5	700.2	43.8	55
Sigri	13.8	13.8	660.9	57.5	70
All	12.14	12.43	660.23	64.84	305
		Swedish			
SSRI	13.1	12.7	627.2	57.7	60
ASEA	16.1	14.5	658.5	53.0	60
Sandvik	13.4	9.6	602.5	64.4	60
All	12.77	11.31	629.39	62.88	180

[a]N = number of specimens in a "set" used in the Weibull calculation.

Table 2. Weibull parameter α, strengths (MPa), and number of specimens for GTE/Wesgo silicon nitride

Laboratories	α (ML)	α (LS)	Standard average	Standard deviation	N[a]
		United States Participating			
GTE	11.7	11.8	651.1	66.6	80
Sohio	10.8	9.3	651.5	79.5	80
Allison	12.5	11.8	667.1	66.9	77
NASA	11.4	10.6	674.2	75.0	80
GTEC	10.3	10.4	582.2	67.2	80
All	10.04	9.89	644.35	78.44	397
		United States Cooperating			
Alcoa	10.6	9.8	651.9	76.6	80
Corning	10.8	10.5	663.6	75.0	80
Norton	10.3	10.6	679.3	77.7	80
All	10.36	10.34	664.30	77.15	240

[a]N = number of specimens in a "set" used in the Weibull calculation.

Table 3. Weibull parameter α, strengths (MPa), and number of specimens for ASEA silicon nitride

Participating laboratories	α (ML)	α (LS)	Standard average	Standard deviation	N[a]
		German			
CFI	12.7	12.9	644.5	60.3	60
DBenz	9.7	10.0	679.0	81.1	60
ESK	12.1	13.2	672.3	61.3	60
Feldml	13.5	14.4	682.1	57.7	60
HCT	11.9	9.2	653.7	73.0	60
All	11.14	11.56	666.31	68.88	300
		Swedish			
SSRI	11.3	12.5	653.4	63.3	60
ASEA	11.7	11.8	667.9	68.1	60
Sandvik	11.3	12.3	618.3	61.0	60
All	10.74	11.79	646.54	67.47	180

[a]N = number of specimens in a "set" used in the Weibull calculation.

was essentially met. All analyses for all five powders are to be completed by all laboratories and the data submitted to the NBS by August 15, 1988. Laboratories not reporting data by August 15 will be excluded from having their data included in the final report, and will not receive copies of the data sets.

Task leaders were identified at the Orlando meeting to help organize and perform the analysis of data differences on the same powder and to identify and further discussion of problem areas in the powder measurements. These task leaders and their responsibilities are:

(1) Chemical characteristics - Dr. A. Dragoo, United States
(2) Particle size distribution, density, and agglomeration - Dr. H. Hausner, Federal Republic of Germany
(3) Surface area, permeametry, aspect ratio, isoelectric point, SEM, and morphology - Dr. R. Pompe, Sweden

These task leaders are to organize activities necessary to meet their responsibilities and be prepared to provide reasonably formal reports at a subtask working group meeting scheduled for October 1988 at Berchtesgaden, Federal Republic of Germany, just prior to the second international meeting on powder science. These task leader reports are to form the basis of the first approximation of the final report for this subtask.

Subtask 3, Chemical Characterization of Sintered Ceramics

At the meeting in Dearborn, Arvid Pasto reported on our chemical analysis characterization results. All but one of the U.S. laboratories have reported measurement results for at least the ESK silicon carbide and ASEA silicon nitride. Several had already completed and reported measurements on the GTE silicon nitride. Pasto provided a preliminary data compilation for the U.S. results, including density, major and minor element analyses, and other data for all three ceramics. Sweden provided density data for all three ceramics and some analytical chemistry results for the ASEA Cerama silicon nitride. Germany did not provide any quantitative results for this subtask. It was agreed that a laboratory which has provided no data by December 31 will be deleted from this subtask.

At the time of the Dearborn meeting, results for the density values were more extensive from the U.S. laboratories than any other property. Many laboratories reported values for the geometric, water immersion, and toluene immersion densities. In addition, Sweden provided summary values for the density of all three ceramics. A brief summary of the preliminary results is given to indicate the general level of agreement for some of the results reported at the meeting.

First, for the ESK silicon carbide, five U.S. laboratories reported water immersion density values, with an average of 3.2014 g/cm^3, and an unbiased standard deviation of 0.0077. These five laboratories, plus a sixth, reported an average toluene immersion density of 3.186 g/cm^3 with a standard deviation of 0.0087. Sweden reported a density of 3.178 g/cm^3

Standard Reference Materials

A. L. Dragoo, D. B. Minor, C. R. Robbins, J. F. Kelly, J. P. Cline, and L.-S. Hsu (National Bureau of Standards)

Objective/Scope

Ceramics have been successfully employed in engines on a demonstration basis. The successful manufacture and use of ceramics in advanced engines depends on the development of reliable materials that will withstand high, rapidly varying thermal stress loads. Improvement in the characterization of ceramic starting powders is a critical factor in achieving reliable ceramic materials for engine applications. The production and utilization of such powders require characterization methods and property standards for quality assurance.

The objectives of the NBS program are (1) to assist with the division and distribution of five ceramic starting powders for an international round-robin on powder characterization; (2) to provide reliable data on physical (dimensional), chemical and phase characteristics of two silicon nitride powders: a reference and a test powder; and (3) to conduct statistical assessment and modeling of round-robin data. This program is directed toward a critical assessment of powder characterization methodology and toward establishment of a basis for the evaluation of fine powder precursors for ceramic processing. This work will examine and compare by a variety of statistical means the various measurement methodologies employed in the round-robin and the correlations among the various parameters and characteristics evaluated. The results of the round-robin are expected to provide the basis for identifying measurements for which Standard Reference Materials are needed and to provide property and statistical data which will serve the development of internationally accepted standards.

Technical Progress

The technical progress covered in this report includes descriptions of work on the preparation of powder samples for the IEA/ANNEX II, Subtask 2, powder characterization round-robin and of the compilation and analysis of round-robin data.

Division, Distribution and Certification of Ceramic Starting Powders. During the current reporting period silicon and silicon carbide powders were riffled, bottled, sealed under dry argon in foil laminate pouches and distributed to the participants in IEA/ANNEX II, Subtask 2, round-robin. Due to serious mechanical deterioration of the flame-sealer, it was necessary to dispense with the flame sealing procedure which had been used to flame-seal previous samples. Approximately 800 samples of each of the two powders were prepared. Each pouch contained 8 samples which were fixed to polystyrene trays with masking tape. The pouches were heat sealed to maintain the inert, dry environment. Due to the large number of samples prepared, all samples had to be packaged for storage outside dry box prior to selecting those for distribution. Samples for distribution were obtained by randomly selecting a number of bags which were opened in a

dry argon ambient. Samples were randomly withdrawn from this subset of bags and repackaged in a similar manner for distribution.

Powder Characterization. Measurement of particle size, surface area, density and chemical composition are in progress for all of the silicon-based powders. Work is in progress to established an improved method for determination of alpha, beta and non-crystalline phase content of silicon nitride powders by x-ray diffraction. The use of Fourier transform infrared (FT-IR) is being studied as a means for analysis of functional groups adsorbed on the surfaces of silicon nitride powders. Installation of a new scanning electron microscope (SEM)/image analysis system is now making possible the production and analysis of high-quality microscopic data for particle size analysis. Figure 1A is a micrograph of SNR, reference silicon nitride, particles dispersed on a 0.2μm Nucleopore[a] polycarbonate filter. Figure 1B is a micrograph of a relatively large agglomerated particle of a type which was observed to constitute a small fraction of the SNR powder. Samples were prepared for SEM observation by ultrasonically dispersing about 100 μg of powder in 25 mL of water containing about 0.1 mL of a 10 percent aqueous solution of Darvan C.

Data Analysis.

1. Data reporting and entry

The status of data reporting for U.S. participants is shown in Table 1A, for all physical characteristics of powders, and in Table 1B, for all chemical characteristics. Also, the number laboratories for which data has been entered into a LOTUS spreadsheet for statistical analysis is shown in each table. Data for yttria-doped zirconia powder (Z3YO) and the reference silicon nitride powder (SNR) was received from the West German and Swedish participants at the IEA meeting Orlando in November, but this data has not been entered into the LOTUS spreadsheet as yet.

All U.S. data for zirconia samples have been entered in the following categories: median particle size (D_{50}) or experimentally computed average particle size values; other physical properties, including surface area, tap density, bulk density and Fisher sub-sieve size; and chemical properties, including bulk chemistry, major, minor and trace impurities, and phase composition. Data from U.S. participants for SNR samples have been entered for median or computed average particle size values and for chemical composition.

---

[a] Certain commercial equipment, instruments, or materials are identified in this report in order to adequately specify the experimental procedure. Such identification does not imply recommendation or endorsement by the National Bureau of Standards, nor does it imply that the materials or equipment identified are necessarily the best available for the purpose.

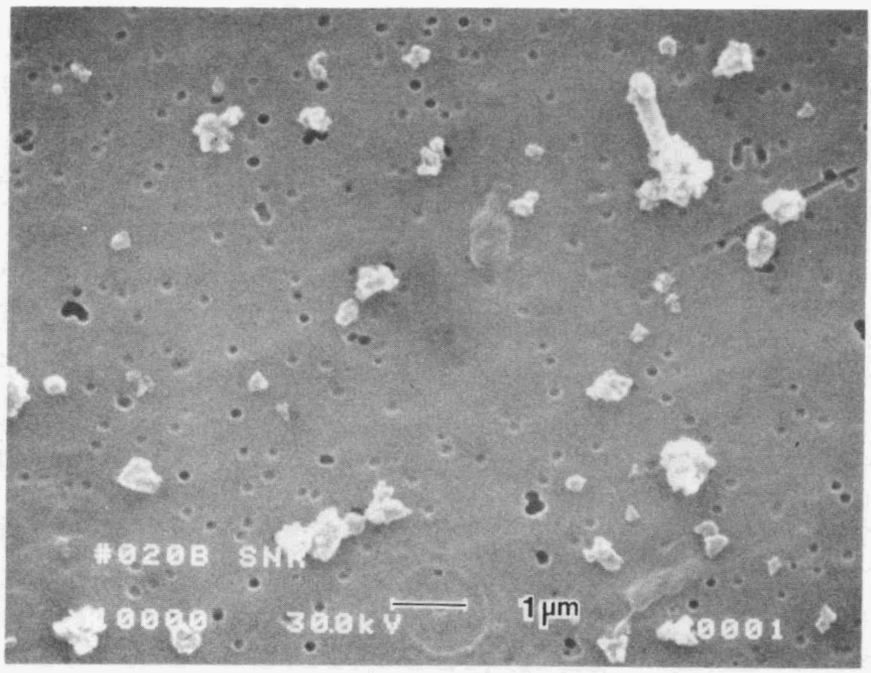

Figure 1A. SEM micrograph of reference silicon nitride (SNR) powder dispersed on Nucleopore polycarbonate filter. Bar marker indicates scale.

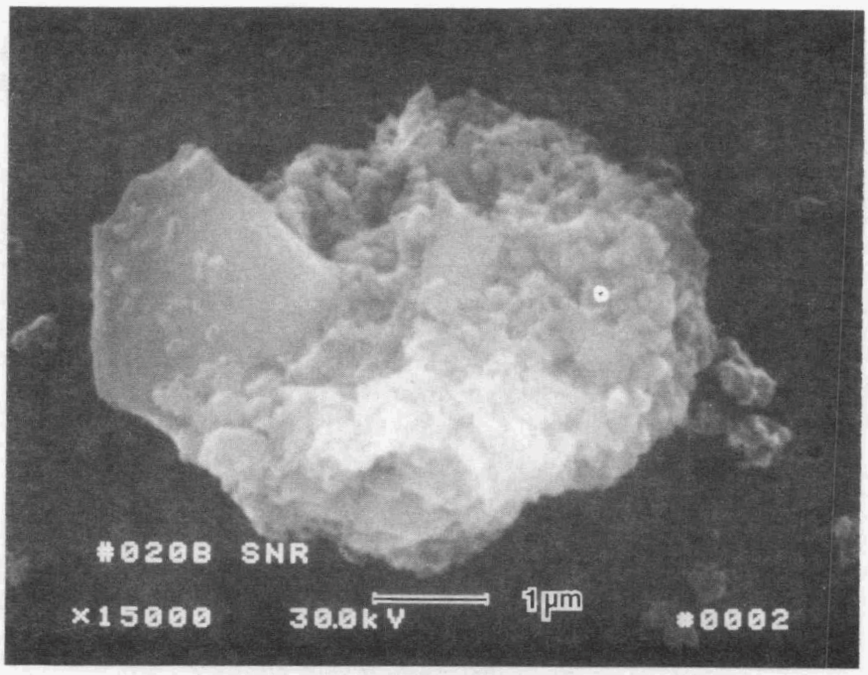

Figure 1B. SEM micrograph of an agglomerated SNR particle showing a coarse particle (2 to 3 μm across) which is embedded in a matrix of particles which are submicron in size.

2. U.S. Working Group

Meetings of the U.S. Working Group for the IEA/Annex II Powder Characterization were held at Orlando, in November; Cocoa Beach, in January; and Pittsburgh, in April. These meetings were held to discuss issues regarding the measurement and interpretation of U.S. data.

3. Revised Lotus 123 templates

Diskettes with revised Lotus 123 templates for particle size, other physical properties and chemical properties were completed and distributed to all participants along with formatted diskettes for reporting data. The templates are written to be used with LOTUS 1-2-3, Release 2, and to be run on IBM-PC compatible computers. Copies to run on other systems can be generated upon special request. The templates systematically organize the data, provided for the computation of some selected parameters and provide a number of macros to aid data entry. A brief description of procedures for the use the templates is presented in the Appendix which follows at the end of this report. As reported in our previous report, the ability to download the LOTUS files to the NBS central computer facility was established.

Table 1A. Status of round-robin results: physical characteristics, including particle size; April 1988

NUMBER OF U.S. LABORATORIES REPORTING

POWDER:	Z3YO	SNR	SN	Si	SiC
NO. OF PARTICIPANTS	11	12	12	11	12
NO. REPORTING	10	9	3	1	1
NO. RECORDED	10	6			

Table 1B. Status of round-robin results: chemical characteristics; April 1988

NUMBER OF U.S. LABORATORIES REPORTING

POWDER:	Z3YO	SNR	SN	Si	SiC
NO. OF PARTICIPANTS	10	12	12	11	12
NO. REPORTING	7	5	3	1	1
NO. RECORDED	7	1	1		

Status of Milestones

Task 1. On schedule. Packaging and distribution of silicon and silicon carbide powders were completed in December and February, respectively.

Publications

T. M. Resetar, G. E. Schaefer, J. W. McCauley, A. L. Dragoo, S. M. Hsu, D. R. Johnson, H. Hausner and R. Pompe. "IEA/ANNEX II Powder Characterization Cooperative Program," First Internatl. Conf. Ceram. Powder Processing; Orlando, Florida, Nov. 1-4, 1987. Am. Ceram. Soc., Basic Sci. Div. Am. Ceram. Soc. and Deut. Keram. G.

Ceramic Characterization

M. D. Vaudin, E. R. Fuller, Jr., J. P. Cline and A. L. Dragoo
(National Bureau of Standards)

Objective/Scope

Ceramics have been successfully employed in engines on a demonstration basis. The successful manufacture and use of ceramics in advanced engines depends on the development of reliable materials that will withstand high, rapidly varying thermal stress loads. Physical and chemical properties, phase characteristics, and microstructural properties of ceramic materials determine to a large extent their mechanical and structural properties, and hence, their high-temperature structural performance and reliability. The reproducibility and precision with which these properties and microstructural characteristics can be measured has not been assessed in a systematic manner for advanced ceramic materials. An initial step in such an assessment is the establishment of a data base for these ceramic properties and microstructural characteristics for a set of standardized specimens.

The objective of this task is to measure and characterize the ceramic properties (crystalline phase composition, grain-boundry properties and possible residual stresses) of a series of standard ceramic specimens to assist in the development of internationally accepted standards for ceramic characterization. This work contributes to an international interlaboratory comparison, IEA/ANNEX II, Subtask 3 on Ceramic Characterization, under the auspices of the International Energy Agency.

Technical Progress

The technical progress covered in this report includes descriptions of work on the analysis of silicon nitride ceramic samples as a part of IEA/ANNEX II, Subtask 3, Ceramic characterization. The following report describes electron microscopy observations of the spatial characteristics of the grain boundaries of two materials: ASEA Cerama silicon nitride and GTE SNW-1000 silicon nitride[a] . Supporting X-ray diffraction data for the bulk phase composition is included.

---

[a] Certain commercial equipment, instruments, or materials are identified in this report in order to adequately specify the experimental procedure. Such identification does not imply recommendation or endorsement by the National Bureau of Standards, nor does it imply that the materials or equipment identified are necessarily the best available for the purpose.

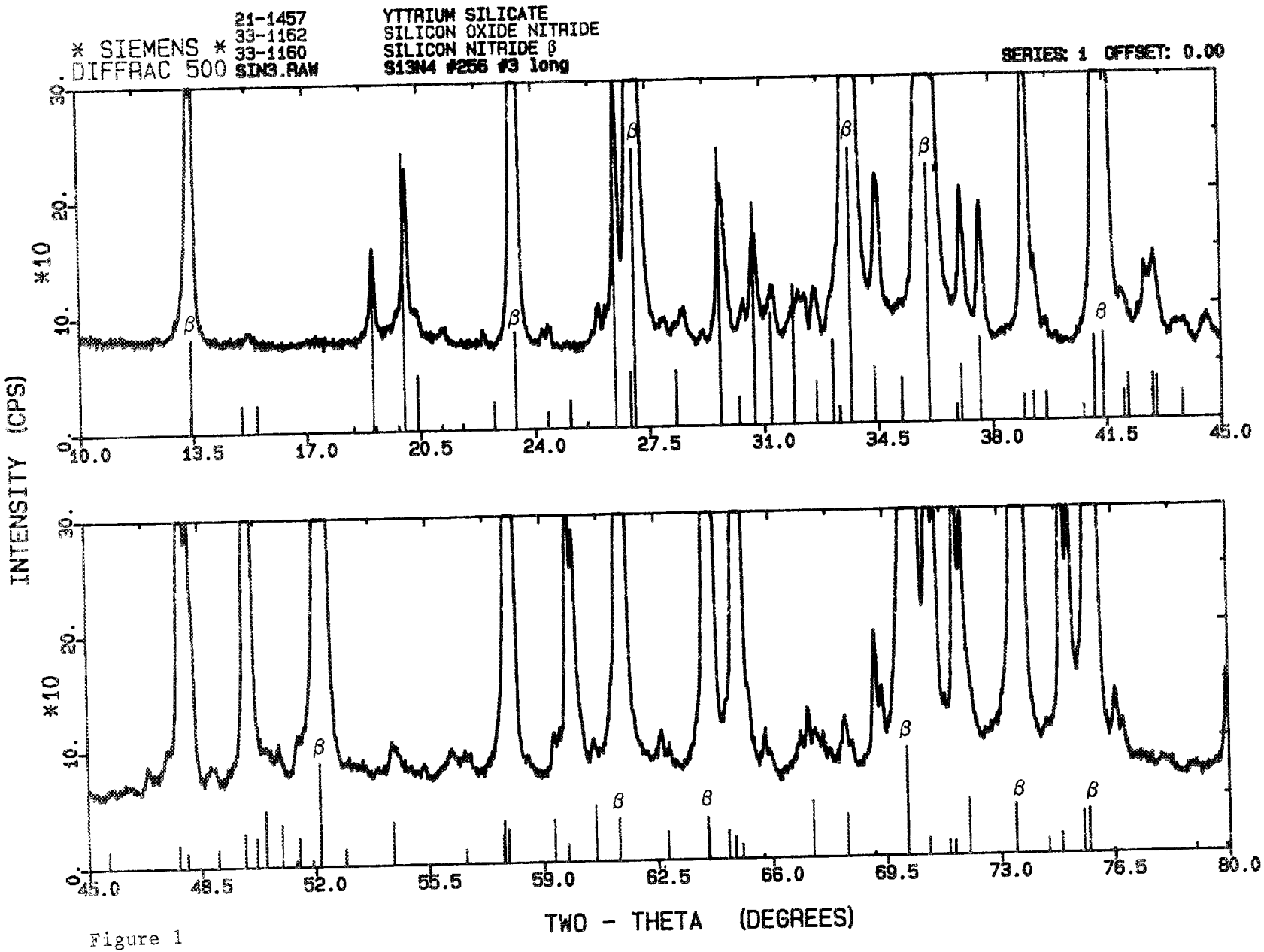
21-1457
33-1162
33-1160
SIN3.RAW
YTTRIUM SILICATE
SILICON OXIDE NITRIDE
SILICON NITRIDE β
S13N4 #256 #3 long
* SIEMENS *
DIFFRAC 500
SERIES: 1 OFFSET: 0.00
INTENSITY (CPS)
*10
TWO - THETA (DEGREES)
β

Figure 1

Electron Microscopy Observation: ASEA Cerama Silicon Nitride.

The X-ray diffraction results in Figure 1 show that this material consists of a primary phase of β-Si_3N_4 and small amounts of two other phases - Si_2N_2O and α-$Y_2Si_2O_7$.

Figure 2 shows a typical microstructure, consisting of equiaxed grains of β-Si_3N_4 with regions of another crystalline phase between many of the grains, particularly at triple junctions. From energy dispersive X-ray analysis it was found that this phase contained approximately equal proportions of yttrium and silicon, and from electron energy loss analysis it was found to contain oxygen, but no nitrogen. It could not be confirmed as α-$Y_2Si_2O_7$ by electron diffraction as the structure of the phase is not known, only some of the d-spacings. Regions of this phase up to 0.5μm thick were found.

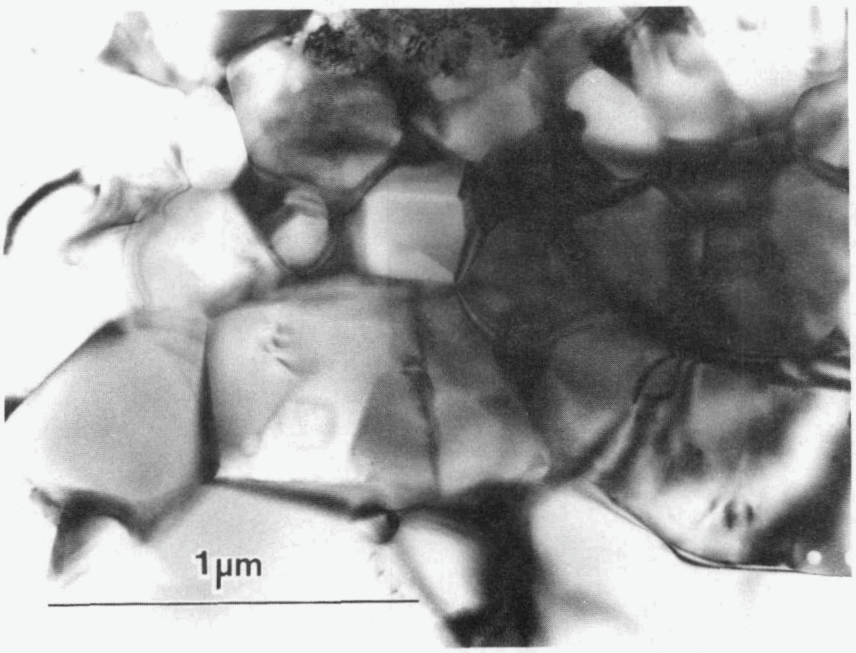

Figure 2. Micrograph showing typical microstructure of ASEA Cerama silicon nitride material.

Figure 3 shows two regions of α-$Y_2Si_2O_7$ about 0.1μm thick. The silicate is seen to be separating grains A and B.

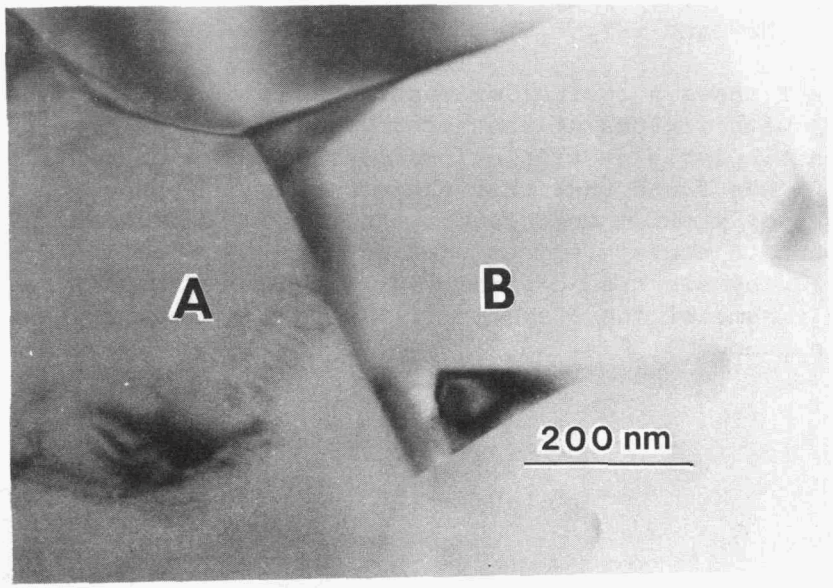

Figure 3. Micrograph of grain boundary between two grains, labeled "A" and "B." Grain-boundary composition was determined to be α-$Y_2Si_2O_7$.

Figure 4 is a high resolution micrograph of one of the yttrium silicate triple junction precipitates in Figure 3, showing that the lower interphase boundary between the nitride and the silicate is parallel to the {1010} plane of the nitride. This was frequently observed in this material and is consistent with the silicate being molten at processing temperatures.

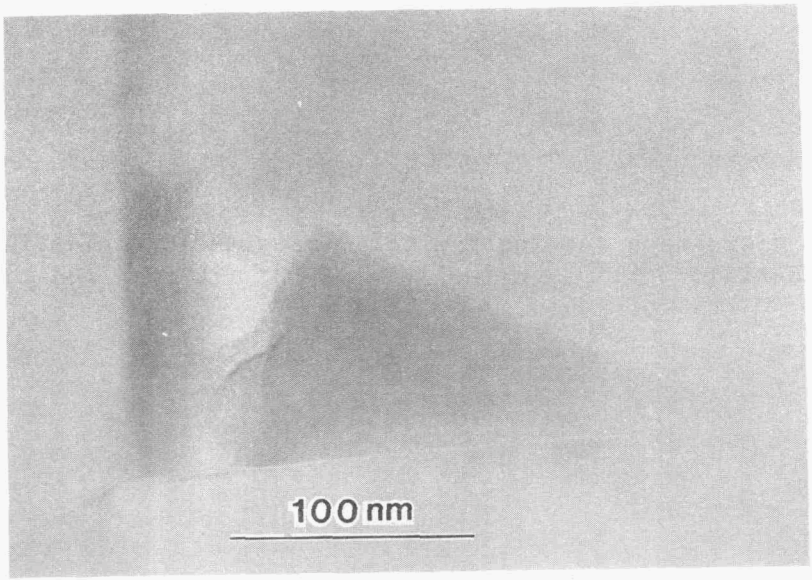

Figure 4. High resolution micrograph of an yttrium silicate triple junction precipitate.

Figure 5 shows two grains of silicon nitride separated by a 1nm thick second phase at the grain boundary. It was not possible to determine the composition and structure of this phase, but it is reasonable to conjecture that it is a silicate glass. The 1010 silicon nitride lattice fringes are visible in one grain. To obtain lattice fringes in both grains and have the grain boundary parallel to the electron beam is an extremely unlikely event.

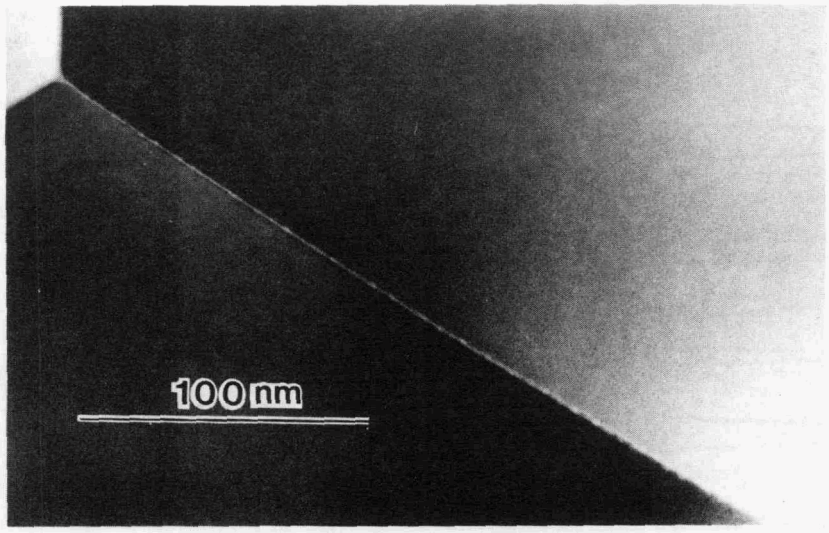

Figure 5. Micrograph showing two grains of silicon nitride separated by a 1 nm thick second phase in the grain boundary.

In general, the grains of silicon nitride were completely dislocation free. Figure 6 is a weak-beam micrograph of a grain in which a small-angle grain boundary is in the process of forming to lower the elastic energy of the dislocations caused by sintering stresses.

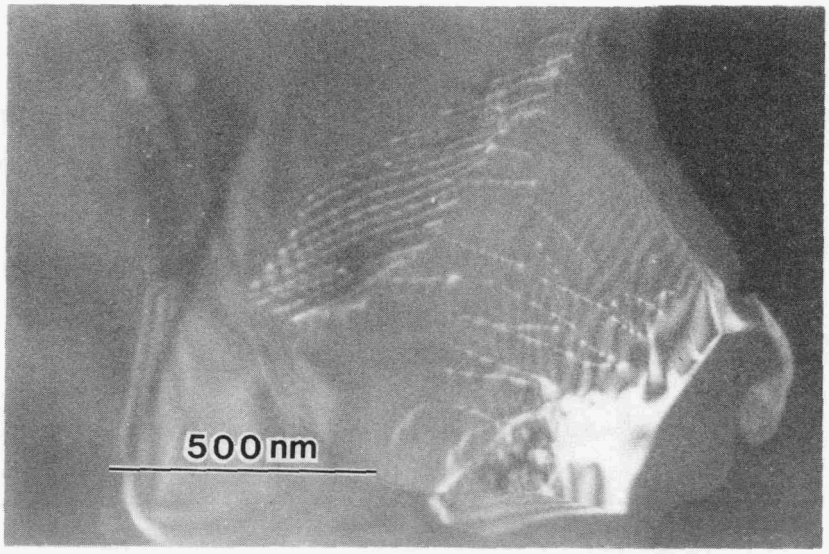

Figure 6. Weak-beam micrograph of a grain in which a small-angle grain boundary is forming.

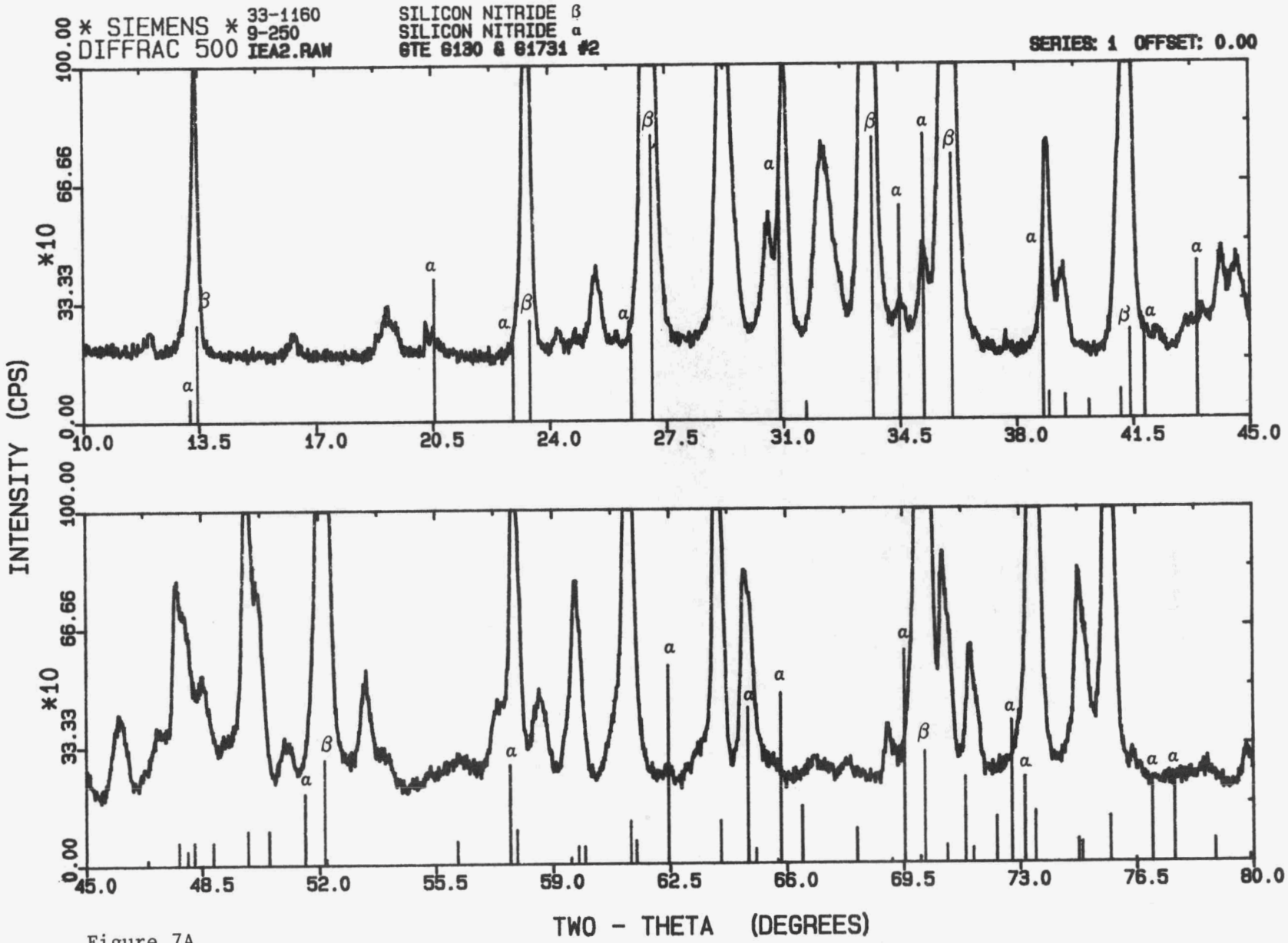
* SIEMENS *
DIFFRAC 500
33-1160
9-250
IEA2.RAW
SILICON NITRIDE β
SILICON NITRIDE α
GTE 6130 & 61731 #2
SERIES: 1 OFFSET: 0.00
INTENSITY (CPS)
*10
100.00
66.66
33.33
0.00
10.0
13.5
17.0
20.5
24.0
27.5
31.0
34.5
38.0
41.5
45.0
48.5
52.0
55.5
59.0
62.5
66.0
69.5
73.0
76.5
80.0
TWO - THETA (DEGREES)

Figure 7A

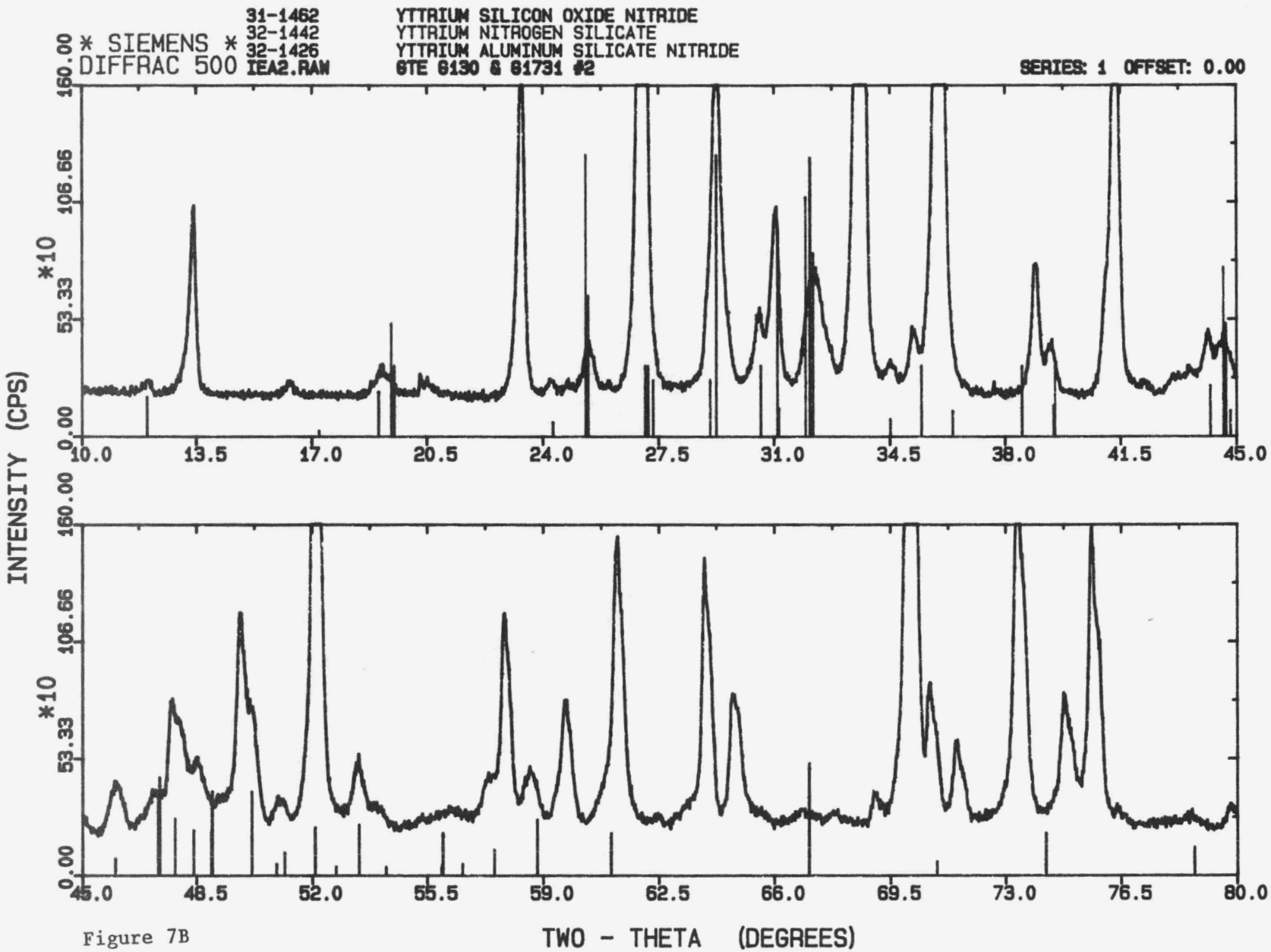
31-1462 YTTRIUM SILICON OXIDE NITRIDE
32-1442 YTTRIUM NITROGEN SILICATE
32-1426 YTTRIUM ALUMINUM SILICATE NITRIDE
* SIEMENS *
DIFFRAC 500
IEA2.RAW
GTE 6130 & 61731 #2
SERIES: 1 OFFSET: 0.00
INTENSITY (CPS)
*10
160.00
106.66
53.33
0.00
10.0
13.5
17.0
20.5
24.0
27.5
31.0
34.5
38.0
41.5
45.0
48.5
52.0
55.5
59.0
62.5
66.0
69.5
73.0
76.5
80.0
TWO - THETA (DEGREES)

Figure 7B

Electron Microscopy Observation: GTE SNW-1000 Silicon Nitride.

As can be seen from the X-ray diffraction results in Figures 7A and 7B, the SNW-1000 silicon nitride is a multiphase material. The primary phase consists of needle-shaped grains of β-Si_3N_4 which are elongated parallel to the c-axis and are often arranged in small bundles. The major secondary phase is crystalline, and contains yttrium, silicon, aluminum, oxygen and a small amount of nitrogen. This elemental analysis agrees with the X-ray identification of $Y_{10}Al_2Si_3O_{18}N_4$, although the d-spacings determined by electron diffraction do not match the JCPDS data. It seems clear that a complex silicate is the major second phase, but that it does not correspond exactly with any of the phase data published to date. Between the bundles of grains there is an amorphous phase containing silicon and yttrium in approximately equal amounts; the fraction of this phase is difficult to estimate.

Figure 8 shows a typical microstructure in which the majority of the Si_3N_4 needles are in cross-section, and the intergranular yttrium-containing phases have darker contrast because of the high atomic number of yttrium (39) compared to silicon (14) and nitrogen (7).

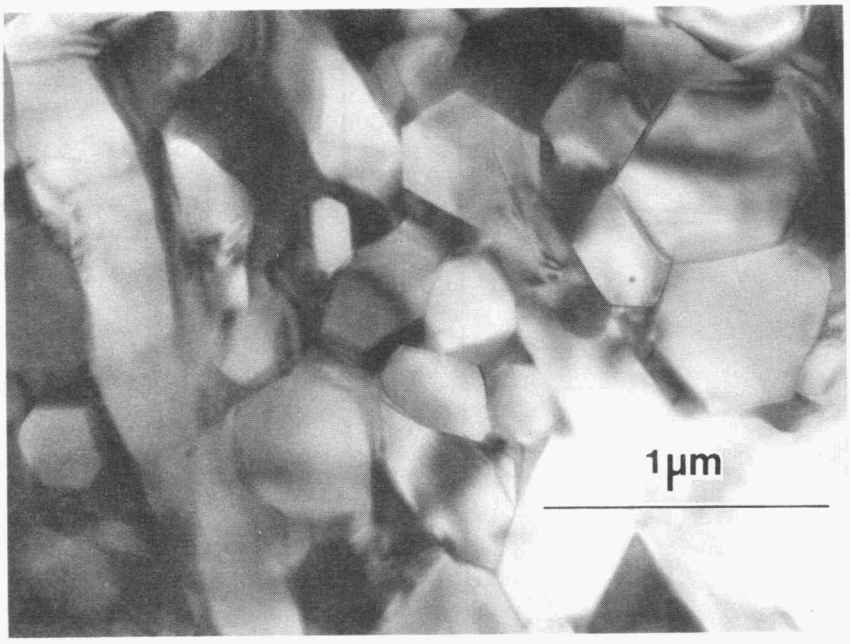

Figure 8. Micrograph of a typical microstructure for SNW-1000 silicon nitride.

In Figure 9 the specimen was oriented so that one region of $Y_{10}Al_2Si_3O_{18}N_4$ was on zone and diffracting strongly. It was found that several neighboring regions of $Y_{10}Al_2Si_3O_{18}N_4$ were at the same orientation and therefore had very dark contrast in the micrograph. Thus one grain of the $Y_{10}Al_2Si_3O_{18}N_4$ phase is encasing several β-Si_3N_4 grains.

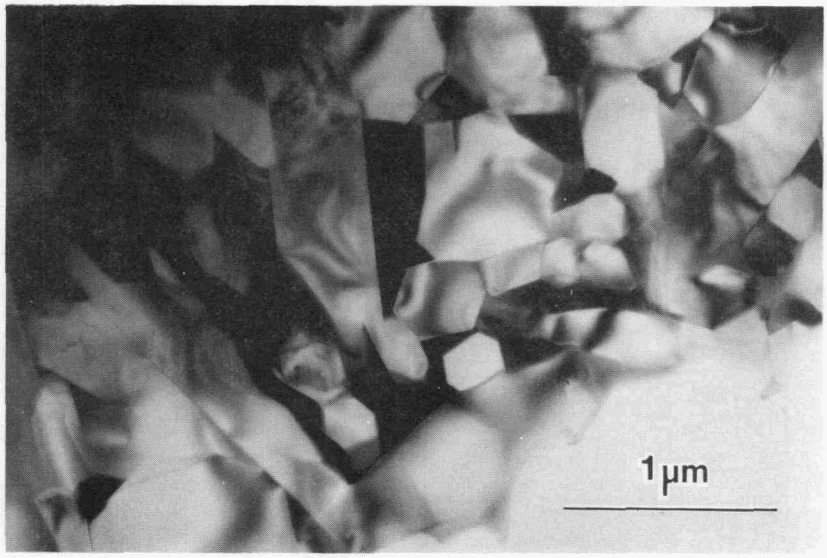

Figure 9. Specimen oriented so that one region of $Y_{10}Al_2Si_3O_{18}N_4$ was on zone and strongly diffracting. Neighboring regions of yttrium-aluminum-silicon oxynitride are seen to have a dark contrast indicating the same orientation as the diffracting region.

Note the hexagonal-shaped grains in both the above micrographs, suggesting that these grains have faceted on {1010} planes. This is confirmed by electron diffraction and lattice fringe imaging. Figure 10 shows a hexagonal-shaped grain with the c-axis normal to the figure.

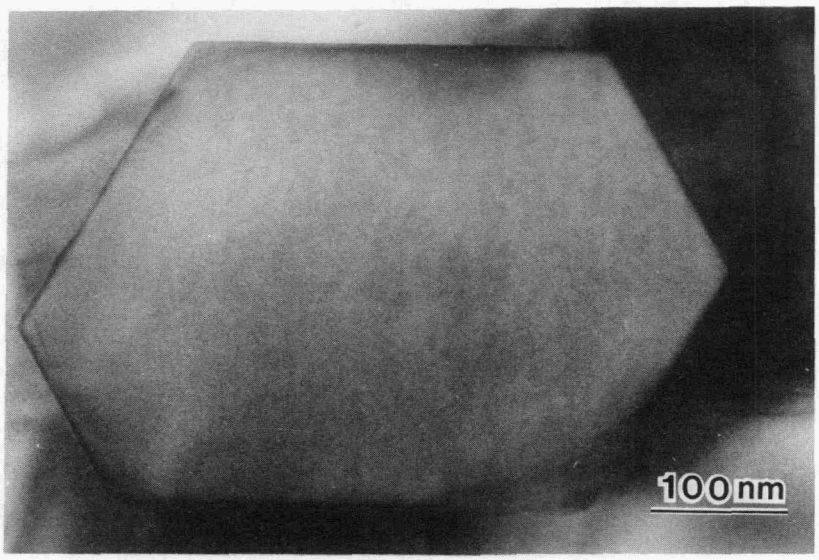

Figure 10. Micrograph of hexagonal-shaped β-Si_3N_4 grain which is faceted on the {1010} planes.

Figure 11 is a higher resolution micrograph of one corner of the grain in Figure 10 indicating that the grain boundaries are lying parallel to 1010 lattice fringes. These fringes are faint because the specimen was thicker than ideal in this region, but they are still visible.

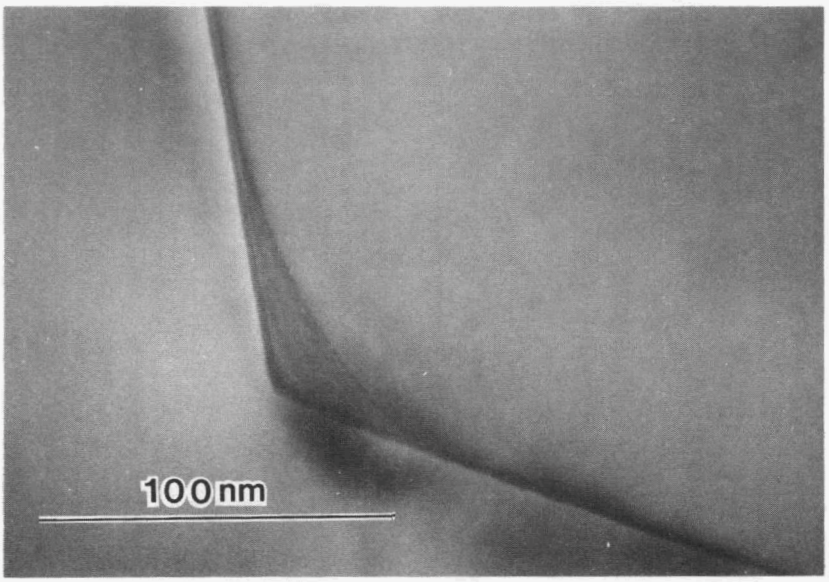

Figure 11. High resolution micrograph of grain shown in Figure 10 showing {1010} lattice fringes which are parallel to the grain boundaries.

In Figure 12 many of the elongated Si_3N_4 grains have been sectioned approximately parallel to the c axis, displaying the needle-shaped morphology of the nitride grains.

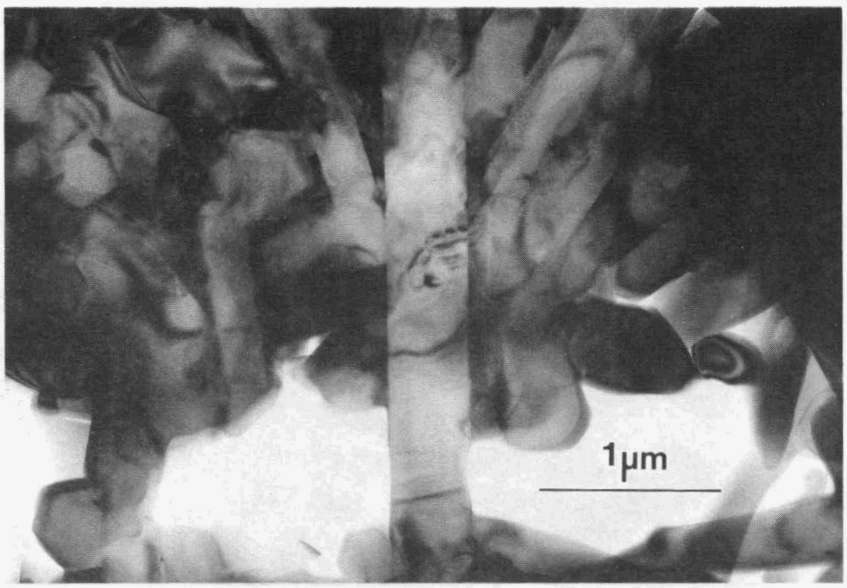

Figure 12. Micrograph showing Si_3N_4 grains elongated parallel to the c axis.

Figure 13 shows a triple junction between two grains of Si_3N_4 (A and C) and a silicate grain (B). The A/B and B/C grain boundaries lie on {1010} silicon nitride planes, suggesting that the silicate was molten at processing temperatures, which are typically about 1750°C for sintered silicon nitride.

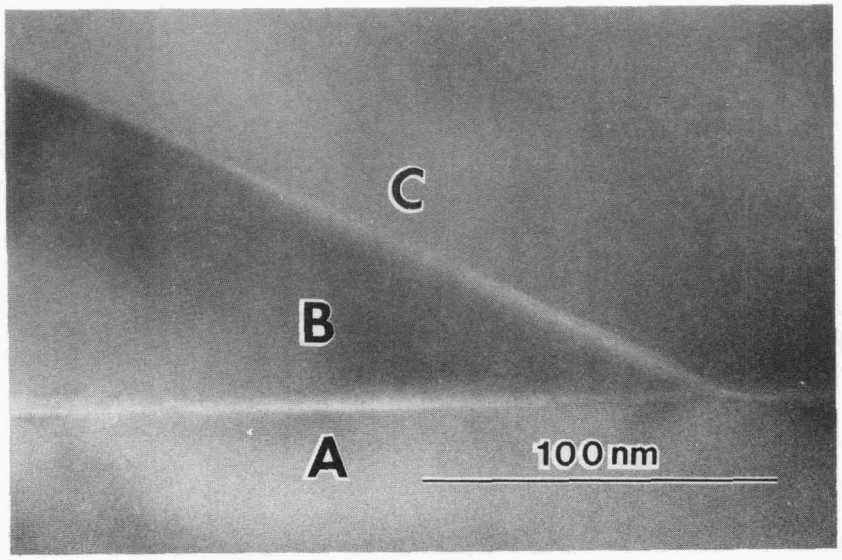

Figure 13. Micrograph showing a triple junction between two grains of Si_3N_4 (A and C) and a silicate grain (B).

High resolution images of selected grain boundaries between silicon nitride grains indicate the presence of a thin amorphous phase. An example is shown in Figure 14 where a boundary parallel to the {1010} plane of one of the grains is wetted by an amorphous phase which is 1.0 - 1.5 nm thick. Insufficient grains were studied to determine the statistics of grain boundary phases.

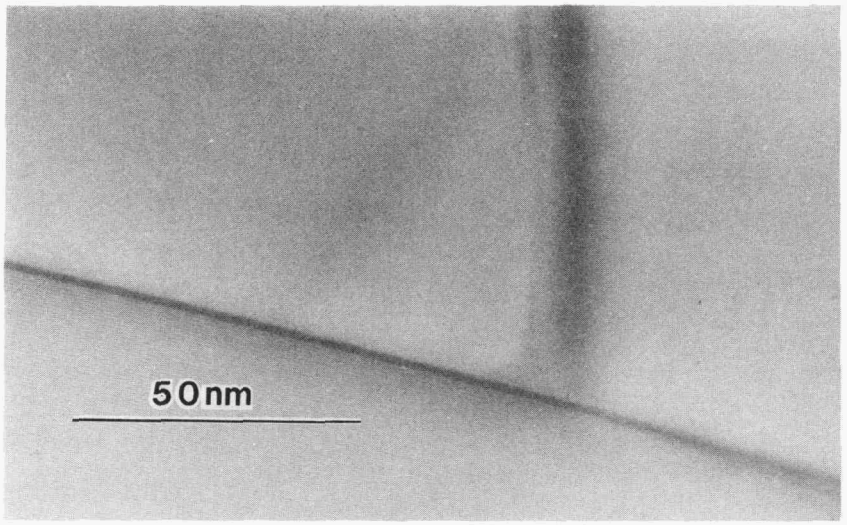

Figure 14. Micrograph of a boundary parallel to the (1010) plane of one grain. The grains are wetted by a 1.0 - 1.5 nm thick amorphous phase.

Status of Milestones

Tasks 1 and 2: ahead of schedule. Electron microscopy observations and X-ray diffraction phase composition analysis of samples were completed to meet IEA requirements for data.

Publications

None

INTERNAL DISTRIBUTION

1-2. Central Research Library
3. Document Reference Section
4-5. Laboratory Records Department
6. Laboratory Records, ORNL RC
7. ORNL Patent Section
8. L. F. Allard, Jr.
9. B. R. Appleton
10. R. L. Beatty
11. P. F. Becher
12. T. M. Besmann
13. P. J. Blau
14. A. Bleier
15. E. E. Bloom
16. K. W. Boling
17-40. R. A. Bradley
41. C. R. Brinkman
42. V. R. Bullington
43. A. J. Caputo
44. R. S. Carlsmith
45. P. T. Carlson
46. J. V. Cathcart
47. G. M. Caton
48. R. H. Cooper
49. S. A. David
50. J. H. DeVan
51. W. P. Eatherly
52. J. I. Federer
53. W. Fulkerson
54. R. L. Graves
55. D. L. Greene
56. M. A. Janney
57-61. D. R. Johnson
62. R. R. Judkins
63. M. A. Karnitz
64. H. D. Kimrey, Jr.
65. T. G. Kollie
66. T. B. Lindemer
67. K. C. Liu
68. E. L. Long, Jr.
69. W. D. Manly
70. D. L. McElroy
71. J. R. Merriman
72. A. J. Moorhead
73. T. A. Nolan
74. J. L. Rich
75. C. R. Richmond
76. J M Robbins
77. M. W. Rosenthal
78. M. L. Santella
79. A. C. Schaffhauser
80. G. M. Slaughter
81. W. B. Snyder, Jr.
82. E. J. Soderstrom
83. D. P. Stinton
84. R. W. Swindeman
85. V. J. Tennery
86-88. P. T. Thornton
89. T. N. Tiegs
90. J. R. Weir, Jr.
91. F. W. Wiffen
92. R. K. Williams
93. S. G. Winslow
94. C. S. Yust

EXTERNAL DISTRIBUTION

95. Donald F. Adams
University of Wyoming
Laramie, WY 82071

96. Jane W. Adams
Corning Glass Works
Corning, NY 14831

97. Donald J. Adrian
High Velocity Corporation
701 Scarboro Road
Oak Ridge, TN 37830

98. Bruce J. Agle
Sundstrand Corporation
Turbomach Division
4400 Ruffin Road
PO Box 85757
San Diego, CA 92138-5757

99. Richard L. Allor
Ford Motor Company
20000 Rotunda Drive
PO Box 2053
Dearborn, MI 48121-2053

100. Richard T. Alpaugh
U.S. Department of Energy
Forrestal Building CE-151
1000 Independence Avenue
Washington, DC 20585

101. H. Arbabi
Brunel University
Uxbridge Middlesex
UNITED KINGDOM UB8 3PH

102. V. S. Avva
North Carolina Agricultural and Technical State University
Greensboro, NC 27411

103. John M. Bailey
Caterpillar Inc.
Technical Center
Post Office Box 1875
Peoria, IL 61656-1875

104. Murray Bailey
NASA Lewis Research Center
21000 Brookpark Road
MS: 77-6
Cleveland, OH 44135

105. R. R. Baker
Ceradyne, Inc.
3169 Red Hill Avenue
Costa Mesa, CA 92626

106. J. Gary Baldoni
GTE Laboratories, Inc.
40 Sylvan Road
Waltham, MA 02254

107. A. L. Bement, Jr.
TRW, Inc.
23555 Euclid Avenue
Cleveland, OH 44117

108. M. Bentele
Xamag, Inc.
259 Melville Avenue
Fairfield, CT 06430

109. Clifton G. Bergeron
University of Illinois
105 South Goodwin Avenue
204 Ceramics Building
Urbana, IL 61801

110. William D. Bjorndahl
TRW, Inc.
One Space Park
Building 01, Room 2060
Redondo Beach, CA 90278

111. James A. Black
American Matrix, Inc.
118 Sherlake Drive
Knoxville, TN 37922

112. Dan Blake
Solar Energy Research Institute
1617 Cole Boulevard
Golden, CO 80401

113. Keith Blandford
Boride Products, Inc.
2879 Aero Park Drive
Traverse City, MI 49684

114. John Blum
Norton Company
High Performance Ceramics
Goddard Road
Northboro, MA 01532-1545

115. Paul N. Blumberg
Integral Technologies Inc.
415 East Plaza Drive
Westmont, IL 60559

116. Wolfgang D. G. Boecker
Standard Oil Engineered Materials Company
Post Office Box 832
Niagara Falls, NY 14302

117. Han Juergen Bossmeyer
BMW Technologies, Inc.
800 South Street
Waltham, MA 02154

118. J.A.M. Boulet
University of Tennessee
310 Perkins Hall
Knoxville, TN 37996

119. S. Bradley
Garrett Ceramic Components Division
19800 S. Van Ness Avenue
Torrance, CA 90509

120. Raymond J. Bratton
Westinghouse Electric Corporation
1310 Beulah Road
Pittsburgh, PA 15235

121. Catherine E. Brown
E. 1. DuPont de Nemours & Company
Wilmington, DE 19898

122. J. J. Brown
Virginia Polytechnic Institute and State University
Blacksburg, VA 24061

123. W. Bryzik
U.S. Army Tank Automotive Command
Warren, MI 48090

124. S. T. Buljan
GTE Laboratories, Inc.
40 Sylvan Road
Waltham, MA 02254

125. John M. Byrne, Jr.
PPG Industries, Inc.
One PPG Place
Pittsburgh, PA 15272

126. Donald J. Campbell
Air Force Wright Aeronautical Laboratory
AFWAL/POX
Wright-Patterson AFB OH 45433

127. Roger Cannon
Rutgers University
Post Office Box 909
Bowser Road
Piscataway, NJ 08855-0909

128. David Carruthers
Allied-Signal Aerospace Company
Garrett Engine Division
111 South 34th Street
Post Office Box 5217
Phoenix, AZ 85010

129. Jere G. Castor
Allied-Signal Aerospace Company
Garrett Engine Company
111 South 34th Street
Post Office Box 5217
Phoenix, AZ 85010

130. Se-Tak Chang
Sundstrand Corporation
Turbomach Division
4400 Ruffin Road
San Diego, CA 92138-5757

131. R. J. Charles
General Electric Company
Post Office Box 8
Schenectady, NY 12301

132. En-sheng Chen
B&C Engineering Research
13906 Dentwood Drive
Houston, TX 77014

133. Albert A. Chesnes
U.S. Department of Energy
Forrestal Building CE-151
1000 Independence Avenue
Washington, DC 20585

134. Frank Childs
EG&G, Inc.
PO Box 1625
Idaho Falls, ID 83415

135. Gilbert Y. Chin
Bell Telephone Laboratories
Murray Hill, NJ 07974

136. Melvin H. Chiogioji
U.S. Department of Energy
Forrestal Building CE-15
1000 Independence Avenue, SW
Washington, DC 20585

137. William J. Chmura
The Torrington Company
59 Field Street
Torrington, CT 06790

138. Eugene V. Clark
Turbine Metal Technology, Inc.
7327 Elmo Street
Tujunga, CA 91042-2204

139. William L. Cleary
ORI, Inc.
1375 Piccard Drive
Rockville, MD 20850

140. Jack L. Clem
J. M. Huber Corporation
PO Box 2831
Borger, TX 79008-2831

141. Philip R. Compton
National Aeronautics and
Space Administration
Washington, DC 20546

142. Harry E. Cook
Chrysler Motors Corporation
1200 Chrysler Drive
Highland Park, MI 48288-1118

143. Stephen Copley
University of
Southern California
Los Angeles, CA 90089-0241

144. John A. Coppola
Standard Oil Engineered
Materials Company
Structural Ceramics Division
PO Box 1054, Bldg 91-2
Niagara Falls, NY 14302

145. Normand D. Corbin
Norton Company
High Performance Ceramics
Goddard Road
Northboro, MA 01532-1545

146. Charles H. Craig
Defense Technology Security
Administration
400 Army-Navy Drive
Suite 300
Arlington, VA 22202

147. William J. Croft
U.S. Army Materials
Technology Laboratory
Arsenal Street
Watertown, MA 02172

148. Gary M. Crosbie
Ford Motor Company
20000 Rotunda Drive
PO Box 2053, Room S-2079
Dearborn, MI 48121-2053

149. Floyd W. Crouse, Jr.
U.S. Department of Energy
PO Box 880
Morgantown, WV 26505

150. Raymond Cutler
Ceramatec, Inc.
163 West 1700 South
Salt Lake City, UT 84115

151. David A. Dalman
The Dow Chemical Company
Midland, MI 48640

152. James I. Dalton
Reynolds Metals Company
Fourth and Canal Streets
PO Box 27003
Richmond, VA 23261

153. Stephen C. Danforth
Rutgers University
Post Office Box 909
Bowser Road
Piscataway, NJ 08854

154. Stanley J. Dapkunas
National Bureau of Standards
Gaithersburg, MD 20899

155. Robert F. Davis
North Carolina State University
232 Riddick Laboratory
Box 7907
Raleigh, NC 27695

156. Evelyn M. DeLiso
Rutgers University
PO Box 909
Bowser Road
Piscataway, NJ 08854

157. Alan L. Dragoo
National Bureau of Standards
Gaithersburg, MD 20899

158. Keith F. Dufrane
Battelle Columbus Laboratories
505 King Avenue
Columbus, OH 43201

159. Edmund M. Dunn
GTE Laboratories Inc.
40 Sylvan Road
Waltham, MA 02254

160. Jeremy D. Dunning
Indiana Memorial Union 662
Indiana University
Bloomington, IN 47405

161. Dr. Sunil Dutta
NASA Lewis Research Center
21000 Brookpark Road
MS: 49-3
Cleveland, OH 44135

162. Paul N. Dyer
Air Products and Chemicals, Inc.
PO Box 538
Allentown, PA 18105

163. Robert J. Eagan
Sandia National Laboratories
Department 1840
PO Box 5800
Albuquerque, NM 87185

164. Christopher A. Ebel
Norton Company
High Performance Ceramics
Goddard Road
Northboro, MA 01532-1545

165. J. J. Eberhardt
U.S. Department of Energy
Forrestal Building CE-12
1000 Independence Avenue, SW
Washington, DC 20585

166. E. E. Ecklund
U.S. Department of Energy
Forrestal Building CE-151
1000 Independence Avenue
Washington, DC 20585

167. William A. Ellingson
Argonne National Laboratory
9700 South Cass Avenue
Argonne, IL 60439

168. Graydon A. Elliott
U.S. Army Research and
Technology Laboratory
(AVSCOM)
Fort Eustis, VA 23604

169. A. Erdely
26 Av. Gore des Eaux-Vives
1208 Geneva
SWITZERLAND

170. Charles D. Estes
U.S. Senate
Washington, DC 20510

171. Peggy Evanich
National Aeronautics and
Space Administration
Washington, DC 20546

172. Anthony G. Evans
University of California
Santa Barbara, CA 93106

173. Robert C. Evans
NASA Lewis Research Center
21000 Brookpark Road
MS: 77-6
Cleveland, OH 44135

174. Katherine T. Faber
Ohio State University
2041 College Road
Columbus, OH 43210

175. John W. Fairbanks
U.S. Department of Energy
Forrestal Building CE-151
1000 Independence Avenue
Washington, DC 20585

176. Larry Farrell
Babcock and Wilcox
Old Forrest Road
Lynchburg, VA 24505

177. H. W. Foglesong
Dow Corning Corporation
3901 South Saginaw Road
Midland, MI 48686

178. Thomas F. Foltz
Avco Corporation
Two Industrial Avenue
Lowell, MA 01851

179. Robert G. Frank
Technology Assessment Group
10793 Bentley Pass Lane
Cincinnati, OH 45140

180. Douglas W. Freitag
LTV Aerospace and Defense
Company
PO Box 225907
MS: TH-85
Dallas, TX 75265

181. George E. Gazza
U.S. Army Materials
Technology Laboratory
405 Arsenal Street
Watertown, MA 02172

182. Charles M. Gilmore
The George Washington
University
Washington, DC 20052

183. Paul Glance
Concept Analysis
950 Stephenson Highway
Troy, MI 48007-7013

184. Fred M. Glaser
U.S. Department of Energy
Washington, DC 20545

185. Joseph W. Glatz
Naval Air Propulsion
Test Center
Box 7176, PE 34
Trenton, NJ 08628

186. W. M. Goldberger
Superior Graphite Company
2175 East Broad Street
Columbus, OH 43209

187. Stephen T. Gonczy
Allied Signal Research Center
50 UOP Plaza
Des Plaines, IL 60016-6187

188. Robert J. Gottschall
U.S. Department of Energy
MS: G-256
Washington, DC 20545

189. Dr. Earl Graham
Cleveland State University
Uclid Ave East 24th Street
Cleveland, OH 44115

190. Kenneth Green
Coors Ceramics Company
17750 West 32nd Street
Golden, CO 80401

191. Robert E. Green, Jr.
Center for Nondestructive
Evaluation
Maryland Hall 107
The Johns Hopkins University
Baltimore, MD 21218

192. Lance E. Groseclose
General Motors Corporation
PO Box 420
Indianapolis, IN 46206-0420

193. T. D. Gulden
GA Technologies, Inc.
PO Box 81608
San Diego, CA 92138

194. P. Ulf Gummeson
Hoeganaes
River Road and Taylors Lane
Riverton, NJ 08077

195. Bimleshwar P. Gupta
Solar Heat Research Division
Solar Energy Research Institute
1617 Cole Boulevard
Golden, CO 80401

196. M. D. Gurney
NIPER
PO Box 2128
Bartlesville, OK 74005

197. John P. Gyekenyesi
NASA Lewis Research Center
21000 Brookpark Road
Cleveland, OH 44135

198. J. J. Habeeb
Esso Petroleum Canada
PO Box 3022
Sarina, Ontario
CANADA N7T 7MI

199. Pennsylvania State University
227 Hammond Building
University Park, PA 16802

200. Nabil S. Hakim
General Motors Corporation
36880 Ecorse Road
Romulus, MI 48174

201. John W. Halloran
Ceramic Process Systems
840 Memorial Drive
Cambridge, MA 02139-3758

202. Kay Hardman-Rhyne
DARPA
1400 Wilson Boulevard
Arlington, VA 22209

203. R. A. Harmon
25 Schalren Drive
Latham, NY 12110

204. Stephen D. Hartline
Norton Company
High Performance Ceramics
Goddard Road
Northboro, MA 01532-1545

205. Willard E. Hauth
Dow Corning Corporation
3901 South Siginaw Road
Midland, MI 48640

206. Kevin L. Haynes
McDonnell Douglas
Astronautics Company
Box 516 E456/HQ/3N/MS329
Saint Louis, MO 63166

207. Norman L. Hecht
University of Dayton
Research Institute
300 College Park
Dayton, OH 45469-0001

208. S. S. Hecker
Los Alamos National
Laboratory
PO Box 1663
Los Alamos, NM 87545

209. Peter W. Heitman
General Motors Corporation
PO Box 420, W-5
Indianapolis, IN 46206-0420

210. Richard L. Helferich
The Duriron Company,
Incorporated
PO Box 1145
Dayton, OH 45401

211. H. E. Helms
General Motors Corporation
PO Box 420
Indianapolis, IN 46206-0420

212. Thomas L. Henson
GTE Products Corporation
Hawes Street
Towanda, PA 18848-0504

213. Thomas P. Herbell
NASA Lewis Research Center
21000 Brookpark Road
MS: 49-3
Cleveland, OH 44135

214. Hendrik Heystek
Bureau of Mines
Tuscaloosa Research Center
PO Box L
University, AL 35486

215. Robert V. Hillery
General Electric Company
One Neumann Way
PO Box 156301
Cincinnati, OH 45215

216. Jonathan W. Hinton
Standard Oil Engineered
Materials Company
Structural Ceramics Division
PO Box 1054
Niagara Falls, NY 14302

217. George Hsu
Jet Propulsion Laboratory
4800 Oak Grove Drive
MS: 512-103
Pasadena, CA 91109

218. Stephen M. Hsu
National Bureau of Standards
Gaithersburg, MD 20899

219. Harold A. Huckins
Princeton Advanced
Technology, Inc.
56 Finley Road
Princeton, NJ 08540

220. Fred Huettic
Advanced Ceramic
Technology, Inc.
17 Deerfield Road
East Brunswick, NJ 08816

221. O. Richard Hughes
Celanese Research Company
86 Morris Avenue
Summit, NJ 07901

222. Joseph E. Hunter, Jr.
General Motors Corporation
12 Mile and Mound Roads
Warren, MI 48090-9055

223. Louis C. Ianniello
U.S. Department of Energy
Washington, DC 20545

224. Robert H. Insley
Champion Spark Plug Company
20000 Conner Avenue
Detroit, MI 48234

225. D. M. Jacques
Norton Company
HPC Library
Goddard Road
Northboro, MA 01532-1545

226. Curt A. Johnson
General Electric Company
PO Box 8
Schenectady, NY 12301

227. Douglas C. Johnson
Sundstrand Corporation
4400 Ruffin Road
PO Box 85757
San Diego, CA 92138-5757

228. Larry Johnson
Argonne National Laboratory
9700 South Cass Avenue
Bldg 362
Argonne, IL 60439

229. R. A. Johnson
General Motors Corporation
PO Box 420
Indianapolis, IN 46206-0420

230. L. A. Joo
Great Lakes Research
Corporation
Post Office Box 1031
Elizabethton, TN 37643

231. A. David Joseph
Sealed Power Corporation
100 Terrace Plaza
Muskegon, MI 49443

232. Roy Kamo
Adiabatics, Inc.
630 South Mapleton
Columbus, IN 47201

233. K. Karasek
Garrett Ceramic Components Division
19800 S. Van Ness Avenue
Torrance, CA 90509

234. Allan Katz
Air Force Wright Aeronautical Laboratory
Materials Laboratory, AFWAL/MLLM
Wright-Patterson AFB, OH 45433

235. R. N. Katz
U.S. Army Materials Technology Laboratory
405 Arsenal Street
Watertown, MA 02172

236. Mr. Kawaguchi
Tokai Carbon
375 Park Avenue
Suite 3802
New York, NY 10152

237. P. Victor Kelsey
Aluminum Company of America
Alcoa Technical Center B
Alcoa Center, PA 15061

238. Frederick L. Kennard, III
General Motors Corporation
1300 North Dort Highway
Flint, MI 48556

239. J. R. Kidwell
Allied-Signal Aerospace Company
Garrett Engine Division
111 South 34th Street
Post Office Box 5217
Phoenix, AZ 85010

240. Max Klein
Gas Research Institute
8600 West Bryn Mawr Avenue
Chicago, IL 60631

241. C. E. Knapp
Norton Company
8001 Daly Street
Niagara Falls, Ontario
CANADA

242. A. S. Kobayashi
University of Washington
Seattle, WA 98195

243. David M. Kotchick
AiResearch Manufacturing Company
2525 West 190th Street
Torrance, CA 90509

244. Bruce Kramer
George Washington University
Washington, DC 20052

245. Saunders B. Kramer
U.S. Department of Energy
Forrestal Building CE-151
1000 Independence Avenue
Washington, DC 20585

246. D. M. Kreiner
Allied-Signal Aerospace Company
Garrett Engine Division
111 South 34th Street
PO Box 5217
Phoenix, AZ 85010

247. Pieter Krijgsman
Ceramic Design Int. Hold., Ltd.
PO Box 68
8050 AB Hattem
THE NETHERLANDS

248. W. J. Lackey
Georgia Tech Research Institute
Atlanta, GA 30332

249. Everett A. Lake
Air Force Wright
Aeronautical Laboratory
AFWAL/POOS
Wright-Patterson AFB
OH 45433

250. Hari S. Lamba
General Motors Corporation
Electro-Motive Division
LaGrange, IL 60525

251. James Lankford
Southwest Research Institute
6220 Culebra Road
PO Drawer 28510
San Antonio, TX 78284

252. John G. Lanning
Corning Glass Works
Corning, NY 14831

253. David C. Larsen
Corning Glass Works
Sullivan Park, FR-51
Corning, NY 14831

254. Dr. S. K. Lau
Standard Oil Engineered
Materials Company
Technology Division
Box 832
Niagara Falls, NY 14302

255. Harry A. Lawler
Standard Oil Engineered
Materials Company
Structural Ceramics Division
PO Box 1054, Bldg 91-2
Niagara Falls, NY 14302

256. Alan Lawley
Drexel University
Philadelphia, PA 19104

257. Daniel Lee Temescon
2850 7th Street
Berkeley, CA 94710

258. June-Gunn Lee
Korea Advanced Institute of
Science and Technology
PO Box 131
Dong Dac Mun, Seoul
KOREA

259. E. M. Lenoe
Air Force Office of
Scientific Research
APO San Francisco
CA 96503-0110

260. Stanley R. Levine
NASA Lewis Research Center
21000 Brookpark Road
Cleveland, OH 44135

261. David Lewis
Naval Research Laboratory
4555 Overlook Avenue, SW
Washington, DC 20375

262. Winston W. Liang
AMERCOM, Inc.
8948 Fullbright Avenue
Chatsworth, CA 91311

263. Bill Long
Babcock and Wilcox
PO Box 1260
Lynchburg, VA 24505

264. L. A. Lott
EG&G, Inc.
PO Box 1625
Idaho Falls, ID 83415

265. Bryan K. Luftglass
Chem Systems, Inc.
303 South Broadway
Tarrytown, NY 10591

266. Robert Lundberg
Svenska Silikatforsknings-
institutet
Swedish Institute for
Silicate Research
Box 5403
S-402 29 Gothenburg
SWEDEN

267. Michael J. Lynch
General Electric Company
PO Box 414, 7B-36
Milwaukee, WI 53201

268. James W. MacBeth
Standard Oil Engineered
Materials Company
Structural Ceramics Division
Box 1054
Niagara Falls, NY 14302

269. Vincent L. Magnotta
Air Products and Chemicals, Inc.
PO Box 538
Allentown, PA 18105

270. Tai-il Mah
Universal Energy Systems
4401 Dayton-Xenia Road
Dayton, OH 45432

271. L. Manes
Commission of the European
Communities
Ispra Establishment
1-21020 Ispra (Varese)
ITALY

272. Gerald R. Martin
Fleetguard, Inc.
Cookeville, TN 38501

273. Dr. John L. Mason
Allied-Signal Aerospace Company
AiResearch Los Angeles Division
2525 West 190th Street
Torrance, CA 90509

274. J. McCauley
U.S. Army Materials Technology
Laboratory
DRXMR-MC
Arsenal Street
Watertown, MA 02172-0001

275. Bryan J. McEntire
Norton Company
TRW Ceramics
Goddard Road
Northboro, MA 01532-1545

276. Thomas D. McGee
Iowa State University
Ames, IA 50011

277. H. Christopher McGowan
Advanced Ceramic
Technology, Inc.
17 Deerfield Road
East Brunswick, NJ 08816

278. Malcolm G. McLaren
Rutgers University
PO Box 909
Bowser Road
Piscataway, NJ 08854

279. Arthur F. McLean
6225 N Camino Almonte
Tucson, AZ 85718

280. Brian L. Mehosky
Standard Oil Engineered
Materials Company
4440 Warrensville Center Road
Cleveland, OH 44128

281. P. K. Mehrotra
Kennametal, Inc.
PO Box 639
Greensburg, PA 15601

282. Joseph J. Meindl
Reynolds International, Inc.
PO Box 27002
6603 West Broad Street
Richmond, VA 23261

283. D. Messier
U.S. Army Materials
Technology Laboratory
DRXMR-MC
Arsenal Street
Watertown, MA 02172

284. Arthur G. Metcalfe
Solar Turbines, Inc.
2200 Pacific Highway
PO Box 80966
San Diego, CA 92138

285. Thomas N. Meyer
Aluminum Company of America
Alcoa Technical Center
Alcoa Center, PA 15069

286. W. Miloscia
Standard Oil Engineered
Materials Company
4440 Warrensville Center Road
Cleveland, OH 44128

287. Bill Moehle
Ethyl Corporation
451 Florida Avenue
Ethyl Tower
Baton Rouge, LA 70801

288. Helen Moeller
Babcock and Wilcox
PO Box 11165
Lynchburg, VA 24506-1165

289. Frederick E. Moreno
Turbo Energy Systems, Inc.
350 Second Street, Suite 5
Los Altos, CA 94022

290. Peter E. D. Morgan
Rockwell International
1049 Camino Dos Rios
PO Box 1085
Thousand Oaks, CA 91360

291. Lawrence M. Murphy
Thermal Systems Research
Branch
Solar Energy Research
Institute
1617 Cole Boulevard
Golden, CO 80401

292. Solomon Musikant
General Electric Company
PO Box 8555
MS: U-1219
Philadelphia, PA 19101

293. Pero Nannelli
Pennwalt Corporation
900 First Avenue
PO Box C
King of Prussia, PA 19406-0018

294. Robert M. Neilson, Jr.
EG&G Idaho, Inc.
PO Box 1625
Idaho Falls, ID 83415

295. William D. Nix
Stanford University
Stanford, CA 94305

296. Richard D. Nixdorf
American Matrix, Inc.
118 Sherlake Drive
Knoxville, TN 37922

297. Brian M. O'Connor
The Lubrizol Corporation
29400 Lakeland Boulevard
Wickliffe, OH 44092

298. W. Richard Ott
Alfred University
Alfred, NY 14802

299. Muktesh Paliwal
GTE Products Corporation
Hawes Street
Towanda, PA 18848-0504

300. Hayne Palmour III
North Carolina State
University
2158 Burlington Engineering
Laboratories
PO Box 5995
Raleigh, NC 27607

301. Joseph N. Panzarino
Norton Company
Goddard Road
Northboro, MA 01532-1545

302. Pellegrino Papa
Corning Glass Works
Corning, NY 14831

303. James G. Paschal
Reynolds Metals Company
PO Box 76154
Atlanta, GA 30358

304. Arvid E. Pasto
GTE Laboratories, Inc.
40 Sylvan Road
Waltham, MA 02254

305. Donald O. Patten
Norton Company
High Performance Ceramics
Goddard Road
Northboro, MA 01532-1545

306. James W. Patten
Cummins Engine Company, Inc.
Box 3005, Mail Code 50183
Columbus, IN 47202-3005

307. Timothy M. Pattison
Textron Lycoming
MS: LSM1
550 Main Street
Stratford, CT 06497

308. Robert A. Penty
Eastman Kodak Company
901 Elmgrove Road
Rochester, NY 14650

309. Gary R. Peterson
U.S. Department of Energy
785 DOE Place
Idaho Falls, ID 83402

310. R. Byron Pipes
University of Delaware
2001 Spencer Laboratory
Newark, DE 19716

311. Robert C. Pohanka
Office of Naval Research
800 North Quincy St, Code 431
Arlington, VA 22217

312. Stephen C. Pred
ICD Group, Inc.
1100 Valley Brook Avenue
Lyndhurst, NJ 07071

313. Karl M. Prewo
United Technologies
Corporation
Silver Lane, MS: 24
East Hartford, CT 06108

314. Hubert B. Probst
NASA Lewis Research Center
21000 Brookpark Road
Cleveland, OH 44135

315. Carr Lane Quackenbush
Norton Company
High Performance Ceramics
Goddard Road
Northboro, MA 01532-1545

316. Brian Quigy
National Aeronautics and
Space Administration
Washington, DC 20546

317. George Quinn
U.S. Army Materials
Technology Laboratory
Arsenal Street
Watertown, MA 02172

318. Dennis T. Quinto
Kennametal, Inc.
PO Box 639
Greensburg, PA 15601

319. S. Venkat Raman
Air Products and
Chemicals, Inc.
PO Box 538
Allentown, PA 18105

320. Dennis Readey
Ohio State University
2041 College Road
Columbus, OH 43210

321. Robert R. Reeber
U.S. Army Research Office
PO Box 12211
Research Triangle Park,
NC 27709

322. K. L. Reifsnider
Virginia Polytechnic Institute
and State University
Blacksburg, VA 24061

323. Paul Rempes
Williams International
2280 West Maple
MS: 6-5
Walled Lake, MI 48088

324. T. M. Resetar
U.S. Army Materials
Technology Laboratory
DAXMA-MC
Arsenal Street
Watertown, MA 02172

325. K. T. Rhee
Rutgers University
PO Box 909
Bowser Road
Piscataway, NJ 08854

326. Roy W. Rice
W. R. Grace and Company
7379 Route 32
Columbus, MD 21044

327. David W. Richerson
Ceramatec, Inc.
163 West 1700 South
Salt Lake City, UT 84115

328. Paul Rieth
Ferro Corporation
661 Willet Road
Buffalo, NY 14218-9990

329. Michael A. Rigdon
Institute for Defense Analyses
1801 Beauregard Street
Alexandria, VA 22311

330. John E. Ritter, Jr.
University of Massachusetts
Amherst, MA 01003

331. Giulio A. Rossi
Norton Company
High Performance Ceramics
Goddard Road
Northboro, MA 01532-1545

332. Barry R. Rossing
Lanxide Corporation
Tralee Industrial Park
Newark, DE 19711

333. David J. Rowcliffe
SRI International
333 Ravenswood Avenue
Menlo Park, CA 94025

334. Donald W. Roy
Coors Ceramics Company
17750 West 32nd Street
Golden, CO 80401

335. Bruce Rubinger
Gobal
50 Milk Street, 15th Floor
Boston, MA 02109

336. Robert Ruh
Air Force Wright
Aeronautical Laboratory
Materials Laboratory
AFWAL/M LLM
Wright-Patterson AFB
OH 45433

337. Robert J. Russell, Sr.
Norton Company
High Performance Ceramics
Goddard Road
Northboro, MA 01532-1545

338. George P. Safol
Westinghouse Electric
Corporation
Pittsburgh, PA 15235

339. J. Sankar
North Carolina Agricultural
and Technical State
University
Greensboro, NC 27411

340. Maxine L. Savitz
Garrett Processing Company
Ceramic Components Division
19800 South Van Ness Avenue
Torrance, CA 90509

341. Richard Schapery
Texas A&M University
College Station, TX 77843

342. J. L. Schienle
Allied-Signal Aerospace Company
Garrett Auxiliary Power Division
2739 East Washington Street
PO Box 5227
Phoenix, AZ 85010

343. Liselotte J. Schioler
Aerojet Tech Systems Company
PO Box 13222
Dept. 9990, Bldg. 2019-A2
Sacramento, CA 95813

344. Richard A. Schmidt
Battelle Columbus Laboratories
505 King Avenue
Columbus, OH, 43201-2693

345. Arnie Schneck
Deere and Company Technical Center
PO Box 128
Wood-Ridge, NJ 07075

346. Matthew Schreiner
Gas Research Institute
8600 West Bryn Mawr Avenue
Chicago, IL 60631

347. John Schuldies
Industrial Ceramic Technology, Inc.
37 Enterprise Drive
Ann Arbor, MI 48103

348-359. R. B. Schulz
U.S. Department of Energy
Forrestal Building CE-151
1000 Independence Avenue
Washington, DC 20585

360. Wesley J.C. Shuster
Thermo Electron Corporation
115 Eames Street
PO Box 340
Wilmington, MA 01887

361. Murray A. Schwartz
Bureau of Mines
2401 Eye Street, N.W.
Washington, DC 20241

362. Douglas B. Schwarz
The Dow Chemical Company
52 Building
Midland, MI 48674

363. Thomas M. Sebestyen
U.S. Army Tank Automotive Command
AMSTA-RGRT
Warren, MI 48397-5000

364. Brian Seegmiller
Coors Ceramics Company
17750 West 32nd Street
Golden, CO 80401

365. S. G. Seshadri
Standard Oil Engineered Materials Company
PO Box 832
Niagara Falls, NY 14302

366. Peter T. B. Shaffer
Advanced Refractory Technologies, Inc.
699 Hertel Avenue
Buffalo, NY 14207

367. Maurice E. Shank
United Technologies Corporation
East Hartford, CT 06108

368. Laurel M. Sheppard
Advanced Materials and Processes
Route 87
Metals Park, OH 44073

369. Dinesh K. Shetty
The University of Utah
Salt Lake City, UT 84112

370. Jack D. Sibold
Coors Ceramics Company
17750 West 32nd Street
Golden, CO 80401

371. Neal Sigmon
U.S. House of Representatives
Rayburn Building, Room B308
Washington, DC 20515

372. Richard Silberglitt
Quest Research Corporation
1651 Old Meadow Road
McLean, VA 22102

373. Maurice J. Sinnott
University of Michigan
438 West Engineering Building
Ann Arbor, MI 48109-2136

374. S. R. Skaggs
Los Alamos National Laboratory
PO Box 1663
Los Alamos, NM 87545

375. J. Thomas Smith
GTE Laboratories, Inc.
40 Sylvan Road
Waltham, MA 02254

376. Jay R. Smyth
Allied-Signal Aerospace Company
Garrett Auxiliary Power Division
2739 East Washington Street
PO Box 5227
MS: 93-172/1302-2K
Phoenix, AZ 85010

377. Rafal Sobotowski
Standard Oil Engineered Materials Company
3092 Broadway Avenue
Cleveland, OH 44115

378. Thomas M. Sopko
Lubrizol Enterprises, Inc.
29400 Lakeland Boulevard
Wickliffe, OH 44092

379. Boyd W. Sorenson
Du Pont Company
Experimental Stat, Bldg 304
Wilmington, DE 19898

380. Dr. Richard M. Spriggs
Center for Advanced Ceramic Technology
New York State College of Ceramics at Alfred University
Alfred, NY 14802

381. M. Srinivasan
Standard Oil Engineered Materials Company
PO Box 832
Niagara Falls, NY 14302

382. Gordon L. Starr
Cummins Engine Company, Inc.
Box 3005, Mail Code 50183
Columbus, IN 47202-3005

383. Harold L. Stocker
General Motors Corporation
PO Box 420, T-23
Indinapolis, IN 46206-0420

384. Paul D. Stone
The Dow Chemical Company
1801 Building
Midland, MI 48674

385. Roger Storm
Standard Oil Engineered Materials Company
PO Box 832
Niagara Falls, NY 14302

386. E. E. Strain
Allied-Signal Aerospace Company
Garrett Engine Division
111 South 34th Street
PO Box 5217
MS: 301-2N
Phoenix, AZ 85010

387. Thomas N. Strom
NASA Lewis Research Center
21000 Brookpark Road, 77-6
Cleveland, OH 44135

388. Jerry Strong
Albright & Wilson
PO Box 26229
Richmond, VA 23260

389. Richard Suddeth
Boeing Motor Airplane Company
PO Box 7730
MS: K-76-67
Wichita, KS 67277

390. Paul Sutor
Midwest Research Institute
425 Volker Boulevard
Kansas City, MO 64116

391. J. J. Swab
U.S. Army Materials
Technology Laboratory
405 Arsenal Street
Watertown, MA 02172

392. John W. Swain, Jr.
Kollmorgen Corporation
PCK Technology Division
15424 Garrison Lane
Southgate, MI 48915

393. Lewis Swank
Ford Motor Company
20000 Rotunda Drive
PO Box 2053
Building SRL, Room S2023
Dearborn, MI 48121-2053

394. Stephen R. Tan
ICI Advanced Materials
PO Box 11
The Heath, Runcorn
Cheshire
ENGLAND WA7 4QE

395. Anthony C. Taylor
U.S. House of Representatives
Rayburn Building, Room 2321
Washington, DC 20515

396. W. H. Thielbahr
U.S. Department of Energy
550 2nd Street
Idaho Falls, ID 83401

397. John K. Tien
Columbia University
1137 S.W. Mudd Building
New York, NY 10027

398. T. Y. Tien
University of Michigan
Dow Building
Ann Arbor, MI 48109-2136

399. Julian M. Tishkoff
Air Force Office of
Scientific Research
(AFOSR/WC) Bolling AFB
Washington, DC 20332

400. Louis E. Toth
National Science Foundation
1800 G Street, N.W.
Washington, DC 20550

401. Richard E. Tressler
Pennsylvania State University
201 Steidle Building
University Park, PA 16802

402. Donald R. Uhlmann
Massachusetts Institute
of Technology
77 Massachusetts Avenue
Cambridge, MA 02139

403. Edward C. Van Reuth
Technology Strategies, Inc.
10722 Shingle Oak Court
Burke, VA 22015

404. Thomas Vasilos
Avco Corporation
201 Towell Street
Wilmington, MA 01887

405. V. Venkateswaran
Standard Oil Engineered
Materials Company
PO Box 832
Niagara Falls, NY 14302

406. John B. Wachtman, Jr.
Rutgers University
PO Box 909
Bowser Road
Piscataway, NJ 08854

407. Richard B. Wallace
General Motors Corporation
36880 Ecorse Road
Romulus, MI 48174

408. Harlan L. Watson
U.S. House of Representatives
Rayburn Building, Suite 2321
Washington, DC 20515

409. John D. Watson
BHP Research & New Technology
Melbourne Research Laboratories
245 Wellington Road
Mulgrave, Vic. 3170
AUSTRALIA

410. Albert R. C. Westwood
Martin Marietta Laboratories
1450 South Rolling Road
Baltimore, MD 21227

411. Thomas J. Whalen
Ford Motor Company
20000 Rotunda Drive
PO Box 2053
Dearborn, MI 48121-2053

412. Sheldon M. Wiederhorn
National Bureau of Standards
Gaithersburg, MD 20899

413. James C. Williams
Carnegie-Mellon University
Schenley Park
Pittsburgh, PA 15213

414. Roger R. Wills
TRW, Inc.
Valve Division
1455 East 185th Street
Cleveland, OH 44110

415. J. M. Wimmer
Allied-Signal Aerospace Company
Garrett Engine Division
111 South 34th Street
Post Office Box 5217
Phoenix, AZ 85010

416. David Wirth
Coors Ceramics Company
17750 West 32nd Street
Golden, CO 80401

417. Thomas J. Wissing
Eaton Corporation
26201 Northwestern Highway
Post Office Box 766
Southfield, MI 48037

418. Dale Wittmer
Southern Illinois University at Carbondale
Department of Mechanical Engineering and Energy Processes
Carbondale, IL 62901

419. George W. Wolter
Howmet Turbine Components Corporation
699 Benston Road
Whitehall, MI 49461

420. James C. Wood
NASA Lewis Research Center
21000 Brookpark Road
MS: 500-210
Cleveland, OH 44135

421. Roger P. Worthen
Eaton Corporation
26201 Northwestern Highway
PO Box 766
Southfield, MI 48076

422. Hun C. Yeh
Garrett Processing Company
Ceramic Components Division
19800 Van Ness Avenue
Torrance, CA 90509

423. Thomas M. Yonushonis
Cummins Engine Company, Inc.
Box 3005, Mail Code 50183
Columbus, IN 47202-3005

424. Don Zabierek
Air Force Wright
Aeronautical Laboratory
AFWAL/POTC
Wright-Patterson AFB
OH 45433

425. Charles Zeh
U.S. Department of Energy
PO Box 880
Morgantown, WV 26505

426. Anne Marie Zerega
U.S. Department of Energy
Forrestal Building CE-15
1000 Independence Avenue
Washington, DC 20585

427. Martin Zlotnick
Nichols Research Corporation
8618 Westwood Center Dr.
Suite 200
Vienna, VA 22180-2222

428. Klaus M. Zwilsky
National Research Council
2101 Constitution Avenue
Washington, DC 20418

429. Department of Energy
Oak Ridge Operations Office
Assistant Manager for Energy
Research and Development
P.O. Box 2001
Oak Ridge, TN 37831

430-439. Department of Energy
Office of Scientific and
Technical Information
Office of Information Service
P.O. Box 62
Oak Ridge, TN 37831

For distribution by microfiche
as shown in DOE/TIC-4500,
Distribution Category UC-95.

☆ U.S. GOVERNMENT PRINTING OFFICE 1988—648-119/80154